Perspectives in Molecular Sieve Science

William H. Flank, EDITOR
Union Carbide Corporation

Thaddeus E. Whyte, Jr., EDITOR
The PQ Corporation

ACS Symposium Series

M. Joan Comstock, *Series Editor*

1988 ACS Books Advisory Board

Foreword

The ACS SYMPOSIUM SERIES was founded in 1974 to provide a
medium for publishing symposia quickly in book form. The
format of the Series parallels that of the continuing ADVANCES
IN CHEMISTRY SERIES except that, in order to save time, the
papers are not typeset but are reproduced as they are submitted
by the authors in camera-ready form. Papers are reviewed under
the supervision of the Editors with the assistance of the Series
Advisory Board and are selected to maintain the integrity of the
symposia; however, verbatim reproductions of previously pub-
lished papers are not accepted. Both reviews and reports of
research are acceptable, because symposia may embrace both
types of presentation.

Preface

THIS STATE-OF-THE-ART book began with some exploratory discussions we had almost three years ago at an executive committee meeting of the Division of Industrial and Engineering Chemistry, Inc., of the American Chemical Society. It gathered support from discussions with people in the Divisions of Petroleum Chemistry, Inc., and Fuel Chemistry, and emerged as a fleshed-out proposal after several brainstorming sessions face-to-face and over the phone. The result, *Perspectives in Molecular Sieve Science*, provides much satisfaction to us as editors.

A unique aspect in which we take some pride is the arrangement with the Books Department of the American Chemical Society to have this book published in time for the meeting at which the symposium sessions will be held. This was made possible by the cooperation of our authors and reviewers, who met the necessary deadlines, as well as some fancy footwork by the editors.

The timing we chose for this book, coming between meetings of the International Zeolite Association during a period of high research activity, has resulted in comprehensive coverage and high quality. We have included a number of reviews that provide some background and introduction to the field of molecular sieves and related materials for those who have entered the field recently. At the same time, significant new work in a number of areas is reported to keep those with experience abreast of new developments and to stimulate discussions which we hope will lead to further progress.

A lot of work went into putting this book and the symposium together as coherent packages. We acknowledge the important contributions of John-Pierre Gilson of Shell Research B.V., who compiled comprehensive lists of reviewers for the draft manuscripts, and of V. Udaya S. Rao of the U.S. Department of Energy, who organized the scheduling details for the symposium program. We were especially pleased to have George T. Kerr write an introduction to the book. We also thank Lillian De Lello and Charlotte Reynolds for their extra effort in helping to make it all

xi

happen. Organizing this book has been a rewarding, if sometimes hectic, experience for us, and we hope our audience will be satisfied with the results.

WILLIAM H. FLANK
Molecular Sieve Department
Union Carbide Corporation
Tarrytown, NY 10591

THADDEUS E. WHYTE, JR.
The PQ Corporation
Lafayette Hill, PA 19444

February 2, 1988

Introduction

by George T. Kerr

Past President, International Zeolite Association

A Brief History

THE TERM "MOLECULAR SIEVE" WAS PROPOSED in 1932 by J. W. McBain to describe the selective adsorption of molecules of relatively small size over molecules of larger size by chabazite, a mineral zeolite, which had been purged free of adsorbed water. At that time, zeolite science or molecular sieve science was rudimentary at best, and zeolite technology was nonexistent. Starting about 1940, R. M. Barrer published a number of papers on the synthesis and adsorptive properties of zeolites, some of which had neither structural nor naturally occurring (mineral) counterparts. Barrer's work attracted the attention of researchers at Union Carbide's Linde Division, who initiated a program in 1949 on the synthesis of zeolites because they hoped to use the selective sorptive or molecular sieve properties of zeolites for the fractionation of air. Fractional distillation of liquid air was a longstanding commercial activity of the Linde Division. About the same time, many coals were reported to be ultramicroporous, similar to zeolites, a fact that led to the preparation of amorphous molecular sieve carbons by the charring of organic polymers.

In 1955 Union Carbide announced the commercial availability of a number of cationic forms of two synthetic zeolites designated A and X, the latter a synthetic form of the rare mineral faujasite. At this announcement, Mobil Research and Development Corporation, as well as the research and development laboratories of other major petroleum companies, hastened to obtain samples from the Linde Division. In 1955 and 1956 Mobil began to explore the potential use of these materials as adsorbents and catalysts and also began its own program on zeolite synthesis.

In 1962 Mobil began using the rare-earth form of zeolite X as a gas-oil cracking catalyst, the first commercial use of a zeolite as a catalyst. By this time a flurry of activity was underway throughout

xiii

the world on zeolite research and development. Barrer, at Imperial College of Science and Technology in London, realized the extent of this activity and organized the first international meeting on molecular sieves in 1967 in London. At the end of this meeting, the participants enthusiastically recommended that another meeting be held in 1970. In that year the Second International Conference on Molecular Sieves was held in Worcester, Massachusetts, and the London meeting has since become known as the First International Conference on Molecular Sieves. The Third International Conference on Molecular Sieves convened in Zurich in 1973 and the fourth in Chicago in 1977. At the Chicago meeting, the participants approved the formation of the International Zeolite Association, which was incorporated in 1982. Since that time, the triennial international meetings have been identified as International Zeolite Conferences, and the numeration already in use for the International Conferences on Molecular Sieves has continued. The Fifth International Zeolite Conference was held in Naples, Italy, in 1980; the sixth in Reno, Nevada, in 1983; and the seventh in Tokyo in 1986. I hope that this historical review is of interest to newcomers in the zeolite or molecular sieve fields.

What Is a Zeolite?

No permanent majority agreement has been reached among workers in these fields as to which term is preferable, zeolite or molecular sieve. "Molecular sieve" is all-inclusive in that it embraces all materials that exhibit shape selectivity, regardless of composition or degree of crystallinity. Traditionally, everyone has agreed that zeolites are crystalline aluminosilicates that have cation-exchange capacities and can reversibly sorb and desorb guest molecules small enough to enter the zeolite pores or channels. In addition, zeolites were recognized as three-dimensional framework structures composed of silicon and aluminum tetrahedra bound to one another by oxygen.

The recent syntheses of zeolitelike crystalline silicas, which contain infinitesimal amounts of aluminum, and the more recent syntheses of zeolitelike crystalline aluminum phosphates, chemical analogues of crystalline silica, have further confused the "zeolite" versus "molecular sieve" question. The conservative position contends that these molecular sieve crystals are not zeolites on two counts: They are not aluminosilicates, and they do not contain exchangeable cations. Furthermore, some of the relatively high silicon-containing materials have an average of less than one

In Perspectives in Molecular Sieve Science; Flank, W., et al.;
ACS Symposium Series; American Chemical Society: Washington, DC, 1988.

aluminum per unit cell, which disqualifies them as zeolites. The liberal view is that the traditional zeolite definition should be updated to state simply that zeolites are crystalline molecular sieves consisting of three-dimensional frameworks composed of tetrahedrally coordinated atoms or ions bound to one another by oxygen. Many of these new substances have frameworks that are isostructural with conventional zeolites. Also, some people argue that some of the high silicon-containing crystals, whose average aluminum contents amount to less than one aluminum per unit cell, have been shown to have aluminum concentration gradients such that some portions of the crystals have at least one aluminum per unit cell, whereas other regions within the same crystal are essentially aluminum-free. Are such crystals both zeolites and nonzeolites? The resolution of this disagreement lies in the future, probably by the participants of a future International Zeolite Conference.

About the Book

Although the title of this book, *Perspectives in Molecular Sieve Science*, avoids the zeolite definition controversy, a large majority of the research reported here centers on traditional zeolites. Only three of the 39 chapters comprising the book deal with materials that are clearly nonzeolitic: Two cover clay-type derivatives, and one deals with carbon molecular sieves. Not surprisingly, interest in these materials lies in their possible use as catalysts. Only four chapters present work on mineral zeolites and three on aluminum phosphate-type molecular sieves. Two of those chapters are by workers from Union Carbide, the laboratory that did the pioneering work in this field. It is surprising that other workers have not submitted papers on the aluminum phosphates, but perhaps this situation indicates that although much activity may be underway, laboratories hesitate to publish until patent positions are established in this potentially lucrative area. Union Carbide's synthetic faujasites (zeolites X and Y) and zeolite A receive the most attention, while ZSM-5-class materials are accorded more attention than zeolite A alone. This reflects the important roles that zeolites X and Y and ZSM-5 materials have already played as catalysts.

Of the phenomena discussed in this book, catalysis and acidity head the list, with sorption a relatively close second, followed by ion exchange. This situation has been the order of activity for the past 20 to 25 years. Studies of crystal structure, crystal and solution chemistry, and crystal growth are presented, indicating that efforts are still underway to make zeolite synthesis a more predictive science than it is at present with only a collection of empirically

derived recipes available. That about a dozen known mineral zeolites have not yet been synthesized is a great challenge to zeolite synthesis scientists. Among relatively new instrumental techniques, magic-angle spinning–nuclear magnetic resonance (MAS–NMR) is the most popular, having already proven its value in confirming earlier research on the mechanism of dealumination and the crystal chemistry of dealuminated zeolites. Several interesting papers in this book deal with recent results using ^{27}Al and ^{29}Si MAS–NMR in further elucidating zeolite crystal and solution chemistry.

One of the most interesting chapters in this book announces the synthesis of a silica that is isostructural with $AlPO_4$–5. This is the first example in which synthesis of a unique aluminum phosphate structure preceded the synthesis of other isostructural chemical analogues. Perhaps the next chapter in this story will be the synthesis of an aluminosilicate that has this structure. What will be the conservative point of view regarding the classification, zeolite or nonzeolite, of a substance whose "parent" is not a traditional zeolite?

February 2, 1988

Chapter 1

NMR Spectroscopy and Zeolite Chemistry

J. B.Nagy and E. G. Derouane

Laboratory of Catalysis, Center for Advanced Materials Research,
Facultés Universitaires Notre Dame de la Paix, Rue de Bruxelles 61,
B–5000 Namur, Belgium

The characterization of catalysts before, during, and after their catalytic evaluation is essentiel. Nuclear magnetic resonance (NMR) is a well-suited technique to observe subtle changes in zeolite catalysts as their composition is made of several NMR-sensitive nuclei such as ^{27}Al, ^{29}Si, and ^{17}O as well as others, i.e., ^7Li, ^{23}Na, etc... corresponding to exchange cations. In addition, the method can also be used to study the behavior of adsorbed molecules and of carbonaceous deposits during or after testing. In this review paper, we focus our attention on the characterization of the as-synthesized zeolites, the changes occurring during their pretreatment and/or subsequent modifications (calcination, steaming, dealumination, isomorphous substitution in their framework), and the conversion of adsorbed reactants.

^{29}Si-NMR enables the determination of the Si/Al ratio of zeolitic frameworks and of the number of crystallographically distinct sites. Indeed the chemical shift of Si is influenced by both the geometry of the sites (Si-O-T angles, T = Si,Al,B, ...) and their chemical environment (substitution of Si by other atoms (Al,B, ...) in the second coordination sphere). The distribution of the Al atoms can be either random or specific (partly or completely). The recognition of this fact may impact on our picture of the zeolite action as catalysts. Finally, the observation of SiOH defect groups in precursor zeolites, and of their modification during calcination, steaming, or dealumination, etc... does largely contribute to our understanding of the chemistry of these materials.

^{27}Al-NMR characterizes aluminium species of different coordination (tetra- or octahedral) and their interaction with the surroundings. Quantification of ^{27}Al-n.m.r. measurements can be achieved in well-defined conditions. The nature of the species resulting from dealumination can be inferred by studying the chemical shift and linewidth variations of the observed resonances.

^7Li- and ^{23}Na-NMR probe the exchange cations compensating the framework ([Si-O-Al]⁻) or defect (SiO⁻) negative charges. The distribution of alkali cations in the as-synthesized catalysts throws some light on their capability to accompany the aluminium atom in the structure. In addition, the method can also be used to investigate the chemical behavior of precursor gels.

Interactions between the molecules occluded during synthesis and the zeolitic framework can be examined by ^{13}C-NMR The behavior of reactants can also be monitored before (mobilities), during (reactivity) and after (reaction products and coking) the catalytic tests. Some typical examples of such in-situ NMR studies will be discussed.

Zeolites are microporous crystalline silicoaluminate materials (1). They have been extensively studied during the last 30 years, leading to the synthesis of novel structural species (1,2) and to a great number of applications (ion-exchange, molecular sieve, catalytic reactions, ...) (1,2).

Microporous materials with optimal properties (composition, acidity, thermal stability, pore size, ...) desired for various applications can be obtained either by modifying classical zeolites (to reach higher Si/Al ratios using various dealumination procedures or substituting Si and/or Al by other elements) or by synthesizing novel zeolitic structures (borosilicates, borosilicoaluminates, gallosilicates, phosphoaluminates, ...) (2-4). In this review paper we focus our attention on the characterization of the as-synthesized zeolites, the changes occurring during their pretreatment and subsequent modifications (calcination, steaming, dealumination, isomorphous substitution in their framework), and the conversion of adsorbed reactants.

Several review papers appeared recently, which deal with the application of NMR to the characterization of zeolites (5-7) or with the study of the adsorbent-adsorbate interaction (7-10). Most of them, however, emphasize the importance of the NMR measurements (5,6,8,9) and only two reviews treat the problems from essentially a catalytic point of view (7,10).

This short review paper will be devoted to our own results obtained in the Laboratory of Catalysis and reference will only be done to illustrative publications in the literature.

EXPERIMENTAL

NMR spectra were recorded at room temperature using a Bruker CXP-200 high power spectrometer. The relevant NMR parameters are described in Table I.

Table I. NMR parameters for the various nuclei

Nucleus	ν(MHz)	Reference	t_{pulse}(μs)	θ(°)	t_{rep}(s)
[29]Si	39.7	TMS	6	$\pi/2$	3
[13]C	50.3	TMS	6	$\pi/2$	4
[27]Al	52.1	Al(NO$_3$)$_3$ aq	7	$\pi/8$	0.1
[23]Na	52.9	NaClO$_4$ aq	6	$\pi/6$	0.2
[7]Li	77.7	LiCl aq	5	$\pi/6$	1

Magic angle spinning (MAS) at ca. 3.5 kHz was used for ^{29}Si- and ^{13}C-NMR measurements, while ^{23}Na-NMR spectra were taken without MAS. For ^{27}Al- and ^{7}Li-NMR both techinques were used. The following parameters were used for cross-polarization ^{13}C-NMR : [13]C (50.3 MHz) and [1]H (200.0 MHz) rf fields were

39.0 G and 9.8 G respectively satisfying the Hartmann-Hahn condition. A single contact sequence comprised 5.0 ms contact time and a recycle time of 4.0 s. The corresponding parameters for the ^{29}Si-NMR cross-polarization experiments are : ^{29}Si (39.7 MHz) and ^{1}H (200.0 MHz) rf fields were 39.3 and 9.8 G respectively, with a contact time of 10.0 ms and a recyle time of 3.0 s.

RESULTS AND DISCUSSION
Characterization of as-synthesized zeolites

The first application of high-resolution solid-state NMR with magic-angle-spinning (MAS-NMR) to the investigation of silicates and silicoaluminates was made by Lippmaa et al. (11). They showed clearly that distinct and well resolved peaks could be observed for ^{29}Si-MAS-NMR spectra of solid silicates and silicoaluminates corresponding to different chemical environments, depending essentially on the number of tetrahedral Al atoms in the second coordination sphere of Si (12,13). In addition, the chemical shifts of the lines belonging to defined Si(nAl) configurations are also influenced by the different crystallographic arrangements of the SiO_4 tetrahedra characterized by the different interatomic distances and angles of the Si-O-T linkages (T = Si or Al) (13,14).

In silicates the total range of ^{29}Si-NMR chemical shifts is appreaciable (from -60 to -120 ppm) and is subdivided into characteristic ranges for monosilicates (Q_0), disilicates and chain end groups (Q_1), middle groups in chains and cycles (Q_2), chain branching sites (Q_3) and the three-dimensional cross-linked framework (Q_4) (12) (Figure 1). Substitution of silicon by aluminium leads to an additional paramagnetic shift. In addition, the sharpness of the resonance lines reflects the degree of crystallinity and depends on the regularity of the Si,Al distribution.

From the relative intensities of the different Si(nAl) NMR lines, quantitative determination of Si/Al ratios is possible, provided the Al avoidance rule of Loewenstein is obeyed (15) :

$$\left(\frac{Si}{Al}\right)_{NMR} = \frac{\sum_{n=0}^{4} I_{Si(nAl)}}{\sum_{n=0}^{4} 0.25\, n\, I_{Si(nAl)}}$$

This formula is easy to understand, if one realizes that each Si-O-Al linkage accounts for 0.25 Al atoms.

For zeolites characterized only by one type of crystallographic site, the computation of the Si/Al ratio is quite obvious. This is illustrated in Figure 2, where the ^{29}Si-NMR spectra of zeolite Y and ZSM-20 are compared. The spectrum of zeolite Y includes five lines corresponding to Si(4Al), Si(3Al), Si(2Al), Si(1Al) and Si(0Al) configurations while that of ZSM-20 consists of four lines of Si(3Al), Si(2Al), Si(1Al) and Si(OAl) configurations. These latter resonance lines are systematically located at lower chemical shifts relative to the lines of zeolite Y (6), due to the higher Si content of the ZSM-20 zeolite. The Si/Al ratio computed from the relative NMR line intensities is equal to 4.3 and agrees quite well with the
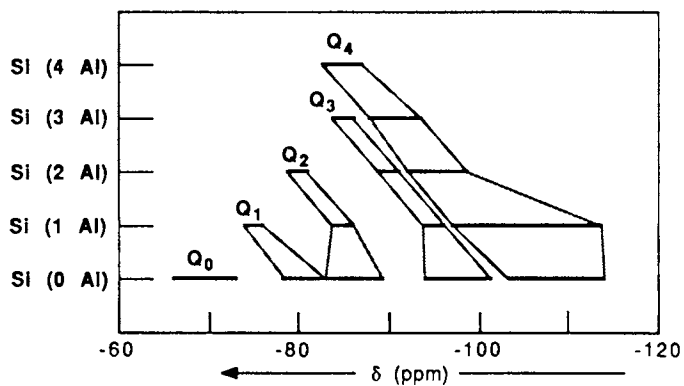
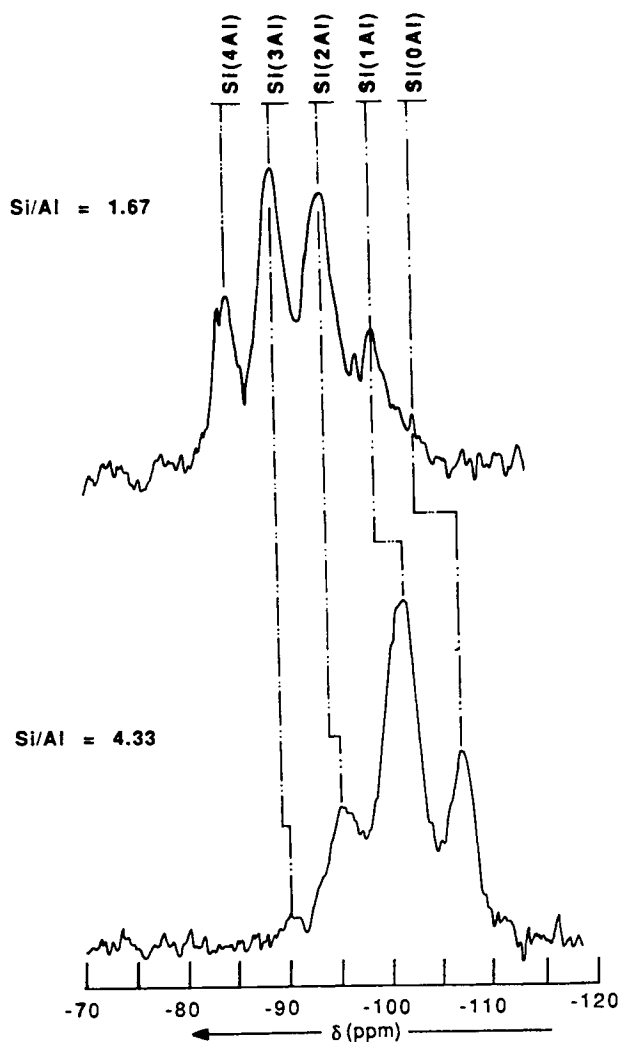Figure 1. ^{29}Si-NMR chemical shifts of silic(oalumin)ates.

Figure 2. ^{29}Si-NMR spectra of zeolites Y and ZSM-20 (Data taken from ref. 16).

chemical EDX analysis (4.2) (16). Indeed, zeolite ZSM-20 is a silica-rich zeolite, possessing a faujasite-like character but having a hexagonal symmetry unit cell (16,17). The high silica content could result in higher (hydro)thermal stability and acid strength, and better resistance to deactivation relative to the Y-type zeolites.

The computation of the Si/Al ratio becomes more tedious, when several crystallographic sites are present, resulting in overlapping of various $Si(nAl)_{T_i}$ configurations (T_i : ith crystallographic site) (18). Several methods have recently been proposed based on one of the following assumptions regarding aluminium site location : specific location of Al on certain crystallographic sites (19,20) (see below), a fully random distribution of Al atoms (20,21) or a random distribution with some preferential location of Al on specific sites (22,23).

The Generalized Random with some Constraint model (GRC) is based on the following hypotheses (23) :
i) On each type of T_i site the Si, Al distribution is random, but the Al per T_i site is different for each i type crystallographic site
ii) The Loewenstein's rule is obeyed.

This model is applied to the study of Al distribution in offretite and omega zeolites, which both possess two different crystallographic sites. The probability p for a Si_{T_i} atom to have an Al atom as a T_j neighbour is described by :

$$p_1 = p[Al_{T1} : Si_{T1}] \quad p_2 = p[Al_{T2} : Si_{T2}]$$

$$p_3 = p[Al_{T2} : Si_{T1}] \quad p_4 = p[Al_{T1} : Si_{T2}]$$

(Note that in ref. 22 only two probabilities p_1 and p_2 were taken into account.)

Including Loewenstein's rule into the calculation, these probabilities have the following simple expressions (23) :

$$p_1 = Al_{T1}/Si_{T1} \qquad p_2 = Al_{T2}/Si_{T2}$$

$$p_3 = (a/b) (Al_{T2}/Si_{T1}) \qquad p_4 = (b/a) (Al_{T1}/Si_{T2})$$

where $a = Si_{T1} + Al_{T1}$ and $b = Si_{T2} + Al_{T2}$ are the numbers of crystallographic sites 1 and 2 per unit cell, respectively. The relative amounts Si_{T_i} and Al_{T_i} can be expressed as a function of two variables, i.e. R = Si/Al (global ratio) and x = Al_{T1}/Al_{T2} (24) :

$$Si_{T1} = [a(R+1) (x+1) - x(a+b)]/(R+1) (x+1)$$

$$Si_{T2} = [b(R+1) (x+1) - (a+b)/(R+1) (x+1)$$

$$Al_{T1} = x(a+b)/(R+1) (x+1)$$

$$Al_{T2} = (a+b)/(R+1) (x+1)$$

Finally the relative intensity of the NMR lines are computed :

$$(I_{Si(nAl)})_{Ti} = [Si_{Ti}/(Si_{T1} + Si_{T2})] \times Si(nAl)_{Ti} \times I_{tot}$$

where I_{tot} is the total line intensity and $Si(nAl)_{Ti}$ the fraction of $Si(nAl)_{Ti}$ atoms, determined by combinational analysis :

$$Si(nAl)_{T1} = \binom{3}{n} (1-p_1)^{3-n} p_1^n (1-p_3) + \binom{3}{4-n} (1-p_1)^{4-n} p_1^{n-1} p_3$$

$$Si(nAl)_{T2} = \binom{2}{n} (1-p_2)^{2-n} p_2^n (1-p_4)^2 + \binom{2}{4-n} (1-p_2)^{4-n} p_2^{n-2} p_4^2$$

$$+ \ \ [\binom{4}{n} - \binom{2}{n} - \binom{2}{4-n}] \ (1-p_2)^{3-n} (1-p_4) p_2^{n-1} p_4$$

These expressions are formally similar to those reported in ref. 22, they differ however in the meaning of the probability p_i.

Finally the spectra are simulated by varying R, x, and w, where w is the linewidth at half maximum. The experimental and theoretical spectra for steam dealuminated omega and offretite samples are illustrated in Figure 3. The correspondence between the experimental and theoretical spectra are excellent. One has also to emphasize, that the computation yields R = Si/Al, where the Al atoms are only those in tetrahedral sites of the structure noted as $(Si/Al)_{IV}$ in Figure 3. The Si/Al ratio determined by chemical analysis corresponds, on the other hand, to global composition including both tetrehedral framework and tetra-and/or octahedral non-framework aluminium atoms. The presence of extraframework Al can be noted in both cases because the Si/Al values are systematically lower than the $(Si/Al)_{IV}$ values.

It was mentioned above that the ^{29}Si-NMR chemical shifts are also sensitive to the different interatomic distances and angles of the Si-O-T linkages (13,14). Indeed, the spectrum of the monoclinic form of highly siliceous ZSM-5 (or silicalite 1) shows as many as twenty one different resonance lines (Figure 4) (25). It is now well known that the structure becomes orthorhombic at higher temperatures (26) and under the influence of adsorbed molecules (27).

The SiOR (R = H, metal or organic cation) defect groups are also readily detected by ^{29}Si-NMR. In zeolites of quite different structures the corresponding resonance line is at ca -103 ppm (13,19,28), due probably to the similar average Si-O-T angles. Cross-polarization enhances the line characterized by a large contribution of SiOH groups (7,28) (Figure 5). The amount of SiOR defect groups increases with decreasing Al content of the ZSM-5 samples (29,30) (Figure 6) and as many as 32 SiOR per unit cell can be detected in highly siliceous samples. As four SiOR groups could correspond to each missing tetrahedral site (see below), this means that some eight T sites would be non occupied in the structure. These results confirm the model previously proposed for the formation of ZSM-5 zeolite, where double five-membered rings were supposed to condense to lead to a structure containing a high number of defect groups (30).

The ^{27}Al-NMR spectra are essentially used to characterize tetrahedral framework and octahedral extraframework Al species (6,31). (Figure 7). However, quite recently, Lippmaa et al. succeded in determining the precise chemical shift of Al using special NMR techniques, such as 2D MAS NMR or measuring the first or second spinning side-bands of the least shifted first satellite (±3/2, ±1/2) transition (32). They found a linear correlation between the chemical shift and the mean Al-O-Si bond angles in framework silicoaluminates. This method will thus be quite complementary to the ^{29}Si-NMR to characterize the zeolite structures. It can also be

modified offretite (Si/Al) = 3.7   modified omega (Si/Al) = 3.8

$(Si/Al)_{IV} = 10.4$ $(Si/Al)_{IV} = 5.1$

$Al_{T1}/Al_{T2} = 2.4$ $Al_{T1}/Al_{T2} = 3.6$
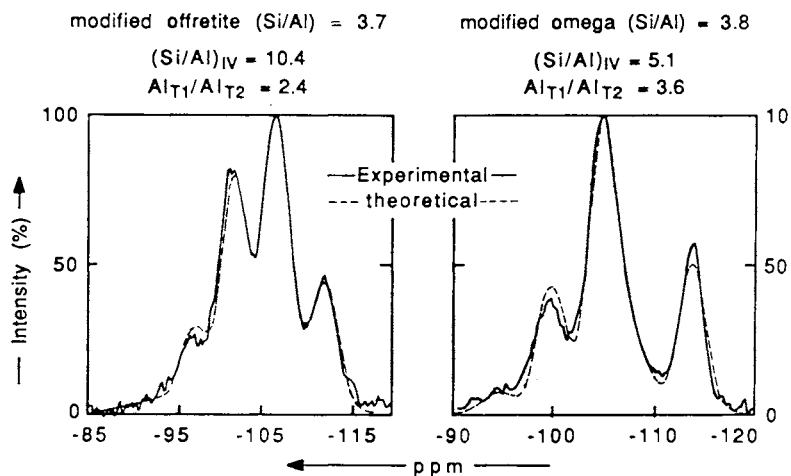
Figure 3. Experimental and theoretical ^{29}Si-NMR spectra of steam dealuminated offretite and omega. (Reproduced with permission from ref. 23. Copyright 1988 Elsevier.)
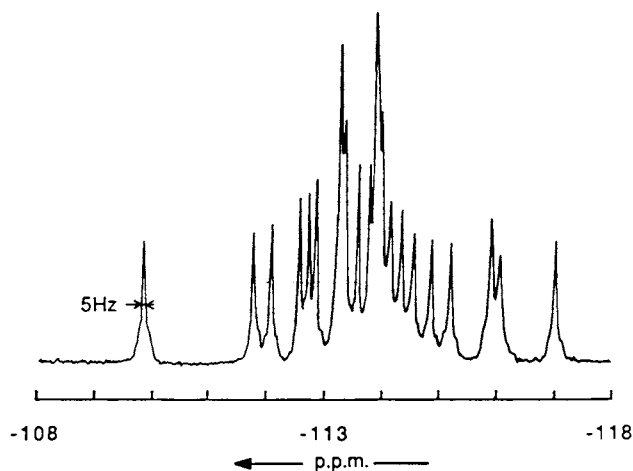
Figure 4. ^{29}Si-NMR spectrum of highly siliceous ZSM-5 zeolite. (Reproduced with permission from ref. 25. Copyright 1987 Macmillan Magazines.)
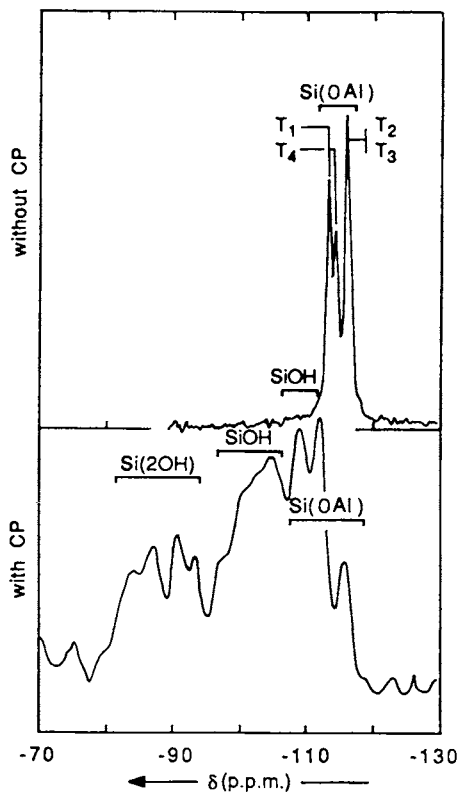
Figure 5. ^{29}Si-NMR spectra of mordenite dealuminated by acid leaching and subsequent steaming. (Reproduced from ref. 19. Copyright 1986 American Chemical Society.)
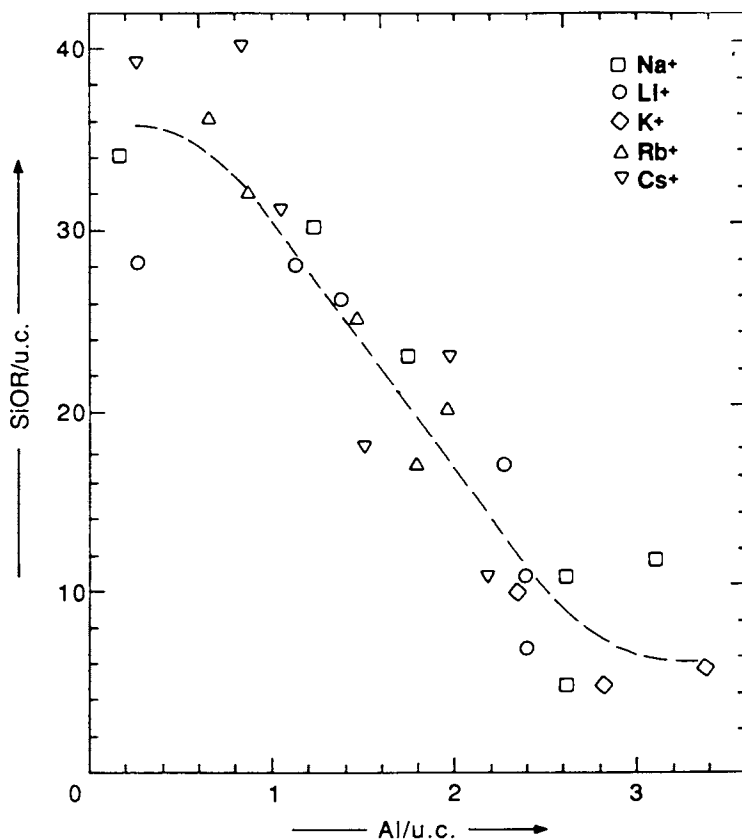
Figure 6. Variation of the SiOR/u.c. (R = H, M, and TPA) as a function of Al/u.c. in the ZSM-5 zeolites. (Reproduced with permission from ref. 41. Copyright 1987 Butterworth.)
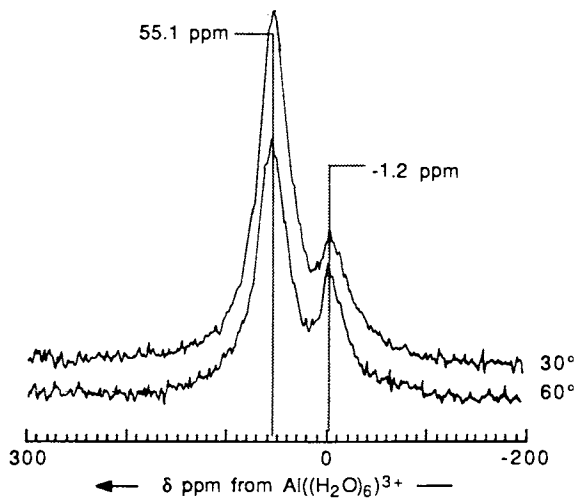
Figure 7. ^{27}Al-NMR spectra of H-Mordenite recorded at two different flip angles. (Reproduced with permission from ref. 34. Copyright 1988 Elsevier.)

used to position Al atoms in the different crystallographic sites, provided the bond angles are accurately determined.

For quantitative measurements, special care should be taken for the flip angle used. Indeed, it was shown previously, that in the case of quadrupolar nuclei the magnetization corresponding to different transitions rotate at different rates around the rf field (33). This results in a large variation of the line intensity. Figure 7 shows the different line intensities for the tetra- and octahedral Al atoms obtained at different flip angles (34). It has to be emphasized, that for adequate quantitative measurements short pulse angles ($\theta \leq \pi/6$) should be used (33,34). Figure 8 illustrates the variation of normalized line intensity as a function of flip angle. It should be noted, that for the two separate components, the intensities are normalized with respect to the total Al atoms in the sample. It is clear that the correct relative intensities can only be computed from small flip angles, id ca. 20° in this case. The method for quantitative analysis is the direct comparison of the initial slopes. From the initial slopes, the ratio of the octahedral to the tetrahedral Al species can be computed as (34) :

$$\frac{\text{slope (octahedral species)}}{\text{slope (tetrahedral species)}} = 27\%$$

^{17}O-NMR has also been applied quite recently to the characterization of zeolites (35,36). Figure 9 shows the wide line NMR spectra of Linde A (having only Si-O-Al bonds), SiO_2 (for Si-O-Si bonds), the sum of these spectra and the spectrum of Linde Y. The quadrupolar coupling constants as well as the chemical shifts of Si atoms in either Si-O-Al or Si-O-Si bonds are sufficiently different and the spectrum of zeolite Y can be decomposed into two contributions. This decomposition also leads to an easy determination of the Si/Al ratio. Indeed :

$$Si/Al = \frac{2[\text{Si-O-Si}] + [\text{Si-O-Al}]}{[\text{Si-O-Al}]}$$

where the concentrations of the Si-O-Si and Si-O-Al bonds are directly determined from the spectra. The ^{17}O-NMR brings thus complementary informations obtained by ^{29}Si- and ^{27}Al-NMR. The basic difficulty resides in the low sensitivity of natural compounds and hence ^{17}O-enriched materials should be used to achieve spectra of high signal to noise ratios.

^{7}Li- and ^{23}Na-NMR techniques are useful to study the hydration state of these alkali cations as well as their interactions with the negative centers of the framework. Relatively few studies have been reported either on the behaviour of Li$^+$ (37-39) or that of Na$^+$ ions (29,37,40). Figure 10 illustrates the ^{7}Li-NMR spectra of the precursor and calcined ZSM-5 zeolite samples. Two lines can be distinguished in the spectrum of the precursor : a broad line ($\Delta H = 4$ kHz) and a narrow line ($\Delta H = 0.5$ kHz) both centered at ca 0 ppm (41). The former is assigned to partially hydrated or anhydrous Li$^+$ cations, while the latter is characteristic of fully hydrated cations. Indeed, thermal gravimetry (TG) data indicate that the available water is not sufficient to hydrate fully the total amount of Li$^+$ cations (Table II). For a full hydration of Li$^+$ cation ca four water molecules are required (42). A relatively slow exchange may occur between the two species. The relative amount of Li$_{hydr}$ decreases with decreasing amount of Al/u.c.. Indeed, it is accompanied by a decrease of the amount of those Li$^+$ ions which are counterions to [Al-O-Si]$^-$ framework negative charges. In this state these ions are then fully hydrated. Similar
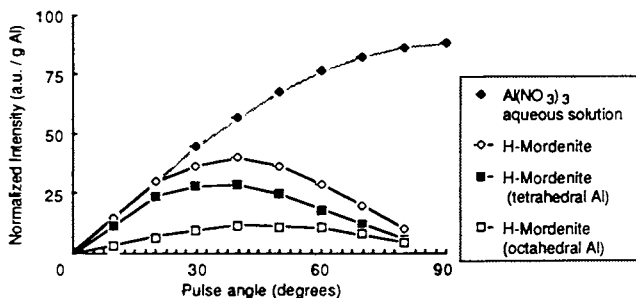
Figure 8. Normalized ^{27}Al-NMR line intensity as a function of flip angles. (The intensities for tetra- and octahedral Al atoms are normalized to the total amount of Al in mordenite.) (Reproduced with permission from ref. 34. Copyright 1988 Elsevier.)
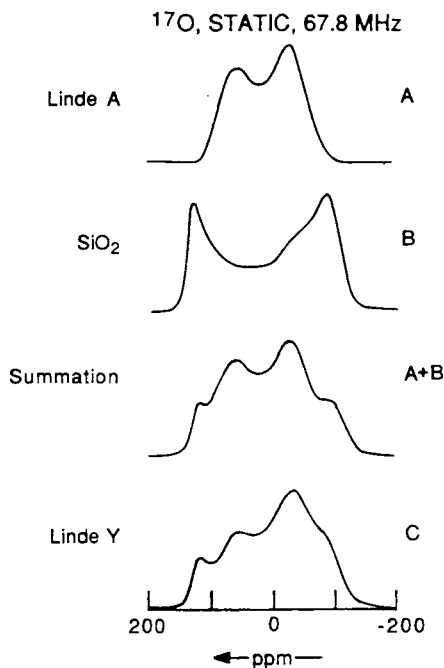

Figure 9. ^{17}O-NMR spectra of zeolites A, Y, and SiO_2. (Reproduced from ref. 36. Copyright 1986 American Chemical Society.)
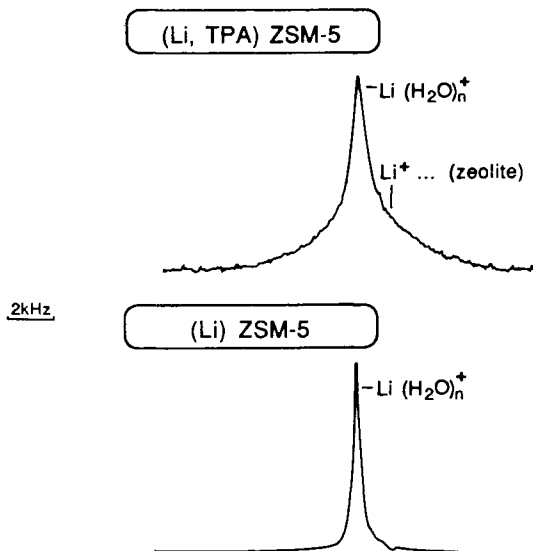
Figure 10. ^{7}Li-NMR spectra of the precursor and calcined ZSM-5 samples (Reproduced with permission from ref. 41. Copyright 1987 Butterworth.)

Table II. ^{7}Li-NMR and chemical analysis of (TPA,Li)-ZSM-5 zeolites

Li$_2$O[a]	Al$_2$O$_3$[a]	^{7}Li-NMR ΔH^b(kHz)	ΔH^c(kHz)	$\dfrac{\text{Li}_{hydr}}{\text{I}_{total}}$×100	Si/Al[d]	Al/u.c.[d]	Li/u.c.[e]	SiOLi/u.c.[f]	Li$^+$...[Al-O-Si][f] /u.c.	H$_2$O[g] /Li$_{total}$
0.25	1	4.0	0.62	28	39	2.4	0.4	0	0.6	2.3
1	1	4.2	0.50	-	39	2.4	1.3	0.6	0.9	0.9
2	1	4.5	0.42	30	41	2.3	1.7	0.9	0.9	0.6
1	0.6	4.1	0.54	15	69	1.4	1.2	1.4	0	2.0
1	0.3	4.2	0.54	15	85	1.1	2.6	3.1	0	1.1
1	0	4.3	0.54	19	390	0.25	1.2	-	-	-

a) Relative amounts in initial gels : xTPABr-y(TPA)$_2$O-zLi$_2$O-wAl$_2$O$_3$-60SiO$_2$-700H$_2$O; x + 2y = 8 (constant TPA content) and y + z = 2 (constant alkalinity)
b) Broad NMR line
c) Narrow NMR line
d) PIGE (proton induced γ-ray emission) measurements
e) Atomic absorption values
f) Values computed from combined chemical analysis, ^{29}Si-NMR and thermal analysis of TPA (41)
g) TG (thermal gravimetry) data combined with chemical analysis

conclusions have been arrived at, when considering the state of Na^+ ions in the ZSM-5 zeolite samples (43,44). It is also clear from Table II, that the non- or less-hydrated Li^+ species are the SiOLi defect groups, where the less delocalized negative charge of the O atom interacts preferentially with less solvated cations (41,45).

Both linewidth and the chemical shift of ^{23}Na depend on the relative amount of Al in the ZSM-5 samples (29,40). A chemical shift close to 0 is obtained for highly siliceous samples, while the high Al-samples exhibit a spectrum characterized by a δ = -15 - -20ppm (29,40,45). The linewidth is also greatly influenced by the relative hydration of the cation. A systematic work is still lacking including both the relative importance of SiONa and $(Si-O-Al)^-Na^+$ groups in the zeolitic samples together with the degree of hydration of the Na^+ cations.

High resolution MAS ^{13}C-NMR is a promising method to investigate the nature of carbon-containing molecules occluded into the zeolitic channels or cavities during the synthesis. The ^{13}C-NMR data show clearly that tetrapropylammonium ions are occluded intact in the ZSM-5 zeolite channels (10,46,47). This is also true for tetrabutylammonium and -phosphonium cations which direct the ZSM-11 structure (10,46). Moreover, two types of methyl groups are distinguished, the difference in chemical shift being due to different chemical environments. In ZSM-5 zeolite every channel intersection is occupied by a tetrapropylammonium ion. Oppositely, tetrabutyl-ammonium and -phosphonium cations occupy preferentially the large cavities in ZSM-11 zeolite, the small cavities being only partially occupied. The alkyl chains of all these organic cations occluded in both ZSM-5 and ZSM-11 zeolites extend in the channel system in order to fill completely the available channel length.

Note that ^{13}C-NMR has also been used to detect the presence of small ZSM-5 particles, which must contain less than 3 or 4 unit cells in thickness, corresponding to a size which is beyond the XRD detection limit (48,49). A change in the interaction occurs between the tetrapropylammonium ions and the ZSM-5 framework during calcination and the doublet splitting of the methyl groups disappears (50,51). The new species formed is described as a relaxed tetrapropylammonium ion occluded in a partially healed ZSM-5 structure (51).

It was shown quite recently that in the synthesis of zeolite ZSM-48 in presence of an alkylamine and tetramethylammonium (TMA) ions, only the n-alkylamine plays a structure-directing role, while TMA^+ ions are the main species incorporated during the growth process, until complete filling of the channels is achieved (52). For example, 0.2 molecule of n-octylamine (2.6 Å) and 1.9 TMA^+ ions (13.1 Å) per unit cell are occluded intact in final crystalline samples.

In contrast to zeolite ZSM-48, the formation of ZSM-39 seems to be exclusively directed by the TMA^+ ions. Indeed, a slight modification in the gel composition (no alkylamine present, increase in the Al content) and in the synthesis procedure, leads to preferential formation of zeolite ZSM-39. Its crystallization is accompanied by the dequaternation of TMA^+ ions, producing trimethylammonium ions in equilibrium with trimethylamine. These latter two organic compounds are essentially occluded in the large cavities of ZSM-39 (52) (Figure 11). Note that the species adsorbed on external surface can be distinguished from those occluded in internal cavities by considering the much broader NMR lines of the former.

In presence of hexamethenium (HM^{++}) $((CH_3)_3{}^+N-CH_2-CH_2-CH_2-)_2$ ions, either zeolite ZSM-48 or ZSM-50 can be formed, depending on the initial

aluminium concentration. A decomposition of HM^{++} ions in the synthesis conditions only occurs if the precursor hydrogel contains ammonium ions (Figure 12). This decomposition leads to the formation of hexyltrimethylammonium ions, which are also occluded into the zeolite crystals. It is concluded, that HM^{++} ions act as structure-directing agents and the total filling of the void volume is achieved in both cases (52).

Dealumination and realumination of zeolites

In order to increase their thermal stability and the strength of their acid sites, high Al content zeolites are submitted to various dealumination treatments (7,19,53-55).Some procedures will be illustrated by the dealumination of zeolite mordenite, where the ^{29}Si-NMR results are shown to lead to the determination of Al distribution in the samples, as well as to the proposition of a dealumination mechanism (19).

The ^{27}Al-NMR spectra of the parent Na-mordenite (commercial Na-Zeolon (Norton)) and of its analogues dealuminated by acid leaching at various temperatures and for various times are presented in Figure 13. The Na-Z spectrum is characterized by a unique resonance line at $\delta = 50$ ppm vs $Al(H_2O)_6^{3+}$, corresponding to tetrahedrally coordinated Al of the framework (Al_T). An additional line at $\delta = 0$ ppm appears in the spectra of acid-treated samples and it belongs to octahedral Al species extracted from the lattice (Al_O). The narrowness of this line (0.8 kHz) suggests that the octahedral Al^{+3} ions are fully hydrated and occupy probably cationic positions. From these spectra, the relative amounts of tetrahedral and octahedral Al atoms can be determined. (Note that all the spectra were taken at small flip angles providing quantitative detection of all Al atoms (34)). These data together with the Si/Al ratios obtained by chemical analyses (Table III) allow one to compute the real composition of the zeolitic framework, if it is assumed that all Al_T atoms belong to the lattice (Table IV).

Table III.   Dealumination of mordenite by acid leaching

sample	exptl conditions	AA	Si/Al[a] EDX	^{27}Al-NMR	av
Na-Z[b]		5.5	5.6	5.4	5.5
H-Z-1	4 M HNO_3, 293 K, 8 h	6.1	6.6	6.3	6.3
H-Z-2	4 M HNO_3, 323 K, 24 h	5.8	7.1	7.1	6.7
H-Z-3	4 M HNO_3, 363 K, 24 h	20.5	19.2	21.6	20.4
H-Z-4	6 M HNO_3, 363 K, 24 h	20.6	22.3	27.6	23.5
H-Z-5	14 M HNO_3, 363 K, 24 h	31.2	28.0	30.7	30.0

[a] AA atomic absorption; EDX energy-dispersive X-ray analysis; ^{27}Al NMR results obtained from a   calibration curve
[b] Commercial Na-Zeolon.
SOURCE: Reproduced from ref. 19. Copyright 1986 American Chemical Society.
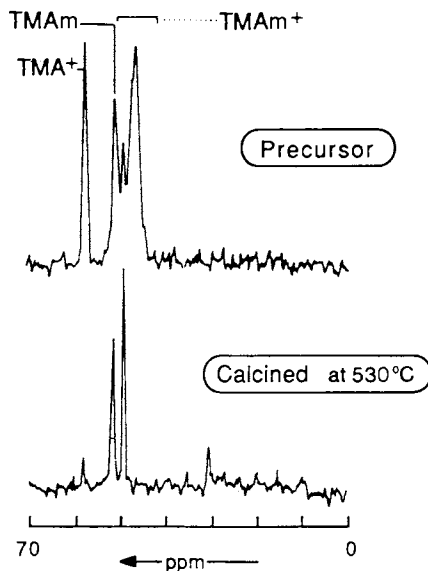
Figure 11. ^{13}C-NMR spectra of zeolite ZSM-39 prepared without *n*-alkylamine: precursors and partially calcined sample at 530 °C to remove externally adsorbed species. (Reproduced with permission from ref. 52. Copyright 1988 Elsevier.)
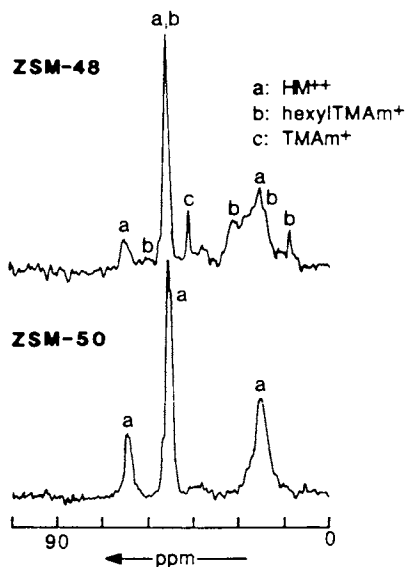
Figure 12. Characteristic ^{13}C-NMR spectra of a ZSM-48 sample prepared in the presence of $(NH_4)_2O$ and low Al content and of a ZSM-50 sample obtained without $(NH_4)_2O$ and with a high Al content in the gel. (Reproduced with permission from ref. 52. Copyright 1988 Elsevier.)
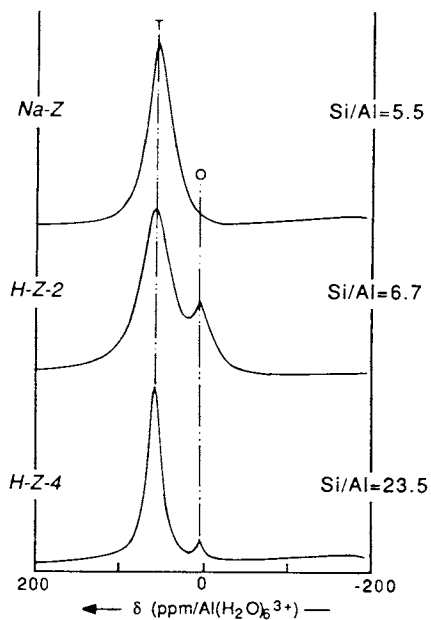
Figure 13. High-power solid-state ^{27}Al-NMR spectra of Na-Zeolon and its dealuminated forms. (Reproduced from ref. 19. Copyright 1986 American Chemical Society.)

Table IV.   Determination of the Si/Al ratios of the zeolite framework from the relative amounts of tetrahedral (T) and octahedral (O) Al and the overall chemical composition of the Na-and acid-treated mordenite samples

samples	chem. compn. Si/Al[a]	^{27}Al NMR		lattice compn	
		Al$_T$ %	Al$_O$ %	Si/Al[b]	Al$_T$/uc[c]
Na-Z	5.5	100	0	5.5	7.4
H-Z-1	6.3	81	19	7.7	5.5
H-Z-2	6.7	75	25	8.9	4.8
H-Z-3	20.4	89	11	22.9	2.0
H-Z-4	23.5	93	7	25.3	1.8
H-2-5	30.0	93	7	32.2	1.4

[a] From Table III
[b] $Si/Al)_{lattice} = [(Al_O + Al_T)/Al_T]$ (Si/Al) global
[c] Al_T/uc = number of tetrahedral Al atoms per unit cell;
$$Al_T/uc = 48/[1 + (Si/Al)_{lattice}]$$

SOURCE: Reproduced from ref. 19. Copyright 1986 American Chemical Society.

Figure 14 shows the high-resolution MAS ^{29}Si-NMR spectra of Na-mordenite and its dealuminated counterparts. The spectrum of Na-Z consists of three resonance lines at -99, -105 and -110 ppm, corresponding to Si(2Al), Si(1Al) and Si(0Al) configurations respectively. In addition, silanol groups at defect lattice sites contribute to the intensity of the NMR line at -105 ppm. As dealumination proceeds, the lines at -99 and -105 ppm decrease, while the relative intensity of the -110 ppm line increases (Table V).

Table V.   Variation of relative HRMAS ^{29}Si-NMR line intensities of mordenite at various degrees of dealumination by acid leaching

samples	Si/Al[a]	relative line intensities[b] (%) at			Si/Al[c]
		δ = -99	δ = -105	δ = -110	
Na-Z	5.5	13	45	42	5.6
H-Z-1	7.7	12	45	43	5.8
H-Z-2	8.9	10	43	47	6.3
H-Z-3	22.9	5	23	72	12
H-Z-4	25.3	4	21	75	14
H-Z-5	32.2	2	16	82	20

[a] Lattice composition (Table IV). [b] Relative to the total NMR intensity.
[c] Recalculated by using the relation Si/Al = It/(Σ 0.25 n I$_{Si(nAl)}$) assuming that SiOH defect groups do not contribute to the -105 ppm line intensity.
SOURCE: Reproduced from ref. 19. Copyright 1986 American Chemical Society.

This shows unambiguously the extraction of Al from the lattice leading to a decrease of the number of Si(1Al) and Si(2Al) configurations and to an increase of Si(0Al) configurations. However, the Si/Al ratios calculated from the general formula (see above) are not in good agreement with those obtained by combined ^{27}Al-NMR and chemical analyses (Table V). The origin of this discrepancy can be explained by assuming a substantial contribution of SiOH groups to the -105 ppm line. Direct evidence for these SiOH groups are obtained by cross-polarization ^{29}Si-^{1}H measurements for samples shown in Figure 5. The acid-leaching was followed by subsequent steaming. Consequently, the line at -105 ppm contains the contribution of both Si(1Al) configuration and defect SiOH groups :

$$I_{-105} = I_{Si(1Al)} + I_{SiOH}$$

and as

$$I_{-99} = I_{Si(2Al)},$$

$I_{Si(1Al)}$ can be computed from

$$Si/Al)_{lattice} = \frac{I_{total}}{2 \times 0.25 \times I_{Si(2Al)} + 1 \times 0.25 \times I_{Si(1Al)}}$$

and

$$I_{Si(0Al)} = I_{-110} + I_{SiOH}$$

The relative intensities of the different configurations so obtained are listed in Table VI. The number of SiOH groups at defect lattice sites per extracted Al atom is shown as a function of the number of extracted Al atoms per unit cell (Figure 15). In the beginning of dealumination up to four SiOH defect groups per extracted Al atom are generated in the structure (56).

Table VI : Evolution of the different Si configurations and tne number of SiOH defect groups generated per extracted Al during mordenite dealumination by acid leaching

samples	lattice compn Si/Al	Al/uc	Si configurations (% of total Si) SiOH	Si(2Al)	Si(1Al)	Si(0Al)[b]	SiOH/Al$_{extd}$[a]
Na-Z	5.5	7.4	0	13	45	42	
H-Z-1	7.7	5.5	17	11	28	61	3.7
H-Z-2	8.9	4.8	18	10	24	66	3.0
H-Z-3	22.9	2.0	15	5	8	87	1.3
H-Z-4	25.9	1.8	14	4	7	89	1.2
H-Z-5	32.2	1.4	8	2	8	90	0.6

[a]Number of SiOH generated per Al extracted, [b]Si(0Al)$_{total}$ = Si(0Al) + SiOH
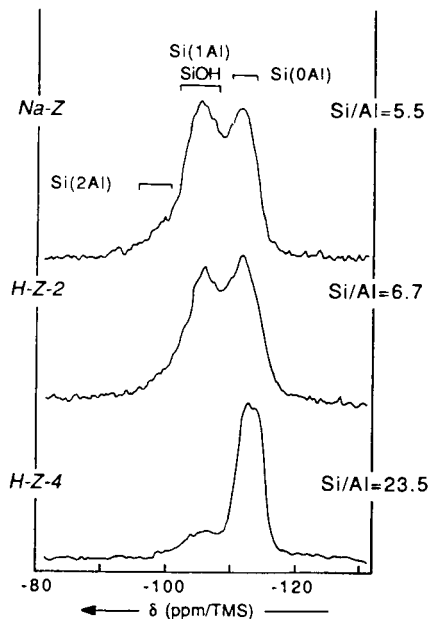
Figure 14. High-resolution MAS ^{29}Si-NMR spectra of Na-Zeolon and its dealuminated forms. (Reproduced from ref. 19. Copyright 1986 American Chemical Society.)
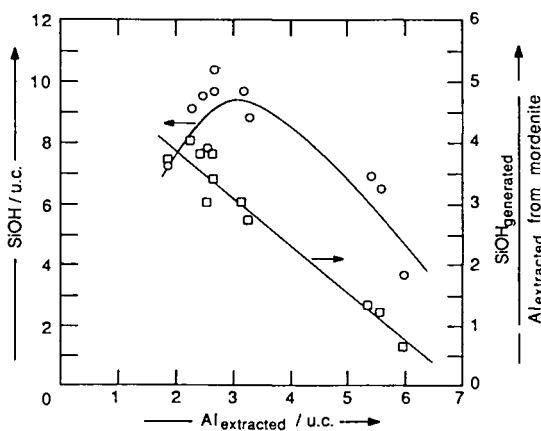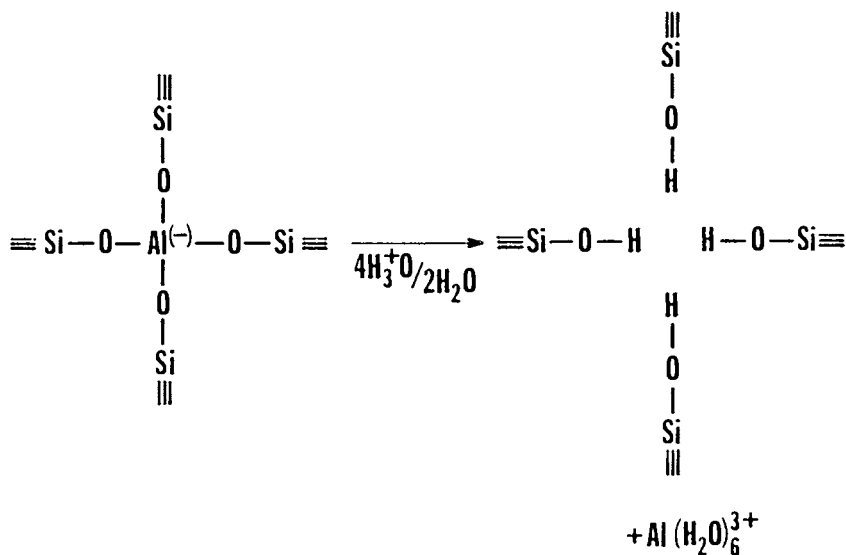

Figure 15. Variation of the total number of SiOH groups and the amount generated per extracted Al atom with the amount of Al extracted per unit cell. (Reproduced from ref. 19. Copyright 1986 American Chemical Society.)

$$
\begin{array}{ccc}
\overset{\text{|||}}{\underset{\text{|}}{\text{Si}}} & & \overset{\text{|||}}{\underset{\text{|}}{\text{Si}}} \\
\text{O} & & \text{O} \\
| & & | \\
\equiv \text{Si}-\text{O}-\overset{\overset{\text{O}}{|}}{\underset{\underset{\underset{\text{Si}}{|}}{\text{|}}}{\text{Al}^{(-)}}}-\text{O}-\text{Si}\equiv & \xrightarrow{\;4H_3^{+}O/2H_2O\;} & \equiv\text{Si}-\text{O}-\text{H} \qquad \text{H}-\text{O}-\text{Si}\equiv
\end{array}
$$

$$+ Al (H_2O)_6^{3+}$$

The decrease of this number as dealumination proceeds is the result of a partial healing of the structure as it was also emphasized by other research groups (57,58). Figure 5 also shows that in addition to SiOH defect groups some $Si(OH)_2$ groups are also present in the highly dealuminated sample. (Although on the basis of chemical shifts some other species like $AlOSi(OH)_2$ or $(AlO)_2SiOH$ could also be present, we regard them as minor components in these highly dealuminatied samples.) In addition, the ^{29}Si-NMR spectrum without cross-polarization reflects the presence of different crystallographic sites, the attribution of the NMR lines was made on the correlation between chemical shifts and mean Si-O-Si angles (59).

When the dealumination is carried out using $SiCl_4$, the extracted Al is deposited in the channels as extra-framework aluminous species. In addition, the $SiCl_4$ treatment only partly removes Al from the lattice. This is caused by both reduced diffusivity of $SiCl_4$ in the channels of mordenite, and by the presence of residual Na^+ cations. The reduced diffusivity of $SiCl_4$ is responsible for the partial dealumination, while the residual Na^+ cations can react with the aluminium chlorides to form $NaAlCl_4$ which is precipitated in the channels. Finally, these chlorides are hydrolyzed during washing to produce $Al(H_2O)_6^{3+}$ species. Note that relative to the acid leaching process the dealumination by $SiCl_4$ generates only a few defect SiOH groups (19).

As it is emphasized above, it is possible to determine the relative ^{29}Si-NMR line intensities from different types of Al distributions in the lattice. Figure 16 shows two possible distributions for which the theoretical and experimental Si(nAl) configurations are compared. It is obvious, that the fully random distribution among all crystallographic T_1, T_2, T_3 and T_4 sites cannot account for the experimental results. The same conclusion holds for a random distribution in the 6-ring sheets, i.e., on sites T_1 and T_2 (19). The random distribution on sites $T_3 + T_4$, i.e. in the 4-membered rings, or on T_1 only or on T_2 only do not reproduce the experimental values of the Si(nAl) configurations either (19). In order to explain adequately the experimental results, it is of paramount importance to include the mechanism of

dealumination in the correct computation of the Al distribution. Figure 16 b shows, that if the Al atoms are only located on sites T_3 and T_4 and the configurations with only one Al atom in the 4-rings are excluded, a very good agreement is found between the calculated and experimental values of the Si(nAl) configurations. (Some discrepancy can be noted for the slightly dealuminated and the initial samples, which suggests that additional informations should be included for the as-synthesized samples. See also ref. 23).

We therefore propose an adequate picture for the mechanism of mordenite dealumination by acid leaching. In the initial sample, nearly all 4-rings contain two Al atoms. As dealumination proceeds, 4-rings with no Al atoms appear in the structure and the remaining 4-rings thus contain two Al atoms. In addition, SiOH defect groups appear, the number of which is close to four per extracted Al atom. The model implies, that both Al atoms are quasi simultaneously extracted from the 4-ring. During subsequent dealumination, the structure is reorganized (even at 353 K) by recombining the SiOH defect groups. Indeed, the number of SiOH per extracted Al atom decreases from 4 to 0.6 during dealumination. Note that both X-ray diffraction studies (60) and theoretical calculations (61) suggest the preferential siting of Al in the 4-rings of the structure.

Very recently, pentacoordinated Al at $\delta = 30$ ppm was shown to exist in steamed crystalline or amorphous silic(oalumin)ate samples (Figure 17) (62). It was suggested that the presence of pentacoordinated Al may reduce the extent of coke formation during hydrocarbon cracking reactions. However, this interpretation is questioned and it is suggested that this line should belong to tetrahedral extraframework Al (63,64). Using 2DNMR, two different tetrahedral Al species can be distinguished in dehydrated Y zeolite samples. They give rise to separate signals in the F1 display where the characteristic lineshapes depend on the ratio of the quadrupole interaction constant and the rf field strength ω_{rf}. The framework tetrahedral Al is characterized by a lower quadrupole constant, while the strong quadrupolar interaction for the non-framework Al nucleus indicates that its tetrahedral symmetry is heavily distorted (64).

Incorporation of Al in the zeolite as a tetracoordinated species by treatment of zeolites with $AlCl_3$ is strongly supported by ^{27}Al-NMR spectroscopy (65-67). The proposed mechanism for the alumination of ZSM-5 involves the reactive hydroxyl nests (see above) both on the external surface and in the internal channels (67). Indeed, the FTIR results also show clearly that the intensity of SiOH groups (at 3740 cm^{-1}) decreases concomitantly to an increase in the Al(OH)Si acidic groups (at 3610 cm^{-1}) (66,67).

Application of ^{13}C-NMR to reactions on zeolites

^{13}C-NMR spectroscopy proves to be a powerful tool to characterize adsorbed species on various zeolites (7-10). The nature of the adsorbed species can be inferred from the usual chemical parameters, i.e. chemical shifts, linewidths and relaxation times. These latter allow one to study the mobility of the molecules on the surface. As an analytical tool, ^{13}C-NMR spectroscopy can also be used to determine the concentration of reactants and products as a function of time and hence kinetic constants can easily be determined.

The reactivity of 2-^{13}C-isopropanol adsorbed on K- and Cs-ZSM-5 zeolites is examined in a batch-reactor (68). Propylene is formed by dehydration at 200°C (Figure 18). The subsequent polymerization of propene to form paraffinic compounds is quite significant on K-ZSM-5, while Cs-ZSM-5 yields only ca 10 %
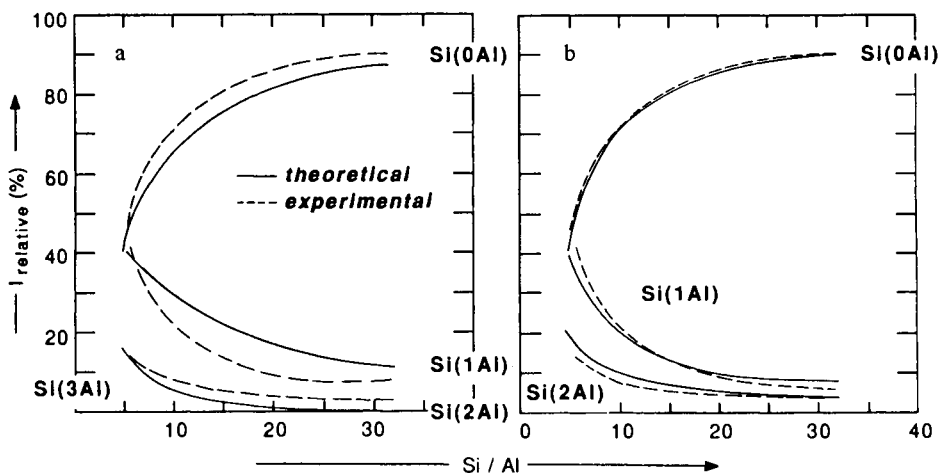
Figure 16. Comparison between the variation of the experimental Si(nAl) configurations and those computed from two Al distributions in the lattice: a) random among all sites and b) Al only on sites T_3 and T_4 with two or no Al atoms in the 4-rings. (Reproduced from ref. 19. Copyright 1986 American Chemical Society.)
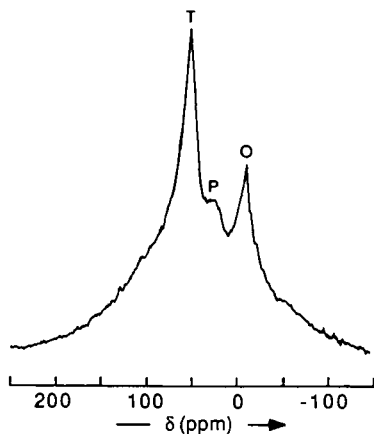
Figure 17. ^{27}Al-NMR spectrum of hydrothermally dealuminated faujasite. (Reproduced with permission from ref. 62. Copyright 1987 The Royal Society of Chemistry.)
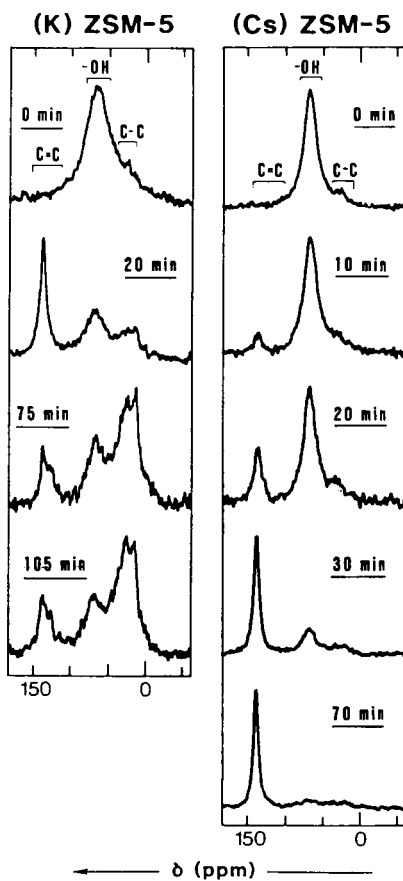
Figure 18. Evolution of high-resolution low-power ^{13}C-NMR spectra of 2-^{13}C-isopropanol adsorbed on K- and Cs-ZSM-5 zeolites. Reaction temperature: 200 °C, measuring temperature: 25 °C. (Reproduced with permission from ref. 68. Copyright 1985 Elsevier.)

of paraffins after 90 % conversion of isopropanol. A certain deactivation of the catalysts occurs, due to probable pore blocking by polymers and/or coke formation (68). On K-ZSM-5, olefins different from propylene are also detected (Figure 18). It is important to note that no diisopropylether has been detected on any of the catalysts. After 90-100 % conversion, the polymerized products are cracked at 370°C. The strongly adsorbed species entrapped in the channels as a result of pore blocking are analyzed by high-resolution MAS solid state ^{13}C-NMR (Figure 19). The Cs-ZMS-5 shows the presence of propene, cis- and trans-2-butenes, and cis-2-pentene, together with some aromatic compounds (35 mol %) and butane (65 %). The K-ZSM-5 only yields cis- and trans-2-butenes as olefins and toluene and ethylbenzene as aromatics (15 %), while the distribution of paraffinic compounds (85 %) is larger, including butane, isobutane, pentane and isopentane. These results emphasize the shape selective role of the alkali cations occluded into ZSM-5 channels.

Molecular traffic control (69), and other network tortuosity effects (70) have been postulated to affect the selectivity of zeolite-catalyzed organic conversion. To investigate and further discuss these hypotheses, the conversion of ^{13}C-labeled ethylene (*CH$_2$=*CH$_2$) is studied on the H-form of three intermediate pore size (ca 0.55 nm) pentasil-type catalysts : H-ZSM-5, H-ZSM-11 and H-ZSM-48. As the Al content (Si/Al = 30,28 and 21 respectively) and the particle size (ca 0.5 μm) of these catalysts are comparable and assuming that non-homogeneous Al distribution (clustering, zoning, etc.) effects are negligible or small, these catalysts thus differ only by their channel network tortuosities and intersection dimensions. Figure 20 shows that the oligomerization product of ethylene at ambient temperature is characterized by three distinct NMR lines, corresponding to terminal methyl (δ = 13.2 ppm), penultimate methylene (δ = 23.5 ppm) and inner methylene groups (δ = 31.9 ppm), respectively (71). H-ZSM-5 and H-ZSM-11 behave analogously, as expected, both having interconnected channels of comparable size and length : the oligomer chains are composed of 36 and 38 carbons respectively. (Note that the methyl and methylene line intensities are semi-quantitatively comparable using cross polarization with 5.0 ms contact time and a recycle time of 4.0 s.) On the other hand, H-ZSM-48 yields shorter oligomers (chain length of 22 carbons) and shows the presence of a rather high amount of unreacted ethylene (Figure 20). These ethylene molecules correspond to species trapped between occluded oligomers, which have no access to active sites because of the one-dimensional nature of the ZSM-48 network. These results provide clear evidence for an augmentation in molecular traffic when the dimensionality of the zeolite channel network increases, and for the need to distinguish between aging resulting from either pore or site blockage (72).

CONCLUSIONS

High resolution MAS multinuclear NMR is a very valuable tool to characterize zeolitic catalysts in the as-synthesized form, to detect changes that occur during their pretreatment and subsequent modifications and to follow the conversion of adsorbed reactants.

The HR ^{29}Si-NMR is able to resolve crystallographically different sites (e.g. highly siliceous ZSM-5) and helps the characterization of new type zeolites (ZSM-20) by comparing spectra with zeolites of known structures (Y zeolite). The Al distribution can be inferred from the ^{29}Si-NMR spectra provided adequate models are elaborated. Finally, a large amount of SiOH defect groups are identified in highly siliceous ZSM-5 samples.The quantitative determination of either tetra- or octahedral Al in the zeolitic samples requires the use of small flip angles for the ^{27}Al

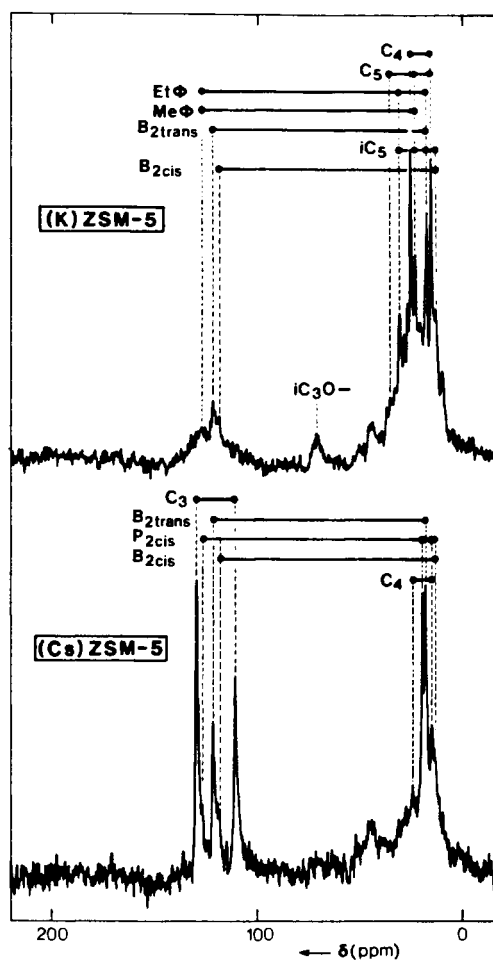Figure 19. High-resolution MAS solid-state ^{13}C-NMR spectra of the cracked products of the dehydration–polymerization products of 2-^{13}C-isopropanol. (Reproduced with permission from ref. 68. Copyright 1985 Elsevier.)
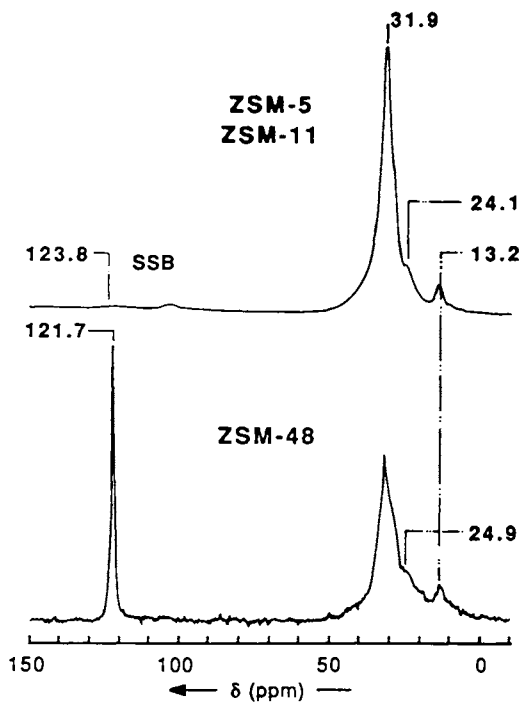
Figure 20. CP^{13}C-MAS–NMR spectra of oligomerized ethylene on H-ZSM-5, H-ZSM-11, and H-ZSM-48 zeolites. (Reproduced with permission from ref. 71. Copyright 1986 Elsevier.)

nuclei. The ^{17}O-NMR, almost unexploited at present, gives encouraging results for the analysis of Si-O-Si and Si-O-Al bonds.

The ^{7}Li- and ^{23}Na-NMR spectra are quite sensitive on the degree of hydration and the nature of the counterions (either SiO^{-} or (Al-O-Si)$^{-}$ groups). The ^{13}C-NMR analysis yields valuable information on the molecules incorporated into the zeolitic cages or channels during the synthesis. These molecules may remain intact (e.g. tetrapropylammonium in ZSM-5 or hexamethonium in ZSM-50) or are partially decomposed (e.g. tetramethylammonium in ZSM-39 and hexamethonium in ZSM-48 in presence of ammonium ions).

The combined used of ^{29}Si- and ^{27}Al-NMR leads to the determination of the silicon-aluminium ordering in mordenite. The Al atoms preferentially occupy tetrahedral positions in the four-membered rings of the structure. In addition, a mechanism of dealumination can be inferred, consisting in removing the Al atoms two by two from the four-membered rings. Four SiOH groups are generated per extracted Al atom in the beginning of dealumination and this number gradually decreases to two, suggesting that a substantial reorganization must necessarily occur for substantial dealumination.

The presence of pentacoordinated Al atoms is suggested by ^{27}Al-NMR in steamed crystalline or amorphous silic(oalumin)ate samples.

The conversion of reactants is illustrated by the dehydration-polymerization of 2-isopropanol adsorbed on K- and Cs-ZSM-5 zeolites as followed by ^{13}C-NMR. On the other hand, the polymerization of ethylene shows a clear-cut difference between three-dimensional channel systems (ZSM-5 and ZSM-11) able to promote the molecular traffic of reactants and on one-dimensional channel systems (ZSM-48) where some unreacted ethylene is still detected after polymerization.

Literature cited
1   Breck, D.W. Zeolites Molecular Sieves, Structure, Chemistry and Use, Wiley, New York, 1974
2   Barrer, R.M. Hydrothermal Chemistry of Zeolites, Academic Press, London, 1982
3   Lok, B.M.; Cannan, T.R.; Messina, C.A. Zeolites, 1983, 3, 282
4   Wilson, S.T.; Lok, B.M.; Messina, C.A.; Cannan, T.R.; Flanigen, E.M., J. Am. Chem. Soc., 1982, 104, 1146
5   Klinowski, J. Prog. NMR Spectrosc. 1984, 16, 237
6   Thomas J.M.; Klinowski, J. Adv. Catal. 1985, 33, 199
7   B.Nagy, J.; Engelhardt, G.; Michel, D. Adv. Colloid Interf. Sci. 1985, 23, 67
8   Pfeifer, H. in "NMR Basic Principles and Progress", Diehl, P.; Fluck, E.; Kosfeld, K., Eds. Springer, Berlin, 1972, p. 53
9   Duncan, T.M.; Dybowski, C. Surf. Sci. Rep. 1981, 1, 157
10   Derouane, E.G.; B.Nagy, J. in "Catalytic Materials : Relationship Between Structure and Reactivity"; Whyte, T.E. Jr.; Dalla Betta R.A.; Derouane E.G.; Baker R.T.K. Eds, ACS Symposium Series 248, Washington, 1984, p. 101
11   Lippmaa, E.T.; Alla, M.A.; Pekk, T.J.; Engelhardt, J. J. Am. Chem. Soc. 1978, 100, 1929

12 Lippmaa, E., Mägi, M.; Samoson, A.; Engelhardt, G.; Grimmer, A.R. J. Am. Chem. Soc., 1980, 102, 4889

13 Lippma, E. Mägi, M.; Samoson, A.; Tarmak, M.; Engelhardt, G. J. Am. Chem. Soc., 1981, 103, 4992

14 Fyfe, C.A.; Gobby, G.C.; Klinowski, J.; Thomas, J.M.; Ramdas, S. Nature 1982, 296, 530

15 Engelhardt, G.; Lohse, U.; Lippmaa, E.; Tarmak, M.; Mägi, M. Z. Anorg. Allg. Chemie, 1981, 482, 49

16 Derouane, E.G.; Dewaele, N.; Gabelica, Z.; B.Nagy, J. Appl. Catal. 1986, 28, 285

17 Ernst, S.; Kokotailo, G.T.; Weitkamp, J. Zeolites, 1987, 7, 180

18 Fyfe, C.A.; Gobbi, G.C.; Murphy, W.J.; Ozubko, R.S.; Slack, D.A. Chem. Lett. 1983, 1547

19 Bodart, P.; B.Nagy, J.; Debras, G.; Gabelica, Z.; Jacobs, P.A. J. Phys. Chem. 1986, 90, 5183

20 Bodart, P.; B.Nagy, J.; Gabelica, Z.; Derouane, E.G. Proc. Int. Conf. on Occurrence, Properties and Utilization of Natural Zeolites, Budapest, 1985, in press

21 Raeder, J.H. Zeolites, 1984, 4, 311

22 Lillerud, K.P., Zeolites, 1987, 7, 14

23 Raatz, F.; Roussel, J.C.; Cantiani, R.; Ferre, G.; B.Nagy, J. in Proc. Int. Symp. "Innovation in Zeolite Materials Sciences", Nieuwpoort, Belgium, Sept. 13-17, 1987

24 Klinowski, J.; Anderson, M.W., J. Chem. Soc., Faraday Trans. 1, 1986, 82, 569

25 Fyfe, C.A.; O'Brien, J.H.; Strobl, H. Nature, 1987, 326, 281

26 Hay, D.G.; Jaeger, H.; West, G.W. J. Phys. Chem. 1985, 89, 1070

27 Fyfe, C.A.; Kokotailo, G.T.; Kennedy, G.J.; Lyerla, J.R.; Fleming, W.W. J. Chem. Soc. Chem. Commun. 1985, 740

28 B.Nagy, J.; Gabelica, Z.; Derouane, E.G.; Jacobs, P.A. Chem. Lett. 1982, 1105

29 Debras, G.; Gourgue, A.; B.Nagy, J.; De Clippeleir, G., Zeolites, 1986, 6, 161

30 van Santen, R.A.; Keijsper, J.; Ooms, G.; Kortbeek, A.G.T.G., Stud. Surf. Sci. Catal., 1986, 28, 169

31 B.Nagy, J.; Gabelica, Z.; Debras, G.; Derouane, E.G.; Gilson, J.-P.; Jacobs, P.A. Zeolites, 1984, 4, 133

32 Lippmaa, E.; Samoson, A.; Mägi, M., J. Am. Chem. Soc. 1986, 108, 1730

33 Schmidt, V.H. Proc. Ampère Int. Summer School II, Basko polje, 1972, p. 75

34 Fernandez, C.; Lefebvre, F.; B.Nagy, J.; Derouane, E.G. in Proc. Int. Symp."Innovation in Zeolite Materials Science", Nieuwpoort, Belgium, Sept. 13-17, 1987

35 Timken, H.K.C.; Turner, G.L.; Gilson, J.-P.; Welsh, L.B.; Oldfield, E. J. Am. Chem. Soc., 1986, 108, 7231

36 Timken, H.K.C.; Janes, N.; Turner, G.L.; Lambert, S.L.; Welsh, L.B.; Oldfield, E. J. Am. Chem. Soc. 1986,108, 7236

37 B.Nagy, J.; Bodart, P.; Gabelica, Z.; Derouane, E.G.; Nastro, A. Stud. Surf. Sci. Catal. 1986, 28, 231

38 Bodart, P. Ph. D. Thesis, Facultés Universitaires de Namur, 1985

39 Melchior, M.T.; Vaughan, D.E.W.; Jacobson, A.J.; Pictorski, C.F. in "Proc. 6th Int. Zeolite Conference", Reno, 1983, D. Olson, A. Bisio, eds. Butterworths, Guildford, 1984, p. 684

40 Scholle, K.F.M.G.J. Ph. D. Thesis, Nijmegen, 1985

41 B.Nagy, J.; Bodart, P.; Collette, H., El Hage-Al Asswad, J.; Gabelica, Z.; Aiello, R.; Nastro, A.; Pellegrino, C. Zeolites, in press

42 Burgess, J. Metal Ions in Solution, Elis Horwood, New York, 1978, p. 141
43 Tianyo, S.; Ruren, X.; Liyun, Lo; Zhaohui, Y. Stud. Surf. Sci. Catal., 1986, 28, 201
44 Nastro, A.; Aiello, R.; Crea, F.; Pellegrino, C. Zeolites in press
45 B.Nagy, J.; Bodart, P.; Collette, H.; Gabelica, Z.; Nastro, A.; Aiello, R. in preparation.
46 Boxhoorn, G.; van Santen, R.A.; van Erp, W.A.; Hays, G.R.; Huis, R.; Clague, D.; J. Chem. Soc. Chem. Commun. 1982, 264
47 B.Nagy, J.; Gabelica, Z.; Derouane, E.G. Zeolites 1983, 3, 43
48 Gabelica, Z.; B.Nagy, J.; Debras, G. J. Catal. 1983, 84, 256
49 Gabelica, Z.; B.Nagy, J.; Debras, G.; Derouane, E.G. Acta Chim. Hung. 1985, 119, 275
50 Boxhoorn, G.; van Santen, R.A.; van Erp, W.A.; Hays, G.R.; Alma, N.C.M.; Huis, R.; Clague, A.D.H. in "Proc. 6th Int. Zeolite Conf., Reno 1983", D. Olson and A. Bisio, eds., Butterworths, Guildford, 1984, p. 694
51 El Hage-Al Asswad, J.; Dewaele, N.; B.Nagy, J.; Hubert, R.A.; Gabelica, Z.; Derouane, E.G.; Crea, F.; Aiello, R.; Nastro, A. Zeolites. in press
52 Dewaele, N.; Gabelica, Z.; Bodart, P.; B.Nagy, J.; Giordano, G.; Derouane, E.G. in Proc. Int. Symp. "Innovation in Zeolite Materials Science", Nieuwpoort, Belgium, Sept. 13-17, 1987
53 Scherzer, J. A.C.S. Symp. Ser. "Catalytic Materials : Relationship Between Structure and Reactivity" (Whyte, J.E., Jr. et al., eds). 1984, 248, 157
54 Kaliaguine, S.; B.Nagy, J.; Gabelica, Z.; in "Keynotes in Energy-Related Catalysis", Stud. Surf. Sci. Catal., in press
55 Debras, G.; Gougue, A.; B.Nagy, J.; De Clippeleir, G. Zeolites, 1986, 6, 241.
56 Kerr, G.T. J. Catal. 1969, 15, 200
57 Beyer, H.K.; Belenykaja, I.M.; Mishin, I.W.; Boberly, Y. Stud. Surf. Sci. Catal. 1984, 18, 133
58 Fejes, P.; Hannes, I.; Kiricsi, I.; Pfeifer, H.; Freude, D.; Oehme, W. Zeolites 1985, 5, 45
59 Thomas, J.M.; Klinowski, J.; Ramdas, S.; Hunter, B.K.; Tennakoon, D.T.B. Chem. Phys. Lett. 1983, 102, 158
60 Schlenker, J.L.; Pluth, J.J.; Smith, J.V. Mater. Res. Bull. 1968, 13, 169
61 Derouane, E.G.; Fripiat, J.G. in Proc. 6th Int. Zeolite Conf., Reno, 1983; Olson, D., Bisio, A.; eds.; Butterworths, Guildford, U.K., 1984, p. 717
62 Gilson, J.-P.; Edwards, G.C.; Peters, A.W.; Rajagopalan, K.; Wormsbecher, R.F.; Roberie, T.G.; Shatlock, M.P.; J. Chem. Soc., Chem. Commun. 1987, 91
63 Freude, D. in Proc. Int. Symp. "Innovation in Zeolite Materials Science", Nieuwpoort, Belgium, Sept. 13-17, 1987, in press.
64 Samoson, A.; Lippmaa, E.; Engelhardt, G.; Lohse, G.; Jerschkewitz, H.G., Chem. Phys. Lett., 1987, 134, 589.
65 Jacobs, P.A.; Tielen, M.; B.Nagy, J.; Debras, G.; Derouane, E.G.; Gabelica, Z. in Proc. 6th Int. Zeolite Conf., Reno, 1983; Olson, D., Bisio, A., eds.; Butterworths, Guildford, U.K., 1984, p. 783
66 Dessau, R.M.; Kerr, G.T., G.T. Zeolites, 1984, 4, 315
67 Chang, C.D.; Chu, C.T.-W. Miale, J.N.; Bridger, R.F.; Calvert, R.B.; J. Am. Chem. Soc. 1984, 106, 8143
68 B.Nagy, J.; Lange, J.-P.; Gourgue, A.; Bodart, P.; Gabelica, Z. Stud. Surf. Sci. Catal. 1985, 20, 127
69 Derouane, E.G.; Gabelica, Z.; J. Catal. 1980, 65, 486
70 Mirodatos, C.; Barthomeuf, D., J. Catal. 1985, 93, 246
71 Derouane, E.G.; Lefebvre, C.; B.Nagy, J. J. Molec. Catal. 1986, 38, 387
72 Beekman, J.W.; Froment, G. Ind. Eng. Chem. Fund. 1979, 18, 245

Chapter 2

Analysis of Cation Position in Ion-Exchanged Y Zeolites by ^{23}Na NMR

L. B. Welsh and S. L. Lambert

Allied-Signal Engineered Materials Research Center, 50 East Algonquin Road, Box 5016, Des Plaines, IL 60017-5016

The results presented here indicate that sodium ions in different cation sites in Y zeolites can be distinguished by their sodium-23 NMR chemical shift at high magnetic fields. As a result, sodium-23 NMR can be used to monitor the sodium cation distribution extant after partial cation exchange. To illustrate this technique, two cation exchanged series of hydrated Y zeolites, ammonium/sodium and calcium/sodium, have been studied by sodium-23 magic angle spinning NMR (MASNMR). Spectral simulations with symmetric lines were used to determine the chemical shift and relative strength of the constituent lines. These NMR lines were then correlated with the specific cation sites of Y zeolite in the supercages, sodalite cages, and hexagonal prisms using cation site locations and occupancies derived from XRD and IR studies. The sodium-23 MASNMR results are consistent with the selective removal of sodium cations from the Y zeolite supercages by the partial cation exchange, and demonstrate that this technique can be used to monitor how cation distributions in Y zeolites change with various sample treatments.

High resolution solids Nuclear Magnetic Resonance (NMR) techniques have been used extensively in recent years to characterize zeolitic materials, by studying the zeolite frameworks. By comparison, relatively little effort has been devoted to the study of cations in zeolites using such NMR techniques. It is the intent of this paper to examine the scope of information which can be obtained via the application of high resolution solids NMR techniques at high magnetic fields to the study of cations in zeolites. Specifically, the use of sodium-23 magic angle spinning NMR (MASNMR) to probe the chemical shift differences of sodium cations in the supercages, sodalite cages and hexagonal prisms of Y zeolite will be discussed.

The location of cations in zeolites is of considerable practical importance since their locations can affect, among others,

cation exchange effectiveness, and the sorption and diffusion properties of organic molecules in zeolites. The cation positions in zeolites have been probed in the past using a number of different techniques. Perhaps the most widely applied is that of x-ray diffraction (XRD) (1-3). Most of the cation location data in the literature which are relevant to this study have been generated by these XRD methods, including what is known about the location of sodium cations in Y zeolite. The work of Mortier et al. (4) and others has shown that there are cations located in the hexagonal prisms, in the sodalite cages and in the supercages of the faujasite structure. The most significant problem encountered in using XRD for this purpose is that only the stationary cations can be located. Since some of the cations in zeolites are very mobile, especially in the presence of water, often fewer than 50% of the cations can be located for hydrated samples by XRD techniques. A higher percentage (nearly 100%) of the cations can often be located if the sample is dehydrated to reduce cation mobility; however, the dehydration step may itself alter the distribution of cations.

IR methods have also been used to study cation locations in zeolites. For example, the work of Roessner et al. (5) follows the migration of calcium and rare earth cations to various sites in Y zeolite. By looking at the double-six-ring vibration band, he shows that the cation locations depend on the exchange procedure and thermal treatment of the samples. Only limited information was obtained for the cations in the supercage and the sodalite cage using IR, the same cations which x-ray techniques have the most difficulty locating. In contrast, as a technique to study cations in zeolites, NMR has the advantage that the mobile cations are the most easily observed. Since the effects of second-order quadrupolar interactions are reduced at high magnetic fields, the use of a high field NMR spectrometer for this study significantly enhances the spectral resolution that can be achieved and increases the percentage of NMR observable sodium cations.

For our high resolution solids NMR studies, two series of samples were prepared in which the locations of the remaining sodium ions were varied in a systematic manner. These series were partially exchanged Y zeolites with either calcium or ammonium ions replacing some of the sodium ions. The exchange isotherms for Y zeolites, with framework Si/Al mole ratios near 2.7, indicate that for calcium and ammonium ions only about 70% of the sodium cations can be exchanged at ambient temperatures (6). Considering the relative populations of the exchange sites in the hexagonal prism (site I), in the sodalite cage (site I') and in the supercage (site II) as determined by XRD (1-4), these data indicate that only the supercage sites are initially exchanged. Sherry has pointed out that this limit may be kinetic, since he achieved 95% exchange of calcium for sodium in a Y zeolite by using an exhaustive exchange procedure (7). His results also indicate that water stripping of cations can play an important role in equilibration of cation locations in Y zeolites. Thermal treatments of partially exchanged Y zeolites are also known to accelerate the redistribution of the cations among all of the exchange sites (7). These data were used to help interpret the NMR data collected in this study.

EXPERIMENTAL

Sample Description and Preparation. All of the samples discussed in
this paper were prepared from a highly crystalline sample of LZY-52,
a Na-Y zeolite from Linde. Two series of partially exchanged
samples were prepared. The same exchange procedure was used in the
preparation of all the samples of a given series. Only the amount
of calcium or ammonium salt added was varied. This procedure
consisted of dissolving the calcium or ammonium salt in 100 cc
deionized water. The solution concentrations ranged from 0.03M to
0.5M for calcium and 0.08M to 1.0M for ammonium salts. The Na-Y
zeolite (10 g, volatile-free) was slurried in the exchange solution
for 72 hours at room temperature. The exchanged Y zeolite was
washed and the samples were dried in a forced air oven at 40°C
overnight to remove the interparticulate water. In the course of
this study we have observed that the exact distribution of cations
in a Y zeolite is very dependent on both the sample preparation and
the handling procedures. Comparison of these data with data
generated from samples whose histories are different or unknown
must proceed with caution.
     A nine-sample series of calcium exchanged Y zeolites and an
eight-sample series of ammonium exchanged Y zeolites were prepared.
The chemical analyses obtained on these samples are given in Table I
along with the calculated percent exchange. The percent exchange
was calculated as the percentage of cation sites which are not
occupied by sodium ions divided by the total number of cation
exchange sites. The ammonium exchanged series extended over the
range of 0 to 56% substitution for sodium while the calcium
exchanged series covered the range of 0 to 62% substitution.
     The samples discussed in this paper were studied in the
hydrated state. All samples were equilibrated at 50% relative
humidity for 18 hours before the NMR data were obtained. This was
done to produce samples with reproducible levels of hydration. The
loss on ignition (LOI) at 900°C of the equilibrated samples was
about 25%. Portions of each preparation were dried at 150°C, which
reduced the LOI at 900°C to 2%. NMR spectra of these dehydrated
samples were also obtained. The interpretation of the dehydrated
sample spectra is complicated by the presence of larger quadrupolar
interactions and broader linewidths. Results on the dehydrated
zeolites will be discussed in a later publication.
     Acquisition, Processing and Simulation of Sodium-23 NMR
Spectra. Sodium-23 MASNMR spectra were obtained on 6.3, 8.45 and
11.7 Tesla multinuclear solids NMR spectrometers at Spectral Data
Services and the University of Illinois in Champaign, Illinois.
Sample spinning rates of 3 to 5 KHz were used in most cases. A
typical spectrum was acquired using 1000 scans, a recycle time of
0.5 sec. and an rf excitation pulse width of 2.0 microsec. Since
the sodium-23 nucleus has a quadrupolar moment, the pulse width was
chosen to be less than 1/4 of a 90 degree pulse of sodium in
solution. The integrated intensity of the sodium NMR lines in the
spectrum then closely approximates the concentration of the sodium
species giving rise to the NMR lines. Spectra were typically
processed using a 25 Hz exponential broadening.

Table I

Cation Exchanged Samples of Y Zeolite

Sample Type	% Exchange (of Sites)	% Na$_2$O (VF)	%SiO$_2$ (VF)	% Al$_2$O$_3$ (VF)	Molarity of Exchange Solution
LZY-52	0	14.02	61.17	20.67	---
(Ca,Na)-Y	11	11.11	---	---	0.028 M
(Ca,Na)-Y	21	9.95	---	---	0.050 M
(Ca,Na)-Y	35	8.20	---	---	0.082 M
(Ca,Na)-Y	45	6.92	---	---	0.123 M
(Ca,Na)-Y	50	6.32	---	---	0.163 M
(Ca,Na)-Y	52	5.99	---	---	0.245 M
(Ca,Na)-Y	56	5.51	---	---	0.299 M
(Ca,Na)-Y	58	5.19	---	---	0.367 M
(Ca,Na)-Y	62	4.81	---	---	0.463 M
(NH$_4$,Na)-Y	9	11.40	---	---	0.080 M
(NH$_4$,Na)-Y	26	9.32	---	---	0.161 M
(NH$_4$,Na)-Y	32	8.56	---	---	0.241 M
(NH$_4$,Na)-Y	41	7.37	---	---	0.361 M
(NH$_4$,Na)-Y	47	6.59	---	---	0.482 M
(NH$_4$,Na)-Y	53	5.95	---	---	0.723 M
(NH$_4$,Na)-Y	55	5.64	---	---	0.883 M
(NH$_4$,Na)-Y	56	5.48	---	---	1.084 M

RESULTS

The sodium-23 MASNMR spectrum of a Na-Y zeolite at 132 MHz (11.7 Tesla) is shown in Figure 1a. As discussed below, the features of this spectrum arise from the presence of at least two separate NMR lines. A simulation of this spectrum, with symmetric lines of mixed Gaussian/Lorentzian character, is also shown in Figure 1a, along with the component lines of the simulation. Such a spectrum is difficult to simulate uniquely because of the overlap of the lines and the errors introduced into the spectrum as a result of spectral phasing and baseline correction.

     To determine if the features of the spectrum of Figure 1a indicate the existence of two or more lines, as simulated, or arise from a single NMR line with a lineshape due to second order quadrupole interactions, sodium-23 MASNMR spectra of a Na-Y zeolite

EXPERIMENTAL SPECTRUM

SIMULATED SPECTRUM

COMPONENT LINES

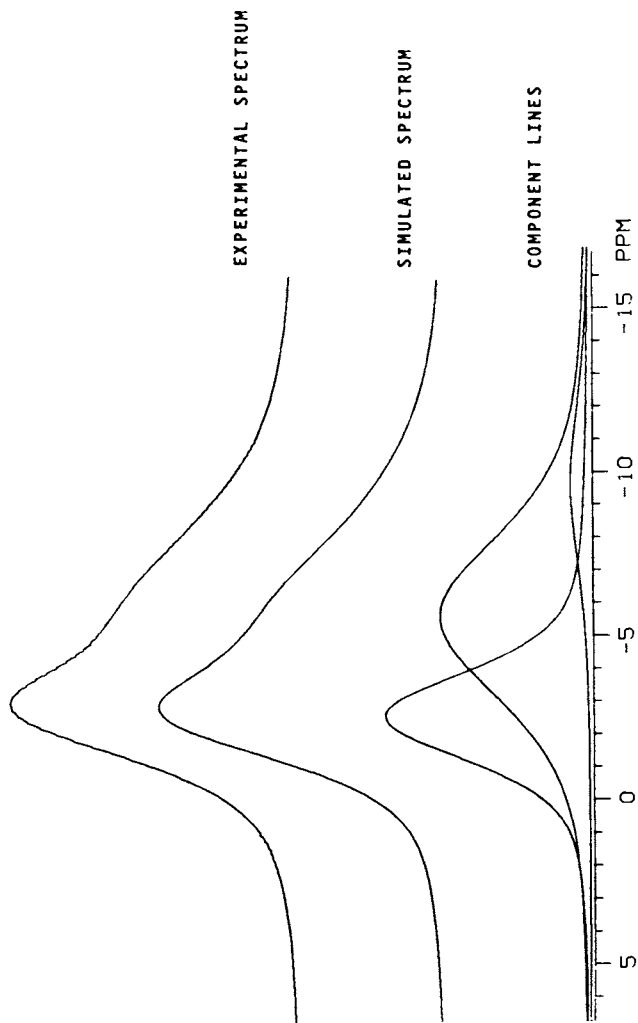PPM

-15   -10   -5   0   5

Figure 1a.   Sodium-23 MAS-NMR spectrum and three-line simulation of hydrated Na-Y zeolite at 132 MHz, with MAS of 4.0 KHz.
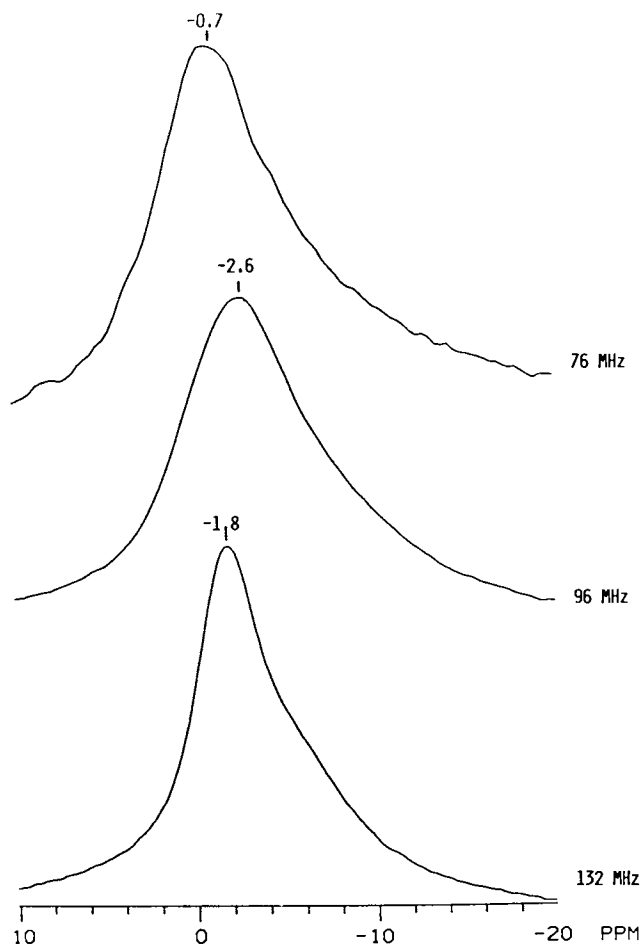
Figure 1b. Comparison of sodium-23 MAS-NMR spectra of the same
sample at 76 MHz (MAS = 2.5 KHz), 96 MHz (MAS = 4.1 KHz), and
132 MHz (MAS = 4.0 KHz).

were obtained at 76, 96 and 132 MHz under similar conditions. Plotted on the ppm scale, spectral features arising from second order quadrupole interaction effects would increase by a factor of 1.9, for the 96 MHz spectrum and 3.4, for the 76 MHz spectrum, when compared with the 132 MHz spectrum. Inspection of the spectra in Figure 1b indicates that this is not occurring, establishing that the spectral features are associated with separate sodium-23 MASNMR lines. This result can be more clearly observed for the partially exchanged, hydrated Y zeolites discussed below.

The sodium-23 MASNMR spectra of the series of hydrated (NH_4,Na)-Y zeolites obtained at 96 MHz, are presented in Figure 2. The order of the spectra are for increasing ammonium concentration from top to bottom. Inspection of this figure clearly shows that the peak near -2 to -3 ppm loses intensity relative to the peak near -7 ppm. At the highest exchange levels, there is little evidence of the line near -2 to -3 ppm. This again demonstrates the existence of more than one line in the spectra of these Y zeolites. (Several of these spectra were rerun two months after the spectra shown in Figure 2 were obtained to determine if the spectra were time dependent. Slight changes were observed in the relative line intensities of the spectra of the samples which were most highly exchanged, suggesting both that a nonequilibrium state of the sodium cations gave rise to the original spectra and that a subsequent equilibration over long periods of time at room temperature caused the observed changes.)

The entire series of spectra shown in Figure 2 have been simulated to determine the NMR properties of each line (chemical shift, linewidth and relative intensity). Various spectral simulations with symmetric lines were examined. Three line simulations were found to give the best fits; however, the simulations cannot be considered to be unique due to both the degree of overlap of the lines and the possible presence of line asymmetry due to quadrupolar interactions. The simulations of these spectra have been performed in the following manner. Since the resolution of the two peaks is highest for the 47% ammonium exchanged Y zeolite, this spectrum was simulated with three lines, and shown in Figure 3. The remaining spectra of the series were then simulated using the same three lines, keeping the linewidth and the line position changes to the minimum required for a reasonable simulation. The Na-Y zeolite was also simulated with the same set of lines. The results of these simulations are discussed later in this paper.

The sodium-23 MASNMR spectra of the series of hydrated (Ca,Na)-Y zeolites are presented in Figure 4, in order of increasing calcium ion concentration from top to bottom. The spectral changes observed in the calcium exchanged series, with increasing calcium concentration, are very similar to the changes observed in the ammonium exchanged series. The chemical shifts of the two pronounced peaks are slightly different, possibly indicating that there is some interaction between the sodium ions and the respective calcium and ammonium ions. The peak near -2 ppm decreases in intensity when compared to the peak near -6 ppm. Simulations of these spectra were performed in a fashion similar to that of the simulations of the spectra of the hydrated (NH_4,Na)-Y zeolite series.

Figure 2. Sodium-23 MASNMR spectra of a series of hydrated, partially ammonium exchanged Na-Y zeolites at 96 MHz. The level of ammonium exchange is as indicated.

EXPERIMENTAL SPECTRUM

SIMULATED SPECTRUM

COMPONENT LINES

10   0   -10   -20   -30 PPM

Figure 3.   Spectral simulation of the hydrated 47% ammonium
exchanged Y zeolite shown in Figure 2.
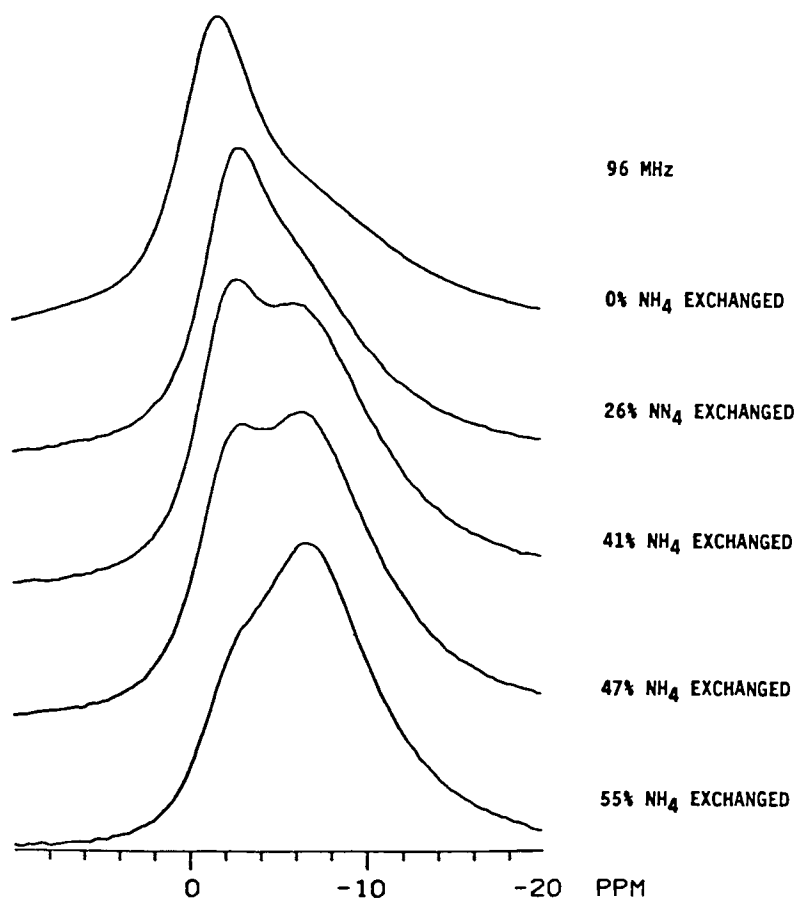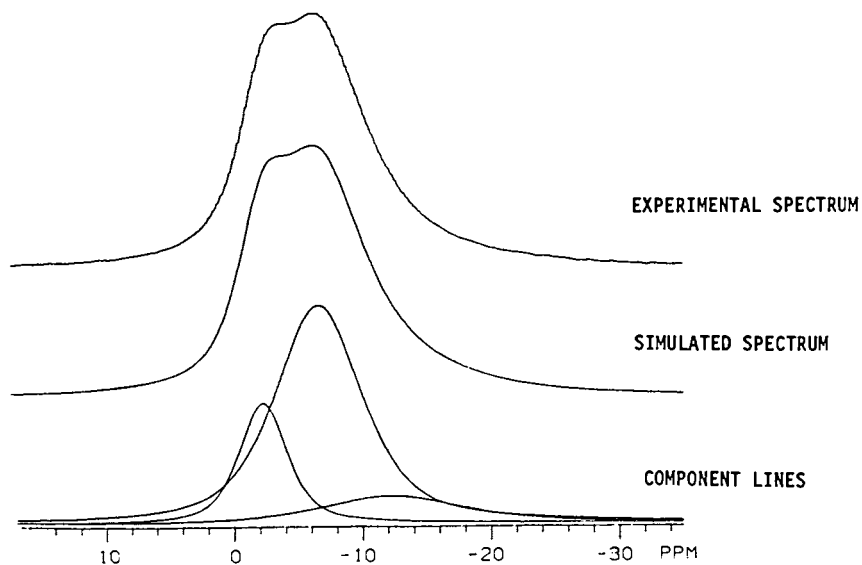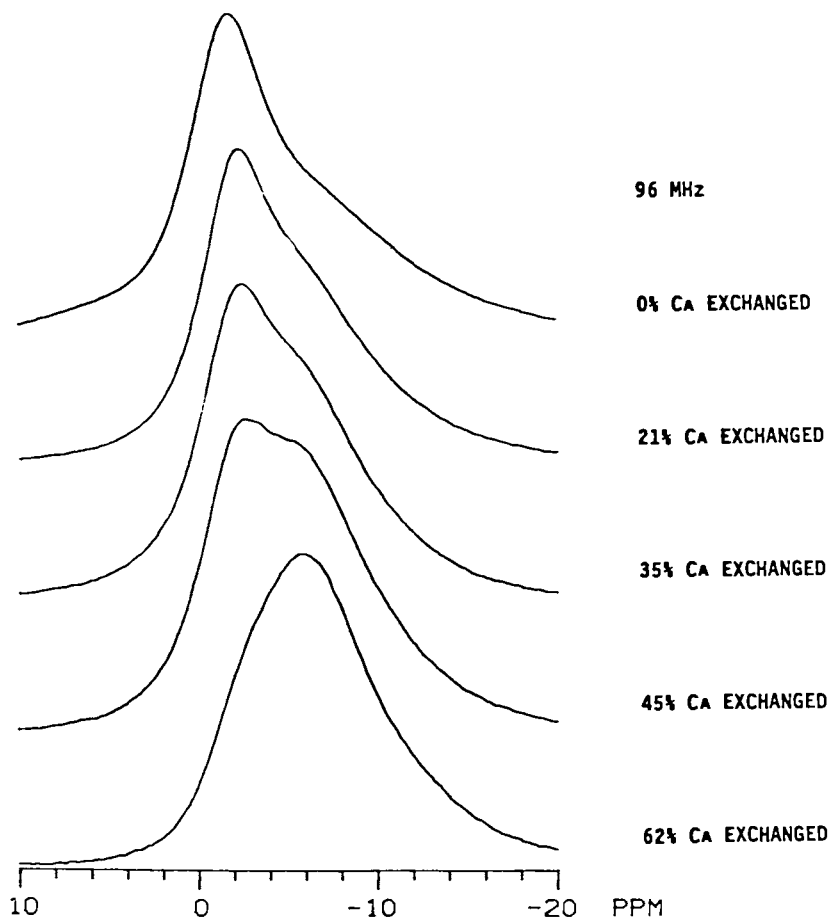
Figure 4. Sodium-23 MASNMR spectra of a series of hydrated,
partially calcium exchanged Na-Y zeolites at 96 MHz. The level
of calcium exchange is as indicated.

DISCUSSION

To understand the information on cation distributions contained in
the sodium-23 MASNMR spectra, requires a knowledge of the sodium-
ammonium and sodium-calcium cation populations resulting from the
cation exchange process. This involves not only the effects of the
actual conditions of cation exchange but the effects of the subse-
quent hydration, drying or other treatments on the cation
distributions. Considerable information on the initial occupancy of
the cation sites is available from the cation exchange isotherms of
the materials as synthesized (6). About 68% of the cations in a
Na-Y zeolite, having a Si/Al mole ratio of 2.7, are removed when the
exchange is performed at 25 to 50°C (10,11). Apparently the sodium
cations in the hexagonal prisms (site I) and in the sodalite cages
(sites I' and II') are not removed. The ammonium ions and the
highly hydrated calcium ions are too large to easily pass through
the six-membered ring restricting access to both the sodalite cages
and the hexagonal prisms. As a result, the sodium cations are
initially removed only from the supercage sites (Type II sites).
Only sodium cations should be found in the Type I, I' and II' sites
of (NH_4,Na)-Y zeolite until sufficiently severe conditions are used
to decompose the ammonium cation and convert the zeolite to a
(H,Na)-Y zeolite.
     Literature results indicate that the situation in a (Ca,Na)-Y
zeolite is considerably more complicated. Various XRD studies
(4,12), and IR studies (5) indicate that the calcium cations prefer
to occupy sites of higher coordination with increasing temperature.
Sodalite cage site I' and hexagonal prism site I appear to be
preferred relative to the supercage site II for calcium cations (5).
The work of Sherry (8) indicates that water stripping of the hydrated
calcium ions plays an important role in controlling the rate at which
calcium ions can penetrate the sodalite cage and then the hexagonal
prism. In dehydrated Y zeolites, the "bare" calcium ion can
penetrate to the Type I sites, which are favored. Sherry (7)
demonstrated that sodium in the sodalite and hexagonal prisms can be
removed by exchanging out 96% of the sodium ions in a Y zeolite with
28 exchanges of 24 hours each at 100°C. This supports the idea that
slow diffusion of calcium ions into the sodalite and hexagonal cages
does occur. Clearly, the sodium distribution for (Ca,Na)-Y zeolites
can be expected to depend on the degree of hydration, the time since
the exchange, and previous thermal treatments. As a result the
samples used in this study were handled at low temperatures to reduce
the thermal redistribution of the cations. All the samples were
prepared simultaneously and the NMR data were collected as quickly
as possible to retain the initial cation distributions.
     Various types of NMR experiments have previously been performed
on the cations of Y zeolites. The work of Basler (9) on hydrated
Y zeolites is particularly relevant. Performing static sodium-23
NMR measurements at 16 MHz, he observed a single NMR line which
disappeared as he exchanged in increasing amounts of calcium. He
concluded that sodium in the supercage was being preferentially
removed, and that sodium in the Type I and I' sites was unobservable
at such a low frequency, due to quadrupolar interactions. In order
to use the sodium-23 NMR spectra of Figures 2 and 4 to determine how

the distribution of sodium is changing as a result of the cation exchange process the sodium concentrations measured from the NMR spectra must be calculated from the spectral intensities. When the sodium NMR spectral intensity is integrated, the total spectral intensity (adjusted for sample weight) of each sample can be compared and plotted. This comparison is shown in Figure 5 for both the calcium and ammonium exchanged series. For each series the decrease in the integrated signal intensity with decreasing sodium concentration is nearly linear and in good agreement with the chemically determined sodium loss. This linear decrease of the integrated intensity of the Na NMR signal with Na loss indicates that all Na species are contributing to the NMR signal. Using these absolute spectral intensity data, the relative intensity of the NMR lines can be plotted, normalized to the sodium content of the Na-Y zeolite. These results are displayed in Figure 6 for the ammonium series and in Figure 7 for the calcium series. These figures then provide the appropriate data for correlation with the existing literature results of sodium ion distributions in Y zeolite. The general features of these two plots are roughly the same. The -2 to -3 ppm line decreases to near zero intensity as the sodium is removed, and the -6 or -7 ppm line shows a more gradual decrease. The low intensity line is roughly constant.

Assignment of the NMR lines to specific cation sites depends critically on two XRD results (3). The first is that XRD indicates cations in a Y zeolite reside only in the Type I, I' and II sites. The second is that XRD determined occupations of the Type I sites indicate that the percentage of the sodium cations in these sites is small, of the order of 15% or less, while the occupations of the Type I' and Type II sites are always substantially higher. With these results the following assignment of NMR lines of specific cation sites is believed to be warranted. The line near -2 ppm is apparently associated with sodium cations in the supercages. These cations are completely exchangeable. These hydrated sodium complexes are probably mobile but may also be associated with Type II sites. The line near -6 or -7 ppm is believed to be associated with sodium cations in the Type I' sites in the sodalite cages. These cations appear to be less readily exchanged than those in the supercages. The broader, less intense, line near -13 ppm is presumably associated with a small number of sodium cations in the Type I sites of the hexagonal cages, as well as any residual sodium residing in the zeolite but not associated with an exchange site.

SUMMARY

Two cation exchanged series of hydrated Y zeolites, ammonium/sodium and calcium/sodium, have been studied by sodium-23 MASNMR methods. The differences in chemical shift of the lines were correlated with the cation locations in Y zeolite using previously published XRD and IR data. As a result, the simulations and various intensity plots discussed in this report provide an analysis of the distribution of the sodium cations among the various Y zeolite cages, and a method of monitoring how these distributions change as a result of zeolite hydration and other treatments. The results presented here strongly indicate that sodium-23 MASNMR can be used as an analytical tool
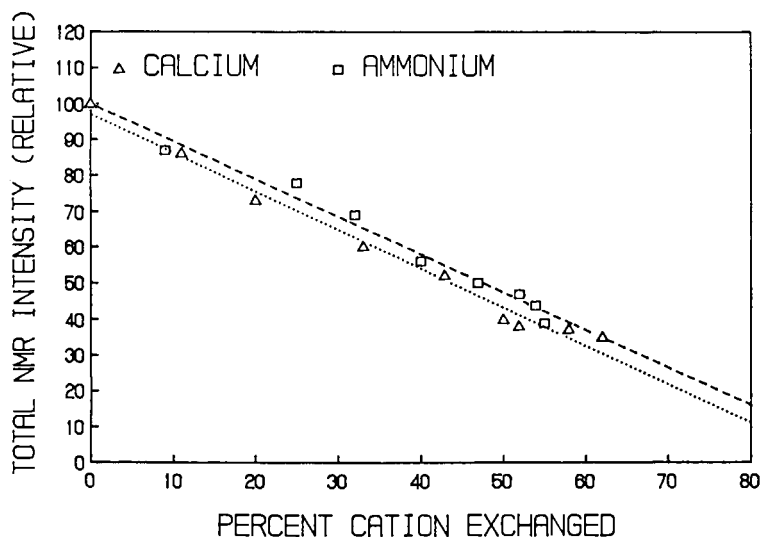
Figure 5.   Total integrated NMR line intensity of the hydrated, partially calcium and ammonium exchanged Na-Y zeolites versus the percent of cation exchange.

Figure 6.   Integrated NMR line intensities of the component NMR lines of the hydrated, partially ammonium exchanged Na-Y zeolite series normalized by the total integrated NMR line intensities given in Figure 5.
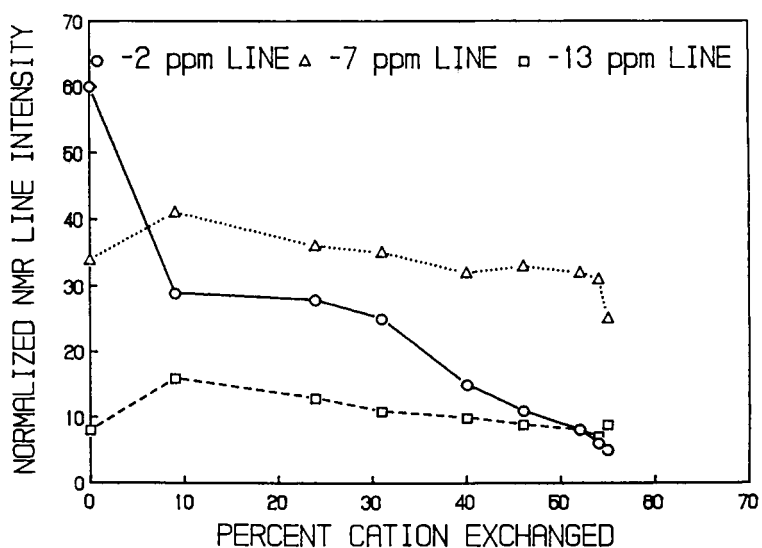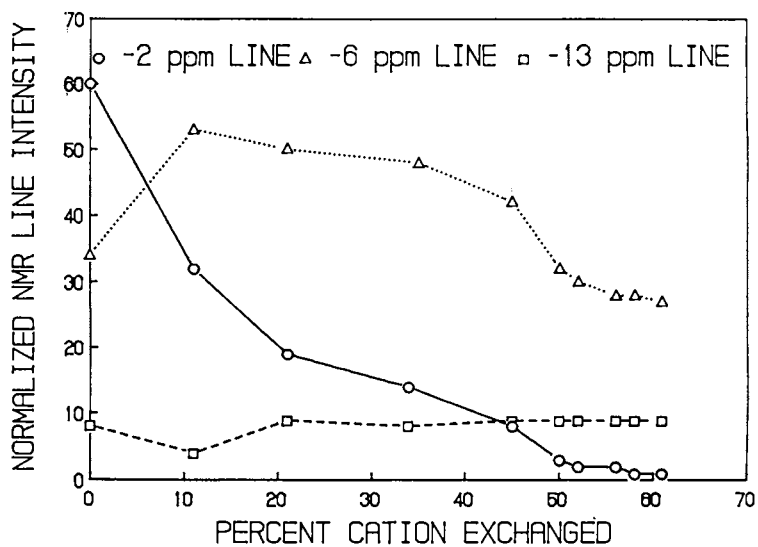
Figure 7. Integrated NMR line intensities of the component NMR lines of the hydrated, partially calcium exchanged Na-Y zeolite series normalized by the total integrated NMR line intensities given in Figure 5.

capable of providing cation distribution information not available by other techniques such as XRD or IR. Sodium-23 MASNMR spectra have also been obtained on these samples in the dehydrated state. The information on cation distributions available on the dehydrated Y zeolites will be presented in a subsequent publication.

LITERATURE CITED

1. Pearce, J. R., Mortier, W. J. and Uytterhoeven, J. B., J. Chem. Soc. Faraday Trans. 1, 1981, 77, 937-946.
2. Mortier, W. J., Van den Bossche, E. and Uytterhoeven, J. B., Zeolites, 1984, 4, 41.
3. Rubio, J. A., Soria, J. and Cano, F. H., J. Coll. and Interface Sci., 1980, 73, 312.
4. Mortier, W. J., "Compilation of Extra-Framework Sites in Zeolites," Butterworths, 1982, p 19.
5. Roessner, F., Steinberg, K. H. and Winkler, H., Zeolites, 1987, 7, 47.
6. Breck, D. W., "Zeolite Molecular Sieves: Structure, Chemistry and Use," Wiley Interscience, New York, 1974.
7. McDaniel, C. V., Maher, P. K., "Molecular Sieves," Society of Chemical Industry, London, 1968, p 168.
8. Sherry, H. S. in "Ion-Exchange - A Series of Advances, Vol. II." J. A. Marinsky, ed., M. Dekker, N.Y., 1969.
9. Basler, W. D., Colloids and Surfaces, 12, 59 (1984).
10. Sherry, H. S., J. Phys. Chem., 70, 1158 (1966).
11. Sherry, H. S., J. Phys. Chem., 72, 4086 (1968).
12. Dendooven, E., Mortier, W. J. and Uytterhoeven, J. B., J. Phys. Chem., 88, 1916 (1984).

Chapter 3

^{29}Si and ^{27}Al Magic-Angle Spinning–NMR Spectroscopic Study of Rare-Earth-Exchanged Y Zeolites

P. S. Iyer, J. Scherzer, and Z. C. Mester

Science and Technology Division, Unocal Corporation, P.O. Box 76, Brea, CA 92621

Lanthanum (La), cerium (Ce), praseodymium (Pr) and neodymium (Nd) exchanged Y zeolites with different rare earth content, as well as mixed lanthanum-cerium exchanged zeolites, have been prepared and characterized. ^{29}Si and ^{27}Al MASNMR spectra, surface area, crystallinity and unit cell size data were obtained for fresh and steamed zeolites. The stability of these zeolites toward steam has been investigated. An increase in lanthanum content from about 14 wt% La_2O_3 to over 20 wt% enhances the stability of the LaY zeolite towards dealumination by steam. A similar effect was observed for NdY and PrY zeolites. The resolution loss of ^{29}Si-NMR signals observed for paramagnetic ions (Nd^{3+}, Pr^{3+}, Ce^{3+}) and higher-valency ions (Ce^{4+}) is discussed. Upon steaming zeolites containing lanthanum-cerium mixtures, dealumination increases and stability decreases with increased cerium content of the zeolite. The differences in observed stability are discussed. XPS data show that steaming induces the migration of both aluminum and rare earths to the surface of the zeolite crystals.

Rare earth (RE) exchanged Y zeolites are of considerable interest due to their high catalytic activity for many reactions (1-4). Such zeolites are the major component of many modern hydrocarbon cracking catalysts (5,6). The structural characteristics of these zeolites have been extensively investigated. The cationic distribution in rare earth exchanged, natural faujasite, as well as in LaY, LaX and CeX zeolites, has been investigated by x-ray crystallography (7-10). The structural characteristics of fresh and hydrothermally treated rare earth Y zeolites have in fact been described in numerous papers (3,10-31). Using a variety of physical methods (e.g., x-ray diffraction, infrared and NMR spectroscopy), it was shown that hydrothermal treatment of rare earth Y zeolites results in framework dealumination. In a recent publication (27), it was shown that steaming of REY zeolites not

only results in framework dealumination but is accompanied by aluminum migration towards the zeolite particle surface. Correlations between structural characteristics (including extra framework aluminum) and catalytic properties of rare earth Y zeolites have been discussed more recently by Corma et al. (29) and Lemos et al. (30).

In their use as catalyst components, rare earth Y zeolites are frequently prepared by ion exchange with commercial rare earth salt solutions. Such commercial salts are mixtures of different rare earths, in which the major components are lanthanum, cerium, praseodymium and neodymium (5). These rare earth elements therefore play a major role in determining the physico-chemical characteristics and stability of Y zeolites that are used in many commercial catalysts.

Most of the published structural studies were done either on lanthanum or mixed rare earth exchanged Y zeolites. Few studies can be found on the effect of individual rare earths on the structural characteristics and stability of Y zeolites.

In this paper, ^{29}Si and ^{27}Al MASNMR spectroscopy is used in conjunction with crystallinity, surface area and unit cell size measurements to study individual rare earth exchanged Y zeolites in order to determine the effect of individual rare earths cations on their structure and stability. These methods are used to further probe rare earth induced structural changes that occur during hydrothermal treatment of the zeolites. The studies were extended to also establish the effect of different lanthanum-cerium mixtures on zeolite stability. The data presented and discussed are for lanthanum, cerium, praseodymium and neodymium exchanged Y zeolites, as well as for zeolites exchanged with different lanthanum-cerium mixtures.

Experimental

Materials. The rare earth exchanged Y zeolites were prepared from commercial NaY zeolite (LZ-Y-52 from Union Carbide Co.) and individual rare earth chlorides (99.9% pure, from Alfa Products). The NaY zeolite had a SiO_2/Al_2O_3 mole ratio of 4.93 and a unit cell composition of $(Na_2O)_{27.5}(AlO_2)_{55}(SiO_2)_{137}$. Portions of water washed NaY zeolite were exchanged twice with the corresponding rare earth chloride solution, according to a procedure described in the literature (10). The partially rare earth exchanged zeolites (RE,NaY) were calcined at 540°C for two hours in air. The calcined material was ammonium exchanged to further reduce the sodium content of the zeolite. The final product was a rare earth, ammonium Y zeolite (RE,NH$_4$Y) and contained between 14 and 15 wt% rare earth oxide. Part of this material was further rare earth-exchanged, resulting in a high-rare earth Y zeolite (Hi-REY).

In the case of cerium exchanged zeolites, the ionic exchanges were carried out under nitrogen, in order to avoid the oxidation of cerium (III) ions. Part of the cerium (III) exchanged zeolite was calcined under oxygen for 6 hours at 540°C in order to convert cerium (III) to cerium (IV) ions. Lanthanum-cerium exchanged zeolites were prepared with the following composition: 75% La, 25% Ce; 50% La, 50% Ce; and 25% La, 75% Ce.

To establish the effect of hydrothermal treatment upon the rare earth exchanged zeolites, portions of these zeolites were steamed at different temperatures under 100% steam, and characterized by different physical methods.

^{29}Si and ^{27}Al NMR Spectroscopy: Instrumentation and Measurements.

^{29}Si MASNMR spectra were obtained on an IBM AF270 NMR spectrometer at a frequency of 53.7 MHz. Samples were spun in 7mm alumina rotors at speeds between 2.5 and 3.5 KHz. Chemical shifts were referenced to external TMS set to 0.0 ppm by sample exchange, using a suitable secondary standard. For each spectrum, 2K data points were digitized during a 51 msec data acquisition. The data were zero filled to 4K and apodization equivalent to 20 to 50 Hz of line broadening was applied prior to Fourier transformation. Typically, 200 to 2000 scans were needed to produce suitable signal to noise levels.

70.4 mHz ^{27}Al MASNMR spectra were also recorded on the same instrument. Typical scan conditions involved 18° (1 μsec) pulse with a recycle delay of 0.2 secs. 2K data points were acquired over 31 msec acquisition time (corresponding to a sweep width of 33.3 kHz). The data were zero filled to 4K and 50 Hz line broadening applied before Fourier transformation. Samples were spun in 7 mm zirconia rotors fitted with vespel end caps, at 3.0 to 3.5 kHz. Chemical shifts reported are referenced to external aqueous $Al^{3+}(H_2O)_6$ (set to 0.0 ppm).

A 18° flip angle was employed to make the ^{27}Al signal intensities as quantitative as possible. In calculating Al^{VI}/Al^{IV} ratios, it was assumed that the spinning sidebands (SSB) were of equal intensities, as observed in the fresh zeolite samples.

Other Measurements. The x-ray diffraction patterns were recorded and unit cell sizes measured on a Siemens D-500 diffractometer. The XPS data were obtained on a Escalab Mark V instrument, made by V.G.

Results and Discussion

The chemical composition and selected properties of the materials prepared are listed in Table 1. The rare earth (RE) content of RE,NH_4Y zeolites shows that about 2/3 of the exchange sites are occupied by rare earth ions. The rare earth content of Hi-REY zeolites shows that over 75% of sites are occupied by rare earth ions. In some of the Hi-REY samples where rare earth exchanges were carried out after calcination, the sum of RE^{3+} and Na^+ equivalents is higher than that required to compensate the framework charge. This is due to formation of lower-valency hydroxyl-ions $[REOH^{2+}, RE(OH)_2^+]$ during calcination. Steaming results in greater unit cell size shrinking for RE,NH_4Y than for Hi-REY. A significant loss of crystallinity occurs during steaming of RE,NaY zeolites, due to their relatively high sodium content.

TABLE I.   COMPOSITION AND SELECTED PROPERTIES
OF RARE EARTH EXCHANGED Y ZEOLITES

REY Type	RE_2O_3, wt%	Na_2O, wt%	STEAMED REY (788°C/5h)[a]		
			% Cryst, (e)	SA, m^2/g	U.C., Å (e)
La, NaY	14.3	3.9	73	630	24.64
La,NH_4Y	14.5	0.3	73	680	24.58
Hi-LaY	25.4	0.6	71	650	24.70
La,Ce,NaY (3:1)[b]	11.7/3.8[c]	4.0	--	330	24.62
La,Ce,NH_4Y (3:1)	103/3.5	0.6	69	660	24.54
Hi-La,CeY (3:1)	16.5/5.4	0.4	54	550	24.63
La,Ce,NaY (1:1)	7.7/8.4	4.2	0	260	24.58
La,Ce,NH_4Y (1:1)	6.7/7.1	0.3	59	645	24.46
Hi-La,CeY (1:1)	10.5/13.6	0.6	36	430	24.61
La,Ce,NaY (1:3)	3.9/12.2	4.0	0	180	24.59
La,Ce,NH_4Y (1:3)	3.5/10.9	0.6	56	600	24.43
Hi-La,CeY (1:3)	5.3/16.6	0.6	21	280	24.59
Ce,NaY	14.2[d]	4.1	<5	40	--
Ce,NH_4Y	15.9	0.2	48	570	24.37
Hi-CeY	22.8	0.4	24	230	24.57
Pr,NaY	14.8	2.9	64	600	24.61
Pr,NH_4Y	14.2	0.2	69	650	24.58
Hi-PrY	19.1	0.4	70	690	24.68
Nd,NaY	16.2	4.2	64	625	24.60
Nd,NH_4Y	15.3	0.3	70	690	24.56
Hi-NdY	19.2	0.3	71	700	24.69

(a) The fresh, non-steamed materials had a surface area between 750 and 850 m^2/g,
     and a unit cell size between 24.68 and 24.72Å.
(b) The numbers in parantheses indicate the approximate La/Ce ratio in the zeolite.
(c) The first number represents wt% La_2O_3, while the second one represents wt% CeO_2.
(d) In the case of cerium exchanged zeolites, the rare earth content is expressed as
     weight percent CeO_2.
(e) Crystallinity and Unit cell sizes were measured according to ASTM 3906 and 3942,
     respectively.

The ^{29}Si NMR spectra of Y zeolites can exhibit up to five distinct signals, which can be assigned to the five possible types of SiO_4 tetrahedra with different numbers of AlO_4 tetrahedra connected to them ([32]). The signals marked Si(nAl), (n = 0-4), correspond to SiO_4 tetrahedra connected to n AlO_4 tetrahedra. From the chemical shifts and corresponding signal intensities, a quantitative distribution of the five Si(n Al) groupings is obtained that allows determination of the Si/Al ratio in the zeolite framework.

The ^{27}Al NMR spectra, on the other hand, exhibit signals that distinguish the presence of tetrahedral and octahedral aluminum species. Since the tetrahedral aluminum signal (∼50 ppm) is generated by framework aluminum, and the octahedral aluminum signal (∼0 ppm) is generated by non-framework aluminum species, the presence of such signals and their intensity can be used to investigate the dealumination process of the zeolite.

LaY Zeolites. The ^{29}Si NMR spectra of different LaY zeolites are shown in Figure 1A. The spectrum of fresh La, NaY shows signals at -89, -95, -101 and -106 ppm, corresponding to Si(3Al), Si(2Al), Si(1Al) and Si(0Al) groups, respectively, with the strongest signals given by Si(1Al) and Si(2Al) structural units. The spectrum is similar to that of NaY zeolite.

The spectrum of fresh La,NH$_4$Y zeolite also resemble that of La, NaY, except for evidence of dealumination and some loss in resolution. Such a loss in resolution can be caused by cationic migration and associated framework distortions during the thermal treatment prior to ammonium exchange ([10]), as well as by a partial loss in crystallinity ([33]). The effect of short-range disorder caused by bond length and angle distortions on ^{29}Si NMR resonances has been reported previously in the literature ([24,34,35,36]). The spectrum of dry Hi-LaY zeolite shows good resolution, similar to the spectrum of La, NaY.

Upon steaming, La,NH$_4$Y zeolite shows a dramatic change in the distribution of structural groups in the framework. The predominant group observed arises from Si(0Al) units at -109.6 ppm. The Si(1Al) and Si(2Al) groups observed at -102.8 and -96.6 ppm, respectively, appear with diminished intensities, clearly reflecting the advanced degree of dealumination (Figure 1A,c). An analysis of the spectrum shows a framework Si/Al ratio of 5.9, compared to 2.5 in the initial zeolite.

The spectrum of steamed Hi-LaY zeolite also shows framework dealumination, but to a lesser extent than steamed La,NH$_4$Y (Figure 1A,e). Besides a strong signal at -110.3 ppm corresponding to Si(0Al) groups, fairly strong signals are also seen at -104.8 and -99.7 ppm, corresponding to Si(1Al) and Si(2Al) structural units, respectively. The framework Si/Al ratio calculated for steamed La,NH$_4$Y is distinctly higher than that of steamed Hi-LaY: 5.9 vs 3.6. The greater dealumination of steamed La,NH$_4$Y is also evident in the lower unit cell size: 24.58A for steamed La,NH$_4$Y vs 24.70A for steamed Hi-LaY. These conclusions are in agreement with structural and infrared data reported in the literature ([10]). Roelofsen et al. ([26]) have found that at rare earth levels below 15% RE$_2$O$_3$, the degree of dealumination induced by steam is not
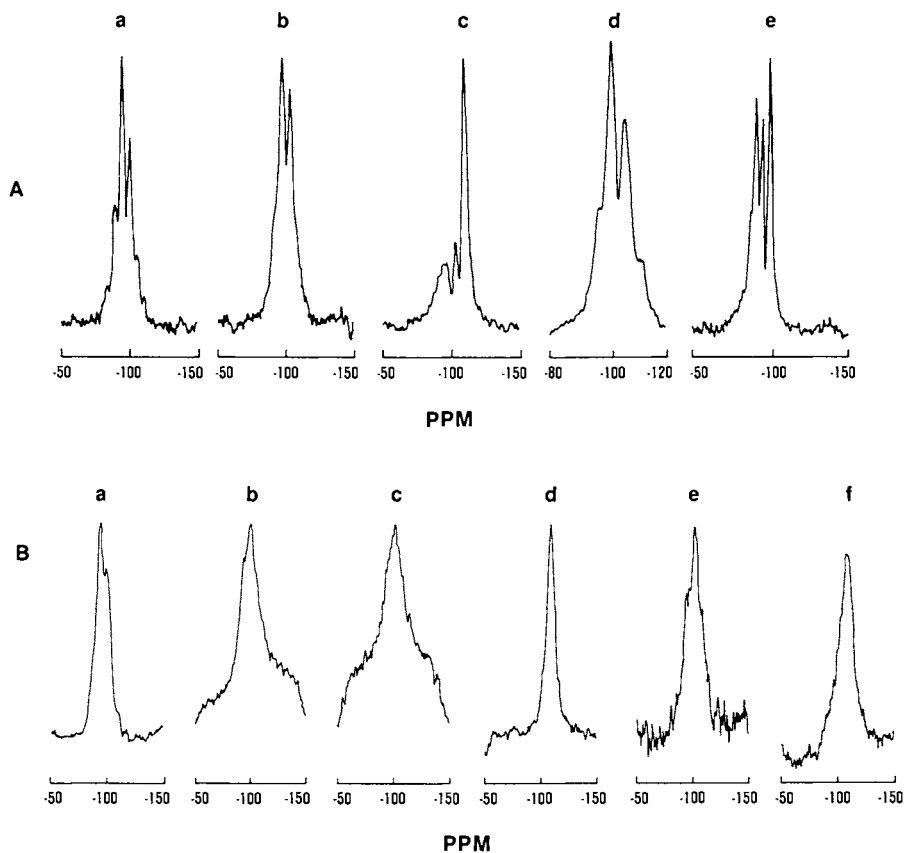
Figure 1: ^{29}Si NMR spectra of LaY and NdY zeolites.

A: (a) La,NaY, fresh; (b) La,NH$_4$Y, fresh;
(c) La,NH$_4$Y, steamed; (d) Hi-LaY, fresh;
(e) Hi-LaY, steamed.

B: (a) Nd,NaY,fresh; (b) Nd,NaY, calcined;
(c) Nd,NH$_4$Y, fresh; (d) Nd,NH$_4$Y, steamed;
(e) Hi-NdY, fresh; (f) Hi-NdY, steamed.

affected by the rare earth content. Our data show that higher
rare earth levels indeed have a strong impact upon the degree of
dealumination.

The lower degree of dealumination observed in steamed Hi-LaY
zeolite can be related to the stronger electrostatic field
generated by the large number of lanthanum ions and the lower
proton concentration in Hi-LaY. The strong electrostatic field
opposes the formation of cationic oxy- or hydroxy-aluminum species
and thus reduces framework dealumination, while the lower proton
concentration reduces the probability of Si-O-Al bond cleavage.
The large number of rare earth ions in the Hi-LaY zeolite also
oppose unit cell shrinking that accompanies framework
dealumination.

The higher thermal stability of LaY zeolites has been
attributed to the presence of lanthanum ions in the sodalite cages
(located at SI' sites) and bridged by one or more extra-framework
hydroxyl groups (3,7,25,31). At higher temperature, the hydroxyl
groups are converted to bridging oxide ions. Each lanthanum ion
in the sodalite cage is also coordinated to three lattice oxygen
atoms of the 6-membered ring that connects the sodalite cage to
the hexagonal prism. It is believed that such a configuration is
responsible for the high thermal stability of LaY zeolites.

NdY Zeolites. The ^{29}Si NMR spectrum of Nd,NaY shows two signals
at ∿-94 and -99 ppm (Figure 1B,a), flanked by weak spinning side
bands (SSBs) spaced approximately 3.2 kHz apart. Upon
calcination, these signals not only broaden considerably but also
display pronounced broad SSBs. This observation is attributed to
interactions between the silicon atoms and the paramagnetic metal
ion. Inspection of the corresponding ^{27}Al NMR spectra (Figure 2)
rules out any major dealumination or structure collapse. Only a
small amount of dealumination is seen to result from calcination
(Al^{VI}/Al^{IV} ∿ 0.17). The stronger interaction between silicon
atoms and metal ions can be attributed to the removal, during
calcination, of the water molecules associated with metal ions,
resulting in a decrease in the effective cationic radius.
Furthermore, the decrease in cationic radius also facilitates the
migration of neodymium ions from the supercages into the smaller
sodalite cages (and possibly hexagonal prisms) through the
6-membered rings (d ∿ 2.2A). Such an ionic migration due to
thermal treatment has been confirmed for lanthanum Y zeolites
(3,10,31).

It is interesting to note that while aqueous ammonium ion
exchange of the calcined Nd,NaY zeolite results in the removal of
the non-framework aluminum, as seen in the ^{27}Al NMR spectrum, the
^{29}Si NMR spectrum remains practically unchanged (Figure 1B,c).
The persistence of the broad resonance and associated SSB suggests
that the paramagnetic cation is irreversibly trapped in the
smaller cages.

Upon steaming, a considerable amount of dealumination occurs,
as evidenced by the broad ^{27}Al signal at ∿0 ppm (Figure 2d). The
^{29}Si peak observed at ∿109 ppm, corresponding to silicon atoms
with no immediate aluminum neighbors also corroborates this. The
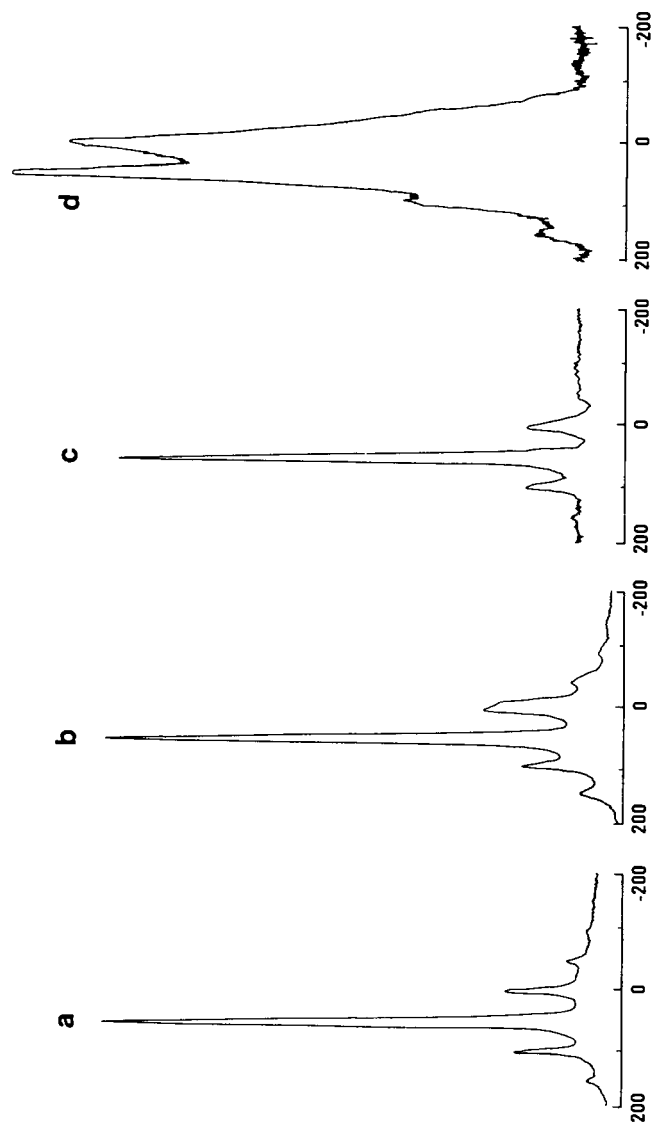
Figure 2: ^{27}Al NMR spectra of NdY zeolites.

(a) Nd,NaY, dry; (b) Nd,NaY, calc; (c) Nd,NH$_4$Y, dry; (d) Nd,NH$_4$Y, steamed. Steaming: 788°C/5 hrs.

signal is fairly sharp since these centers do not interact closely with the neodymium cations in the absence of aluminum atoms.

Similar to LaY zeolites, the steamed Hi-NdY zeolites show less dealumination than steamed Nd,NH$_4$Y as seen from the NMR spectra and unit cell size data (Table I).

PrY Zeolites. The ^{29}Si NMR spectrum of fresh Pr,NaY zeolite shows signals at -88.4, -93.8, -99.9 and -106.9 ppm (Figure 3A). The ^{29}Si and ^{27}Al spectra of fresh and steamed PrY zeolites are similar to those obtained for the corresponding NdY zeolites. Noticeably absent are SSBs in the spectra of PrY zeolites.

CeY Zeolites. The ^{29}Si-NMR spectra of different CeY zeolites are shown in Figure 3B. The spectra of all CeY zeolites show considerable line broadening. Such severe line broadening has also been observed by Roelofsen et al. (26). As in the case of LaY, steamed Ce,NH$_4$Y shows stronger dealumination than steamed Hi-CeY zeolite. The difference in the degree of dealumination is also reflected in the corresponding unit cell sizes: 24.37A for steamed Ce,NH$_4$Y vs 24.57A for steamed Hi-CeY. Steaming of partially oxidized CeY zeolite with about 1/3 of total cerium as cerium (IV) also shows dealumination and peak broadening.

A comparison of the spectra of steamed La,NH$_4$Y and Ce,NH$_4$Y suggests considerably stronger dealumination in the latter material, in spite of the poor quality of spectra obtained with cerium containing zeolites. The lower unit cell size of steamed CeNH$_4$Y with the same rare earth content supports this conclusion. The strong signal at -110 ppm in the spectrum of steamed Hi-CeY is indicative of the presence of amorphous silica, resulting from partial structural collapse (33).

A structure similar to that of LaY zeolites has been suggested for CeY zeolites (3,7). However, structural x-ray studies of CeX zeolites have shown (9) that the presence of trivalent and especially tetravalent cerium results in a considerable distortion of the 6-membered ring. Such a distortion could explain the lower hydrothermal stability and stronger dealumination of CeY zeolites vs LaY zeolites. Indeed, the loss in crystallinity and surface area observed for steamed CeY zeolites as compared to corresponding LaY zeolites (Table I) is indicative of significant structural collapse. Furthermore, the paramagnetism of trivalent cerium ions and the local framework distortions, caused primarily by tetravalent cerium ions, will result in a deterioration of spectral resolution.

La,CeY Zeolites. ^{29}Si MASNMR spectra for a series of fresh and steamed zeolites at different La-Ce ratios are presented in Figure 4. For fresh RE,NH$_4$Y, two clearly resolved peaks appeared around 97 ppm and 103 ppm. These chemical shifts can be assigned to Si(2Al) and Si(1Al) environments. The Si(2Al) signal decreases in intensity as the cerium content of the zeolite increases. This is most likely due to increased interactions between the paramagnetic cerium ions and high-aluminum containing structural units of the framework, leading to a weakening of the corresponding ^{29}Si NMR signal. Steam treatment resulted in dealumination as indicated by

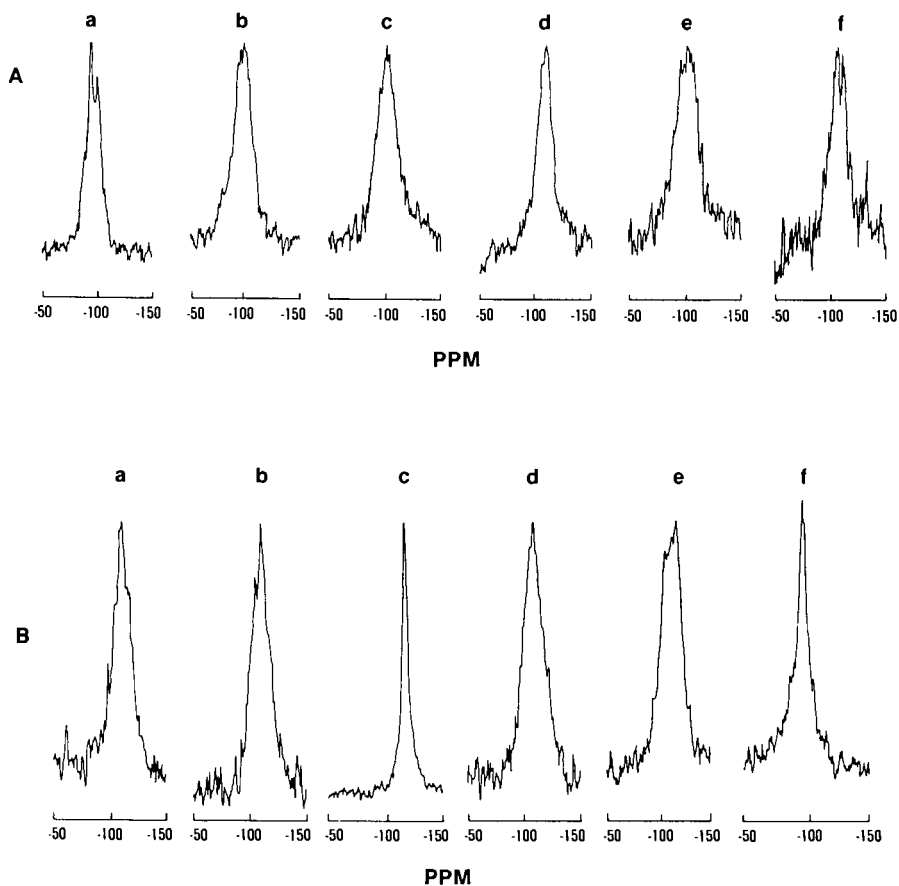Figure 3: ^{29}Si NMR spectra of PrY and CeY zeolites.

A: (a) Pr,NaY, fresh; (b) Pr,NaY, calc; (c) Pr,NH$_4$Y, fresh; (d) Pr,NH$_4$Y, steamed; (e) Hi-PrY, fresh; (f) Hi-PrY, steamed. Steaming: 788°C/5 hrs; calcination: 540°C/2 hrs.

B: (a) Ce,NaY, fresh; (b) Ce,NH$_4$Y, fresh; (c) Ce,NH$_4$Y, steamed; (d) Ce,NH$_4$Y oxidized, steamed; (e) Hi-CeY, fresh; (f) Hi-CeY, steamed. Steaming: 788°C/5 hrs.

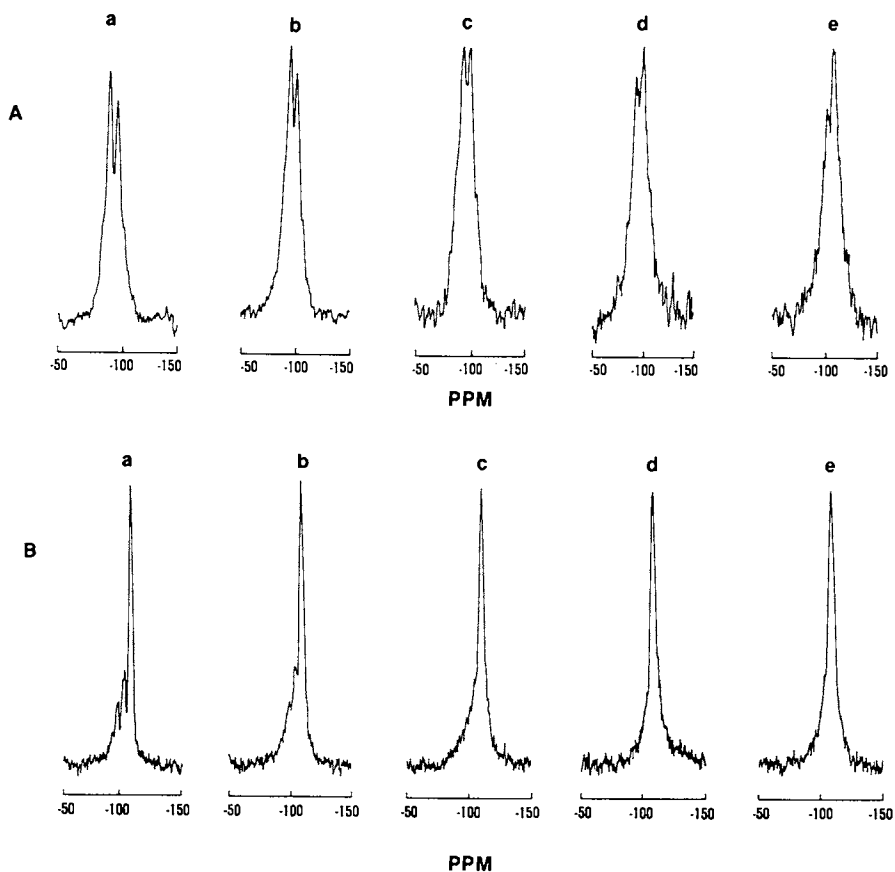the emergence of a narrow peak between 105-110 ppm. This range for chemical shifts is characteristic of Si(OAl) environments including amorphous silica. The degree of dealumination in steamed zeolites increases as the cerium content increases. This is reflected in the ^{29}Si-NMR and ^{27}Al-NMR spectra of the steamed zeolites (Figures 4 and 5). The peak around 57 ppm corresponds to tetrahedral (framework) aluminum (Figure 5), while the one around 0 ppm corresponds to octahedral aluminum. The ratio between the octahedral and tetrahedral aluminum peak areas increases in the order LaY < La,CeY (3:1) < La,CeY (1:3) < CeY from 0.035 to 0.26, indicating a corresponding increase in framework dealumination. Although the accuracy and absolute values of these ratios are debatable (38), the trend shown by them is in agreement with other physical data (vide supra).

The effect of steaming severity on dealumination is shown in Figure 6. The ^{29}Si NMR spectra show that, for a specific zeolite composition, framework dealumination increases with increasing steaming severity.

The fresh RE,NaY samples all displayed spectra similar to a NaY sieve. For the lanthanum-cerium binary exchanges, only two peaks were well resolved at 94-98 and 100-103 ppm. Steam treatment of Hi-REY, similarly to RE,NH$_4$Y, resulted in de-alumination characterized by the appearance of a peak at 108-111 ppm. Substantial retention of the Y zeolite framework was observed for 100% La and 75% La/25% Ce exchanges indicating the stabilizing influence of lanthanum over cerium.

Crystallinity, surface areas and unit cell constants of the steam treated zeolites are shown in Table I. Hydrothermal treatment diminished surface areas and crystallinity more severely for Hi-REY and RE,NaY than for Lo-REY. The greater decrease in crystallinity and surface area of Hi-REY compared to RE,NH$_4$Y, upon steaming, reflects the lower stability of Hi-REY due to its higher cerium content. Surface areas of steamed RE,NH$_4$Y, Hi-REY and RE,NaY decreased with increasing cerium content indicating declining stabilities in this direction. The crystallinity of the steamed zeolites showed a similar trend (Figure 7A). At similar sodium content of about 4% Na$_2$O, the surface area of steamed materials are higher for zeolites with higher La/Ce ratios, indicating higher hydrothermal stabilities.

Unit cells, similar to surface areas, also shrank with increasing relative cerium content upon steaming (Figure 7B). Unit cell size measurements refer only to the crystalline fraction of the material and do not reveal loss of crystallinity as do surface area measurements. At a fixed La-Ce ratio, steamed RE,NH$_4$Y shows the strongest unit cell decrease. The relatively small change in unit cell size for RE, NaY may seem surprising but the higher level of sodium in the zeolite prevented extensive lattice contraction (37). At low sodium and low rare earth exchange levels, however, such contractions are quite pronounced. For the steamed Hi-REY, unit cell constants decreased with increasing cerium content.

The experimental data obtained for La,CeY zeolites suggest the existence of a correlation between hydrothermal stability and degree of dealumination under steam. The less stable zeolites are
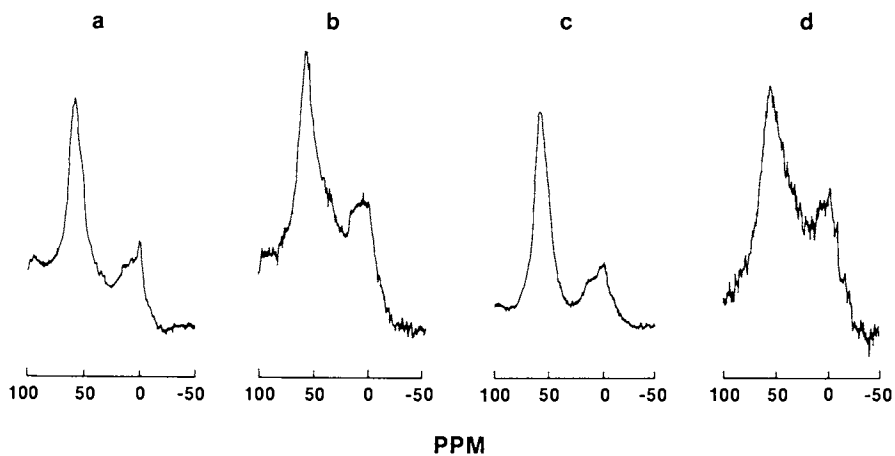
Figure 5: ^{27}Al NMR spectra of steamed La,Ce,Y zeolites.
(a) La,NH$_4$Y; (b) La,CeNH$_4$Y (3:1); (c) La,Ce,NH$_4$Y
(1:3); (d) Ce,NH$_4$Y.
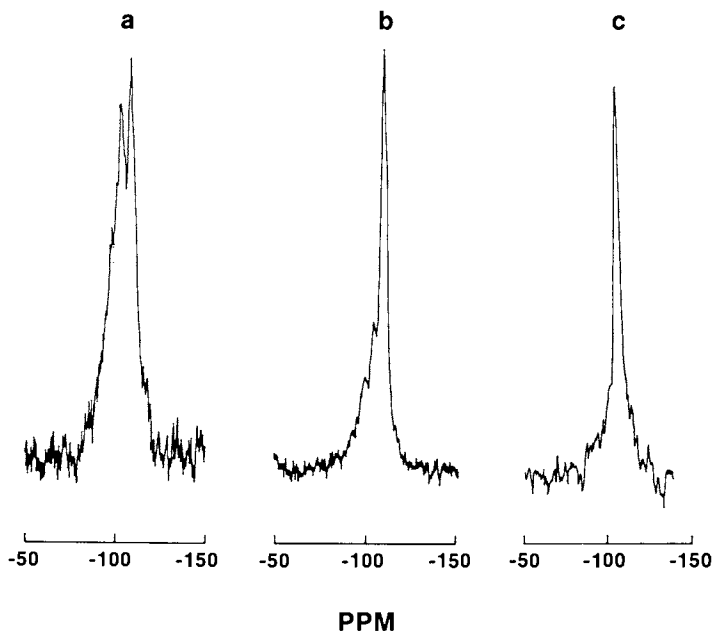
Figure 6: ^{29}Si NMR spectra of La,Ce,NH$_4$Y (3:1) zeolite
steamed under different severities.
Steaming conditions: (a) 540°C/2 hrs;
(b) 788°C/2 hrs; (c) 788°C/5 hrs.
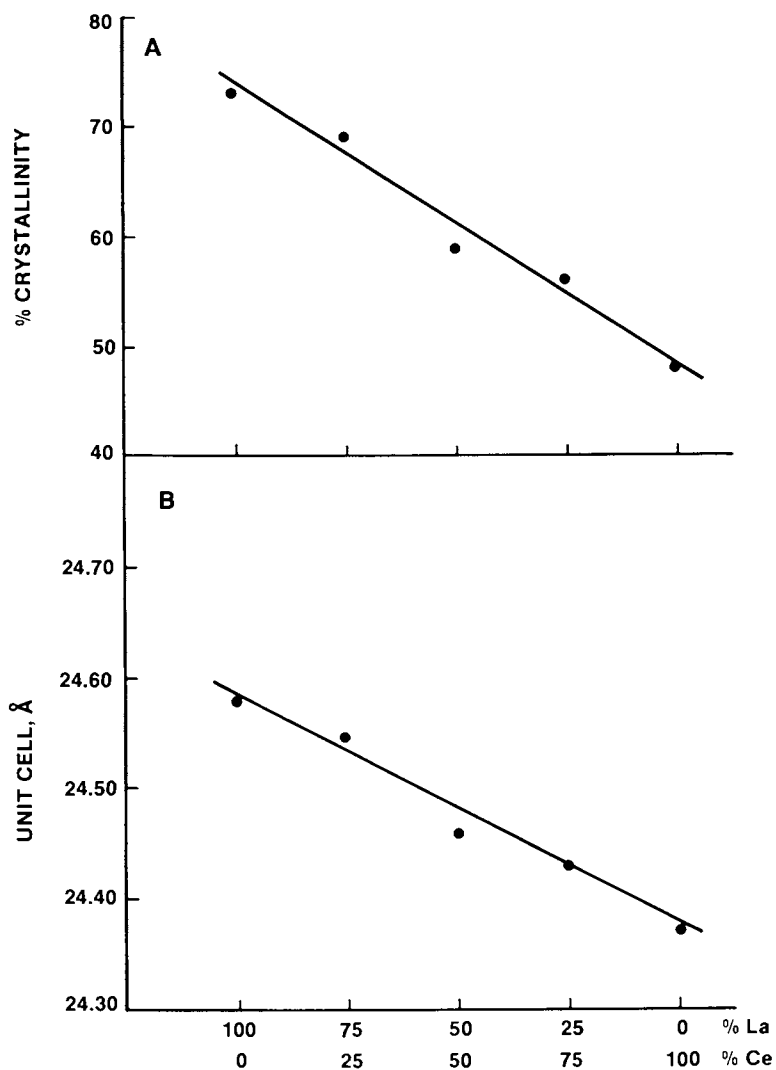
Figure 7: Variation of crystallinity (A) and unit cell size (B) of steamed La,CeNH$_4$Y zeolites as a function of La-Ce ratio. Steaming: 788°C/5 hrs.

TABLE II. XPS DATA FOR La AND Ce EXCHANGED Y ZEOLITES

Zeolite	Pretreat	Surface mole, % (Carbon-free normalization)		
		Al	La	Ce
Hi-LaY	Fresh	7	1	--
	Steamed 788°/5h	10	0.9	--
Lo-LaY	Fresh	7.5	0.4	--
	Steamed 788°/5h	13	0.6	--
Lo-CeY	Fresh	7	--	0.5
	Steamed 788°/5h	20	--	1

more readily dealuminated than the hydrothermally more stable ones under identical treatment. Furthermore, the structural collapse of the zeolite is more likely to affect preferentially the aluminum-containing structural units in the framework and be preceded by dealumination.

XPS data for fresh and steamed LaY and CeY zeolites are shown in Table II. The steamed samples show an enrichment in surface aluminum when compared to the fresh samples. This is indicative of steam induced non-framework aluminum migration to the crystal surface. The aluminum enrichment of the surface of steamed zeolites increases in the order Hi-LaY<Lo-LaY<Lo-CeY, and follows qualitatively the increase in framework dealumination (vide supra).

The data in Table II also show that steaming results in a surface enrichment of rare earths for Lo-LaY and Lo-CeY, while leaving practically unchanged Hi-LaY. The surface enrichment in rare earths of the steamed materials is more significant for Lo-CeY than for Lo-LaY zeolite. This corresponds to stronger dealumination and loss in crystallinity of the CeY zeolite. The migrating rare earths are likely to originate in the structurally collapsed regions of the zeolite crystals. The data indicate that steaming of these zeolites induces the migration of both aluminum and rare earths to the crystal surface. The surface composition of Hi-LaY zeolite crystals shows the least change upon steaming, due to its higher structural stability.

These data point out a striking difference between hydrothermal dealumination of rare earth exchanged Y zeolites (with over 14 wt% RE_2O_3) and ammonium exchanged zeolites. While, in the first case, framework dealumination precedes or is accompanied by loss of structure, in the latter case, dealumination leads to a more stable structure (ultrastable Y zeolite).

Acknowledgment

Literature Cited

1. J. A. Rabo, P. E. Pickert, D. N. Stamires and J. E. Boyle, Actes Congr. Int. Catal. 2nd, 1960, 2, 2055 (1961).
2. P. B. Venuto, L. A. Hamilton, P. S. Landis and J. J. Wise, J. Catal. 5, 484 (1966).
3. J. A. Rabo, C. L. Angel and V. Shomaker, Proc. Int. Congr. Catal., 4th, 1967 (1968).
4. D. A. Hickson and S. M. Csicsery, J. Catal. 10, 27 (1965).
5. J. S. Magee and J. J. Blazek, "Preparation and Performance of Zeolite Cracking Catalysts," in Zeolite Chemistry and Catalysis, ACS Monograph No. 171, ed. J. A. Rabo, 1976.
6. J. W. Ward, "Molecular Sieve Catalysts" in Applied Ind. Catalysis, V. 3, ed. B. E. Leach, Acad. Press, 1984.
7. D. H. Olson, G. T. Kokotailo, and J. F. Charnel, J. Colloid. Interface Sci. 28, 305 (1968).

8. J. M. Bennett and J. V. Smith, Mater. Res. Bull., 3, 865 (1968); 4, 7, 77, 343 (1969).
9. F. D. Hunter and J. Scherzer, J. Catal. 20, 246 (1971).
10. J. Scherzer, J. L. Bass and F. D. Hunter, J. Phys. Chem., 79, (12), 1194 (1975).
11. J. W. Ward, J. Phys. Chem. 72, 4271 (1968).
12. A. P. Bolton, J. Catal. 22, 9 (1971).
13. J. Scherzer, J. L. Bass, J. Phys. Chem. 79 (12) 1200 (1975).
14. G. H. Kuhl, Zeolites, 5, No. 1, 4 (1985).
15. V. P. Shiralkar and S. B. Kulkarni, J. Therm. Anal., 25 (2), 399 (1982).
16. D. Das, M. C. Ugreti, Proc. Catsympo 80, Natl. Catal. Symp., 5th, 1980, p. 24.
17. A. Dyer, M. Shesheniah, J. G. Brown, J. Inorg. Nucl. Chem. 40(1), 99 (1978).
18. M. L. Costenoble, M. L. Mortier, J. Wilfried, J. B. Uytterhoeven, J. Chem. Soc. Faraday Trans. 1, 74 (2), 466 (1978).
19. T. Batiashvili, Therm. Anal. Proc. Int. Conf., 4th, v.2, 611 (1974).
20. J. Marti, J. Soria and F. H. Cano, An. Fis. 72 (2), 130 (1976).
21. D. Ballivet, P. Pichat and D. Barthomeuf, Adv. Chem. Ser. 121, 469 (1973).
22. P. P. Lai and L. V. C. Rees, J. Chem. Soc., Faraday Trans. I, 72, 1809 (1976).
23. P. Marynen, A. Maes and A. Cremers; Zeolites, 4 (3), 287 (1984).
24. C. A. Fyfe, G. C. Gobbi, W. J. Murphy, R. S. Ozubko and D. A. Slack, J. Am. Chem. Soc., 106, 4435 (1984).
25. F. Maugé, P. Gallezot, J. C. Courcelle, P. Engelhard and J. Grosmangin, Zeolites, 6, (4), 261 (1986).
26. J. W. Roelofsen, H. Mathies, R. L. de Groot, P. C. M. Jane Woerkom and E. Angad Gaur, in "New Developments in Zeolite Science (Studies in Surface Science & Catalysis, v. 28), p. 337 (1986); Elsevier.
27. T. H. Fleisch, B. L. Meyers, G. J. Ray, J. B. Hall and C. L. Marshall, J. Catal., 99, 117 (1986).
28. H. Winkler, K. H. Steinberg, G. Kapphahn, J. Colloid. Interf. Sci., 98 (1), 144 (1984).
29. A. Corma, V. Fornes, J. B. Monton and A. V. Orchillés, Ind. Eng. Chem. Prod. Res. Dev. 25, 231 (1986).
30. F. Lemos, F. Ramoa Ribeiro, M. Kern, G. Giannetto and M. Guisnet, Applied Catalysis, 29, 43 (1987).
31. J. W. Smith, J. M. Bennett and E. M. Flanigen, Nature, 215, 241 (1967).
32. E. Lippmaa, M. Magi, A. Samoson, M. Tarmak and G. Engelhardt, J. Am. Chem. Soc. 103 (17) 4992 (1981).
33. G. Engelhardt, U. Lohse, M. Magi, E. Lippma, in "Structure and Reactivity of Modified Zeolites, Ed. P. A. Jakobs, et al, Elsevier, Amsterdam, 1984, p. 23.
34. A. R. Grimmer, R. Peter, E. Fechner and G. Molgedey, Chem. Phys. Let. 77, 331 (1981).

35. I. V. Smith and C. S. Blackwell, Nature, <u>303</u>, 223 (1983).
36. G. T. Kokotailo, C. A. Fyfe, G. J. Kennedy, G. C. Gobbi, H.
     Strobl, C. T. Pasztor, G. E. Barlow and S. Bradley, "New
     Development in Zeolite Science," (Studies in Surf. Science &
     Catalysis), 5. <u>28</u>, p. 361 (1986), Elsevier.
37. Zeolite Chemistry and Catalysis (Ed. by J. Rabo), ACS, 1976,
     p. 319.
38. G. J. Ray, B. L. Meyers, C. L. Marshall, Zeolites, <u>7</u>, 307
     (1987).

Chapter 4

Structural and Sorptive Properties of Some MFI- and AEL-Type Materials

Jacques C. Vedrine [1], Gisèle Coudurier [1], and Bernard F. Mentzen [2]

[1]Institut de Recherches sur la Catalyse, Centre National de la Recherche Scientifique, 2 Avenue Albert Einstein, F-69626 Villeurbanne, Cedex, France

[2]Laboratoire de Physico-Chimie Minérale IA, Unité Associée No. 116 du Centre National de la Recherche Scientifique, Université Claude Bernard Lyon I, Bat. 731, 43 boulevard du 11 Novembre 1918, F-69622 Villeurbanne, Cedex, France

Pentasil MFI (ZSM-5) type materials exhibiting different crystallite sizes and AEL (SAPO-11) type materials have been studied. Structural investigations using X-ray diffraction techniques, developed for polycrystalline powdered samples, allow one to determine precisely the structure and crystallinity of the samples and the effect of adsorbates (e.g., p-xylene, n-hexane, etc) on the framework topology (monoclinic towards orthorhombic for MFI) and unit-cell dimensions.
The diffusion rates of hydrocarbons have been studied by thermogravimetry as a function of crystallite size. Acidity of the materials has been determined by ir and thermodesorption of ammonia and their catalytic proper-ties for toluene alkylation with methanol have been studied. Relations between acidic strength, diffusion rate, catalytic shape selectivity and structural featu-res are discussed. It is suggested that the microporous framework has to be considered as a "living material" under catalytic reaction conditions.

Zeolites and molecular sieve materials exhibit fascinating properties, particularly as sorbents or catalysts. From a fundamental point of view, they represent a family of crystallographically well-defined solid materials (this is not always the situation for most of the metallic oxides). When considering catalysis, two main factors play an important role, i.e., the nature of the active sites (particularly acidic sites) and the topology (cavities, channels, pores ...).

Many investigations have already been devoted to the modification of zeolites, either during or after their synthesis. The aim was to change their catalytic properties, either by creating active sites or by monitoring the pore size (shape selectivity). For instance, it has been shown that substituting B, Fe, Ga ... for Al in pentasil-type zeolites results in a decrease of the acidic strength (1-3), parti-cularly in the case of boron (2). Moreover, the presence of an extra-

framework phase within the pores or at the pore-openings, modifies
the diffusivity features, thus altering the selectivity of reaction
processes, e.g. toluene alkylation into xylene isomers. Hydrothermal
treatment, or even calcination, was shown to extract aluminum from
framework positions and result in the formation of amorphous alumina
or silicoalumina, deposited within the pores (4). Such a deposit
could also be responsible for specific catalytic properties. This is
very probably the case for the gallo- (5,6), zinco- (7), ferri- (8)
or titanosilicates (9) of the pentasil MFI family, which promote
bifunctional type catalysis, e.g., propane aromatization (Ga - or
Zn-ZSM-5) or direct hydroxylation of aromatic hydrocarbons with hydro-
gen peroxide (Ti-ZSM-5). On the other hand, some elements of the
deposited oxide may react with the microporous matrix and produce
framework T-atom substitution. This was shown to occur for boron-
impregnated ZSM-5 samples (2,10) and one must be aware of this when
some binders (clays, alumina) are used for industrial catalyst formu-
lations.
    Another feature that one must also keep in mind, is the possible
crystal structure modifications induced by hydrocarbon adsorption,
which might result in changes in some catalytic properties. Therefore,
it appeared very important to us, to characterize the structural
properties of zeolitic-type materials versus chemical, hydrothermal
or adsorptive modifications, and subsequently to determine the chan-
ges in acidic and catalytic properties. The aim of this paper is to
present some examples of our own, in order to illustrate the changes
observed for the ZSM-5 (MFI) and SAPO-11 (AEL) type materials (11).

Adsorption Investigations

Experimental. Pentasil MFI (Al or B substituent) samples, A to F,
were prepared in a fluoride medium, in the Laboratory of Prof. Wey
(Mulhouse) (12). Sample G was prepared in basic medium conditions
(13, example 1) in our Laboratory. SAPO-11 material (sample H) was
synthesized in our Laboratory, as described in reference (14) with
di-n-propylamine as template.
    In order to obtain the H-form, the samples A to F and H were
calcined under nitrogen flow at 550°C, and then under air flow for
16 hours at the same temperature. Sample G (after the same treatment)
was ammonium-exchanged and recalcined at 550°C.
    Chemical analyses were performed using atomic absorption spec-
troscopy. The morphology of the crystallites was determined by
scanning electron microscopy (CAMECA). Adsorption capacities and
sorption kinetics of n-hexane, p-xylene and 3-methyl-pentane were
determined gravimetrically with a SARTORIUS microbalance, at room
temperature using p/p_0 varying from 0.1 to 0.2. Acidities of the
samples were studied by infrared (hydroxyl groups) ammonia adsorption-
desorption and thermoprogrammed desorption of ammonia (TPDA). Alkyla-
tion of toluene with methanol was performed at 400°C in a flow-
microreactor using a methanol/toluene ratio of 1/4, in order to favor
alkylation over direct conversion.

Results. Chemical analysis data, size, morphology of the crystallites
and adsorption capacities are given in Tables I and II.

Table I. Formulae calculated according to the chemical analyses

	Sample	Composition
A	H–B.ZSM–5	$H_{1.4}Al_{0.02}B_{1.38}Si_{94.6}O_{192}$
B	H–Al.ZSM–5	$H_{3.56}Na_{0.05}Al_{3.61}Si_{92.39}O_{192}$
C	H–B.ZSM–5	$H_{3.20}Al_{0.02}B_{3.18}Si_{93.40}O_{192}$
D	H–Al.ZSM–5	$H_{4.83}Al_{4.80}B_{0.03}Si_{91.17}O_{192}$
E	H–Al.ZSM–5	$H_{3.14}Al_{3.11}B_{0.03}Si_{92.86}O_{192}$
F	Silicalite	$Na_{0.11}Al_{0.11}Si_{96.89}O_{192}$
G	H–Al.ZSM–5	$H_{3.8}Na_{0.3}Al_{4.10}Si_{91.90}O_{192}$
H	SAPO–11	$H_{0.9}Al_{18.8}P_{19.1}Si_{2.1}O_{80.6}$

In the MFI framework, the adsorption capacities of n-hexane and p-xylene are close to 8 molecules/unit-cell, and 5 molecules/uc for 3-methyl-pentane, indicating that the n-hexane and the p-xylene gain access to both channel systems, while the branched paraffin, due to its size, has a restricted adsorption in the sinusoidal channel (15). The adsorption kinetics agree with these observations since p-xylene and n-hexane adsorption is very fast.

Table II. Crystallite sizes and adsorption capacities

Sample	size (μm)	A/V* (μm⁻¹)	adsorption capacities (mol/uc)		
			n-hexane	3-Me-pentane	p-xylene
A	90x15x15	0.28	7.4	5.3	–
B	38x20x12	0.32	8.2	5.1	–
C	30x12x8	0.48	–	4.7	7.5
D	17x7x5	0.8	–	5.0	8.3
E	2.5x.8x.6	6.6	8.7	6.3	–
F	5x1x.3	9.0	8.2	4.8	–
G	1x.6x.35	11.0	7.5	5.8	–
H	10–15	0.2–0.3	1.9	–	2.7

*All ZSM-5 samples are rhombic prisms more or less expanded along their c axis. The SAPO-11 sample consists of spherical agglomerates. A and V are the external surface and volume of the crystallites, respectively.

For 3-methyl-pentane, the initial ranges of the adsorption kinetics are shown in figure 1. It is observed that except for sample C, the kinetics strongly depend on the crystallite size of the samples. The curves may be analyzed in terms of the Fickian diffusion law (16) at small time values (17) :

$$m_t/m_\infty = (2A/V) \ (D/\Pi)^{1/2} \ t^{1/2}$$

Here : - m_t and m_∞ are the amounts adsorbed at time t and at equilibrium,
- A and V are the external surface area and the volume of the crystallites,
- D is the diffusion coefficient.

According to figure 2 the m_t/m_∞ versus $t^{1/2}$ plots are straight lines for initial adsorption periods.

The slopes of these lines roughly depend on A/V (figure 3). This allows us to calculate an average diffusion coefficient for 3-methyl-pentane in MFI topologies, i.e., $D = 1.1 \times 10^{-11}$ cm^2 s^{-1}. In the same way, the diffusion coefficient $D = 2.4 \times 10^{-10}$ cm^2 s^{-1} is obtained for p-xylene (samples C and D).

In catalytic alkylation of toluene with methanol, all the Al-ZSM-5 samples were observed to be active and to yield high para-xylene selectivity. For sample G, the activity remained for several days with the following selectivity for xylene isomer distribution : 52/36.5/11.5 (for p-, m- and o-xylene, respectively). In contrast, for samples B and D, activity was observed to decrease down to a tenth after one day, while selectivity was very high in favor of the para isomer (92 %). The increase in para-selectivity may easily be explained when considering the rate of 3-methyl-pentane adsorption (see fig. 1) which characterizes the change in intracrystalline diffusivity. The deactivation rate characterizes the blocking of the pore-openings and therefore obviously increases per weight-unit, when the A/V ratio decreases, i.e., when the crystallite size increases.

B-ZSM-5 samples (A and C) were observed to be inactive for the alkylation, even at 600°C, with a very low methanol conversion yielding light olefins. The SAPO-11 sample (H) gave very low alkylation conversion with thermodynamic para-xylene equilibrium selectivity. The latter result obviously arises from the pore dimensions (6 x 6.2 Å), larger than for MFI samples.

TPDA experiments allowed us to compare the acidity of the samples. The TPDA peaks correspond to 190, 200-340 and 230-430°C, respectively, for the B-ZSM-5, SAPO-11 and the Al-ZSM-5 samples (11). These data clearly show that acidic strength is in the order B-ZSM-5 < SAPO-11 << Al-ZSM-5 for the H-form of zeolites. In IR spectroscopy hydroxyl group bands were observed near 3740 and 3700 cm^{-1} for B-ZSM-5 (2), 3740, 3710, 3675 and 3605 cm^{-1} for SAPO-11 (14) and 3740 and 3605 cm^{-1} for Al-ZSM-5 (18). The 3740 cm^{-1} band corresponds to non acidic silanol groups, the 3700 cm^{-1} band to weak acid sites and the 3605 cm^{-1} to strong acidic sites for MFI-type samples.

These data are quite consistent with the catalytic properties for acid type reactions, as summarized above. It shows that substituting Al for B in a ZSM-5 sample, results in low acidity. This was explained (2) on the basis of tri-coordination of framework boron, as schematized on the insert. This also explains the relative instability of framework boron under reaction conditions (10) or under calcination.
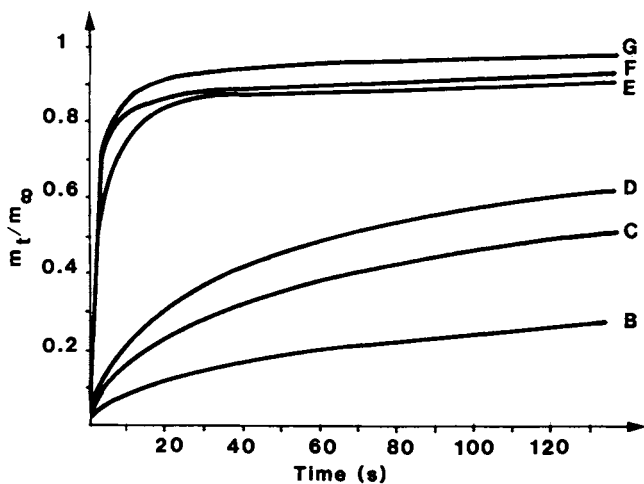
Figure 1. Kinetics of 3-methyl-pentane adsorption at room temperature determined by thermogravimetry. Labels refer to Table I.
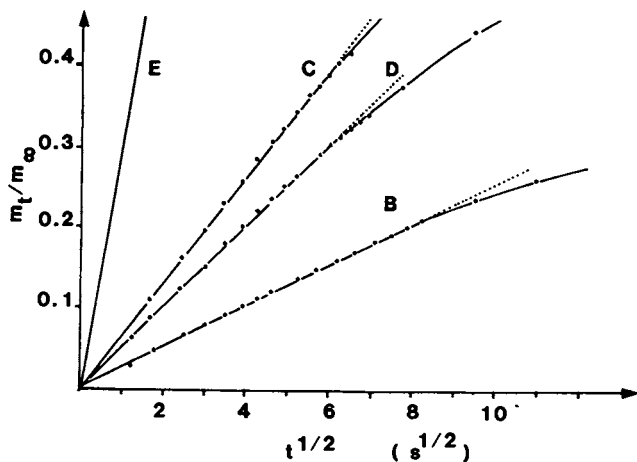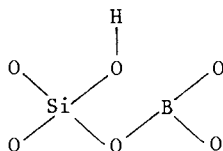

Figure 2. Fickian plots for 3-methyl-pentane adsorption at room temperature (letters as in figure 1 and Table I).

H
|
O   O   O
 \   / \   /
  Si   B
 /   \ /   \
O   O   O

In the case of SAPO-11 materials, silicon was observed to incor-
porate the AEL framework with some difficulty, in order to induce
medium strength acidity by substitution for P. It could also corres-
pond to specific Al environments, i.e., not all the Al atoms are
tetracoordinated, but some have six neighbors or even five. Such a
concept may broaden the field of AlPO-type materials which exhibit
novel topologies.

Structural investigations

In order to get a better knowledge of the behavior of zeolitic mate-
rials in catalysis, sorbate/sorbate and/or sorbate/ framework interac-
tions have to be investigated by several complementary techniques.
Among these, techniques such as masNMR, XPS(ESCA), ESR, IR give local
information whereas others like X-ray and neutron diffraction techni-
ques give global information. If a sorbed molecule in a zeolitic
framework yields a stable complex, it might then be possible to in-
vestigate the solid phase by diffraction techniques, and get informa-
tion about the localization of the sorbed species. Of course, the
best starting material for ab initio structure determinations is the
"single crystal". Unfortunately, when available, most crystals of
synthetic zeolites are usually twinned, and in the case of sorption
complexes, the single crystal is out of the question ! For these
reasons, the powder diffraction technique has been extensively develo-
ped, and the well-known Rietveld-type full-pattern-fitting structure
refinement procedure has been applied to moderately complex structu-
res.
     Recently, by using neutron powder-diffraction, it has been
possible to localize the perdeuterated benzene (19) and pyridine (20)
guests in high symmetry zeolites. In the case of MFI type frameworks
(silicalite, ZSM-5, boralites, etc) the problem is somewhat different,
since extensive peak-overlap occurs throughout the pattern (vide
infra). In that case, most of the refinable parameters are highly
correlated. These parameters form two distinct groups : one corres-
ponds to the profile parameters, which must first be varied : the
second corresponds to all the structural atomic parameters (x, y, z,
thermal factors, occupancy). Some of which must be severely constrai-
ned.
     In our case, the most widely used experimental techniques are
conventional X-ray and neutron powder-diffractions.Very recent
equipment using high-resolution devices (e.g., Brookhaven NSLS, Chess,
Grenoble ILL, Orsay LURE, etc) have shown promise and are now widely
exploited for the present purpose. Nevertheless, these installations
are very sophisticated, and their accessibility is somewhat limited.
However, conventional X-ray equipment is less useful, but it is
essentially immediately available at most colleges, universities and

industrial research laboratories. Therefore, in the following
discussion, only this latter technique will be considered.

    The very first problem is to have "a good quality zeolitic sam-
ple". Let us suppose that we have one ! The next problem is to get a
"good quality diffraction pattern". Most of the commercially availa-
ble X-ray diffraction equipment is likely to yield moderately-
resolved step-scanned patterns, which provide a starting point for
the structural investigations. To the best of our knowledge, the very
first succes in localizing extra-framework material in an MFI frame-
work, by using conventional X-rays, is the work of BAERLOCHER on a
silicalite/TPA-template complex (21). Our purpose here is to show
that with standard routine equipment and computer programs, one has a
means of locating "some butterflies" sitting in microporous materials.

MFI materials. X-ray investigations have shown that the powder
diffraction patterns are very sensitive to sorbate-induced structural
modifications (22-24). Figure 4 represents the $9.5 < 2\theta < 22.5°$ XRD
(X-ray powder diffraction) domains corresponding to the as-synthesized
(TPA) and calcined+air-equilibrated (WAT) forms of sample A (also
called boralite (25) (cf. Table I)) having the $H_{1.40}B_{1.38}Al_{0.02}Si_{94.6}$
O_{192} framework composition. Both patterns correspond to orthorhombic
phases (Pnma space group). If the just-calcined B-ZSM-5 is analysed
by XRD, its structure appears to be monoclinic ($P2_1/n$ space group)
(see Table III). These three (TPA, CAL, and WAT) forms are commonly
observed and their XRD patterns represent a good criterion for crys-
tallinity estimations of newly prepared samples. The difference
between the TPA (tetrapropylammonium) and WAT forms is the replacement
of the TPA template by water molecules. These striking differences
in the XRD patterns provide indirect evidence that the TPA ions are
localized on fixed sites in the framework (21,26).

    As a typical example of sorbate-localization in a MFI framework
let us now consider the p-xylene/ZSM-5 complexes. It is well-
established that the adsorption of p-xylene in MFI type materials
takes place in two steps (22,27,29). The first one corresponds to the
formation of a low-coverage complex (XYL I) (Figure 5) containing up to
four molecules/unit-cell, and the second one to the formation of a high-
coverage complex (XYL II) containing up to eight molecules/unit-cell
at ambient temperature. Recently, one of us was able to localize the
p-xylene guest molecule in two B-ZSM-5 samples by trial-and error
methods (30,31) and by a direct characterization method described
elsewhere (32-34). In order to propose reasonable localizations for a
sorbate molecule the symmetry-compatible elements between the sorbent
and the sorbate have to be considered. If we assume four p-xylene
molecules/unit-cell as in (31), it appears that the best fit might be
obtained if one of the mirror planes of the molecule coincides with
the m plane of the MFI framework. The three possible assumptions are
S1 - the long-axis of the p-xylene (methyl-methyl line) is parallel
to the (010) direction, S2 - the long-axis is on the m plane of the
Pnma space group, and the planar p-xylene is normal to m, S3 - the
aromatic cycle and the long-axis are on the mirror plane. In all
cases the centroid of the molecule is on the mirror plane (4c sites).
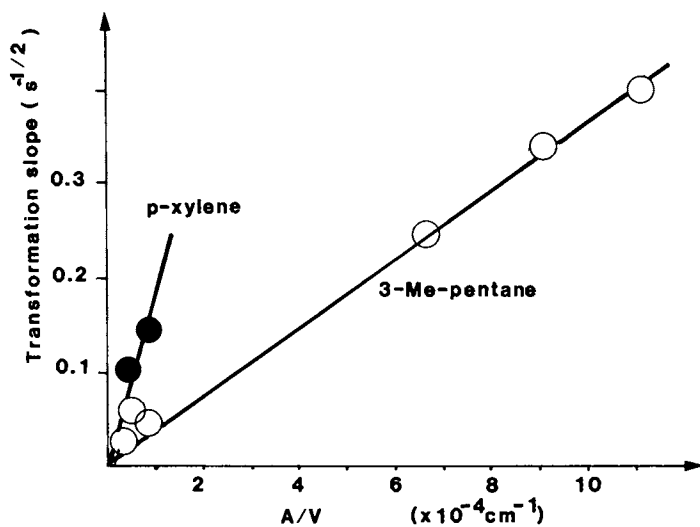These three situations are represented in Figures 6 (number pairs

Figure 3. Slopes of the linear transformation (figure 2) of adsorption curves (figure 1) versus A/V values.
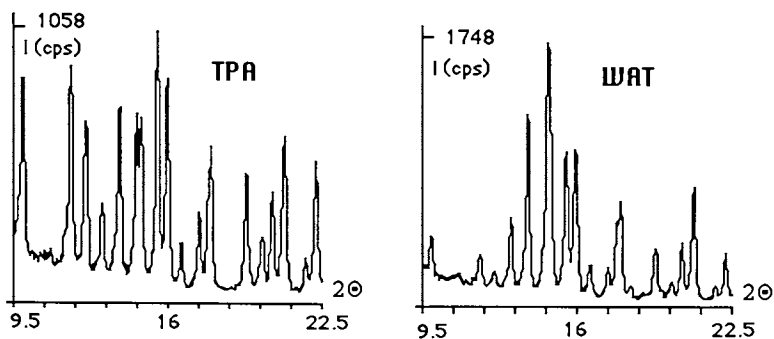

Figure 4. Details of the XRD patterns for the TPA and WAT forms of a synthetic B-ZSM-5.
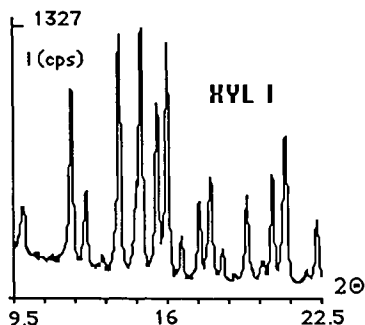
Figure 5. XRD pattern details for the XYL I form of B-ZSM-5 sample A.

Table III. Unit-cell parameters of several B-ZSM-5/sorbate complexes containing 1.38 B/uc

form	a(Å)	b	c	α(°)	V(Å³)	δa(%)[*]	δb(%)	δc(%)
CAL	20.081(6)	19.854(3)	13.366(4)	90.58	5329	0	0	0
TPA	20.040(5)	19.904(3)	13.377(3)	90.00	5336	-.20	+.25	+.08
XYLI	20.013(3)	19.928(3)	13.378(2)	90.00	5335	-.34	+.37	+.09
XYLII	20.105(2)	19.826(2)	13.440(2)	90.00	5357	+.12	-.14	+.55
TOLI	20.079(6)	19.881(7)	13.399(7)	90.12	5345	-.01	+.13	+.24
TOLII	20.096(9)	19.86(1)	13.44(1)	90.00	5364	+.07	+.03	+.55
BNZI	20.021(3)	19.805(3)	13.383(2)	90.00	5307	-.30	-.25	+.13
BNZII	19.934(3)	19.875(3)	13.325(2)	90.00	5279	-.73	+.11	-.31
HEX	20.128(5)	19.881(2)	13.400(8)	90.44	5362	+.23	+.16	+.18
WAT	20.058(3)	19.886(3)	13.373(2)	90.00	5334	-.11	+.16	+.05

[*] the reference corresponds to the CAL (calcined) form.

CAL : calcined for 24 h at 550°C - immediate XRD spectrum
TPA : as-synthetized form (tetrapropylammonium ion template)
       (3.55 mol/uc)[a]
XYLI : p-xylene low-coverage[a] form (2.67 mol/uc)[a]
XYLII : p-xylene high-coverage[b] form (8 mol/uc)[a]
TOLI : toluene low-coverage form[b]
TOLII : toluene high-coverage form[c]
BNZI : benzene low-coverage form (3.78 mol/uc)[a]
BNZII : benzene high-coverage form[c]
HEX : n-hexane form (7.16 mol/uc)[a]
WAT : calcined form after 1 week air-equilibration

[a]
[b] x-ray refinement of the occupancy factors
    low-coverage   :   0 - 4 guest molecules/unit-cell
[c] high-coverage :   4 - 8 guest molecules/unit-cell

Compared to the calcined (empty) monoclinic form the parameter variations are non-predictable and anisotropic. This is some evidence for sorbent/sorbate interactions.

are for T atoms), 7 and 8. For each solution, the corresponding
calculated XRD pattern using the atomic coordinates reported in (21)
is also presented for comparison with the experimental one (figure 5).
    It appears that the best fit is obtained for the first solution
(S1) where the p-xylene is sitting at the channel-intersection with
its long-axis parallel to the straight channel. It must be emphasized
here that for the three theoretical solutions the most important
detail when localizing the p-xylene molecule is the orientation of
its long-axis : for each case, the calculated XRD pattern is not very
sensitive to the rotation of the molecule about this axis. The S2.65/
S3.0 and S2.155/S3.65 patterns are almost identical, and it appears
that the tilt of the long-axis between the S2.65 and S3.0 solutions
(15°) is not too significant. The results obtained by this trial-and-
error method have been verified by the direct characterization method
which yields essentially the same results, i.e., the p-xylene guest is
disordered (partially hindered rotational disorder) and localized at
the channel intersections, as shown in figure 9 (hatched circles
stand for possible sites of Al or B heteroatom).
    The direct-characterization method used for the detection and
the localization of adsorbed molecules in zeolitic frameworks pre-
sents three relevant points : 1-refinement of the X-ray powder profile
using the "monochromatic" approximation for the α_1-α_2 doublet and
the DBW3.2 program (35), thus avoiding numerical monochromatization
methods ; in that case the apparent FWHM (full-width at half-maximum)
is about 1.3-1.4 times that of α_1 recordings ; 2-investigations of
the most "sensitive" angular domain corresponding possibly to at
least 100 hkl triplets ; for MFI materials the 6-48°(2θ) domain is
usually sufficient (about $\approx$ 444 hkl), and the preliminary investiga-
tions (visual fit) correspond mostly to the 9.5-22.5°(2θ) domain
($\approx$ 48 hkl) ; 3-computer runs by combining full-profile refinements
(34), extraction of the integrated intensities (modified DBW3.2 pro-
gram) and conventional difference-Fourier synthesis (any of the
available single-crystal structure-refinement programs). This method
has now been used with success for several sorbent/sorbate complexes,
including n-hexane (32,34), TPA (34), benzene (33) and high-coverage
p-xylene/ZSM-5 phases (36,37). It is hard to imagine a more democra-
tic method for the investigation of sorbent/sorbate complexes, and
accordingly, this simplified procedure was named butterfly-hunting
(chasse aux papillons) (31,33) when we first started using it !
    Even if one might be sceptical when considering our direct-
characterization method, it works correctly and so far yields consis-
tent results. The aim of this method is two-fold : 1-obtain the best
information concerning the whereabouts of sorbed molecules in molecu-
lar sieve materials, by using mostly "routine" equipment, and 2-be
able to investigate a whole series of materials for varying composi-
tion and/or sorbate. This second criterion is, of course, the more
important : it is always better to have valuable preliminary results
on such complex systems, by choosing the best-suited specimen before
going to highly sophisticated X-ray synchrotron, pulsed-neutron,
time-of-flight and other advanced installations where the success
of the operation is only evident after a costly run. However, it
must not be considered that the apparent simplicity of our method
precludes a precise knowledge of materials science and solid-state
chemistry and physics, nor that it is a cure-all procedure for
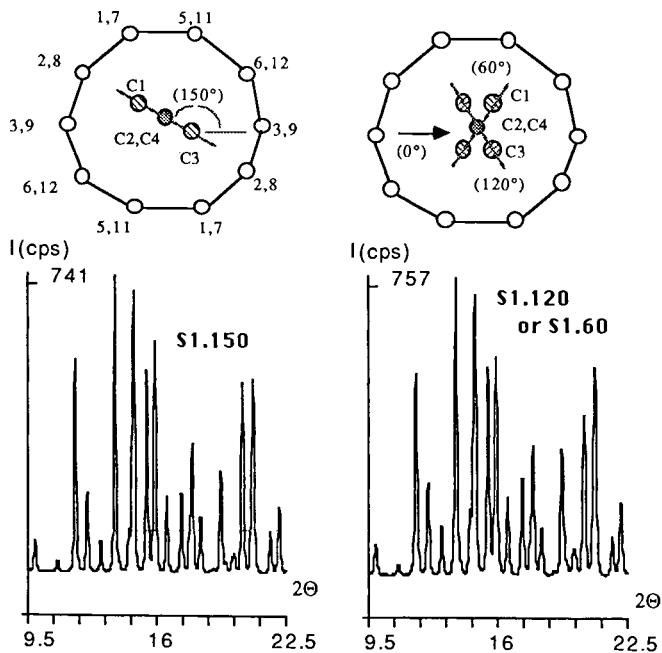
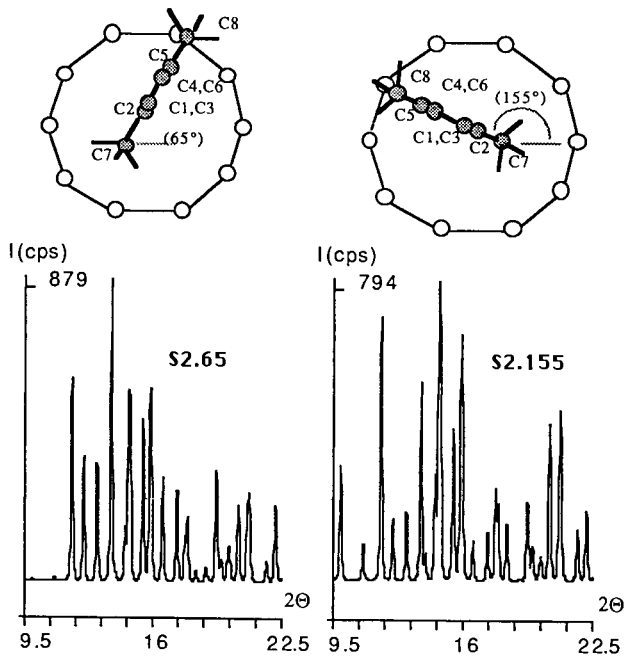Figure 6.   The S1 solution.

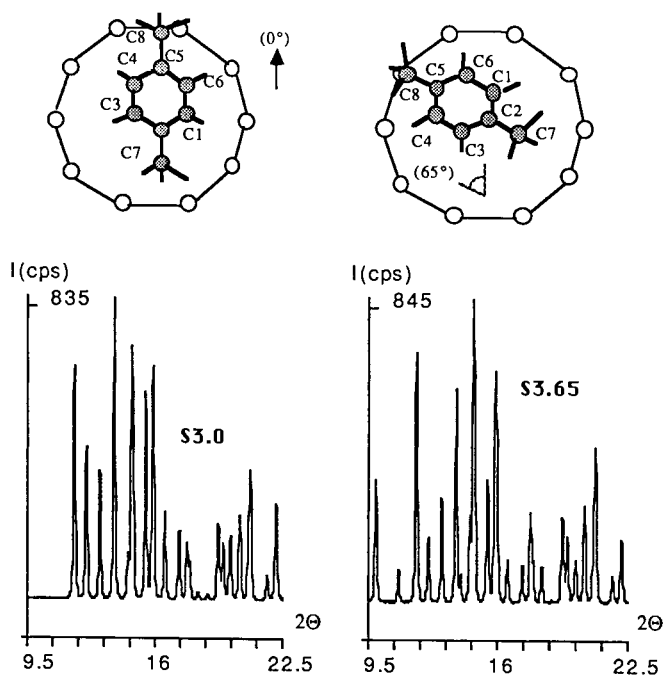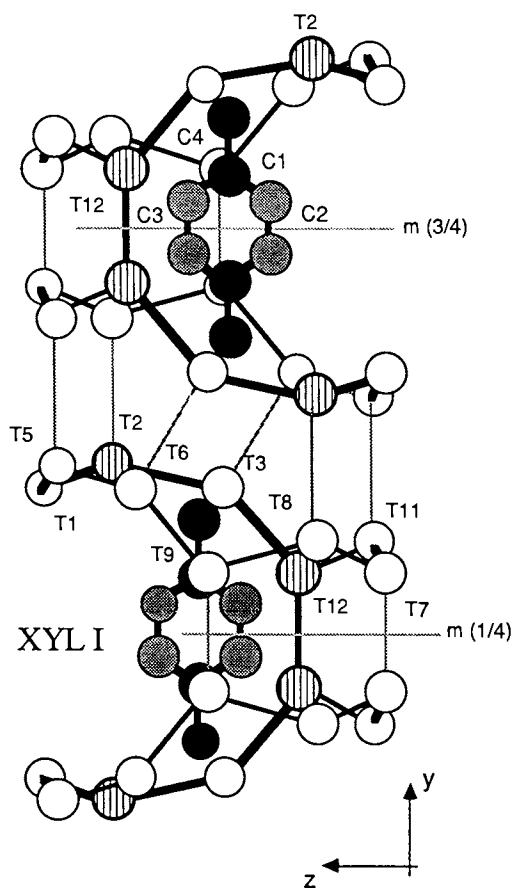Figure 7.   The S2 solution.

Figure 8. The S3 solution.

Figure 9.   p-xylene in the MFI framework.

inexperienced workers. It must be recalled again that there can be
severe peak-overlap occuring for MFI type frameworks :
viz.ca. 15, 25, 40, 63 and 73 reflections overlapping, respec-
tively, at 27, 37, 48, 62 and 70° 2θ (38).

SAPO-11 (AEL) materials.   SAPO-11 type molecular sieves are now
widely investigated and at the time we started investigating their
synthesis and structure, only information about their T-atom topology
was available (39,40). It appeared to us that the as-synthesized SYN
(di-n-propylamine) and calcined+air-equilibrated WAT forms correspond
to different XRD patterns which could be unambiguously indexed in,
respectively, the Ima2 and Pna2₁ (in both cases the origin has to be
fixed by postulating arbitrarily the z coordinate of one atom)
orthorhombic space groups (assuming strict Al/P alternation). In order
to investigate sorbent/sorbate complexes of SAPO-11 materials (AEL
topology) with several molecules (see Table IV) we needed some better
structural information.
    The above-mentioned method has been applied by using the
graphically-determined coordinates of the T atoms (alternating P, Al)
calculated from distances and angles close to those reported for
AlPO₄-5 materials (41). Surprisingly, in both cases (synthesized and
calcined) the difference-Fourier maps reveal all the framework
oxygen atoms, and consequently, just before the paper of BENNETT et
al. appeared in Zeolites (42) we proposed partially refined atomic
coordinates for these materials (43,44). Ab initio calculations using
a distance-least-squares (DLS) program (45) have been shown to yield
very comparable coordinates, but in our opinion the intimate structu-
re of AlPO₄-11 derived materials is a rather difficult question
(due to severe structure-defect problems) (42,43,46,47), but for
preliminary sorbent/sorbate investigations these defects do not
hamper too severely the profile-refinements.
    A general observation is that several calcination-adsorption
cycles on the same sample yield better profile-fits than the prepared
raw material. Furthermore, when the just-calcined material is analy-
sed by XRD before its air-equilibration, drastic time-resolved
structural changes are observed (46) : it might accordingly be
supposed that the true calcined form is even more complicated than
the WAT form reported in Table IV. Figure 10 represents partial XRD
patterns corresponding to the SYN, WAT and CYC (cyclohexane adsorbed)
forms.
    Similar results on p-xylene, n-hexane and isopropanol complexes
show that for the Ima2 (AEL topology) phases there are no evident
nor visual sorbate-induced structural modifications as those observed
for MFI topology materials. Most surprisingly, if a single, and
always the same site (interpreted as a carbon atom), detected by
difference-Fourier (in the straight channel) is introduced in the
refinement cycle, the Rp (profile) and Rb (Bragg) values (cf. ref.
(35)) drop systematically from 16-12 % to 6-3 %. Accordingly, some
hosts in the 1D channel system must be present but cannot be locali-
zed precisely. Here we must remember the symmetry-compatible crite-
rion mentioned above : most of the sorbed molecules have no evident
matching symmetry elements with the AEL framework, so that they might
all be considered as completely disordered, i.e., as spherical
diffracting centers. Another possible visualization is to consider

Table IV. Unit-cell parameters of several forms of
a SAPO-11 containing 2Si/uc (sample H)

form	a(Å)	b	c	V(Å^3)	δa(%)*	δb(%)	δc(%)	sp.gr
SYN	18.671(3)	13.373(2)	8.422(1)	2102	0	0	0	Ima2
WAT	18.056(8)	13.799(5)	8.126(3)	2024	−3.29	+3.18	−3.51	Pna2₁
CYC	18.660(2)	13.514(2)	8.3762(8)	2112	−.06	+1.05	−.54	Ima2
XYL	18.586(3)	13.543(2)	8.377(1)	2108	−.45	+1.27	−.53	Ima2
IPRA	18.559(2)	13.517(2)	8.3753(9)	2101	−.60	+1.08	−.55	Ima2
HEX	18.647(2)	13.509(2)	8.3724(9)	2109	−.13	+1.02	−.60	Ima2

*SYN : as-synthetized (di-n-propylamine as template)
        ($\approx$ 2 DPA/uc)[a,b]
        reference for parameter variation
WAT   : 1 week air-equilibrated calcined form
CYC   : cyclohexane form (1.78, 2.00 mol/uc)[b]
XYL   : p-xylene form (2.74 mol/uc)[a] (2.48 mol/uc)[a]
IPRA : isopropanol form (2.72 mol/uc)[a] (2.72 mol/uc)[a]
HEX   : n-hexane form (2.04 mol/uc)[a] (2.64 mol/uc)[a]

[a]X-ray refinement of the occupancy factor
[b]chemical analysis

Both the SYN and CAL forms are orthorhombic. If we accept that these
phases present exact Al/P alternation (ordered structures), then
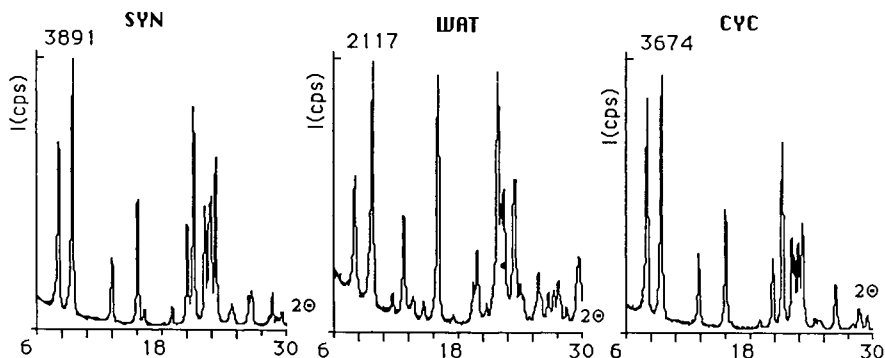their respective space groups are Ima2 and Pna2₁.

Figure 10. XRD pattern details of the SYN, WAT and CYC forms
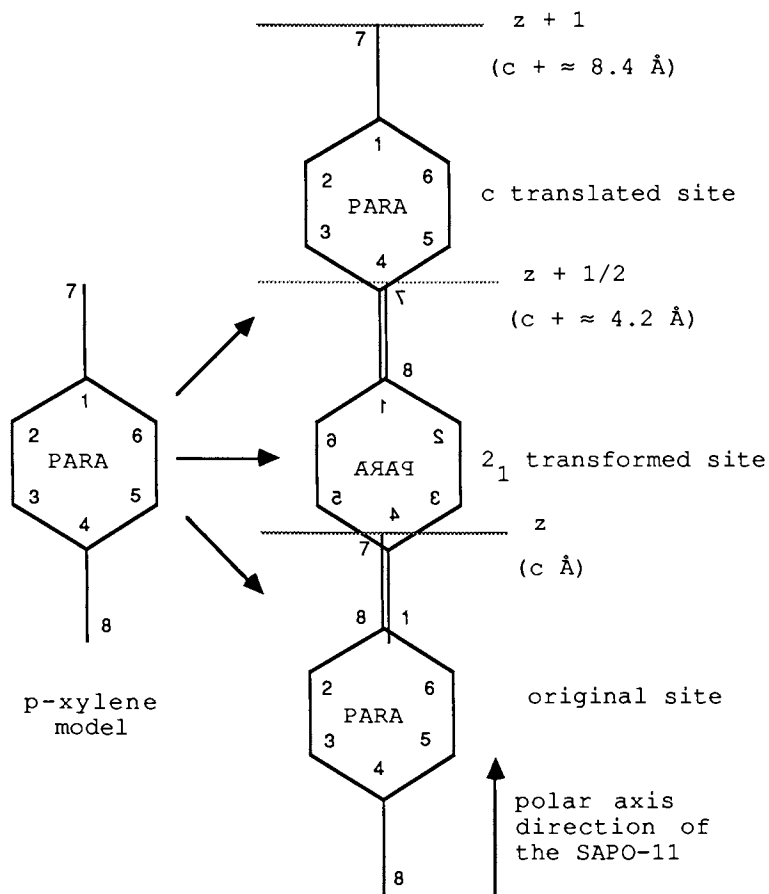of a SAPO-11 molecular sieve.

Figure 11. Possible disorder model for the p-xylene molecule in a SAPO-11 material.

the channel volume as a diffracting continuum ; in other terms the sorbed molecules are in an endless movement possibly induced by the polar 2_1 axis in the channel. For instance, figure 11 represents a possible situation where the p-xylene molecule has to obey the local symmetry elements (for a better visualization the original and the 2_1-transformed molecule are slightly displaced). Whatever the solution might be, materials of AEL topology appear to have very attractive properties (47) which need to be more extensively investigated by powder diffraction and other techniques.

Conclusion

Several conclusions may now be drawn from the present work. First of all, the crystallite size plays an important role in the diffusivity of reactant or product molecules, and subsequently in catalytic shape selectivity and deactivation rate. When the crystallite size increases, diffusion rate decreases, while shape selectivity and deactivation rate increase. These features obviously arise from an enhancement in the molecule pathway within the zeolite matrix, and from a decrease in the number of pore openings per unit weight when the crystallite size increases.

    Another important suggestion may be proposed on the basis of structural data. It was shown that upon adsorption of different molecules (p-xylene, benzene, toluene, pyridine, etc.) the zeolitic framework symmetry is closely related to the amount of sorbed organic guests, e.g. b axis compression and a and c axis expansion when filling MFI materials with more than four p-xylene molecules/uc (see Table III). Moreover, if a sample filled with a given hydrocarbon remains in air under atmospheric pressure and at room temperature, the guest hydrocarbon may be expelled by itself without heating or outgassing. For instance, p-xylene is desorbing from 8 to 4 molecules/uc with a diffusion coefficient about equal to that for adsorption (48).

    It thus turns out that the zeolitic matrix exhibits some relaxation strength resulting in the automatic desorption of adsorbates. For instance, in the high-coverage form, p-xylene was shown to be localized both at the channel-intersections and in the sinusoidal channel-junctions of a B-ZSM-5 matrix, but to desorb only via the straight channels, and even more via one direction only (48). This might be related to the molecular traffic control (MTC) concept proposed several years ago by Derouane and Gabelica (49).

Literature Cited

1.   Chu, C.T. ; Chang, C.D. J. Phys. Chem. 1985, 89, 1569.
2.   Coudurier G. ; Védrine J.C. Pure and Appl. Chem. 1986, 58, 1389.
3.   Tielen, M. ; Geelen, M. ; Jacobs P.A., In Proc. Intern. Symp. Zeolite, Siofolk, 1985, p. 1.
4.   Scherzer, J. In Catalytic Materials, Whyte, T.E. et al. Ed., ACS Symposium Series, n° 248, American Chemical Society : Washington, DC 1984 ; p. 157.
5.   Ball, W.J. ; Dwyer, J. ; Garforth, A.A. ; Smith, W.J., Ibid, p. 137.

6. Shibata, M. ; Kitagawa, H. ; Sendoda, Y. ; Ono, Y., Ibid, p. 717.
7 Hayashi, S. ; Suzuki, K. ; Shin, S. ; Hayamizu, K. ; Yamamoto, O. Bull. Chem. Soc. Japan., 1985, 59, 52.
8. Ball, W.J. ; Barri, S.A.I. : Cartlidge, S. ; Maunders, B.M. ; Walker, D.W. In Proc. 7th IZC; Murakami, Y. et al. Ed., Elsevier, Amsterdam, 1986, p. 951.
9. Perego, G. ; Bellussi, C. ; Corno, C. ; Taramasso, M. ; Buonomo, F. ; Esposito, A., Ibid, p. 159 and references therein.
10. Sayed, M.B. ; Auroux, A. ; Védrine, J.C., Appl. Catal., 1982, 12, 49.
11. Barrer, R.M., Pure and Appl. Chem., 1986, 58, 1317.
12. Guth, J.L. ; Kessler, H. ; Wey, R., In Proc. 7th 12C, Murakami, Y. et al., Elsevier, Amsterdam, 1986, p. 121.
13. Argauer, R.J. ; Landolt, G.R. US Patent 3 702 886, 1972.
14. Khouzami, R. ; Coudurier, G. ; Mentzen, B.F. ; Védrine, J.C. In Proc. Symposium on Innovation in Zeolite Materials Science ; Nieuwpoort, Studies in Surface Science and Catalysis, Elsevier, Amsterdam 1988 in press.
15. Derouane, E.G. In Catalysis by Zeolites ; Imelik B., et al. Ed. in Surf. Sc. and Catal., N° 5, Elsevier, Amsterdam, 1980, p. 5.
16. Crank, J.   In Mathematics of Diffusion ; Oxford University Press, London, 1956, p. 86.
17. Barrer, R.M. In Advances in Chemistry Series ; N° 102, American Chemical Society, Washington, DC, 1971, p. 1.
18. Auroux, A. ; Bolis, V. ; Wierzchowski, P. ; Gravelle, P.C. ; Védrine, J.C. J. Chem. Soc., Faraday Trans II, 1979, 75, 2544.
19. Fitch, A.N. ; Jobic, H. ; Renouprez, A. J. Phys. Chem., 1986, 90, 1311.
20. Wright, P.A. ; Thomas, J.M. ; Cheetham, A.K. ; Nowak, K. Nature, 1985, 318, 611.
21. Baerlocher, C. In Proc. 6th IZC ; Olson, D.H. ; Bisio, A. Ed, Butterworths, London, 1984, p. 823.
22. Olson, D.H., ; Kokotailo, G.T. ; Lawton, S.L. ; Meier, W.M. J. Phys. Chem., 1981, 85, 2238.
23. WU, E.L. ; Lawton, S.L. ; Olson, D.H. ; Rohrman, A.C. ; Kokotailo, G.T. J. Phys. Chem., 1979, 83, 2777.
24. Fyfe, C.A. ; Kennedy, G.J. ; De Schutter, C.T. ; Kokotailo, G.T. J. Chem. Soc., Chem. Commun., 1984, p. 541.
25. Taramasso, M. ; Perego, G. ; Notari, B. In Proc. 5th IZC ; Rees, L.V., Ed. ; Heyden, London, 1980, p. 74.
26. Chao, K.J. ; Lin, J.C. ; Wang, Y. ; Lee, G.H. Zeolites, 1986, 6 359.
27. Mentzen, B.F. ; Védrine, J.C. ; C.R. Acad. Sci., Paris, 1985, 301(II), 1017.
28. Pope, C.G. J. Phys. Chem., 1986, 90, 635.
29. Eckman, R.R. ; Vega, A.J. J. Phys. Chem., 1986, 90, 4679.
30. Mentzen, B.F. C.R. Acad. Sci., Paris, 1986, 303 II, 681.
31. Mentzen, B.F. ; Vigné-Maeder, F. Mater. Res. Bull., 1987, 22, 309.
32. Mentzen, B.F. C.R. Acad. Sci., Paris, 1986, 303 II, 1299.
33. Mentzen, B.F. Mater. Res. Bull., 1987, 22, 337.
34. Mentzen, B.F. Mater. Res. Bull., 1987, 22, 489.
35. A local modified version of the DBW3, 2 Code of Wiles D.B. and Young, R.A. J. Appl. Cryst., 1981, 14, 149.

36. Mentzen, B.F. ; Bosselet, P. ; Bouix, J., <u>CR. Acad. Sci., Paris</u>, 1987, <u>305(II)</u>, 51.
37. Mentzen, B.F. ; Bosselet, F. <u>Mater. Res. Bull.</u>, 1988, <u>23</u>, in press.
38. Baerlocher, C. ; Mentzen, B.F. ; Unpublished work.
39. Bennett, J.M. ; Smith, J.V. <u>Z. für Kristallogr.</u>, 1985, <u>171</u>, 65.
40. Bennett, J.M. ; Dytrych, W.J., Pluth, J.J. ; Richardson, Jr. J.W. ; Smith, J.V. <u>Zeolites</u>, 1986, <u>6</u>, 349.
41. Bennett, J.M. ; Cohen, J.P. ; Flanigen, E.M. : Pluth, J.J. ; Smith, J.V. ACS Symposium Series N° 218 American Chemical Society, Washington, DC, 1983, p. 109.
42. Bennett, J.M. ; Richardson, Jr. J.W. ; Pluth, J.J. ; Smith, J.V., <u>Zeolites</u>, 1987, <u>7</u>, 160.
43. Mentzen, B.F. ; Védrine, J.C. ; Khouzami, R. <u>C.R. Acad. Sci., Paris</u>, 1987, <u>304(II)</u>, 11.
44. Mentzen, B.F. ; Védrine, J.C. ; Khouzami, R. ; Coudurier, G. <u>C.R. Acad. Sci., Paris</u>, 1987, <u>305(II)</u>, 263.
45. Meier, W.M. ; Willinger, H. <u>Z. fürKristallogr.</u>, 1969, <u>129</u>, 411 and Baerlocher, Ch., Hepp, A. ; Meier, W.M. ; DLS-76, a program for the simulation of crystal structures by geometric refinement, Zürich, 1977.
46. Mentzen, B.F. ; et al. to be published.
47. Flaningen, E.M. In <u>Synthesis and properties of new molecular sieves</u>, In <u>Proc. Symposium on Innovation in Zeolite Materials Science</u>, In Studies in Surf. Sci. and Catal., Grobet P. et al. Ed., Elsevier, Amsterdam, 1988 in press.
48. Mentzen, B.F. ; Bosselet, F. ; Bouix, J. <u>C.R. Acad Sci., Paris</u>, submitted.
49. Derouane, E.G. ; Gabelica, Z. <u>J. Catal.</u>, 1986, <u>65</u>, 486.

Chapter 5

Studies of Molecular Sieve Catalysis by Diffuse Reflectance IR Spectroscopy

V. A. Maroni, K. A. Martin[1], and S. A. Johnson

Materials Science Division, Argonne National Laboratory, Argonne, IL 60439

Diffuse reflectance infrared Fourier transform spectroscopy is being used to investigate the interaction of
hydrocarbons with catalytically active zeolites, such as
H-ZSM-5. The experiments are carried out in a controlled environment (temperature, gas composition) diffuse
reflectance cell. The reactivity of alcohols, light
olefins, and ethers on ZSM-5- and offretite-type
zeolites has been probed by observing the changes in
intensity of the framework O-H stretching vibrations as
a function of the type of reactant, temperature, and
product mix (determined by gas chromatography/mass
spectrometry). C-H stretching vibrations of organic
fragments retained in the zeolite channels and pores are
also observed in these experiments, and they too are
correlated with reactant, temperature, and product mix.

This paper presents examples of the application of diffuse reflectance infrared Fourier transform (DRIFT) spectroscopy to the study
of acid site chemistry and catalysis by product-selective molecular
sieve materials. The most attractive features of the DRIFT method
are that (i) uncompacted, high-surface-area powders can be studied
in controlled chemical environments and over a wide range of temperatures; (ii) reactants can be passed through a bed of the powdered
sample and infrared spectra recorded simultaneously at temperatures
in excess of 500°C with high species detection sensitivity; and
(iii) the sample can be repeatedly regenerated and exposed to
reactants without being removed from the diffuse reflectance (DR)
cell assembly.
    The DRIFT method has proven to be extremely useful for studies
of the O-H, O-D, C-H, and C-D stretching region (nominally 2000 to
4000 cm^{-1}) of molecular sieve materials (1-3). Kazansky and co-
workers (4-6) have employed the DRIFT technique to investigate the
combination and overtone structure of the O-H and O-D band systems

of zeolites in the near-infrared region. However, in the application of DRIFT spectroscopy to the spectral region below 2000 cm^{-1}, problems with anomalous specular reflectance and other light scattering phenomena are often encountered when studying molecular sieve materials (2,3). While these effects can be overcome in most cases by 10- to 100-fold dilution of the sample in a powder matrix of a material having very low absorbance over the spectral range of interest, such dilution leads to a significant reduction in the intensity of spectral features originating from the sample. Also, for the types of investigations described in this paper, the diluent chosen must be one that does not (i) ion exchange or react with the molecular sieve material (at or below ~600°C), (ii) react directly with the hydrocarbons fed to the diffuse reflectance cell, or (iii) have catalytic activity of its own under the reaction conditions and at the temperatures of interest.

The results and discussion which follow show how DRIFT spectroscopy in a controlled environment cell can be used to probe the active sites in synthetic zeolite catalysts, the nature and temperature dependence of the organic species (referred to herein as fragments) bound within the zeolite framework during and after exposure of the zeolite to light hydrocarbons, and, in conjunction with gas chromatography/mass spectrometry (GC/MS), the rate, product speciation, and mechanism of the zeolite-induced reforming reactions.

The authors recognize that some of the results presented in this paper parallel published findings based on other types of infrared spectroscopic techniques, but feel that their presentation in the context of this paper serves to establish the credibility of the DRIFT/GC/MS procedure in advance of the publication of similar studies currently under way on other molecular sieve systems that have not been investigated in detail by such methods.

Experimental Methods

The alcohols used in this work were obtained from Aldrich Chemical Co. (99+% grade). The ethylene and dimethyl ether were Matheson C.P. grade. The H-ZSM-5, the H-offretite, and their aluminoferrisilicate analogs were synthesized by standard methods that are described in the literature (7-11). The sodium substituted forms of these same zeolites were prepared by repeated washing of the protonated form of the zeolite in 1 M NaCl.

The apparatus used for the DRIFT studies consists of a controlled environment diffuse reflectance cell (Harrick Scientific Corp., Model HVC-DRP) interfaced with optics (Harrick Scientific Corp., Model DRA-SID) that allow adaptation to a BOMEM D3A FTIR spectrometer. A sketch of the diffuse reflectance (DR) cell is shown in Figure 1. A powdered specimen (8 to 10 mg) of the zeolite is placed on the screen in the sample cup at the top of the sample post (see Figure 1). To introduce a light hydrocarbon reactant which is a liquid at room temperature, a stream of dry nitrogen is bubbled through a glass trap containing the liquid and then passed on to the DR cell. Gaseous reactants (e.g., ethylene, dimethyl ether) contained in their as-received lecture bottles are fed directly into the DR cell through a bleed valve. The reactant stream flows into the cell at its base (gas entrance port), upwards along the heated sample post, through the powdered sample, and into an annular space

O-RING SEAL

WINDOW

SAMPLE CUP

CHAMBER

THERMOCOUPLE

SAMPLE POST

COOLANT (OUT)

GAS
ENTRANCE PORT

COMPRESSION NUT

WINDOW

SCREEN

HEATING ELEMENT

COOLANT CHAMBER

O-RING SEAL

COOLANT (IN)

GAS
EXIT PORT
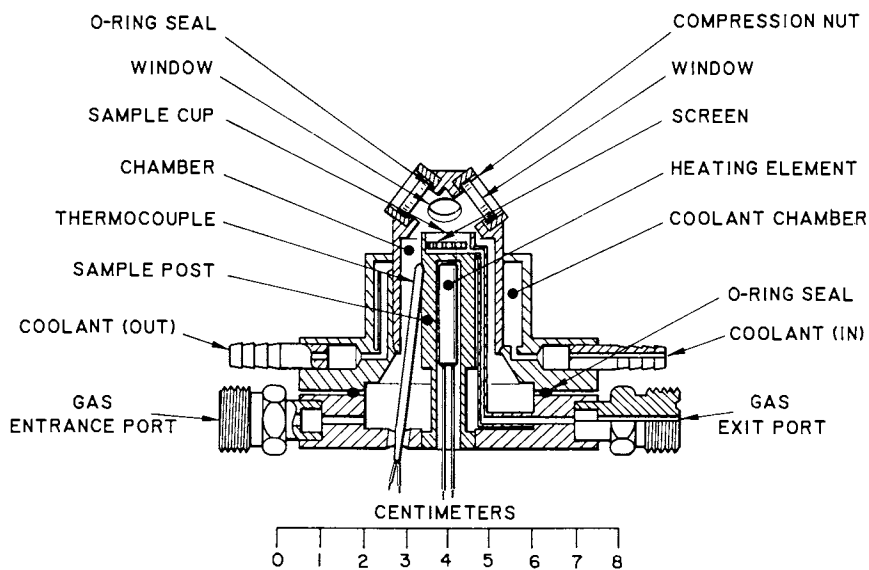
CENTIMETERS

0   1   2   3   4   5   6   7   8

Figure 1.   Controlled environment diffuse reflectance cell
(Harrick Scientific Corp., Model HVC-DRP).

below the screen which is connected (via a small diameter tube) to
the gas exit port.

The thermocouple built into the Harrick Model HVC-DRP cell is
attached to the outside surface of the sample post at a point below
the sample cup (as shown in Figure 1). In order to get a more
accurate reading of the actual sample temperature, an auxiliary
thermocouple (not shown in Figure 1) was epoxied into a fitting that
attached to a third port in the base of the cell. The section of
this auxiliary (iron/constantan) thermocouple inside the cell was
strapped to the gas exit tube that runs from the upper portion of
the sample post to the gas exit port, after which the tip end was
bent into a small semicircle so that the tip of the thermocouple
could be positioned at the surface of the powdered specimen in the
sample cup. The built-in thermocouple was used as the control
thermocouple, but its temperature setting was adjusted to give the
desired temperature at the sample surface as measured by the
auxiliary thermocouple. All temperatures reported in this paper
were those measured by the auxiliary thermocouple.

The DRIFT spectra consist of 500 co-added scans taken at 4 cm^{-1}
resolution. Each sample spectrum is ratioed against the DRIFT
spectrum of powdered KBr (under dry N_2 flush) recorded in the DR
cell at a temperature near that at which the sample spectrum was
taken. This procedure is beneficial in reducing the thermal back-
ground enhancement due to infrared emission, which becomes progress-
ively more troublesome as the temperature is increased. These
effects are, however, less severe in the 2000 to 4000 cm^{-1} region
than at frequencies below 2000 cm^{-1} where thermal emission consti-
tutes a significantly greater fraction of the total infrared power
reaching the detector. The major spectral features in Figures 2
through 5, i.e., the O-H and C-H stretching bands are typically 0.1
to 0.2 absorbance units (peak-to-baseline). This sensitivity is
achieved for a loading of ~10 mg of zeolite packed into a circular
well ~3 mm in diameter and 2 mm deep.

In a typical experiment, the zeolite sample is first heated
slowly in flowing dry air to 525±25°C where it is held for 20 to 30
minutes; the air flush is then switched to a dry N_2 flush to purge
the system of O_2. During this treatment, hereafter called "condi-
itioning," all adsorbed water and organic matter (e.g., from prior
exposures to light hydrocarbons) are removed, leaving the zeolite
pores and channels free of physi- and chemi-sorbed species. The
zeolite is then cooled to the desired temperature for the next
exposure experiment, a DRIFT spectrum is taken, and the reactant is
introduced. The rate of delivery of a liquid reactant can be con-
trolled by adjusting the N_2 flow rate and/or the temperature of the
glass trap; bleed valve adjustments are made in the case of gaseous
reactants. After a 5 to 15 minute exposure of the catalyst sample
to the reactant stream, the flow of reactant is terminated, the DR
cell is purged with dry N_2 for several minutes, and a second DRIFT
spectrum is taken. In experiments where product speciation is
studied, the reactant-plus-product stream coming out of the gas exit
port is passed through a glass catch bulb which is designed to
collect specimens for subsequent analysis by gas chromatography/mass
spectrometry (using a Finnegan Model 4021C GS/MS system).

Results and Discussion

One of the most interesting and informative features of the infrared
spectra of protonated (or acid) form molecular sieve catalysts is
the character of the O-H stretching vibrations. For example, it is
usually the case that the acid form of a molecular sieve material is
the most active catalytically; for zeolites this acidity is primari-
ly Bronsted in nature and can have a fairly wide acid effectiveness
range. For a given zeolite framework structure, the Bronsted acidi-
ty can be correlated with the frequency of the O-H stretching vibra-
tion--the lower the frequency the more weakly bound (more acidic)
the proton. Two types of O-H vibrational sites are normally detec-
ted by infrared spectroscopy, those associated with hydroxyls con-
nected only to silicon atoms and those associated with hydroxyls
connected to aluminum atoms. The former type (SiOH) are found
mainly on the outer periphery of zeolite crystallites and in essence
terminate the disrupted framework structure at the surface. The
latter type, those involving aluminum, are for the most part located
intrastructurally at silicon-oxygen-aluminum bridges (Si-OH-Al),
where the attached proton balances the negative charge associated
with the aluminate subunit.
     DRIFT spectroscopy is especially useful for probing the acid
character of zeolite O-H vibrations. This utility can be illus-
trated by comparison of results for three zeolite systems having the
following framework structures and metal atom stoichiometries:
H-ZSM-5 with Si/Al$\simeq$10 and Fe = 0, AFS-H-ZSM-5 with Si/Fe$\simeq$43 and
Al$\simeq$0, and H-offretite with Si/Al$\simeq$4. DRIFT spectra of these three
zeolites in the O-H stretching region (Figure 2) demonstrate how
hydroxyl site character is affected by metal atom substitution in a
fixed framework structure (H-ZSM-5 vs. AFS-H-ZSM-5) and by variation
of aluminosilicate framework (H-ZSM-5 vs. H-offretite). It is well
established (5,6,10,12-17) that the band at ~3745 cm^{-1} in each spec-
trum (Figure 2) is the O-H stretching mode of the terminal silanol
(SiOH) sites on the outer surfaces of the zeolite crystallites. The
frequency of the silanol O-H stretch shows little sensitivity to
zeolite structure and composition when it is measured on the same
instrument using the same sampling technique. With the DRIFT method
applied in this work, it invariably appears at 3745 $\pm$ 5 cm^{-1} for a
wide range of zeolites and related silicates.
     The remaining O-H bands in Figure 2 lie at frequencies below
the silanol stretch and have been attributed to the framework
hydroxyl groups that exhibit Bronsted acidity. The prominent bands
at 3610 cm^{-1} for H-ZSM-5 and 3630 cm^{-1} for the AFS-H-ZSM-5 arise
from the O-H stretch of a particularly active M-OH-Si hydroxyl site
(M = Al and Fe, respectively). The shift to higher frequency when
the Al(III) is replaced by Fe(III) reflects the reduced Bronsted
acidity of AFS-H-ZSM-5 compared to that of H-ZSM-5 (10).
     The weak O-H band at 3660 cm^{-1} in the H-ZSM-5 spectrum is seen
with varying intensity in most preparations of this synthetic zeo-
lite (1,5,6,12,17). It seems to gain intensity with increasing
silicon-to-aluminum ratio in the framework (5,12) and several
explanations have been offered concerning its origin. Sayed et al.
(12) suggest that this mode is due to water-perturbed nests of
silanol sites, while Kazansky et al. (5) claim that it should be
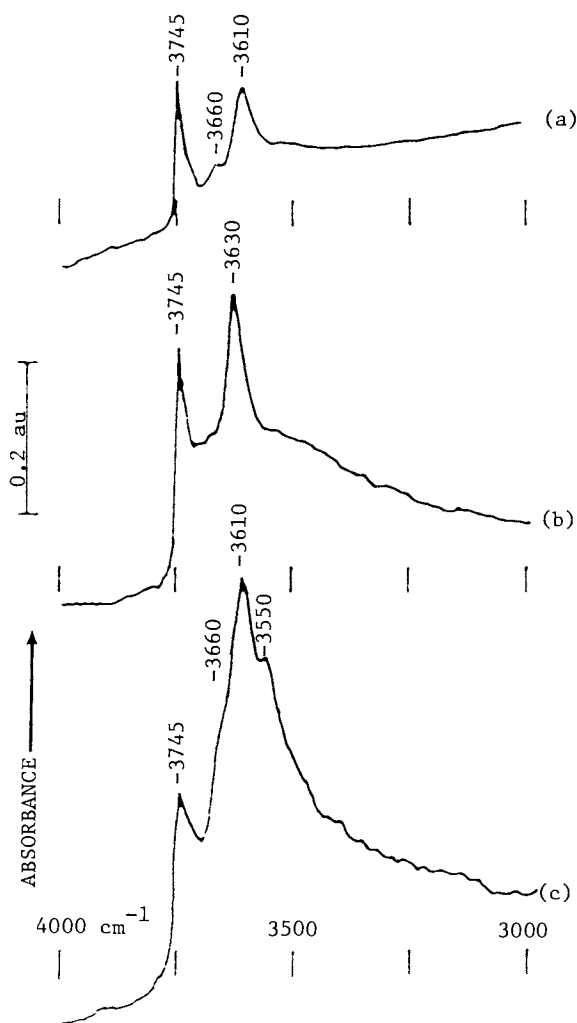ascribed to O-H vibrations of nonframework aluminate species.

Figure 2. DRIFT spectra (3000 → 4000 cm^{-1}) of (a) H-ZSM-5,
(b) AFS-H-ZSM-5, and (c) H-offretite.

Another possibility (related to the one proposed by Kazansky) is that the 3660 cm^{-1} band arises from small amounts of amorphous or poorly crystallized phases containing terminal -AlOH sites.

The O-H spectrum of H-offretite (Figure 2) is dominated by the absorption envelope between 3500 and 3700 cm^{-1} which appears to consist of at least three individual components--3550, 3610, and 3660 cm^{-1}, in good accord with the findings of Mirodatos et al. (18). The much greater combined intensity of these bands versus that of the silanol stretch at 3745 cm^{-1} must be due in part to the low silicon-to-aluminum ratio for the H-offretite (~4). However, when making such comparisons it is important to keep in mind that the silanol peak intensity can be as much a function of the surface area-to-volume ratio of the zeolite crystallites as it is of the silicon-to-aluminum ratio (13).

The DRIFT method can also be employed in conjunction with gas chromatography/mass spectrometry (GC/MS) to correlate acid site occupancy and organic fragment structure with the rate of reaction and the speciation of products. This type of application is illustrated in Figure 3 for the reaction of a 50/50 mixture of CH_3OH and CH_3OD on the ferrisilicate (AFS) form of ZSM-5 with Si/Fe = 43 and Fe/Al >>1. The figure includes results for the acid form of the ferrisilicate zeolite (AFS-H-ZSM-5) at 200 and 350°C and for the sodium-substituted form (AFS-Na-ZSM-5) at 350°C. DRIFT spectra of the respective forms of the AFS zeolite recorded after 15 minutes of exposure to CH_3OH/CH_3OD followed by a five-minute purge with N_2 are shown on the right-hand side of the figure. The corresponding reconstructed ion chromatograms (RICs) from GC/MS analyses of the gas flushed from the DR-cell just prior to the recording of each DRIFT spectrum of the exposed zeolite sample are presented to the left of the corresponding spectrum. GC/MS and DRIFT results obtained at 200°C and 350°C for the inactive AFS-Na-ZSM-5 are nearly the same in appearance and hence only the 350°C set is presented in Figure 3. Also, since the spectral profiles in the O-H and O-D stretching regions are identical in each DRIFT spectrum, only the O-D region is shown in Figure 3.

At 200°C, the RIC for the active AFS-H-ZSM-5 indicates a product mix consisting of a wide range of paraffinic, olefinic, and aromatic compounds having four (C_4) to twelve (C_{12}) carbon atoms. At 350°C the product RIC is reduced to that of a mixture of alkyl substituted benzenes. RICs of the flush gas taken following the methanol/AFS-Na-ZSM-5 exposure show little evidence of C_4 or greater products at either 200 or 350°C. The corresponding DRIFT spectra contain the SiOH and SiOD vibrations for both zeolites at each reaction temperature, but the O-H vibrations of the Fe-OH-Si and Fe-OD-Si sites only appear for the active (AFS-H-ZSM-5) form of the zeolite at 350°C. Another key feature of the DRIFT spectra in Figure 3 is that restructuring of the C-H stretching band accompanies the temperature increase for AFS-H-ZSM-5, but there is very little evidence of restructuring in the C-H region when the AFS-Na-ZSM-5 reaction temperature is increased from 200 to 350°C.

The relative number of counts obtained from the integrated RICs for each experiment represented in Figure 3 were >10^5 for AFS-H-ZSM-5 at 350°C, >10^4 for AFS-H-ZSM-5 at 200°C, <10^3 for AFS-Na-ZSM-5 at 350°C and <10^2 for AFS-Na-ZSM-5 at 200°C. These results imply a >100-fold reactivity difference between the protonated and sodium
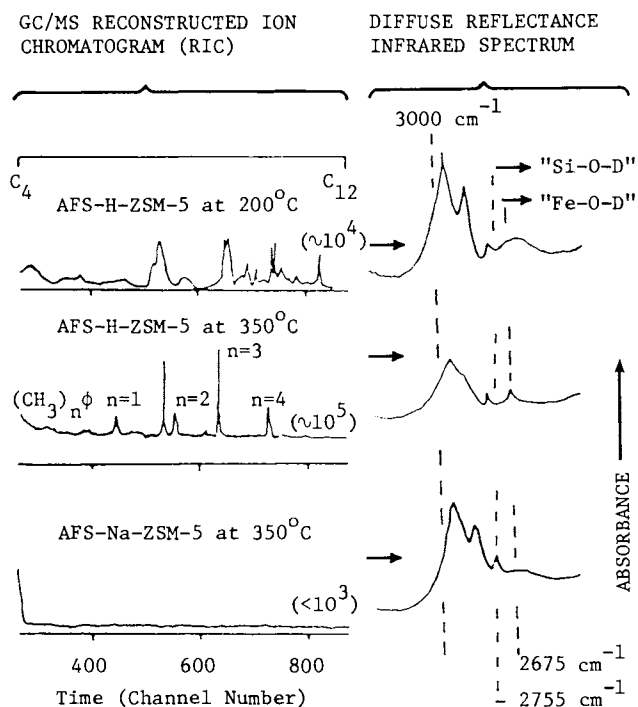
Figure 3. DRIFT and GC/MS study of the reaction of CH_3OH/CH_3OD on AFS-H-ZSM-5 and AFS-Na-ZSM-5. Numbers in parentheses on each RIC indicate the total number of counts in the C_4 to C_{12} range.

forms of the AFS material (with the residual activity of the sodium
form most probably a result of incomplete exchange of the protons).
They also highlight the clear correlation between C-H band structure
and reactivity.

The DRIFT technique that is most definitive for elucidation of
the intraframework interactions and species that accompany adsorp-
tion and reaction of light hydrocarbons on shape selective molecular
sieve catalysts is one based on the application of spectral subtrac-
tion procedures to the DRIFT spectra recorded prior to and following
exposure of the zeolite sample to a reactant. Typically, the spec-
trum recorded prior to exposure is subtracted from the post-exposure
spectrum. The resulting difference spectrum provides a signature of
the changes in protonated site occupancy and gives evidence of the
formation of organic fragments that tend to remain in the zeolite at
moderate temperatures even after purging of the reactant. Results
for exposures of H-ZSM-5 to isopropanol, n-butanol, and n-pentanol,
which illustrate the effects typically observed in these spectral
differencing experiments, are shown in Figure 4. These spectra
cover the spectral region of the O-H and C-H stretching vibrations.
They show that the silanol (3745 cm^{-1}) and aluminol (3610 cm^{-1}) site
occupancies are reduced in the presence of the "trapped" organic
fragments, that all O-H sites tend to recover their occupancies as
the trapped fragments desorb at higher temperatures, and that the
highly acidic 3610 cm^{-1} site is the last one to recover its initial
proton occupancy. For reactions involving light alcohols and ole-
fins on H-ZSM-5, the temperature at which fragment retention and
protonated site occupancy reach zero (as determined by DRIFT differ-
ence spectra) is generally around 400°C.

Experiments of the type described above and illustrated in
Figure 4 have been carried out for a series of zeolites which
included H-ZSM-5, H-offretite, and their iron substituted analogs,
using light alcohols, dimethyl ether, and ethylene as reactants.
From one zeolite to another, only subtle differences are seen in the
shape and intensity of the C-H band envelope as a function of reac-
tant and temperature. The response pattern depicted in Figure 4 --
a double-peaked C-H band envelope at lower temperatures (usually up
to ~200°C) which broadens to a single band at higher temperatures
and eventually disappears (circa 400°C) -- is typical of what is
observed in every case investigated where there is paralleling evi-
dence (from downstream GC/MS) that the reactant is being converted
into higher molecular weight products.

Greater differences are seen in the response of the framework
O-H stretching vibrations to various types of reactants and to the
presence of water in the incoming reactant stream. Some of these
responses are shown in Figure 5. Dry olefins exposed to conditioned
H-ZSM-5 and its iron-substituted analog leave a fragment that
depletes the protons at the aluminol (site) but does not signifi-
cantly alter the proton occupancy of the silanol site. This effect,
exemplified by spectra a and b of Figure 5, is interpreted as evi-
dence that the retained fragment is a carbocation which has assumed
the charge balancing role formerly played by the aluminol proton.
The C-H band structure of this carbocation fits the pattern of many
light parafins; and the lack of any significant infrared absorption
in the 3000 to 3200 cm^{-1} region precludes the presence of signifi-
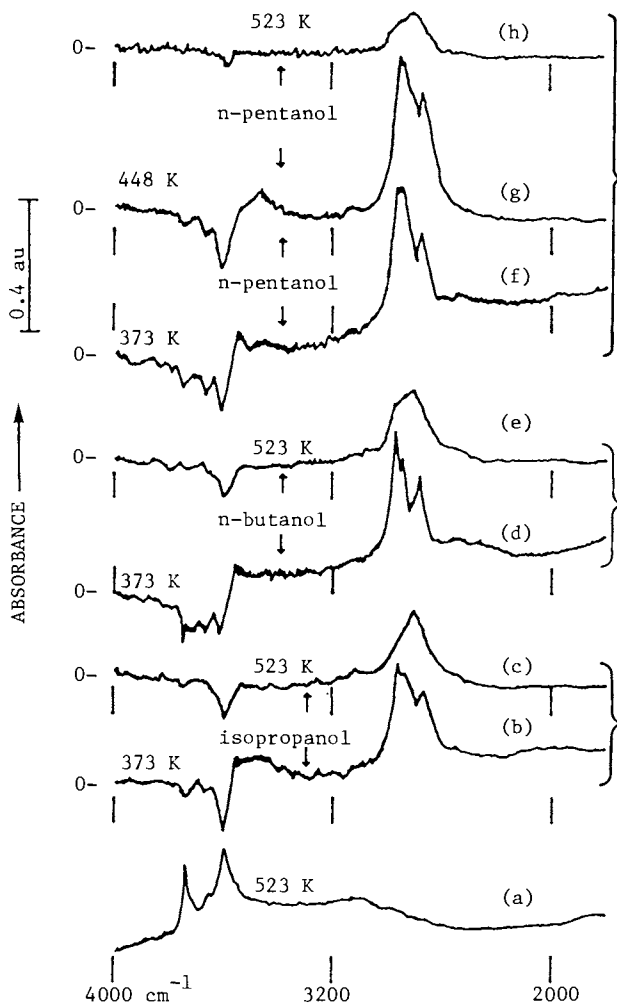cant amounts of olefinic or aromatic entities.

Figure 4. DRIFT spectrum of conditioned H-ZSM-5 at 523 K
(Curve a) and difference spectra of H-ZSM-5 taken after
exposure to isopropanol, (b) and (c); n-butanol, (d) and (e);
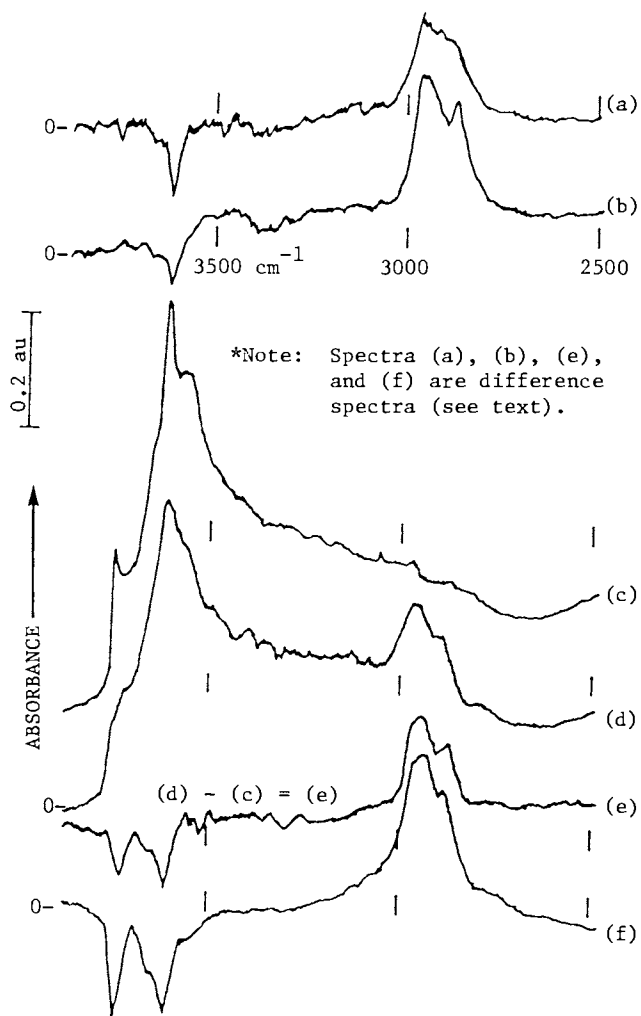and n-pentanol, (f), (g), and (h) at various temperatures.

Figure 5. DRIFT difference spectra for C_2H_4 on H-ZSM-5 at (a) 373 K and (b) 473 K; DRIFT spectra of H-offretite (c) before and (d) after exposure to C_2H_4 at 573 K; (e) = (d) – (c); (f) DRIFT difference spectrum for $(CH_3)_2O$ on H-offretite at 573 K.

DRIFT spectra of H-ZSM-5, H-offretite, and the AFS analog of
H-ZSM-5 taken after exposure to light alcohols or dimethyl ether
reveal retained organic fragments with C-H structures very much like
those observed following exposure to ethylene. These spectra also
show depletion of the aluminol protons (3610 cm^{-1}) but often give
evidence of depletion of the silanol site (3745 cm^{-1}) as well. This
effect, seen in Figure 4 and in spectra $\underline{e}$ and $\underline{f}$ of Figure 5, has
been tied to the presence of traces of water in the incoming reac-
tant stream and in the case of H-ZSM-5 is more prevalent at tempera-
tures below 150°C, the temperature at which water appears to freely
desorbed from H-ZSM-5 that is actively being exposed to a light
alcohol, olefin, or ether.

The results in Figure 5 for the C_2H_4/H-offretite exposure
(spectra $\underline{c}$ and $\underline{d}$ and their difference curve, spectrum $\underline{e}$) are parti-
cularly interesting because the negative peak structure in the 3600
to 3750 cm^{-1} region is very closely matched with the O-H region of
H-ZSM-5 (see spectrum $\underline{a}$ in Figure 2) but strikingly different from
that of spectrum $\underline{c}$ in Figure 5. Much of the intensity in the O-H
region of spectrum $\underline{c}$ (Figure 5), i.e., that remaining in spectrum $\underline{d}$
(Figure 5), must, therefore, be due to protonated sites that are
either not accessible to the reactant or not exchangeable. This
behavior is identical to that observed by Mirodatos et al. ([18]) and
is nicely summarized in Table 1 of their paper. The essence of
their explanation is that the 3745 cm^{-1} band is accessible, i.e., to
exchange with labile protons, but nonacidic (just like in H-ZSM-5);
the 3660 cm^{-1} band is not accessible to hydrocarbons (possibly
located in the hexagonal prisms); the 3610 cm^{-1} band is both acces-
sible and acidic (just like the 3610 cm^{-1} band of H-ZSM-5); and the
3550 cm^{-1} band is acidic but largely inaccessible (possibly located
in the cancrinite cages).

Concluding Remarks

The results presented in this paper show that diffuse reflectance
infrared Fourier transform spectroscopy, used in conjunction with
controlled environment techniques and gas chromatography/mass
spectrometry, can be a powerful tool for the study of catalysis by
product (shape) selective molecular sieve materials. By utilizing
spectral differencing techniques it is possible to track the vari-
ations in protonated site occupancy and the formation of stable
organic species that occur during exposure of molecular sieve
catalysts to organic reactants.

Acknowledgments

Literature Cited

1. Klier, K. In <u>Vibrational Spectroscopies for Adsorbed Species</u>;
    Bell, A. T., Hair, M. L., Eds.; ACS Symposium Series No. 137;
    American Chemical Society: Washington, DC, 1980, pp 141-162.
2. Kubelkova, L., Hoser, H., Riva, A., Trifiro, F. <u>ZEOLITES</u>
    1983, <u>3</u>, 244.
3. Chalmers, J. M., Mackenzie, M. W. <u>Applied Spectroscopy</u> 1985,
    <u>39</u>, 634.
4. Kustov, L. M., Borovkov, V. Y., Kazansky, V. B. <u>J. Catal</u>.
    1981, <u>72</u>, 149.
5. Kazansky, V. B., Kustov, L. M., Borovkov, V. Yu. <u>ZEOLITES</u>
    1983, <u>3</u>, 77.
6. Kazansky, V. B., Minachev, K. M., Nefedov, B. K., Borovkov, V.
    Y., Kondrat'ev, D. A.,Chukin, G. K., Kustov, L. M., Bondarenko,
    T. N., Konoval'chikov, L. D. <u>Kinetics and Catalysis</u> 1983, <u>24</u>,
    572.
7. Argauer, R. J., Landolt, G. R. U.S. Patent 3 702 886, 1972.
8. Derouane, E. G., Janos, B. N., Dejaifve, P., Nagy, J. B., van
    Hooff, J. H. C., Spekman, B. P., Vedrine, J. C., Naccache, C.
    <u>J. Catal</u>. 1978, <u>53</u>, 40.
9. Barrer, R. M., Harding, D. A. <u>Sep. Sci</u>. 1974, <u>9</u>, 195; Aiello,
    R., Barrer, R. M. <u>J. Chem. Soc</u>. (A) 1970, 1470.
10. Chu, C. T.-W., Chang, C. D. <u>J. Phys. Chem</u>. 1985, <u>89</u>, 1569.
11. Iton, L. E., Beal, R. B., Hodul, D. T. <u>J. Molecular Catal.</u>
    1983, <u>21</u>, 151.
12. Sayed, M. B., Kydd, R. A., Cooney, R. P. <u>J. Catal</u>. 1984, <u>88</u>,
    137.
13. Qin, G., Zheng, L., Xie, Y., Wu, C. <u>J. Catal</u>. 1985, <u>95</u>, 609.
14. Nunan, J., Cronin, J., Cunningham, J. <u>J. Catal</u>. 1984, <u>87</u>, 77.
15. Ono, Y., Mori, T. <u>J. Chem. Soc. Faraday Trans. I</u> 1981, <u>77</u>,
    2209.
16. Grady, M. C., Gorte, R. J. <u>J. Phys. Chem</u>. 1985, <u>89</u>, 1305.
17. Woolery, G. L., Alemany, L. B., Dessau, R. M., Chester, A. W.
    <u>ZEOLITES</u> 1986, <u>6</u>, 14.
18. Mirodatos, C., Abou-Kais, A., Vedrine, J. C., Barthomeuf, D. <u>J.</u>
    <u>Chem. Soc. Faraday Trans. I</u> 1978, <u>74</u>, 1786.

Chapter 6

Strong Acid Sites of Dealuminated Y Zeolites Prepared by Conventional Treatments and Isomorphous Substitution

Microcalorimetric Study

A. Macedo[1], A. Auroux[2], F. Raatz[1], E. Jacquinot[1], and R. Boulet[1]

[1]Institut Français du Pétrole, Boîte Postale 311, 92506 Rueil-Malmaison, Cedex, France
[2]Institut de Recherches sur la Catalyse, Centre National de la Recherche Scientifique, 2 Avenue Albert Einstein, F-69626 Villeurbanne, Cedex, France

The acidity of dealuminated Y zeolites prepared either by conventional treatments or isomorphous substitution has been characterized in detail through a microcalorimetric study of the adsorption of ammonia.

In agreement with previous studies, microcalorimetry confirms that in steamed products, most of the strong acid sites are poisoned by cationic extra-framework Al species. These sites can be recovered by an optimized post-steaming acid leaching. Isomorphously substituted HY which is free of extra-framework cationic species possesses more acid sites than conventionally dealuminated solids with similar framework Si/Al^{IV} ratio.

The catalytic performances of the solids in the conversion of cyclohexene are in qualitative agreement with their acidic properties as determined by calorimetric experiments or other techniques such as TPD of ammonia and infrared spectroscopy.

It is well known, that depending on the post-synthesis treatments, the acidity of zeolitic materials in terms of type, strength, localization and number of acid sites can vary over a wide range (1-5). The modification of the acidity of zeolites through various treatments is indeed widely used to design efficient FCC, hydrocracking , isomerization catalysts (6,8), etc. Since in solids, the acidity concept involves various aspects, several complementary characterization techniques have to be used. Over the last decade the acidic properties of zeolites have been the subject of extensive work (9-12) which has led to a deep understanding of the acidity of a large variety of solids (13,14). However, a limited number of systematic studies,

based on a multitechnique approach, have been devoted to the detailed determination of the evolution of the acidic properties of modified zeolites at each step of the post synthesis dealumination procedures (15-17).

In this work we will specifically focus on the acidic properties of fully characterized Y zeolites dealuminated by i) – conventional treatments (steaming, acid leaching) and ii) – isomorphic substitution (fluorosilicate). To achieve a detailed description of the acidity of these series of solids and of the mechanisms involved, complementary techniques have been retained : TPD of NH_3, IR of the hydroxyls, IR of adsorbed probe molecules with various basic strengths and adsorption of NH_3 followed by microcalorimetry. Results concerning TPD and IR have either been already published (18) or are the scope of another paper presented at the present conference (19). Here we will restrict ourselves to microcalorimetry. This powerful technique has proved to give reliable direct information on the acid strength distribution of zeolites with various structures (12,15,20,21). Our main aim here is to follow the evolution of the acid strength distribution (ASD) in dealuminated Y zeolites at each step of the dealumination procedures. We will also attempt to determine whether a direct link exists, at least on a semi-quantitative basis, between the acid strength distributions given by microcalorimetry of adsorbed NH_3 and the catalytic performance in a model reaction such as the conversion of cyclohexene.

EXPERIMENTAL

Solids. Starting from a low sodium, (% Na $<$ 0.17 wt), NH_4Y (Si/Al – 2.5), dealuminated solids have been prepared according to the two previous routes : i) – hydrothermal treatment, (HT), at various temperatures (773 K to 1123 K) followed by two successive acid leachings at 353 K in 1.5 N (HTA1) and 4 N (HTA2) HCl solutions, and ii) – isomorphic substitution (IS) in $(NH_4)_2SiF_6$ solutions buffered with $CH_3 CO_2NH_4$ at 348 K. All these solids have been characterized by chemical analysis, XRD, ^{29}Si MAS NMR and N_2 adsorption.

Microcalorimetry. Following a pretreatment at 623 K under vacuum ($<10^{-5}$ torr) overnight, the differential heat of adsorption of ammonia was measured at 423 K using a SETARAM – Tian-Calvet type microcalorimeter associated with a volumetric equipment allowing the simultaneous determination of the adsorption isotherm.

Model reaction. A Geomecanique microtest unit adapted to the study of reactions giving rise to a rapid catalyst deactivation was used (22). The reaction was conducted at a total pressure of 10^2 kPa with a cyclohexene partial pressure of $0.2 \cdot 10^2$ kPa, contact times in the range 0.5 to 1.5 s, at 643 K. Sampling was performed at various times on stream (2, 5, 8, 11 min).

Further details on the dealumination procedures, the characterization techniques and the model reaction studies can be found in ref. (23,24).

RESULTS

The main consequences of each step of the preparation procedures on the physicochemical properties of the solids (unit cell parameter, X-ray crystallinity, etc.) have already been described in ref. (18). However for the sake of clarity, the most important characteristics of the solids are given again in Tables I and II together with the dealumination operating conditions.

Conventional dealumination (HT, HTA1, HTA2 solids).
Steaming : As should be expected (18), steaming at increasing temperature leads to a loss of acid sites (Figure 1). More specifically, while a rather sharp peak is evident near 150 KJ mole^{-1} in the acid strength distribution (ASD) of (HT) solids treated below about 973 K (figure 3-a-c, table I), the (HT) solids treated at higher temperature exhibit a quite uniform ASD (Figure 3-e-h, Table I). However it should be noted that these (HT) solids with a highly dealuminated framework (Si/Al^{IV} $\geqslant$ 30) still possess a small amount of very strong acid sites in the 200 kJ mole^{-1} range (Figure 3-e-h).

Acid leaching : Providing that the steaming temperature is higher than about 800 K, the selective acid leaching conducted under mild conditions (no or very little framework Al^{IV} extraction) results in a significant increase of the number of acid sites (Figures 1, 2). All these (HTA1) solids, even those derived from (HT) solids characterized by a uniform ASD (steaming at temperature higher than about 973 K), are characterized by an intense peak located roughly between 150 and 200 kJ mole^{-1} in their ASD (Figure 3-b-d-f-i). An important point emerges from Figure 3 : the gain in strong sites (Q >100 kJ mole^{-1}) resulting from the mild acid leaching decreases gradually as the steaming temperature increases.
    In contrast with the mild acid leaching, the second and more severe acid treatment leads to (HTA2) solids possessing a very small amount of strong sites and characterized by a very flat ASD. The ASD of these solids illustrated in the case of HY52 on Figure 3-g does not depend on the X-ray crystallinity obtained after the acid treatment (Table I).

Isomorphic substitution (IS solids)

From Figure 4, it appears clearly that the (IS) solids which are only dealuminated up to about 50 %, possess a much larger quantity of acid sites with chemisorption energy in the 150-200 kJ mole^{-1} range than the (HT) or (HTA1) solids. The higher quantity of acid sites still holds true even for (IS) and (HT) or (HTA1) solids with comparable unit cell parameter (Figures 1, 2, 4, Tables I, II). Another important feature of most of the (IS) solids is a two- peak ASD (Figure 5). The progress of the isomorphic substitution affects this ASD in two ways :
    - the two peaks are moved to higher acid strength
    - the area of the least "acidic" peak decreases more rapidly

TABLE I

PHYSICO-CHEMICAL AND ACIDITY CHARACTERISTICS OF THE (HT) AND (HTA) SOLIDS

(HT) solids	Steaming temperature (°K)	XRD % crystallinity	Unit cell parameter (nm)	Si/Al total	Si/Al^{IV} (NMR)	V_{NH_3} ml.g^{-1} (P=1 torr)	NH$_3$/Al total	NH$_3$/Al^{IV}; y = Si/Al Amorphous phase
HY10	773	70	2.443	2.37	8	23.1	0.20	0.74 (y=0.20)
HY30	873	75	2.438	2.37	12	14.2	0.12	0.57 (y=0.04)
HY50	1043	86	2.428	2.37	35	7.9	0.07	1.01 (y = 0)
HY60	1123	75	2.423	2.37	>100	8.8	0.08	n.d.

(HTA) solids	Acid leaching concentration	XRD % crystallinity	Unit cell parameter (nm)	Si/Al total	Si/Al^{IV} (NMR)	V_{NH_3} ml.g^{-1} (P=1 torr)	NH$_3$/Al total	NH$_3$/Al^{IV}; y = Si/Al Amorphous phase
HY11	1.5 N	37	2.443	4.0	8.5	25.1	0.32	1.52 (y=1.5)
HY31	1.5 N	77	2.436	4.8	12	19.5	0.29	0.88 (y=0.5)
HY51	1.5 N	82	2.428	5.1	37	12.0	0.19	1.36 (y=0.14)
HY61	1.5 N	71	2.424	4.7	>100	10.5	0.15	n.d.
HY52	4 N	84	2.425	62	>100	4.5	0.73	1.39 (y=20)

TABLE II

PHYSICO-CHEMICAL AND ACIDITY CHARACTERISTICS OF THE (IS) SOLIDS

(IS) solids	Theoretical rate of dealumination	XRD % crystallinity	Unit cell parameter (nm)	Si/Al total	Si/Al^{IV} (NMR)	V_{NH_3} $ml.g^{-1}$ (P=1 torr)	NH_3/Al total
HYF1	15 %	91	2.466	3.2	3.0	74	0.76
HYF2	30 %	90	2.458	4.1	4.0	65	0.82
HYF3	45 %	91	2.450	5.5	5.4	48	0.91
HYF4	50 %	89	2.445	6.7	6.8	45	0.96
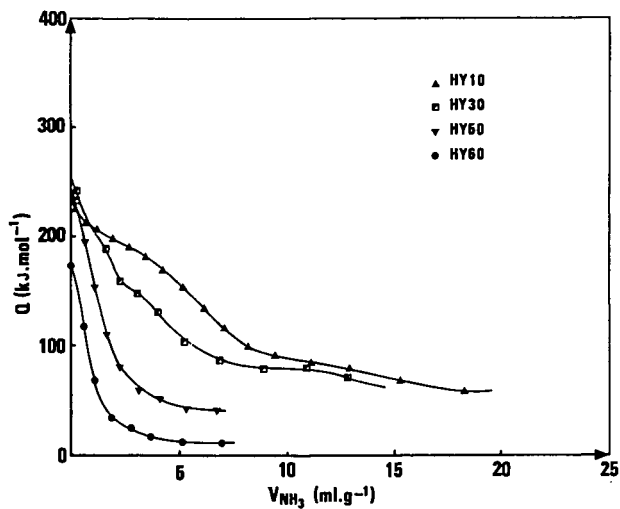
Figure 1. Heat of adsorption of ammonia versus coverage for the steam dealuminated solids (HT.)
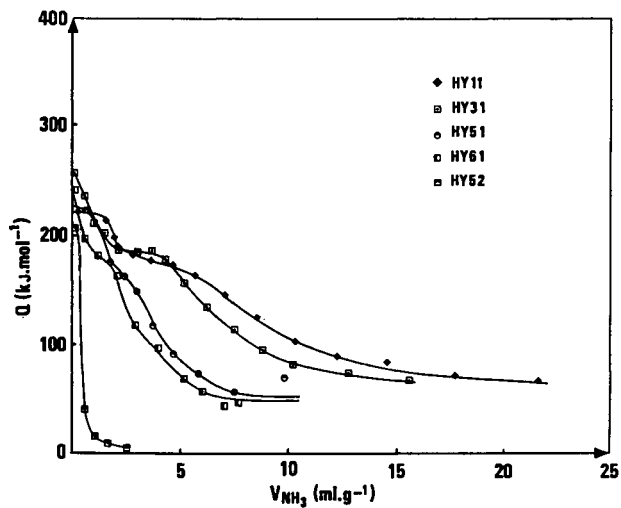
Figure 2. Heat of adsorption of ammonia versus coverage for the steamed and acid leached solids (HTA).
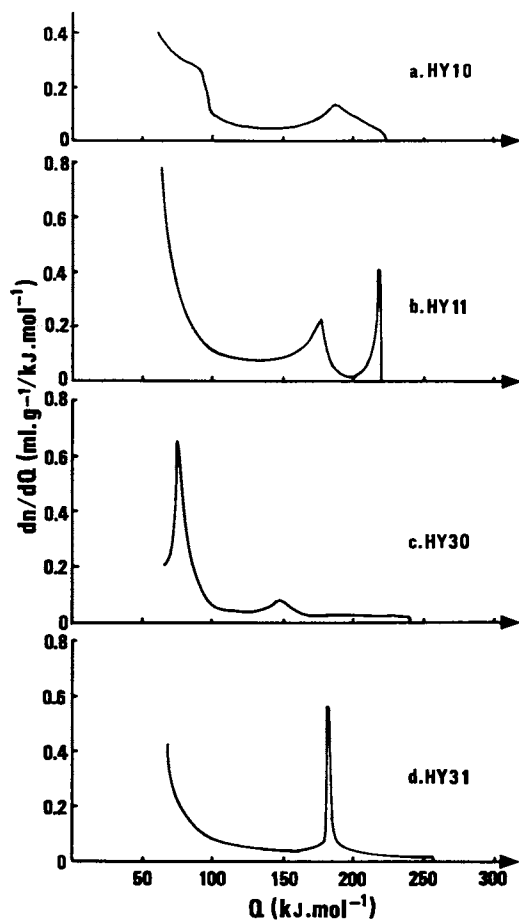
Figure 3. Acid strength distribution (ASD) of the (HT) and (HTA) solids.
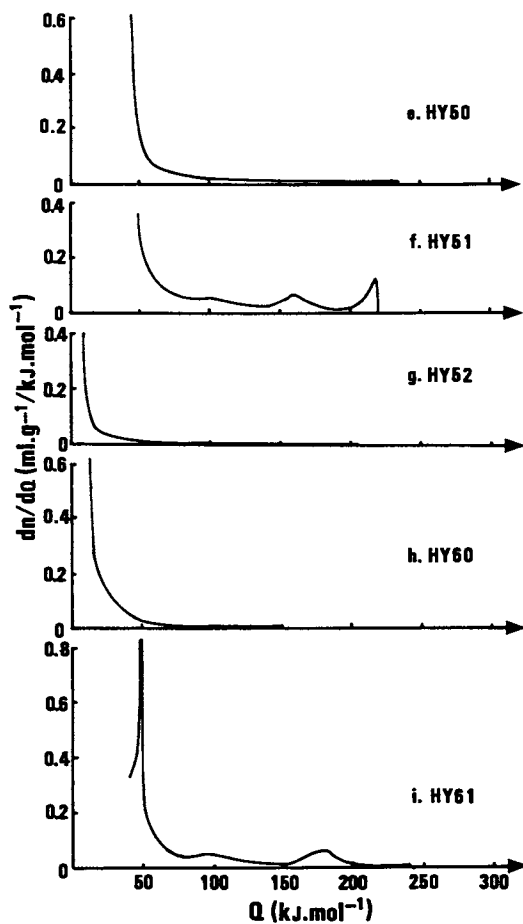
Figure 3. Continued. Acid strength distribution (ASD) of the (HT) and (HTA) solids.
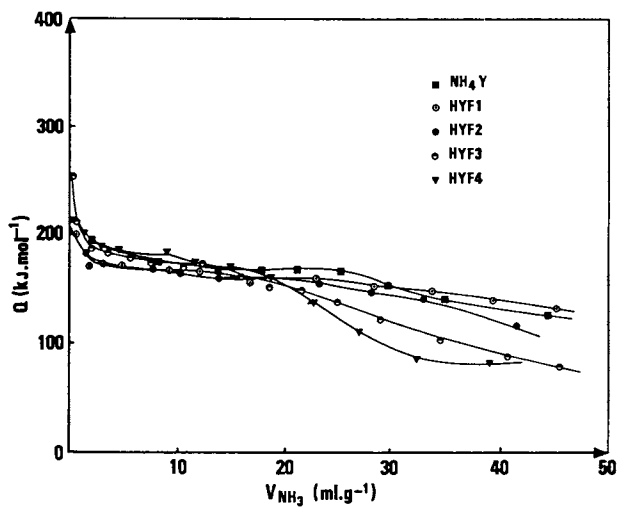
Figure 4.   Heat of adsorption of ammonia versus
coverage for the isomorphously substituted solids
(IS).
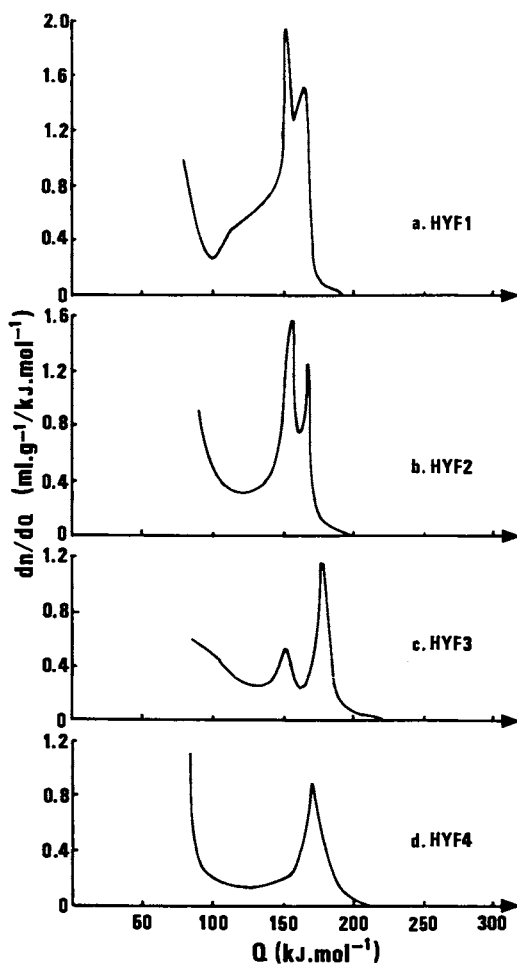
Figure 5. Acid strength distribution (ASD) of the (IS) solids.

than that of the most "acidic" peak; for dealumination levels
higher than about 40 % only the most "acidic" peak remains.

DISCUSSION

Before discussing the microcalorimetric experiments it would be
helpful to summarize briefly the main results which have been
previously obtained by other techniques on the same solids (18).
        Concerning the conventional dealumination method, it has
been shown that the loss of acid sites arising from steaming does
not only result from the extraction of framework Al atoms.
Another mechanism is involved, namely the poisoning of the
strongest structural Brönsted sites by cationic extra-framework
aluminium species which are likely to be mainly located in the
supercages (25). This poisoning effect is especially important
for (HT) solids treated below about 973 K. Providing that the
post-steaming acid leaching is selective enough, most of the Al
poisoning species can be eliminated without any further
appreciable framework dealumination (18). Such an optimized acid
leaching could result in an increase of the number of strong
sites (18). In contrast a non selective acid attack always leads
to solids possessing very few acid sites whatever the retention
of the X-ray crystallinity (18).
        In contrast to the (HT), (HTA1), (HTA2) solids, the
isomorphously substituted (IS) solids, which are nearly free from
extra-framework species, only exhibit Brönsted acidity without
any significant amount of Lewis sites (18). Moreover compared to
the (HT), (HTA1), (HTA2) solids, they show a two-peak NH_3 TPD
spectrum (18).
        It is important at this stage to emphasize that the
isomorphic substitution by $(NH_4)_2SiF_6$ gives solids with limited
dealumination levels : up to about 60 %, which corresponds to
unit cell parameters not smaller than about 2.442 nm (26,27),
whereas a total framework dealumination could be easily achieved
by conventional treatments (unit cell parameter down to 2.423 nm
(4)). It is not entirely clear at the moment, whether this
limited dealumination level for the (IS) solids results from the
experimental conditions we used or is specific to the
fluorosilicate technique. Nevertheless this situation renders
difficult the detailed comparison between the acidic properties
of solids with identical framework dealumination levels prepared
by the two techniques. However, as will be seen later, important
trends can be derived.

Isomorphic substitution. Since the (IS) solids only possess
framework Brönsted sites the first point to be discussed is :
        Do the framework Al^{IV} account for the total quantity of
strongly chemisorbed ammonia ?
        The NH_3 adsorption isotherms are not perfectly rectangular,
thus the precise estimation of the quantities of strongly
chemisorbed ammonia is somewhat difficult. We have retained for
this estimation a pressure of 1 torr which corresponds to the
pseudo-plateau region of the isotherms. The calculated NH_3/Al^{IV}
ratios are close to 0.80 (Table II) and a nice linear correlation

is found between the total ammonia chemisorbed volume $(P = 1$ torr) and the unit cell parameter a_o; slope 1480 $cm^3 g^{-1}$ nm^{-1}, theory ($NH_3/Al^{IV} = 1$) 2275 $cm^3 g^{-1}$ nm^{-1}. These results obviously support the idea that in (IS) solids, the framework Al sites only are responsible for the acidity which is, in that case, of Brönsted character exclusively (18).

In agreement with their NH_3 TPD spectra (18), the (IS) solids exhibit a two-peak ASD (Figure 5). Since these solids also show two structural Al-OH bands in their IR spectra (14,18,27,28), the so called h.f. and l.f OH, it would be tempting to attribute the " most acidic" calorimetric peak to the most acidic IR band, i.e, h.f. and the "least acidic" calorimetric peak to the least acidic IR band, i.e, l.f. (18,19). This attribution is, however, not entirely satisfactory since (IS) solids with framework Si/Al^{IV} ratio higher than about 6 only show a one-peak ASD (Figure 5-d) while the h.f. and l.f. OH bands are still present in the IR spectra (18). Additional work is needed to clarify this situation. Whatever the exact attribution of the calorimetric peaks in terms of IR OH bands, it appears clearly that framework dealumination does not lead to a loss of sites keeping a constant acid strength. On the contrary (Figure 5) the least acidic Brönsted sites are preferentially eliminated while the strengths of the two types of sites increase in the course of the dealumination procedure. These rather clean results (no interference with extra-framework species) would directly support the generally accepted, but still not completely proven, scheme according to which the framework dealumination gives less structural Brönsted sites but with a stronger acid strength. An elegant theoretical model has been recently proposed by D. Barthomeuf (29) to rationalize such a behaviour. According to our experiments the increase in acid strength is quite significant since it corresponds to an increase of about 12 kJ $mole^{-1}$ for the heat of adsorption of NH_3 on the two types of sites (Figures 5).

Conventional dealumination. NH_3 is known to be a non-selective probe: it can interact with Brönsted as well as with Lewis sites (30). Under such conditions the amounts of ammonia which interact strongly ($P = 1$ torr) with the (HT), (HTA1) and (HTA2) solids cannot be directly attributed to the neutralization of the framework Brönsted sites. To address that problem a possible preliminary approach is to evaluate NH_3/Al_T and NH_3/Al^{IV} ratios (where Al_T and Al^{IV} stand respectively for the total amount of aluminium present in the solids and the amount of framework Al atoms).

First, whatever the treatments the NH_3/Al_T ratios are always much smaller than 1.0 in the (HT), (HTA1) solids, to be compared with the 0.80 value found for the (IS) Y zeolites (Tables I, II). This indicates, in agreement with previous results (18,19), that a limited amount of extra-framework species possess a strong acidic character .

The evaluation of the NH_3/Al^{IV} ratio is much more difficult since one has not only to know the framework Si/Al^{IV} ratio of the zeolite but also the proportion of the zeolitic phase in the dealuminated material. Indeed from a material balance point of

view, a (HT) or (HTA1) HY can be formally considered as being formed by two phases :

    i) – a weight fraction (1 – z) of a zeolitic phase free from any extra-framework species, with a Si/Al^{IV} ratio x.

    ii) – a weight fraction z of amorphous phase with a Si/Al ratio equal to y.

    According to these scheme, the amount of framework Al^{IV} is given by :

$$Al^{IV} (\% \, wt) = \frac{0.45}{1 + x + \left(\dfrac{x - x_0}{x_0 - y}\right) * (1 + y)} * 100$$

where x_0 is the (Si/Al)total ratio of the solid.

    Since the Si/Al material balance leads to the relation :
$$(1-z)* \, x + z*y = x_0$$
only two among the three variables (x, y, z) are needed   to evaluate the amount of framework AI^{IV} in the composite system. While x can be readily measured (XRD, ^{29}Si MAS NMR), y and z can only be roughly estimated by indirect methods. Most often y is implicitly considered as being equal to zero. However, depending on the operating conditions HY dealuminated by conventional techniques always contain significant amounts of extra-framework Si atoms, which means that in most cases y is not equal to zero.

    In a very rough approach, the amorphous phase Si/Al ratios y have been chosen so that the zeolitic fraction (1-z) is equal to the XRD crystallinity of the solids. It appears, from these calculations, that y varies from 0 to about 2 for (HT) and (HTA1) solids, (Table I) which is in qualitative agreement with STEM results (31). Concerning the (HTA2) solids, y can reach very large values, (>20), which is consistent with the fact that the severe acid leaching extracts most of the extra-framework Al^{IV} species. With these values for y, only approximate NH$_3$/Al^{IV} ratios can be calculated (Table I).

    However some qualitative trends can be extracted from the results reported in Table I. For the (HT) solids, the NH$_3$/Al^{IV} ratios are smaller than 1, which would mean that some Al^{IV} atoms do not interact with NH$_3$. Higher NH$_3$/Al^{IV} ratios are obtained after a mild acid leaching ; a possible explanation could be that in (HTA1) solids a higher proportion of framework Brönsted sites are able to interact with ammonia. This result is in agreement with the elimination, in the course of the mild acid leaching procedure, of cationic poisoning species (18), an effect which is discussed in more details below.

    Since the (IS) solids with low unit cell parameters close to 2.445 nm are characterized by a one-peak ASD, one would also expect for the (HT) solids (a < 2.442 nm) a one-peak ASD. This is indeed the case for (HT) solid treated at low temperature (T < 973 K). For (HT) solids treated at higher temperatures the ASD is very flat (Figure 3). This does not mean that these (HT) solids are free from framework Al atoms. These framework sites still exist but, as has already been proved by indirect techniques (25) and more recently by a direct one, namely Rietvelt analysis (32),

they are poisoned by extra-framework cationic Al species and to a much less extend by residual Na cations. An optimized acid leaching, which does not extract appreciable amounts of framework Al, allows an almost complete elimination of the poisoning species, giving rise to an important peak in the ASD between 150 and 180 kJ mole^{-1} (Figure 3- b-d-f). The gain of strong acid sites is especially important for the solids steamed at low temperature because these conditions favor the formation of extra-framework Al cations while higher steaming temperatures more likely lead to neutral polymeric species. Contrary to the (IS) solids, in the case of (HTA1) HY, the heat of adsorption corresponding to the ASD peak does not vary monotonically with the unit cell parameter ; it shows a more complex behaviour (Figure 3).

At this stage an important question has to be addressed : from the NH_3 probe point of view how do the (HT), (HTA1) solids compare with the (IS) materials ? Restricting ourselves to solids with similar framework Si/Al^{IV} ratios, it appears clearly that both type of solids possess acid sites with very similar strengths. They show a one-peak ASD located near 175 kJ mole^{-1}. However conventional HY, even those which have been submitted to an optimized acid leaching, possess less acid sites than the (IS) solids. This is not surprising since (HT) and (HTA1) HY are not purely zeolitic, they contain variable amounts of extra-framework material. This extra-framework material is mainly responsible for the Lewis acidity of (HT) and (HTA1) solids while the (IS) solids are nearly pure Brönsted acids.

Up to now we have focussed on acid sites characterized by heat of adsorption of ammonia in the range 150 to 190 kJ mole^{-1}. However, whatever the dealumination procedures or the framework dealumination levels, all the solids possess a very small amount of very strong acid sites in the range 190 to 220 kJ mole^{-1} (Figures 3 and 5). The origin of these very strong sites, which represent a very small proportion of the framework Brönsted sites, is not clear. One can argue that they either correspond to isolated framework Al atoms or to the very first framework sites which are not surrounded by NH_3 neutralized sites (coverage effect). It is very difficult experimentally to measure with a high precision the heat of adsorption of NH_3 on these very strong sites and the derivative plots are approximative in that region. To compare the strength of these strongest sites one possible rough approach is to plot the cumulative heat of adsorption (ΣQ) versus the adsorbed amount (Figure 6). On such a plot it appears that, whatever the solids (HY11 is an exception), the slope at the origin is nearly always the same, i.e., about 10 J.cm^{-3}. This roughly indicates that the strength of the very few strongest sites is not very much affected either by the dealumination procedure or the framework dealumination level. In other words even highly dealuminated solids with unit cell parameter close to 2.423 nm possess very strong sites.

It is important to determine at least on a qualitative basis how do the ASD given by microcalorimetry of adsorbed NH_3

correlate with the catalytic properties of the solids. Cyclohexene transformation is a model reaction which is well adapted to easily characterize the acidity of catalysts and to determine the hydrogen transfer tendency of FCC catalysts. Here we will not discuss the selectivity results (hydrogen transfer versus isomerization), we will only examine briefly what are the main effects of the preparation procedures on the conversion levels.

Let us first consider the effect of the acid leaching of the (HT) solids (Figure 7). In agreement with NH_3 adsorption, the selective acid leaching (HTA1) leads to a very significant increase of the conversion levels, whereas an important decrease is evidenced for solids which have been submitted to a non-selective dealumination (HTA2). These results directly illustrate the benefit arising from a selective elimination of the cationic poisoning species formed in the course of the steaming procedure.

As far as the strength of the acid sites in the 150-180 kJ range is concerned, our microcalorimetric experiments (Figure 6) suggest that some sort of continuity may exist between (IS) and conventional HY. Indeed an almost continuous curve is obtained when the conversion levels in cyclohexene transformation are plotted against the unit cell parameter for (IS) and (HTA) solids. The detailed interpretation of Figure 8 is obviously outside the scope of the present paper. However it should be noted that the rather low conversion levels of the (IS) solids do not only result from a surprisingly low acidity (microcalorimetric experiments tell us that it is not the case) but more likely from higher deactivation rates. Additional work is obviously needed to better compare the catalytic activity of (IS) and (HTA1) solids with similar unit cell parameter. The aim of Figure 8 is only to give preliminary results on the relative catalytic performances of (IS) and conventional HY.

CONCLUSION

Adsorption of ammonia followed by microcalorimetry has proved to be a very useful tool to determine quantitatively the acid strength distributions of HY zeolites dealuminated either by conventional treatments or isomorphic substitution. Concerning the conventional dealumination route, it has been confirmed that the post steaming acid leaching plays a very important role. When conducted under optimized conditions it leads, through the elimination of extra-framework cationic species, to a recovery of strong framework sites. The elimination of these poisoning species gives rise to an improvement of the catalytic performance. Isomorphously substituted (IS) HY nearly behave as ideal Brönsted acids (NH_3/Al^{IV} close to 1) and possess more acid sites than conventional HY with similar unit cell parameter. At least for the (IS) solids, the strength of the residual acid sites increases significantly with the dealumination level.
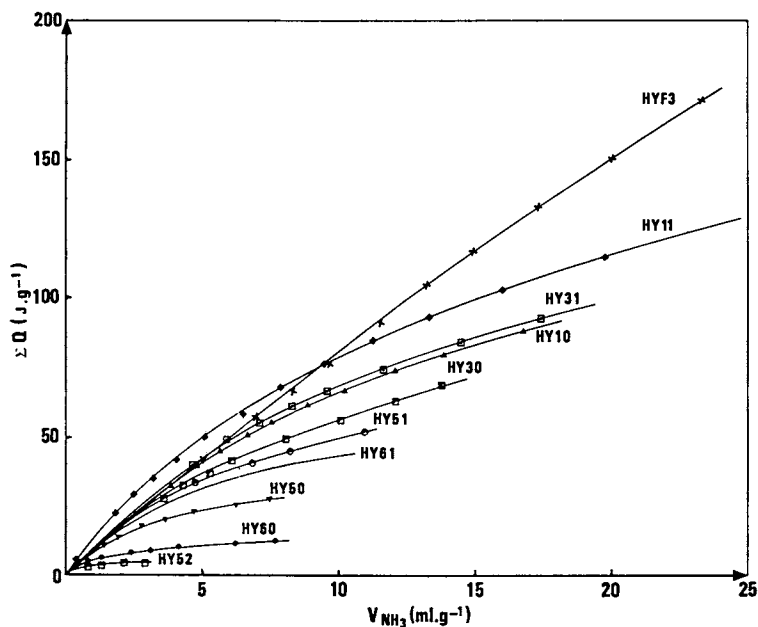
Figure 6. Cumulative heat of adsorption for the (HT), (HTA) and (IS) solids.
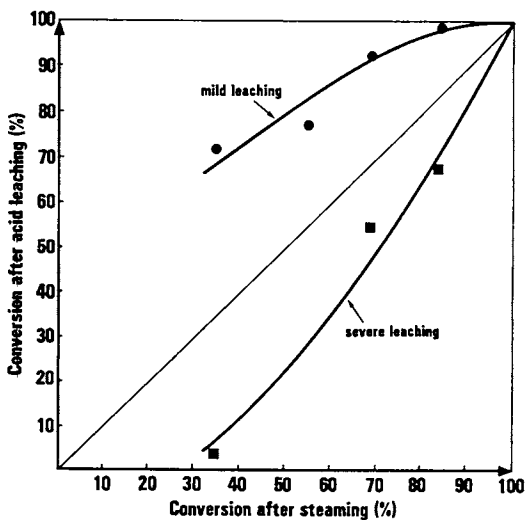

Figure 7. Conversion level in cyclohexene transformation after acid leaching versus conversion level after steaming for the (HTA1) and (HTA2) solids (time on stream 2 min.).
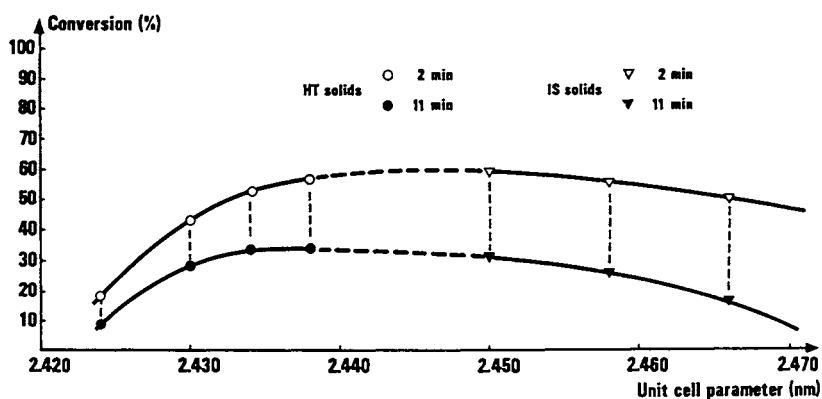
Figure 8. Conversion in cyclohexene transformation
against unit cell parameter for the (HT) and (IS)
solids (times on stream 2 and 11 min.).

LITERATURE CITED

1. Barthomeuf, D., in Molecular Sieves II, ACS Symposium Series n° 40 ; American Chemical Society : Washington, DC, 1977, 453.
2. Hey, M.J.; Nock, A.; Rudham, R.; Applleyared, I.; Haines, G.; Harris, R.; J. Chem. Soc. Faraday Trans I, 1986, 82, 2817.
3. Kubelkova, L., J. Chem. Soc. Faraday Trans I, 1984, 80, 1367.
4. Scherzer, J. in A.C.S. Symposium Series n° 248, 1983, 157.
5. Ashton, A.; Batmanian, S; Clark, D.M.; Dwyer, J.; Fitch, F.; Hinchcliffe, A.; Machado, F.; in Catalysis by Acids and Basis; B. Imelik et al ed; Elsevier : Amsterdam;,1985, 101.
6. Habib, E; Venuto, P.B. in"Fluid Catalytic Cracking with Zeolite Catalysts"; Marcel Dekker : New-York; 1979.
7. Ribeiro, F; Rodrigues, A; Rollmann, L. Naccache, C; in Zeolites Science and Technology; Martinus Nijhoff Publishers, 1984.
8. Drzaj, B.; Hocevar, S.; Pejovnik, S.; in Zeolites, Synthesis, Structure, Technology and Application; Elsevier Amsterdam, 1985.
9. Ghosh, A.; Curthoys, G.; J. Chem. Soc. Faraday Trans I, 1984, 80, 99.
10. Pfeifer, H.; Freude, D.; Hunger,M.; Zeolites, 1985, 5, 274.
11. Jacobs, P.A.; Mortier,W.J.; Zeolites, 1982, 2, 226.
12. Klyachko, A.L.; Kapustin, A ; Brueva, T.; Rubinstein, A.; Zeolites, 1987. 7, 119,
13. Skeels, G.; Flank, W.; in Intrazeolite Chemistry, ACS Symposium Series n° 218, American Chemical Society : Washington DC, 1983, 369.
14. Akporiaye, D.; Chapple, A.; Clark, D.; Dwyer, I; Elliot, I.; Rawlence, D.; Stud. Surf. Sci. Catal.,1986, 28, 351.
15. Vedrine, J.C.; Auroux, A.; Bolis, V. J. Catal., 1979, 59, 24
16 Hidalgo, C.V.; Hitoh, H.; Hattori, T.; Niwa, M.; Murakami Y.; J. Catal., 1984, 85, 362.
17. Lok, B.M.; Marcus B.K.; Angell,C.L.; Zeolites, 1986, 6, 185.
18. Macedo,A.; Raatz, F.; Boulet, R.; Lavalley, J.C.; Janin, A.; Symposium on Innovation in Zeolite Materials Sciences, Nieuwport (Belgium), Sept. 14-17 (1987), to be published
19. Janin,A.; Lavalley, J.C.; Macedo, A.; Raatz F.; Symposium Perspectives in Molecular Sieve Science, Toronto (Canada June 1988.
20. Auroux, A.; Ben Taarit, Y.; Thermochimica Acta, in press.
21. Masuda, T.; Taniguchi, H.; Tsutsumi, K.; Takakashi, H.; Bull. Chem. Soc. Japan, 1979, 10, 2849.
22 Mercier des Rochettes, B.; PhD, ENSPM Rueil-Malmaison, France, 1983.
23. Macedo, A. ; PhD, ENSPM, Rueil-Malmaison, France, in preparation.
24. Jacquinot, E.; DEA, ENSPM Rueil-Malmaison, France 1986.

25.   Macedo, A.; Raatz, F.; Boulet,R.; Freund E.; Marcilly,
      in New Developments in Zeolite Science and Technology :
      preprint of poster papers ; Japan Association of
      Zeolite ed.,1986, 91.
26.   Lynch,J.; Raatz F.; Delalalande,C.; IUPAC Symposium on
      Characterization of porous solids, Bad-Soden (FRG)
      26-29th April, 214, 1987, to be published.
27.   Skeels, G.W.; Breck,D.W.; Proc. 6th Int. Zeolite Conf.,
      1983, 87.
28.   Baizoumi, Z. PhD, Paris VI, 1987.
29.   Barthomeuf, D. Mat. Chem. Phys.,1987, 17, 49.
30.   Ward,J.W.; in A.C.S. Monograph n° 171, American Chemical
      Society : Washington DC; 1976 118,.
31.   Lynch, J.; Raatz F.; Delalande, C.; IFP unpublished results.
32.   Merlen, E.; IFP unpublished results.

Chapter 7

FT–IR Study of the Brönsted Acid Sites in Dealuminated HY Zeolites Using Specific Probe Molecules

A. Janin[1], J. C. Lavalley[1,3], A. Macedo[2], and F. Raatz[2]

[1]Laboratoire de Spectrochimie, Groupe Catalyse et Spectrochimie, Unité Associée No. 414, I.S.M.Ra, Université de Caen, 14032 Caen, Cedex, France
[2]Institut Français du Pétrole, Boîte Postale 311, 92506 Rueil-Malmaison, Cedex, France

The Brönsted acid sites of HY zeolites dealuminated either by conventional treatment (steaming + acid leaching) or isomorphous substitution (fluorosilicate) have been characterized at each step of the preparation procedures through IR spectroscopy of probe molecules with various basic strengths (pyridine, C_2H_4, H_2S). In contrast to pyridine, which cannot easily discriminate between OH groups with similar acid strength, C_2H_4 and H_2S lead to a much more specific interaction. Whatever the dealumination procedures, the structural high-frequency OH is likely to be the most acidic and its acid strength smoothly increases with the framework dealumination level. Some of the extra-framework Al-OH groups present in conventional HY treated at low temperature indeed possess a pronounced acidic character since they can interact with C_2H_4 or H_2S. Finally two components at 3738 and 3743 cm^{-1} appear to contribute to the Si-OH at 3740 cm^{-1}; they correspond respectively to SiOH groups attached to the framework and to an extra-framework silicon-containing phase.

It is well known that the number, type and strength of the Brönsted acid sites which are present in modified H zeolites do not only depend on the Si/Al^{IV} ratio of the framework (1, 2). The nature and the amount of non-framework species such as residual alkaline cations,

[3]Correspondence should be addressed to this author.

cationic or neutral Al species also play an important role on the acidity of the solids (3, 4).

   To characterize the Brönsted acidity of modified zeolites two methods can mainly be used : IR spectroscopy (4-7) and MAS-NMR (8, 9) with or without the use of probe molecules. Concerning more specifically modified HY zeolites, these two techniques have led to a rather clear description of the hydroxyls in terms of framework and non-framework species (10). Moreover very useful informations on the acid strength of the hydroxyls have been obtained through pyridine adsorption followed either by IR (5) or MAS NMR (8). Pyridine can discriminate between OH groups with very different acid strengths such as for example framework Al-OH and Si-OH groups of defects (11). However, since it is too basic, OH groups with a slightly different acid strength cannot be easily distinguished (12). In the course of a more general study devoted to the acidity of modified zeolites (4, 12), adsorption of basic probe molecules with various basic strength (alcohols, ethers, sulfides, thiols, hydrocarbons...) followed by FT-IR spectroscopy has been investigated. Of these probes, H_2S and C_2H_4 (adsorbed at about 210 K to avoid polymerization) appeared to be more appropriate (12).

   In this work, using H_2S and C_2H_4 as probes, we aim to characterize the strongest Brönsted acid sites of HY solids, dealuminated either by conventional treatment (steaming followed by acid leaching) or isomorphous substitution (by fluorosilicate) and to compare the results with those obtained with pyridine.

Experimental

Starting from a low sodium (% Na $\leq$ 0.17 wt) NH_4Y (Si/Al = 2.5) zeolite, dealuminated solids have been prepared either by i) hydrothermal treatment (HT) at various temperatures (773 to 1123 K) followed by a leaching at 353 K in 1.5 N or 3 N HCl solution (HTA), or by ii) isomorphous dealumination (ID) in $(NH_4)_2SiF_6$ solutions buffered with CH_3COONH_4 at 348 K (13).

   Infrared spectra have been recorded on a NICOLET MX-1 Instrument (Caen) or on a DIGILAB FTS-15E one (IFP). Self supporting pressed discs (ca. 5 mg cm^{-2}) have been activated by heating under vacuum at 723 K for 12 hours. Pyridine (10^2 Pa at equilibrium) was introduced at room temperature, then immediately evacuated at the same temperature and at 423 K to eliminate physisorbed species. Analysis of the spectra then obtained allows for the determination of OH bands insensitive to pyridine. Subtraction of spectra after pyridine desorption from those obtained before pyridine adsorption evidences well bands due to acidic OH groups.

   In the case of H_2S and C_2H_4, a partial pressure of 3 10^2 Pa has been introduced on the activated solids in the

IR cell at room temperature (H_2S) or in the cell frozen at 210 K by a methanol circulation (C_2H_4). The species formed were reversible. Their spectra were recorded under such conditions. Those spectra reported in the figures were obtained after subtraction of the gas phase spectra.

All the spectra have been normalized to the same amount of solid (10 mg).

Results

The evaluation at each step of the dealumination procedures, of the physicochemical characteristics of the solids together with their acidic properties followed by IR spectra of the OH, TPD of NH_3 and microcalorimetry of adsorbed NH_3, has already been described (4). However, for the sake of clarity, we report in Table I the main physicochemical characteristics of the solids. We will first summarize briefly the results related to the infrared study of the OH groups.

Table I - Physicochemical characteristics of the (HT), (HTA) and (ID) solids

(HT) Solids	(HT) T° (K)	% Crystal-linity	Unit cell parameter (nm)	Si/Al total	Si/Al^{IV} (NMR)	Na (ppm)
HY_{10}	773	70	2.443	2.37	8	1700
HY_{20}	823	75	2.440	2.37	9.4	1700
HY_{30}	873	75	2.438	2.37	12	1700
HY_{40}	973	75	2.434	2.47	15	<300
HY_{50}	1043	86	2.428	2.37	35	1700

(HTA) Solids	Acid leaching concent.	% Crystal-linity	Unit cell parameter (nm)	Si/Al total	Si/Al^{IV} (NMR)	Na (ppm)
HY_{11} *	1.5 N	37	2.443	4.0	8.5	880
HY_{21}	1.5 N	52	2.439	6.0	9.4	560
HY_{31}	1.5 N	77	2.436	4.8	12	960
HY_{41}	1.5 N	77	2.434	6.7	15	<300
HY_{51}	1.5 N	82	2.428	5.1	37	730
HY_{42}	3 N	80	2.425	40	90	<300

(ID) Solids	% Crystal-linity	Unit cell parameter (nm)	Si/Al total	Na (ppm)
HYF_1	105	2.468	2.95	<300
HYF_2	105	2.458	3.50	<300
HYF_3	102	2.448	4.70	<300

* HY_{11} is derived from HY_{10}, HY_{21} from HY_{20}, and so on.

OH groups.   Spectra in the 3800-3500 cm^{-1} range of the
HT, HTA and ID solids are reported on figure 1A, 1B, 1C.

- HT, HTA solids.   For these solids all the spectra
present at least the three classical bands assigned to
silanols (3742 cm^{-1}) and to the structural (h.f. : 3630
cm^{-1} ; l.f. : 3560 cm^{-1}) bridged OH groups (figures 1A,
1B). However, for solids treated below about 873 K
additional bands resulting from extra-framework materials
(10, 11) are evidenced near 3600 cm^{-1} (strong), 3660 cm^{-1}
(sharp) and 3680 cm^{-1} (shoulder). The intensities of
these additional bands increase as the steaming
temperature decreases (figure 1A).
    As far as the three previous classical bands are
concerned, the effect of the acid leaching is to increase
the number of silanol groups (3742 cm^{-1}) and h.f. OH
groups (3630 cm^{-1}). As discussed elsewhere (4), the
increase of the h.f. band is due to the elimination of
poisoning cationic Al species mainly located in the
supercages. Concerning the three additional bands, the
main effect of the acid leaching is to decrease their
intensity (figure 1B).

- ID solids.   The ID solids which are nearly exempt from
structural defects and extra-framework species present,
in agreement with (13, 14), the two structural h.f. and
l.f. bands with a very weak silanol band (figure 1C).
    As expected, the intensities of the structural h.f.
and l.f. bands decrease as the framework dealumination
level increases for the HT, HTA as well as for the ID
solids (figure 1).

Pyridine.
- HT, HTA solids.   It has been found that the l.f. band,
in contrast to the h.f. one, is insensitive to pyridine
in the case of non dealuminated HY zeolites (5,11);
however, it tends to be sensitive after dealumination
(5,11). In our case, the structural bands (h.f.,l.f.)
disappear completely after pyridine adsorption what-
ever the physicochemical characteristics of the solids
(figure 2). More surprising is the behaviour of the
silanol band (3742 cm^{-1}). While the low frequency part of
it (3738 cm^{-1}) appears to be insensitive to pyridine, the
high frequency part (3743 cm^{-1}) does interact with
pyridine. This interaction persists even after evacuation
at higher temperatures up to 723 K. Thus, two components
are responsible for the silanol band.
    Among the three additional OH groups which are
present in the HT and HTA solids two appear to be acidic:
they are characterized by bands at 3600 and 3660 cm^{-1} (HT
solids) or at 3670 cm^{-1} (HTA solids), while that at 3680
cm^{-1} does not interact with pyridine (figure 2). Another
ill-defined non acidic component is revealed in HT as
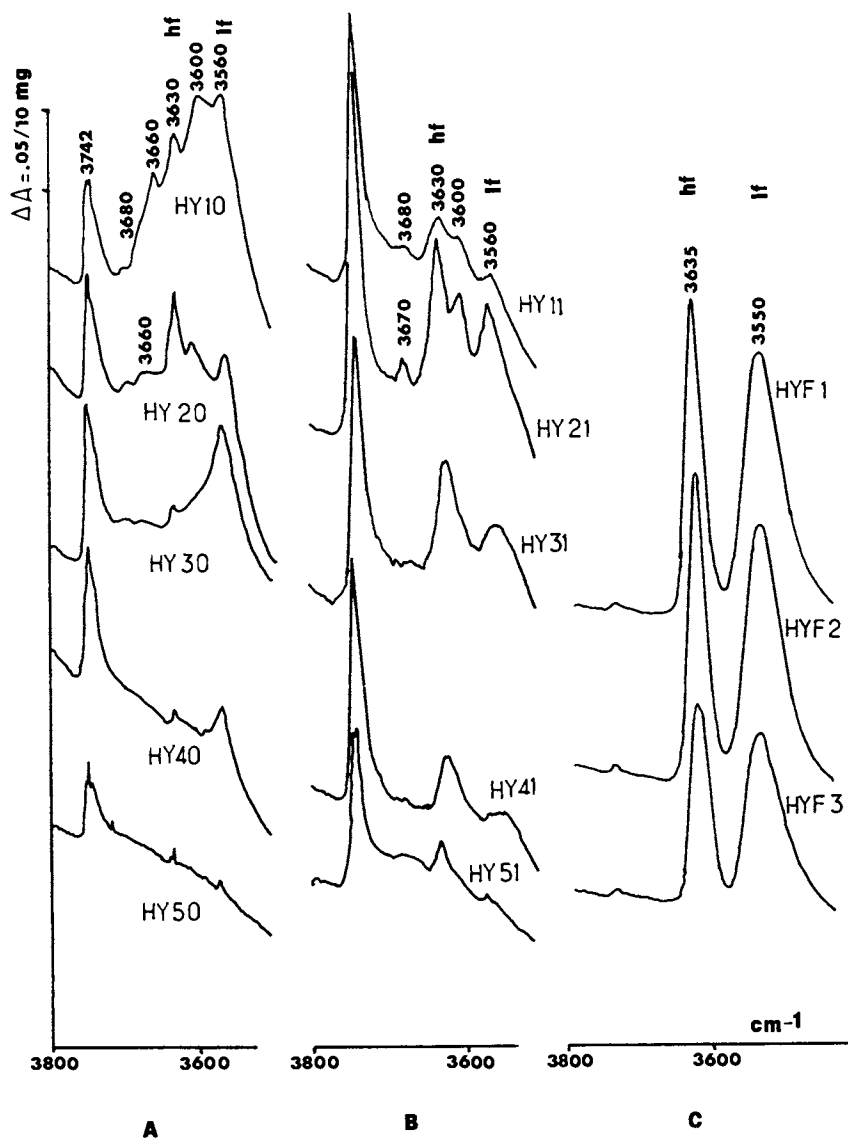
Figure 1. ν_{OH} bands of zeolites activated at 723 K.
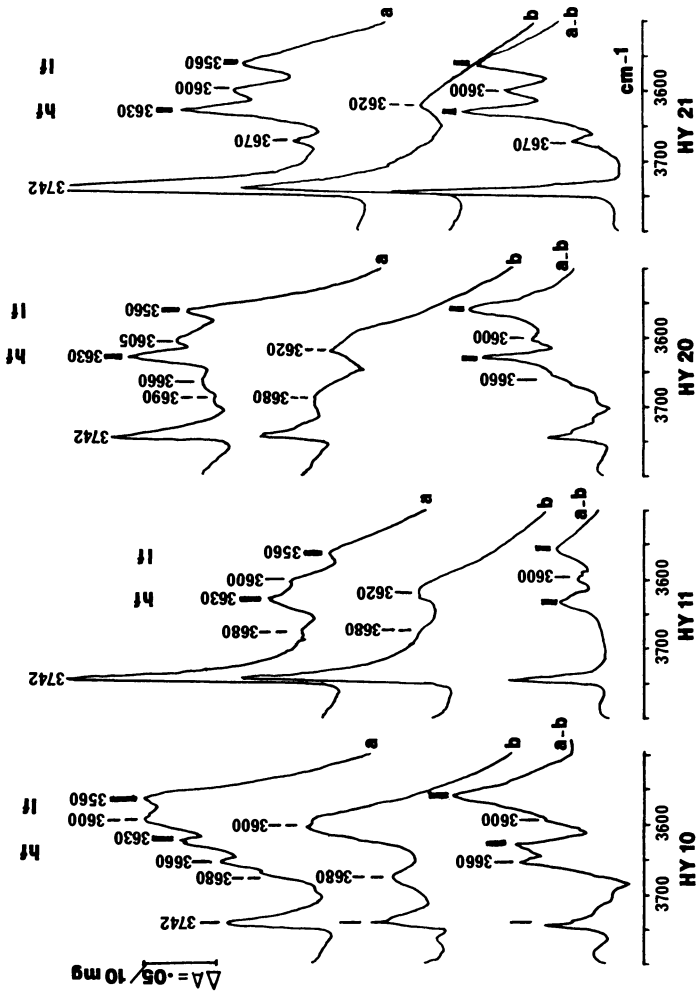A: HT ; B: HTA and C: ID series.

Figure 2. Sensitivity of OH bands towards pyridine :
zeolites steamed at moderate temperature
a: ν_{OH} bands of the activated zeolites
   before adsorption.
b: ν_{OH} bands insensitive after pyridine
   desorption at 423 K.
a-b: ν_{OH} bands sensitive to pyridine.

well as in HTA solids near 3620 cm^{-1} through pyridine adsorption (figure 3).

Although the effect of the acid leaching on these additional bands depends on the steaming temperature, some clear trends can be extracted from the spectra : the acidic component (3600 cm^{-1}) only slightly decreases after the leaching. On the contrary, a severe reduction of the intensity of the bands corresponding to non acidic groups (3620, 3680 cm^{-1}) is evidenced. The intensity of the ill-defined 3620 cm^{-1} band decreases as the steaming temperature increases, however it still persists even in solids treated up to 973 K (figure 3).

- ID solids. As for the HT and HTA solids, the h.f. and l.f. bands interact with pyridine. However for these solids with a limited dealumination level (< 50 %), the l.f. band appears to be composite since its low frequency part is not completely affected by pyridine.

Ethylene. While pyridine interacts with framework as well as with non-framework sites, ethylene gives rise to a more specific interaction. Whatever the solids HT, HTA, ID, as illustrated on figure 4A, the only band to be perturbed by ethylene is the structural h.f. Al-OH band. The only exception concerned HY_{21} where the extra-framework 3600 cm^{-1} band seems to be partly involved in the interaction (figure 5). Adsorption of ethylene does not lead to any protonation and the interacting OH groups are involved in a hydrogen bond with ethylene π electrons.

The bond strength between ethylene and interacting hydroxyls can be estimated by the following frequency difference (figure 4) (15):

$$\Delta \nu_{OH} = \nu_{h.f.} - \nu_a$$

where :
$\nu_{h.f.}$: is the frequency of the h.f. OH (before ethylene adsorption)
ν_a : is the frequency of the perturbed OH, after ethylene adsorption.

The $\Delta \nu_{OH}$ shift can therefore be considered as an approximate measure of the acid strength of the interacting OH.

Hydrogen sulfide. H$_2$S leads to results very similar to those observed for C$_2$H$_4$. For all the HT, HTA and ID solids, it interacts mainly through hydrogen bonding with the structural h.f. OH (figure 6). In the case of HY_{21}, a partial interaction with the structural l.f. band and the extra-framework 3600 cm^{-1} band may occur.

As for C$_2$H$_4$, no definite conclusion can be drawn for the interaction with the silanol groups since adsorption
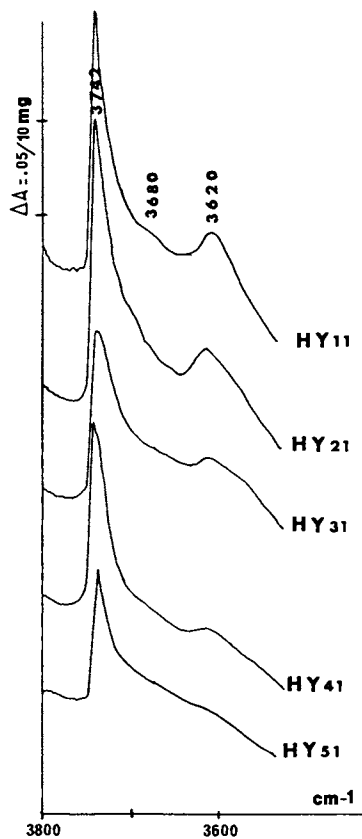
Figure 3. ν_{OH} bands insensitive to pyridine after
              desorption at 423 K (HTA series).
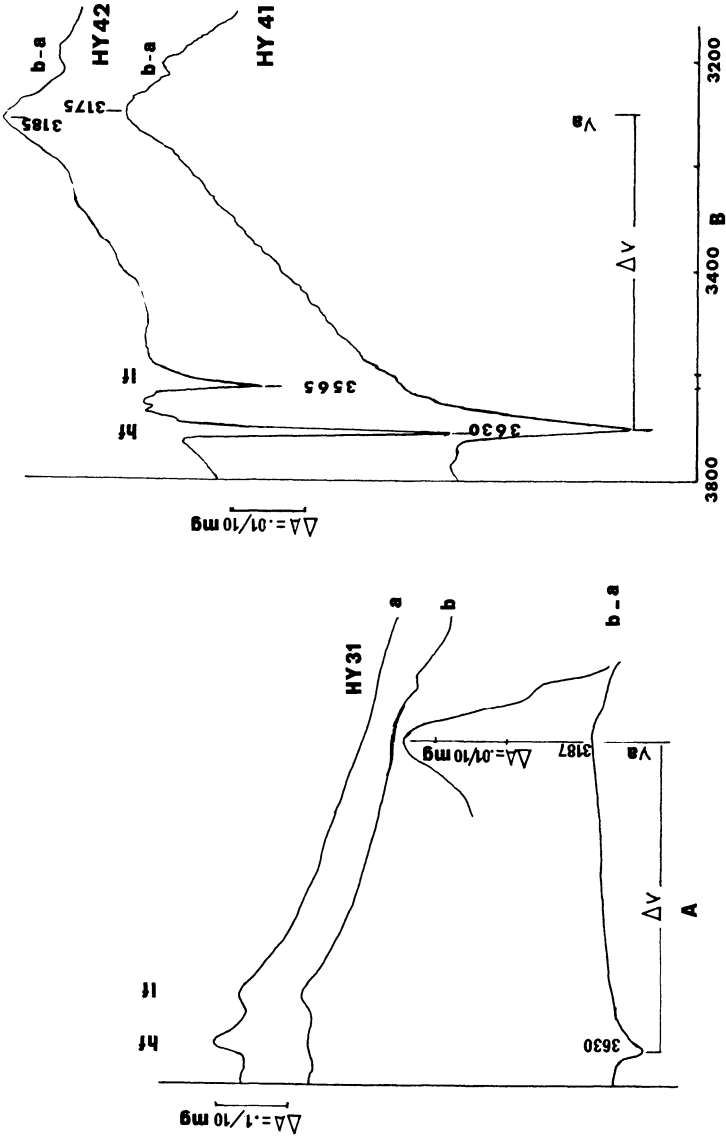
Figure 4. Ethylene adsorption on :
A: HY31 ; B: HY41 and HY42:
a: before ethylene adsorption.
b: after ethylene adsorption.
b-a: subtracted spectra for the
determination of the interacting OH and
the shift (ν_a).
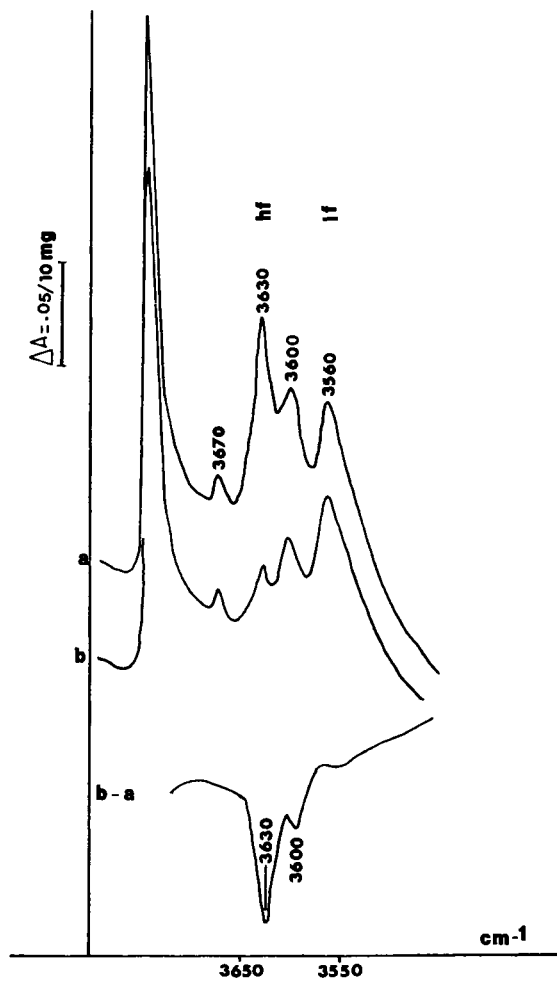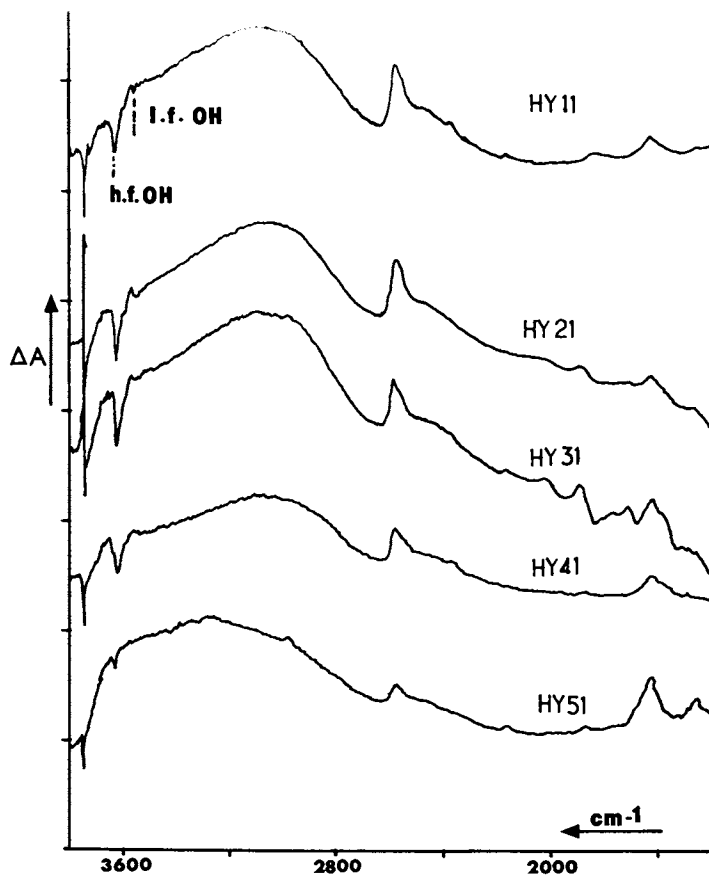
Figure 5.   Ethylene adsorption on HY_{21}.

Figure 6.   Effect of H$_2$S adsorption on HTA solids (subtracted spectra).

of H_2S leads to a slight shift of this rather sharp band. Under such conditions, the interpretation of the subtracted spectra is very delicate.

The shift of the $\nu_{h.f.}$ band, which is located near 3100 cm^{-1} after interaction, is more important than for C_2H_4. This means that the interaction with H_2S is stronger. The ν_a band observed in the case of H_2S adsorption is broader which renders the determination of the frequency of its maximum more difficult than for C_2H_4.

Discussion

The mechanism responsible for the genesis of the various OH groups present in modified HY is out of the scope of this paper. Details on that topic can be found elsewhere (4). We aim here to focus on the respective acid strength of the HY hydroxyls and on the evolution of the strength of the strongest sites in the course of the various dealumination procedures. In the following, we will consider successively the structural h.f. and l.f. OH, the extra-framework OH and the silanol groups.

Structural h.f. and l.f. OH. It is now well accepted that the h.f. and l.f. OH arise from framework OH located respectively in the supercages and in the hexagonal prisms / or the sodalite cages (16). Moreover proton mobility allows the less accessible l.f. OH to interact with bulky basic molecules (17). While adsorption of pyridine at temperatures lower than 573 K does not discriminate between h.f. and l.f. OH acid strength, adsorption of less basic probes (C_2H_4, H_2S for example) gives rise to a more specific interaction. For the HT, HTA and ID solids investigated in this work, h.f. OH groups appear to be the most acidic. This directly confirms previous studies (4) which have shown that a severe decrease of the strong acidity occurs when the h.f. OH are poisoned by extra-framework cationic species formed in the course of the steaming treatments.

On the basis of the clean experiments (specific interaction with h.f. OH), the evolution of the acid strength versus the framework dealumination level can be followed. For such a study, it is important to use the HTA solids (figure 7) instead of the HT solids since the latter may contain the poisoning cationic species mentioned above. On figure 8, the $\Delta\nu_{OH}$ frequency difference is reported versus the $Al^{IV}/Si+Al^{IV}$ ratio for the HTA and the ID solids. Two important results emerge from figure 8; first, in agreement with microcalorimetric experiments performed on the same solids (18) and other independent determinations (19), the strength of the strongest Brönsted acid sites increases with the framework dealumination level. Secondly, as far as the strength of the strongest acid
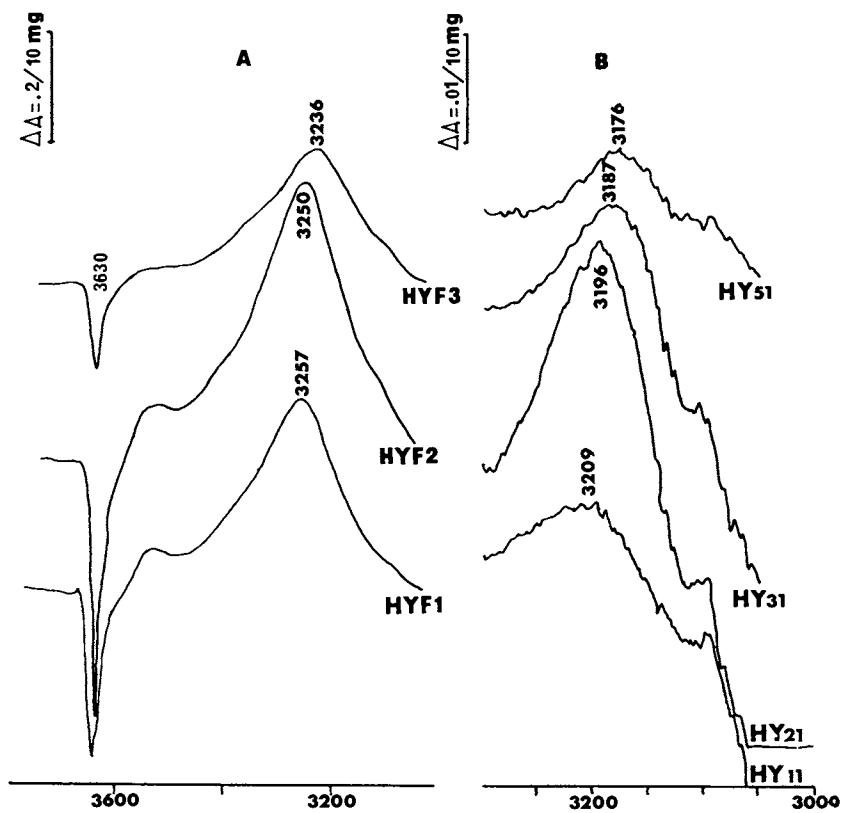
Figure 7. ν_a band after ethylene adsorption :
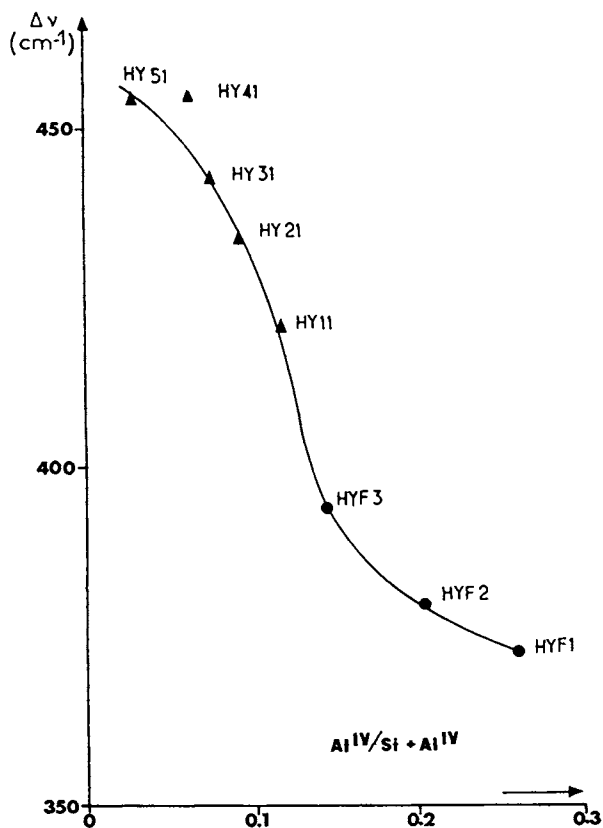A: HYF solids
B: HTA solids.

Figure 8.   Variation of the $\Delta\nu_{OH}$ shift due to ethylene adsorption with the $Al^{IV}/Si+Al^{IV}$ ratio of various dealuminated zeolites.

sites is concerned, no discontinuity exists between HTA and ID solids. These results are qualitatively confirmed by the H_2S experiments.

From the results discussed above, it could have been concluded that whatever the dealumination procedures or the physicochemical characteristics of the solids, the l.f. OH groups are always much less acidic than the h.f. OH groups. However, as it is shown below, this is not entirely true : at this stage, it should be emphasized that the highly dealuminated solids we have investigated (HT, HTA) still contain a low but significant amount of residual sodium cations (> 800 ppm). For instance, if we focus on the HT series, the Na/Al^{IV} ratio increases to about 50 % when the unit cell parameter decreases to 2.428 nm. This means that poisoning of framework sites and, more specifically, of the less accessible ones, i.e. l.f. OH groups, is likely for HT or HTA solids with an unit cell parameter below about 2.430 nm. To verify this important aspect, HT and HTA solids with a very low sodium content (< 300 ppm) have been prepared. Providing that these new solids have a unit cell parameter lower than about 2.430 nm (HY_{42}), the l.f. OH begins to interact with C_2H_4 (figure 4B). On the other hand, C_2H_4 does not interact with the l.f. band of the ID solids which are also characterized by a very low sodium content (< 300 ppm). Therefore the interaction, which is evidenced between C_2H_4 and the l.f. band of highly dealuminated HT or HTA solids with a very low sodium content, is likely to result from the increase of the acid strength of the l.f. OH with the dealumination level of the framework.

Taking into account all these results, it appears that framework dealumination leads to an increase of the acid strength of the h.f. as well as of the l.f. OH groups.

Extra-framework Al-OH groups.   Acidic and non-acidic extra-framework Al-OH groups are evidenced in solids steamed at moderate temperatures, i.e. below about 973 K. Such groups are not detected in solids treated at higher temperatures since under these conditions they are likely to dehydroxylate. The mild acid leaching does not eliminate all the extra-framework OH bands but leads to a severe decrease of the non-acidic contribution.

The first question to be answered concerns the interpretation of these Al-OH bands. Clearly, as shown by independent experiments (4), extra-framework alumina and/or silica-alumina species are present in dealuminated materials. Indeed, interpretation in terms of alumina-like species has already been proposed in the literature for the non-acidic components (11). However, to our knowledge, the frequency of the various extra-framework Al-OH does not exactly correspond to any Al-OH frequency already known for alumina, silica or amorphous silica-

alumina materials. This renders difficult the reliable interpretation of the spectra.

We tentatively suggest that the non acidic Al-OH would result from highly dispersed alumina-rich silica-alumina phases while the acidic Al-OH would be due to a more silica-rich phase. This approximative interpretation would explain why the non-acidic Al-OH bands assigned to alumina-rich phases are more easily eliminated by the acid leaching.

Silanol groups. The so-called non-acidic Si-OH band at 3742 cm^{-1} is more complex than expected : it results from two components located at 3738 and 3743 cm^{-1}. The 3738 cm^{-1} is predominant for well crystalline materials while the 3743 cm^{-1} band is only detected in the case of nearly amorphous samples (figure 9). This would mean that the 3738 and 3743 cm^{-1} bands correspond to Si-OH attached to the framework (defects sites) and to Si-OH attached to an extra-framework phase containing silicon, respectively.

According to this interpretation a small proportion of the non-framework Si-OH is able to interact with pyridine. Does this mean that these Si-OH groups behave as Brönsted sites ? Such a surprisingly acidic behaviour is unlikely. Adsorption experiments performed on silica-rich amorphous silica-alumina indicate that the Si-OH band located at 3745 cm^{-1} is partly affected by pyridine adsorption, even after evacuation at 723 K. Taking into account that non-protonated pyridine species are detected under such conditions, the perturbation of the Si-OH would result from an indirect interaction with pyridine adsorbed on near-by Lewis acid sites. The same phenomenon is likely to occur for non-framework Si-OH present in modified zeolites since the solids are known to contain a large amount of extra-framework Lewis sites (4). Moreover this interpretation would support the presence of a silica rich extra-framework phase in HT as well as in HTA solids.

Conclusion

Methods generally used to study the zeolites acidity, such as titration in aprotic solvent (19), and temperature programmed desorption of basic probe molecules (20) reveal a heterogeneity of Brönsted acid sites. The present results show that IR spectroscopy of adsorbed probe molecules with various basic strengths gives direct informations on the respective acid strengths of the different types of OH groups. They allow to compare their evolution with the $Al^{IV}/Si+Al^{IV}$ ratio of HY zeolites dealuminated by conventional treatment or isomorphous substitution. Figure 8 demonstrates a monotonic increase in the acid strength of the OH groups indicated by the high-frequency band with decreasing
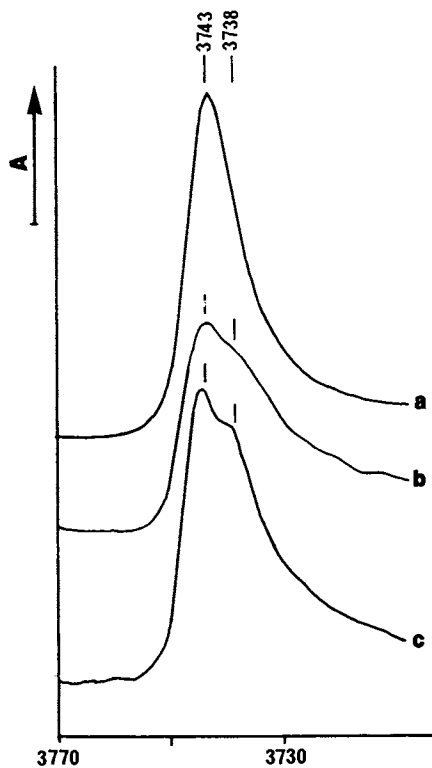
Figure 9. Silanol ν_{OH} bands of solids :
a: SiO_2-Al_2O_3 90:10 ; b: HY_{30} and ; c: HY_{31}

$Al^{IV}/Si+Al^{IV}$. Interestingly, the acid strength continues to increase when $Al^{IV}/Si+Al^{IV} < 0.1$, although for such ratios NMR studies concluded that the strength of acidity remains constant (9). Our results relative to the h.f. OH groups are confirmed by those relative to the l.f. ones, since the latter also become more acidic (sensitive to ethylene) for high degrees of dealumination level.

Extra-framework Al-OH groups are present in conventional HY treated at low temperatures. Most of these OH groups are non- or weakly acidic. However, under some specific preparation conditions, some of these extra-framework Al-OH groups behave as strong acid sites. The Si-OH band appears to be more complex than expected since a framework and an extra-framework component are involved.

Literature Cited

1. Ghosh ,A. K.; Curthoys, G. J. Chem. Soc., Faraday Trans I 1984, 80, 99.
2. Barthomeuf, D. Molecular Sieves II, ACS Symposium 1977, 40, 453.
3. Scherzer, J. ACS Symposium Series No. 248, 1983, 157.
4. Macedo, A.; Raatz, F.; Boulet, R.; Janin, A.; Lavalley, J.C. Proc. Innovation in Zeolite Materials Science Nieuwpoort (Belgium), 1987.
5. Anderson, M. W. ; Klinowski, J. Zeolites 1986, 6 455.
6. Topsoe, N. Y.; Pedersen, K.; Derouane, E. G. J. Catal. 1981, 70, 41.
7. Dakta, J.; Tuznik, E. J. Catal. 1986, 102, 43.
8. Pfeifer, H.; Freude, D.; Hunger, M. Zeolites 1985, 5, 274.
9. Freude, D.; Hunger, M.; Pfeifer, H.; Schwieger, W. Chem. Phys. Letters 1986, 128, 62.
10. Lohse, U.; Löffler, E.; Hunger, M.; Stöckner, J.; Patzelova, V. Zeolites 1987, 7, 11.
11. Kubelkova, L.; Seidl, V.; Novakova, J.; Bednarova, S.; Jiru, P. J. Chem Soc., Faraday Trans I 1984, 80, 1367.
12. Cornac, M. Ph.D. Thesis, I.S.M.Ra, Caen, 1986.
13. Skeels, G. W.; Breck, D. W. Proc.6th Int.Zeolite Conf., Reno, 1983, p 87.
14. Akporiaye, D.; Chapple, A. P.; Clark, D. M.; Dwyer, J.; Elliott, I. S.; Rawlence, D. J. Stud. Surf. Sc. Catal. 1986, 28, 351.
15. Rouxhet, P. G.; Sempels, R. E. J. Chem. Soc., Faraday Trans I 1974, 70, 2021.
16. Jacobs, P. A.; Uytterhoeven, J. B. J. Chem. Soc., Faraday Trans I 1973, 69, 359.
17. Ward, J. W. J. Phys. Chem. 1969, 73, 2086.
18. Macedo, A.; Auroux, A.; Raatz, F.; Jacquinot, E.; Boulet, R. In this book, pp 98-116.

19. Beaumont, R.; Barthomeuf, D. J. Catal. 1972, 26, 218; J. Catal. 1972, 27, 45.
20. Dondur, V.; Karge, H. G. Surface Sci. 1987, 189/190, 873.

Chapter 8

FT–Far IR Spectroscopic Studies of Alkali and Alkaline Earth Linde Type A Zeolites

Probing Extraframework Cations in Molecular Sieves

Mark D. Baker, John Godber, and Geoffrey A. Ozin

Lash Miller Chemical Laboratories, Department of Chemistry, University of Toronto, Toronto, Ontario M5S 1A1, Canada

The FT–FAR-IR spectra (350–30 cm^{-1}) of self-supporting wafers of alkali and alkaline earth Linde Type A zeolite and some of their binary combinations are reported for the first time. The sensitivity of this region of the vibrational spectrum to metal cation type, location, coordination number, geometry and population, provides a convenient diagnostic for probing metal cation site distributions, the sequence of metal cation replacement resulting from ion-exchange and metal cation mobility and reorganization during the removal of intrazeolitic water. Systematic trends in the far-IR spectra of the metal cations in conjunction with cation frequency, intensity, mass, charge, bond-length relationships, enables the establishment of an internally consistent set of vibrational signatures for different cations in specific sites of alkali and alkaline earth Linde Type A zeolites. Studies of this kind are likely to find utility in the identification and manipulation of pore blocking cations in Linde Type A zeolites; a science at the centre of their application for gas separation and purification, (1).

Pinpointing the siting of cations in Linde Type A zeolites is crucial in the design and understanding of experiments aimed at fine tuning the dimensions of the entrance windows of the supercages. The window sizes can be precisely adjusted by the controlled placement of cations at strategic locations in the A-zeolite lattice, thereby permitting only molecules with suitable dimensions to penetrate the crystal. This is exemplified by K_8Na_4-A and Na_{12}-A which both contain monovalent cations partially blocking the eight-ring windows between supercages, thus restricting entrance to molecular diffusants with a maximum kinetic diameter of 3Å and 4Å (2) respectively (Figure 1). In contrast the cations preferentially occupy six-ring sites in Ca_4Na_4A, removed from the window, resulting in an expanded entrance, allowing molecules with up to 5 Å kinetic diame-

ter to enter the supercage. A judicious selection of co-cations
therefore is a prerequisite for precise adjustment of the blocking
action at the 0.1 Å level. Once this has been achieved, these ma-
terials can be further exploited in gas separation and purification
applications (1).

The far-IR spectra (350-30 cm^{-1}) of Linde Type A zeolites can be
divided into two regions based on the origin of the observed vibra-
tional modes. Framework vibrations occur above about 230 cm^{-1} and
are essentially decoupled from the extra-framework cation modes. The
cation translational vibrations occur below 230 cm^{-1}. This useful
division of the vibrational spectra of zeolites into framework and
extra-framework modes has been discussed previously (3-5). In this
paper the far-IR spectral signatures of alkali and alkaline earth
exchanged Linde Type A zeolites will be examined in a designed ef-
fort to address the question of cation site location and population.
The unit cell of Linde Type A shown in Figure 1 contains charge bal-
ancing cations, which are located on the Figure in bold lettering
(6).   These lie in the following positions: a) On the C_{3v} axis of
the single six-rings (sites A, B and C) b) In the plane of the
eight-rings (site E) c) On the four fold axis of the four-rings,
(site H, α-cage), (site G, β-cage). (23)

Results: Na-A and Li, Na-A

The far-infrared spectra of hydrated and dehydrated Na_{12}-A are shown
in Figure 2,(24). Framework vibrations of the unit cell that are rath-
er insensitive to the nature of the metal cation guest occur between
350-250 cm^{-1}. The hydrated sample exhibits four well defined cation
related absorptions which shift slightly upon dehydration of the
zeolite. The largest change occurs for the vibration at 133 cm^{-1}
shifting to 142 cm^{-1} upon removal of water. Crystallographic deter-
minations of site locations for hydrated and dehydrated Na-A are
compiled in Table I.

Table I. Crystallographically identified cation sites and
populations for Na-A.   The numbers in this table refer to
the number of cations per pseudo-unit cell. Deh. is dehy-
drated, Hyd. is hydrated

Form	Site A	Site E	Site H	Reference
Deh.	7.8	2.9	0.8	7
Deh.	8.0	4.0	–	8
Deh.	8.0	4.0	–	9
Hyd.	8.0	–	–	10
Deh.	8.0	4.0	–	11
Deh.	8.0	3.0	1.0	12
Deh.	8.0	3.0	1.0	13

Essentially, these locate 7-8 cations in site A, 3 in site E and the
remainder in site H.

The most intense band in the far IR spectrum of Na-A is logi-
cally ascribed to a Na^+(A) vibration. Its position compares to that
seen for sodium ions in site II in zeolite Y (blue-shifted due to
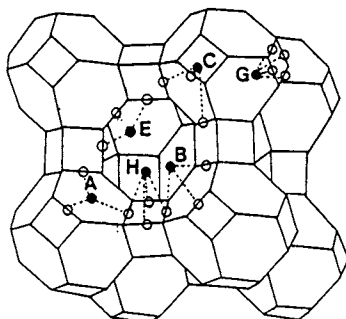the higher lattice anionicity of A relative to Y). Confirmation

Figure 1. Representation of the pseudo-cell of zeolite A, (Space Group Pm3m) illustrating the framework structure surrounding a large cage. The cation positions are shown in bold face lettering using the formalism of Mortier (6). The extent of projection of cations in sites B,C and G is exaggerated for clarity.
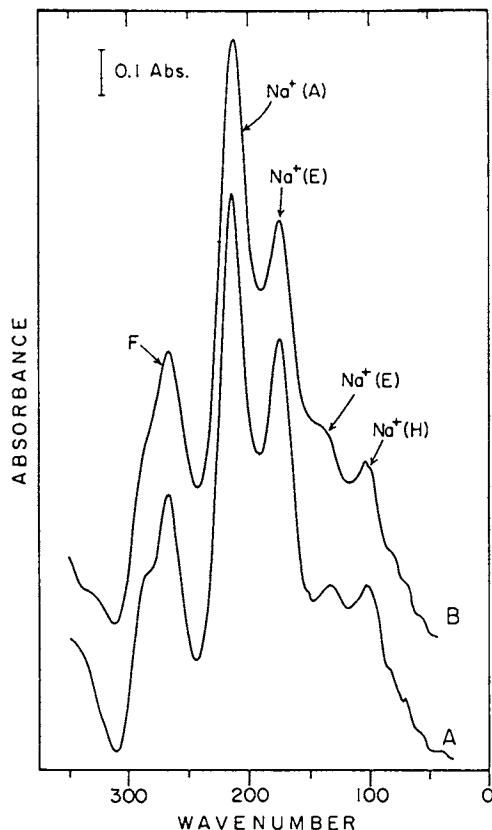

Figure 2. Far-ir spectra of Na-A, recorded at room temperature (A) Hydrated (B) After a 400°C in situ vacuum dehydration. F denotes a framework band.

of this assignment comes from an intensity analysis of the asymmetric and symmetric absorption bands of the site A vibrations (3). This leads to an anticipated pyramidal angle of 113° compared to that determined crystallographically of 119.2° (7). (For band positions see Figure 3). Further support for this assignment comes from the far-IR spectra of progressively Li^+ ion-exchanged Na-A. The location of Li^+ in the A lattice is known from crystallography to be restricted to the six-ring sites (14), and does not show any far-IR Li-O stretching vibrations, (22).

In Figure 4 the spectra of dehydrated Na_{12}-A, Na_9Li_3-A and Na_6Li_6-A are displayed. Here it is observed, that upon progressive loading with Li^+ ions, the $Na^+(A)$ vibration first decreases in intensity, followed by changes in the low frequency region.

Therefore the siting of Li^+ ions in the LTA six-rings is found to proceed at the expense of the $Na^+(A)$ ions. In the region around 100 cm^{-1}, other changes are occurring upon progressive replacement of Na^+ by Li^+ ions, signalling the exit of sodium ions from another site. Bands in this region are ascribed to the site H cation based on two considerations: i) The local symmetry of $Na^+(H)$ is reminiscent of site III in Na-Y. In the latter case an absorption at 90 cm^{-1} is ascribed to this cation (3,4). ii) The low intensity of this cation vibration is consistent with the low population of this site.

In Na_{12}-A, site E is the second most populous site accommodating about three ions per pseudo-unit cell. Based on this population, one would anticipate the site E absorption band to be the second most intense, pinpointing it at 177 cm^{-1}.

A cation bound at site E, as shown in Figure 5, is interacting primarily with two O1 and one O2 lattice oxygens in local C_{2v} symmetry. In this symmetry the following cation-oxygen stretching vibrations are infrared active.

$$\Gamma_1 \ (A_1) = 1/\sqrt{2} \ (\Delta r_1 + \Delta r_2) \ (\nu_1)$$

$$\Gamma_2 \ (A_1) = \Delta R \qquad\qquad (\nu_2)$$

$$\Gamma_3 \ (B_1) = 1/\sqrt{2} \ (\Delta r_1 - \Delta r_2) \ (\nu_3)$$

An analysis of the two A_1 modes using the sum and product intensity rules (15) shows that the band at 142 cm^{-1} in the observed spectrum is due to the ν_2 mode. The lower intensity ν_1 mode occurs as a weak, curve resolvable band at 110 cm^{-1}.

Potassium-Exchanged A

The far IR spectra of the dehydrated forms of $Na_{12}A$, K_8Na_4A and $K_{11.6}Na_{0.4}A$ are shown in Figure 6. The crystallographic observations of potassium ions in materials similar to those described here are listed in Table II. The spectrum of K_8Na_4A (Figure 6B) exhibits a strong band at 213 cm^{-1} which is clearly due to sodium ions in site A. Of the remaining bands, the most intense at 179 cm^{-1} is attributed to $K^+(B)$ for a number of reasons.
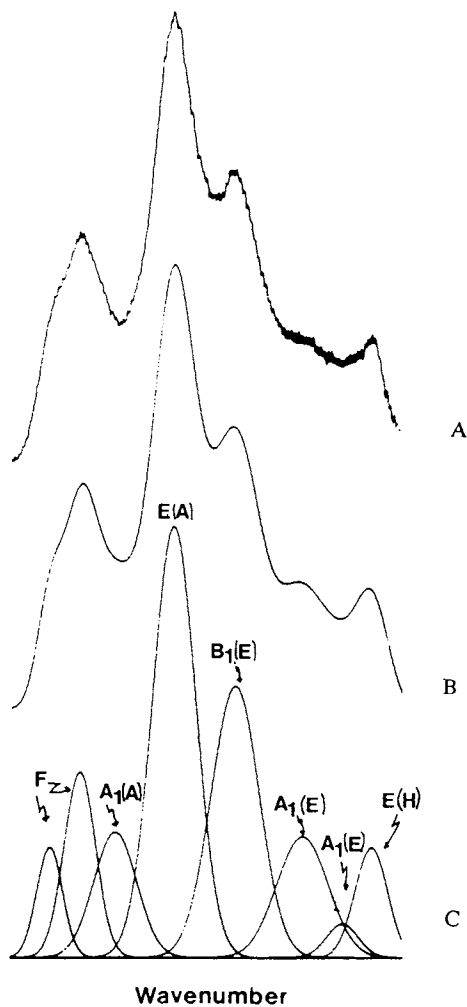i) This is the most populated site and will therefore give rise to the most intense absorption.

Figure 3. Curve resolved spectrum of dehydrated Na-A.   (A) observed (B) simulation (C) curve resolution.
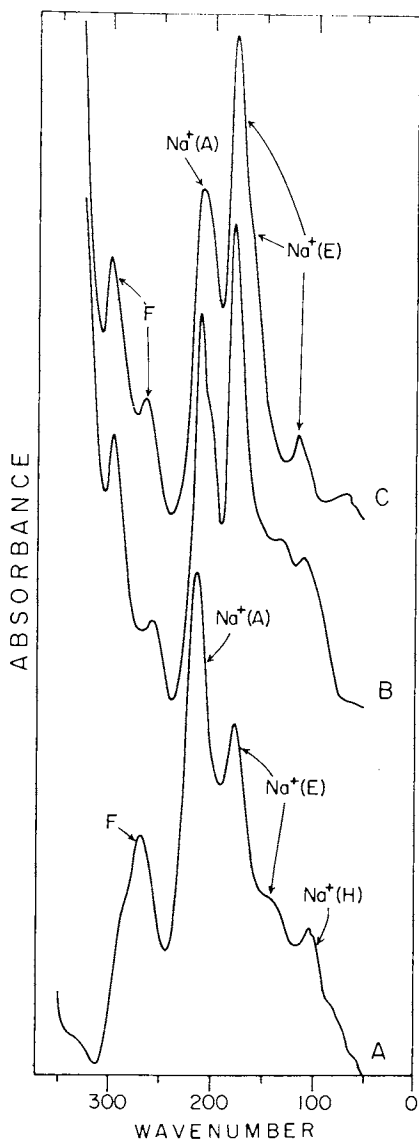
Figure 4. Far-ir spectra of dehydrated Na_{12}-A (A), Na_9Li_3-A (B), and Na_6Li_6-A (C). Note that the Na^+(A) vibration decreases first.
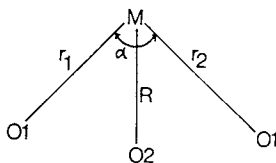
Figure 5. Representation of the geometry of a cation in site E, illustrating the internal coordinate definitions used in the frequency and intensity calculations.
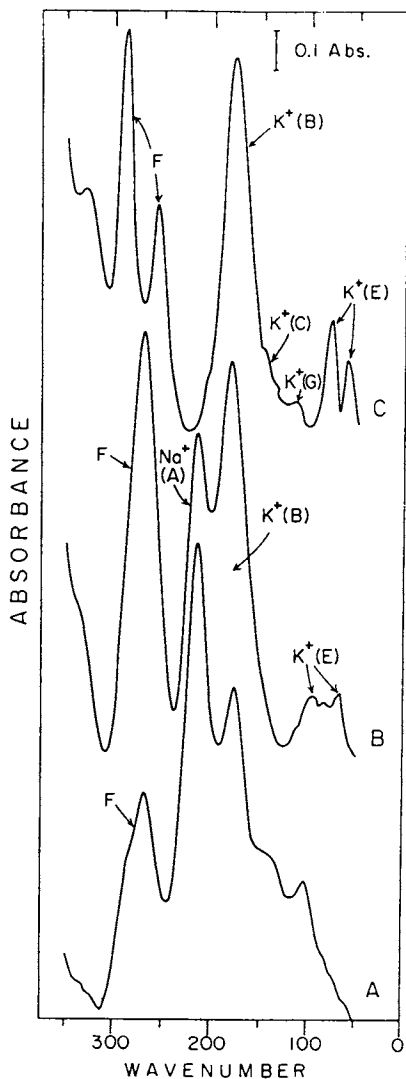

Figure 6. Far-ir spectra of dehydrated: (A) Na_{12}-A; (B) Na_4K_8-A; (C) K_{12}-A.

ii) The calculation (3) of the frequency of $K^+(B)$ using the $Na^+(A)$
    observed frequency leads to an anticipated frequency of 173 cm^{-1}.

Table II. Crystallographically identified cation sites and
           populations for K-A.   The numbers in this table
           refer to the number of cations per pseudo-unit cell.
           Deh. is dehydrated, and Hyd. is hydrated. The last
           entry in the Table is for a $K_{7.5}Na_{4.5}^-$ A sample

Form	Site A	Site B	Site C	Site E	Site G	Site H	Reference
Hyd.	–	8.0	–	–	–	–	[16]
Deh.	1.0	6.0	2.0	3.0	–	–	[16]
Deh.	–	6.3	1.4	3.0	0.1	0.3	[17]
Deh.	4.4Na	3.6	–	2.0	–	0.6	[18]

The unresolved shoulder on the low frequency side of the main absorp-
tion, signals the presence of another site which is probably $K^+(C)$.
The remainder of the far-IR spectrum contains a poorly resolved ab-
sorption below 100 cm^{-1}, which in the curve resolution (21) is shown
to probably contain two bands, and is due to vibrations of the pore
blocking potassium cation.
     The far-IR spectrum of essentially fully exchanged KA (Figure 6C)
clearly indicates that the Na^+ ions have been replaced since the
$Na^+(A)$ band at 213 cm^{-1} seen in K_8Na_4-A (Figure 6B) is absent. The
dominant feature of the K-A spectrum is a broad intense absorption
at 172 cm^{-1}, due to $K^+(B)$ ions (6.3K^+ ions, Table II) with a small
contribution from $K^+(C)$ producing a weak shoulder at about 147 cm^{-1}
(see Figure 6B). Curve resolution (21) reveals that $K^+(B)$ is made
up of two components. These are the A_1 and E symmetry IR active vib-
rations (3). Intensity analyses give a pyramidal angle of 110.3°,
where the crystallographic determination (17) gives 110.8°.
     Of the remaining cations in K_{12}-A the most populous are the im-
portant pore blocking K^+ ions in site E. In K_8Na_4-A, vibrations at
98 and 72 cm^{-1} were assigned to the B_1 and A_1 symmetry vibrations
respectively of $K^+(E)$. In K_{12}-A, absorptions at 77 and 61 cm^{-1} are
attributed to these same vibrations of $K^+(E)$. The red shift of these
bands is indicative of either a force constant, or geometry change of
this site in K_{12}-A relative to K_8Na_4-A. If the differences are
purely angular in origin, then one can estimate the O1-K-O1 angle in
K_8Na_4-A using the frequencies of the B_1 modes in K_{12}-A and K_8Na_4-A
and the crystallographically determined angle in K_{12}-A of 102.5°
(17).   This calculation predicts a value of 110.5° for $K^+(E)$ in
K_8Na_4-A and therefore suggests that the potassium ion in the fully
exchanged material is held less strongly in site E, and thus projects
further into the eight-ring window, implying that the pore size would
be slightly smaller.
     Of the remaining cations in K_{12}-A, there are 0.3 K^+ ions per
pseudo unit cell in site H and 0.1 K^+ ions per pseudo cell in site
G. The vibrational frequency of $Na^+(H)$ cations would translate to a
$K^+(H)$ cation vibration at 49 cm^{-1}. It appears from the spectrum that
a weak band at about 117 cm^{-1} is best ascribed to $K^+(G)$, with $K^+(H)$

either overlapped by the $K^+(E)$ bands around 77-60 cm^{-1} or that it occurs at still lower frequencies (Figure 6C).

Rubidium-Exchanged A

The far-IR spectra of hydrated and dehydrated Rb,Na-A are shown in Figure 7. The spectrum of the latter can be divided into two regions. The higher frequency shows characteristic bands due to $Na^+(A)$ and $Na^+(E)$ as seen earlier at 217 and 180 cm^{-1} respectively (Figure 2). The lower frequency region, (110-30 cm^{-1}) shows bands due to the motion of Rb^+ ions. Crystallographic determinations have shown that rubidium ions occupy sites B/C and E and the absorption bands are assigned to these sites (see Figure 7). It is interesting to note that the frequencies of the Na^+ and Rb^+ modes fall in distinct regions. This observation indicates that monitoring intensity changes in a series of Rb, Na-A samples with varying unit cell cation complements would allow for a firm statement to be made regarding the populations of the different ions in their extra-framework positions. In conjunction, adsorption experiments on these materials, would serve as a useful method for investigating and optimizing the sieving properties of the samples with respect to a specific separation process. In this context, the far IR spectra suggest that the pore size of the dehydrated Rb, Na-A sample is more constrained than in the parent Na_{12}-A zeolite, based on the observation of a substantial far-IR absorption (site population) due to $Rb^+(E)$. Further statements in this spirit will surface when more data have been collected concerning these samples.

Calcium Exchanged A

Divalent ions mainly occupy the six-ring sites, and are exclusively found in these positions in A zeolites.

Ca_4Na_4A

The crystallography of Ca4Na4-A demonstrates that the cations are distributed only in the three-fold sites, on the six-rings of the sodalite cages (19,20). The divalent Ca^{2+} ions locate near the plane of the six-ring (site A), while the sodium ions are displaced into the supercage (site B). A neutron diffraction study of Ca4Na4-A (20) also showed that the six-rings containing the Ca^{2+} were severely distorted, and that the Ca^{2+}-O3 bond length was quite short at 2.9 Å. The far-IR spectra of the hydrated and dehydrated Ca4Na4-A sample are shown in Figure 8. In addition to the framework absorption at 260 cm^{-1}, two bands dominate the spectrum. These are logically associated with $Na^+(B)$ ions (191 cm^{-1}) and $Ca^{2+}(A)$ cations (237 cm^{-1}).

The assertion of these assignments is founded on the following criteria: i) Similar single six-ring frequencies were observed in CaX and CaY (3,4,9). ii) A good fit of observed (237 cm^{-1}) and calculated (207 cm^{-1}) frequencies. iii) The high frequency of the Ca^{2+} ion is rationalized by a large interaction of the 2+ ion with the anionic lattice compared to the sodium ion.
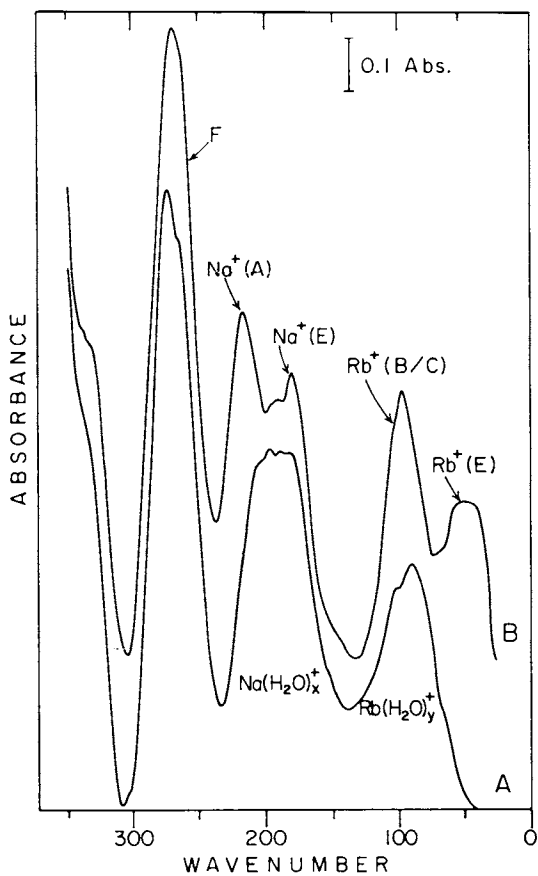
Figure 7. Far-ir spectra of (A) hydrated and (B) dehydrated Na, Rb-A.

Ca$_6$A

In the dehydrated form 4.4 Ca^{2+} ions per pseudo unit cell are found
in site B, (Ca^{2+} - O3 = 2.27 Å), almost in the plane of the O3 oxy-
gens of the six-ring, and 1.2 Ca^{2+} ions are located in site C in the
sodalite cage (Ca^{2+} - O3 = 2.32 Å). The far-IR band at 198 cm^{-1}
(Figure 9) is ascribed to the Ca^{2+} ion with the longer bond length,
namely site C. Using the Ca^{2+}(C) asymmetric cation frequency and
the crystallographic details of Ca^{2+}(B) one can estimate the Ca^{2+}(B)
asymmetric vibrational frequency at 250 cm^{-1}. This fits quite well
with the assignments above for the Ca$_4$Na$_4$-A sample, as well as the
observation of a band in this region in the curve resolved spectrum
of Ca$_6$-A (Figure 9).

Sr$_6$A

The far-IR spectra of hydrated and dehydrated SrA are displayed in
Figure 10. The form of the spectra aside from red shifts are re-
markably similar to those of the Ca-A described above. This is not
surprising as the siting and populations of Sr^{2+} ions are identical
to Ca^{2+} in Ca$_6$-A (19b). The Sr^{2+} ions are located in the six-rings,
with 4.5 ions per pseudo-cell in site B, and 1.2 ions per pseudo-cell
in site C. Together the Ca^{2+} and Sr^{2+} -A zeolites yield a consis-
tent picture of the divalent cation far-IR vibrational frequencies,
and are useful models for the investigation of the transition metal
(2+) -A systems. Strontium cation vibrations anticipated to occur
at 175 cm^{-1} (site B) and at 145 cm^{-1} (site C) compare quite well
with the observed bands at 182 and 142 cm^{-1} respectively.

Conclusion

In this paper the far-IR spectra of a series of alkali and alkaline
earth exchanged -A zeolites have been described and assignments of
cation related bands diagnostic of specific binding sites have been
proposed. The requirement of a reliable basis from which to make
comparisons is crucial in this type of study. In this regard, the
Na-A far-IR spectrum and unit cell cation dynamics have been studied
and discussed in detail (5). It is still difficult at this stage
however, to separate or gauge the effect of both geometry and force
constant changes·at a cation binding site on the far-IR spectra.
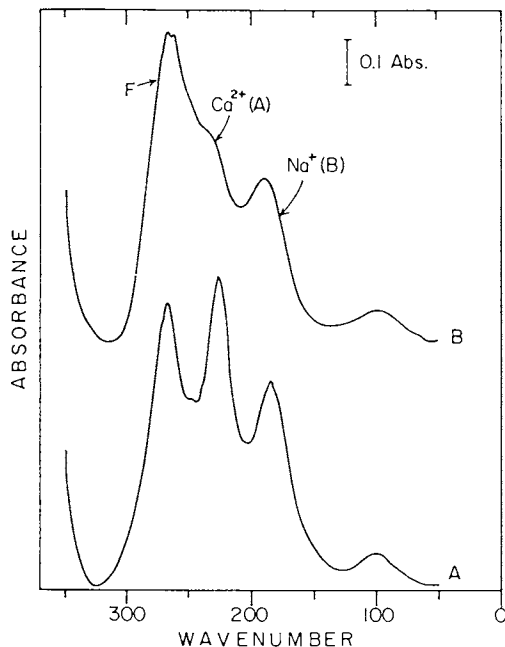Further progress in this regard is anticipated from complementary
Raman data.

Acknowledgments

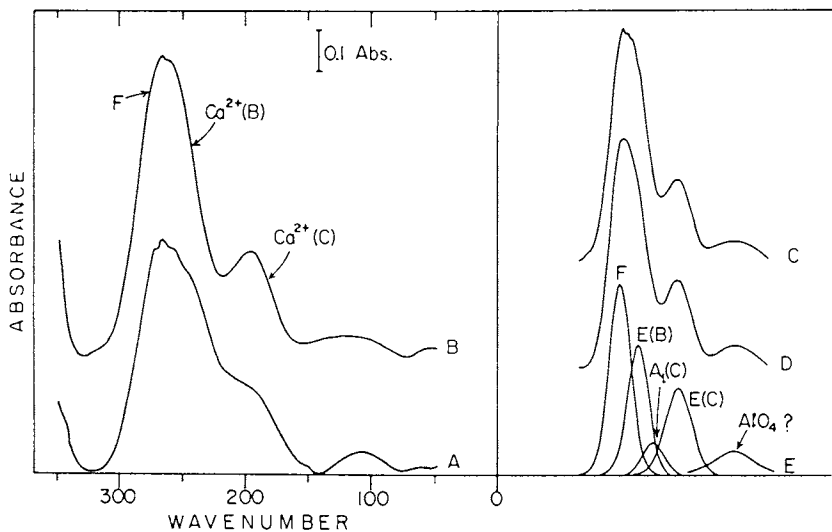Figure 8.   Far-ir spectra of (A) hydrated and (B) dehydrated, Ca_4Na_4-A.

Figure 9.   Far-ir spectra of :   (A) hydrated and (B) dehydrated Ca_6-A. (C) observed spectrum (D) simulation   (E) curve resolution. Note that the A,(B) mode probably lies within the framework vibration.
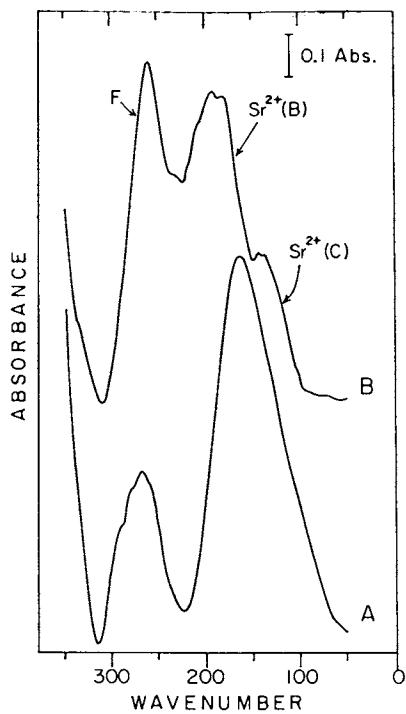
Figure 10. Far-ir spectra of: (A) hydrated and (B) dehydrated Sr_6A.

Literature Cited

1. (a) Dwyer, J.; Dyer, A., Chemistry & Industry, p.237 (1984).
    (b) D.W. Breck, "Zeolite Molecular Sieves", J. Wiley and Sons,
    New York, (1974).
2. The kinetic diameter is defined as the intermolecular distance
    of closest approach for two molecules colliding with zero ini-
    tial kinetic energy (see Ref. 1(b) and is calculated from a
    Lennard – Jones potential. The difference between the apparent
    pore diameter (from crystallography) and the kinetic diameter
    is explained on the basis of activated diffusion of adsorbates
    into the zeolite pores.
3. Ozin, G.A., Baker, M.D. and Godber, J., J. Am. Chem. Soc., 107,
    3033 (1985).
4. Baker, M.D., Ozin, G.A. and Godber, J., Catal. Rev. Sci. Eng.,
    27, 591 (1985).
5. Ozin, G.A. and Godber, J., J. Phys. Chem. (submitted).
6. Mortier, W.J., "Compilation of Extra Framework Sites in
    Zeolites"; Butterworths, Surrey, 1982.
7. Pluth, J.J. and Smith, J.V., J. Am. Chem. Soc., 102, 4704 (1980).
8. Reed, T.B. and Breck, D.W., J. Am. Chem. Soc., 78, 5972 (1956).
9. Howell, P.A. Acta, Cryst., 13, 737 (1956).
10. Broussard, L. and Shoemaker, D.P., J. Am. Chem.Soc., 82, 1041
    (1960).
11. Smith, J.V. and Dowell, L.G., Kristallogr, Z., 126, 1 (1968).
12. Yanagida, R.Y., Amaro, A.A. and Seff, K., J. Phys. Chem., 77,
    805 (1973).
13. Subramanian, Y. and Seff, K. J. Phys. Chem., 81, 2249 (1977).
14. Jirak, Z.; Nosacek, V.; Vratislav, S., Herden H.,; Schollner,
    R.; Mortier, W.J.; Gellens, L. and Uytterhoeven, J.B., Zeolites,
    3, 255 (1983).
15. Wilson, E.B., Decius, J.C. and Cross, P.C., "Molecular
    Vibrations", McGraw-Hill, New York (1955).
16. Leung, P.C.W.; Kunz, K.B.; Seff, K. and Maxwell, I.E., J. Phys.
    Chem., 79, 2157 (1975).
17. Pluth, J.J. and Smith, J.V., J. Phys. Chem., 83, 741 (1979).
18. Adams, J.M. and Haselden, D.A., J. Solid State Chem., 47, 123
    (1983).
19. a) Pluth, J.J. and Smith, J.V., J. Am. Chem. Soc., 105, 1192
    (1983). b) Pluth, J.J. and Smith J.V., J. Am. Chem. Soc., 104,
    6977 (1982).
20. Adams. J.M. and Haselden, D.A., J. Solid State Chem., 51, 83
    (1984).
21. Baker, M.D. , Ozin, G.A. and Godber, J., J. Phys. Chem., sub-
    mitted.
22. Godber, J., PhD Thesis 1987, U of Toronto.
23. The spectra described in this paper were recorded using a
    Nicolet 200SXV Ft far IR spectrometer. The vacuum infrared
    cell, and sample handling techniques used have been described
    in detail in a recent review of this subject.(4)
24. The spectra of the former will not be discussed here, but are
    addressed in more depth elsewhere. (21).

Chapter 9

Studies of Cu(II)-Doped Zeolites A, Rho, and ZSM-5 by Electron Spin Resonance and Electron Spin Echo Modulation Spectroscopies

Cocation Effects and Coordination with Adsorbates

Michael W. Anderson[1] and Larry Kevan

Department of Chemistry, University of Houston, Houston, TX 77004

Electron spin resonance (ESR) coupled with electron spin echo modulation (ESEM) spectroscopies have been used as tools to probe both crystallographic siting of Cu^{2+} in zeolites A and rho and its dependence on cocation and the solvation structure of Cu^{2+} with water and various organic adsorbates. In both hydrated and dehydrated zeolite A it is found that the Cu^{2+} is located inside the β-cage close to the zeolite six-ring between the α and β-cages. In zeolite rho no cocation effect of H^+, Na^+, K^+ or Ca^{2+} is found for water adsorbate solvating Cu^{2+} but some cocation effect is found for methanol and ethylene adsorbates. Direct coordination is only observed with polar adsorbates such as methanol and ammonia which can gain access to the α-cage by solvating the cocation. In dehydrated zeolite Na-ZSM-5 the Cu^{2+} is recessed from the main channels in sites not directly accessible to adsorbates but exposure to polar molecules causes the Cu^{2+} to migrate into the main channels where it forms directly coordinated complexes.

The catalytic importance of zeolites from an industrial standpoint resides both in the ability to subtly tailor their properties to described characteristics and in the consequent high activities and selectivities(1). These last two attributes are primarily a result of the large internal surface area of the zeolites and their microporosity, respectively. The aspect of tailoring zeolites to desired characteristics demands an intimate knowledge of both their structural and chemical properties.

One major branch of zeolite catalysis is that of non-acid catalysis(2), either over exchanged metal cations or over impregnated metal clusters. When the catalytic center is paramagnetic such as Cu^{2+}, the system is amenable to investigation by electron spin res-

[1]Current address: Department of Chemistry, University of Connecticut, Storrs, CT 06268

onance (ESR) techniques. The aim of this work is to combine continuous wave ESR and pulsed ESR, known as electron spin echo modulation (ESEM) spectroscopy, to obtain a better understanding of both the cation siting of Cu^{2+} and its interaction with potential organic reactants with the ultimate goal of tailoring better catalysts.

   This paper is organized as follows. First ESEM spectroscopy is briefly described. Then the location of Cu^{2+} in zeolite A by ESEM data on ^{133}Cs modulation is illustrated. This allows determination of the Cu^{2+} location in zeolite A under different hydration conditions and in the presence of Na^+ versus K^+ as the major cocations present in addition to Cu^{2+}. A strong cocation effect is found. The location of Cu^{2+} in A zeolite is then contrasted with its location in zeolite rho and zeolite ZSM-5 in succeeding sections. In addition to the Cu^{2+} siting in these other two zeolite types, the coordination with various deuterated adsorbates is determined by ESEM methods using analysis of deuterium modulation. Cocation effects on the adsorbate coordination are assessed and discussed.

Electron Spin Echo Modulation Spectroscopy

Since the ESEM technique is only now becoming commercially available, a short description illustrating its potential for the study of zeolite systems seems appropriate. ESEM is a pulsed ESR technique (3,4). When an appropriate sequence of two or three short (ca 40 ns) resonant, microwave pulses is applied to a paramagnetic sample a subsequent burst of magnetization known as a spin echo may be formed.

   A direct analogy can be drawn with the spin echoes formed in the more widely used pulsed nuclear magnetic resonance techniques. The magnitude of this echo is a function of the time between these pulses, τ for a two-pulse experiment, and the magnitude decays with increasing τ. This decay provides information about various relaxation processes but is not of prime interest for structural studies. If in the vicinity of the paramagnetic center (Cu^{2+}) there is a nucleus with a nuclear spin, e.g. ^2H, ^{27}Al, ^{133}Cs etc, there will be an echo intensity modulation superimposed on the echo decay. This modulation is due to weak dipolar hyperfine interaction between the Cu^{2+} and this neighboring nucleus. It is possible to simulate this ESEM pattern and extract important chemical information about the surroundings of the paramagnetic species out to about 0.6 nm. The modulation depends on three fundamental chemical properties of the system, (i) the type of interacting nucleus, (ii) the distance from the paramagnetic center to the interacting nuclei, and (iii) the number of interacting nuclei. Therefore in the case of adsorbed, specifically deuterated organics specific numbers of interacting molecules may be determined as well as their orientation. Orientation information is obtained by using two or more specific deuterations of the same molecule such as CH_3OD and CD_3OH. Such quantitative information greatly enhances the information available from continuous wave ESR alone (5-10).

Crystallographic Location of Cu^{2+} in Zeolite A

Several reports pertain to x-ray crystallographic studies of Cs^+ in zeolite A (11-13). In all cases, the crystallographic siting of the
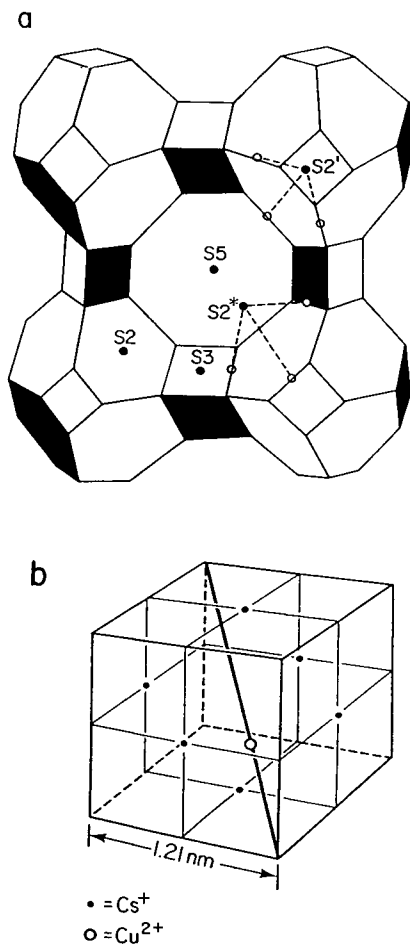
Cs^+ has been well defined. There are several sites for Cs^+ in fully exchanged Cs_7Na_5-A. But for a loading of less than three Cs^+ per unit cell x-ray diffraction evidence shows that all the Cs^+ cations are located at the center of the single eight-ring faces, site S5 in Figure 1a. Cu^{2+} is then introduced into the zeolite and into this matrix of Cs^+ cations; see Figure 1b. As indicated, ^{137}Cs has a nuclear spin and can modulate the spin echo amplitude. Since the distribution of Cs^+ cations is known, by simulating the ESEM pattern and determining both the number of interacting Cs^+ cations and their distance from the Cu^{2+} cation, the Cu^{2+} site location may be determined. If more than one Cu^{2+} species is present with separately resolved ESR lines, the ESEM experiment may be carried on on individual species by selecting the appropriate magnetic field. From analysis of ^{137}Cs modulation it has proved possible to determine Cu^{2+} locations to within ± 0.01 nm (5).

    Figure 2a shows a field-swept ESEM spectrum of Cu^{2+} in a hydrated CsNa-A sample; this shows two Cu^{2+} species. For each species the ESEM pattern has been determined at both $g_\parallel$ and $g_\perp$ and satisfactorily simulated with the same parameters. One Cu^{2+} species is located at site S2 at the center of the six-ring. The second Cu^{2+} species is located at site S2' displaced 0.09 nm into the β-cage. From previous ESEM work with adsorbed D_2O it is known that these two Cu^{2+} species are coordinated to two and three water molecules respectively.(14) The Cu^{2+} species at S2 is a trigonal bipyramidal species with three equatorial lattice oxygens and two axial water molecules. The species at S2' is a distorted octahedral species coordinated to three lattice oxygens and three water molecules.

    In this manner the crystallographic siting of all Cu^{2+} species in hydrated and dehydrated zeolites Na-A and K-A were determined(5). The two following dehydration sequences were determined in which the subscript on Cu denotes the number of coordinated waters. Note the cocation effect. The distances in brackets indicate the displacement from site S2 into the β-cage.

CuNa-A $Cu_{III}(S2')$ $\xrightarrow{\Delta}$ $Cu_{II}(S2)$ $\xrightarrow{\Delta}$ $Cu_0(S2')$
           [0.09 nm]   [0.02 nm]

           $Cu_{II}(S2)$ ─────────────────────────────

CuK-A $Cu_I(S2')$ ─────── evac. ───────→ $Cu_{II}(S2)$ $\xrightarrow{\Delta}$ $Cu_0(S2)$
           [0.02 nm]

                     ─────── evac. ───────→ $Cu_{III}(S2')$
                                              [0.05 nm]

Cu^{2+} in Zeolite Rho

Similarities exist between the structure of zeolite rho (15) shown in Figure 3a and that of zeolite A. Zeolite rho consists of α-cages

Figure 1. (a) Crystal structure of zeolite A showing cation positions. Site S2 is at the center of a six-ring face with sites S2' and S2* displaced into and out of the β-cage along the triad axis, respectively. Site S3 is in a four-ring site while S5 is in an eight-ring site. (b) Schematic representation of the distribution of Cs^+ cations (dark circles) in A zeolite located at the centers of the faces of a cube of edge length 1.21 nm. The Cu^{2+} (open circle) is located on the body diagonal. (Reproduced from Ref. 5. Copyright 1987 Am. Chem. Soc.)
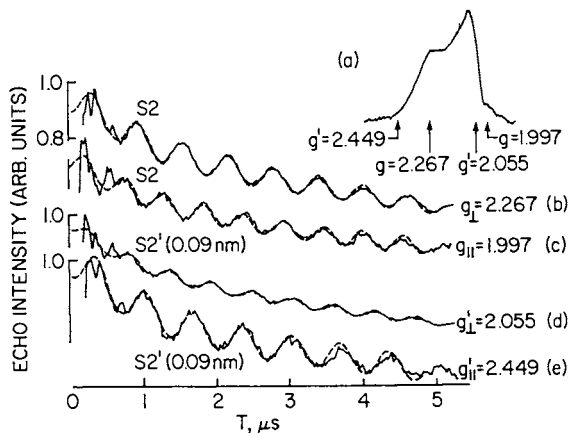
Figure 2. (a) Field-swept ESEM spectrum of fresh CuCsNa-A showing two different Cu^{2+} species differentiated by g and g' components. (b) - (e) Experimental (———) and simulated (-----) three-pulse ESEM spectra of fresh CuCsNa-A. Distances in brackets indicate displacement of Cu^{2+} from S2 to S2'. (Reproduced from Ref. 5. Copyright 1987 Am Chem. Soc.)
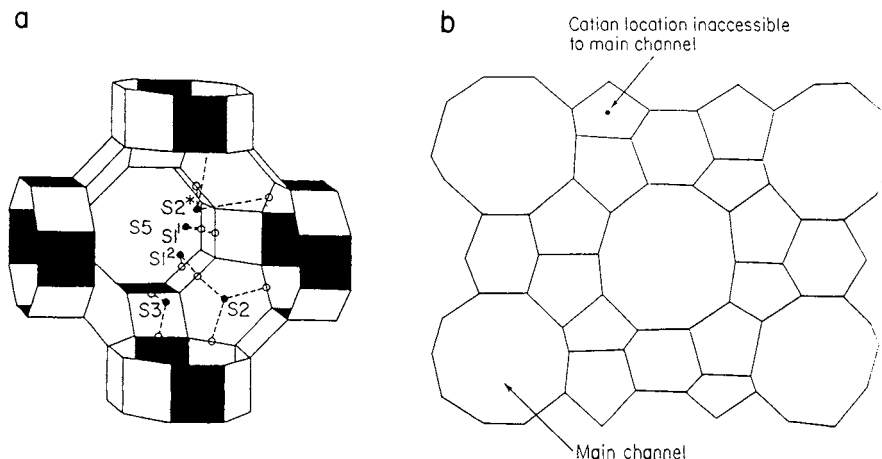
Figure 3. (a) Crystal structure of zeolite rho showing cation positions. Site S2 is at the center of a six-ring face with site S2* displaced slightly along the triad axis into the α-cage. Sites S1^1 and S2^2 are adjacent to four-rings in the octagonal prism, and site S5 is at the center of the octagonal prism. Site S3 is adjacent to a four-ring in the α-cage. (b) Schematic representation of the (100) - face of ZSM-5 showing the ten-membered ring main channels that are accessible to adsorbates and the smaller five-membered units that are inaccessible to adsorbates. (Reproduced from Refs. 7 and 8. Copyright 1987 Am. Chem. Soc.)

connected in a cubic arrangement by double-eight rings which affords
the same eight-ring pore opening as in zeolite A. However, there
are no small β-cages and therefore no parts of the intrazeolite sys-
tem which are accessible only to molecules capable of passing through
the six-ring entrance diameter. This is catalytically attractive as
there are no cation sites where Cu^{2+} is inaccessible to reactant
molecules. A similar study of the Cu^{2+} cation location in zeolite A
was performed by partial exchange with Cs^+ which is preferentially
located at sites either S2, S2* or S3.
        In hydrated forms of Cu^{2+}-doped H-, Na-, K- and Cs-rho a small
part of the Cu^{2+} is octahedrally coordinated to six water molecules
and undergoes free rotation at room temperature (6,7). This Cu^{2+}
is located in the α-cages and has little interaction with the cage
walls. The major part of the Cu^{2+} is coordinated to two water mole-
cules and to oxygens in the zeolite lattice. This species is most
likely either a square-planar complex located at site S3 or less
likely a square-based pyramid located at site S2*. An interesting
feature of zeolite rho is that the nature of the hydrated species is
independent of the nature of the cocation. This is quite different
from the case in zeolite A where the location and hydration number
of the major hydrated species is governed by the type of cocation.
It has been established that the hydrated species in zeolite A are
formed in the β-cage whereas the hydrated species in zeolite rho are
formed in the α-cage. It appears that the cocation effects in zeo-
lite A are due to the closer proximity of cocations to the Cu^{2+} in
the β-cage of zeolite A. There is greater steric hinderance in
smaller β-cages than in the larger α-cages.
        The coordination of Cu^{2+} in zeolite rho with other adsorbates
than water has also been studied by ESEM methods. Table I summarizes
the adsorbate coordination number of water and other adsorbates for
Cu^{2+} in rho zeolites with various cocations (6,7).

Table I. Cu^{2+} Coordination Number to Various Adsorbates in Rho
          Zeolites

Zeolite	CsH-rho	H-rho	Na-rho	K-rho	Ca-rho
H_2O	2	2	2	2	2
CH_3OH	–	2	1	1	1
C_2H_4	0	1	0	0	0
NH_3	3	3	∿3	∿3	∿3

The coordination number of ammonia is determined by resolved nitro-
gen hyperfine in the ESR spectra. The other coordination numbers
are determined by ESEM analysis. Ammonia appears to show no cocat-
ion effect as does water. Both are small, highly polar molecules.
        However, methanol and ethylene both show some cocation effect.
The coordination of each is larger in H-rho than for other cocations.

Figure 4 shows the ESEM results for specifically deuterated metha-
nols in CuH-rho. The data for CH_3OD indicate two coordinated metha-
nols through the oxygen. This is confirmed by the CD_3OH data for
the N = 6 fit. However, the CD_3OH data require a two shell fit and
the N = 3 shell corresponds to indirect coordination to a third mol-
ecule with its methyl group oriented toward the Cu^{2+}. Molecular
models suggest that the Cu^{2+} is located at $S2^*$ coordinated to two
methanols through their oxygens in the same α-cage and weakly inter-
acting with the methyl group of a third methanol located in an ad-
jacent α-cage on the other side of the six-ring associated with the
$S2^*$ site. This third methanol is presumably coordinated to a coca-
tion in the adjacent α-cage and its hydroxyl deuterium is too far to
contribute to the ESE modulation pattern.
    Note that ethylene only coordinates to Cu^{2+} in H-rho. In H-rho
ethylene can enter the α-cage whereas for CsH-, Na-, K- and Ca-rho
the larger cocations, which are located in the eight-rings, block
access to the α-cage. It appears that this blocking is effective
for nonpolar molecules like ethylene whereas polar molecules like
water, ammonia, methanol and even ethanol can solvate the cation,
perhaps transiently, and gain access to the α-cage.

Cu^{2+} in Zeolite NaH-ZSM-5

ZSM-5 provides a quite different zeolite structure involving a chan-
nel network instead of a cage network in which to accomodate Cu^{2+}
cations. Probably most significant is the absence of neighboring
cocations owing to the low ion-exchange of these zeolites, with Si/
Al = 26 in our synthesis.
    In hydrated CuNaH-ZSM-5 a hexa-aquo Cu^{2+} complex is observed
which has an isotropic ESR line at room temperature (8). The ESEM
data in Figure 5a confirms the six-water coordination. This species
must be located at the channel intersections since the main channels
are too small. After evacuation at room temperature the Cu^{2+} be-
comes anchored to the zeolite framework and shows coordination to
only three water molecules as shown by the ESEM data in Figure 5b.
The ESR parameters still indicate approximately octahedral coordina-
tion so the Cu^{2+} is coordinated to three water and three zeolite
framework oxygens. This partial dehydration procedure is totally
reversible by saturating the zeolite with water vapor.
    After complete dehydration the coordination of varous other ad-
sorbates was studied. Adsorption of methanol and ethanol produces
Cu^{2+} complexes containing two and three molecules respectively (8).
In both cases all the Cu^{2+} becomes complexed to the alcohol within a
few minutes. In contrast, adsorption of both ethylene and benzene
resulted in a very slow complexation with Cu^{2+}. In the case of ben-
zene even after two days much of the Cu^{2+} remained uncomplexed. To
test whether this is due to steric effects slowing down the diffu-
sion of benzene into the intrazeolite voids, pyridine was studied
because it has a similar kinetic diameter to benzene. However, pyr-
idine complexed Cu^{2+} within a few minutes. This suggest that the
Cu^{2+} in dehydrated ZSM-5 is not located in particularly accessible
positions and requires a polar molecule to interact with it and
cause it to migrate into the main channel. If Cu^{2+} were in an ac-
cessible position in dehydrated ZSM-5, the adsorption of nonpolar
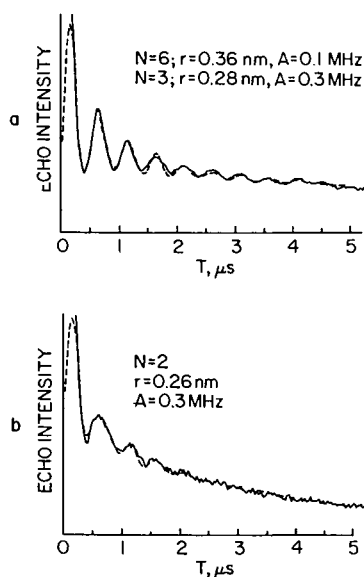
Figure 4. Experimental (———) and simulated (-----) three-pulse ESEM spectra of CuH-rho showing deuterium modulation (a) with adsorbed CD_3OH and (b) with adsorbed CH_3OD. (Reproduced from Ref. 6. Copyright 1986 Am. Chem. Soc.)
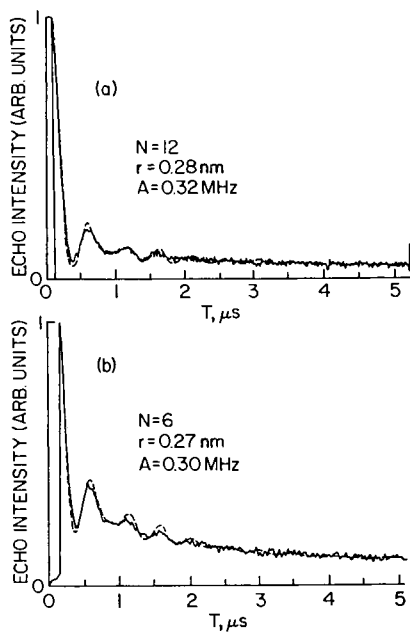
Figure 5.   Experimental (———) and simulated (-----) three-pulse ESEM spectra of CuNaH–ZSM–5 (a) with adsorbed D_2O, and (b) with adsorbed D_2O followed by evacuation at room temperature.   (Reproduced from Ref. 8.   Copyright 1987 Am. Chem. Soc.)

molecules would also result in rapid complexation of Cu^{2+} as happens in cage type zeolites. Possible, less accessible cation positions in the ZSM-5 structure are illustrated in Figure 3b.

The ESR spectra after adsorption of ammonia and pyridine show nitrogen superhyperfine splitting which is indicative of direct Cu^{2+}-N interaction. The number of superhyperfine components suggests that the Cu^{2+} is coordinated to three molecules of pyridine and four of ammonia.

In order to establish whether Cu^{2+} is internally exchanged into the zeolite and not just deposited on the external surface, deuterated ortho-xylene, a molecule too large to enter the zeolite channels, was adsorbed. No complexation of Cu^{2+} was observed by ESR and no modulation was observed by ESEM which supports the conclusion that Cu^{2+} is internally exchanged.

It is significant that ^{27}Al modulation is not observed by ESE spectroscopy in CuNaH-ZSM-5. Since Cu^{2+} must exchange for two monovalent cations it may site itself about midway between their presumed monovalent sites near negative aluminum lattice centers. This middle location would site the Cu^{2+} too far from aluminum lattice centers to observe ^{27}Al modulation. In contrast, when Na^+ is exchanged by Ca^{2+} the Cu^{2+} does show ^{27}Al modulation (16). This striking effect on cocation control of the Cu^{2+} location in zeolite ZSM-5 is currently being studied.

Overview

This work demonstrates the power of the ESEM technique when used in conjunction with ESR for the study of paramagnetic species in zeolites. Accurate measurements of the Cu^{2+} locations in zeolite A have been determined via cesium modulation. Assignments have been made to many ESR spectra in terms of coordination numbers and orientation of interacting species by ESEM analysis. In many cases unique structural data can be obtained by combined ESR and ESEM methods.

Acknowledgment

Literature Cited

1. Jacobs, P.E. Carbioniogenic Activity of Zeolites; Elsevier: Amsterdam, 1977.
2. Maxwell, I.E. Advan. Catal. 1982, 31, 1.
3. Kevan, L. In Time Domain Electron Spin Resonance; Kevan, L. and Schwartz, R.N., Eds.; Wiley-Interscience: New York, 1979; Chapter 8.
4. Mims, W.B. In Electron Paramagnetic Resonance; Geshwind, S., Ed.; Plenum Press: New York, 1972; Chapter 4.
5. Anderson, M.W.; Kevan, L. J. Phys. Chem. 1987, 91, 1850.
6. Anderson, M.W.; Kevan, L. J. Phys. Chem. 1986, 90, 6452.
7. Anderson, M.W.; Kevan, L. J. Phys. Chem. 1987, 91, 2926.
8. Anderson, M.W.; Kevan, L. J. Phys. Chem. 1987, 91, 4174.

9.   Goldfarb, D.; Kevan, L. J. Phys. Chem. 1986, 90, 264.
10. Ichikawa, T.; Kevan, L. J. Phys. Chem. 1983, 87, 4433.
11. Vance, T.B.; Seff, K. J. Phys. Chem. 1975, 79, 2163.
12. Fior, R.L.; Seff, K. J. Am. Chem. Soc. 1977, 99, 6249.
13. Subramanian, V.; Seff, K. J. Phys. Chem. 1980, 84, 2928.
14. Narayana, M.; Kevan, L. J. Chem. Soc. Faraday I. 1986, 82, 213.
15. Parise, J.B.; Prince, E. Mater. Res. Bull. 1983, 18, 841.
16. Sass, C.; Kevan, L. J. Phys. Chem., in press.

Chapter 10

Determining the Structure
of Molecular Sieve Materials
Using High-Resolution Powder Data

J. M. Bennett

Union Carbide Corporation, Old Saw Mill River Road,
Tarrytown, NY 10591

Molecular sieve compounds are a class of crystalline solids
which because of their porous nature have wide uses for
catalytic and adsorption processes. The size and shape of
these pore openings range from small six ring channels which
will only adsorb water to 18-ring channels which are 1.2nm
across. The determination of the framework topology which
yields both the pore size and shape is critical for
understanding and predicting uses for these materials. Single
crystal x-ray techniques have been used to determine the
topology of over 60 different microporous materials.
Unfortunately many molecular sieve materials are synthesized
with crystals that are too small to be used with single
crystal techniques, and powder techniques have to be used.
The framework topologies of the two most widely used molecular
sieve materials, type A and type Y zeolites, were first
determined from a combination of powder and single crystal
techniques in the 1950's by scientists at Union Carbide
Corporation. Since then only a relatively few new framework
topologies have been determined using powder data. Most are
determined from single crystal data using very small crystals.

Within the last few years high resolution data collected
either from synchrotron or neutron sources has allowed new
structures to be solved from powder samples. Powder data from
these new sources are superior to that collected from a
conventional x-ray source both in resolution and peak to
background ratio; these improvements in data quality have the
capability of making the determination of new molecular sieve
topologies easier but not necessarily routine. Synchrotron
radiation has possible future capabilities of being used to
collect data from crystals that are only a few microns in
size. At that time most newly synthesized molecular sieve
materials will be solved by single crystal techniques instead
of powder techniques. At the present time an acceptable
structure refinement can be obtained from a crystal with a

volume greater than 40,000 cubic microns using a sealed x-ray tube. The topology of silicalite was first determined using a twinned crystal roughly 20×20×70 microns in size. With a crystal of this size, data collection is measured in weeks, not hours and because the material contains only light atoms which do not diffract strongly, the data collection statistics are poor. If the crystals are large enough to obtain an adequate structure refinement, then single crystal techniques should still be used in preference to powder techniques.

DISCUSSION.

There are many steps in the determination of an unknown framework topology from diffraction data, and especially with powder data each step has many difficulties. The steps can be summarized as follows:

1. Collection of the data.
2. Determination of the cell dimensions and space group.
3. Determination of the correct trial model.
4. Refinement of the data and solution of the structure.

Usually each step must be successfully achieved before the next can be started. When the powder pattern of the new material matches that of a previously simulated hypothetical material it is possible to bypass stage 2 and go directly to stage 3. These steps are the same for both single crystal and powder data determination of a structure, but the techniques used with powder data are far less formalized. For example, with single crystals a suitable crystal is chosen, mounted on one or more cameras and the unit cell dimensions and space group determined. With a powder sample this information has to be derived either from three dimensional deconvolution of the one dimensional information contained in a powder pattern or reconstructed from information obtained from many different crystals using electron diffraction techniques. This simple step with single crystal data has therefore become complex with powder data. The determination of the structure of a molecular sieve material using single crystal techniques is very involved and tedious, and it is even more so with powder data. However the results supply information that cannot be obtained using any other technique.

COLLECTION OF DATA. It should be emphasized that the correct choice and preparation of the sample combined with careful collection of data will greatly aid in the total process. It is extremely important that the sample is pure, or if not, that all the impurity phases are known. Figure 1 shows a comparison of data collected from a typical 1970's diffractometer, a modern computer controlled diffractometer and a high resolution diffractometer using synchrotron radiation at the National Synchrotron Light Source. The excellent resolution and high peak to background ratio (typically 1000:1) obtained from the synchrotron data enable very weak peaks to be easily observed.
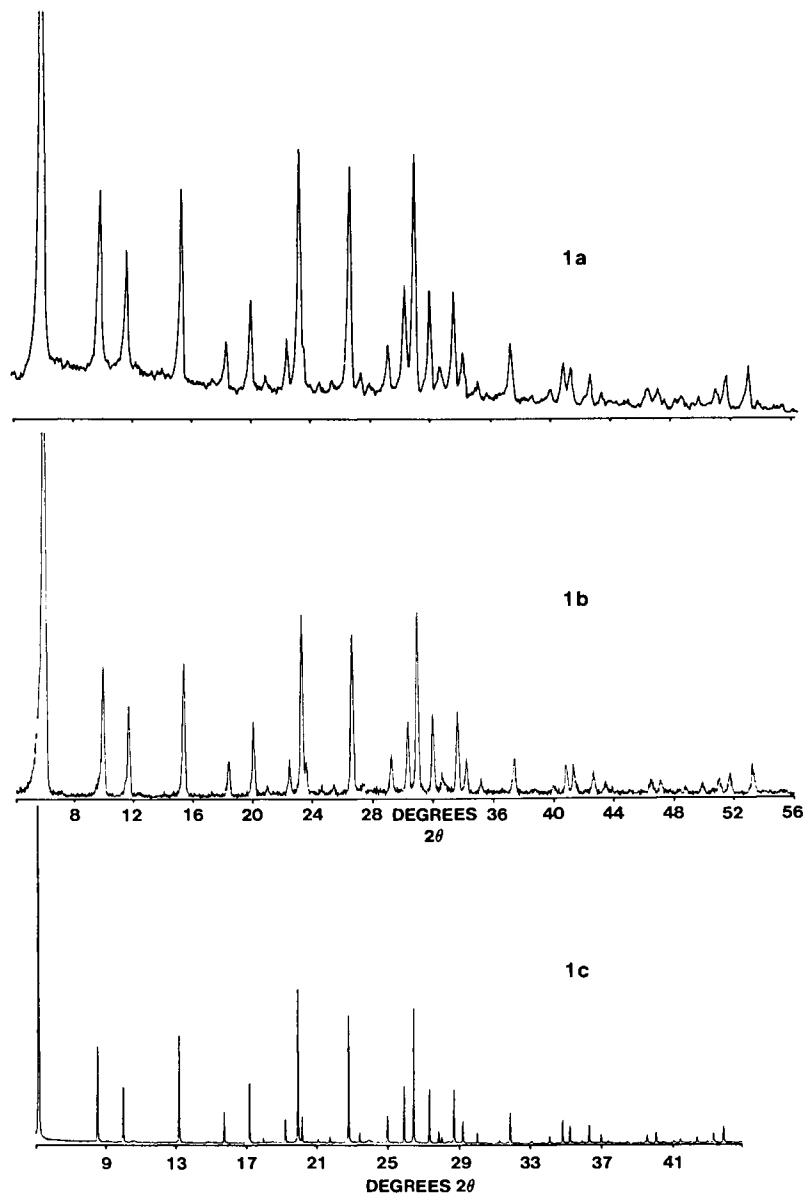
Figure 1:   A comparison of data collected from typical
diffractometers: (a) a 1970's diffractometer, (b) a modern
computer controlled diffractometer and (c) a high resolution
diffractometer using synchrotron radiation.
Note: Trace c has been scaled to simulate data collected with
copper radiation.

If   the   material under   examination   has   an   unknown
framework topology and therefore unknown cell dimensions, weak
peaks   in   a   diffraction   pattern   could   come either from an
impurity phase or from the sample. The presence of one peak
from an impurity phase can prevent the crucial determination
of the cell dimensions if computer indexing programs are used
routinely   without   sequential   testing   for   possible   stray
diffractions.   The   state   of   the   sample   must   also   be
considered.   Since   most   molecular   sieve materials are also
adsorbents,   the   atmosphere   around   the   sample   must   be
controlled   to   prevent   changes   in   sample   hydration with
humidity changes. This sorption/ desorption process results
in a compositional change of the sample during data collection
that will hinder the modelling of the non-framework density.
It   is   preferable   to   determine   the topology of a new phase
using   an   anhydrous   and,   if   possible,   a   cation free sample.

The   collection   of   high   resolution   data   is partially
machine dependent, however   certain   generalizations   can   be
made.   It is advantageous to use the focussing properties of a
monochromater such that for use with computer autoindexing
programs,   the   conditions   are   set   to   yield   the best angular
resolution at low two theta values. For data collection the
conditions   are changed so that the best angular resolution is
obtained at high two theta values where overlap of the peaks
will   be   the   greatest.   It must be remembered that particle
size affects the resolution,   and   it   is   advisable   to   have
crystallites   larger   than   one micron. Data are collected in
the   usual   way   by   step-scanning   at   appropriate
intervals; however, because of the extremely small divergence
of the incident beam, the sample is usually rotated if it is
mounted   in   a   capillary   or oscillated if it is a flat plate
mount   to   correctly   average   over   a   large   number   of
crystallites. The geometry of the diffractometer, the type of
detector and the operating conditions for the irradiating beam
affect   the   maximum resolution, the peak to background ratios
and the maximum intensity that can be obtained.   All these
have to be considered in determining the most effective way to
collect the data. If care is taken both with the choice and
preparation   of   the   sample   and   with   the   data   collection
technique, then many hours of frustration can be saved in the
final   stages   of   data   processing.

DETERMINATION OF THE CELL DIMENSIONS AND THE SPACE GROUP. The
best   means   for   determining   the   cell   dimensions   and   the
possible space group uses selected area electron diffraction
techniques; this   is   equivalent   to   using   single   crystal
techniques   on   a   powder sample. The other possibility is to
use either manual   or   computer   indexing   processes.   Manual
indexing   techniques   are   usually limited to materials having
cubic   or   hexagonal   symmetry   even   though   lower   symmetry
materials   were   often   correctly indexed using Bunn charts in
the   early days of structural   studies.   One   difficulty with
using   computer   indexing   programs   is   obtaining   sufficient
accuracy with the low angle peak   positions.   Typically with
synchrotron   data   these   peak   positions can be determined to
better than $0.005°$ 2θ. Computer indexing programs can be used

with almost any symmetry, however all programs will usually supply several different answers. Tests can be carried out to check the validity of each solution; unfortunately often several solutions appear equally probable. Thus the crystallographer is left with a choice between several possible unit cell dimensions and is often forced to decide between them using intuition and/or luck. Even when only one unit cell appears probable it may not be recognized that the cell has higher symmetry. Algorithms are available that can aid in recognizing that the cell has higher symmetry, and should be used to augment the proceedures present in the autoindexing programs. Most molecular sieve materials have high symmetry; in fact when the topologies are idealized more than 50% have either hexagonal or cubic symmetry, while none have triclinic symmetry. 80% of molecular sieve structures have orthorhombic or higher symmetry and it is reasonable to expect that a new topology could also have high symmetry. This requires a check of all unit cells determined by computer indexing programs for possible higher symmetry. If computer indexing programs have to be used as the sole method for determining the unit cell dimensions, then it is best to employ more than one program using different techniques and to compare the results. If identical results are obtained from two different programs, then it improves the confidence level. Currently the two most widely used autoindexing programs are Vissers(1) and Treor(2). The techniques required to use either program are given in the program writeups.

Selected area electron diffraction techniques have to be used to obtain the single crystal patterns from powder samples. unit cell dimensions can be measured directly. In the best situation electron diffraction techniques can supply the correct cell dimensions and all of the systematic absences. With high symmetry space groups, knowing all the systematic absences does not mean that the space group can be determined unambiguously. For example, if the cell dimensions indicate a geometrically hexagonal cell with no systematic absences, there are 21 possible space groups. In the worst situation, electron diffraction techniques can usually determine several of the cell dimensions and some of the major systematic absences. Using this partial unit cell dimension information in conjunction with the results of the computer indexing is probably the best technique for determining the cell dimensions and the symmetry of an unknown molecular sieve material. Even partial electron diffraction data will greatly reduce the number of possible 'correct solutions' derived by any computer indexing program.

Once the unit cell dimensions have been determined, it is necessary to determine the space group. This involves completely indexing the powder pattern and examining all possible sets of hkl values for each peak to see if they are consistent with the chosen space group. In patterns with high symmetry or ones that have two dimensions that are related by a constant, this will usually result in multiple hkl values for most peaks. This multiple indexing of peaks will result in several equally possible space groups. If it is necessary

to choose between several possible space groups, then an examination of reported space groups of idealized molecular sieve topologies suggests that several space groups are preferred. This is a result of the restrictions placed upon the framework atom positions by the need to maintain a tetrahedral framework. If one of the several possible space groups has already been observed for a molecular sieve material it should be tried first.

Each choice of a space group and a set of cell dimensions attempted requires an effort equivalent to that necessary to solve the structure. If the structure determination effort is unsuccessful, it is not known whether the combination of space group and cell dimensions is wrong or whether the crystallographer has failed in his task, therefore it is desirable to have the minimum number of combinations.

Fortunately, in the initial stages of a structure determination it is not always necessary to use the correct space group. With a completely ordered molecular sieve material it is often easier to determine the topology making the assumption that all tetrahedral atoms are of the same type; the use of an idealized space group will produce an idealized topology. However, the determination of the topology is the limiting step in determining a new structure from powder data.

DETERMINATION OF THE CORRECT TRIAL MODEL. Before this stage can be started, all noncrystallographic structural information which can aid in producing the correct topology should be obtained. For example, this information should include data from sorption studies which can help to predict both the maximum pore opening and the framework density and solid state NMR studies which can show the number of crystallographically unique atoms or the coordination state of the framework atoms.

There are two general techniques that can be used to successfully determine a trial model: ab initio calculations and modelling techniques. At the present time a combination of the two is most effective, as neither can be used exclusively.

Ab Initio Techniques. The use of ab initio techniques is possible with high resolution neutron and synchrotron data because more non-overlapping reflection data can be obtained than is possible from a standard diffractometer. As the resolving power of these diffractometers further increases, so will the successful use of ab initio calculations.

Ab initio techniques imply the use of either a Patterson function or direct methods techniques. Recently both of these techniques have been used to solve structures(3,4) using high resolution powder data; these initial successes do not mean that either technique can now be used routinely. The possibility of success with either technique is increased if 1) the unit cell is small, 2) the space group is centered and 3) the unit cell has relatively low symmetry. These

requirements greatly reduce the possibility of overlap of
reflections. Unfortunately when used with molecular sieve
materials, direct method techniques may fail to provide a
useful solution since many materials have one or more large
cell dimensions and also have high symmetry. To solve these
structures it has been found to be useful to include the
correct number of TO_2 units (as T atoms surrounded
tetrahedrally by four half weight oxygen atoms) as a fragment
of the structure.

Modelling techniques. There are several modelling techniques
that can be used. The first technique is recognition that the
new material has a known topology. This is not always
trivial, because the powder patterns may appear to be
different due to either compositional differences or changes
in symmetry resulting from framework distortions. This can be
illustrated by comparing the following sets of powder patterns
in which the materials in each set have the same idealized
framework topology:

1) Zeolite F(Linde) and Edingtonite.(Figure 2)
2) Amicite, Gismondine, Gobbinsite and Na-P1(see 5).

Likewise, in cases where the two materials have have similar
unit cell dimensions and symmetry, such as Zeolite Q(Linde)
and MAPO-46, the topologies can not be assumed to be identical
unless proven by carrying out a full structure determination.

        Another modelling technique is to compare the cell
dimensions, maximum symmetry and maximum pore opening with
hypothetical tetrahedral framework structures such as those
detailed by J. V. Smith et. al.(6) and others(7). It should
be noted that if the cell dimensions have been determined only
from a model of the hypothetical structure and not refined
using the DLS technique, then they can easily differ from the
idealized values by more than 1Å. For example, the c
dimension of $AlPO_4$-5(8) is 8.48Å as compared to the model
value of 10Å.

        A better technique is to have available the simulated
powder patterns of all the possible tetrahedral structures so
that they can be used in the same way as the JCPDS file is
used to identify unknown materials. If these simulated powder
patterns were available, it might not even be necessary to
determine the cell dimensions and space group of an unknown
molecular sieve material. For example, if the simulated
powder pattern of JVS81-1 had been available, and if it
matches the observed powder pattern of dehydrated VPI-5 then
there would be no need to determine the correct idealized cell
dimensions and symmetry. This simple comparison would have
yielded the correct topology and shown that the material was
an 18-ring structure.
        Unfortunately there are over 500 hypothetical framework
topologies presently enumerated, and the effort required to
simulate all of these powder patterns and match them with the
50 unknown frameworks would be extensive. It is necessary to
find a method that would determine the probability of
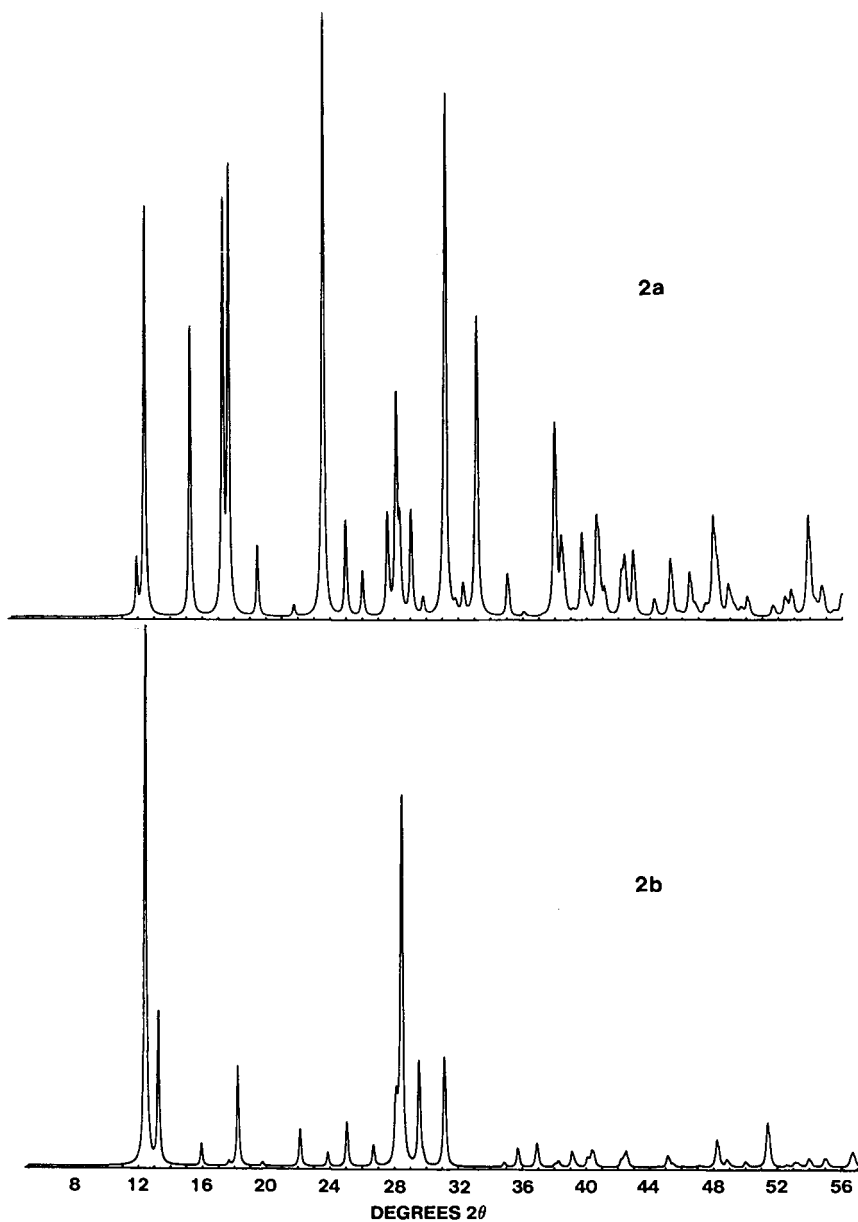
Figure 2: A comparison of the diffractometer pattern of
zeolite F(Linde) and Edingtonite.

synthesizing a hypothetical topology. As an example, if the
ABC-6 ring family of hypothetical structures is considered,
all can be satisfactorally idealized using DLS; therefore, all
are theoretically possible. However, the number of observed
members of this family is only about 12, and all of these have
both high crystallographic symmetry and high geometrical
symmetry. If we describe structures having these symmetries
as being 'elegant', then it may be a lack of elegance in many
of the hypothesized topologies that suggests that they may
never be synthesized. Table I contains a list of all ABC-6
ring hypothetical structures that can be postulated out to a
repeat sequence of 12.

Table I: List of all possible hypothetical ABC-6 nets

number of layers	number of possibilities	number of topologies	observed structures
2	1	1	CAN
3	2	2	SOD,OFF
4	3	2	GME,LOS
5	5		
6	10	4	CHA,EAB,ERI,LIO
7	20		
8	45	1	AFG
9	96	1	LEV
10	230	1	Franzinite?
11	529		
12	1303	(?)	

If we apply the elegance test to the 12 layer repeat sequence,
we find that there are 20 topologies that have the highest
possible symmetry ($P6_3/mmc$) and one of these is built only
from double six rings. By definition this would be the most
elegant of the 1303 possible sequences. As an example Figure
3 shows the observed powder pattern for a calcined dehydrated
$AlPO_4$ material and the DLS simulated pattern for this most
elegant sequence. The close similarity between the two
patterns is sufficient justification to attempt a solution
using as a starting model the postulated sequence. It may
also indicate that it is possible to reduce the large number
of postulated hypothetical structures down to a more
manageable number of practical possibilities.

     The final technique used at Union Carbide was developed
in conjunction with V. Schomaker (U. of Washington, Seattle).
The Bennett/Schomaker method extends the concept of the DLS(9)
method which is currently restricted to refining atom
parameters and/or cell dimensions from a known topology, to
use with a powder pattern simulation program(10). The DLS
method is successful because, when correctly set up, the
number of interatomic distances is always larger than the
number of unknown atom parameters. The Bennett/Schomaker
method is restricted to use with molecular sieve materials
having tetrahedral frameworks. The method requires that the
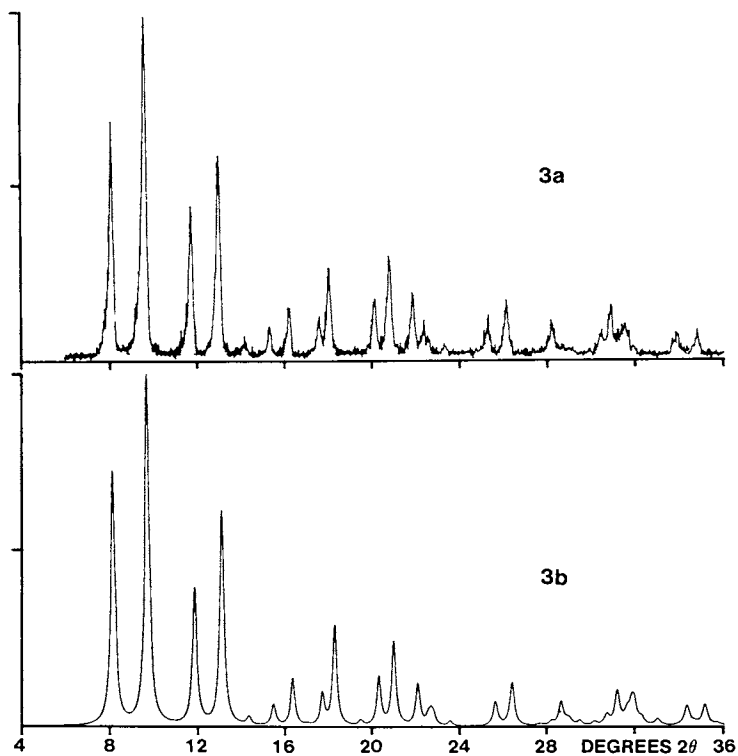
Figure 3: A comparison of the diffractometer pattern of a calcined AlPO$_4$ material and the simulated pattern of a 12 layer ABC-6 net topology.

cell dimensions, symmetry and cell contents are known and can sucessfully predict a new framework topology by making the following assumptions:
1) The method is restricted to tetrahedral frameworks such that each T atom has only four near T neighbours bonded by oxygen atoms.
2) The positions of these framework oxygen atoms can be ignored.
3) All the T-T interatomic distances are assumed to be equal.
4) and finally we have only to place the T atoms in the chosen asymmetric unit, since symmetry relationships can be derived such that atoms in the asymmetric unit correctly bond to the T atoms in the neighbouring asymmetric units. This allows interatomic distance equations to be set up that can be solved to yield the correct positions of all of the T atoms in the asymetric unit cell and ultimately, the complete topology.

The Bennett/Schomaker method is not easy to describe and can be illustrated by the first example (see the Appendix) which derives the idealized faujasite topology. The method derives starting x,y,z parameters for the tetrahedral atom of (.125,-.050,.038), which compare with refined parameters of (.125,-.054,.037). The second example derives parameters for the RHO topology of (¼,.102,.398) as compared to refined parameters of (¼,.1014,.3986). The third example derives idealized parameters for AlPO$_4$-16 of (.114,.114,.114) as compared to refined parameters of (.1139,.1139,.1139) and (.1156,.1156,.1156). In these three examples the derived parameters are more than adequate to completely describe the idealized framework topology and can even be used as a starting set in a structure refinement.

Miscellaneous techniques. The structure of Theta one(11) was solved with neither ab initio calculations nor modelling, but by permuting all possible assignments of phases for a small number of reflections and then examining the Fourier maps. This may seem a tedious way to solve an unknown structure, but it was successful. The technique may indeed be a way of solving molecular sieve structures with centric space groups should all else fail.

REFINEMENT OF THE DATA AND SOLUTION OF THE STRUCTURE. Once the correct framework topology has been determined, the data must be refined to get the complete solution. Data collected using high resolution synchrotron radiation are easier to process and refine than standard x-ray data 1) because it is highly monochromatic and the peak shapes can be well described by the convolution of Gaussian and Lorentzian functions and 2) because it has excellent resolution and there is less overlap of reflections.

The major difficulty with refining powder data from molecular sieve materials is determining the positions of all of the non-framework atoms. In hydrated or as-synthesized samples, the non-framework atoms are usually disordered such that they occupy a variety of possible positions and orientations. Therefore, they must be modeled to make both

chemical sense (i.e. valid interatomic distances and angles) and to also duplicate the filling of the voids within the structure. This is difficult with single crystal data and even more so with powder data; the refinement of $AlPO_4$-16 data illustrates this. The as-synthesized material contains quinuclidine as the template; it was originally placed in the center of the cavity and aligned along a 3-fold axis. However, the best refinement was obtained when the quinuclidine was rotated a few degrees off the 3-fold axis. The difference between the two orientations of the quinuclidine resulted in the second orientation creating a spherically disordered region which better modelled the actual disorder. In many cases it is not possible to get as sophisticated a model for the non-framework atoms. Often it is sufficient for the first structure determination of a new framework topology using powder data to model this disorder with a series of carbon atoms with large temperature factors, since the correct determination of the non-framework atoms is not necessary. Once the framework topology has been correctly determined from a anhydrous and/or calcined sample, then the position of the non-framework atoms can be determined using the as-synthesized material and the use of another data set.

SUMMARY.

Most new molecular sieve phases are synthesized with crystals only a few microns in size. It is not possible to determine the framework topology of such a phase using present single crystal techniques, and powder techniques are becoming increasingly important. With new high resolution diffractometers the technique to collect excellent data are available. The increase in resolution makes it practical to use autoindexing programs to determine the cell dimensions and to better determine the symmetry. The improvements being made to Rietveld programs give the capability of relatively easy processing of the data. The major stumbling block to the use of powder techniques is the difficulty of determining a new topology. At the present time ab initio techniques as applied to powder data for molecular sieve materials have not been used with enough structures to demonstrate the capability of the techniques. Modelling techniques require a wide knowledge of many molecular sieve topologies and few molecular sieve crystallographers have this information readily available. It would be very helpful if simulated powder patterns were available for all hypothetical topologies, but this is a large undertaking. The most productive tool may be the Bennett/Schomaker method described herein, especially if it can be automated. It may not be possible to teach the computer to apply symmetry operations to derive the correct interatomic relationships, so it will be necessary for the computer to permute all the possible symmetry operations to see if a solution can be obtained. The number of calculations may be large, but a week or even a month of a micro VAX computer time to do the task will be considered by many to be a timesaver for structure determinations.

Literature cited

1. Visser, J. W. J. Appl. Cryst. 1969, 2, 89-94
2. Werner, P. E. Z. Krst. 1964, 375-387
3. Lightfoot, P.; Cheetham, A. K.; Sleight, A. W.
   Inorg. Chem, 1987, 26, 3544-3547
4. Rudolf, P. R.; Saldarriage-Molina, C.; Clearfield,
   A. J. Phys. Chem. 1986, 90, 6122-6125
5. von Ballmoos, R. Collection of simulated XRD powder
   patterns for zeolites, Butterworth Ltd., 1984
6. Smith, J. V.; Rinaldi, F. Min. Mag. 1962, 33, 202-212
   Smith, J. V. Min. Mag. 1968, 36, 640-642
   Smith, J. V. Am. Min. 1977, 62, 703-709
   Smith, J. V. Am. Min. 1978, 63, 960-969
   Smith, J. V. Am. Min. 1979, 64, 551-562
   Smith, J. V.; Bennett, J. M. Am. Min. 1981,66,777-788
   Smith, J. V. Z. Krst. 1983, 165, 191-198
   Smith, J. V.; Bennett, J. M. Am. Min. 1984,69,104-111
   Smith, J. V.; Dytrych, W. J. Nature 1984, 309,607-608
   Bennett, J. M.; Smith, J. V. Z. Krst. 1985, 171,65-68
   Hawthorne, F. C.; Smith, J. V. Z. Krst.1986,175,15-30
   Smith, J. V.; Dytrych, W. J. Z. Krst. 1986, 175,31-36
7. Kerr, I. S. Nature 1963, 197, 1194-1196
   Sherman, J. D.; Bennett, J. M. Molecular Sieves
   Adv. in Chem. 121, 1973, p.52-65
   Rechsteiner, H. Diplomarbeit thesis, ETH, Zurich,
   Switzerland, 1979
   Gramlich-Meier, R. Z. Krst. 1986 177, 237-245
   McCusker, L. B.; Meier, W. M.; Rechsteiner, H.
   Mat. Res. Bul. 1987, 22 1203-1207
8. Bennett, J. M.; Cohen, J. P.; Flanigen, E. M.;
   Pluth, J. J.; Smith, J. V. Intrazeolite Chemistry
   ACS Symp. Ser. 218, 1983, p.109-118
9. Baerlocher, Ch.; Heep, A.; Meier, W. M. DLS-76,
   A program for the simulation of crystal structures
   by geometric refinement. ETH, Zurich, p.124 (1978)
10 Smith, D. K.; Nicols, M. C.; Zolensky, M. E.
   A Fortran Program for Calculating X-ray Powder
   Diffraction Patterns - Version 10
11. Highcock, R. M.; Smith, G. W.; Wood, D.
    Acta. Cryst. 1985, C41, 1391

APPENDIX

THE IDEALISED FAUJASITE TOPOLOGY. The following assumptions
are made 1) the space group is Fd3m (second setting) and 2) all
192 T atoms are in general positions. The cell dimensions are
known and the T-T interatomic distance is assumed to be 3·1Å.
For convenience the atom coordinates (x,y,z) are expressed in
Ångstroms, and not in fractions of the unit cell dimensions.

Description of the asymmetric unit.   The space group has a
natural double asymmetric unit, a tetrahedron bounded by four
mirror planes.   If one such tetrahedron is chosen with
vertices, in 1/8's, of $(0,0,0)$, $(4,0,0)$, $(2,2,2)$ and $(2,-2,2)$,
the tetrahedron has a two-fold axis running through the points
$(1,1,1)$ and $(3,-1,1)$.   This twofold axis divides the double
asymmetric unit into the two asymmetric units.

Derivation of topology. Consider the plane with $z = 1$, and the
part of the tetrahedron with z greater than 1, finally for
mathematical convenience during the calculation, the origin is
shifted by $(1,1,1)$, then we find:

1.   The x-projection.
The choice of asymmetric unit causes
y to be zero.   The T atom (x,y,z) in
the chosen asymmetric unit cell
bonds across a mirror plane to
another T atom (x,z,y) in the next
asymmetric unit cell:

$$d = \sqrt{(2z)}.$$

2.   The y projection.
The T atom (x,y,z) bonds across a
mirror plane to another T atom
(z,y,x) in the next asymmetric unit
cell, since $y=0$,

$$d' = \sqrt{[2(z-x)]}.$$

3.   Equating d and d', we find that
$x = 2z$.

4.   The z projection.
The T atom (x,y,z) bonds to the T
atom in the twin asymmetric unit
which is at $(2-y,2-x,2-z)$.

$$d'' = \sqrt{[(2-x-y)^2+(2-x-y)^2+(2-2z)^2]}.$$

substituting $2z$ for x, and 0 for y.

$$d'' = \sqrt{[3(2-2z)^2]}.$$

5.   Equating d and d''

$$\sqrt{(2z)} = \sqrt{[3(2-2z)^2]}.$$

Therefore $z = 0\cdot7$Å and $x = 1\cdot4$Å
Therefore the T atom(x,y,z) has parameters of $(1\cdot4,0,0\cdot7)$Å and
the tetrahedral atom in the second asymetric cell is
$(2,0\cdot6,1\cdot3)$Å. If the origin shift of $(1,1,1)$ is removed, then
the tetrahedral atom in the second asymetric unit cell becomes
$(1,-0\cdot4,0\cdot3)$Å; which is $(\cdot125,-\cdot50,\cdot038)$ in fractions of a
cell edge.
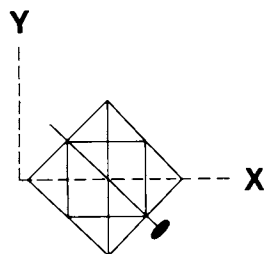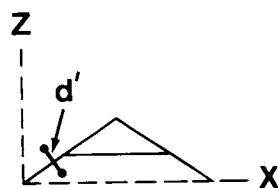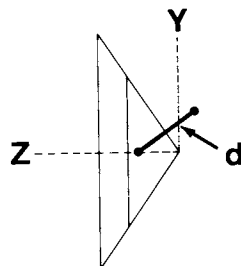
Comparison of results.   Typical refined tetrahedral atom
parameters for a faujasite structure are (0·125,-0·054,0·037),
so the parameters derived by the Bennett/Schomaker technique
are more than adequate to both build the topology and to be
used as a starting set in a refinement.

THE IDEALISED RHO TOPOLOGY. The following assumptions are made
1) the space group is Im3m and 2) the 48 atoms are on a special
position. There are 3 possible special positions and it can be
shown that there is no solution for the first two. The T atom
is therefore assumed to be on a (x,¼,½-x) position. Because
the T atom is on a special position the problem reduces to a
one parameter solution. It can be shown that the atom at
(x,¼,½-x) bonds to another at (¼,x,½-x). The final
Bennett/Schomaker result is (¼,0·102,0·398) as compared to
refined parameters of (¼,0·1014,0·3986).

MULTIPLE ATOM SOLUTIONS. When there are two atoms in the
asymmetric cell, the problem becomes more complex.   If
necessary, seven distance equations can be derived for a
maximum of six unknown framework parameters. As the number of
atoms in the asymmetric cell increases so does the number of
possible interatomic distances.   There is always (4n-1)
distances for 3n unknown parameters (where n is the number of
atoms in the asymmetric unit cell).
THE IDEALISED AlPO$_4$-16 TOPOLOGY. Structural studies showed
that the unit cell contains 40 atoms and the symmetry is face
centered cubic, maximum symmetry Fm3. 40 atoms in a unit cell
can be arrived at by having 32 T atoms at (x,x,x) and either 8
T atoms at (¼,¼,¼) or 4 T atoms at (0,0,0) and another 4 T
atoms at (½,½,½).

     The following assumptions are made 1) the space group is
Fm3 with a = 13·4Å and 2) 32 of the 40 atoms are on a special
position(x,x,x). Consider the 32 T atoms:
The atom(x,x,x) bonds to three others at (x,x,x̄), (x,x̄,x) and
(x̄,x,x) across mirror planes. The interatomic distance is d =
2x, assuming an interatomic distance of 3·07Å, x = 0·114 in
fractional coordinates. This atom at (·114,·114,·114) will
also bond to the atom at (¼,¼,¼) with a suitable interatomic
distance, but not to atoms either at (0,0,0) or (½,½,½). It
can be easily shown that the atom at (¼,¼,¼) bonds to four
other atoms at (x,x,x), (½-x,½-x,x), (x,½-x,½-x) and
(½-x,x,½-x).

The structure was refined using the space group F23 because of
the need to maintain aluminum and phosphorus ordering; the
final results were x = 0·1139 and 0·1156 compared to the 0·114
obtained by the Bennett/Schomaker method.

Chapter 11

Cesium Vapor Reacts with K+-Exchanged Zeolite A To Give Fully Cs+-Exchanged Zeolite A Containing $(Cs_4)^{3+}$ Clusters

Nam Ho Heo and Karl Seff

Chemistry Department, University of Hawaii, Honolulu, HI 96822-2275

The K^+ ions in dehydrated K_{12}-A were all reduced by 0.1 torr of cesium vapor at 350 °C to give dehydrated fully Cs^+-exchanged zeolite A containing extra cesium atoms at least primarily as $(Cs_4)^{3+}$ clusters. The crystal structure of Cs_{12}-A•$\underline{x}$Cs ($\underline{x}$ $\underline{ca}$ 3/4; $\underline{a}$ = 12.281(1) Å) has been determined by single-crystal x-ray diffraction methods in the cubic space group $\underline{Pm3m}$; $\underline{R}_w$ = 0.054. Cs_{12}-A•$\underline{x}$Cs may be viewed as a homogeneous mixture of Cs_{13}-A and Cs_{12}-A whose populations are about 3/4 and 1/4, respectively. In each of these, per unit cell, three Cs^+ ions are located at the centers of the 8-rings. Within the sodalite unit, two Cs cations are found 4.05(2) Å apart on a unique threefold axis. Each sodalite-unit Cs cation in Cs_{13}-A associates further with a large-cavity cation at 3.85(1) Å to give the linear $(Cs_4)^{3+}$ cluster. All eight 6-ring sites in the large cavity are occupied by Cs cations in Cs_{13}-A, but only six are found there in Cs_{12}-A. In Cs_{12}-A, one Cs^+ lies opposite a 4-ring in the large cavity between two adjacent 6-rings which are occupied only on their sodalite-unit sides by Cs cations. Less than thirteen cesiums are found per unit cell. Perhaps Si/Al = 1.00 and some unit cells have failed to sorb a cesium atom. Alternatively, if each cell has sorbed a cesium atom, the Si/Al ratio of the zeolite framework is about 1.04 and some $(Cs_2)^+$ clusters must be present.

The concept of 'ion-sieving' originally proposed by R. M. Barrer ([1]) has not been supported by crystallographic studies of various partially Cs^+-exchanged zeolite A's. ([2]-[7]) The 6-ring windows of the sodalite cage (mean van der Waals aperture = 2.2 Å) were thought to be too small to allow large cations like Cs^+ (d = 3.34 Å) to enter. It was for this reason, it was believed, that all of the Na^+ ions in zeolite 4A could not be replaced by Cs^+ when ion-exchange from aqueous solution was attempted. However, zeolite A always contains one Cs^+ ion in each sodalite unit when more than three Cs^+ ions per 12.3-Å unit cell are introduced by conventional ion-exchange methods from aqueous solution. ([2]-[7]) Perhaps water molecules participate in a mechanism which allows Cs^+ ions to pass through the narrow 6-rings of the sodalite cage.

Cs^+ ions can pass through 6-rings even in the absence of water, however, according to recent results on the reactions of various dehydrated zeolite A's with cesium vapor. ([8]-[11]) Cs^+ ions introduced by redox reaction between zeolitic cations and cesium metal vapor readily locate in the sodalite cages. ([8]-[11]) It appears that the zeolite framework allows easier passage to cations than it does to molecules according to the concept of 'molecular sieving'. ([12])

Furthermore, fully dehydrated, fully Cs^+-exchanged zeolite A containing two Cs^+ ions in each sodalite unit has been successfully prepared by the reaction of dehydrated Na_{12}-A with cesium vapor. ([8]-[10]) With twelve large Cs^+ ions per 12.3 Å unit cell, zeolite A accepted extra cesium atoms to relieve its cation-crowding in both the large and the small cavities by forming weak metal-metal bonds between Cs^+ ions in the form of the linear cluster $(Cs_4)^{3+}$. ([8]-[10]) These clusters were found to be stable up to 850 °C. ([11],[13]) However, for reasons which are unclear, only about half of the unit cells of Cs_{12}-A•1/2Cs contained extra cesium atoms.

The K^+ ions in dehydrated K_{12}-A, because of their size, can be considered to be more loosely associated with the zeolite A framework than Na^+ ions. Perhaps then K^+ would react more readily than Na^+ with Cs, even though the electrochemical potential (aqueous) for the reaction is much less. The reaction of dehydrated K_{12}-A with cesium vapor was carried out to determine the generality of the reaction of cations in zeolite A with cesium and with the hope of preparing a product of different, perhaps integral stoichiometry such as Cs_{12}-A•Cs.

Experimental

Fully K$^+$-exchanged zeolite A (14,15) was prepared by flow methods using aqueous 0.1N KOH solution and a single crystal of zeolite 4A (actual or idealized stoichiometry: $Na_{12}Si_{12}Al_{12}O_{48} \cdot 27H_2O$ (16)) synthesized by Charnell's method. (17) This crystal, a cube 85 μm on an edge, was then evacuated in a fine Pyrex capillary on a vacuum line at 350 °C and 1×10^{-5} torr for 48 hours.

After complete dehydration, (14) cesium (99.98% purity, Johnson Matthey Inc.) was distilled from a side-arm breakseal ampoule to the glass tube extension of the crystal-containing capillary. This glass reaction vessel was sealed off under vacuum and placed within two cylindrical coaxially attached horizontal ovens. The oven around the crystal was maintained at 350 °C for 16 hours, while the oven around the distilled cesium was at 209 °C to give 0.1 torr of cesium vapor in the entire reaction vessel. (18) The capillary was then allowed to cool (after the cesium source had cooled) and was sealed off from the reaction vessel with a small torch while still under vacuum at 25 °C. An examination of the product under the microscope showed that the colorless crystal of dehydrated K_{12}-A had become black.

A Syntex four-circle computer-controlled diffractometer with a graphite monochromator and a pulse-height analyzer was used for preliminary experiments and for the subsequent collection of diffraction intensities. Molybdenum radiation ($\underline{K}\alpha_1$, λ = 0.70930 Å; $\underline{K}\alpha_2$, λ = 0.71359 Å; $\underline{K}\bar{\alpha}$, λ = 0.71073 Å) was used.

Fully dehydrated, fully Cs$^+$-exchanged zeolite A has been shown to have far less "b" reflection intensity for its $\underline{Fm3c}$ superstructure than hydrated zeolite 4A. (2) For this reason, as well as for others discussed previously, (16,19) the space group $\underline{Pm3m}$ (no systematic absences) was used for data collection and structure solution. The final structure was examined using both space groups.

The cell constant, $\underline{a}$ = 12.283(1) Å, was determined by a least-squares treatment of 15 intense reflections for which 20° < 2θ < 30°. The θ-2θ scan technique was used for data collection. Each reflection was scanned at a constant rate of 1.0° min^{-1} from 1° (in 2θ) below the calculated $\underline{K}\alpha_1$ peak to 1° above the $\underline{K}\alpha_2$ maximum. Background intensity was counted at each end of a scan range for a time equal to half the scan time. The intensities of three reflections in diverse regions of reciprocal space were recorded after every 47 reflections to monitor crystal and instrument stability. Only small random fluctuations of these check reflections were observed during the course of data collection. The intensities of all lattice points for which 2θ < 70° were recorded.

The raw data were corrected for Lorentz and polarization effects, including that due to incident beam monochromatization (assuming the graphite monochromator crystal to be half perfect and half mosaic in character). Standard deviations were assigned to individual reflections by the formula

$$\sigma(\underline{I}) = [\omega^2(CT + \underline{B}_1 + \underline{B}_2) + (\underline{p}\underline{I})^2]^{1/2}$$

where CT is the total integrated count, $\underline{B}_1$ and $\underline{B}_2$ are the background counts, and $\underline{I}$ is the intensity. The value of $\underline{p}$ = 0.02 was found to be appropriate for the instrumentation used. [20]   Other details regarding   data   treatment   and   reduction   are   as   previously described. [21,22]   Absorption   corrections   were   judged   to   be unnecessary for this crystal (μR ca 0.33) [23] and were not applied; psi scan data collected on crystals of similar composition prepared by the reaction of Na_{12}-A with Cs had been featureless.   Only those reflections for which $\underline{I}$ > 3$\sigma(\underline{I})$ (303 reflections) were used in structure solution and refinement.

Structure Determination

Full-matrix least-squares refinement was begun using the atomic parameters of the framework atoms [(Si,Al), O(1), O(2), and O(3)] and of the Cs^+ ions at Cs(1), Cs(2), and Cs(3) in Cs_{12}-A•1/2Cs. [8] This model quickly converged to the error indices

$$\underline{R}_1 = \Sigma|\underline{F}_o - |\underline{F}_c||/\Sigma\underline{F}_o = 0.062 \quad \text{and} \tag{1}$$

$$\underline{R}_2 = (\Sigma\underline{w}(\underline{F}_o - |\underline{F}_c|)^2/\Sigma\underline{w}\underline{F}_o{}^2)^{1/2} = 0.054 \tag{2}$$

with occupancies of 3.12(4), 7.73(8), and 2.14(5) for Cs(i), i = 1 to 3, respectively.   A subsequent refinement was carried out with the occupancy at Cs(1) fixed at 3 (its maximum value by symmetry) and that at Cs(3) fixed at 2 (the maximum number that a sodalite cavity can accommodate; otherwise three Cs^+-Cs^+ contacts of about 3.2 Å would exist instead of one at about 4.1 Å; 3.2 Å is an impossibly short distance, even less than the sum of the ionic radii of two Cs^+ ions, and ionic radii are short because they represent cation-to-anion contacts -- cation-to-cation distances must be substantially longer). This refinement converged with the occupancy at Cs(2) = 7.52(6), $\underline{R}_1$ = 0.063, and $\underline{R}_2$ = 0.056.   A difference Fourier function revealed a new peak of height 1.7 eÅ^{-3} at (0.27, 0.27, 0.5).   Inclusion of Cs(4) at this position reduced the error indices to $\underline{R}_1$ = 0.061 and $\underline{R}_2$ = 0.053 with occupancies converged at 7.44(7) and 0.29(9) for Cs(2) and Cs(4), respectively.   Final least-squares refinement, done with fixed occupancies (G(i)) of 3.00, 7.50, 2.00, and 0.25 for Cs(i), i = 1 to 4, respectively, resulted in $\underline{R}_1$ = 0.061 and $\underline{R}_2$ = 0.054.   These occupancies are consistent with the packing requirement that

$$G_{Cs(2)} + 2 \, G_{Cs(4)} \leq 8. \tag{3}$$

All adjustments to the least-squares occupancies have been of 3σ or less; correlations between thermal and occupancy parameters have therefore not been a serious problem.
     Refinements in the space group $\underline{Fm3c}$ led to the same occupancies as above for all Cs^+ equipoints.   Although least-squares was unstable in this subgroup of $\underline{Pm3m}$, it was well enough behaved, with

Table I. Positional, Thermal, Occupancy Parameters[a] of Cs_{12}-A•3/4Cs

	Wyckoff Position	x	y	z	β_{11}[b] or B_{iso}[c]	β_{22}	β_{33}	β_{12}	β_{13}	β_{23}	Occupancy[d] Fixed	Varied
(Si,Al)	24(k̲)	0	1841(3)	3719(3)	20(3)	19(3)	12(3)	0	0	12(5)	24[e]	
O(1)	12(h̲)	0	2266(13)	5000[f]	88(16)	36(12)	33(12)	0	0	0	12	
O(2)	12(i̲)	0	2949(8)	2949(8)	37(12)	30(8)	30(8)	0	0	0	12	
O(3)	24(m̲)	1125(6)	1125(6)	3427(8)	33(5)	33(5)	42(9)	22(14)	32(11)	32(11)	24	
Cs(1)	3(c̲)	0	5000[f]	5000[f]	94(4)	71(2)	71(2)	0	0	0	3	3.12(4)
Cs(2)	8(g̲)	2760(1)	2760(1)	2760(1)	49(1)	49(1)	49(1)	12(2)	12(2)	12(2)	7.5	7.73(8)
Cs(3)	8(g̲)	951(6)	951(6)	951(6)	103(5)	103(5)	103(5)	-49(10)	-49(10)	-49(10)	2	2.14(5)
Cs(4)	12(i̲)	2714(80)	2714(80)	5000[f]	8(4)						0.25	0.29(9)

[a] Positional and anisotropic thermal parameters are given x 10^4. Numbers in parentheses are the estimated standard deviations in the units of the least significant figure given for the corresponding parameter. The anisotropic temperature factor is $\exp[-(\beta_{11}\underline{h}^2 + \beta_{22}\underline{k}^2 + \beta_{33}\underline{\ell}^2 + \beta_{12}\underline{hk} + \beta_{13}\underline{h\ell} + \beta_{23}\underline{k\ell})]$.

[b] R.m.s. displacements can be calculated from β_{ii} values using formula $\mu_i = 0.255\underline{a}(\beta_{ii})^{1/2}$, where $\underline{a} = 12.3$ Å.

[c] Isotropic thermal parameter in units of $Å^2$.

[d] Occupancy factors are given as the number of ions per unit cell.

[e] Occupancy for (Si) = 12, occupancy for (Al) = 12.

[f] Exactly 1/2 by symmetry.

selected parameters held fixed at values found in previous $\underline{Fm3c}$
refinements, for the occupancy parameters to be stable.

   A final difference Fourier function was featureless except for
some residual peaks around large-cavity Cs^+ ions. All shifts in the
final cycle of refinement were less than 0.1% of their corresponding
estimated standard deviations. Final structural parameters are
presented in Table I; selected interatomic distances and angles are
tabulated in Table II.

<p align="center">Table II. Selected Interatomic Distances (Å)</p>

<p align="center">and Angles (deg) in Cs_{12}-A•3/4Cs[a]</p>

(Si,Al)-O(1)	1.657(7)	O(1)-(Si,Al)-O(2)	106.4(8)
(Si,Al)-O(2)	1.658(2)	O(1)-(Si,Al)-O(3)	111.6(5)
(Si,Al)-O(3)	1.677(4)	O(2)-(Si,Al)-O(3)	108.0(4)
		O(3)-(Si,Al)-O(3)	110.0(6)
Cs(1)-O(1)	3.358(16)		
Cs(1)-O(2)	3.562(15)	(Si,Al)-O(1)-(Si,Al)	143.3(11)
Cs(2)-O(2)	3.406(2)	(Si,Al)-O(2)-(Si,Al)	159.6(10)
Cs(2)-O(3)	2.957(9)	(Si,Al)-O(3)-(Si,Al)	145.0(7)
Cs(3)-O(2)	3.663(15)		
Cs(3)-O(3)	3.057(12)	O(3)-Cs(2)-O(3)	85.1(3)
Cs(4)-O(1)	3.38(11)	O(3)-Cs(3)-O(3)	81.7(4)
Cs(4)-O(3)	3.37(11)		
		Cs(2)-Cs(3)-Cs(3)	180.0[b]
Cs(1)-Cs(2)	5.161(6)		
Cs(1)-Cs(4)	4.359(12)		
Cs(2)-Cs(2)	5.502(3)		
Cs(2)-Cs(3)	3.850(12)		
Cs(3)-Cs(3)	4.046(24)		

[a] The numbers in parentheses are the estimated standard deviations
    in the units of the least significant digit given for the
    corresponding parameters.

[b] Exactly 180° by symmetry.

   The goodness-of-fit = $(\Sigma \underline{w}(F_o-|F_c|)^2/(\underline{m}-\underline{s}))^{1/2}$ = 2.3.   (4)
The number of observations, $\underline{m}$, is 303, and the number of parameters,
$\underline{s}$, is 31. The quantity minimized in least-squares is $\Sigma \underline{w}(F_o-|F_c|)^2$,
and the weights ($\underline{w}$) are the reciprocal squares of $\sigma(F_o)$, the
standard deviation of each observed structure factor. Atomic
structure factors for Cs^+, O^-, and $(Si,Al)^{1.75+}$, the mean of the
Si^{4+}, Si^0, Al^{3+}, and Al^0 functions, were used. ($\underline{24}$,$\underline{25}$)   All

scattering factors were modified to account for the real component (f') of the anomalous dispersion correction. ($\underline{26},\underline{27}$) (The effect of the imaginary component (f") of the anomalous dispersion correction would have been negligible for this crystal (centric) as had been noted previously for Cs_9Tl_3-A. ($\underline{4}$)) A table of observed and calculated structure factors is available. ($\underline{28}$)

   The structures reported are consistent with the site occupancies observed, but are not required by them and are not unique crystallographic solutions. Only by combining the crystallographic results with the most basic of crystal packing considerations do the structures reported uniquely emerge. That consideration is that cations be placed as far apart as possible within their equipoints of partial occupancy to minimize their intercationic repulsions. Because of the high concentration of cations in this structure, this consideration has become simpler and more imperative, namely that cations should not be placed far closer together than had ever been observed before. The figures show the relative Cs^+ positions in and about each cavity; arrangements in neighboring cavities of the same kind may be the same or may be related by symmetry, e.g., rotation or reflection, to those shown.

Discussion

The K^+ ions in dehydrated K_{12}-A were completely reduced by 0.1 torr of cesium vapor at 350 °C. The product, fully dehydrated, fully Cs^+-exchanged zeolite A, Cs_{12}-A•3/4Cs, contains extra cesium atoms which associate with Cs^+ ions to form, at least predominantly, the linear cationic clusters $(Cs_4)^{3+}$.

   In the crystal structure of Cs_{12}-A•3/4Cs, Cs^+ ions are found at four crystallographically distinct sites common to partially Cs^+-exchanged zeolite A's ($\underline{2}-\underline{7}$) and Cs_{12}-A•1/2Cs. ($\underline{8}$) They are on fourfold axes at the centers of 8-rings (local symmetry $\underline{C}_{4h}$ ($\underline{D}_{4h}$ in $Pm3\underline{m}$)), on threefold axes ($\underline{C}_{3v}$), both on the large- and sodalite-cavity sides of 6-rings, and finally on twofold axes opposite 4-rings in the large cavity.

   Cs_{12}-A•3/4Cs can be viewed as a homogeneous mixture of Cs_{12}-A and Cs_{13}-A whose populations are about 1/4 and 3/4, respectively (see Table III for the distribution of Cs^+ ions in the component "unit cells"). In both "unit cells", the centers of three 8-rings are fully occupied by Cs^+ ions at Cs(1); each Cs^+ ion is 3.36 and 3.56 Å from four framework oxygens at O(1) and O(2), respectively (see interatomic distances in Table II). These positions are well-established experimentally, ($\underline{2}-\underline{7}$) although their distances to the framework oxygens are substantially longer than the sum of the ionic radii of O^{2-} and Cs^+, 2.99 Å. ($\underline{29}$) Theoretical calculations

also support this observation of a potential energy minimum at these positions. (30,31)   Each sodalite cage contains two Cs^+ ions at Cs(3) opposite 6-rings. These are placed on the same threefold axis on opposite sides of the origin 4.04 Å apart.   This short intercesium distance is exemplary of the ion-crowding which was anticipated for fully Cs^+-exchanged zeolite A.

Table III.   Distribution of Cs^+ ions in Cs_{12}–A•3/4Cs

Crystal (component)	in 8-rings Cs(1)	Number of Cs^+ ions opposite 6-rings in the α-cage Cs(2)	β-cage Cs(3)	opposite 4-rings Cs(4)	Total
Cs_{12}–A•3/4Cs	3	7.5	2	0.25	12.75
(Cs_{12}–A)	3	6	2	1	12
(Cs_{13}–A)	3	8	2	0	13

In about three-fourths of the unit cells (Cs_{13}–A), the eightfold equipoint opposite the 6-rings in the large cavity is fully occupied by Cs^+ ions with intercesium distances of 5.50 Å.   Each Cs^+ ion is coordinated to three O(3) framework oxygens at 2.96 Å and extends 1.84 Å into the large cavity from the [111] plane at O(3) (see Table IV).   A stereoview of this is shown in Figure 1.

Table IV.   Deviations of Atoms (Å) from the [111] Plane at O(3)[a]

O(2)	0.16
Cs(1)	3.07
Cs(2)	1.84
Cs(3)	-2.00
Cs(4)	3.37

[a] The negative deviation indicates that Cs(3) lies on the same side of the plane as the origin, that is, inside the sodalite unit.
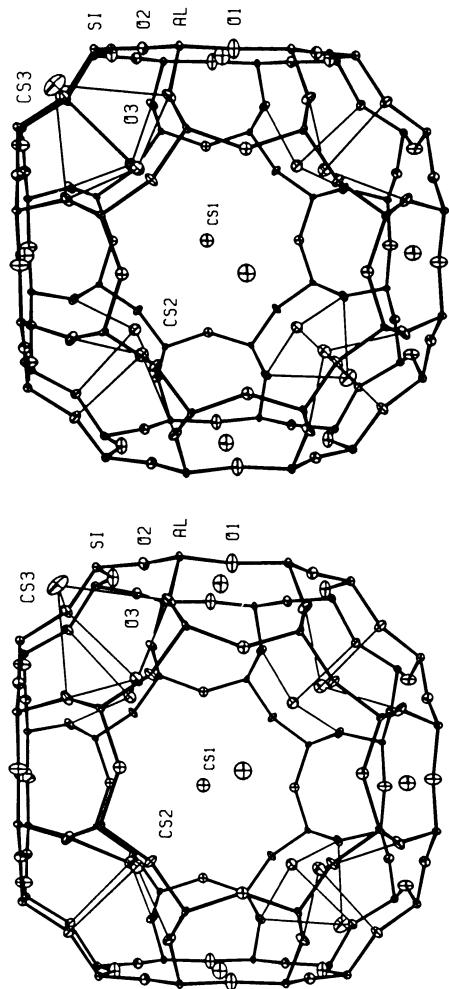
Figure 1. A stereoview of a large cavity of Cs_{13}–A. The zeolite A framework is drawn with heavy bonds between tetrahedrally coordinated (Si,Al) and oxygen atoms. Cs^+ ion coordination by framework oxygens is indicated by fine lines. Ellipsoids of 20% probability are shown.

With one excess electron, two of these eight Cs^+ ions associate with two sodalite-unit Cs^+ ions at Cs(3), all on the same threefold axis, to form a linear cationic cluster $[Cs(2)-Cs(3)-Cs(3)-Cs(2)]^{3+}$ with intercesium distances of 3.85 and 4.04 Å for Cs(2)-Cs(3) and Cs(3)-Cs(3), respectively. (This cluster must be present and must be linear in three-fourths of the unit cells because (1) the Cs(2) equipoint is fully occupied and (2) the two ions at Cs(3) must be on opposite sides of the origin.) These distances are much shorter than those in cesium metal (5.31 Å). (32) The cesium atom must facilitate the condensation of three Cs^+ ions into a relatively small volume of space. The total energy of the $(Cs_4)^{3+}$ cation within the zeolite must therefore be less than that of three linearly arranged Cs^+ ions, which would have a large electrostatic repulsive contribution to its total energy, and one atom of cesium gas. Figure 2 is a stereoview of the $(Cs_4)^{3+}$-containing sodalite unit.

The $(Cs_4)^{3+}$ clusters are apparently responsible for the black color of $Cs_{12.75}$-A. A simple particle-in-a-box calculation (8) for a single electron in a one-dimensional box of length 15.4 Å indicates an allowed electronic transition in the middle of the visible range. Vacuum heating at 1000 °C causes the extra cesium atom per unit cell to be lost (this is observed directly in the vacuum system as well as crystallographically), and the crystal becomes colorless. (10,13) This experiment also displays the unusually high thermal stability of fully Cs^+-exchanged zeolite A.

In the remaining one-fourth of the "unit cells" (Cs_{12}-A), only six such large-cavity Cs^+ ions are found per unit cell at Cs(2). One Cs^+ ion at Cs(4) is found opposite a 4-ring in the large cavity. This 4-ring lies between two adjacent 6-rings which are occupied by Cs^+ ions on their sodalite-unit sides only. Stereoviews of these large and sodalite cavities are presented in Figures 3 and 4, respectively.

These Cs_{12}-A "unit cells" are either $Cs_{12}Si_{12}Al_{12}O_{48}$ in composition, which for some reason have not reacted with a cesium atom to form Cs_{13}-A, or they are $Cs_{11}Si_{13}Al_{11}O_{48} \cdot Cs$. The latter would be the case if recent Si^{29} MASNMR results (33) indicating that Si/Al is greater than one for the crystals used in this work (17) is correct. Then, taking the crystallographic occupancies to be 7.5 for Cs(2) and 0.25 for Cs(4), satisfying equation (3), Si/Al = 1.045, consistent with the MASNMR result (1.03(1)) and other evidence therein referenced (1.04(1)) (33). The sodalite unit in such a Cs_{12}-A "unit cell" is likely to contain a $(Cs_2)^+$ ion; $(Cs_4)^{3+}$ and $(Cs_3)^{2+}$ are also possible for these unit cells but are
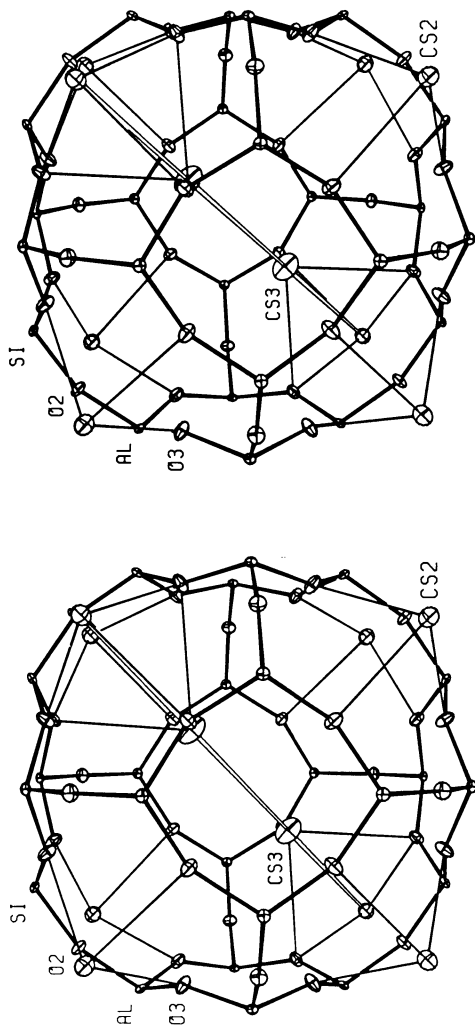
Figure 2. A stereoview of a sodalite unit of Cs_{13}–A. The linear cesium cluster $(Cs_4)^{3+}$ is shown on a threefold axis passing through the sodalite cavity of Cs_{13}–A. See the caption to Figure 1 for other details.
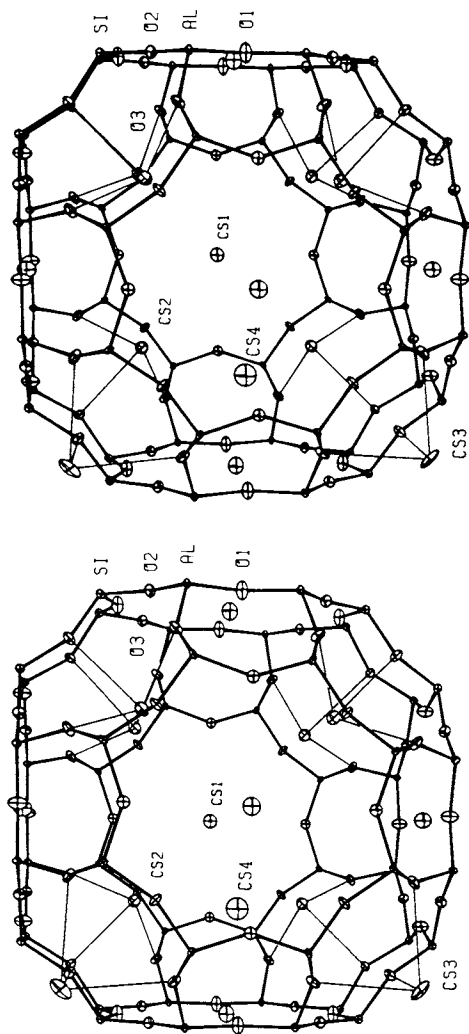
Figure 3.   A stereoview of a large cavity of Cs_{12}–A.   See the caption to Figure 1 for other details.
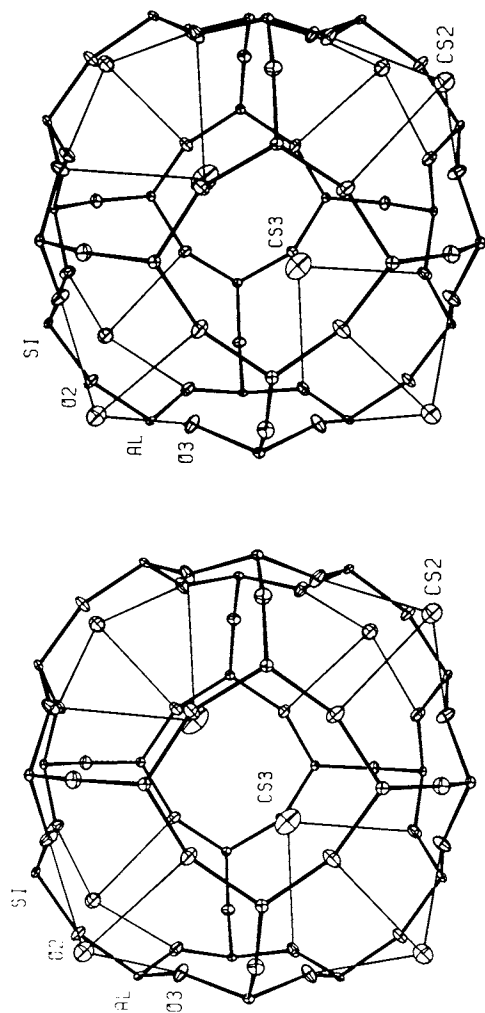
Figure 4.   A stereoview of a sodalite unit of Cs_{12}–A.   See the caption to Figure 1 for other details.

considered less likely (the additional intercesium repulsions involved are expected to override the small increase in delocalization energy). Crystals of stoichiometry closer to Cs_{12}–A•1/2Cs ($\underline{8}$–$\underline{11}$) must then either have Si/Al ratios higher than 1.04 or have failed to reach equilibrium in the sorption of cesium. If equilibrium was not achieved in Cs_{12}–A•1/2Cs ($\underline{8}$–$\underline{11}$), perhaps it has not been achieved in Cs_{12}–A•3/4Cs either, in which case Si/Al would be unity for these crystals. To resolve this question, further attempts will be made to prepare Cs_{12}–A•Cs.

Acknowledgments

Literature Cited

(1) Breck, D. W. <u>Zeolite Molecular Sieves: Structure, Chemistry, and Use</u>; Wiley: New York, 1974, pp 579-80.
(2) Vance, T. B.; Jr.; Seff, K. <u>J. Phys. Chem.</u> 1975, <u>79</u>, 2163-7.
(3) Firor, R. L.; Seff, K. <u>J. Am. Chem. Soc.</u> 1977, <u>99</u>, 6249-53.
(4) Subramanian, V.; Seff, K. <u>J. Phys. Chem.</u> 1979, <u>83</u>, 2166-9.
(5) Kim, Y.; Seff, K. <u>Bull. Korean Chem. Soc.</u>, 1984, <u>5</u>, 117-21.
(6) Kim, Y.; Seff, K. submitted for publication.
(7) Dejsupa, C.; Seff, K. <u>J. Phys. Chem.</u> submitted for publication.
(8) Heo, N. H.; Seff, K. <u>J. Am. Chem. Soc.</u> 1987, <u>109</u>, December.
(9) Heo, N. H.; Dejsupa, C.; Seff, K. <u>J. Phys. Chem.</u> 1987, <u>91</u>, 3943-3944.
(10) Heo, N. H.; Seff, K. <u>J. Chem. Soc. Chem. Commun.</u> 1987, 1225-6.
(11) Heo, N. H., Ph.D. Thesis, University of Hawaii, 1987.
(12) Reference 1, pp 633-45.
(13) Heo, N. H.; Seff, K. <u>J. Phys. Chem.</u> submitted for publication.
(14) Leung, P. C. W.; Kunz, K. B.; Maxwell, I. E.; Seff, K. <u>J. Phys. Chem.</u> 1975, <u>79</u>, 2157-62.
(15) Pluth, J. J.; Smith, J. V. <u>J. Phys. Chem.</u> 1979, <u>83</u>, 741-9.
(16) Seff, K.; Mellum, M. D. <u>J. Phys. Chem.</u> 1984, <u>88</u>, 3560-3.
(17) Charnell, J. F. <u>J. Cryst. Growth</u> 1971, <u>8</u>, 192-4.
(18) <u>Handbook of Chemistry and Physics</u>; Chemical Rubber Co.: Cleveland, OH, 1983; 64th ed., pp D157-8.
(19) Cruz, W. V.; Leung, P. C. W.; Seff, K. <u>J. Am. Chem. Soc.</u> 1978, <u>100</u>, 6997-7003.
(20) Peterson, S. W.; Levy, H. A. <u>Acta Crystallogr.</u> 1957, <u>10</u>, 70-6.
(21) Seff, K. <u>Accounts Chem. Res.</u> 1976, <u>9</u>, 121-8.
(22) Firor, R. L.; Seff, K. <u>J. Am. Chem. Soc.</u> 1977, <u>99</u>, 4039-44.
(23) <u>International Tables for X-ray Crystallography, Vol. II</u>; Kynoch Press: Birmingham, England, 1974; p 132.
(24) Doyle, P. A.; Turner, P. S. <u>Acta Crystallogr., Sect. A</u> 1968, <u>24</u>, 390-7.
(25) Reference 23, <u>Vol. IV</u>, pp 73-87.
(26) Cromer, D. T. <u>Acta Crystallogr.</u> 1965, <u>18</u>, 17-23.

(27) Reference 23, Vol. IV, pp 149–50.
(28) Shannon, R. D.; Prewitt, C. T. Acta Crystallogr., Sect. B 1969, B25, 925–46.
(29) See Appendix
(30) Ogawa, K.; Nitta, M.; Aomura, K. J. Phys. Chem. 1978, 82, 1665–70.
(31) Takaishi, T.; Hosoi, H. J. Phys. Chem. 1982, 86, 2089–94.
(32) Interatomic Distances, Supplement; The Chemical Society, London, 1965, p S–5s.
(33) Blackwell, C. S.; Pluth, J. J.; Smith, J. V. J. Phys. Chem. 1985, 89, 4420–2.

Appendix

Observed and calculated structure factors for fully dehydrated, fully Cs^+-exchanged zeolite A, Cs_{12}–A•3/4Cs. In the table, the Miller indices, $\underline{h}$, $\underline{k}$, and ℓ appear in the first three columns. The fourth column is $10F_c$, the fifth column is $10KF_o$ where K is the scale factor (3.01317) from least-squares which puts the observed structure factors on an absolute scale, and the last column is $100K\sigma_{hk\ell}$; $\sigma_{hk\ell}$, the estimated standard deviation of the corresponding F_o, was calculated from counting statistics.

H	K	L	10FC	10KFO	100KSIG	H	K	L	10FC	10KFO	100KSIG
0	0	1	1176	1160	124	0	5	13	671	751	268
0	0	2	-1439	1425	157	0	5	16	861	855	301
0	0	3	2169	2222	232	0	6	6	1895	1868	226
0	0	4	3032	3027	313	0	6	7	-962	904	199
0	0	5	-2363	2390	256	0	6	8	579	544	274
0	0	6	656	678	163	0	6	9	312	328	419
0	0	7	1652	1595	196	0	6	10	558	542	277
0	0	8	2336	2434	271	0	6	13	504	626	301
0	0	9	-1255	1251	196	0	6	15	-425	372	554
0	0	10	1850	1802	232	0	6	16	672	673	553
0	0	11	2461	2451	236	0	7	7	850	851	214
0	0	13	-781	808	247	0	7	9	-1651	1727	235
0	0	14	802	695	286	0	7	11	722	751	256
0	0	16	337	356	551	0	7	12	-674	609	304
0	0	17	200	357	551	0	7	13	-548	591	331
0	0	18	559	649	371	0	8	9	-455	522	289
0	1	1	-864	787	105	0	8	10	324	318	479
0	1	3	-537	585	157	0	8	11	412	441	333
0	1	4	-2225	2337	247	0	8	13	-519	469	404
0	1	5	-751	772	148	0	9	9	805	793	244
0	1	6	-224	231	353	0	9	11	-777	663	256
0	1	7	-1456	1424	137	0	9	14	-568	504	431
0	1	15	-393	360	503	0	9	15	-461	560	404
0	2	2	3427	3535	359	0	10	10	523	470	368
0	2	3	-2644	2765	286	0	10	11	359	355	438
0	2	4	-1706	1690	190	0	11	11	1214	1282	259
0	2	5	1427	1372	172	0	11	13	-234	304	573
0	2	6	1869	1846	214	0	11	14	236	362	538
0	2	7	-2793	2717	292	1	1	1	615	649	108
0	2	8	-311	286	380	1	1	3	2261	2323	244
0	2	9	1079	1057	196	1	1	4	-1217	1290	160
0	2	10	263	324	404	1	1	5	282	245	319
0	2	11	-1252	1228	214	1	1	6	-778	734	160
0	2	12	475	441	334	1	1	7	253	209	347
0	2	13	409	404	353	1	1	9	392	406	310
0	2	14	-504	506	340	1	1	10	-570	520	286

H	K	L	10FC	10KFO	100KSIG	H	K	L	10FC	10KFO	100KSIG
0	2	15	-616	654	322	1	1	13	328	311	491
0	2	16	498	485	428	1	2	2	-205	289	268
0	3	3	-430	429	193	1	2	3	306	377	220
0	3	4	827	866	145	1	2	4	230	223	340
0	3	5	-1116	1151	160	1	2	5	-408	372	223
0	3	6	-444	450	220	1	2	6	-517	495	202
0	3	7	912	927	175	1	2	7	255	252	377
0	3	8	-479	433	286	1	2	8	185	272	404
0	3	9	-1277	1274	202	1	3	3	982	1010	148
0	3	10	410	335	407	1	3	4	-410	441	193
0	3	11	720	720	232	1	3	5	897	883	157
0	3	12	-399	350	413	1	3	7	1319	1305	184
0	3	13	-571	568	319	1	3	9	934	886	208
0	4	4	3818	3923	404	1	3	11	357	404	337
0	4	5	-1021	1021	163	1	4	4	-295	278	298
0	4	7	989	956	184	1	4	5	-369	353	205
0	4	8	813	776	205	1	4	6	-504	516	208
0	4	9	-2276	2232	262	1	4	7	-307	357	304
0	4	11	522	535	286	1	4	10	-392	379	362
0	4	12	-388	314	470	1	4	11	-704	636	253
0	4	13	-471	558	316	1	4	12	-304	357	443
0	4	14	588	535	344	1	5	5	1040	1014	172
0	4	17	-343	437	494	1	5	7	613	599	229
0	5	5	2822	2800	301	1	5	10	-323	365	377
0	5	6	1661	1675	206	1	5	11	452	369	398
0	5	7	-1428	1441	202	1	5	12	-491	472	328
0	5	8	-157	281	452	1	6	6	-431	464	268
1	6	9	-391	433	325	2	9	15	406	443	494
1	6	10	-304	300	453	2	11	11	-414	469	419
1	6	12	-457	437	330	2	11	13	191	400	509
1	7	7	310	324	416	2	13	13	-401	466	491
1	7	9	422	394	365	3	3	3	801	868	148
1	7	10	-440	369	398	3	3	4	584	594	172
1	7	13	392	418	440	3	3	7	1254	1292	190
2	2	2	-1580	1608	181	3	3	8	-1650	1553	211
2	2	4	3387	3302	340	3	3	9	-350	359	380
2	2	5	-1777	1746	202	3	3	11	356	291	482
2	2	6	-658	613	184	3	3	13	-369	436	383
2	2	7	1511	1460	193	3	4	4	1124	1116	166
2	2	8	750	745	202	3	4	5	-1005	1018	169
2	2	9	-1105	1078	199	3	4	7	820	839	199
2	2	11	644	635	256	3	4	9	-411	405	353
2	2	13	-815	858	250	3	4	14	329	326	530
2	2	14	482	379	461	3	5	5	1537	1562	199
2	2	15	540	642	328	3	5	6	493	516	244
2	2	16	-467	491	434	3	5	7	-312	350	362
2	2	18	383	443	506	3	5	8	-807	825	214
2	3	3	-1869	1968	217	3	5	9	515	459	310
2	3	4	-1165	1208	163	3	5	14	-363	333	524
2	3	5	261	278	307	3	6	6	434	431	298
2	3	7	-744	688	196	3	6	7	-368	334	404
2	3	8	-1129	1105	193	3	6	8	-541	535	230
2	3	9	644	678	232	3	7	7	1697	1627	223
2	3	11	-813	796	229	3	7	10	305	327	440
2	3	12	293	350	416	3	7	11	576	597	295
2	3	14	-557	532	353	3	7	17	199	294	410
2	4	5	947	947	166	3	8	8	-1036	1096	214
2	4	6	1429	1358	187	3	8	9	-431	435	359
2	4	7	-1167	1115	137	3	8	13	-652	593	356
2	4	8	442	417	313	3	8	14	-493	486	428
2	4	9	1357	1325	211	3	9	9	733	784	250
2	4	10	329	341	395	3	11	11	604	633	350
2	4	11	-1244	1248	217	4	4	4	1875	1852	217
2	4	12	612	583	289	4	4	5	-2244	2279	256
2	4	13	597	613	301	4	4	6	-492	405	307
2	5	5	-714	686	181	4	4	7	841	881	202
2	5	6	-739	750	190	4	4	8	1552	1557	217
2	5	7	750	801	202	4	4	9	-384	384	374

H	K	L	10FC	10KFO	100KSIG
2	5	9	-1107	1115	208
2	5	11	709	734	244
2	5	12	-326	362	422
2	5	13	-591	665	283
2	6	7	389	297	431
2	6	8	634	575	265
2	6	9	-747	742	232
2	6	11	364	348	443
2	6	13	-400	375	464
2	7	7	-945	936	214
2	7	8	-466	460	325
2	7	9	1178	1145	214
2	7	11	-942	991	229
2	7	13	510	576	334
2	8	8	-462	331	395
2	8	10	228	469	265
2	8	11	-464	419	374
2	8	12	420	282	395
2	8	13	-161	469	331
2	9	9	-581	629	277
2	9	11	466	537	334
2	9	13	-374	457	437

H	K	L	10FC	10KFO	100KSIG
4	4	10	361	391	368
4	4	13	-370	339	512
4	4	14	616	617	334
4	4	16	-340	390	545
4	4	17	-149	361	588
4	4	18	395	396	576
4	5	7	-1727	1733	226
4	5	9	575	532	283
4	5	10	-304	296	464
4	5	11	-638	650	280
4	5	14	-357	419	452
4	5	15	-389	407	521
4	6	6	526	465	307
4	6	7	-1176	1201	208
4	6	9	314	387	371
4	6	11	-652	709	265
4	6	15	-402	403	527
4	7	7	1090	1023	211
4	7	8	467	469	307
4	7	9	-496	542	298
4	7	14	397	369	554
4	7	16	-382	447	500

H	K	L	10FC	10KFO	100KSIG
4	8	8	407	401	362
4	8	10	410	394	398
4	8	12	425	411	440
4	8	15	197	483	389
4	9	9	634	467	268
4	9	11	-852	525	253
4	9	13	582	611	328
4	11	12	-391	377	452
4	11	13	-323	481	437
5	5	5	382	414	328
5	5	7	715	561	292
5	5	8	526	487	313
5	5	10	347	314	488
5	5	11	1508	1510	244
5	6	8	338	372	395
5	6	9	-557	539	307
5	6	11	766	714	286
5	7	7	-702	690	244
5	7	9	798	800	253
5	7	11	-364	465	371
5	7	14	-429	370	573
5	8	8	-271	383	398
5	9	9	-775	717	280
5	9	11	407	514	377
5	9	12	-328	384	506
5	9	13	-210	352	582
5	11	13	361	390	569
6	6	8	671	723	244
6	6	9	-508	505	319
6	6	11	461	469	380
6	7	7	-652	638	256
6	7	9	395	424	380
6	7	11	-464	527	350
6	8	10	414	394	437
6	8	17	161	453	470
7	7	7	1518	1509	232
7	7	8	278	324	482
7	7	11	566	527	377
7	7	12	-247	362	524
7	7	14	462	469	482
7	7	15	270	425	533
7	7	16	-396	395	603
7	9	9	-907	991	256
7	9	11	-550	577	377
7	9	13	487	512	449
7	11	11	452	471	476
8	8	8	-543	462	386
8	8	9	-322	346	497
8	8	13	-591	619	389
9	9	11	336	490	458
11	11	11	758	770	383

RECEIVED January 25, 1988

Chapter 12

Long-Range Versus Short-Range Effects in the Distribution of K Ions in Hydrated KY Zeolites

W. J. Mortier[1,3], D. E. W. Vaughan[2], and J. M. Newsam[2]

[1]Laboratorium voor Oppervlaktechemie, Katholieke Universiteit Leuven, Kardinaal Mercierlaan 92, B-3030 Leuven (Heverlee), Belgium
[2]Exxon Research and Engineering Company, Route 22 East, Annandale, NJ 08801

The cation site population is used for monitoring the cation-framework interaction energy in hydrated K-Y-type zeolites with varying Si/Al ratio. The K-ion content of a series of Y-type zeolites was modified by (i) changing the framework Al content (by direct synthesis or by dealumination) and by (ii) exchange with NH_4 cations, and their structures determined with X-ray powder methods. The population of site I with K ions depends primarily on the framework Al content, and is empty for Si:Al ratios over 2.7. The sites I' and II depopulate much more slowly. The cation distribution pattern seems to be determined by the short-range cation-framework interaction energy only, independent of the details of the population of the other sites (at high cation loading, the site I-site I' repulsion becomes important however). This is in agreement with recent statistical-thermodynamical developments.

The cation distribution in zeolites is the result of an energy-minimization process. The site energy is determined by the interaction of the cations with the framework, with the adsorbed molecules and by the mutual repulsion between them. Provided that an equilibrium distribution is possible, we may expect that the cation distribution contains information about the energy levels of the sites.

Recently, a statistical mechanical model was proposed for explaining the cation distribution in zeolites as a function of

the temperature (1). For dehydrated faujasite-type zeolites, it was possible to write an exact expression for the partition function, and therefore also for all derived thermodynamic functions. If we assume that N_i cations are located at site i (energy level e_i depending on cation-framework interactions only) with a maximum occupancy of B_i cations at this site (the site population $P_i=N_i/B_i$), we may then enumerate the total number of configurations i.e. the product of the number of ways we can permute N_i cations on B_i-sites as

$$\Omega = \prod_i \frac{B_i!}{N_i!(B_i-N_i)!} \tag{1}$$

Maximizing Ω, subject to the restrictive condition that $N=\sum N_i$, we obtain the most probable equilibrium distribution as:

$$\frac{P_i}{1-P_i} = \exp(\mu+e_i)/kT \tag{2}$$

where μ represents the chemical potential of the cations in the zeolite phase. μ enters this expression through the Lagrange multiplier α associated with fixing N: α can be identified using standard thermodynamic formulae with $\alpha=-\mu/kT$.

   The equations become gradually more complicated if cation-cation repulsions as well as cation-molecule interaction energies have also to be considered. In these cases, e_i will have to be modified to include contributions from adjacent sites. In the Bragg-Williams approximation (which proved to give an excellent analysis of the cation variation in dehydrated NaY-type zeolites (1), and we assume to apply equally well to the hydrated state), the relation between the site population, the energy levels and the temperature can be readily written down as soon as the structure is known. The site energies are then modified to include contributions from the neighbouring sites. For site I, this requires that e_I would have to be modified to include contributions from the two adjacent sites I', depending on its repulsion energy w and site population $P_{I'}$.
In this case the population expression is modified and becomes:

$$\frac{P_I}{1-P_I} = \exp(\mu+e_I+2P_{I'}w)/kT \tag{3}$$

The similar relationship for site I', considering one adjacent site I and three sites II' occupied with water molecules (attraction energy w') is:

$$\frac{P_{I'}}{1-P_{I'}} = \exp(\mu+e_{I'}+P_Iw+3P_{II'}w')/kT \tag{4}$$

Similar relationships for site II, and unlocalized supercage cations
in "site III", exclude cation-cation repulsions because the nearest
neighbours are too far away to influence the interaction energies.
If in Equation 2 we assume e_i includes the contributions from the
adsorbed water molecules, this then also applies to site II and site
III. The population ratios depend only on the energy level
differences $(e_{I'}-e_I)$, $(e_{II}-e_I)$, $(e_{III}-e_I)$ and the magnitude
of the cation-cation repulsion energy (w) and the cation water
attraction energy (w'). Knowing these, and the number of cations
per unit cell N $(N = 16P_I + 32P_{I'} + 32P_{II} +$ (cations in site
III)), the population ratios can be calculated.

For the hydrated state, we can reasonably expect that the site
I' and site II cations are completely solvated with (three) water
molecules. The interaction energy w' can therefore be incorporated
into $e_{I'}$ e_{II} and e_{III}, such that the above equations formally
reduce to those of the dehydrated state. Van Dun et. al. (2) found
that as a function of the Al content, the cation distributions in
dehydrated Na-exchanged FAU-type zeolites could be accurately
predicted if it was assumed that the energy level differences
relative to site I varied linearly with the framework negative
charge. At around 48 Al/unit cell, the site preference changes from
II > I' > I (low Al content) to I > II > I' (high Al content).
This was understood by realizing that the effect of the Al
substitution will have twice the effect in site I (double six-ring)
than in the single six-ring (sites I' and II) and wall sites ("site
III").

This paper will be concerned with investigating the K-ion
distributions in hydrated K-exchanged FAU-type zeolites with varying
Al content. It is an equilibrium situation (hydrated state) so that
we can apply the prior model developed for the dehydrated state.

Experimental

Sample preparation

     h-K$_{34.9}$FAU

This material was obtained by direct synthesis using a modified
organic template procedure previously reported (3). Its Al
content, and of all others, was determined from the variation of the
unit cell constant with Al content for a range of fully K-exchanged
hydrated zeolites (5). The Al content is then calculated as
$(a_o - 25.127)/0.011388$, which applies only to h-K-FAU-type
zeolites. ^{29}Si NMR and chemical analyses confirmed these data.

     h-K$_{32.5}$FAU

This is a Union Carbide sample obtained by dealumination of an
NH$_4$Y sample with $(NH_4)_2SiF_6$ (4). From a characterization
with solid state magic-angle spinning ^{29}Si nuclear magnetic
resonance, a Si/Al ratio of 4.8 was found. No extra-lattice
aluminum was determined in the ^{27}Al spectrum. Double exchanges
with KCl (10 wt % solution, 10 wt % zeolite) were performed at 70°C,

followed by drying (110°C), calcining (3 h at 400°C), and twice
re-exchanging with KCl as above.

h-K$_{13.3}$FAU

This sample is a shallow-bed steamed version (600°C, 3 h) of the
LZ 210 parent material used for h-K$_{32.5}$FAU. A dilute mineral room
temperature acid exchange (pH = 2.5) was used to remove detrital Al.
After a second steam-leach treatment the sample was K-exchanged as
described above.

h-K$_{15}$H$_{40}$FAU

This is a regular commercial Y-type zeolite, twice exchanged
with a 15 wt % KCl solution (zeolite/solution = 7 %) at 60°C, then
double exchanged with NH$_4$Cl at 22°C (10 wt % solution; 10 %
zeolite) followed by filter washing with 5 % NH$_4$OH to convert the
NH$_4^+$ to H$_3$O$^+$.

X-ray data sampling and refinement. The diffraction profiles were
recorded in two parts by using an automated powder diffractometer
(Siemens D-500) with Ni- filtered Cu radiation in steps of 0.01°
2θ (0.1° incident beam divergence slit below 35° 2θ and 1.0°
above 35° 2θ; receiving slit 0.05 mm; typical counting times
respectively 25s and 65s). The X-ray data sampling (peak-fitting
of the individual peaks using an experimental profile) and
refinement procedures have been described extensively elsewhere
(6-7). Agreement factors are defined as:

$$R_G = \frac{\sum ||G^o| - |G^c||}{\sum |G^o|} \tag{5}$$

$$wR_G = \left[\frac{\sum (w_i^{1/2}||G^o| - |G^c||)^2}{\sum (w_i^{1/2}|G^o|)^2} \right]^{1/2} \tag{6}$$

where $w = 1/s_G^2$ and G stands for F_{hkl} or I_N, i.e.
intensities summed for coinciding reflections (N = h^2 + k^2
+ l^2); o for observed and c for calculated. For the four
compositions, in the sequence given in the experimental section, 96,
128, 112 and 128 reflections were measured, i.e. for max. 2θ 66°,
77°, 73°, and 77°, respectively. All four structures were refined
in the space group Fd3m. The scattering lengths of the tetrahedral
sites were fixed at the values calculated from the unit cell
compositions. Radial distribution functions were applied to account
for the unlocalized scattering matter (water molecules and cations)
(8). The water in the large cage and also in the sodalite cage
was supposed to be distributed randomly throughout a sphere, with a
radius of 5.7 and 2.3 Å^2, respectively. The distribution of the
water molecules between the sodalite cages and the large cages was
also fitted to obtain a best agreement. For the spheres an
additional temperature factor of 15 Å^2 was applied.

Results

Positional parameters, population poarameters, isotropic temperature factors and agreement factors are compiled in Table 1. A list of selected interatomic distances, bond angles and unit cell parameters is given in Table 2.

Discussion

All bond lengths, bond angles and structure parameters fall within the expected ranges and experimental errors, and need not be discussed further. We will focus on the correlation between the cation distributions obtained from these four structures, together with previously determined distributions (h-$K_{48.2}$FAU, h-$K_{54.7}$FAU, h-$K_{69.8}$FAU and h-$K_{86.5}$FAU (5) and h-$K_{15.2}$(NH$_4$)$_{39.5}$FAU (9)), and the model outlined in the introduction.

From a knowledge of the cation distribution changes with temperature, the energy level differences and the interaction energies can be determined using Equations 1-4. This requires the site energies to remain constant in that temperature range. For the hydrated state, this would require measurements at high steam partial pressures, over an extended temperature range, in order to maintain the water coordination at the sites – obviously a major experimental problem. For a room-temperature equilibrium partial pressure of water, it has been shown that the cation populations for NaY and CaY zeolites evolves from a hydrated condition at room temperature to a dehydrated situation after a temperature increase of several hundred degrees C (10-11). Specific values for the energy level differences therefore cannot be assigned at this time. However, a qualitative comparison with the dehydrated state (d-Na-FAU (2)) allows us to elucidate definite trends.

The K-populations, as a function of the Al content are plotted in Figure 1 and summarized in Table 3. These qualitatively agree with the variation of the Na distribution in the dehydrated FAU-type zeolites (Figure 2). There is one important exception however: the site I' now varies similarly to the site I in the dehydrated state. The site I' K$^+$ population peaks at about 50 Al/unit cell which is also the case for the Na$^+$ population in site I (dehydrated). In the dehydrated state, the Na population of site I' increases in a similar manner (except for the inflection, also at around 50 Al/unit cell) as for the site I population. The site II variation is for both cases one of a progressively increased loading, reaching a maximum at about 50 Al/unit cell in the de-hydrated state, and at about 60 Al/unit cell in the hydrated state. The site III (supercage, unlocated) serves as an overflow site in the dehydrated state, but seems to be consistently populated throughout for the hydrated state (also showing an increase with Al content however). The site I-site I' inversion above 50 Al/unit cell is primarily dictated by the cation-cation repulsion energy w. The cation-water attraction energy w' (Equation 3) obviously plays a major role for (i) making site I' more favourable than the site I and (ii) providing an extra stabilization for the site III which

Table 1: Positional parameters[a], population parameters (P),
temperature factors (B, 10^{-2} nm^2) and agreement factors

		h-$K_{34.9}$FAU	h-$K_{32.5}$FAU	h-$K_{13.3}$FAU	h-$K_{15}H_{40}$FAU
T=Si,Al	x	0.1240(7)	0.1247(6)	0.1240(7)	0.1244(6)
(192i)	y	0.9453(7)	0.9453(6)	0.9459(6)	0.9455(5)
	z	0.0363(6)	0.0359(6)	0.0361(5)	0.0364(5)
	B	2.1 (3)	2.18 (21)	2.18 (19)	2.23 (20)
O(1)	x=-y	0.1089(12)	0.1082(10)	0.1089(12)	0.1076(10)
(96h)	B	2.6 (1.5)	4.30(1.45)	4.84(1.38)	3.46(1.39)
O(2)	x=y	0.2512(18)	0.2518(12)	0.2521(11)	0.2518(12)
(96g)	z	0.1395(17)	0.1409(13)	0.1418(16)	0.1382(16)
	B	5.5 (1.5)	4.14(1.25)	3.33(1.69)	4.61(1.38)
O(3)	x=y	0.1752(13)	0.1746(9)	0.1749(11)	0.1735(9)
(96g)	z	0.9686 (15)	0.9676(13)	0.9665(15)	0.9664(13)
	B	0.72(1.05)	2.38(1.07)	0.99(0.98)	0.86(95)
O(4)	x=y	0.1791(12)	0.1820(9)	0.1813(11)	0.1806(10)
(96g)	z	0.3224(21)	0.3243(13)	0.3221(16)	0.3256(14)
	B	2.4 (1.3)	1.76 (90)	2.1 (1.4)	2.7 (1.2)
K I'	x=y=z	0.0832(24)	0.0861(25)	0.055(19)	0.0816(16)
(32e)	P	0.237(40)	0.215(36)	0.034(40)	0.362(37)
	B	1.7 (2.8)	2.6 (2.5)	5.0	3.0 (1.6)
K II	x=y=z	0.2621(20)	0.2665(20)	0.2465(108)	0.2592(17)
(32e)	P	0.247(31)	0.224(31)	0.048(32)	0.269(29)
	B	0.0 (2.6)	2.1 (2.7)	0.0 (15.8)	0.4 (1.9)
O II'	x=y=z	0.1817(56)	0.1815(35)	0.1866(52)	0.1783(64)
(32e)	P	0.210(81)	0.299(40)	0.223(77)	0.193(90)
	B	0.0 (7.5)	2.3 (5.2)	0.0 (10.3)	2.5 (8.3)
H_2O[b]	P	2.05 (1.23)	1.4 (0.8)	0.59 (5)	2.4 (7)
(8a)	B	15.	15.	15.	15.
H_2O[c]	P	37.7 (8.6)	34.0 (5.0)	17.4(4.5)	40.0 (4.3)
(8b)	B	15.	15.	15.	15.
R_I		0.2021	0.1903	0.1962	0.1662
wR_I		0.2290	0.2223	0.1674	0.2119
R_F		0.1383	0.1360	0.1445	0.1233
wR_F		0.1182	0.1250	0.0908	0.1184

[a] : Space group Fd3m ; the standard deviation of the last signifi-
cant digit between brackets.
[b,c] : Unlocalized scattering matter, statistically distributed in a
sphere with a radius of 2.3 (b) or 5.7 Å(c) respectively.

Table 2: Selected interatomic distances (Å), bond angles (°) and unit cell parameters (Å) a

	$h-K_{34.9}FAU$	$h-K_{32.5}FAU$	$h-K_{13.3}FAU$	$h-K_{15}N_{40}FAU$
T-O(1)	1.639(17)	1.628(15)	1.636(15)	1.643(14)
T-O(2)	1.647(37)	1.640(27)	1.625(29)	1.643(28)
T-O(3)	1.637(29)	1.641(23)	1.599(23)	1.626(22)
T-O(4)	1.653(24)	1.649(21)	1.659(21)	1.691(20)
T-O(1)-T	132 (2)	134 (2)	131 (2)	135 (2)
T-O(2)-T	147 (3)	146 (2)	145 (3)	150 (3)
T-O(3)-T	137 (3)	139 (2)	141 (3)	142 (3)
T-O(4)-T	140 (3)	135 (2)	137 (2)	134 (2)
O(1)-T-O(2)	113 (1)	113 (1)	113 (1)	112 (1)
O(1)-T-O(3)	115 (2)	114 (2)	114 (2)	114 (2)
O(1)-T-O(4)	105 (2)	103 (1)	103 (2)	103 (2)
O(2)-T-O(3)	102 (2)	104 (2)	107 (2)	104 (2)
O(2)-T-O(4)	108 (3)	107 (2)	105 (2)	110 (2)
O(3)-T-O(4)	114 (2)	116 (1)	115 (2)	114 (1)
K(I')-3 O(3)	2.83(6)	2.93(7)	2.26(11)	2.85(5)
K(I')-3 O(2)	3.23(5)	3.33(4)	2.88(23)	3.23(3)
K(I')-3 O(II')	2.47(14)	2.42(10)	3.19(47)	2.41(18)
K(II)-3 O(2)	3.03(4)	3.12(3)	2.55(25)	3.00(4)
K(II)-3 O(4)	3.23(5)	3.25(3)	2.90(17)	3.20(3)
O(II')-3 O(2)	2.62(10)	2.63(6)	2.50(9)	2.75(12)
a	24.525	24.497	24.278	24.686

a : Standard deviation of the last significant digit between brackets

Table 3: Site populations for the hydrated K-exchanged FAU-type zeolites with varying Al content and K-loading

	K(I)	K(I')	K(II)	n° unlocated
$h-K_{86.5}FAU$	0.5572	0.2236	0.7237	46.3
$h-K_{69.8}FAU$	0.4391	0.3754	0.7578	26.5
$h-K_{54.7}FAU$	0.0834	0.4144	0.6289	20.0
$h-K_{48.2}FAU$	-	0.4260	0.5563	16.8
$h-K_{34.9}FAU$	-	0.2379	0.2471	19.4
$h-K_{32.5}FAU$	-	0.2154	0.2244	18.4
$h-K_{13.3}FAU$	-	0.0340	0.0480	10.7
$h-K_{15}H_{40}FAU$	-	0.3615	0.2685	-
$h-K_{15.2}(NH_4)_{39.5}FAU$	-	0.2625	0.2188	-
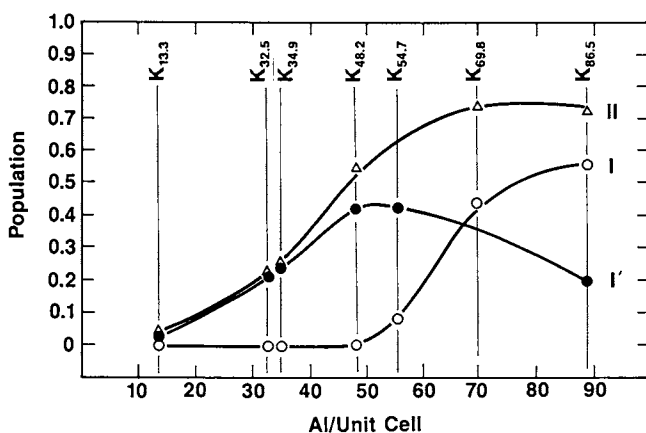
Figure 1   Variation of the site I, I' and II K-ion population
as a function of the Al content for the fully cation-
exchanged FAU-type zeolites.
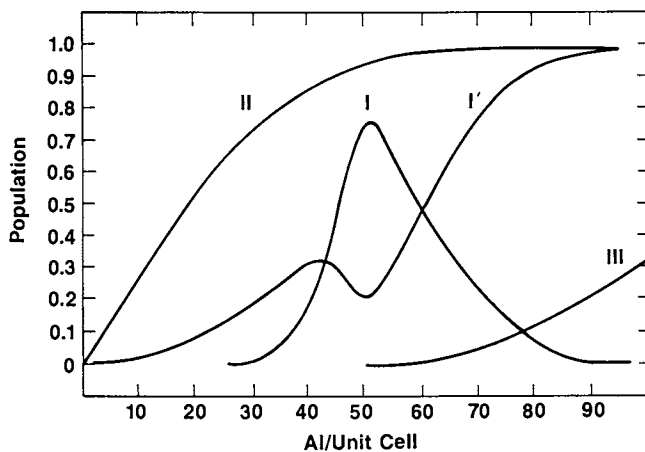
Figure 2   Predicted variation of the site I, I', II and III
(overflow site) Na-ion population as a function of
the Al content for the dehydrated Na-exchanged FAU-
type zeolites.

now has a higher population than the traditional framework sites at
low Al content (where obviously the cation-framework interaction
energy is lower).

It should be reminded here that the variation in cation
distribution with Al content is explained by considering short-range
interactions only. The dominance of these forces is demonstrated by
the h-KY samples with depleted K loading (with H/NH_4 replacement
for K): for a regular Y composition, the sites I' and II are the
predominant sites, and this remains so for h-$K_{15}H_{40}$FAU and
h-$K_{15.2}$(NH_4)$_{39.5}$FAU (Figure 1 and Table 3).

We can now conclude that the model developed by Van Dun (1) for
the dehydrated state can also be applied (and formally also in an
exact way if the water-cation interaction energies are included in
e_i) to the hydrated state. The water molecules seem to stabilize
(w') single six-ring and wall sites. At the same time this
qualifies, relative to water molecules, the framework as a weak
ligand.

Acknowledgments

Literature cited

1. Van Dun, J.J. Ph.D. thesis, K.U. Leuven, Belgium 1987.
2. Van Dun, J.J.; Dhaeze, K.; Mortier, W.J.; Vaughan, D.E.W., in
   preparation
3. Vaughan, D.E.W.; Strohmeier, K.G. Proc. 7th. Int. Zeolite Conf.
   Murakami, Y.; Iijima, A.; Ward, J.W., Eds.; Kodansha-Elsevier:
   Tokyo, 1986; p. 207.
4. Skeels, G.W.; Breck, D.W. Proc. 6th Int. Zeolite Conf.,
   Olson, D.H.; Bisio, A., Eds.; Butterworths: London, 1984; p 87.
5. Mortier, W.J.; Bosmans, H.; Uytterhoeven, J.B. J. Phys. Chem.
   1971, 75, 3327-3334.
6. Pearce, J.R.; Mortier, W.J.; Uytterhoeven, J.B. J. Chem. Soc.
   Faraday Trans. I 1979, 74, 898-906.
7. Mortier, W.J. N.B.S. Spec Pub (U.S.) 1980, No 567, 315-324.
8. Simpson, H.D.; Steinfink, H. Acta Crystallogr., Sect A. 1970,
   26, 158.
9. Mortier, W.J.; Costenoble, M.L.; Uytterhoeven, J.B. J. Phys.
   Chem. 1973, 77, 2880-2885.
10. Mortier, W.J.; Van den Bossche, E.; Uytterhoeven, J.B. Zeolites
    1984, 4, 41-44.
11. Dendooven, E.; Mortier, W.J.; Uytterhoeven, J.B. J. Phys. Chem.
    1984, 88, 1916-1921.

Chapter 13

Coordination of Cu²⁺ to Oxygen Six-Rings of Zeolites

D. Packet and R. A. Schoonheydt

Laboratorium voor Oppervlaktechemie, Katholieke Universiteit Leuven, Kardinaal Mercierlaan 92, B-3030 Leuven (Heverlee), Belgium

An analysis of the ESR parameters and the d-d absorption bands of Cu^{2+}, coordinated to oxygen six-rings of dehydrated zeolites, is presented in the framework of the ligand field theory and the angular overlap model theory. Two six-rings are considered : type I', on the hexagonal prism and type II, on the supercages. The ideal C_{3v} point symmetry of the sites is distorted by a dynamic Jahn-Teller effect and spin-orbit coupling, the former being much more important than the latter. The sum of the ligand field stabilisation energy and the Jahn-Teller stabilisation energy is 7545 cm^{-1} for type II six-rings in CuNaA and 7669 cm^{-1} for type I' six-rings in Cu-chabazite. With these numbers the site preference of Cu^{2+} for six-rings sites over hexagonal prisms can be explained but not the experimentally found preference for site I' over site II in zeolites X and Y. There is a non-negligible contribution of the 3 oxygens in the second coordination sphere of the six-rings to the overall ligand field. The coordinative bond of the 3 oxygens in the first coordination sphere has a strong σ-donor character and a weak π-donor character. The coordinative bond of the 3 oxygens in the second coordination sphere has a more pronounced π-donor character.

For about 20 years Cu(II) has been used as a probe to study the coordination sites of zeolites. Attention has been primarily given to zeolites X and Y and, to a lesser extent, zeolite A, Chabazite and Mordenite. The techniques used were X-ray diffraction (XRD), electron spin resonance (ESR) and diffuse reflectance spectroscopy (DRS) (1-11). The results of these techniques are not directly comparable, because e.g. small Cu-loadings have to be used to obtain

well resolved ESR spectra, while high loadings are required for DRS and, especially, XRD.

We have been able to match the ESR data and the DRS spectra on a large number of zeolites by taking the spectra on samples with the same Cu-loadings, which underwent the same pretreatment in the same cell before recording the spectra (12-14). In that way, it has been possible to determine unambiguously the g-values, hyperfine coupling constants A and d-d transitions of Cu^{2+} coordinated to the oxygen six-rings of dehydrated zeolites.

It turns out that these experimental parameters (Table I) are almost independent of the type of zeolite, the Si:Al ratio and the type of co-exchanged cation. They reflect only the type of coordination i.e. the place of Cu^{2+} in the structure. The 2 most important coordination types of Cu^{2+} are (12-14) : type II, at the oxygen six-ring of the large cavities in zeolites A, X and Y; type I', at the oxygen six-ring, which forms part of the hexagonal prisms in zeolites Y and Chabazite.

Table I. ESR parameters and d-d transition energies of CuNaA and Cu-chabazite

Sample	$g_{//}$	$A_{//}$	$g_\perp$	$A_\perp$	d-d transitions		
		mT		mT	(cm^{-1})		
CuNaA	2.386	12.6	2.064	0.25	10500	12200	15100
Cu-chab.	2.340	16.0	2.073	2.00	10700	12900	14800
CuNaY							
II	2.397	11.9	2.070	1.50	10400	12600	15000
I'	2.328	15.5	2.065	1.90	10700	12600	15000
CuNaX							
II	2.384	12.7	2.074	1.20	10300	12500	15100
III'	2.354	14.3	2.068	1.50	11100	12500	15100
CuNa-mord.							
VI	2.327	15.5	2.068	1.50	13680		14460

Table I gives the ESR parameters and d-d transitions of Cu^{2+} in dehydrated CuNaA, exemplifying Cu^{2+} on type II six-rings and of Cu^{2+} in dehydrated Chabazite, exemplifying Cu^{2+} on type I' six-rings. This data set is used for interpretation in the framework of the angular overlap model (AOM) theory and the ligand field (LF) theory.

Our goals are (1) to obtain details of the site geometry; (2) to gain insight into the Cu-O coordinative bond; (3) to calculate the ligand field stabilisation energy (LFSE) i.e. the contribution of the d-orbital energy splitting to the overall lattice energy of Cu^{2+} on types II and I' six-rings and to deduce the site preference of Cu^{2+}.

Geometricl model and methods of calculation

Model. The CuO_6 unit is constructed with 3 oxygens in the first coordination sphere at a distance r_1 from Cu^{2+} and 3 oxygens in the second coordination sphere at a distance r_2 from Cu^{2+} with $r_2 > r_1$ (Figure 1). The geometrical parameters, derived from the XRD data (8-11) are shown in Table II. They support our hypothesis, that the 6 oxygens are located in one plane. Cu^{2+} is situated on the trigonal axis, common to the 2 sets of equilateral triangles of oxygens. The point symmetry of the CuO_6 unit is C_{3v}. It is an extension of

Table II. Bond angles and bond distances of Cu^{2+} in dehydrated chabazite and zeolite A

Sample	r_1 (nm)	θ_1 (°)	r_2 (nm)	θ_2 (°)	ref.
CuA	0.214	119	0.285	119	10
Cu-chab.	0.197	119	0.283	120	11

Klier's CuO_3 complex, also with point symmetry C_{3v} (15). Because the point symmetries are the same, the calculations on CuO_3 and on CuO_6 are formally identical. Thus, LF and AOM parameters derived from CuO_3 calculations contain information about the oxygens of the second coordination sphere and, more generally, of the complete zeolitic lattice as far as it influences the coordinative bond. We will, therefore, present first AOM calculations on the CuO_3 complex to obtain AOM parameters, which are directly comparable with Klier's LF parameters of the same unit. In the second part the CuO_6 complex is explicitly calculated to look for second coordination sphere effects.
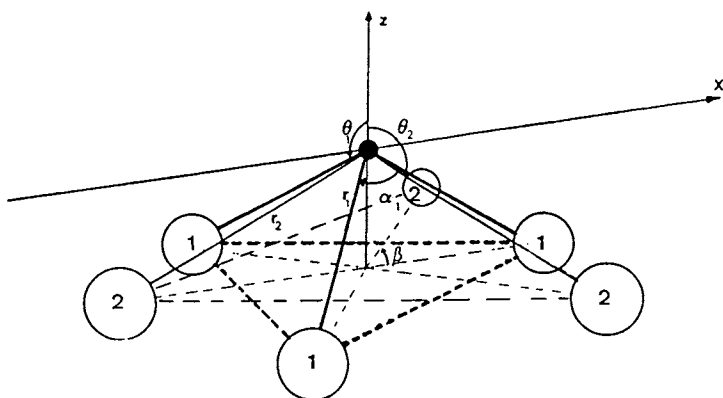
Figure 1. Geometrical model of Cu^{2+} coordinated at an oxygen six-ring in zeolites.

Angular Overlap Model. In AOM the matrix elements V_{pq} of the total ligand field potential in the d-orbital basis (V_{LF}) are decomposed according to the number of ligands and the type of individual metal-ligand interactions in the complex, σ and π ([16,17]) :

$$V_{pq} = \langle d_p [V_{LF}] d_q \rangle$$

$$= \sum_{i=1}^{N} \left[\sigma F_\sigma(d_p, L_i) F_\sigma(d_q, L_i) + \pi F_\pi(d_P, L_i) F_\pi(d_q, L_i) \right] \quad (1)$$

N is the number of ligands and $F_{\sigma,\pi}$ is the fraction of maximum overlap in the particular geometry. σ and π are the energy changes for maximum overlap. For the C_{3v} point group the matrix elements V_{pq} are explicitly calculated by Vanquickenborne et al. ([18]). There authors, as well as Klier et al. ([15]) and Strome and Klier ([7]) have shown that the ground-state of Cu²⁺ in C_{3v} is doubly degenerate (^2E) and subjected to a Jahn Teller (JT) distortion. That is, it couples with the doubly degenerate vibrations e of the $CuO_{3(6)}$ complex and the C_{3v} point group is distorted to C_s ([19]). In the case of a static JT effect and ESR signal with 3 g-values is expected but never observed ([12-14]). Our hypothesis is that at the temperature of the measurement, 110K, a dynamic JT effect is operative, which averages out the non-axial distortions. For our calculations we have retained only the linear JT coupling as explicitly discussed by Strome and Klier ([7]), because the energy contributions of the higher anharmonicity terms are expected to be negligible.

There are 2 doubly degenerate vibrational modes which interact with the electronic states ^2E in C_{3v}, a stretching and a bending. We have collected them formally into one vibration with force constant k. The JT stabilisation energy is then $E_{JT} = (1/2) kR^2$, where R is the JT radius, a measure of the distortion of the complex. At equilibrium the energy separation of the 2 energy levels, split from ^2E, is $4E_{JT}$ ([20]). For most of the Cu-O complexes k is in the range 50-150 Nm^{-1} ([21-23]). We have taken 70 Nm^{-1}. This value is kept constant during the calculations, whereas R was taken as a variable. This is because k and R are not linearly independent.

Finally, because the ESR parameters are also calculated the 5*5 matrix of the AOM + JT effect is extended to a 10*10 matrix to

include spin-orbit (SO) coupling to second order of perturbation, the Zeeman energy matrix elements and the hyperfine interaction matrix elements ($\underline{18,24}$).

The experimental parameters that are fitted in the calculations are the 3 d-d transitions and the ESR parameters, $g_{//}$, $g_{\perp}$ and $A_{//}$. $A_{\perp}$ is not fitted, because the accuracy of the experimental values is too low. The reason is that the computer program that we used to simulate the ESR spectra, does not include forbidden transitions, which are known to be important in the perpendicular region of the spectrum ($\underline{12\text{-}14,25}$).

The theoretical parameters that are used as variables in the least squares procedure are : (1) the AOM σ and π parameters; (2) the angle θ_1 (see Figure 1); (3) the JT radius R; (4) the SO coupling constant λ. The free ion value is -829 cm^{-1}, but this value may considerably be reduced due to covalency and the JT effect ($\underline{26}$); ($\underline{5}$) the Fermi contact parameter κ, which quantifies the isotropic contact interaction or the interaction of the unpaired electron with the nuclear magnetic moment of Cu at the nuclear site. Theoretical calculations suggest a value of 0.43 for the free ion. The dipolar hyperfine interaction parameter P is fixed at 0.036 cm^{-1}, a value adopted by most authors ($\underline{27,28}$).

We have then a set of 6 experimental data and 6 adjustable parameters. There exists a unique solution for the set of normal equations, which fits the experimental data exactly. This solution is found by a least squares procedure. For each parameter set the 10*10 matrix is calculated and diagonalised 4 times : (1) in the absence of an external magnetic field in order to fit the 3 d-d transitions; (2) with the Zeeman terms of the parallel region of the ESR spectrum in order to fit $g_{//}$; (3) with the Zeeman terms of the perpendicular region of the ESR spectrum to fit $g_{\perp}$; (4) as under (2) + the hyperfine interaction terms of the parallel region to calculate $A_{//}$.

Ligand Field Theory. The details of the LF calculations have been discussed by Klier et al. ($\underline{7,15}$) and need not be repeated here. The matrix elements of the C_{3v} LF potential, V_{pq}, in the d-orbital basis

are expressed in terms of LF parameters, G_2 and G_4, referred to 1 coordinate frame, centered on Cu^{2+}. In the point charge approximation :

$$G_{1i} = \frac{z_i \, e^2}{r_i^{\,1+1}} \int \left[R_{3d}(r) \right]^2 \, r^1 \, dr \tag{2}$$

with 1 = 2 or 4 (<u>29</u>). $R_{3d}(r)$ is the normalized radial part of the 3d wavefunctions; r is the distance from the origin of the coordinate frame (= the Cu nucleus) to the 3d electron and r_i to the ligand i; i = 1 refers to the oxygens of the first coordination sphere and i = 2 to those of the second coordination sphere. It is also useful to consider $K_i = G_{2i}/G_{4i}$.

 If we assume that the 6 oxygens of the six-rings have the same partial charge, which is upported by CNDO calculations (<u>30,31</u>), the ratio of the ligand field parameters of the 2 sets of oxygens is proportional to the bond distances :

$$\frac{G_{41}}{G_{41}} = \left(\frac{r_2}{r_1} \right)^5 \qquad \text{and} \qquad \frac{G_{21}}{G_{22}} = \left(\frac{r_2}{r_1} \right)^3 \tag{3}$$

With the relevant XRD data of table II, r_1, r_2 and θ_2 can be calculated for each value of θ_1 under the hypothesis that the positions of the oxygens of the six-rings are fixed. Since the JT and SO couplings and the Zeeman and hyperfine interactions are identically expressed in LF and in AOM, the LF calculations can be restricted to the fitting of the unperturbed C_{3v} energy levels from the AOM calculations. Thus, only 3 independent parameters have to be varied in these calculations : G_{41}, G_{21} and θ_1.
There exists a parametric equivalence between the LF and the AOM theories :

$$\sigma_i = (4/7) \; G_{2i} + (5/21) \; G_{4i}$$

$$\tag{4}$$

$$\pi_i = (3/7) \; G_{2i} - (5/21) \; G_{4i}$$

These equations will be used in the conversion of the LF parameters G_{1i} of the CuO_6 complex in the corresponding AOM parameters σ_i and π_i (32).

The CuO_3 model in AOM

All the calculations are performed on the CuO_3 complex to make a direct comparison with Klier's LF calculations (7). The energy level diagram which gives the best fit for CuNaA is shown in figure 2. The corresponding parameters and the best fit parameters of Cu-Chabazite are summarized in Table III. The following discussion is pertinent for figure 2 and the data of Table III.

Table III. Parameters of the AOM calculations for CuNaA and Cu-chab

Sample	σ (cm^{-1})	π/σ	λ (cm^{-1})	θ $(°)$	R (nm)	κ
CuNaA	10797	0.147	-287	107.8	0.0203	0.413
Cu-chab.	10003	0.041	-269	110.3	0.0165	0.549

We first remark that the position of Cu^{2+} on the trigonal axis, characterized by the angle θ_1, leads to O-Cu-O bond angles of 111° and 109° for CuNaA and Cu-chab. respectively. This is below the values of Table II. These geometrical parameters can be improved with the CuO_6 model as we shall see later.

At first sight, the σ-donor strength of the lattice oxygens, expressed by the parameter σ, is unusually high. For most complexes values in the range 4000-6000 cm^{-1} are obtained. The reason is that the 3 oxygens of CuO_3 give d-orbital splittings of the same order of magnitude as the 6 O-ligands in octahedral or tetragonal Cu-complexes. This suggests that there might be a considerable contribution from the oxygens in the second coordination sphere to the overall LF potential. This point will be explored in the next section. The strong σ-donor capacity is accompanied by a weak π-donor strength, especially in the case of Cu-Chab. or type I' six-rings. Usually π/σ values range between 0.15 and 0.25 (33,34). The consequence is that the sequence of energy levels, unperturbed by JT and SO couplings, is $^2E_1 < {}^2A_1 < {}^2E_2$. Strome and Klier
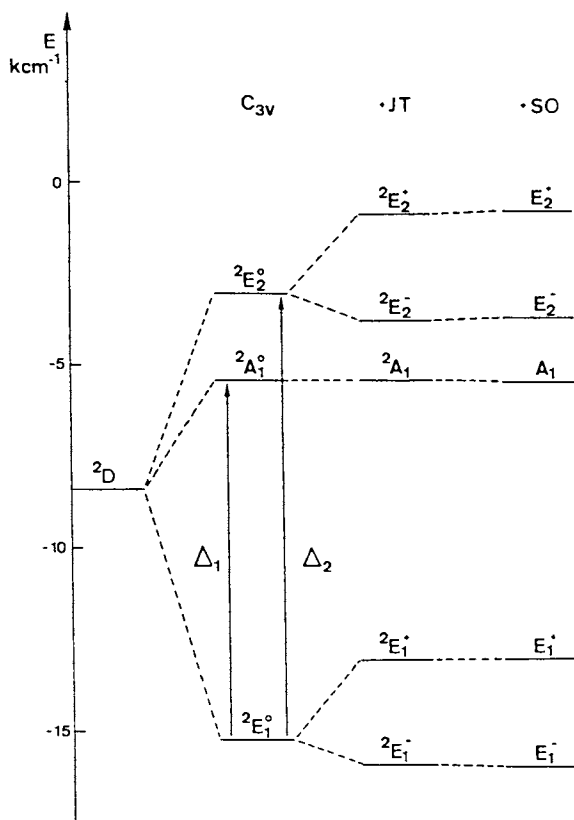
Figure 2. Energy level diagram of Cu^{2+} at an oxygen six-ring in dehydrated CuNaA. The effect of the Zeeman and hyperfine interaction is not shown.

obtained the sequence $^2E_1 < {}^2E_2 < {}^2A_1$ (7). The reason for the reversal of $^2E_2$ and $^2A_1$ is illustrated in figure 3. This figure shows, that Strome's sequence is obtained for $\pi/\sigma \geqslant 0.35$, an unusually high value when compared with literature values (33,34).

The JT effect and SO coupling. The JT effect is by far the most important perturbation of the ideal C_{3v} point symmetry as shown in figure 2. It has been impossible to fit the d-d band maxima by admitting SO coupling only. Both effects mutually influence each other and cannot be separated in this discussion.

      The JT effect leads to a considerable quenching of the orbital contribution to the g-factors and the hyperfine splitting constants (26). This is shown by the values of the spin-orbit coupling constants of Table III, which have to be compared with the free ion value of -829 cm^{-1}. Thus, 2 effects contribute to the decrease of λ : the JT interaction and the covalency of the Cu-O coordinative bond. The latter is expected to be relatively strong in view of the large σ-donor strength of the lattice oxygens. It is therefore remarkable that the isotropic contact interaction parameter is almost equal to the free ion value or even exceeds it as in the case of type I' six-rings. The value of κ is of course dependent on the value chose for the dipolar interaction parameter P. When we take $P = 0.039$ cm^{-1} (28), κ is decreased to 0.51 for Cu-Chab. Clearly this does not explain everything and other factors come into play.

      The magnitude of the JT effect itself, as expressed by the JT radius, is in the expected range. Holuj and Wilson (35) found a value of 0.019 nm for a trigonal distortion of $Cu(OD)_2$. With our assumed force constant of 70 Nm^{-1}, the JT radius calculated from Strome and Klier's data is 0.016 nm (7).

Ligand Field and Jahn-Teller stabilisation energies. The lattice energy determines the distribution of Cu^{2+} over the various sites and, thus, its reducibility, its coordinative ability and its availability for adsorption and catalysis. It is determined by a large number of factors, the LFSE and the JT stabilisation energy
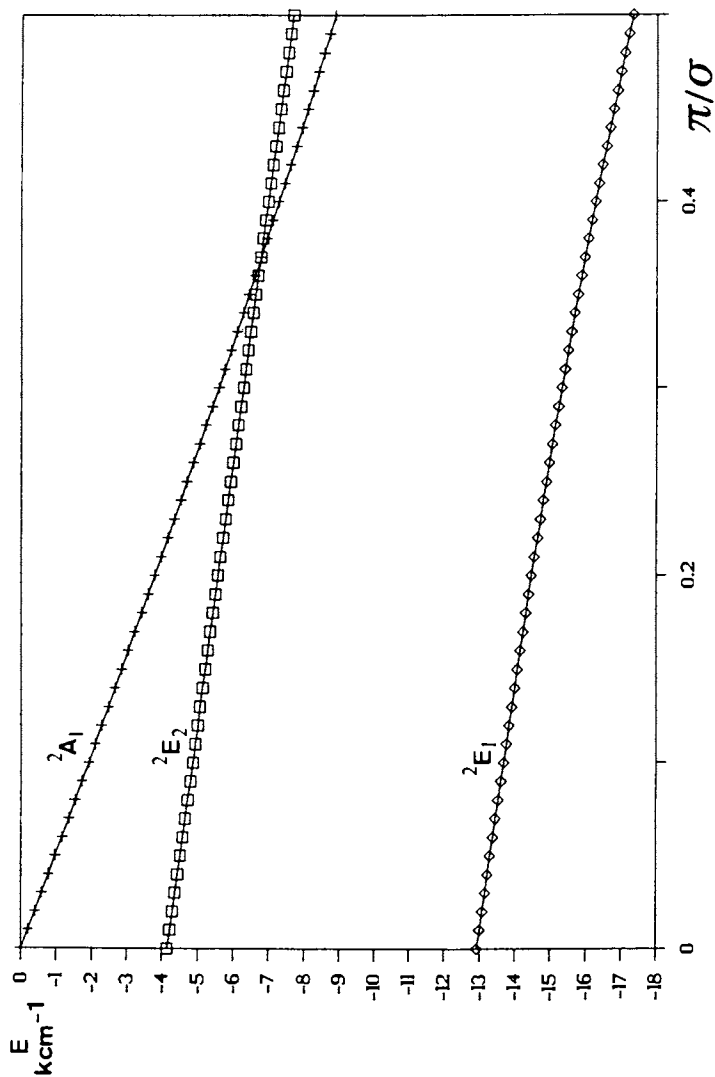
Figure 3. Ordering of the C_{3v} energy levels as a function of π/σ for $\sigma = 10000$ cm^{-1} and $\theta = 107°$.

being 2 of them. They can be derived from diagrams like that of figure 2. The values are shown in table IV.

Table IV. Calculated transitions of Cu^{2+} in a C_{3v} ligand field and ligand field and JT stabilization energies (all energies are expressed in cm^{-1})

Sample	Δ_1	Δ_2	LFSE	E_{JT}	$LFSE+E_{JT}$
CuNaA	9798	12149	6819	726	7545
Cu-chab.	10230	12857	7189	480	7669

It is shown in that table that the LFSE of type I' six-rings exceeds that of type II six-rings by 370 cm^{-1}, but this difference is almost completely offset by the difference in JT stabilisation energy. Thus, on the basis of these calculations, and all other factors being equal, there is no site preference between type I' and type II six-rings and one expects an almost equal occupancy of them. This is obviously not the case. At the high Cu^{2+} loadings of the XRD studies site I' is always preferentially occupied (8,9), while at the low loadings of our combined ESR-DRS studies site II is preferentially occupied (14). When it is assumed that these experimentally determined site occupancies are thermodynamic equilibrium distributions, it follows that they are not primarily determined by the LFSE + JT stabilisation energy. The most important factor is probably the Madelung energy. It was shown to be different for type I' and type II six-rings and to be strongly dependent on the Si:Al ratio and the exchangeable cation composition of the zeolites (36). Another important factor is the preference of Cu^{2+} for type I' six-rings over the hexagonal prisms. The latter can be regarded as an octahedral site with 6 oxygens in the coordination sphere. According to Gallezot et al. (8), the average coordination distance is 0.2545 nm. In $(NH_4)_2(Cu(OH_2)_6)(SO_4)_2$ the average $Cu-OH_2$ bond distance is 0.2092 nm (37). The d-d transition of this $Cu(OH_2)_6$ chromophore is at 12600 cm^{-1} (38) and the corresponding LFSE is 7560 cm^{-1}. For the tetragonally distorted CuO_6 chromophore in perovskites LFSE's range from 5920 cm^{-1} to 7280 cm^{-1} at small Cu-loadings (39). Our values of the six-ring sites are at the high energy side of

those of perovskites. Thus, as far as the LFSE's are concerned, the six-ring sites behave as CuO_6 chromophores. This lends credit to our previous suggestion that the 3 oxygens in the second coordination sphere cannot be neglected. On the other hand, in view of the difference in bond distance Cu-O in the hexagonal prisms and in perovskites or in $Cu(OH_2)_6$, the LFSE of Cu^{2+} in the hexagonal prisms is certainly smaller than those of Cu^{2+} in perovskites or in the water complex, and thus also than those of Cu^{2+} on six-ring sites. We conclude that Cu^{2+} strongly prefers type I' and type II six-rings above the hexagonal prisms, conclusion which is experimentally confirmed by the XRD studies on dehydrated Cu-exchanged zeolites (8,9).

The CuO_6 model in LF.

That the LFSE of Cu^{2+} on a six-ring is of the same order of magnitude than that of other CuO_6 chromophores, indicates not only a strong coordinative bond but also, that oxygens of the second coordination sphere i.e. the 3 oxygens of the six-rings at a distance r_2 (Figure 1) make a non-negligible contribution to the overall ligand field experienced by the Cu ion. We have checked this by LF calculations on the CuO_6 model of figure 1. The parameters, which fit the energy differences Δ_1 and Δ_2 of Table III are shown in Table V. They allow the following comments.

Table V. Parameters of the ligand field calculations for Cu^{2+} on a C_{3v} site with six oxygens

	CuNaA	Cu-chab.
G_{41} (cm^{-1})	15050	16010
G_{21} (cm^{-1})	10535	11207
K_1	0.70	0.70
G_{42} (cm^{-1})	3863	2852
G_{22} (cm^{-1})	4659	3980
K_2	1.21	1.40
θ_1 $(°)$	105.9	105.9
θ_2 $(°)$	102.0	101.2
r_1 (nm)	0.221	0.204
r_2 (nm)	0.291	0.288

1. The geometrical model, which comes out of the calculations, is better than for the CuO_3 complex. The calculated Cu-O bond distances are slightly longer than those determined by XRD (Table II). The calculated O_1-Cu-O_1 bond angle is 112.8°, in good agreement with the value of 115.9°, found by Gallezot for Cu^{2+} on site I' in CuNaY ($\underline{8}$). Perfect agreement should not be expected, as the geometrical parameters of the XRD studies are determined on samples with high Cu loadings.

2. The contribution of the oxygens of the second coordination sphere is not negligible. This is borne out by the values of the corresponding radial integrals, G_{22} and G_{42}, in Table V. One might argue that this is – at least partially – due to our assumption of 2 sets of chemically equivalent oxygens. However, the effect of next nearest neighbors on the LF has been recognized more than 20 years ago ($\underline{40}$). In fact, the LF is made up of the complete zeolitic lattice and the LF or AOM parameters taken from CuO_6 or CuO_3 chromophores contain the information of the lattice in which they are embedded. Thus, σ and π or G_2 and G_4 are products of 2 terms : one, characterizing the oxygens in the coordination sphere and one, characterizing the zeolitic lattice. Electronegativities of atoms in solids also contain information about the lattice in which the atoms are embedded ($\underline{41}$). It is an interesting research subject to see if the LF or AOM lattice parameters can be quantified via the electronegativity values.

3. The AOM parameters of the CuO_6 complex are calculated from the corresponding LF parameters by equations (4) and given in Table VI. Again, the values of σ_1 are indicative of the strong σ-donor strength of the nearest neigboring oxygens. However $\pi_1/\sigma_1 < \pi_2/\sigma_2$. Thus, the π-donor strength of the next nearest neighboring oxygens significantly exceeds that of the first coordination sphere oxygens. This is due to the fact that $\theta_2 < \theta_1$ (Table V) and it is known that the π-character increases when θ approaches 90° ($\underline{42}$). The difference in π-character could also

mean a chemical difference between the 2 sets of oxygens. We know, for instance, that there are 4 types of oxygens in zeolite Y and that protons prefer O_1 and O_3 oxygens (43). The six-rings are made up of O_3 and O_2 oxygens. Some chemical inequivalence is, therefore, not unexpected.

Table VI. AOM parameters of Cu^{2+} on a C_{3v} site with six oxygens

Sample	σ_1 (cm^{-1})	π_1	π_1/σ_1	σ_2 (cm^{-1})	π_2	π_2/σ_2
CuNaA	9601	932	0.10	3582	1077	0.30
Cu-chab.	10216	991	0.10	2953	1027	0.35

Conclusions

The d-d transitions and ESR parameters of Cu^{2+}, coordinated to oxygen six-rings in zeolites, can be explained quantitatively in the framework of the LF and AOM theories in the point symmetry C_{3v}, provided the linear JT effect and SO coupling are taken into account. The JT effect is a far more important perturbation than SO coupling. In type I' and type II six-rings the 3 oxygens of the second coordination sphere have a non-negligible contribution to the overall ligand field. The LFSE of Cu^{2+} on a six-ring is of the same order of magnitude as that of other CuO_6 chromophores. There is no significant difference between type I' and type II six-rings as far as LFSE is concerned. But the stability of Cu^{2+} on a six-ring exceeds its expected stability in hexagonal prisms. This explains the preference of Cu^{2+} for six-ring sites, but cannot explain the difference in site occupancies between sites I' and II in zeolite Y. We think that long range Madelung effects come into play. The Cu-O bond is a strong σ bond and a weak π bond. The LFSE is somewhat larger for Cu^{2+} on type I' six-rings than for type II six-rings, which is indicative of a stronger coordinative bond. Conversely, the JT distortion is more pronounced for type II six-rings, at least judged from the JT stabilisation energy. When all the data are taken together the differences in bonding characteristics between type I' and type II six-rings are minor.

Literature Cited

1. Mikheikin, I.D.; Zhidomirov, G.M.; Kazanskii, V.B. Russian Chem. Rev. 1972, 41, 468-483.
2. Herman, R.G.; Flentge, D.R. J. Phys. Chem. 1978, 82, 720-9.
3. Conesa, J.C.; Soria, J. J. Chem. Soc. Faraday Trans. I 1979, 74, 406-22.
4. Morke, W.; Vogt, F., Bremer, H. Z. Anorg. Allg. Chem. 1976, 422, 273-82.
5. Kevan, L. Acc. Chem. Res. 1987, 20, 1-7.
6. Chao, C.C.; Lunsford, J.H. J. Phys. Chem. 1972, 57, 2890-8.
7. Strome, D.H.; Klier, K. in Adsorption and Ion Exchange with Synthetic Zeolites; Flank, W.H., Ed.; A.C.S. Symposium Series no. 135; American Chemical Society: Washington, D.C., 1980; p 155-176.
8. Gallezot, P.; Ben Taarit, Y.; Imelik, B. J. Catalysis 1972, 26, 295-302.
9. Maxwell, I.E.; De Boer, J.J. J. Phys. Chem. 1975, 79, 1874-9.
10. Pluth, J.J.; Smith, J.V.; Mortier, W.J. Mat. Res. Bull. 1977, 12, 1001-7.
11. Lee, H.J.; Seff, K. J. Phys. Chem. 1981, 85, 397-405.
12. Packet, D.; Schoonheydt, R.A. in Structure and Reactivity of Modified Zeolites; Jacobs, P.A.; Jaeger, N.; Jiru, P.; Kazanskii, V.B.; Schulz-Ekloff, G., Eds.; Studies in Surface Science and Catalysis no. 18; Elsevier: Amsterdam, 1984; p 41-8.
13. Packet, D.; Dehertog, W.; Schoonheydt, R.A. in Zeolites : Synthesis, Structure, Technology and Applications; Drzaj, B.; Hocevar, S.; Pejovnik, S., Eds.; Studies in Surface Science and Catalysis no. 24; Elsevier: Amsterdam, 1985; p 351-8.
14. Packet, D.; Schoonheydt, R.A. in New Developments in Zeolite Science and Technology; Murakami, Y.; Iijima, A.; Ward, J.W.; Eds.; Proc. 7th Int. Zeolite Conf.; Kodansha: Tokyo, 1986; p 385-392.
15. Klier, K.; Hutta, P.J.; Kellerman R. in Molecular Sieves II; Katzer, J.R., Ed.; A.C.S. Symposium Series no. 40; American Chemical Society: Washington, D.C., 1977; p 108-119.
16. Larsen, E.; LaMar, G.N. J. Chem. Ed. 1974, 51, 633-40.
17. Gerloch, M.; Woolley, R.G. Progress Inorg. Chem. 1983, 31, 371-446.
18. Vanquickenborne, L.G.; Gorller-Wallrand, C.; Debuyst, R. J. Chem. Soc. Dalton 1979, 1150-4.

19. Ceulemans, A.; Beyens, D.; Vanquickenborne, L.G. J. American Chem. Soc. 1984, 106, 5824–37.
20. Reinen, D.; Friebel, C. Structure and Bonding 1979, 37, 1–60.
21. Deeth, D.J.; Hitchmann, M.A. Inorg. Chem. 1986, 25, 1225–33.
22. Nakagawa, I.; Shimanouchi, T. Spectrochim. Acta 1964, 20, 429–39.
23. Mikami, M.; Nakagawa, I.; Shimanouchi, T. Spectrochim. Acta 1967, 23A, 1037–53.
24. Atherton, N.M. Electron Spin Resonance, Theory and Applications; J. Wiley: New York, 1973; chapters 6 and 7.
25. Rollmann, L.D.; Chan, S.I. in Electron Spin Resonance of Metal Complexes; Teh Fu Yen, Ed.; Plenum Press: New York, 1969; p 175–200.
26. Ham, F.S. in Electron Spin Resonance; Geschwind, S., Ed.; Plenum Press: New York, 1972; p 1–119.
27. Abragam, A.; Horowitz, J.; Pryce, M.H.L. Proc. Royal Soc. London 1955, 230A, 169–87.
28. McGarvey, B.R. J. Phys. Chem. 1967, 71, 51–67.
29. Krishnamurthy, R.; Schaap, W.B. J. Chem. Ed. 1970, 47, 433–46.
30. Mortier, W.J.; Geerlings, P.; Van Alsenoy, C.; Figeys, H.P. J. Phys. Chem. 1979, 83, 855–61.
31. Mortier, W.J.; Geerlings, P. J. Phys. Chem. 1980, 84, 1982–6.
32. Steenkamp, P.J.; Gonsalves, J.W. J. Chem. Ed. 1981, 58, 380–2.
33. Ford, P.J.; Hitchmann, M.A. Inorg. Chim. Acta 1973, 33, L167–L170.
34. Deeth, R.J.; Gerloch, M. Inorg. Chem. 1984, 23, 3846–53.
35. Holuj, F.; Wilson, R.G. Phys. Rev. B 1973, 7, 4065–72.
36. Dempsey, E. J. Phys. Chem. 1969, 73, 3660–8.
37. Alcock, N.W.; Duggan, A.; Murray, A.; Tyagi, S.; Hathaway, B.J.; Hewat, A. J. Chem. Soc. Dalton 1984, 4–14.
38. Lever, A.B.P. Inorganic Electronic Spectroscopy; Elsevier: Amsterdam, 1984.
39. Propach, V.; Reinen, D. Z. Anorg. Allg. Chem. 1969, 369, 278–94.
40. Ferguson, J.; Knox, K.; Wood, D.L. J. Chem. Phys. 1961, 35, 2236–7.
41. Mortier, W.J. in New Developments in Zeolite Sciences and Technology; Murakami, Y.; Iijima, A.; Ward, J.W., Eds.; Proc. 7th Int. Zeolite Conf.; Kodansha: Tokyo, 1986; p 423–8.
42. Grefer, J.; Reinen, D. Z. Naturforschung 1973, 28A, 464–71.
43. Mortier, W.J.; Schoonheydt, R.A. Progress in Solid State Chemistry 1985, 16, 1–125.

Chapter 14

Effect of Alkali Metal Cations on Silicate Structures in Aqueous Solution

A. V. McCormick, A. T. Bell, and C. J. Radke

Center for Advanced Materials, Lawrence Berkeley Laboratory, and Department of Chemical Engineering, University of California, Berkeley, CA 94720

By means of ^{29}Si NMR spectroscopy, it is established that the distribution of silicate anions in alkaline silicate solutions is a moderate function of base composition. At a fixed SiO_2 concentration and silicate ratio, the proportion of Si present in oligomeric and cage-like structures increases in progressing from Li to Cs hydroxide. This trend is ascribed to cation-silicate anion pairing and to a higher selectivity for ion pairing by large silicate anions as cation size increases.

It is widely believed that the nucleation and growth of zeolites occur through the reactions of dissolved silicate and aluminosilicate anions (1,2). Supporting this view, several experimental studies have shown that the structure of dissolved silicate species can influence the structure of solid aluminosilicate intermediates present in the gel from which a zeolite may form (3-5). As a consequence, determination of the structure and distribution of such anionic species has become a subject of considerable interest. Studies utilizing ^{29}Si NMR have revealed a wide variety of silicate species in aqueous solutions of silica at high pH (1,6-10). Anions resembling the secondary building units of zeolites have been observed and it has been shown that the concentrations of these species, as well as others, are highly sensitive to the pH of the solution (7,9). The structures of aluminosilicates are less well known than those of silicates but some information about the simpler aluminosilicates has been obtained from ^{29}Si and ^{27}Al NMR (11,12).

Cation size and charge are known to influence the selectivity of zeolite synthesis (1). For instance, faujasite synthesis is quite specific to sodium systems, whereas zeolite L is formed in the presence of potassium. The effects of cation composition on the distribution of silicate species has been examined by only a few authors. Ray and Plaisted (13), using trimethylsilation/

chromatography, have found that the proportion of silicon observed in oligomeric species increases as the base is changed from LiOH to CsOH.   Differences in the distribution of silicate species of Na silicate and K silicate solutions can also be deduced from differences in the high resolution ^{29}Si NMR spectra of K silicates (8) and Na silicates (9).

The work presented here was aimed at establishing the influence of different alkali metal cations on the distribution of silicate anions in aqueous solutions such as those used in zeolite synthesis. Changes in the extent of silicate oligomerization were identified using ^{29}Si NMR spectroscopy.   The results obtained indicate that the influence of cation composition is expressed through the formation of cation-anion pairs.   Direct evidence for the presence of such ion pairs has been obtained using alkali metal cation NMR spectroscopy and is presented elsewhere (14).

EXPERIMENTAL

Alkali metal silicate solutions were prepared from Baker analyzed SiO_2 gel, reagent grade alkali metal hydroxides, and deionized water. Stock solutions at about 3 mol% SiO_2, SiO_2/M_2O = 3 (M = alkali metal) were aged in polypropylene bottles for periods of several weeks, to assure that all the SiO_2 had dissolved.   Samples were then formulated with extra water and base to achieve a desired composition.

^{29}Si NMR spectra were obtained with a Bruker AM-500 spectrometer at 99.36 MHz.   About 100 70° pulses were used with relaxation delays of about 5 times the spin-lattice relaxation time, T_1.   Values of T_1 were estimated from inversion recovery experiments.   Relaxation times varied from 0.5 s for very alkaline Na silicates to 7 s for Li silicates.   All spectra were recorded at room temperature.

A glass membrane electrode was used to measure the pH of the silicate solutions.   Adsorption of the smaller alkali metal cations, K, Na, and Li, caused an underestimation of the pH.   The pH error reached several pH units for the most alkaline Li silicate samples. On the other hand, the errors for Na silicates were around 0.5 pH unit and the errors for larger cations were relatively small. Corrections to the measured pH were made by comparison of the electrode response for the silicate solutions with that for alkali metal hydroxide solutions of known concentration.   Since the hydroxide content of the base solutions is known, the interference from cation adsorption was calculated and added to the pH measured for the silicate solutions (16).

RESULTS

Figures 1, 2, and 3 show ^{29}Si NMR spectra of alkali metal silicate solutions with silicate ratios (R = $[SiO_2]/[M_2O]$) of R = 0.4, 1.5, and 2.0, respectively.   The total SiO_2 concentration is 1.75 mol%
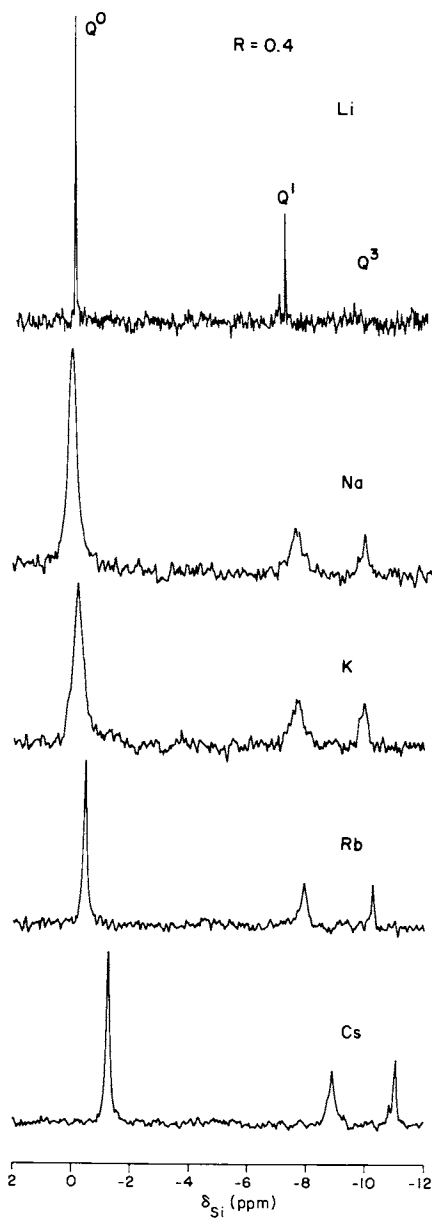
Figure 1. ^{29}Si NMR spectra of 1.75 mol% SiO_2, R=0.4 alkali metal silicate solutions.
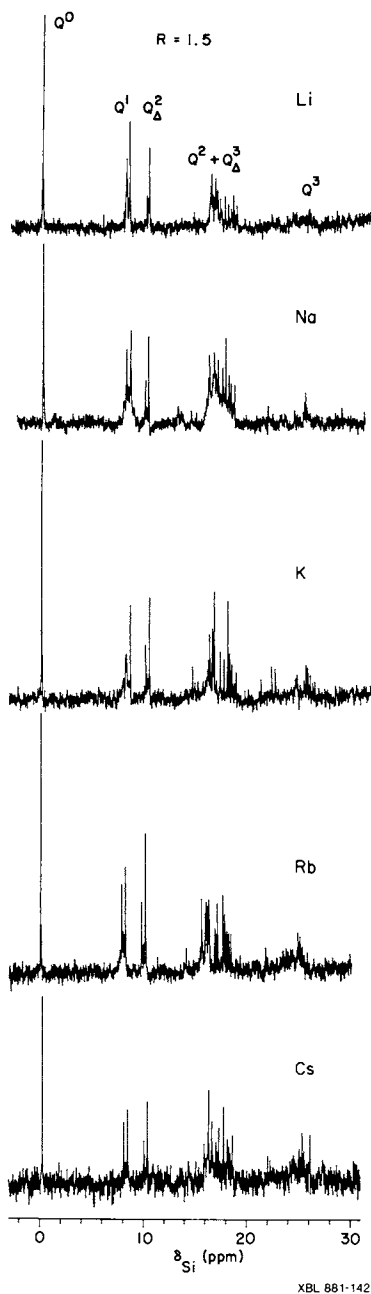
Figure 2. ^{29}Si NMR spectra of 3.0 mol% SiO_2, R=1.5 alkali metal silicate solutions.
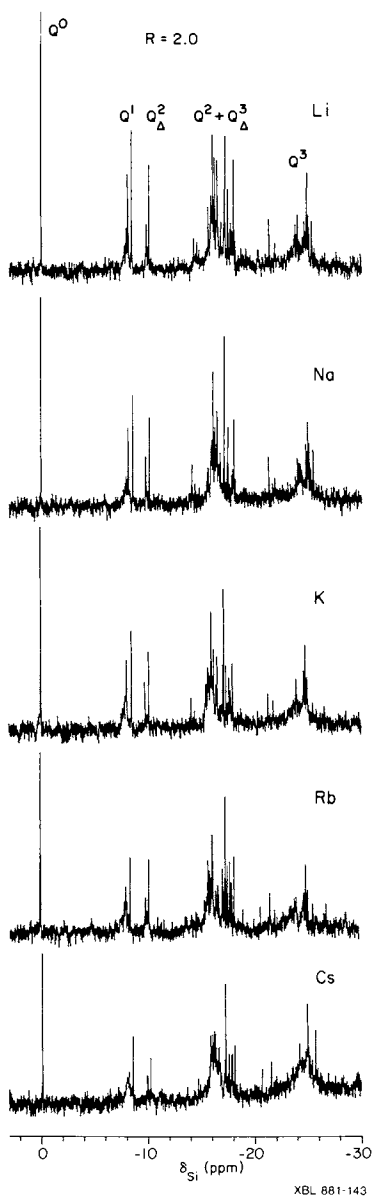
Figure 3. ^{29}Si NMR spectra of 3.0 mol% SiO_2, R=2.0 alkali metal silicate solutions.

for R = 0.4, and 3.0 mol% for R = 1.5 and 2.0. Each peak in these spectra represents a distinct silicon environment. In each figure, the chemical shift is referenced to that of the monomer in the Li silicate solution (which appears at 72 ppm relative to TMS). The distribution of silicon connectivities was determined by integrating the peaks occurring in the regions designated by Q^i in Figures 1 through 3 ($\underline{7}$). The results of these calculations are presented in Figures 4 through 6. Because Q^2 and Q^3_Δ peaks occur in overlapping regions, the amount of silicon present in Q^2 and Q^3_Δ environments is shown as a single bar.

The silicate solutions at R = 0.4 exhibit only three peaks, assignable to the monomer, dimer and cyclic trimer ($\underline{9}$). The linear trimer is ruled out because of the absence of Q^2 resonances. The larger cations produce higher concentrations of the cyclic trimer than do the smaller cations. The Li silicate spectrum in Fig. 1 ought not be compared directly with the other spectra, since a substantial amount of lithium inosilicate precipitated from the solution. The resulting supernatant solution was found to have a composition of only 0.03 mol% SiO_2 and a silicate ratio of 0.02.

The peaks in the spectra of Figure 1 become progressively shielded with increasing cation size; the monomer peak is about 1.5 ppm further shielded in the Cs silicate solution compared to the Na silicate solution. This trend is readily apparent only at low values of silicate ratio and so is not seen in Figs. 2 and 3. It is also apparent from Fig. 1 that the full width at half maximum (FWHM) of the peaks is a strong function of the cation. The FWHM is large in the presence of intermediate size cations (Na and K) and is small in the presence of Li and Cs.

At R = 1.5 the spectra display resonances in all of the connectivity regions except Q^4 (-34 ppm). As the cation size increases, silicon is displaced from lower connectivity states to states with Q^3_Δ and Q^3 connectivity. At R = 2.0, the amount of Si in the Q^3 environment increases whereas the amounts in Q^0, Q^1, and Q^2_Δ environments decrease with increasing cation size. The portion of Si in the sum of the Q^2 and Q^3_Δ environments decreases, but it is evident from the spectra that the strong Q^3_Δ resonance at -18 ppm, assignable to the prismatic hexamer ($\underline{8}$), increases with cation size. Hence we observe that the population of cagelike species increases at the expense of smaller chain species with increasing cation size.

To investigate whether the addition of a neutral alkali metal salt causes a redistribution of the silicate species, a 1.75 mol% SiO2, R = 0.4 Cs silicate solution was doped with 46 wt% LiCl solution to achieve lithium cation mole fractions of 0.42 and 0.59. The resulting connectivity distributions obtained from band integrals are shown in Figure 7. This figure shows that Li^{+} addition causes a moderate depolymerization of the silicate species present in the Cs silicate solution.
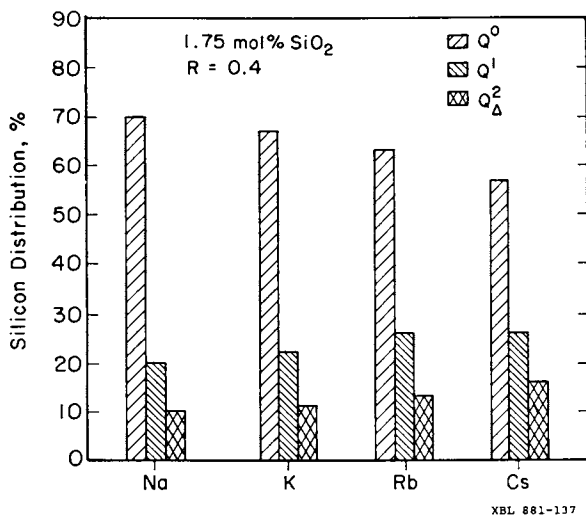
Figure 4. The influence of the cation on the distribution of Si among the connectivity states at the composition 1.75 mol% SiO_2, R=0.4.
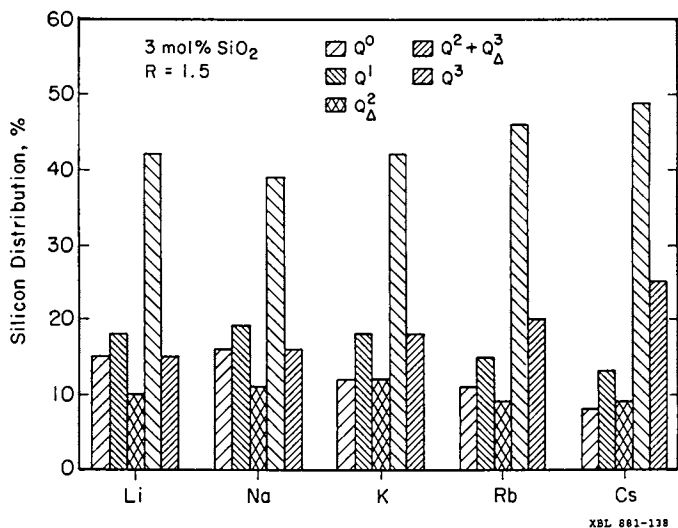
Figure 5. The influence of the cation on the distribution of Si among the connectivity states at the composition 3.0 mol% SiO_2, R=1.5.

The pH of the silicate solutions with R = 2.0 and R = 1.5 are given in Table 1. The listed values are corrected for cation interference. Accurate pH determinations for Li silicate solutions and silicate solutions for which R = 0.4 could not be made because the error due to cation interference was on the order of 2 pH units.

Since cation-adsorption induced errors in pH measurements were small at R = 2.0, the corrected pH values for these solutions were used to estimate the average charge per Si atom in solution. This was done by subtracting the OH$^-$ concentration, determined from the pH, from the total anion concentration required to balance the concentration of cations in solution and then dividing by the concentration of dissolved SiO_2. (The pH values for R = 1.5 are not considered precise enough for this calculation but are useful in discerning whether monotonic pH changes with cation size occur.) As shown in Table 1, these calculations indicate that the average charge per silicon atom does not decrease as the cation size increases.

DISCUSSION

The results presented in Figures 1-3 demonstrate that the distribution of silicate anions in alkaline silicate solutions is affected to a moderate degree by the choice of the alkali metal cation. It is evident from Figures 4-6 that the proportion of Si present in single and double rings increases progressing from Li to Cs, i.e., in the direction of increasing cation radius. Further demonstration that cation composition influences the distribution of silicate structures is evident from Figure 7, which shows the effects of introducing LiCl to a Cs silicate solution. With increasing presence of Li$^+$ cations there is a moderate redistribution of the silicate anions to lower molecular weight species. Figure 7 shows as well that when Li$^+$ constitutes 59% of the cations in solution there is a notable decrease in the proportion of cyclic trimer relative to dimer anions. The present results are consistent with those of Ray and Plaisted ([13]), who showed by means of trimethylsilation/ chromatography that the fraction of Si present in oligomeric structures increases with increasing cation size. Also, in agreement with the trends of the present work, these authors observed that the addition of KCl to a Na silicate solution resulted in a modest increase in the degree of silicate oligomerization.

Since pH is known to influence strongly the distribution of silicate anions in alkaline solutions ([7,9]), one might expect the observed changes in silicate anion distribution with cation size to be a result of changes in pH. Reference to Table 1 shows, however, that for a fixed silicate ratio, the pH of the solutions is relatively independent of the base composition and certainly does not increase with cation size, as might be expected from a consideration of hydroxide dissociation constants ([17]). This suggests that the influence of cation composition is a consequence of direct cation-anion interactions, rather than an effect of pH.

It is well known that cation-anion pairs can form in concentrated solutions of ionic compounds ([18]). The extent of ion
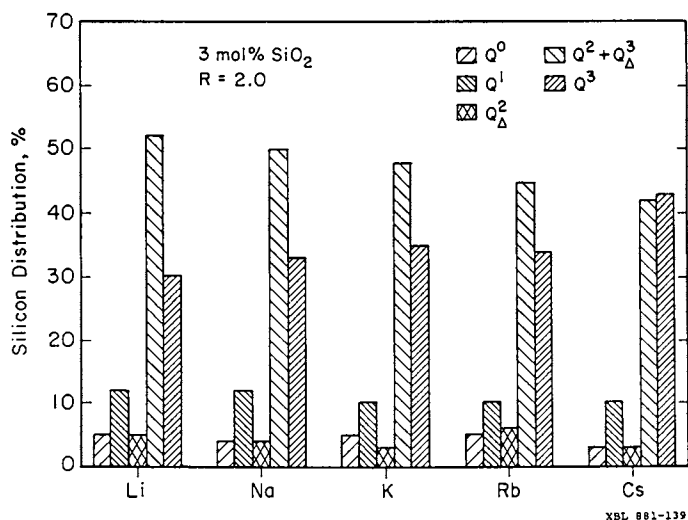
Figure 6. The influence of the cation on the distribution of
Si among the connectivity states at the composition 3.0 mol%
SiO_2, R=2.0.

Table 1. pH of Silicate Solutions

Cation	pH	Charge/Si
3 mol% SiO_2, R=2.0		
Na	12.8	0.46
K	13.0	0.46
Rb	13.2	0.45
Cs	13.0	0.47
3 mol% SiO_2, R=1.5		
Na	14.1	-
K	13.6	-
Rb	13.7	-
Cs	13.9	-
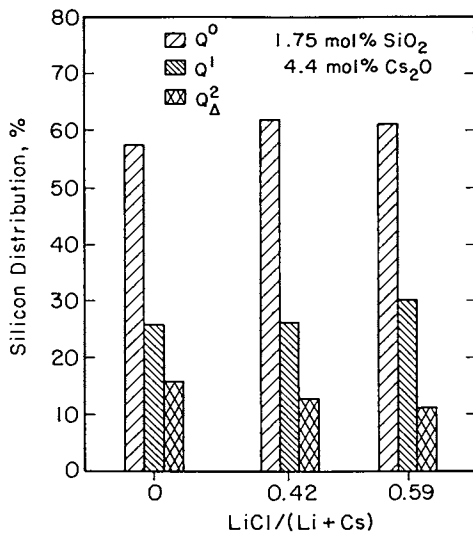
Figure 7. The influence of LiCl addition on the distribution of Si among the connectivity states of the Cs silicate solution with the composition 1.75 mol% SiO_2, R=0.4.

concentrated solutions of ionic compounds (18). The extent of ion pair formation increases with increasing ion concentration, decreasing cation size, and decreasing dielectric strength of the solvent (18). Kinrade and Swaddle (19) have invoked the proximity of alkali metal cations to silicates to explain anomalously short ^{29}Si spin lattice relaxation times. Direct evidence of pairing between alkali metal cations and silicate anions has recently been presented by McCormick et al. (14) using alkali metal NMR spectroscopy (14). The formation of cation-anion pairs was found to influence both the chemical shift and spin-relaxation time of the cation. Additional manifestations of ion pairing were observed in studies of the silicon spin relaxation and exchange between silicate anions (15). This work revealed that cation-anion contacts affect the silicon T_2 values, an effect also seen in Figure 1.

The way in which cation-anion pairs might influence the distribution of silicate anions can be illustrated with the aid of reactions 1-5 below:

1. $M^- + H_2O = M + OH^-$

2. $M + M^- = D^- + H_2O$

3. $D^- + H_2O = D + OH^-$

4. $M^- + C^+ = CM$

5. $D^- + C^+ = CD$
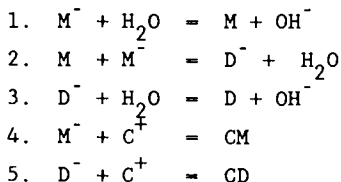
Here M^- and D^- represent the anionic species $Si(OH)_3O^-$ and $(HO)_3SiOSi(OH)_2O^-$, respectively, and M and D are the corresponding neutral species $Si(OH)_4$ and $(HO)_3SiOSi(OH)_3$. C^+ is the cation and CM and CD are cation-anion pairs formed with M^- and D^-, respectively. It is recognized that reactions 1-5 exclude the possibility that M and D exist in multiply, as well as singly, ionized states; to include such multiply ionized species would complicate the subsequent discussion, without contributing additional insight.

Reactions 1-3 indicate that dimerization is preferred at low pH. If one includes reactions for the formation of higher order oligomers and their neutralization (i.e., the analogs of reaction 2 and 3), then it is concluded that the extent of oligomerization increases with decreasing pH. This trend is in excellent agreement with the literature on silicate chemistry (7,9,20) and is exemplified by the results presented in Figures 1-3 for individual cations.

Reactions 4 and 5 represent the formation of cation-anion pairs. If the equilibrium constants for these reactions, K_4 and K_5, are identical, cation-anion pair formation will have no influence on the extent of dimerization at a fixed pH. On the other hand, if $K_5/K_4 > 1$, then the formation of dimers will be enhanced. The question to be posed, then, is what is the effect of cation size on K_4 and K_5, and more importantly, on K_5/K_4.

Based on Bjerrum's model of ion pairing (18), it is expected that the equilibrium constant for ion pair formation of a given

anion with a cation decreases with increasing cation size. As a consequence K_4 and K_5 would both be expected to decrease in magnitude as one proceeds from Li^+ to Cs^+. Direct experimental confirmation of this trend is not available, but support for it can be inferred from the following observations. First, the precipitation of the Li inosilicate salt at solution compositions (R = 0.4) which remain stable in the presence of larger cations indicates that Li^+ cations bind to small silicate anions more strongly than do larger cations. Second, using a Born-Haber cycle and measured heats of formation of alkali metal orthosilicates ($\underline{21}$), we have estimated that the heat of formation of a $Li^{+-}OSi$ ion pair is 25.5 kcal/mol higher than that of a $K^{+-}OSi$ pair in the absence of the moderating effects of hydration. From this we would infer that K_4 for Li^+ is larger than for K^+.

   For hard sphere ions, the ion pairing equilibrium coefficient is roughly inversely proportional to the distance between charge centers in the ion pair. This relationship allows us to predict that for hard spheres K_5/K_4 increases with increasing cation size. Silicate anions, though, cannot be treated as spherical. Cations may attach at small charged sites on the surface of the anion, and as a consequence the distance between charge centers is an unknown function of the cation size.

   The effects of cation size on K_5/K_4 for silicate anions cannot be determined directly, since the necessary thermochemical information is unavailable. Indirect evidence for an increase in K_5/K_4 with increasing cation size can be drawn, however, from NMR observations of the interactions between alkali metal cations and silicate anions ($\underline{14}$). These studies indicate that oligomeric anions shield the nucleus of Cs^+ more efficiently than Na^+ and that Cs^+-silicate pairing exhibits higher selectivity for large oligomers than does Na^+-silicate pairing. Moreover, Liebau ($\underline{22}$) has suggested that large polarizable cations can bind more effectively than small cations with rigid ring and cage silicate anions. Thus we are led to propose that K_5/K_4 can increase with cation size to cause the observed anion distribution shift to larger silicates.

   The information presented in Table 1 indicates that for a fixed silica concentration and silicate ratio, the pH and thus the average negative charge per dissolved Si atom is nearly independent of cation composition. Since the extent of silicate oligomerization increases proceeding from Li^+ to Cs^+, this implies that the negative charge per silicate anion increases with cation size. Estimates of this effect show that at R = 2.0, the average charge per anion in the Cs-silicate solution is 8-10% greater than that in the Li-silicate solution. The corresponding increase in average charge per anion is about 31% at R = 1.5.

   Further evidence for the change in average charge per anion with increasing cation size can be drawn from the observed increase in the chemical shift (increasing shielding) of the peaks with increasing cation size, shown in Figure 1. Harris ($\underline{8}$) has observed that the shielding of Si nuclei increases with solute concentration

at a constant silicate ratio. Since the pH (23) and the silicate distribution [9] remain roughly constant in such a case, the observed shift can be attributed to an increase in the charge on each anion. This suggests that the shielding of the Si nucleus increases in the order $\equiv$SiOH $<$ $\equiv$SiO$^-$. Thus the shielding trend observed in Figure 1 is consistent with the theory that the silicate anions in the Cs-silicate solution have a greater number of ionized surface oxygens than in the Na-silicate solution.

CONCLUSIONS

The distribution of silicate anions in alkaline silicate solutions changes with the composition of the base. At a fixed SiO_2 concentration and silicate ratio, the proportion of Si present in high molecular weight and cage-like structures increases in progressing from Li to Cs hydroxide. This trend is ascribed to cation-silicate anion pairing and to the higher selectivity to ion pairing by large silicate anions as cation size increases. An elementary estimate of the energetics of ion pairing confirm that major differences in pairing equilibrium are to be expected as the cation size is changed. Increasing cation size also increases the degree of ionization of individual anion structures. These trends may contribute to the cation selectivity of zeolite synthesis.

Literature Cited

1. Barrer, R. M. The Hydrothermal Chemistry of Zeolites; Academic Press: London, 1982.
2. Zhdanov, S. P. In Molecular Sieves I, Advances in Chemistry Series No. 101; American Chemical Society: Washington, DC, 1971, p20.
3. Derouane, E. Zeolites 1982, 2, 299.
4. Engelhardt, G. Zeolites 1985, 5, 49.
5. Wieker, W.: Fahlke, B. In Zeolites: Drzaj, H.; Hocevar, S.; Pejovnik, S., Eds.; Elsevier: New York, 1987; p 161.
6. Marsmann, T. Z.Naturforschung 1974, 295, 495.
7. Engelhardt, Z. An Allg. Chem. 1975, 418, 17.
8. Harris, R. K.; Knight, C. T. G., J. Chem. Soc., Faraday 2 1983, 79, 1525 and 1539.
9. McCormick, A. V.; Bell, A. T.; Radke, C. J. Zeolites 1987, 7, 183.
10. McCormick, A. V.; Bell, A. T.; Radke, C. J., to be published.
11. Dent Glasser, L. S.; Harvey, G. Proc. 6th Intl. Zeol. Conf.; Bisio. A.; Olson, D.H., Eds.; Butterworth: Guildford, U.K., 1984; p 925.

12. McCormick, A. V.; Bell, A. T.; Radke, C. J. In <u>New Develop-ments in Zeolite Science and Technology</u>; Murakami, Y.; Iijima, A.; Ward, J.W., Eds.; Studies in Surface Science and Catalysis Vol. 26; Elsevier: 1986; New York, p 247.
13. Ray, W.H.; Plaisted, R. J. <u>J. Am. Chem. Soc.</u> 1986, <u>108</u>, 7159
14. McCormick, A. V.; Bell, A. T.; Radke, C. J. to be published.
15. McCormick, A. V.; Bell, A. T.; Radke, C. J. to be published.
16. Heydweiler, A. <u>Ann. Phys.</u> 1915, <u>48</u> (4), 688.
17. <u>Gmelin Handbuch der Anorganische Chemie</u>; Springer-Verlag: Berlin, 19 .
18. Bockris, J. O'M.; Reddy, A. K. N. <u>Modern Electrochemistry</u>; Plenum: New York, 1970.
19. Kinrade, S. D.; Swaddle, T. W. <u>J. Am. Chem. Soc.</u>. 1986, <u>108</u>, 7159.
20. Iler, R. K. <u>The Chemistry of Silica</u>; Wiley: New York, 1979.
21. McCormick, A.V. Ph.D. Thesis, University of California, Berkeley, CA 1987.
22. Liebau, F. <u>The Structural Chemistry of the Silicates</u>; Springer-Verlag: Berlin, 1986.
23. Weldes, H. H.; Lange, K. R. <u>Ind. Eng. Chem.</u> 1969, <u>61</u> (4), 29.

Chapter 15

An All-Silica Molecular Sieve That Is Isostructural with AlPO$_4$-5

Robert A. Van Nordstrand, Don S. Santilli, and Stacey I. Zones

Process Research Department, Chevron Research Company, Richmond, CA 94802

The aluminum phosphate molecular sieve AlPO$_4$-5 has been the subject of much recent interest. Some substitution of Si for the tetrahedral Al and P has been accomplished leading to the SAPO-5 sieves. Now an all-silica sieve, SSZ-24, has been found which is isostructural with AlPO$_4$-5. Syntheses, XRD patterns and unit cell parameters, IR spectra, SEM photos and adsorption properties of AlPO$_4$-5 , SAPO-5 and SSZ-24 are compared. Although many organic templates and a wide variety of synthesis conditions lead to AlPO$_4$-5, and many elements may be substituted for a significant portion of its tetrahedral Al or P, the conditions for synthesis of SSZ-24 are very restricted; only one type of organic template has proven successful, and substitution for the tetrahedral Si is very limited. Adsorption studies show that both AlPO$_4$-5 and SSZ-24 have a preference for 2,2-dimethylbutane over n-hexane, in contrast to most large pore molecular sieves. IR spectra in the lattice vibration range are significantly different.

The composition, synthesis, properties and structure of the aluminum phosphate molecular sieve AlPO$_4$-5 have been reported over the past five years by workers at the Union Carbide Corporation (1-5). The SAPO series of sieves, reported by Lok, Messina, Patton, Gajek and Flanigen (6,7), contains Si substituted in AlPO$_4$ structures. There have been some studies regarding the location of silicon in these structures. Two possibilities have been considered - first, the replacement of an occasional P^V by a Si^{IV} to produce a strong acid site - and second, the replacement of a pair, Al^{III} - P^V, by a pair, Si^{IV} - Si^{IV}, to produce a neutral or

a much weaker acid site (8). This pair-replacement concept may
face criticism as it brings about the P-O-Si linkage which
Flanigen (9) has characterized as "unlikely". Recent work of
Martens, Mertins, Grobet and Jacobs (10) suggests that synthesis
of SAPO-5 may occur with replacement of up to 40% of the Al-P
pairs by Si-Si pairs, the silica existing in small clusters that
retain the $AlPO_4$-5 structure. Now an all-silica sieve, SSZ-4, is
found with the $AlPO_4$-5 structure (11,12).

   Details of synthesis, XRD patterns and unit cell parameters,
SEM photos, IR spectra and adsorption properties of $AlPO_4$-5,
SAPO-5 and SSZ-24 are compared.

   SSZ-24 may be the first instance in which a silica type sieve
has been discovered after its $AlPO_4$ structural analog was known.
The reverse sequence is well known, $AlPO_4$ structural analogs being
found for previously known faujasite, chabazite, erionite, soda-
lite, gismondine, levynite and Linde type A zeolites.

   A related sequence involves the sodalite structure. Here the
structure was determined for sodalite (Al:Si = 1:1). $AlPO_4$-20 was
then discovered, with the same structure. And more recently Bibby
and Dale (13) have reported an all-silica form of sodalite.

Synthesis

The $AlPO_4$-5 synthesis takes place starting with phosphoric acid,
aluminum hydroxide (pseudoboehmite) and an organic template such
as tetrapropylammonium cation. The pH starts out on the acid
side, going gradually to neutral. A wide variety of templates may
be used. Conditions such as temperature, dilution and agitation
may be varied widely.

   Conditions for synthesis of SAPO-5 are not as flexible, if
one is committed to introducing silicon into the structure. The
modes of Si introduction mentioned above, isolated Si or pairwise
Si (even cluster Si) each require special and restricted synthesis
conditions.

   Conditions for synthesis of the all-silica version of $AlPO_4$-5
(SSZ-24) are still more critical and restricted. The synthesis is
carried out on the basic side. A critical feature is the tem-
plate, N,N,N-trimethyl-1-adamantammonium hydroxide.
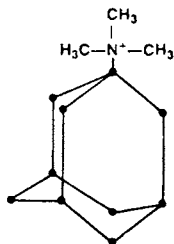
This template is just one of many directing the synthesis to AlPO$_4$-5 (11) but is the only one found which directs to SSZ-24. As described in the patents (11,12), a preferred recipe for SSZ-24, given in atomic or molecular ratios, is: Al/Si = 0.000, K or Na/Si = 0.10, template N/Si = 0.15, H$_2$O/Si = 15 to 44, OH$^-$/Si = 0.25, Cabosil M-5 as the silica source (Cabot Corp., less than 2 ppm Al), 6 days at 150-160°C, with or without mild agitation. The adamantammonium template is found within the sieve pore system at a level which indicates complete pore filling. The formula for this organo-sieve is RN-24SiO$_2$. Here RN is trimethyladamantammonium hydroxide. The corresponding formula for AlPO$_4$-5 is RN-12AlPO$_4$ (4). Here RN is tetrapropylammonium hydroxide.

The reason for the narrow crystallization field for SSZ-24 is the intrusion of fields of other molecular sieves and non-porous materials. With aluminum present or with higher OH$^-$/Si, SSZ-23 (11,14), SSZ-25 (11,15), and SSZ-13 (16) (a high silica chabazite) may intrude. Higher temperatures and vigorous stirring accelerate the Hoffmann degradation reaction of the quaternary cation. The degradation products lead to other zeolites, ZSM-5 and ZSM-39 (17). These latter zeolites are found by NMR to contain the neutral amine degradation products. Quartz, cristobalite, and kenyaite have also been produced in trying to define the crystallization field of SSZ-24.

SSZ-24 has been produced along with various impurities when aluminum at a level of Al/Si = 0.01 was introduced into the syntheses. A variety of aluminum sources were used including aluminum sulfate, metakaolin, colloidal alumina dispersed on silica (Nalco ISJ612), and even other zeolites (K-L, K-A, and K-offretite). However, accompanying zeolites and other impurities could not account for the catalytic activity and selectivity found in a constraint index test, described in Example 7 of the patent reference (12). The assumption then is made that the catalysis is caused by a low alumina form of the large pore SSZ-24.

Crystal Structure

XRD patterns of organic-free AlPO$_4$-5 and SSZ-24 are shown in Figure 1. The isostructural relationship of these two sieves is deduced from the matching of these powder patterns and the matching of the hexagonal unit cells. Table I contains a list of the XRD peaks and their hexagonal indices for SSZ-24 with and without the template. Hexagonal unit cell parameters for both AlPO$_4$-5 and SSZ-24 are given in Table II.

Both d-spacings and cell parameters are in angstrom units.
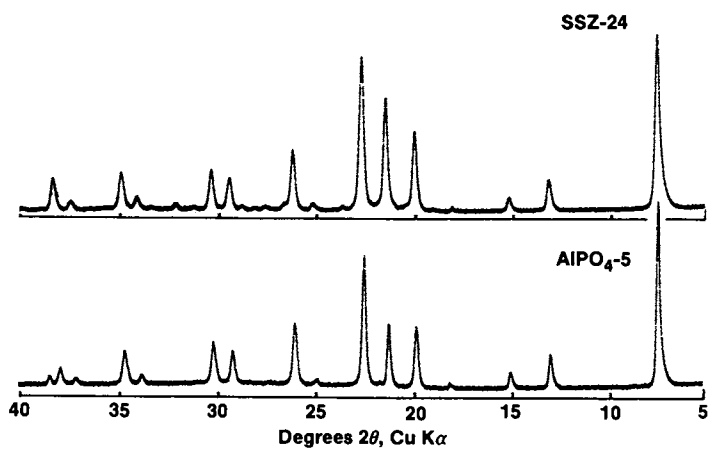
Figure 1. X-ray powder diffraction patterns of AlPO$_4$-5 and SSZ-24.

Table I. XRD Patterns for SSZ-24 With and
Without the Adamantammonium Hydroxide

With Template		Calcined		Index
d	Intensity	d	Intensity	(hkl)
11.79	98	11.79	100	(100)
6.81	10	6.82	17	(110)
5.906	46	5.906	8	(200)
4.459	100	4.464	34	(210)
4.148	36	4.162	27	(002)
3.927	87	3.934	71	(211)
3.544	4			(112)
3.406	44	3.410	40	(220)
3.041	13	3.046	12	(311)
2.949	30	2.953	30	(400)
2.631	5	2.637	4	(222)
2.574	20	2.576	20	(321)
2.404	4	2.408	3	(402)
2.351	7	2.355	6	(213)
2.152	4	2.156	3	(421)
2.118	4	2.118	3	(510)

Table II. Lattice Parameters for the
Hexagonal Unit Cells of $AlPO_4$-5 and SSZ-24
(Template for $AlPO_4$-5 is tetrapropylammonium
hydroxide.)

	a	c
$AlPO_4$-5		
With Template (4)	13.726	8.484
Calcined (21)	13.77	8.38
SSZ-24		
With Template	13.62	8.296
Calcined	13.62	8.324

$AlPO_4$-5 and SSZ-24 are isostructural with the predicted
framework type 81 of Smith (18). It is composed predominantly of
6-ring SBU. This is unexpected in the case of the SSZ-24 because

most known high silica molecular sieves contain predominantly 5-ring SBU. The high silica chabazite, SSZ-13, can also be produced using this adamantammonium template, and consists of 4- and 6-ring SBU. This suggests that the adamantammonium template may control the silica ring type in the synthesis. A similar point was raised by Bibby and Dale (13) regarding the absence of 5-ring SBU in their silica-sodalite.

SEM photos in Figure 2 show resemblance in morphology among $AlPO_4$-5, SAPO-5 and SSZ-24. These photos, while typical, are not representative of all preparations of these molecular sieves, but were selected to show this similarity in morphology.

Infra-Red Spectra

Comparisons of the IR spectra in the lattice vibration range are provided in Figure 3. The spectra include those of SSZ-24, $AlPO_4$-5 and a SAPO-5 (with Si corresponding to 4% of the T atoms). The spectra were obtained on an FT IR instrument (Digilab FTS-20C). The samples were examined in the form of KBr discs with 0.3 mg sample in 300 mg KBr. The spectrometer was equipped with CsI optics, resolution 2 cm, with triangular apodization.

Spectra of the $AlPO_4$-5 and SAPO-5 show minor distinctions. However, the absorption maxima of SSZ-24 are significantly displaced from, and are sharper than those of the phosphates.

Adsorption Characteristics

Initial reports on adsorption studies suggested that $AlPO_4$-5 has a moderately hydrophilic surface (1). Recently, Lohse, Noack, and Jahn (19) have described the surface as non-polar but suggested that the aluminum atoms undergo a chemical interaction with water.

The set of test molecules used here for port gauging of zeolites all enter freely at room temperature into the $AlPO_4$-5, SAPO-5, and SSZ-24 sieves. These molecules include six C-6 hydrocarbons - n-hexane (nC6), benzene, 3-methylpentane (3MP), methyl cyclopentane, cyclohexane and 2, 2-dimethylbutane (22DMB) - and iso-octane. The total adsorption of this mixture of hydrocarbons is about 0.12 ml/g for these sieves. The admission of the larger molecules such as 22DMB is compatible with the 12-ring pore openings of the sieves.

A surprising characteristic of these three sieves was found by using our "pore probe" technique (20). At 127°C the contents of the pores in equilibrium with a vapor phase equimolar mix of 22DMB, 3MP and nC6 are given in Table III. The SAPO-5 sample here contained Si corresponding to 10% of the T atoms.
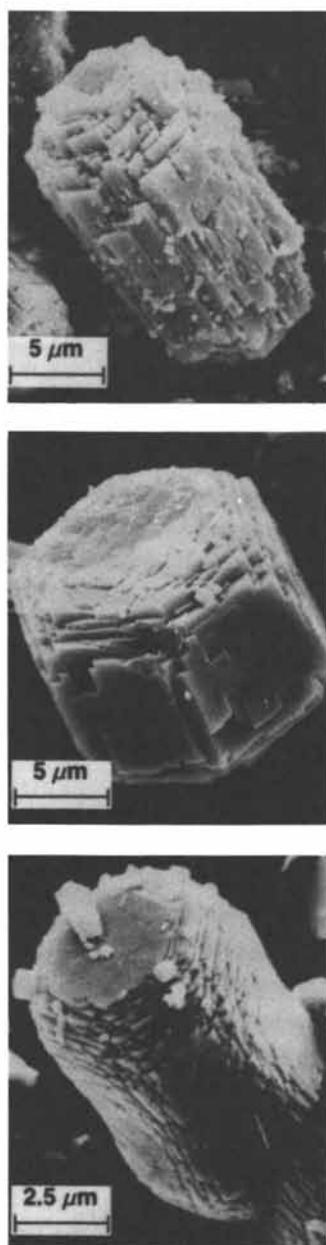
Figure 2.   SEMs of AlPO$_4$-5, SAPO-5, and SSZ-24 (top to bottom).
Photographs courtesy of Lun-Teh Yuen.
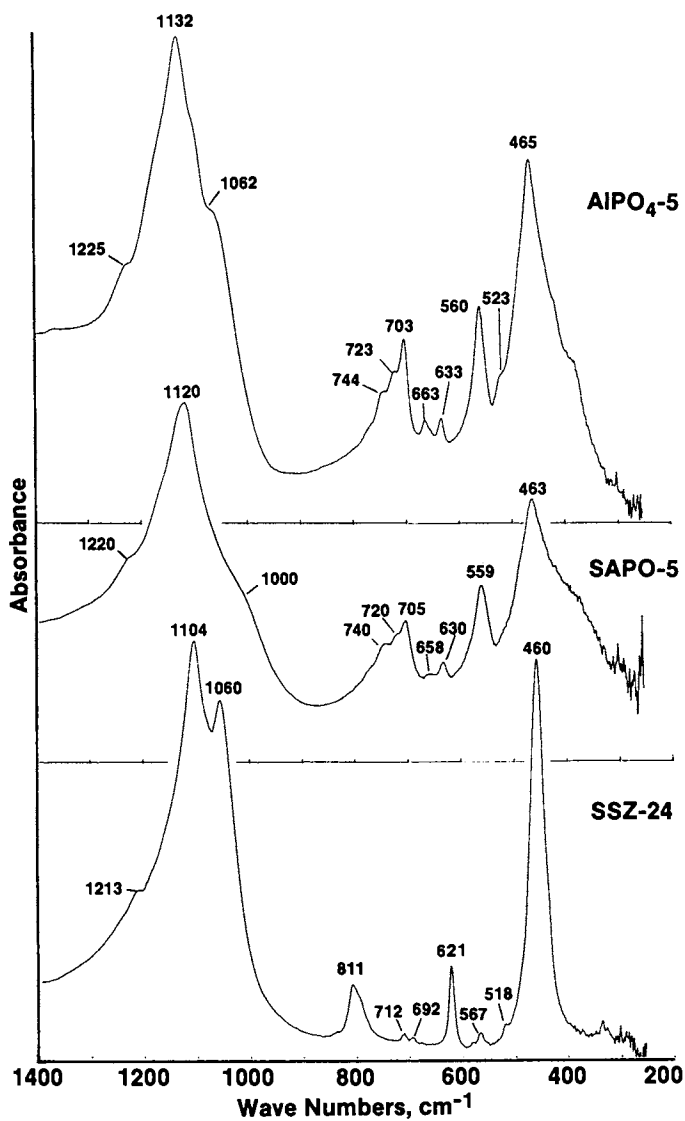
Figure 3. IR spectra of AlPO$_4$-5, SAPO-5, and SSZ-24.

Table III.   Pore Probe Data at 127°C in Units of mg/g

	$AlPO_4$-5	SAPO-5	SSZ-24
22DMB	27	21	26
3MP	13	12	15
nC6	6	9	12

Other large pore zeolites studied do not show this preference for 22DMB over nC6. For example, NaY prefers nC6 over 22DMB by a factor of 2.0 under these conditions. The pore structure is the common feature in SSZ-24, $AlPO_4$-5, and SAPO-5, and may account for this preference for branched-chain hydrocarbons.

Acknowledgments

Literature Cited

1.   Wilson, S. T.; Lok, B. M.; Messina, C. A.; Cannan, T. R.; Flanigen, E. M. J. Am. Chem. Soc. 1982, 104, 1146-1147.
2.   Wilson, S. T.; Lok, B. M.; Flanigen, E. M. U.S. Patent 4 310 440, 1982.
3.   Wilson, S. T.; Lok, B. M.; Messina, C. A.; Cannan, T. R.; Flanigen, E. M. Am. Chem. Soc. Sympos. Ser. 1983, 218, 79-106.
4.   Bennett, J. M.; Cohen, J. P.; Flanigen, E. M.; Pluth, J. J.; Smith, J. V. Am. Chem. Soc. Sympos. Ser. 1983, 218, 109-118.
5.   Bennett, J. M.; Dytrych, W. J.; Richardson, Jr., J. W., Smith, J. V. Zeolites 1986, 6, 349-360.
6.   Lok, B. M.; Messina, C. A.; Patton, R. L.; Gajek, R. T.; Cannan, T. R.; Flanigen, E. M. U.S. Patent 4 440 871, 1984.
7.   Lok, B. M.; Messina, C. A.; Patton, R. L.; Gajek, R. T.; Cannan, T. R.; Flanigen, E. M. J. Am. Chem. Soc. 1984, 106, 6092-6093.
8.   Flanigen, E. M.; Lok, B. M; Patton, R. L.; Wilson, S. T. "New Developments In Zeolite Science and Technology", Elsevier, 1986; pp 103-112.
9.   Flanigen, E. M. Presented at Symposium on Innovation in Zeolite Materials Science, Nieuwport, Belgium, September 1987, in press.

10.   Martens, J. A.; Mertens, M.; Grobet, P.; Jacobs, P. A.
      Presented at Symposium on Innovation in Zeolite Materials
      Science, Nieuwpoort, Belgium, September 1987, in press.
11.   Zones, S. I. U.S. Patent 4 665 110, 1987.
12.   Zones, S. I. European Patent Application 0 231 019 A2,
      published 1987.
13.   Bibby, D. M.; Dale, M. P. Nature (London) 1985, 317, 157–
      158.
14.   Zones, S. I. European Patent Application 0 231 018 A2,
      published 1987.
15.   Zones, S. I. European Patent Application 0 231 860 A2,
      published 1987.
16.   Zones, S. I. U.S. Patent 4 544 538, 1985.
17.   Dwyer, F. G.; Jenkins, E. E. U.S. Patent 4 287 166, 1981.
18.   Smith, J. V. Am. Mineral. 1978, 63, 960–969.
19.   Lohse, U.; Noack, M.; Jahn, E. Adsorption Sci. and Tech.
      1986, 3, 19–24.
20.   Santilli, D. S. J. Catalysis 1986, 99, 335–341.
21.   Richardson, Jr., J. W.; Pluth, J. J.; Smith, J. V. Acta
      Cryst. 1987, C 43, 1469–1472.

Chapter 16

Silica–Alumina Ratio Effects on Zeolite Crystallization in the Presence of Trioctylamine

IR and NMR Characterization

M. L. Occelli [1], G. P. Ritz [1], P. S. Iyer [1], and J. V. Sanders [2,3]

[1]Science and Technology Division, Unocal Corporation, P.O. Box 76, Brea, CA 92621
[2]Division of Material Science and Technology, Commonwealth Scientific and Industrial Research Organisation, Clayton, Victoria 3168, Australia

X-ray and NMR analyses of several Si-rich (Na, K, TOA)-mordenites and Al-rich (Na,K,TOA)-pentasils did not reveal the presence of significant amounts of amorphous material or occluded reactants. Phase impurities (feldspar) are believed responsible for the appearance of a relatively strong band at about 585 cm^{-1} in the MID-IR spectra of (Na,K,TOA)-mordenites. Shifts to lower frequencies in the T-O band region correlates well with the presence of faults in several of the mordenite crystals studied. Aluminum-27 MAS NMR spectra show a single resonance at 50-53 ppm typical of Al(IV) in these zeolites. IR spectra indicate that after calcination, the pentasils exhibit bands only at 3733 and ~3588 cm^{-1}. After NH_4-exchange and calcination at 500°C, all the samples examined showed an aluminum-27 NMR resonance near 0 ppm typical of Al(VI) indicating dealumination of the crystal lattice. This is accompanied by IR bands appearing at 3630-3635 cm^{-1} in the OH-stretching region. Only when in their H-form, do the pentasils show an IR band at ~3635 cm^{-1} which, on the basis of Al-NMR results, is attributed to stretching vibrations of Al-OH groups resulting from extra lattice aluminum generated during zeolite activation.

Alumina-rich zeolites of the pentasil family and siliceous mordenite crystals can be synthesized from near stoichiometric hydrogels of composition Al_2O_3:$xSiO_2$:1.5 Na_2O:2.2 K_2O:250 H_2O containing four moles of trioctylamine (TOA) per mole Al_2O_3 (1). Gels with x < 10 (x = SiO_2/Al_2O_3) gave analcime or analcime-offretite-mordenite mixtures after heating at 150-200°C for a period of four weeks (1).

From hydrogels with x in the 12-20 range, the crystallization of mordenite over ZSM-11 is favored while for x in the 20-25 range, the opposite is observed; ZSM-5 was obtained from gels with x = 30 ([1]). In the synthesis of zeolites with the pentasil structure, it is believed that the nucleation step is initiated by the reaction of an aluminosilicate anion and an organic base ([2]). Gels prepared without (or with very low) Al content will generate weakly charged silicate anions which cannot react with weakly basic protonated amines ([3]). Thus trioctylammonium cations can act as counter ions only for strong anions like those present in aluminosilicate solutions. In fact, the crystallization of TOA-containing zeolites with the pentasil structure requires the presence of Al in the gel ([1,3]). As a result, when the gel x value was raised to 60 from 30, an amorphous product was obtained ([1]). Gels with x = 1000 yielded magadiite ($NaSi_7O_{13}(OH)_3H_2O$) instead of silicalite crystals ([1]). It is the purpose of this paper to investigate and report the use of IR and NMR techniques in the characterization of several zeolites synthesized from TOA-containing hydrogels.

Experimental

All crystallization reactions were performed at 150-200°C for 7d, in 750 ml teflon-lined autoclaves equipped with a magnetic stirring mechanism ([1]). Gels were prepared by dissolving commercial grade $NaAlO_2$ (containing 25% H_2O) into a mixed NaOH-KOH alkaline solution. Following trioctylamine ($(C_{24}H_{51}N)$ addition, colloidal silica (Ludox HS-40) was introduced dropwise; the gel formed was first allowed to cold age for 10h and then placed in the autoclave for crystallization. TOA-containing crystals with low Si/Al ratio are hydrophobic and tend to agglomerate into large particles during the washing step ([1]). Excess reactants (NaOH and KOH) occlusion in these aggregates occur and, as a result, the crystals Al/(Na+K+TOA) ratio often exceed 1.0 ([1]). After calcination at 600°C/10h in air, crystals were reacted with a 1M NH_4NO_3 solution; H-zeolites were obtained by heating for 10h the NH_4-exchanged crystals at 500°C in air. Results have been summarized in Table I.

TABLE I. Surface Area (SA) and Crystal Composition
(per Al_2O_3 mole) Before and After
NH_4-Exchange and Calcination at 500°C/10h ([1])

S No.	Gel x Value	Before Exchange				After Exchange			Area m²/g	Phase(s) Present
		SiO_2	Na_2O	K_2O	$(TOA)_2O$	SiO_2	Na_2O	K_2O		
1.	6	5.0	1.1	0.03	0.01	4.7	0.82	0.03	--	Analcime
2.	12	9.2	0.38	0.67	0.28	10.6	*	*	440	Morden. +Q+F
3.	15	8.4	0.41	0.51	0.33	9.5	0.29	0.03	293	Mordenite
4.	15	13.3	0.84	0.0	0.08	13.3	*	0.0	432	Mordenite
5.	15	--	--	--	0.00	10.4	0.03	*	441	Mordenite
6.	20	17.3	0.58	0.53	0.10	16.9	*	*	409	Mordenite
7.	24	20.0	0.78	0.0	0.25	19.9	*	*	359	ZSM-11+ZSM-5
8.	24	21.1	0.49	0.50	0.22	21.4	*	*	390	ZSM-11+M
9.	24	21.2	0.61	0.49	0.00	20.1	*	*	336	ZSM-11
10.	30	27.1	0.47	0.43	0.23	28.2	*	*	357	ZSM-5
11.	60	--	--	--	--	--	--	--	--	Amorphous
12.	1000	14.0	1.0	--	--	--	--	--	17	Magadiite

*Less than 0.01; Q = Quartz; M = Mordenite; F = Feldspar

Electron diffraction patterns of heavily and weakly faulted mordenite crystals were obtained with a JEOL 100 CX transmission electron microscope fitted with a top entry two-axis tilting stage and a UHR objective pol piece (C_s = 0.7 mm). In this situation, electron diffraction patterns can be obtained from crystals tilted by about ± 35° from the horizontal. Experimental details have been discussed elsewhere (2).

Mid-IR spectra were obtained using the KBr wafer technique and a Nicolet 3600 spectrometer. Zeolites were used after drying in air at 100°C or in their H-form. At least two spectra were obtained from each sample before accepting the results as being representative of the zeolite under study. Surface acidity was examined with a Nicolet 170 SX spectrometer. As with mid-infrared data, spectra were acquired with 2 cm^{-1} resolution (8192 data points) and apodised using the Happ-Genzel algorithm. Self supporting wafers (4-8 mg/cm^2 in density) were prepared by pressing samples between 25 mm diameter die for one minute at ∿6,000-7,000 lbs pressure. Prior to pyridine sorption, the wafers were mounted in an optical cell and degassed by heating at 200°C for 2h at 10^{-4} torr. The pyridine-loaded wafers were then heated (in vacuo) in the 200-500°C temperature range for periods of 1h and the spectra recorded at each temperature. Spectra of the O-H stretching region were smoothed with a five points Savitzky-Grolay algorithm and baseline slope corrected; peak intensities were normalized to the sample density.

Silicon-29 NMR spectra were recorded at 53.7 MHz on an IBM AF-270 FTNMR spectrometer equipped with Doty Scientific MAS solids probe. Samples were spun in cylindrical 7mm alumina (saphire) rotors equipped with vespel caps at 3.0 to 3.5 kHz. Since neither high power proton decoupling nor cross-polarization ((CP) was employed, the observed signal intensities are uncorrected for the possible presence of Si-OH groups. A 60° pulse (6 μs) and 5 sec recycle delay was used in all cases. 2K data points were acquired during a 51 msec acquisition time (corresponding to 20 kHz spectral width) and zero filled to 4K data points with apodization equivalent to 20-50 Hz line broadening applied prior to Fourier transformation. Chemical shifts were referenced to external TMS (taken as 0.0 ppm) by sample exchange using a secondary standard (set to -108.2 ppm).

Experimental Silicon-29 NMR signals were deconvoluted into Gaussian components using the LINESIM program (courtesy of Dr. Peter Barron, Griffith University, Natham, Australia) that was written for an ASPECT-3000 computer. The best fitting simulated spectra were obtained using an iterative simplex routine. The Si/Al ratios were calculated from the derived line intensities using the relation:

$$Si/Al = I_{TOT} / \sum_{n=1}^{4} 0.25 \ n \ I_{Si[nAl]}$$

where I_{TOT} is the total intensity of the spectrum and $I_{Si[nAl]}$ is the intensity contributions from Si atoms with nAl neighbors in their second coordination sphere.

The same spectrometer was also used to record Aluminum-27 MAS NMR spectra at 70.4 mHz. Typical scan conditions involved 18° (1 μsec) pulse with a recycle delay of 2 secs to obtain near

quantitative results. In calculating Al(VI)/Al(IV) ratios, it was
assumed that spinning side bands (SSB) were of equal intensities.
Justification for this assumption is based on the observation of
equal intensity SSB in all the TOA-containing zeolites. 2K data
points were acquired over 31 msec acquistion time (corresponding to
a sweep width of 33.3 kHz). Data was zero filled to 4K and
exponential apodization equivalent to 50 Hz line broadening applied
before Fourier transformation. Left shifting was not performed on
the acquired data. Samples were spun in 7mm zirconia rotors fitted
with vespel end caps, at 3.0 to 3.5 kHz. Chemical shifts reported
are referenced to external aqueous $Al^{3+}(H_2O)_6$ (set to 0.0 ppm).

Results and Discussion

Electron Diffraction.   A variety of different preparations of
TOA-containing mordenites were examined by TEM in order to compare
their morphology and fault concentration with those of natural
mordenite. Natural mordenite crystals in the form of long laths
give streaks in diffraction patterns taken at almost any random
orientation, but most strongly in an okl orientation, Figure 1A.
This is because faults produce two dimensional sheets of scattering
in reciprocal space (2) so that the intensity of the streaks is not
very sensitive to the tilt of the crystal. It is, therefore,
possible to assess quantitatively the concentration of the faults by
the intensities of the streaks in the diffraction patterns. To do
this, selected crystals were tilted in the electron microscope, and
diffraction patterns recorded at convenient orientations. The
examples shown in Figures 1B and 1D show that samples 3 and 2 (Table
I) give quite strong streaks, but not as intense as those from the
natural mordenite sample, so that the crystals must be faulted, but
rather less than natural mordenite. In Figures 1E and 1F, the
streaks can just be discerned, indicating a very low concentration
of faults in these crystals. In sample (6) (Table I), the
morphology of the crystals is such that their c axis lies parallel
to the electron beam, and it is not possible to obtain diffraction
patterns comparable with the others, Figure 1C.
     The morphologies of the crystals are shown in Figure 2. The
natural mordenite is in the form of very long laths, with the
channels parallel to the length of the crystal. Sample (2) is
similar, but with a smaller length/width ratio, Figure 2D. Sample
(3) consists of mainly irregular fragments with some short laths,
Figure 2B. The lath habit of individual crystals is apparent also
in Figure 2F, but the crystals are, in general, aggregated into
irregularly shaped flat particles (1).

Lattice Vibrations.   The IR spectra for analcime in the framework
absorption region is shown in Figure 3. Frequency shifts observed
with respect to published results (3) are attributed to the sample's
higher (4.7 vs 4.0) SiO_2/Al_2O_3 ratio. IR lattice vibrational bands
and spectra for mordenites and pentasils with different SiO_2/Al_2O_3
ratios are given in Table II and Figures 4-7. Bands at 950-1250
cm^{-1}, 650-720 cm^{-1} and 420-500 cm^{-1} have been assigned by Flanigen
and coworkers (3,4) to asymmetric stretching, symmetric stretching
and Al-O and Si-O bending vibrations in internal AlO_4 and SiO_4
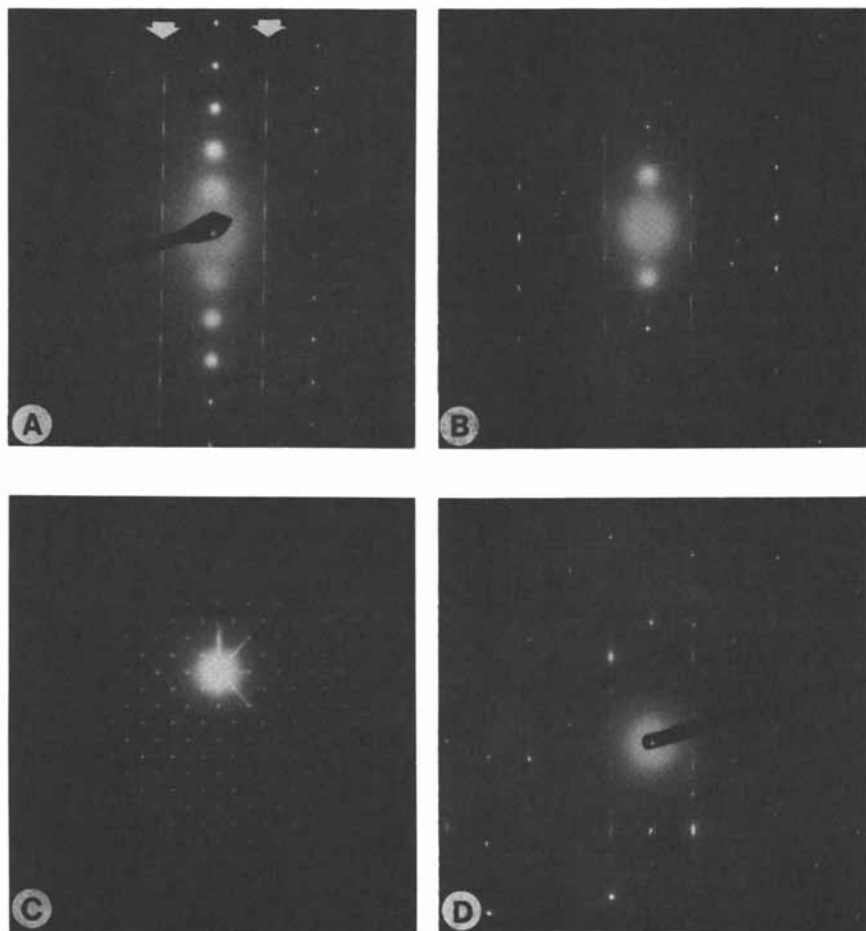
Figure 1.   Electron diffraction patterns of several mordenite
crystals.   (A) Natural mordenite from Hicknoi, New Zealand,
(B) Sample 3, (C) Sample 6, (D) Sample 2.   Faulting in the
crystals produces streaks in the diffraction patterns.   Since
these streaks come from sheets of diffuse scattering in
reciprocal space (2), their appearance and intensity is not
very sensitive to the tilt of the crystal.   Because sample
(C) is in the form of plates that lie in the electron micro-
scope with the c axis parallel to the electron beam, streaks
from the faults do not appear in the pattern because they
are not visible in this orientation.   The short streaks
through the intense central spot come from the sharp edges of
the crystal.
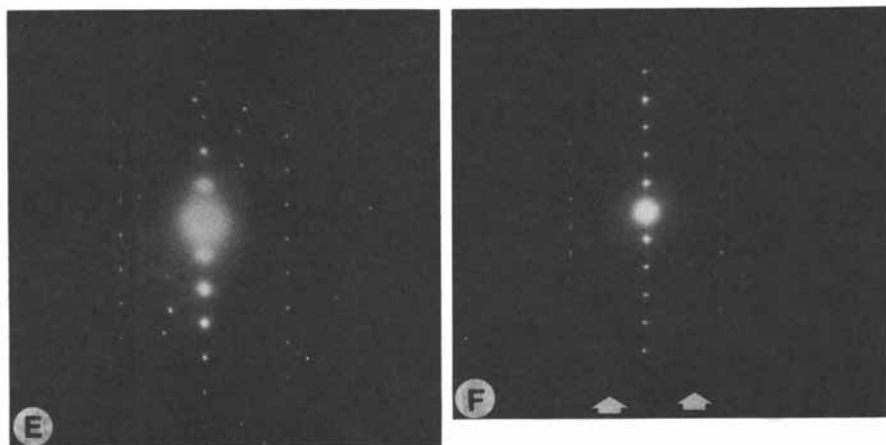
Figure 1. Continued. (E) Zeolon 900, (F) Sample 4.
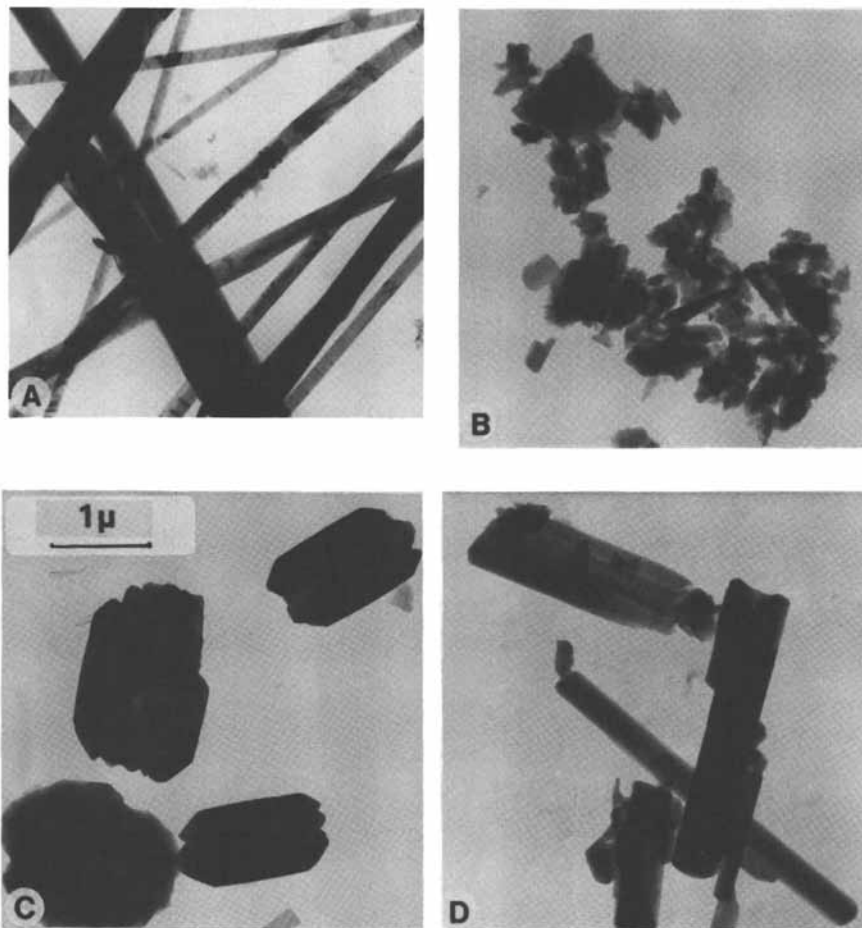
Figure 2.   Electron micrographs of several mordenite crystals.
(A) Natural mordenite from Hicknoi, New Zealand, (B) Sample 3,
(C) Sample 6, (D) Sample 2.   In (A) and (B), the main channels
are parallel to the length of the crystals, the c axis.   In
(C), the channels are normal to the plates, which are shown
looking down the c axis.   The magnifications vary slightly
between the micrographs, but are about that shown by the micron
scale in (C).
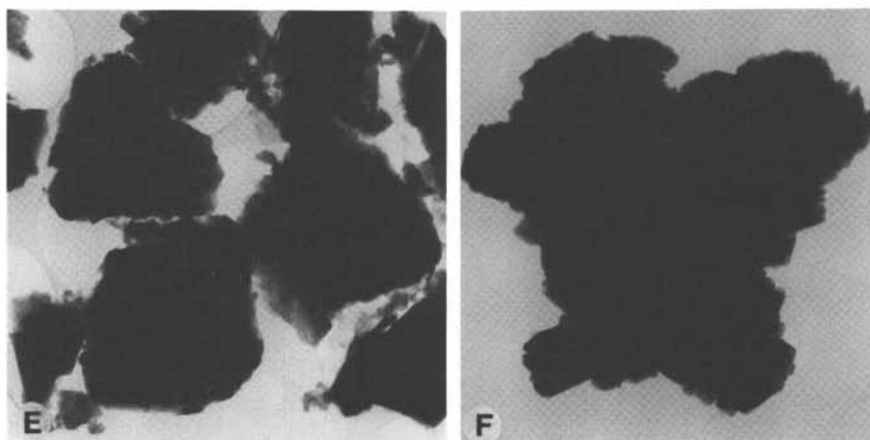
Figure 2. Continued. (E) Zeolon 900, (F) Sample 4.
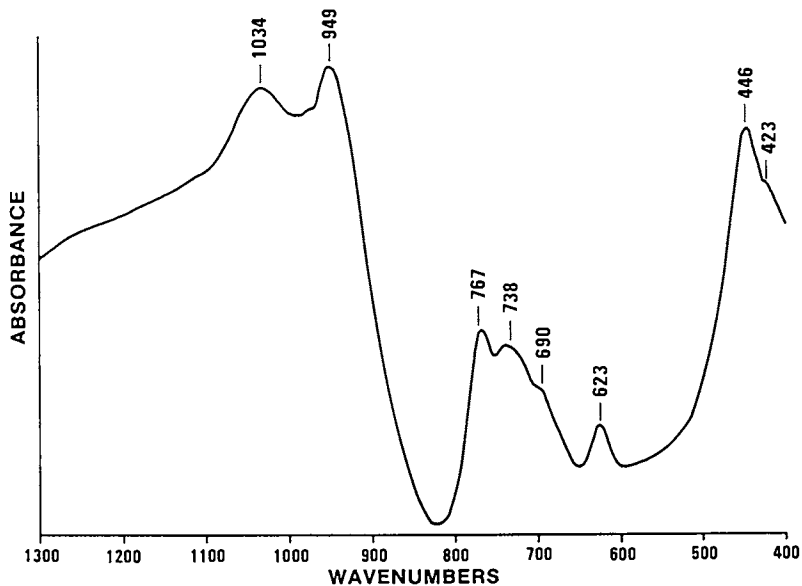
Figure 3. Mid infrared spectra of analcime, Sample No. 1,
Table I.
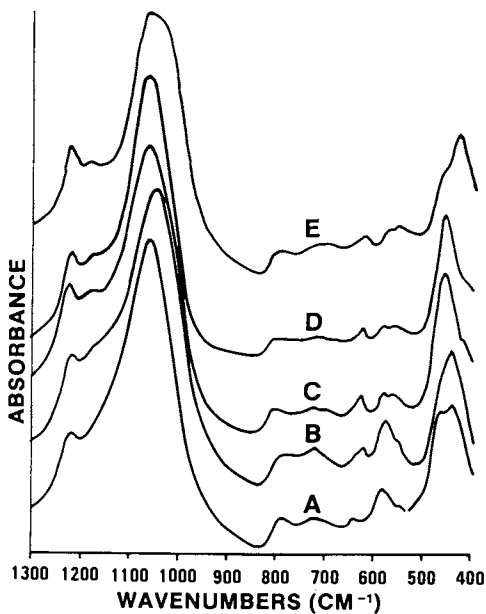
Figure 4. Mid infrared spectra of several pentasils from
Table I: (A) Sample No. 8; (B) Sample No. 9; (C) Sample No. 10
and (D) Sample No. 10, seeded. (E) is the spectrum of an x-ray
amorphous material obtained from a gel with x = 60.

TABLE II. MID-INFRARED SPECTRAL FREQUENCIES (CM^{-1}) OF SEVERAL MORDENITE AND PENTASIL CRYSTALS (ASSIGNMENTS MADE AFTER FLANIGEN ET AL., (3))

| | Heavily Faulted Mordenites | | | Weakly Faulted Mordenites | | | ZSM-11 | ZSM-5 |
Natural*	Natural**	Sample 2	Sample 3	Sample 4	Sample 5	Commercial***	Sample 8	Sample 10
435 (ms)	441 (ms)	441 (ms)	440 (ms)	----	----	----	----	----
460 (bsh)	462 (bsh)	461 (vwsh)	457 (vwsh)	458 (ms)	457 (ms)	460 (ms)	453 (ms)	452 (ms)
557 (bm)	547 (vwsh)	545 (vwsh)	545 (vwsh)	559 (w)	556 (w)	558 (w)	546 (m)	546 (ms)
574 (vwsh)	581 (bm)	580 (bm)	584 (bm)	578 (w)	578 (w)	582 (w)	582 (wsh)	582 (wsh)
624 (w)	----	623 (w)	624 (w)	627 (w)	625 (w)	626 (bw)	615 (vwsh)	614 (vwsh)
----	642 (w)	639 (wsh)	648 (w)	----	----	----	----	----
----	----	----	----	692 (bvw)	688 (bvw)	----	----	----
716 (bvw)	714 (bw)	723 (bvw)	722 (bvw)	723 (bvw)	722 (bvw)	726 (bvw)	----	----
798 (bmw)	790 (bmw)	780 (bmw)	788 (bmw)	806 (bmw)	802 (bmw)	810 (bmw)	790 (bmw)	792 (bmw)
1065 (vs)	1061 (vs)	1047 (vs)	1079 (vs)	1064 (vs)	1060 (vs)	1082 (vs)	1087 (vs)	1091 (vs)
1182 (w)	----	1171 (bvwsh)	1176 (bvwsh)	1178 (bwsh)	1178 (bwsh)	1182 (bvwsh)	----	----
1224 (mw)	1221 (sh)	1218 (sh)	1222 (sh)	1220 (sh)	1219 (bsh)	1223 (bsh)	1217 (mw)	1218 (mw)

*Natural mordenite from Hickuoi, New Zealand. The sample contains less than 5% quartz impurities.
**Natural mordenite from Lovelock, Pershing Co., Nevada, USA. The sample contains about 20-30% ferrierite and 10-15% feldspar.
***Na-mordenite from Laport (Laposil 3000).
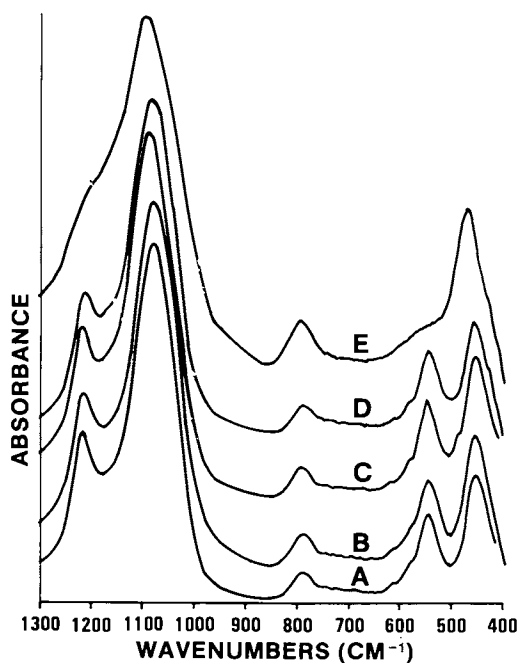
Figure 5. Mid infrared spectra of several mordenites (see Table I). (A) Natural mordenite from Lovelock, Nevada, USA; the sample contains ferrierite and feldspar impurities. (B) Sample No. 2; (C) Sample No. 4, (D) Sample No. 5, and (E) Natural mordenite from Hicknoi, New Zealand; the sample contains small amounts of quartz impurities.
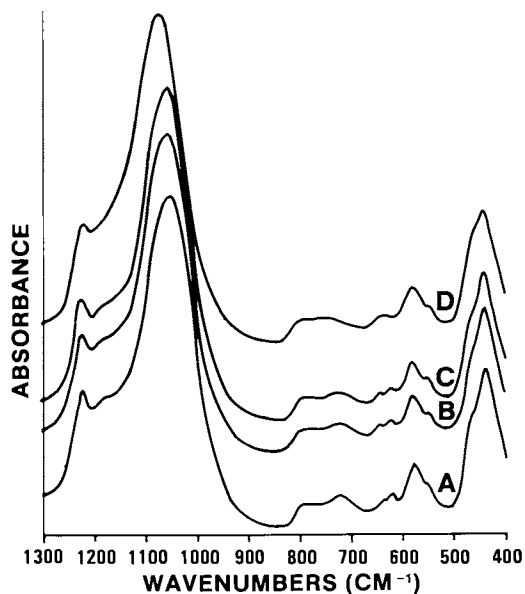
Figure 6. Mid infrared spectra of faulted mordenite (sample No. 2) crystals: (A) (Na,K,TOA)-Mordenite, (B) (Na,K)-Mordenite, (C) NH$_4$-Mordenite and (D) H-Mordenite. This sample contains small amounts of feldspar impurities.
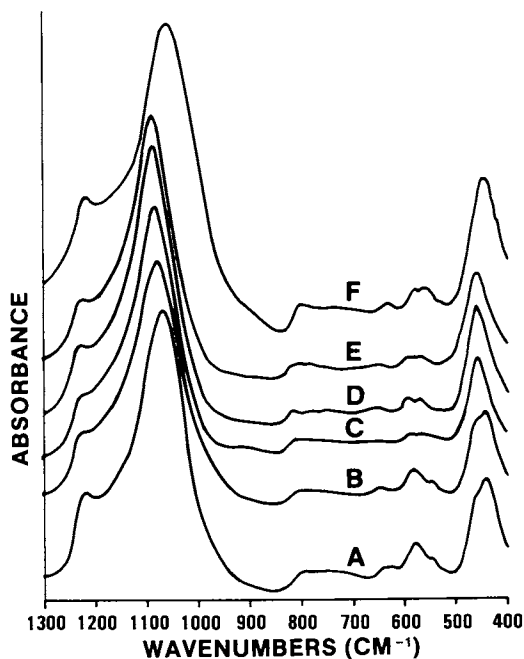
Figure 7. Mid infrared spectra of several mordenites (see Table
I) in their H-form: (A) Sample No. 2; (B) Sample No. 3; (C) Sample
No. 4; (D) Sample No. 5, (E) Sample No. 6 and (F) Zeolon 900.

tetrahedra, respectively. Bands at 750-820 cm^{-1} represent symmetric stretching of external Al-O and Si-O linkages in double 6-rings (D6R) and in double 4-rings (D4R) units (3).

In Table II, the asymmetric stretching band at about 1215-1225 cm^{-1} is typical of zeolites containing 5-membered rings, (5-7) and in analogy to the assignments made by Jacobs and coworkers, (5) bands at 545-585 cm^{-1}, and at 630-650 cm^{-1} are also attributed to external vibrations of double 5-rings (D5R) units. The pentasil structure sensitive band at 550 cm^{-1} is shifted to 546 cm^{-1} probably because of the low SiO_2/Al_2O_3 ratio. The frequency dependence of framework vibrations on the Si/Al ratio for bands in the mid-infrared region has been discussed by Datka and coworkers (8). In weakly faulted mordenites, this band is observed between 578 and 582 cm^{-1}. The weak absorption band at about 580 cm^{-1} seems to be unaffected by the different SiO_2/Al_2O_3 ratios.

Bands between 620 and 650 cm^{-1} in mordenite are present as weak shoulders (at about 615 cm^{-1}) in the pentasils studied. Similarly, the structure sensitive band at ∿546 cm^{-1} in the pentasils is present as a weak shoulder in mordenite, Figures 2-4. Therefore, the band at 550 cm^{-1} is diagnostic of the presence of mainly D5R units containing nearly parallel 5R units (Type A blocks (7)) whereas bands at 575-580 cm^{-1} and 625-630 cm^{-1} indicate the presence of D5R units containing puckered 5R units in the envelope mode (Type B blocks, ref. 7). Furthermore, results in Figure 4 show that an x-ray amorphous material (sample 11, Table I) gives a spectrum similar to that of silica gel which differs from a spectrum of a fully crystallized pentasil only because it lacks bands at about 580 and 1220 cm^{-1}, Figure 4E. Thus, these two structure sensitive bands could prove useful in monitoring the extent of the crystallization reaction also during the synthesis of these TOA-containing pentasils (6, 9, 10).

MID IR spectra do not distinguish between ZSM-5 and ZSM-11 crystals (5), see Figure 4. However, as observed in zeolites belonging to the offretite-erionite family (11), mid-infrared results may prove useful in studying the existence of faulting or phase impurities in mordenite crystals. The high surface area mordenites (samples No. 4,5 and 6) with similar electron diffraction patterns (1) also have IR spectra very similar to each other (Figures 7C-7E) and to samples of weakly faulted, commercially available, large-port mordenites like Norton's Zeolon 900 (and Laporte's Laposil-3000). In contrast, spectra from sample No. 2 and 3 contain a much stronger band between 580 and 585 cm^{-1} with a shoulder at ∿545 cm^{-1}, see Figures 5-7. In addition, the low frequency band shifts to ∿440 cm^{-1} from ∿458 cm^{-1} and bands at 800 and 1180 cm^{-1} broaden. After NH_4-exchange and calcination, the two weak bands in the 600-650 cm^{-1} region broaden and overlap and the band at about 722 cm^{-1} becomes a very weak shoulder, Figure 6D; however, the aforementioned spectral differences are still evident, Figures 6 and 7. In addition to being faulted, Sample No. 3 (Table 1) probably contains some occluded material thus explaining its low (293 m^2/g) surface area (ref. 1).

Electron microscopy examination of the two mordenites, samples 2 and 3, along the (okl) orientation revealed the existence of streaks (Figures 1D and 1B) due to faulting (1) as commonly seen in

natural mordenite crystals. Diffraction patterns are of the type previously described by Sanders (2) who concluded that natural mordenite contained linear faults. However, MID-IR spectra of the two (faulted) synthetic mordenites more closely resemble that of a sample of a natural mordenite containing feldspar and ferrierite impurities (Figure 5A) than that of a sample of a relatively pure and faulted natural mordenite, see Figure 5E. Therefore, the aforementioned spectral differences in the 500-600 cm^{-1} regions are probably due to phase impurities and intergrowths. Small amounts of feldspar and (quartz) impurities have been observed in the x-ray diffractogram of this mordenite sample (1). Furthermore, the relatively intense band at ~585 cm^{-1} can be obtained by adding 10-20% feldspar crystals (orthoclase, $KAlSi_3O_8$) to a fault-free synthetic mordenite like Laporte's Laposil-3500.

Shifts to lower frequencies in the T-0 bending band region (420-550 cm^{-1}) seem to be fairly independent of the zeolite's SiO_2/Al_2O_3 ratio:

	Heavily Faulted		Weakly Faulted Mordenites			
	Sample 2	Sample 3	Sample 4	Sample 5	Sample 6	Laposil
SiO_2/Al_2O_3	10.6	9.5	13.3	10.4	16.9	20.5
ν_{T-0} (cm^{-1})	441	440	458	457	458	459

Thus, the position of the T-0 bending band near or below 440 cm^{-1} correlates well with the presence of faults in these synthetic and natural mordenite crystals, see Table II.

Stretching Vibrations. All H-mordenites after rehydration and degassing in vacuo at 200°C/1h show a broad IR band in the 3500-3800 cm^{-1} region containing two partially resolved bands at 3609 and 3632 cm^{-1} and a broad shoulder at ~3720 cm^{-1}, Figure 8. After degassing at 500°C/1 h in vacuo, the high frequency (h.f.) band increases relative to the intensity of the bands at 3632 and 3609 cm^{-1}; at 500°C, some Si-0-Si bonds could break, thus forming new SiOH groups, Figure 9. Karge (12), for an H-mordenite sample with SiO_2/Al_2O_3 = 8.54, reported similar results and observed bands at 3735, 3650 and 3610 cm^{-1}. Ghosh and Curthoys (13), in their study of dealuminated mordenites, reported OH stretching bands at 3609 and 3738 cm^{-1}, together with a weak band at 3650 cm^{-1}. The stretching vibration band at 3735 cm^{-1} was attributed to surface Si-OH groups while the low frequency (l.f.) bands at 3610 and 3650 cm^{-1} were assigned to Si-OH-Al groups located in the large 12-membered ring channels and in the smaller side channels, respectively (12). On the basis of relative band intensities, it can be said, at least in a qualitative sense, that OH-density in the main channels is somewhat lower than in the smaller channels, see Figure 9. Protonated TOA, because of its size, is probably limited to charge compensate Al(IV) only in the main channels where it is believed that, because of its size, it can promote isomorphous substitution of Na^+Al^{+3} and K^+Al^{+3} with Si^{+4} ions generating, in this way, siliceous mordenite crystals.
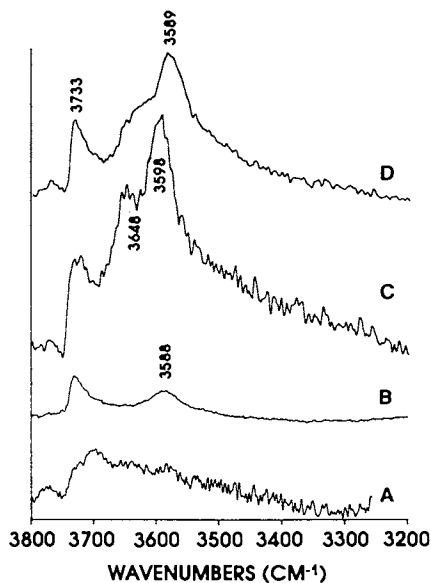
Figure 8.   Hydroxyl absorption bands for several mordenites in their H-form after drying in vacuo at 200°C/2h. (A) Sample No. 2, (B) Sample No. 4, (C) Sample No. 5 and (D) Sample No. 6.
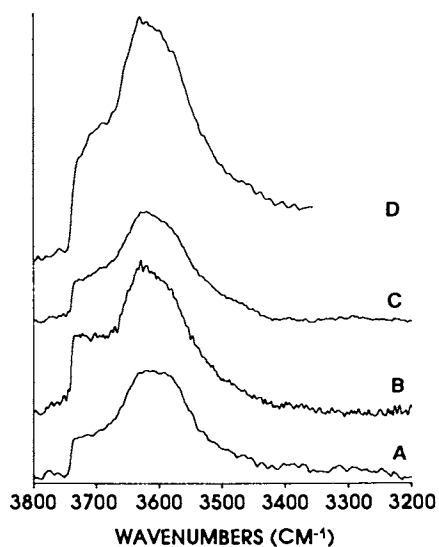
Figure 9.   Hydroxyl absorption bands of several H-mordenites after drying in vacuo at 500°C/2h: (A) Sample 2, (B) Sample 4, (C) Sample 5 and (D) Sample 6.

After washing and drying at 200°C, the (Na,K,TOA) ZSM-5 crys-
tals give a non-descriptive spectra in the OH-region with a broad
band between 3670 and 3730 cm^{-1}, Figure 10A. Heating in air at
500°C generates two well defined bands at about 3720 and 3588 cm^{-1}
attributed to surface SiOH and bridging SiOH-Al groups generated
during the oxidative decomposition of occluded TOA, Figure 10B. The
appearance of a sharp band at ∿3720 cm^{-1} after calcination, suggests
the formation of SiOH groups due to the presence of surface SiO$^-$-
$(C_8H_{17})_3NH^+$ groups in these crystals. Following NH_4^+-exchange and
calcination, the intensity of the l.f. band increases significantly
and a new band appears at ∿3648 cm^{-1} which decreases in intensity on
heating at 500°C, Figures 10C-10D. Similar results have been
observed with TOA-containing pentasils of the ZSM-11 type, Figure
11.

In their H-form, all the pentasils studied show (after rehy-
dration and degassing at 200°C/1h in vacuo) three OH-stretching
bands at 3600, 3650 and 3734 cm^{-1}, Figure 12. Heating at 500°C (1h,
in vacuo) decreases band intensity significantly and the two l.f.
bands shifts toward lower values, Figure 13. In contrast, the SiOH
band at ∿3733 cm^{-1} becomes sharper and more intense probably because
of the breakage of additional Si-O-Si linkages.

Bands at about 3600, 3660 and 3720 cm^{-1} in the OH-stretch
region of HZSM-5 crystals with SiO_2/Al_2O_3 ratio equal to 38.2 and
23.6 have been reported by several workers (14-16). In contrast,
Jacob and von Ballmoos (17) reported IR-spectra of pentasils con-
taining only one type of hydroxyl group vibrating at 3600 cm^{-1} and
suggested that additional bands (at ∿3720 cm^{-1}) result from the
presence of impurities. Guanlin Qin and coworkers (18) have pro-
posed instead that the intensity of the 3720 cm^{-1} band depends on
synthesis conditions and on crystallite sizes. Kazansky et al. (14)
have attributed the l.f. band in HZSM-5 to Si-OH-Al groups contain-
ing only silicon atoms in their second coordination sphere. Heating
above 547°C an HZSM-5 (with SiO_2/Al_2O_3 = 60) a band at 3680 cm^{-1}
appeared which was assigned to stretching vibration of Al-OH groups
resulting from aluminum removed from the crystal lattice (14).

Pyridine Sorption. After pyridine sorption and degassing in vacuo
at 200°C (to remove physisorbed pyridine), the intensity of the
OH-stretch bands decreased and the l.f. band in both mordenites and
pentasils disappeared. Bands at about 3635-3665 cm^{-1} were almost
unaffected by pyridine. In the 200-500°C temperature range, pyri-
dine removal (as well as dehydroxylation) occurred with partial
restoration of band's intensity. At 500°C, most of the pyridine was
removed and spectra with OH stretching bands typical of the calcined
samples were obtained.

Spectra of chemisorbed pyridine show, as expected, bands
characteristic of Bronsted (B, at 1542 cm^{-1}) and of Lewis (L, at
1453 cm^{-1}) acid. Ghosh and Curthoys (13) reported an additional
Lewis band at 1462 cm^{-1} in dealuminated mordenites degassed above
400°C; this band was not observed in any of the siliceous H-
mordenites (containing Al(VI)) examined in this study, lending some
support to the correlation between the 1462 cm^{-1} band and the
existence of hydroxyl nests in the crystal lattice proposed by these
authors (13).
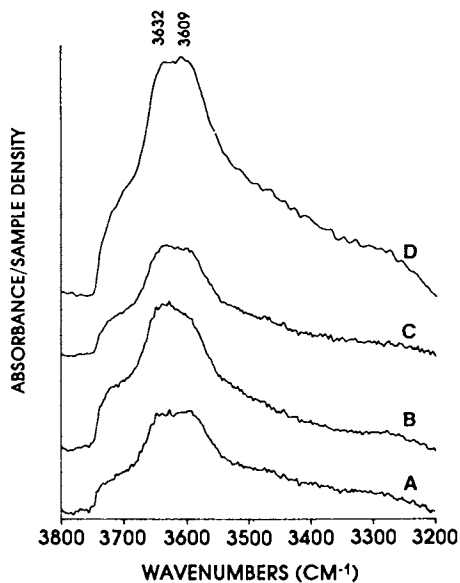
Figure 10. Hydroxyl absorption bands for (Na, K, TOA)-ZSM-5 (Sample No. 10, Table I) after (A): crystallization and drying at 100°C/24h and (B) calcination in air at 500°C/10h; bands of the crystals in their H-form degassed at 200°C and 500°C/1h are shown in (C) and (D), respectively.
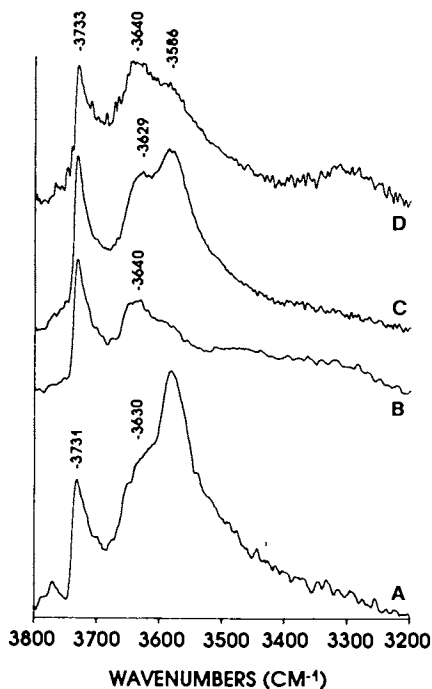
Figure 11. Hydroxyl absorption bands for (Na,K,TOA)-ZSM-11 (Sample No. 10, Table I) after: (A) crystallization and drying at 100°C/24h and (B) calcination in air at 500°C/10h; bands of the crystals in their H-form degassed at 200°C and 500°C/1h are shown in (C) and (D), respectively.
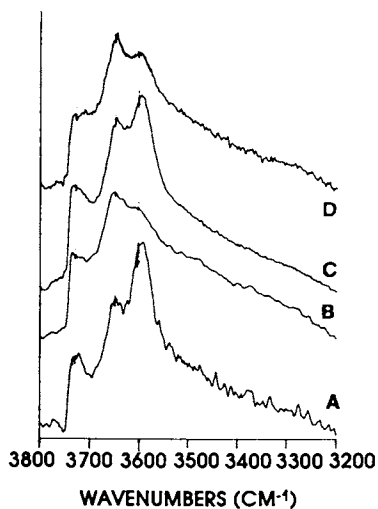
Figure 12. Hydroxyl absorption bands for several pentasils in their H-form after drying in vacuo at 200°C: (A) Sample No. 10; (B) Sample No. 7; (C) Sample No. 8; and (D) Sample No. 9.
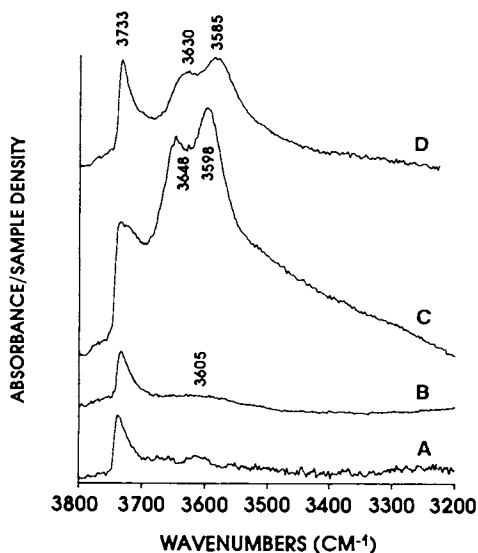
Figure 13. Hydroxyl absorption bands of several pentasils in their H-form after drying in vacuo at 500°C: (A) Sample No. 10; (B) Sample No. 7; (C) Sample No. 8; and (D) Sample No. 9.

Acidity was examined from pyridine desorption measurements in the 200-500°C temperature range, results are given in Figure 14. Acid site density (as measured from the integrated absorbance at 1542 and 1453 cm^{-1}) decreased with increasing SiO_2/Al_2O_3 ratio in the H-mordenites. However, acid sites strength increased with the crystal's SiO_2/Al_2O_3 ratio. Thermodesorption of pyridine from Bronsted acid sites was more facile than from Lewis sites and at 500°C, pyridine was retained mainly on Lewis acid centers. In mordenites synthesized in the presence of TOA, the SiO_2/Al_2O_3 ratio has little effect on the relative distribution of B and L acid sites and the B/L ratio monotonically decreased with desorption temperature.

Silicon-29 and Aluminum-27 NMR. Results from NMR analyses of all the crystals studied have been collected in Table III and representative silicon-29 and aluminum-27 NMR spectra shown in Figures 15-19. With the exception of analcime (Sample 1) and magadiite (Sample 13), resonances observed at about -99, -106 and -113 ppm have been assigned to silicon atoms present in Si[2Al], Si[1Al] and Si[0Al] units, respectively, (19-23). Of the zeolites under study, analcime is the richest in aluminum content with a measured Si/Al ratio of 2.4 (chemical analysis). Its silicon-29 spectrum consists of five signals at -86.3, -91.7, -97.1, -102.8 and -107.6 ppm that may be assigned to Si[4Al], Si[3Al], Si[2Al], Si[1Al] and Si[0Al] units, respectively (Figure 15A). The Si/Al ratio calculated from the relative signal intensities computes to 2.1, in close agreement with chemical analysis. A natural sample of analcime (from San Bernardino, CA) gave a very similar Silicon-29 spectrum and a calculated Si/Al ratio of 2.5.

The Silicon-29 spectrum of Magadiite, the most siliceous member of the group, on the other hand, shows two well resolved peaks at -101.5 and -111.8 ppm (Figure 15F). While the peak at -111.8 ppm represents silicon atoms within the layers and sharing all its four oxygen atoms with neighboring SiO_4 tetrahedra, the downfield resonance at -101.5 ppm is attributed to $Si(SiO_4)_3OH$ groupings with the OH group pointing towards the interlamellar space (24,25). The observed 1:3 intensity ratio of the two peaks $[Si(SiO_4)_3OH:Si(SiO_4)_4]$ is in agreement with Pinnavaia's results (24). The disappearance of the downfield peak upon calcination at 500°C is accompanied by a substantial broadening of the signal at -112.2 indicating loss of the hydroxyl groups due to siloxane bridges forming between adjacent layers.

Inspection of the calculated Si/Al ratios for most of the fresh materials show that they are in reasonably good agreement with chemical analyses data (Table III). Furthermore, aluminum-27 MAS NMR spectra show only a single signal at about 52 ppm corresponding to the presence of lattice Al(IV) atoms. Evidence for the presence of possible impurities such as $NaAlO_2$ (normally seen at ~77 ppm), dehydroxylated $Al(OH)_3$ or x-ray amorphous gel could not be found in any of the spectra examined. Thus, all the aluminum atoms are probably in tetrahedral coordination and directly incorporated in the zeolite lattice framework; only minor amounts of Si-OH defects (26-28) exist in these TOA containing crystals. In the case of sample 4, (Na,TOA) mordenite, the calculated Si/Al ratio is 5.6 if
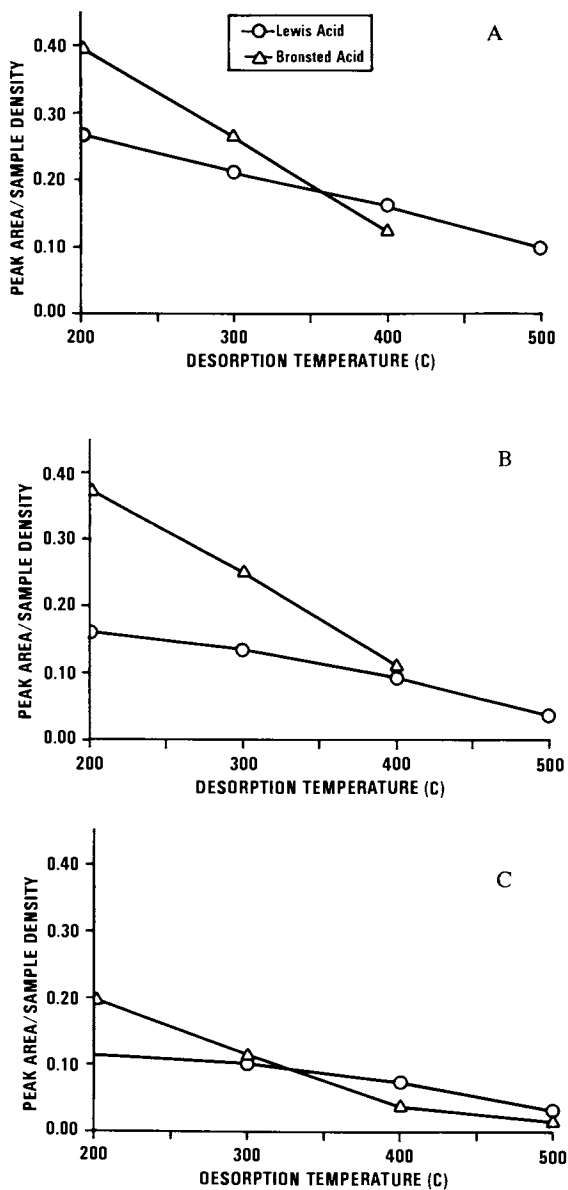
Figure 14. Acid sites strength in several mordenite and pentasil crystals. (A) Sample 2, (B) Sample 5, (C) Sample 4. Continued on next page.
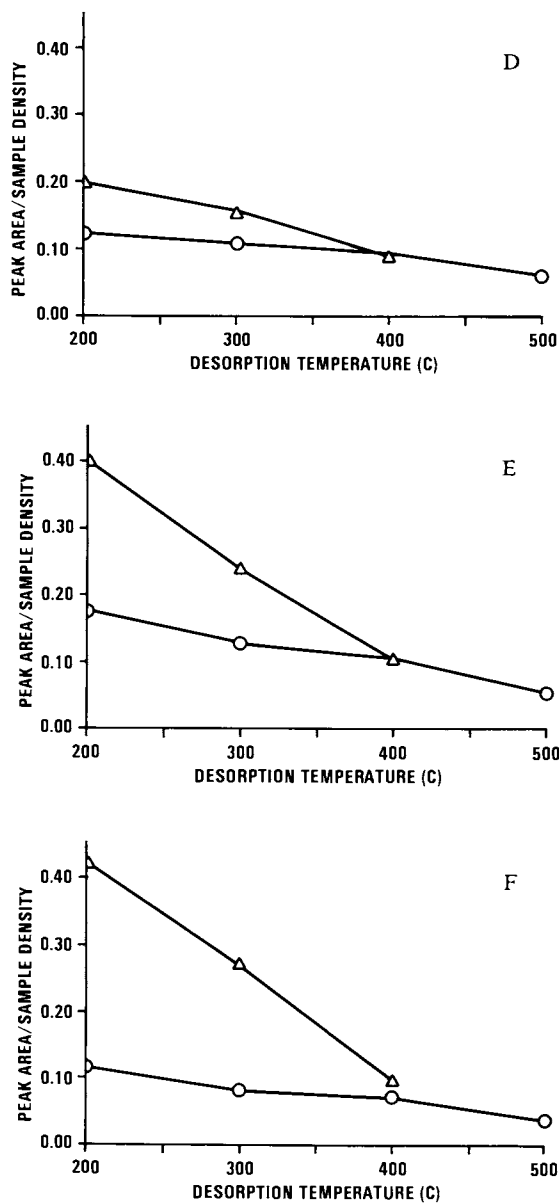
Figure 14. Continued. Acid sites strength in several mordenite and pentasil crystals. (D) Sample 6, (E) Sample 8, (F) Sample 10.
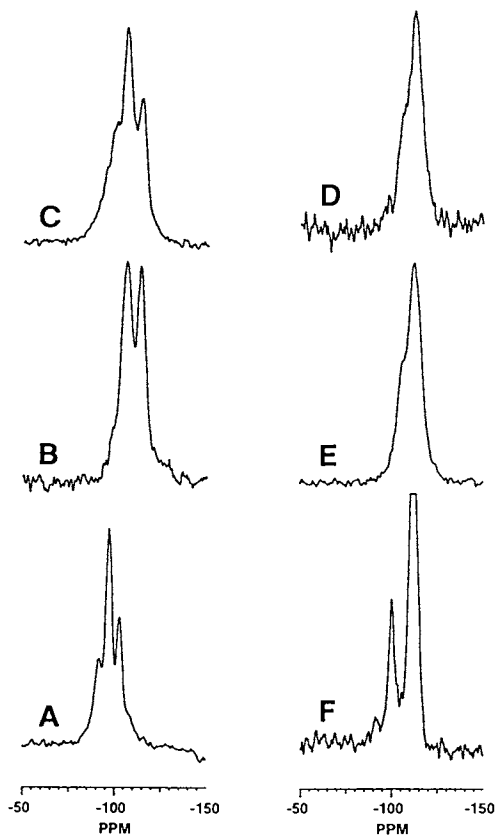
Figure 15. Silicon-29 spectra of: (A) Analcime, (B) (Na,K,TOA)-Mordenite, (Sample No. 4) unfaulted; (C) (Na,K,TOA)-Mordenite, faulted (Sample No. 2); (D) (Na,K,TOA)-ZSM-11 (Sample No. 8), (E) (Na,K,TOA)-ZSM-5 (Sample No. 9) and (F) Magadiite.
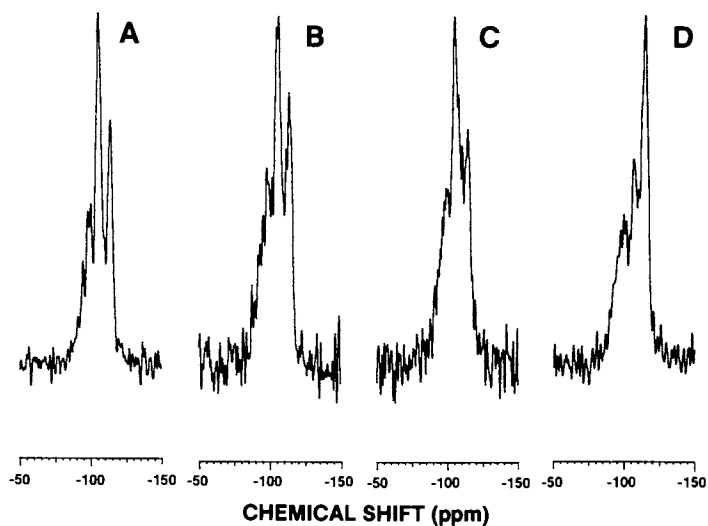
Figure 16. Silicon-29 MAS NMR spectra of a sample of faulted mordenite (Sample No. 2): (A) (Na,K,TOA)-Mordenite, (B) (Na,K)-Mordenite, (C) NH$_4$-Mordenite and (D) H-Mordenite.
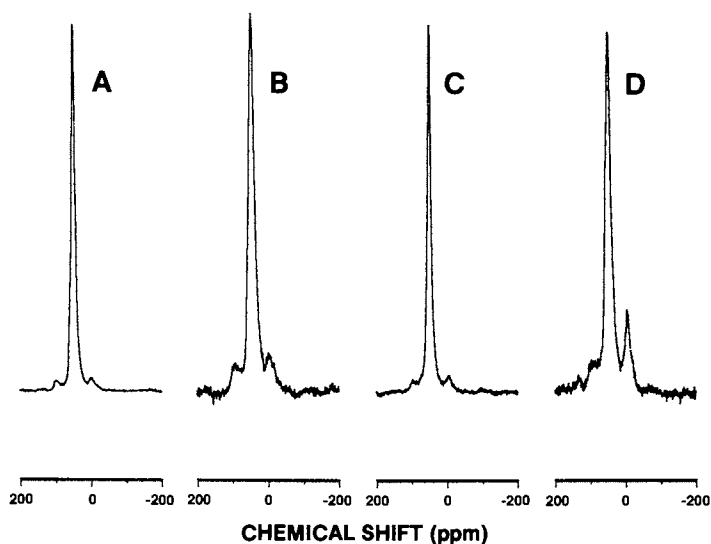
Figure 17. Aluminum-27 MAS NMR spectra of a sample of faulted mordenite (Sample No. 2): (A) (Na,K,TOA)-Mordenite, (B) (Na,K)-Mordenite, (C) NH$_4$-Mordenite and (D) H-Mordenite.
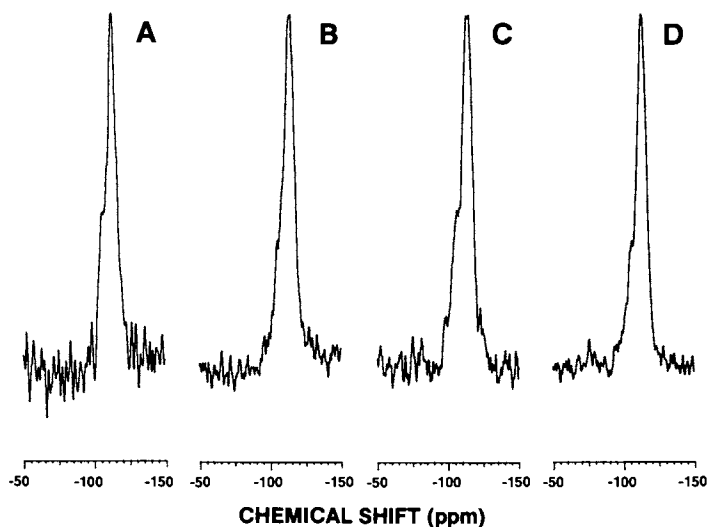
Figure 18. Silicon-29 MAS NMR spectra of: (A) (Na,K,TOA)-ZSM-11,
(B) (Na,K)-ZSM-11, (C) (NH$_4$)-ZSM-11 and (D) H-ZSM-11.
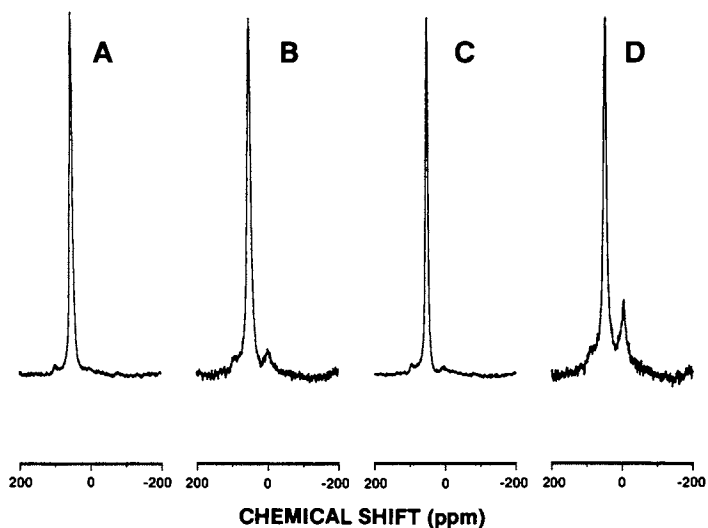
Figure 19. Aluminum-27 MAS NMR spectra of: (A) (Na,K,TOA)-ZSM-11,
(B) (NA,K)-ZSM-11, (C) NH$_4$-ZSM-11 and (D) H-ZSM-11.

TABLE III: SILICON-29 AND ALUMINUM-27 NMR DATA

S.N.	Crystal Type[a]	Silicon-29 Chemical Shifts (Rel. % Intensities)					Si/Al		Al-27 Chem. Shift	Al-27 Line-widths	Al(IV)/Al(VI)
		Si[4Al]	Si[3Al]	Si[2Al]	Si[1Al]	Si[0Al]	NMR	Chem.			
1	(Na,K)-Analcime	-86.3 (4)	-91.7 (21)	-97.1 (42)	-102.8 (24)	-107.6 (9)	2.1	2.4	N.A.	N.A.	N.A.
2	(Na,K,TOA)-Mordenite	-85.0(5)[a]	-90.0 (7)[a]	-98.4(19)[a,b]	-105.8 (37)	-114.2 (32)	3.4[a]	5.3	50.9	809	0
3	(Na,K,TOA)-Mordenite	-	-	98.0(11)	-105.9 (44)	-113.4 (45)	6.0[a]	4.8	N.A.	N.A.	N.A.
3	H-Mordenite	-	-92.0[a]	-96.0[a]	-107.3 (10)	-114.2 (90)	42.1[a]	---	53.3	1359	0.24
4	(Na,TOA)-Mordenite	-	-	-98.8 (8)	-106.3 (56)[c]	-113.9 (36)	6.6[a]	6.7	52.5	728	0.0
4	H-Mordenite	-	-	-	-106.0 (21)[c]	-113.4 (79)	19.2	---	52.8	744	0.19
5	(Na,K)-Mordenite	-	-	-98.0(16)	-106.3 (42)[c]	-113.7 (42)	5.4	5.2	52.6	728	0.0
5	H-Mordenite	-	-	-	-106.0 (12)[c]	-113.5 (88)	34.5	---	52.5	1052	0.32
6	H-Mordenite	-	-	-	-106.0 (12)[c]	-113.6 (88)	33.3	---	53.1	728	0.45
	Zeolon-900	-	-	-98.0(18)	-106.2 (31)	-113.5 (51)	6.1	8.5	52.3	728	0.10
8	(Na,K,TOA)-ZSM-11	-	-	-99.0 (8)[d]	-106.0 (23)[c]	-112.0 (69)[d]	10.4	10.7	52.6	647	0.0
8	(Na,K)-ZSM-11	-	-	-	-106.0(26)[c]	-112.2 (74)	15.4	---	51.9	841	0.07
8	NH-ZSM-11	-	-	-	-106.0(26)[c]	-113.7 (74)	15.4	---	53.0	550	0.0
8	H-ZSM-11	-	-	-	-106.0(15)[c]	-112.5 (85)	27.0	---	51.6	809	0.38
9	(Na,K)-ZSM-11[e]	-	-	-98.0(10)[d]	-106.0 (21)	-112.7 (69)[d]	9.9	10.1	53.7	582	0.0
9	H-ZSM-11	-	-	-98.0 (2)	-107.1 (9)	-113.1 (89)	30.8	---	51.2	874	0.28
10	(Na,K,TOA)-ZSM-5	-	-	-98.0 (8)	-106.7 (14)[c]	-113.3 (78)	13.3	14.1	52.5	663	0.0
10	H-ZSM-5	-	-	-	-106.0 (13)[c]	-113.5 (77)	29.6	---	52.5	647	0.35
(g)	H-ZSM-5	-	-	-	-106.0 (19)[c]	-113.1 (81)	21.0	30.0	53.7	485	0.0
12	Magadiite	-	-	-	-101.5 (25)[f]	-111.8 (75)	---	---	No signal		---
12	Magadiite (500°C)	-	-	-	-	-112.2 (h)	---	---	No signal		---

(a) See text for discussion; (b) broad featureless peak seen downfield of this signal; ~-106 ppm; (c) broad low intensity shoulder; (d) multiple (2-5) shoulders observed; (e) seeded; (f) assigned to Si [SiO$_4$]$_3$OH unit (see text); (g) Mobil's HZSM-5; (h) broad.

signal contribution from all three peaks is considered. Ignoring the contribution from the weak resonance at -98.8 ppm (assuming it arises from a SiOH group), however, gives a calculated Si/Al ratio of 6.6 in close agreement with the chemical analyses result of 6.7. Similar analyses of these crystals in their H-form clearly reflect the extent of dealumination. This is further corroborated by the presence of an additional resonance in the corresponding aluminum-27 MAS NMR spectra at about 0 ppm derived from extra lattice aluminum formed after calcination of the NH_4-exchanged zeolites. The calculated Si/Al ratios of these samples are presented with a cautious reservation since the 4 sec recycle delay employed may not always be sufficient to overcome long silicon-29 T_1's that highly siliceous materials sometimes possess (29).

The two heavily faulted mordenites (Samples 2 and 3) gave a calculated Si/Al ratio different from that obtained from chemical analyses (Table III). Both samples displayed a single resonance at about 52 ppm in their corresponding aluminum-27 spectrum. Besides the expected silicon-29 resonances at -98.4, -105.8 and -114.2 ppm, Sample 2 displayed a broad signal envelope that extended almost up to -85 ppm (Figure 15C). A total of 8 overlapping peaks had to be co-added to simulate the experimental spectrum resulting in the calculated Si/Al ratio of 3.4. Gaussian transformation resolved additional peaks at -94.7, -100.4 and -109.8 ppm (Figure 16A). In its H-form, crystals gave silicon-29 signals at -96.8, 100.7, -106.2, -108.3, -112.8, -114.4 and -119.3 ppm (Figure 16D). Dealumination in this sample is evidenced by a marked decrease in the silicon-29 signal intensity at -106.2 ppm and by the appearance of a new signal at ∿0 ppm in the corresponding aluminum-27 spectrum that gives rise to a Al(VI)/Al(IV) ratio of ∿0.24 (Figures 16D-17D). The silicon-29 signals observed at -112.8 and -114.4 ppm could be assigned to T_1 and T_4 sites (19). Resonances for T_2 and T_3 sites (expected at ∿-115 ppm) however remained unresolved.

While the calculated Si/Al ratio of 6.0 for Sample 3 is higher than chemical analysis, signals downfield of -98 ppm were not observed. In its H-form, this mordenite, however, showed two weak resonances at -92 and -96 ppm. The electron diffraction pattern of both samples indicate the presence of faults. More experiments, including CP studies, are necessary to possibly correlate NMR results with structural differences in mordenite crystals. An alternate explanation for the observed discrepancies is the presence of phase impurities (30). In fact, a sample of natural mordenite containing 10-15% feldspar (and 20-30% ferrierite) gave a silicon-29 NMR spectrum closely resembling that obtained from Sample 2. All other mordenites gave consistent results (Table III). The commercial H-mordenite sample (Norton Zeolon 900) not only showed the least dealumination but also afforded a relatively sharp extra framework Al(VI) signal at ∿0 ppm reflecting a high symmetry about these aluminum atoms.

The use of silicon-29 MAS NMR to distinguish between ZSM-5, ZSM-11 and silicalite structures has been the subject of several publications (23,27,31,32). A resonance at about -105 ppm has been attributed to Si(1Al) units. The presence of Si-OH defect sites gives a resonance at about -103 ppm which could interfere with this signal often resulting in a decrease in the calculated Si/Al ratio

(26,28). Though 6-7 overlapping peaks were needed to simulate the
experimentally observed spectra, the calculated Si/Al ratio seem to
agree quite closely with chemical analyses (Table III).   Longer
silicon-29 T_1's in dealuminated zeolites could, however, increase
discrepancies in these values (see Sample g, Table III).   Compared
to the well resolved resonances obtained in the case of highly
siliceous (Si/Al >1000) pentasils (23), only three resonances from
Si(OA1) units could be resolved (by resolution enhancement) at
-109.5, -112.4 and -116.7 ppm for (Na,K,TOA)-ZSM-11 crystals (Sample
number 8, Figure 18). The low Si/Al ratio of the HZSM-5 and HZSM-11
samples precluded their ready distinction.   In all cases, evidence
for dealumination in the corresponding aluminum-27 NMR spectra were
observed only in crystals in their H-form.   Comparing the line
widths of all the fresh pentasils, the narrowest signals are seen
from Mobil's (Na, TPA)-ZSM-5 (485 Hz) and Sample no. 9 (582 Hz)
which contained no TOA. Samples nos. 8, and 10 displayed relatively
broader peaks.
     The aluminum-27 spectra of some ZSM-11 crystals after various
thermal pretreatments are shown in Figure 19.   All crystals exhibit
a resonance at ∿50 ppm corresponding to framework tetrahedral
aluminum atoms; only when in its H-form, the ZSM-11 shows evidence
for the presence of excluded non-framework aluminum by exhibiting an
additional signal at ∿-3 ppm; Figure 19D.   Inspection of the
corresponding line widths shows that (Na,K,TOA)-ZSM-11 and
(NH_4)-ZSM-11 have relatively narrow lines (e.g. ∿809 and ∿744 Hz)
compared to (Na,K)-ZSM-11 and H-ZSM-11 which are ∿1327 Hz (see Table
III).   While Debras et al (33) reported an opposite trend in their
study of mordenite crystals, Engelhart et al (26) described a
similar observation for ZSM-5. This signal broadening is attributed
to heat induced symmetry distortion about the observed aluminum
atoms.

Summary

Siliceous mordenite crystals (with 9 < SiO_2/Al_2O_3 < 20) and Al-rich
pentasils (with 20 <SiO_2/Al_2O_3 <30) have been synthesized from
trioctylamine (TOA) containing hydrogels.   Crystallization is
favored by the presence of Al and gels with high SiO_2/Al_2O_3 ratio
crystallize into magadiite instead of forming silicalite.   The
presence of TOA generates irregularly shaped (hydrophobic) crystals
which facilitate the forming of these zeolites into extrudates with
the crush strength resistance required for catalytic evaluation in
pilot-plant units (1).

Electron diffraction patterns indicate that heavily and weakly
faulted mordenite crystals were obtained; weakly faulted mordenites
patterns resemble those of commercially-available large port
mordenites. The absence of odd order spots or streaks in the h00
rows of the ZSM-11 diffraction pattern has been taken as evidence of
the presence of ZSM-11 crystals essentially free from ZSM-5
intergrowths. The (Na,K,TOA)ZSM-5 crystal morphology is different
from that of typical (Na,TPA)ZSM-5; the relative lengths of straight
and tortuous channels are interchanged (1).

Mid infrared spectra do not distinguish between pentsils and mordenites; however, it proved useful in indicating the presence of phase impurities. Furthermore, shifts to lower frequencies (below 440 cm^{-1}) in the T-O bending region correlate well with the presence of faults in both synthetic and natural mordenite crystals.

After NH$_4$-exchange and calcination in air, all H-mordenites (after rehydration and degassing in vacuo at 200°C/1h) show a broad IR band in the 3500-3800 cm^{-1} region containing two partially resolved bands at 3609 and 3632 cm^{-1} and a broad shoulder at ∿3720 cm^{-1}. Similarly (in their H-form), the pentasils studied show three OH-stretching bands at 3600, 3650 and 3734 cm^{-1}. The high and low frequency bands have been attributed to vibration of surface SiOH and bridging SiOH-Al groups, respectively. Bands in the 3625-3655 cm^{-1} region are believed to represent stretching vibrations of Al-OH groups resulting from extra framework aluminum generated during the activation step. As expected, spectra of chemisorbed pyridine contained both bands characteristic of Bronsted and Lewis acid sites with pyridine thermodesorption being more facile from Bronsted acid centers. Thus, at high temperature (500°C), pyridine is retained mainly on Lewis acid sites. Whereas acid site density decreased with the crystals SiO$_2$/Al$_2$O$_3$ ratio, acid site strength (as inferred from pyridine retention with temperature) increased.

Aluminum-27 NMR spectra show that after crystallization, all the TOA-containing zeolites exhibit a well resolved resonance at ∿50 ppm, corresponding to framework Al(IV) atoms. However, following NH$_4$- exchange and calcination in air at 500°C, a new band appears at about 0 ppm due to Al(VI) resulting from aluminum removed from the crystal lattice. In general, calculated Si/Al ratio from silicon-29 NMR data are in reasonable agreement with chemical analysis results. Thus, all the aluminum atoms in these siliceous mordenite and Al-rich pentasils are believed to be in tetrahedral coordination and incorporated into the zeolite lattice.

References

1. Occelli, M. L., Pollack, S. S., and Sanders, J. V. in "Innovation in Zeolite Material Science" Symposium, Nieuwpoort, Belgium (1987), in press.
2. Sanders, J. V., Zeolites, 5, 81, 1985.
3. Flanigen, E. M., Khatami, H. and Szymanski, H. A., Adv. Chem. Ser., 1971, 101,201.
4. Flanigen, E. M., "Zeolite Chemistry and Catalysis," J. A. Rabo, Ed.; Am. Chem. Soc., Washington, D.C. 1976, 80.
5. Jacobs, P. A., Beyer, H. K. and Valyon, J., Zeolites, 1981, 1, 161.6. Coudurier, G., Naccache, C. and Vedrine, J. C., J. Chem. Soc., Chem. Comm., 1982, 1413.
7. Jansen, J. C., van der Gaag, F. J. and van Bekkum, H., Zeolites, 1984, 4, 379.
8. Datka, J., Geerkings, D., Mortier, W. and Jacobs, P., J. Phys. Chem. 89, 3483 (1985).
9. Jacobs, P. A., Derouane, E. G. and Weitkamp, J., J. Chem. Soc. Chem. Comm. 591 (1981).

10. Scholle, K. F. M. G. J., Veeman, W. S., Frene Ken, P. and Van der Valden, G. P. M., Appl. Catal.
11. Occelli, M. L., Iyer, P. S., Walker, J. S. and Gerstein, B. C., Zeolites (1987) to be submitted.
12. Karge, H., Z. Phys. Chem. Neue Folge 76, 133 (1971).
13. Ghosh, A.K. and Curthoys, G., J. Chem. Soc., Farad. Trans. 1, 79, 805 (1983).
14. Kazansky, V.B., Kustov, L.M. and Borovkov, V. Yu, Zeolites, 3, 77, (1983).
15. Vedrine, J. C., et al., J. Catal, 59, 248 (1979).
16. Topsoe, N. Y., Pedersen, K. and Derouane, E. G., J. Catal, 70, 41 (1981).
17. Jacobs, P. A., and Ballmoos, R. V., J. Phys. Chem., 86, 3050 (1982).
18. Qin, G., Zheng, L., Xie, Y. and Wu, C., J. Catal, 95, 609 (1985).
19. Bodart, P.; Nagy, J. B.; Debras, G.; Gabelica, Z.; Jacobs, P., Phys. Chem., 90, 5183 (1986) and references therein.
20. Thomas, J. V.; Khinowski, J., Adv. Catalysis, 33, 199 (1985).
21. Hays, G. R.; E&P, W. A. Rain, Alma, N. C. M.; Couperus, P. A.; Huis, R.; Wilson, A. E., Zeolites, 4, 377 (1984).
22. Debras, G.; Nagy, J. B.; Gabelica, Z.; Bodard, P.; Jacobs, P. A., Chem. Lett., 199, (1983).
23. Fyfe, C. A.; Kokotailo, G. T.; Kennedy, G. J.; Schutter, C. D. E., JCS. Chem. Comm., 306, (1985).
24. Pinnavaia, T. J. et al, J. Solid State Chem. 63, 118 (1986).
25. Rojo, J. M., Sauz, J., Ruiz-Hitzky, E. Serratosa, J. M., Z. Anorg. Allg. Chem. 540,227 (1986).
26. Engelhart, G.; Fahlke, B.; Magi, M.; Lippmaa, Z. Phy. Chimie, 266, 239 (1985).
27. Nagy, J. B.; Gabelica, Z.; Derouane, E. G.; Jacobs, P. A., Chem. Lett, 2003 (1982).
28. Nagy, J. B.; Gabelica, Z.; Derouane, E. G., Chem. Lett., 1105 (1982).
29. van de Ven, L. J. M.; Post, J. G.; van Hoof, H. C.; de Haan, J. W., ICS, Chem. Comm., 214 (1985).
30. Kirkpatrick, R. J.; Kinsey, R. A.; Smith, K. A.; Henderson, D. M.; Oldfield, E., Am. Mineralogist, 71, 712 (1986).
31. Fyfe, C. A.; Gobbi, G. C.; Kennedy, G. J.; Chem. Lett., 1551, 1555 (1983).
32. Fyfe, C. A.; Kennedy, G. J.; Kokotailo, G. T.; Lyerla, J. R.; Fleming, W. W., J. C. S. Chem. Comm., 740 (1985).
33. Debras, G.; Gourque, A.; Nagy, N. B.; Clippeleir, G. De; Zeolites, 6, 161 (1986).

Chapter 17

Effect of NaOH, TPAOH, and TPABr Concentration on the Growth Rate and Morphology of Silicalite-1

D. T. Hayhurst [1], R. Aiello [2], J. B.Nagy [3], F. Crea [2], G. Giordano [2], A. Nastro [2], and J. C. Lee [1]

[1]Department of Chemical Engineering, Cleveland State University, Cleveland, OH 44115
[2]Dipartimento di Chimica, Università della Calabria, Arcavacata di Rende, 87030 Rende (CS), Italy
[3]Laboratory of Catalysis, Center for Advanced Materials Research, Facultés Universitaires Notre Dame de la Paix, Rue de Bruxelles 61, B–5000 Namur, Belgium

The influence of NaOH, TPAOH and TPABr on the formation of silicalite-1 was studied using the reaction batch mixture
$xM_2O-yTPABr-100SiO_2-1000H_2O$ where M was either Na or TPA, x ranged from 0.5 to 4.0 and y ranged from 0.5 to 16. Reactions were carried out at 170C in unstirred teflon-lined autoclaves. For all runs, silicalite-1 was the only phase found to crystallize. TPA ions were found to have both a structure-directing and space-filling role. At low initial TPA concentrations $(TPA/100SiO_2<4.0)$, crystallization stopped when TPA was exhausted from the reaction mixture. For changes in base concentration (either NaOH or TPAOH), the rates of crystal growth and crystal morphology were found to be strong functions of hydroxide concentration. As the hydroxide content of the reaction mixture was reduced, the aspect ratio (length/width) of the crystals increased from 1.0 for $4M_2O$ to 6.7 for $0.5M_2O$. Additionally, for synthesis runs made without sodium, both nucleation and crystallization occured more rapidly. From these results, some insights into the crystallization mechanism are proposed.
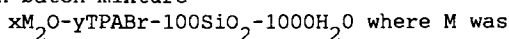
Reports on the roles played by individual reaction components in the synthesis of ZSM-5 and silicalite are abundant. Aiello et al. (1-3) and Nastro et al. (4) have reported on the role of alkali$_+$ cations in ZSM-5 synthesis. The structure directing role of Na$^+$ and other alkali cations in the formation of ZSM-5 has also been

investigated (5-9). Reports on the synthesis of ZSM-5 without the addition of an organic template have also appeared in the literature (10-16); although the addition of an organic appears to be required for the synthesis of silicalite-1 (14,17,18).

Even though the structure-directing role played by each of these reactants has been investigated extensively, reports on their effect on the crystal size and morphology of ZSM-5 and silicalite have been much more limited. Fegan and Lowe (19) have reported that the size and morphology of silicalite vary with system alkalinity. They observed that the crystals produced in batch mixtures of lower alkalinity were relatively larger than those formed at higher alkalinity and were elongated. Aspect ratios (length/width) were reported to vary from 1.0 to 2.5. Kuehl (20) has also reported that crystals formed at low pH are more elongated.

The objective of this study was to systematically vary the concentrations of NaOH, TPAOH and TPABr in the synthesis of silicalite-1 and to evaluate how these changes affect the crystal size, morphology and growth rate. A simple reaction system was chosen (xM_2O-$yTPABr$-$100SiO_2$-$1000H_2O$ where M was either Na^+ or TPA^+) using compositions known to crystallize only silicalite-1. From these results, a mechanism for silicalite crystallization is proposed.

EXPERIMENTAL

Materials. The two silicas used in this study were a precipitated silica (BDH Ltd.) containing 0.1 wt.% Na_2O and 1.0 wt.% H_2O and Ludox AS-40. The remaining materials were a 30 wt.% NaOH solution reagent grade (Erba), tetrapropylammonium bromide, 99% purity (Fluka, AG) and tetrapropylammonium hydroxide, 20% in water (Fluka, AG).

Synthesis. Silicalite was prepared from three different reaction batch mixtures. The first used sodium hydroxide as the alkali source. It had the general formula (oxide basis) xNa_2O-$8TPABr$-$100SiO_2$-$1000H_2O$ where x was varied from 0.5 to 4.0 (S-series). To evaluate the effect of sodium on silicalite crystallizaiton, a second batch mixture using TPAOH as the alkali source was also tested. It had the formula $yTPA_2O$-$(8-2y)TPABr$-$100SiO_2$-$1000H_2O$ where y was varied from 0.5 to 4.0 (T-series).

In the third series, the amount of template was varied (B-series). The formula for this series was $1.4Na_2O$-$zTPABr$-$0SiO_2$-$1000H_2O$ where z was varied from 16 to 0.5. For most runs, the precipitated silica was used as the silica source. The suffix A is added to the run number of those syntheses using Ludox AS-40. Specific batch compositions for each run are listed in Table 1.

For each composition tested, the following experimental protocol was followed. Water and TPABr were combined with mixing until the salt was dissolved. This was followed by the addition of either the NaOH or TPAOH. To this solution, silica was added with agitation until a uniform gel was formed. The gel was rapidly

transferred into a series of 35ml teflon-lined Morey-type
autoclaves. The vessels were sealed and placed into a
forced-convection oven preset to 170±2C. The mixtures were allowed
to react quiescently. At predetermined times, the vessels were
removed from the oven. The contents were washed a minimum of four
times with 10ml aliquots of distilled water using a Buchner funnel.
After washing, samples were dried overnight at 110C. Prior to SEM
and chemical analysis, product crystals were separated from
unreacted gel using a sonication procedure as outlined elsewhere
(16).

Table 1. Batch Compositions for the B-, S-. and T- Series with

$$XNa_2O-YTPA_2O-ZTPABr-100SiO_2-1000H_2O$$
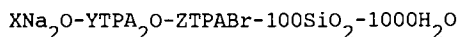
Run No.	$X(Na_2O)$	$Y(TPA_2O)$	$Z(TPABr)$
B-16	1.4	0	16
B-8	1.4	0	8
B-4	1.4	0	4
B-2	1.4	0	2
B-1	1.4	0	1
B-0.5	1.4	0	0.5
S-4	4	0	8
S-2	2	0	8
S-1	1	0	8
S-0.5	0.5	0	8
T-4	0	4	0
T-2	0	2	4
T-1	0	1	6
T-0.5	0	0.5	7

Analysis. Product materials were tested for degree of
crystallinity by powder x-ray diffraction, using $CuK\alpha_1$ radiation.

The instrument was a Philips Model PW1730/10 x-ray generator
equipped with a PW1050/70 vertical goniometer. Diffractograms were
measured for the as-synthesized product; that is, zeolite plus gel.
The percent crystallinity was determined using a peak-height
analysis software routine developed by Phillips. Morphology and
crystal size were determined by scanning electron and optical
microscopy. The electron microscope was an AMRay Model 1200B.
     Thermal analysis (DTA) was performed both on the dried
unreacted gel and on the product crystals to determine water and
TPA content. Measurements were made using a NETZSCH Model STA 409
thermogravimetric analyzer. Samples were scanned from 30 to 700C
at a rate of 10C/min. under a 10ml/min. flow of dry nitrogen.
Details of the experimental protocol are listed elsewhere (21).
     The sodium content of the fumed silica and the product
crystals were determined using atomic absorption (Perkin-Elmer
Model 380 AA). The protocol was to digest approximately 100mg of
the sample with four drops of conc. (96%) H_2SO_4 and 2ml. of 48% HF

solution. The mixture was heated in an open polyethylene beaker to
60C overnight to eliminate the HF. The digested zeolite solution
was diluted to an appropriate concentration and then analyzed for
sodium using the precalibrated spectrophotometer.

RESULTS AND DISCUSSION

     The crystallization curves for the different systems are
illustrated in Figure 1. Both crystallization rates and induction
periods are influenced by the alkalinity (S and T series), TPA
concentration (S and B series) and the presence of sodium (S and T
series). A summary of crystallization and induction rates is
listed in Table 2. Higher crystallization rates and shorter
induction periods are obtained at higher TPA concentrations (B
series) and at higher alkalinity (S series) while the presence of
sodium in the reaction mixture increases the time required for both
nucleation and crystallization (S and T series). In addition, the
crystallization stops when one of the system components (TPA or
OH^-) is exhausted. For example, crystallization stops in the
B-series for low initial TPABr concentrations. From Figure 1, it
appears that silicalite stops crystallizing when TPA is consumed by
the reaction; that is, when the limit of 4TPA/u.c. (as reported by
Lok (22)) is reached. For the B-series at high initial TPABr
contents and for series S and T at low initial OH^- concentrations,
complete crystallization is never achieved. This is because the
amount of OH^- in the reaction solution is below that required for
complete silica dissolution (Fig. 1 and Table 2); therefore,
complete reaction of the silica to silicalite-1 is impossible.

        Table 2. Crystallization Rate, Induction Period, Sodium And TPA
                        Content per Unit Cell

SAMPLE	CRYSTALLIZATION RATE ($\%x1/h$)	INDUCTION PERIOD(h^{-1})	Na^+ per u.c.	TPA^+ per u.c.
B - 16	4.5	5	0.35	3.9
B - 8	3.1	6	0.40	4.2
B - 4	2.2	12	0.35	4.1
B - 2	1.2	17	0.50	3.9
B - 1	0.7	23	0.40	4.0
B - 0.5	0.2	24	0.45	3.8
S - 4	5.3	6	2.10	3.8
S - 2	1.8	17	0.57	3.9
S - 1	0.4	25	0.25	3.9
S - 0.5	0.05	100	0.2	--
T - 4	9.4	4	1.19	3.8
T - 2	6.0	10	0.52	3.9
T - 1	1.4	14	0.15	3.8
T - 0.5	0.2	40	0.08	3.5
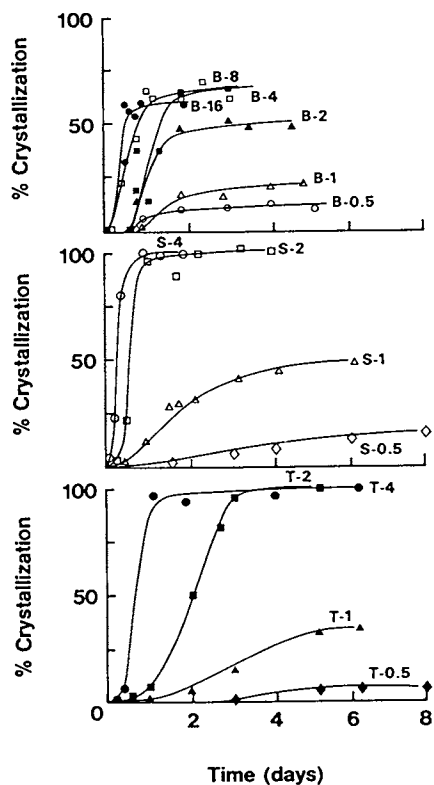
Figure 1. X-ray crystallization curves for synthesis made with varying TPABr (B—series, top), with varying sodium hydroxide (S—series, middle), and with varying TPAOH, no sodium (T—series, bottom). (Reproduced with permission from Ref. 7. Copyright 1986 Kokansha-Elsevier.)

The dimensions of the silicalite which is crystallized are strongly influenced by changes in reactant concentrations (Fig. 2 and 3, Table 3). These differences are most pronounced in the aspect ratios (i.e. length/width) of crystals synthesized. Aspect ratios were found to differ considerably for the S- and T-series where the alkalinity was varied over an extensive range. For constant alkalinity, a rather constant aspect ratio is observed (B-series). Constant values of aspect ratios were observed for batches with identical alkalinities but where the source of silica was changed from precipitated silica to Ludox. High aspect ratios have been reported previously for silicalite crystallized at low alkalinities (19,20).

The differences observed in aspect ratios should correlate directly with crystallization rates measured separately for crystal length and width. These rate data are summarized in Table 3.

Table III. Average Product Dimension and Growth Rate for All Synthetic Runs (The suffix A in the sample number indicates runs made using Ludox AS-40 as the silica source)

SAMPLE Number	CRYSTAL SIZE(μm) Length	Width	ASPECT Ratio(L/W)	GROWTH RATE (μm/h) Length(R_L)	Width (R_W)
B-16	18	10	1.8	1.2	0.7
B-8	32	16	2.0	1.1	0.6
B-4	50	26	1.9	1.1	0.5
B-2	50	25	2.0	1.3	0.8
B-1	60	30	2.0	1.0	0.5
B-0.5	75	28	2.7	1.3	0.6
S-4	12	13	0.9	1.0	1.2
S-2	74	30	2.5	1.5	1.0
S-1	160	37	4.3	1.7	0.4
S-0.5	100	15	6.7	1.0	0.2
T-4	17	15	1.1	2.2	1.8
T-2	47	28	1.7	2.2	1.4
T-1	78	25	3.1	2.1	1.4
T-0.5	101	15	6.7	1.2	0.1
S-4A	17	15	1.1		
S-2A	30	15	2.0		
S-1A	43	10	4.3		
S-0.5A	94	10	9.4		
T-4A	60	45	1.3		
T-2A	43	22	2.0		
T-1A	53	15	2.9		
T-0.5A	65	10	6.5		
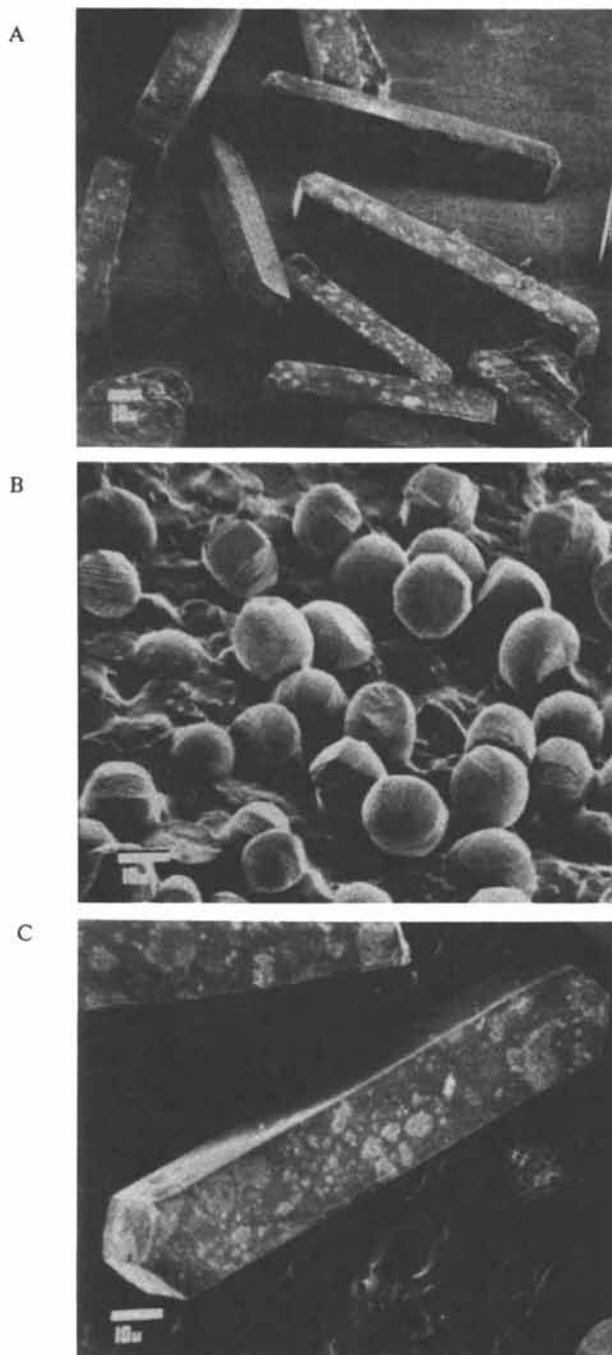
Figure 2. Scanning electron micrographs of silicalite produced from all three series. (A) S-0.5, (B) S-4.0, (C) T-0.5. Continued on next page.
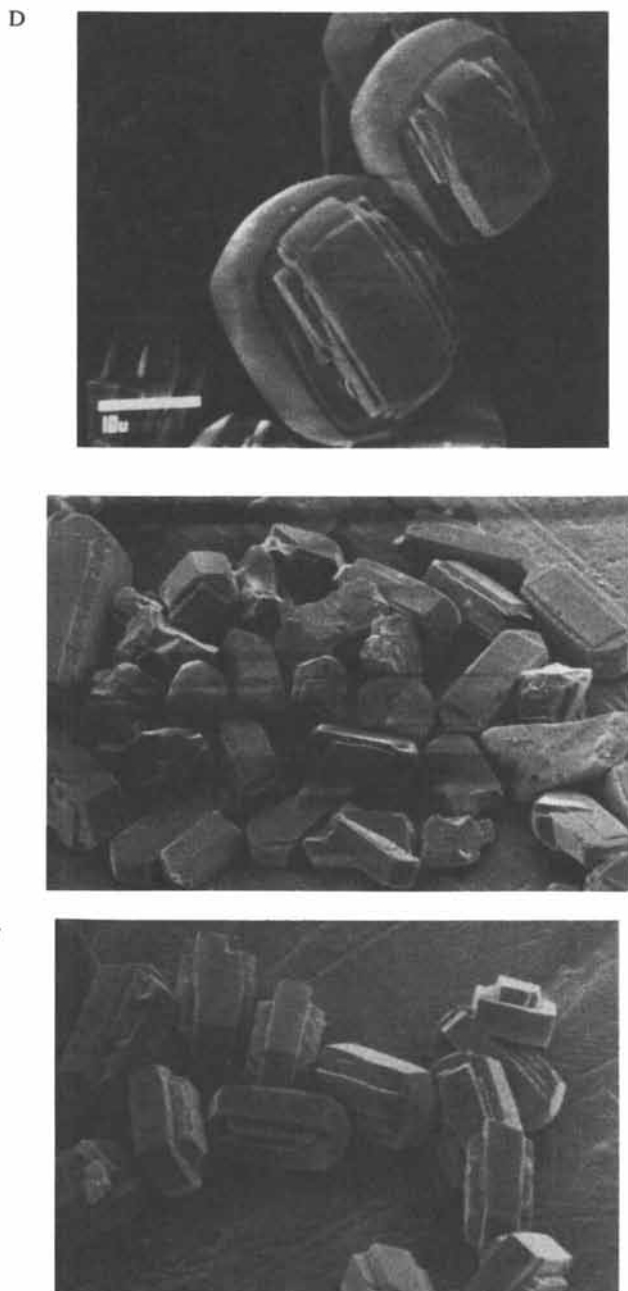
Figure 2. Continued. Scanning electron micrographs of silicalite
produced from all three series. (D) T-4.0, (E) B-0.5,
(F) B-16.
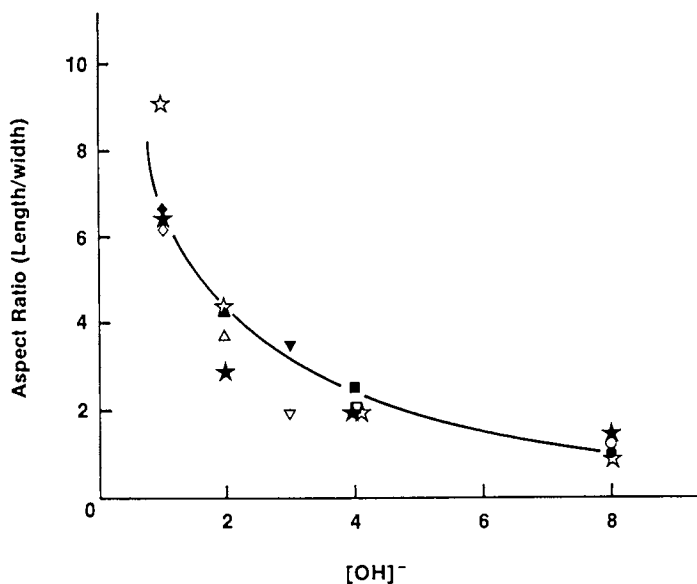
Figure 3. Aspect Ratios of Silicalite synthesized
(T-series ◇ △ □ ○, S-series ◆ ▲ ■ ●,

B-series ▼ ▽ ,   TA-series ☆ SA-series ★).

It should be noted that the crystallization rate for the length (R_L) is essentially independent both of the TPA concentration (B and T series) and the OH concentration (S and T series). The crystal width growth rate, (R_w) however, is strongly dependent on the OH^- concentration. All these data can be rationalized if one accepts a model of silicalite formation which is based on the condensation of double five-membered rings (D5R) as depicted in Figure 4. Groenen et al. (23) has shown that under conditions favoring ZSM-5 synthesis, double five-rings are stabilized in the solution containing TPA cations. It is hypothesized that these D5R units can then condense into chains which then link together to form the silicalite structure. A perfect structure comprising 96 tetrahedral sites, however, cannot be obtained from direct condensation of these D5R's and chains. Van Santen et al. (7) have indicated that as many as 16 empty tetrahedra (T-site) per idealized unit cell, $(Si_{96}O_{192})$ can occur upon chain condensation. One missing T-site corresponds to four $SiOR^+$ (where $R^+ = H^+$, Na^+ or TPA^+) groups. These missing sites will result in about 64 SiOR groups per unit cell. Such large numbers of defect sites have not been reported to date. Nevertheless, recent work has clearly shown that as high as 30-40 defect SiOR groups can be obtained for low aluminum ZSM-5 zeolites (24,25). During the formation of silicalite, it therefore must be necessary to eliminate about half of the approximate 64 SiOR sites.

Figure 4 shows that the growth of the D5R chain is along C-axis. This axis corresponds to the longest of the crystal axes (26). The rate of crystal growth along this axis is independent of both TPA and OH concentrations. It may, therefore, be assumed that the concentration of D5Rs in solution is always high enough to achieve similar a condensation rate. It is also clear from Figure 4 that the increase in crystal width corresponds to growth along the a-axis (i.e. "along" the zig-zag channels, Fig. 4B). This increase is made by condensing the preformed D5R-chains (Fig. 4a) and by replacing (at least in part) the missing T-sites with free silanols. It is the rate of growth along the a-axis that depends on the OH content. This process can be considered as filling the missing T-sites with monomeric silicate species. Indeed, it is rather well known that the concentration of monomeric species increases with increasing alkalinity (27) and this should favor the rate of condensation of the D5R-chains along the a-axis.

Figure 5 illustrates the DTA curves for gels prepared from $TPAOH-100SiO_2-1000H_2O$ (Fig. 5A), $Na_2O-TPABr-100SiO_2-1000H_2O$ (Fig. 5B), $NaBr-TPABr-100SiO_2-1000H_2O$ (Fig. 5C) and for the corresponding final silicalite-1 samples (Fig. 5D for S-series and 5E for T-series). As can be seen from this figure, the gel obtained in absence of Na ions is quite different from that obtained in its presence. In the former case (Fig. 5A), an endotherm is obtained at approximately 160C. This peak can be attributed to TPA-silicate, where the TPA group is fully hydrated. Gabellica et al. (28) and B.Nagy et al. (29) have assigned an endotherm peak at about 135C to TPA ions acting as counter-ions to negative charges. These charges result from the presence of Al in gels which form
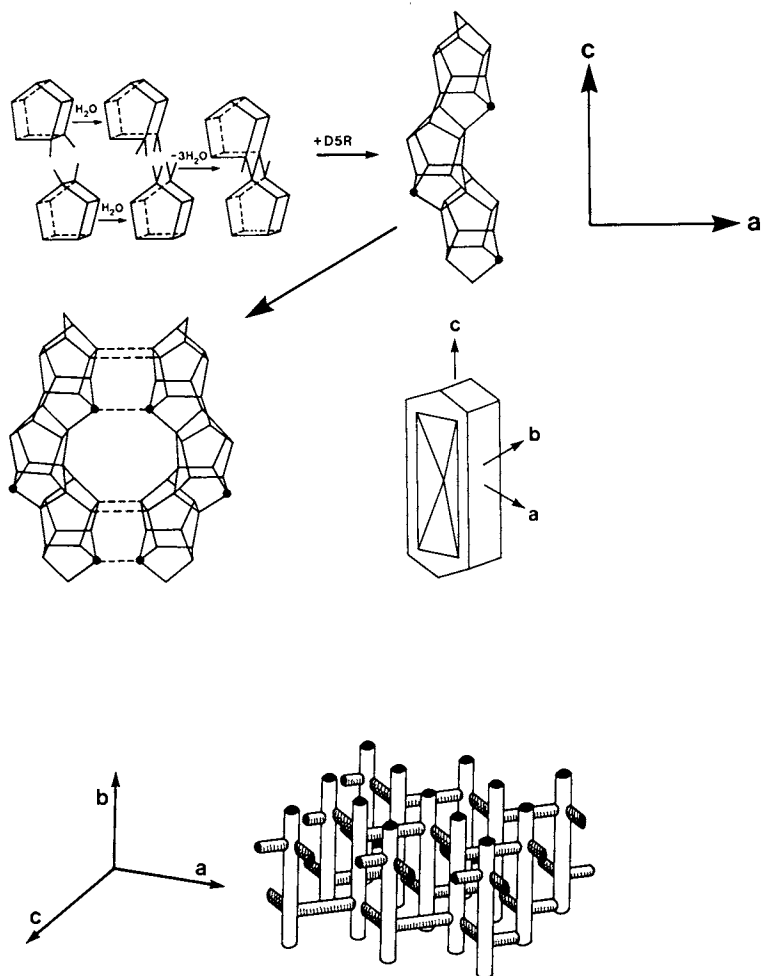
Figure 4. Model for the growth of silicalite from D5R (adapted from Ref. 25, 28)
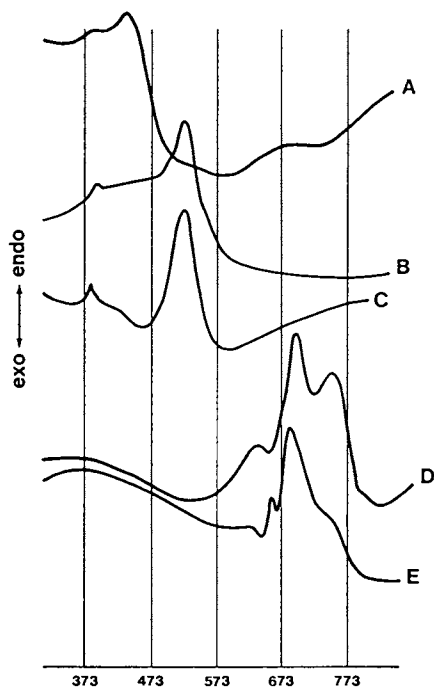
Figure 5.   DTA curves for A. TPAOH-100SiO$_2$-1000H$_2$O gel,
            B. Na$_2$O-TPABr-100SiO$_2$-1000H$_2$O gel, C.

            NaBr-TPABr-100SiO$_2$-1000H$_2$O gel, D. Silicalite

            from S-series, E. Silicalite from T-series.

ZSM-5. For gels containing sodium (Fig. 5B and 5C) a peak at 240C is obtained. This peak is characteristic of both monomeric and crystalline TPAOH, and it is the only one detected in the gel containing TPABr in the presence of Na. The small endotherms at 110C in this system (Fig. 5B and 5C) show clearly the presence of crystalline TPABr (28). Note, that in the final crystalline product (Fig. 5D and 5E), the DTA peaks are similar for both the S- and T-series. This indicates that the state of TPA ions is essentially identical in these silicalite-1 samples. These occluded TPA ions have been shown to be counter-ions to SiO$^-$ defect groups (25,30).

The presence of hydrated TPA$^+$ silicate in the T-series is quite interesting, as the crystallization rate is consistently higher for the T-series than for the S-series where sodium is also included in the gel. It was shown previously that monomeric TPA ions may lead to the formation of ZSM-5 zeolites (30,31), and that the concentrations of TPA ions required to crystallize ZSM-5 is indeed much higher in the sodium-free system. Sodium has also been shown to reduce the rate of ZSM-5 crystallization. This is due in part to the preferential formation of sodium silicate, which leads to the formation of dense structures (29). Moreover, the hydrophillic interaction of sodium with the precursor silicate gels has an inhibiting effect on the formation of the hydrophobic silicalite framework. The results emphasize the dual role of TPA ions both in their structure directing and space-filling functions.

CONCLUSIONS

Results presented in this report represent a comprehensive, systematic study on the effects of NaOH, TPAOH and TPABr addition on the synthesis of silicalite-1. From these data, the following conclusions may be drawn. First, the length to width (aspect) ratio of silicalite increases with decreasing alkalinity of the reaction mixture. This ratio is in reasonable agreement with the growth rate ratios for the crystal length (R_L) and width (R_w).

Similar results have been reported by other investigators (19,20). Secondly, the rates of nucleation and crystallization are lowered by the addition of sodium to the reaction mixture. This suggests that the presence of highly hydrophillic sodium cations may interfere with the formation of the hydrophobic silicalite structure. Thirdly, the incorporation of TPA into the silicalite structure is independent of hydroxide concentration and is near the theoretical limit of four molecules per unit cell as reported by Lok et al. (22). In fact, crystallization of silicalite ceases prematurely when the amount of TPA in the initial batch mixture falls below four per unit cell. Finally, results from this study support the crystallization mechanism proposed by van Santen et al. (7), and provide a reasonable explanation of the variations observed in crystal morphology with changes in reaction mixture alkalinity.

LITERATURE CITED

1. Aiello, R.; Nastro, A.; Colella, C. Proc. 17th Natl.
    Cong. Inorg. Chem., 1984, p 339.
2. Nastro, A.; Colella, C.; Aiello, R. Stud. Surf. Sci. Catal.
    1985, 24, 39.
3. Aiello, R.; Crea, F.; Nastro, A.; Pellegrino, C. Chimica ed
    Ingegneria dei Nuovi Materiali, 1986, p 97.
4. Aiello, R.; Crea, F.; Nastro, A.; Pellegrino, C.
    ZEOLITES 1987, 7, 549.
5. Grose, R.W.; Flanigen, E.M. U.S. Patent 4 257 885, 1981.
6. Liang, J. Stud. Surf. Sci. Catal. 1985, 24, 611.
7. van Santen, R.A.; Keysper, J.; Ooms, J.; Kortbeek, A.G.T.G.
    In Proc. 7th Int. Zeolite Conf., "New Developments in
    Zeolite Science and Technology"; Murakami, Y. et al., Eds.;
    Kokansha-Elsevier: Tokyo, 1986; p 169.
8. Dai, F.Y.; Suzuki, M.; Takahashi, H.; Saito, Y. ibid., p 223.
9. Tianyou, S.; Ruren, X.; Liyun, L.; Zhaohui, Y. ibid., p 201.
10. Hayhurst, D.T.; Lee, J.C. ibid., p 113.
11. Gabelica, Z.; Blom, N.; Derouane, E.G. Appl. Catal.
    1983, 5, 227.
12. Erdem, A.; Sand, L.B. J. Catal. 1979, 60, 241.
13. Erdem, A.; Sand, L.B. In Proc. Fifth Int. Conf. Zeolites;
    Rees, L.V.C., Ed.; Heyden: London, 1980; p 64.
14. B.Nagy, J.; Bodart, P.; Collette, H.; ElHage-AlAsswad, J.;
    Gabelica, Z.; Aiello, R.; Nastro, A.; Pellegrino, C. in
    preparation.
15. B.Nagy, J.; Bodart, P.; Collette, H.; Gabelica, Z.;
    Nastro, A.; Aiello, R. in preparation.
16. Nastro, A.; Gabelica, Z.; Bodart, P.; B.Nagy, J.
    Stud. Surf. Sci. Catal. 1984, 19, 131.
17. Grose, R.W.; Flanigen, E.M. U.S. Patent 4 061 724, 1977.
18. Bodart, P. Ph.D. Thesis, Facultes Universitaires de Namur:
    Namur, 1985.
19. Fegan, S.G.; Lowe, B.M. J. Chem. Soc. Faraday Trans. 1
    1986, 82, 785.
20. Kuehl, G.H. European Patent Application 93519, 1983.
21. Gabelica, Z.; Gilson, J.P.; Debras, G.; Derouane, E.G.
    Proc. 7th ICTA, 1982, p. 1203.
22. Lok, B.M.; Cannon, T.R.; Messina, C.A. ZEOLITES 1983, 3, 282.
23. Groenen, E.J.J.; Kortbeek, A.G.T.G.; Mackay, M.;
    Sudmeijer, O. ZEOLITES 1986, 6, 403.
24. Debras, G.; Gourgue, A.; B.Nagy, J.; De Clippeleir, G.
    ZEOLITES 1986, 6, 161.

25. B.Nagy, J.; Bodart, P.; Collette, H.; ElHage-AlAsawad, J.; Gabelica, Z.; Aiello, R.; Nastro, A.; Pellegrino, C. in preparation.

26. Price, G.D.; Pluth, J.; Bennett, J.M.; Patton, R.L.; J. Am. Chem. Soc. 1982, 104, 5971.

27. Harris, R.K.; Knight, C.T.G.; Hull, W.E. in Soluble Silicates; Falcone Jr., J.S., Ed.; ACS Symposium Series No. 194; American Chemical Society: Washington, DC, 1982; p 73.

28. Gabelica, Z.; B.Nagy, J.; Bodart, P.; Dervalle, N.; Nastro, A. ZEOLITES 1987, 7, 67.

29. B.Nagy, J.; Bodart, P.; Gabelica, Z.; Derouane, E.G.; Nastro, A. In Proc. 7th Int. Zeolite Conf., "New Developments in Zeolite Science and Technology"; Murakami, Y. et al., Eds.; Kokansha-Elsevier: Tokyo, 1986; p 231.

30. ElHage-AlAsawad, J.; Devalle, N.; B.Nagy, J.; Hubert, R.A.; Gabelica, Z.; Derouane, E.G.; Crea, F.; Aiello, R.; Nastro, A. in preparation.

Chapter 18

Stability and Ion-Exchange Capacity of Natural Sedimentary Zeolites in Acidic Solutions

R. M. Carland[1] and F. F. Aplan[2]

[1]Indusmin, Spruce Pine, NC 28777
[2]Mineral Processing Section, Pennsylvania State University, University Park, PA 16802

The stability of four natural sedimentary zeolites in acidic solutions (pH 0.75-5) was found to be
mordenite > clinoptilotite > erionite > chabazite.
Their ability, however, to extract Cu^{2+} from these same acidic solutions was
erionite $\geq$ chabazite > clinoptilolite >> mordenite.
Contact with acidic solutions (pH 4) removed significant quantities of Na^+ and Si^{4+}, lesser amounts of K^+ and Fe^{+n} and only small amounts of Al^{3+} and Ca^{2+} from the erionite sample. The cation exchange capacity of the natural erionite sample for Cu^{2+} was improved substantially by elution with Na^+ salts or by a pretreatment in hot NaCl.

Large quantities of sedimentary zeolites are known in the western United States ($\underline{1}$). One of the more attractive of their potential uses is as an inexpensive, cation-exchange material for metals in environmental improvement. This use includes the removal of heavy metal ions from acid mine-drainage waters and the treatment of industrial waste solutions. Inasmuch as solutions containing unprecipitated heavy metal ions are typically acidic, the stability of zeolites in an acidic environment is an important consideration in evaluating their potential as a cation exchanger in such systems.

The most common of the natural sedimentary zeolites found in the United States in mineable quantities are chabazite, clinoptilolite, erionite, and mordenite ($\underline{2}$). Many crystalline zeolites decompose in acids, although mordenite and, to a lesser extent, erionite have been reported to be stable in acid solutions ($\underline{3}$). The goal of this research was to evaluate the stability and cation-exchange capabilities of these common, natural, sedimentary zeolites in acidic solutions. The basic concepts of zeolite ion-exchange, usually emphasizing synthetic zeolites, may be found elsewhere ($\underline{3-6}$); several studies of cation exchange by natural zeolites are also available ($\underline{7-10}$).

EXPERIMENTAL MATERIALS AND METHODS

The zeolite samples used here (see Table I) were collected in the field by R. H. Olson (Golden, CO), F. A. Mumpton (SUNY-College at Brockport, NY), and one of the authors. The mineralogy of the raw samples was determined by X-ray diffraction (XRD) and confirmed by petrographic microscope studies. The amount of the zeolite present after contact with acid was determined from the diminution of two characteristic XRD peaks for the sample in question. The values selected were unique to each zeolite in the specific mineral assemblage under study. The evaluation was facilitated by use of XRD data for natural zeolites and their associated gangue minerals assembled by F. A. Mumpton (SUNY-Brockport, unpublished data). Because the crystallinity of a given zeolite type may vary from deposit to deposit, a highly purified zeolite fraction was prepared from each source by sizing and specific gravity beneficiation methods. Its purity was determined by optical microscopy, and the sample was used as an internal standard. This purified fraction was mixed with varying proportions of glass (amorphous to X-rays), and a standard composition vs. peak height curve developed. The procedure was simplified because, with the exception of the Bowie, AZ sample, the deposits contained only one major zeolite.

For the destruction studies a 3 g sample of 10 x 48 mesh (1680 x 295 μm) zeolite was placed in 150 ml of a sulfuric acid solution of the desired pH and agitated, slowly, for periods as long as 48 hr. Batch Cu^{2+} uptake experiments were carried out by conducting parallel experiments in solutions also containing 10^{-2} mol 1^{-1} of $CuSO_4 \cdot 5H_2O$. The pH of each solution was monitored periodically and adjusted to the desired value when necessary. Column ion exchange experiments were made using the method proposed by Dow Chemical Co. (11). Usually, 20 g of 10 x 48 mesh zeolite (10 g for the column stability tests) was placed in a 50-ml buret (0.95 cm i.d.), and Cu^{2+} containing solutions passed through the buret at a rate of 3 ml/min. Desorption was accomplished at the same flowrate. Preliminary testing had indicated that the cation-exchange capacity (CEC) was not appreciably altered by column dimensions (0.95 and 1.91 cm columns), amount of zeolite (5 to 35 cm in height) or influent concentration (10^{-3} to 10^{-1} mol 1^{-1} Cu^{2+}).

A few tests were made in which the zeolite was pretreated to place it in essentially the Na form. In this method 30 g of zeolite and 200 ml of 1 mol 1^{-1} NaCl contained in a 250-ml beaker were placed in a household pressure cooker which was used as a water bath. The sample in solution was heated to $\sim$ 120°C for 2 hours at a pressure of $\sim$ 2 atm., using a method similar to that used by Starkey (12). A 5-minute cool-down time was then used before opening. Each sample was then washed thrice with distilled water, and the procedure repeated twice more before the zeolite was dried for subsequent use.

Chemical analysis of the Eastgate, NV erionite sample was made by the Mineral Constitution Laboratories, The Pennsylvania State University, using DC plasma emission spectrometry.

TABLE I. Composition of Raw Zeolite Samples

Sample	Minerals	Approx. Content, %
Eastgate, NV	Erionite	96
	Chabazite	1
	Calcite	1
	Quartz	2
Bowie, AZ	Chabazite	60
(High grade bed)	Erionite	36
	Feldspar	2
	Quartz	2
Hector, CA	Clinoptilolite	80
	Mordenite	5
	Feldspar	2
	Calcite	2
	Quartz	4
	Volcanic glass	7
Trinity Basin, NV	Mordenite	80
	Feldspar	10
	Quartz	10

EXPERIMENTAL RESULTS AND DISCUSSION

SAMPLE COMPOSITION. The compositions of the four raw zeolite
samples were determined largely by XRD but adjusted by petrographic
microscopy for those minerals present in low percentages (< ~5%) or
amorphous to x-rays (volcanic glass). As seen in Table I, the
samples are composed largely of zeolites (range: 80-90% zeolite),
and, with the exception of the Bowie, AZ sample, they all contain
only one prominent zeolite. The Bowie, AZ deposit is known to be
largely a chabazite deposit, although in parts of the deposit rather
large quantities of erionite are also present ($\underline{13}$).

ZEOLITE STABILITY AND Cu^{2+} SELECTIVITY PROPERTIES IN ACIDIC
SOLUTIONS. Using the batch procedure described above, the percen-
tage destruction of the zeolites at various pH values was determined
based on the diminution of the characteristic XRD peak height com-
pared to that of the original sample. The results, given in Figure
1, indicate that the Eastgate, NV erionite sample is reasonably
stable at pH>1, even after 48-hr contact with acidic solutions. The
loss of crystallinity was ~10% at pH 4 and ~30% at pH 1. At pH<1,
however, the crystal structure was significantly destroyed. The
Bowie, AZ sample, containing mostly chabazite, but also some
erionite, retained its crystallinity well only at pH>3. Its loss of
structure was substantial and rapid at pH<1. The Hector, CA, clino-
ptilolite sample was very stable in acidic solutions except in a
strongly acid (pH <1) environment, and the Trinity Basin, NV morden-
ite sample was stable in all solutions tested, even in solutions of
pH 0.6 - 0.75 (~50 g/liter H_2SO_4). This is not surprising because
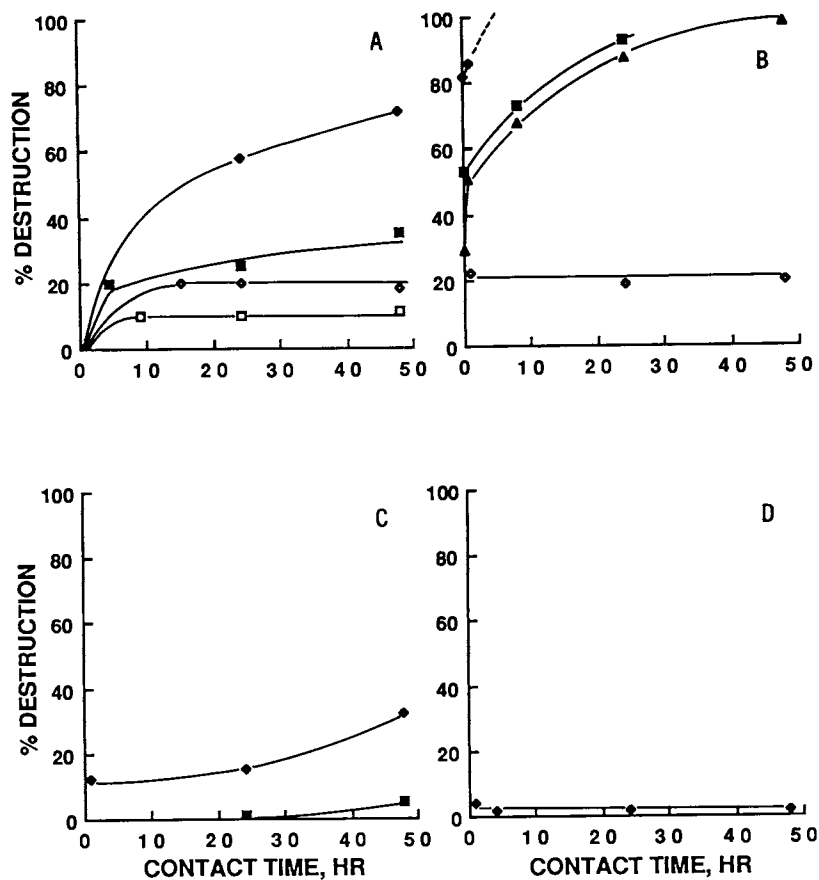
Figure 1. Stability of various zeolites in acidic solutions.
A. Eastgate, NV erionite   ◆ pH 0.75   ◇ pH 3.0
B. Bowie, AZ chabazite   ■ pH 1.0   □ pH 4.0
C. Hector, CA clinoptilolite   ▲ pH 2.0
D. Trinity Basin, NV erionite

mordenites, having a Si/Al ratio >5, are the most siliceous of the common zeolites ($\underline{3}$).

Parallel experiments were run in acidic solutions of 10^{-2} mol 1^{-1} Cu^{2+} to evaluate the ability of these zeolites to remove heavy metal ions from solution (Figure 2). At pH≥3, the ion-exchange capability of the Eastgate, NV and Bowie, AZ samples was not much affected, whereas the Hector, CA clinoptilolite and Trinity Basin, NV mordenite samples gave their highest ion-exchange capability at pH≥4 and 5, respectively. Whereas the erionite, chabazite, and clinoptilolite samples showed comparable Cu^{2+} uptake at pH≥4, the former two samples were superior at pH 3, and the Eastgate, NV erionite extracted a modest amount of Cu^{2+} even at pH 2. Other than their decomposition, the inability of the zeolite samples to extract Cu^{2+} from strongly acidic solutions is likely due to the preferred exchange of H^+ over Cu^{2+} which is approximated by:

$$100[Cu^{2+}] \geq \sim[H^+] \qquad\qquad (1)$$

All the zeolites except the Eastgate, NV erionite sample showed an initial increase in Cu^{2+} uptake in slightly acid solutions as a function of time. This initial increase may be due to the purging of some of the less readily exchangeable cations from the structure, or reduction in pore blockage. The presence of a small amount of calcite in the raw Eastgate, NV and Hector, CA zeolite samples would result in the ready availability of Ca^{2+} in acid solutions, and as will be subsequently demonstrated (see Table IV), the presence of exchangeable Ca^{2+} is deleterious for subsequent cation exchange by e.g. Cu^{2+}. This circumstance probably influenced the shape of the Eastgate, NV curve at pH 2 and the Hector, CA curve at pH 3 since both raw samples contained calcite.

The mordenite sample, though exceedingly stable in acid solution, showed relatively poor exchange for Cu^{2+} even at pH 5. Although erionite, chabazite and clinoptilolite showed good ion exchange capabilities ($>\sim$ 60% Cu^{2+} uptake) in moderately acid solutions (pH≥3 for the former two, pH≥4 for the latter), two factors likely make them poor exchangers: (1) partial structural destruction and (2) the preference of H^+ over Cu^{2+} (see Equation 1). Overall, the Eastgate, NV erionite was probably the best of the samples tested here for use in an acidic environment (see Figure 1), because its destruction in acidic solutions was modest and it shows a reasonable affinity for Cu^{2+} even at pH 2 (see Figure 2).

REMOVAL OF ADSORBED OR STRUCTURAL CATIONS.

The Eastgate, NV erionite sample was selected for further testing because of its minimal destruction and high Cu^{2+} uptake in acid solutions (see Figures 1 and 2). A detailed description of the geology and mineralogy of this deposit was given by Papke ($\underline{14}$). H^+ exchange was studied using the column technique. Passing water at pH 3 through the column, gave an initial effluent having a pH of 9.2, which decreased to $\sim$6 after flushing with about 320 ml of solution/g zeolite. The pH thereafter remained constant at pH $\sim$6
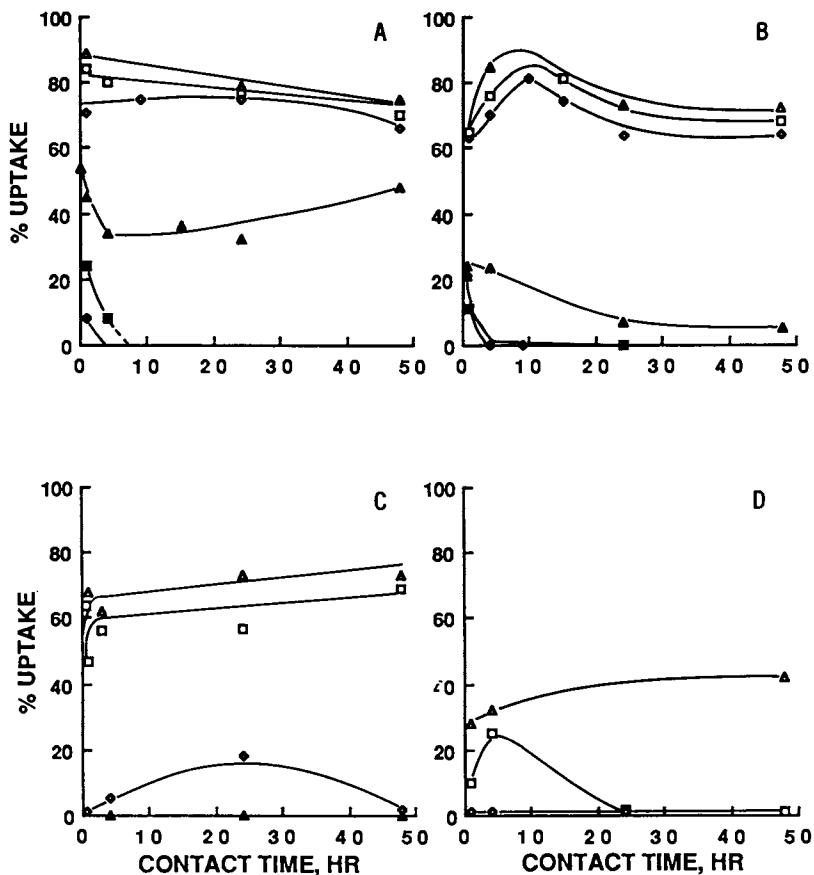
Figure 2.   Influence of pH on the uptake of Cu^{2+} from a 10^{-2} mol l^{-1} solution.
A.   Eastgate, NV erionite
B.   Bowie, AZ chabazite
C.   Hector, CA clinoptilolite
D.   Trinity Basin, NV erionite

◆ pH 0.75   ◇ pH 3.0
■ pH 1.0   □ pH 4.0
▲ pH 2.0   △ pH 5.0

until 800 ml of solution/g of zeolite had been passed through the column at which time ($\sim$ 44 hr) the test was discontinued. Both H_2SO_4 and HCl gave similar results. This pattern may have been due to preferential exchange of H^+ or H replacement of Al sites (3) but was more likely due to a modest, but continual, destruction of the basic erionite structure (see Figure 1A). In contrast, if a clinoptilolite sample was used, the effluent pH decreased to the feed solution value (pH 3) after the passage of $\sim$ 400 ml/g zeolite. This result prompted a more thorough study of the removal of exchangeable or structural cations by acidic solutions. Analyses of a raw and a beneficiated sample of Eastgate, NV erionite are given in Table II. The

TABLE II.   Chemical Analysis of Eastgate, NV Erionite Sample
            Using DC Plasma Emission Spectrometry

Component	Beneficiated	Raw
SiO_2	58.5	--
Al_2O_3	12.6	--
Fe_2O_3	2.42	--
Na_2O	4.15	4.13
K_2O	4.25	4.20
CaO	0.51	0.75
MgO	--	0.79

beneficiation was by gravity methods; and the procedure removed essentially all of the associated gangue minerals. The principal exchangeable cations appear to be Na^+, K^+, Ca^{2+}, Mg^{2+} and, possibly, Fe^{2+} or Fe^{3+}. Figure 3A shows that relatively large amounts of Na^+ (30-40 ppm) were removed by the passage of a pH 3 solution and this effluent concentration persisted even after the passage of 800 ml/g of zeolite ($\sim$44 hr). Only small amounts of K^+ ($\sim$ 1 ppm) were removed continually from the zeolite and very small amounts of Ca^{2+}. Figure 3B shows the removal of Fe^{n+} and Al^{3+}. Initially $\sim$ 3 ppm Fe^{n+} was found in the effluent solution, which decreased with time ($\sim$ 6 hr) to $\sim$ 1 ppm which persisted even after the passage of 700 ml/g zeolite of solution ($\sim$ 39 hr). Less Al^{3+} was found initially ($\sim$ 1 ppm) in the effluent and this decreased to $\sim$ 0.1 ppm in $\sim$ 5 hr.

Figure 3C shows that a significant amount of Si^{4+} was initially removed from the zeolite during treatment with either H_2SO_4 or HCl at pH 3. Even after prolonged treatment an effluent containing 10-20 ppm Si^{4+} persisted, undoubtedly due to the destruction of the structure at this pH (see Figure 1A). To demonstrate that the high Si content was not due to fine particulates, a sample of one of the early effluents was passed through a Millipore filter capable of removing particles coarser than $\sim$1 μm. The Si^{4+} content decreased only from 140 to 125 ppm, indicating that the relatively high Si content in the effluent was present either in the ionic form or as a fine colloid.
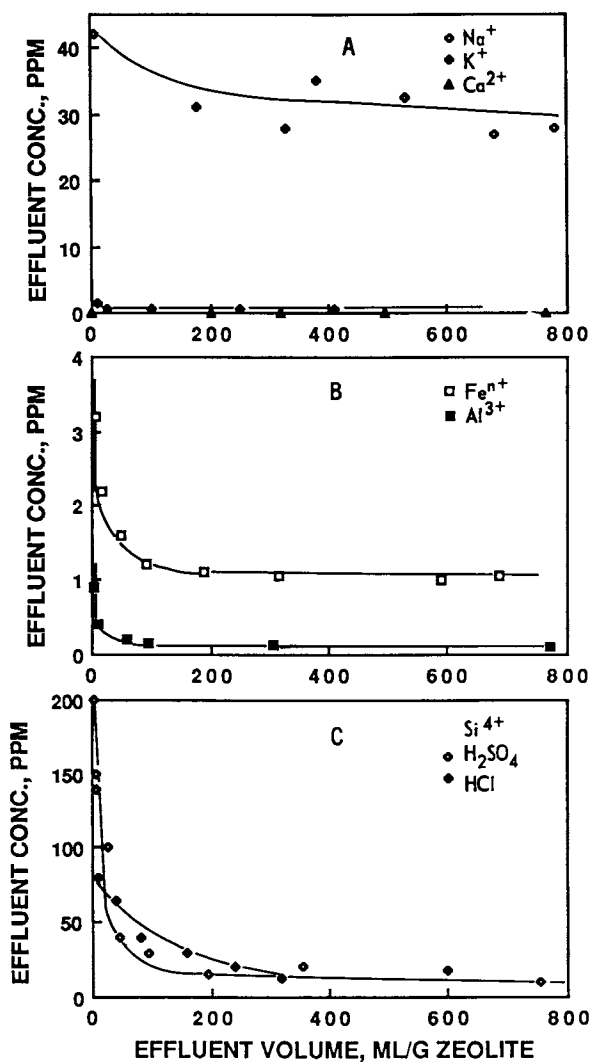
Figure 3. Removal of exchangeable or structural cations from raw Eastgate, NV erionite samples by an acidic solution (pH 3). A. Na^+, K^+ and Ca^{2+}; B. Fe^{n+}, Al^{3+}; C. Si^{4+}

Using the column technique and 20 g of 10 x 48 mesh zeolite, the breakthrough curve shown in Figure 4 (as Δ) was developed. The cation-exchange capacity (CEC) (in milliequivalents (meq)/100g zeolite) was calculated assuming a step function passing through an effluent value of 50% of the influent value and adjusting for the included and excluded areas(15). A value of 78 meq/100 g of solid was found for this zeolite (Table III). The concentration of the

TABLE III. Cu^{2+} Exchange and Regeneration Data for As Received Eastgate, NV Eronite*

Elution Solution		CEC (meq/100g)	Avg, Cu^{2+} conc. eluted (mol l^{-1})	Approx. Cu^{2+} eluted (%)
salt	(mol l^{-1})			
NaCl	1	78	5.7×10^{-2}	70
NaCl	5	78	1.1×10^{-1}	100

* Exchange solution: 8.5×10^{-3} mol l^{-1} $CuSO_4 \cdot 5H_2O$, pH 4

Cu^{2+} EXCHANGE CAPACITY AND ELUTION FROM EASTGATE, NV ERIONITE

effluent before breakthrough was ∿ 0.1 ppm. The Cu^{2+} taken up by the zeolite was then removed by elution with a salt solution. The use of 5 mol l^{-1} NaCl solution doubled both the maximum and the average Cu^{2+} concentration of the solution eluted compared with that using 1 mol l^{-1} NaCl. The amount of Cu^{2+} eluted reached ∿ 100% with the stronger solution.

As noted above, H^+ commonly has a stronger preference for the zeolite exchange site than does Cu^{2+}, and batch testing (Figure 2) has indicated the order of preference between $[H^+]$ and $[Cu^{2+}]$ (Equation 1). Thus, when Cu^{2+} is no longer being extracted, the pH should decrease to that of the feed solution. Figure 4 shows that the Cu^{2+} breakthrough can be estimated from the effluent pH alone (see ◆ and ◇ data, Figure 4). Numerous other tests on a variety of zeolites (data not given here) indicate that this observation can be generalized.

Following Cu^{2+} loading onto the zeolite, the effect of regeneration by elution on subsequent column loading was determined using a variety of salts. The data of Table IV show that regeneration with Na^+ compounds increased the subsequent exchange capacity by 15 to 50%, K^+ had no effect, but Ca^{2+} and Mg^{2+} decreased the CEC substantially. Mg^{2+} was a strong poison. Thus, zeolite material containing large amounts of exchangeable cations other than Na^+ appear to be deleterious to heavy metal cation exchange, with Ca^{2+} and Mg^{2+} being especially disadvantageous.

The improvement in the CEC value for Cu^{2+} after regeneration with NaCl solution is likely due to the purging of deleterious ions from the natural zeolite by Na^+. Accordingly, the pressure pretreatment method described in the experimental methods section was used to place
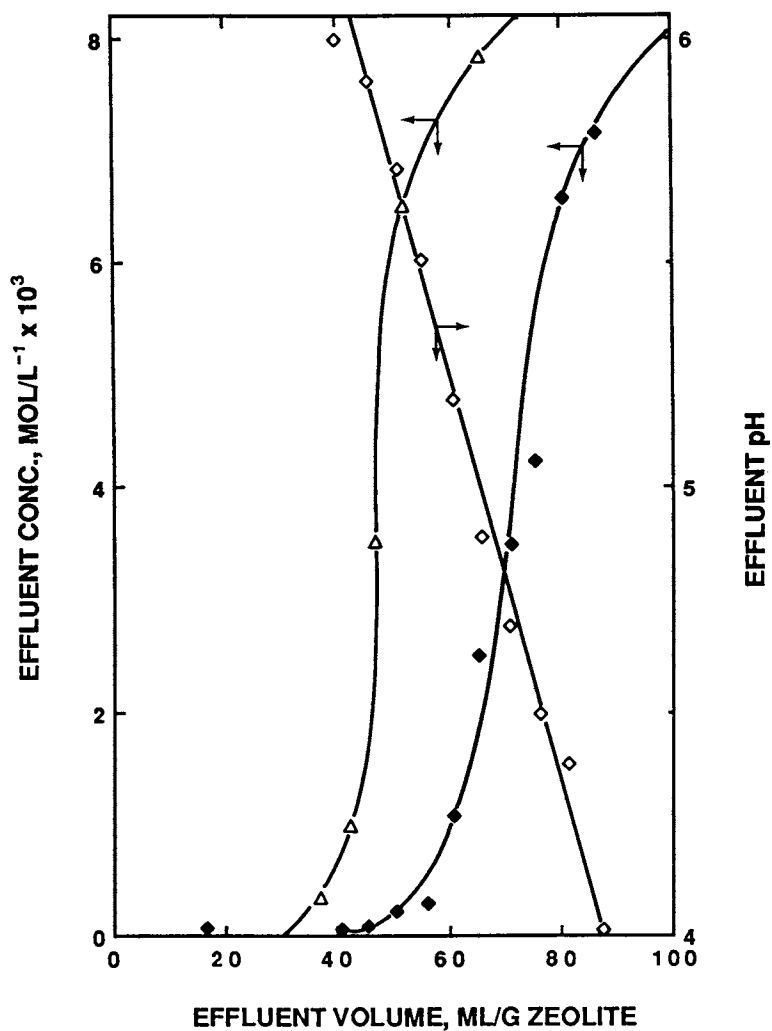
Figure 4. Cu^{2+} breakthrough curves for Eastgate, NV erionite samples showing correlation with effluent pH.
△   as received sample
◆   2 atm. Na$^+$ pretreated sample
◇   effluent pH of pretreated sample

the raw zeolite in essentially the Na^+ form. Analysis of the leach-
ates indicated that about half the original amount of K^+ and Mg^{2+} and
nearly all of the Ca^{2+} was removed by this treatment. The break-
through curve for Cu^{2+} is given in Figure 4 (◆) and loading and
elution results are shown in Table V. This treatment increased the
CEC of this zeolite by 56% to 122 meq/100 g. It also increased the
concentration of the eluted solution and resulted in the easy elution
of essentially all the Cu^{2+} from the zeolite.

The Na^+ pre-treatment, and to a lesser extent elution with Na^+ salts,
improved the CEC by removal of K^+; Ca^{2+} and Mg^{2+}. The superior CEC
of the sodium form of the natural erionite over these other forms is
related to the differing strengths of adsorption and pore diffusion
rates of the various cations, and to the removal of fine particulates
(e.g., clays) that might block passageways. K^+ is an inherently
large ion (0.133 nm) (16), though its hydrated radius is about the
same as that for hydrated Na^+ ion (18) (Table VI). The different
action of K^+ compared with Na^+ was probably due to a stronger attach-
ment of K^+ at the exchange site. This is partially confirmed by
other data (Carland and Aplan, unpublished data) that indicates K^+
elutes a higher percentage of Cu^{2+} from a natural zeolite than does
Na^+. The deleterious effect of Ca^{2+} and Mg^{2+} on the CEC may be
explained by their larger hydrated radius and their tightly held
water (17-19), which would result in slow diffusion through the
zeolite pores. The effect would be magnified by structural imper-
fections likely present in these natural zeolites.

SUMMARY AND CONCLUSIONS

1. A study of the stability of four natural sedimentary zeolites
    indicated the order of stability in an acidic environment was
    found to be Trinity Basin, NV mordenite > Hector, CA clinoptilo-
    lite > Eastgate, NV erionite > Bowie, AZ chabazite.

2. The mordenite sample was stable for a 48 hr period even at pH
    0.75. The clinoptilotite, erionite and chabazite were similar-
    ly stable at or above pH 1,2 and 3, respectively.

3. The ability of these zeolites to remove Cu^{2+} from solution at
    pH≥3 was found to be

        erionite ≥ chabazite > clinoptilolite >> mordenite

    The clinoptilolite adsorbed Cu^{2+} significantly only at pH≥4 and
    the mordenite only at pH 5.

4. Overall, the Eastgate, NV erionite sample would be rated best be-
    cause its destruction by acid was modest above pH 1 and it showed
    a reasonable ability to remove Cu^{2+} from solution even at pH 2.

5. Column tests showed that acidic water at pH 4 removed significant
    quantities of Na^+ and Si^{4+}, modest amounts of K^+ and Fe^{n+} and
    small amounts of Al^{3+} and Ca^{2+} from the Eastgate, NV erionite
    sample.

TABLE IV.   Influence of Elutant on the Regeneration and Subsequent
Exchange Capacity of Eastgate, NV Erionite*

Elutant (Regenerant)		Cation-exchange capacity (meq/100g zeolite)		change in CEC from as rec'd state(%)
salt	(mol 1^{-1})	as rec'd	after regeneration	
NaCl	1	78	90	+15
NaCl	5	78	117	+50
Na_2SO_4	1	78	102	+31
$NaNO_3$	1	78	102	+31
KCl	1	78	78	0
$CaCl_2$	1	78	46	-41
$Mg(NO_3)_2 \cdot 6H_2O$	1	78	14	-82

* Exchange solution: 8.2×10^{-3} mol 1^{-1} $CuSO_4 \cdot 5H_2O$, pH 4

TABLE V.   Improvement in Cu^{2+} Exchange Performance After Two
Atmosphere Pretreatment *

Sample	CEC (meq/100 g zeolite)	Incr. in CEC(%)	Max. Conc. Cu^{2+} eluted (mol 1^{-1})	Incr. in eluate strength(%)	Cu^{2+} eluted, (%)
as received	78	–	1.62×10^{-1}	–	70
pretreated	122	+56	4.62×10^{-1}	+185	100

*Exchange solution: 8.2×10^{-3} mol 1^{-1} $CuSO_4 \cdot 5H_2O$, pH 4
Elution solution: 1 mol 1^{-1} NaCl, pH 5.6
Pretreatment described in experimental methods section

TABLE VI.   Radii and Hydration Data for Various Ions

Ion	Ionic radius (nm) (16)	Hydration No. (17)	Hydration radius (nm) (18)	Hydration energy (kcal/g-ion)(19)
Na^+	0.097	3	0.228	203
K^+	0.133	1	0.217	183
Ca^{2+}	0.099	14	0.310	593
Mg^{2+}	0.066	14	0.309	672

6. The cation exchange capacity (CEC) of the Eastgate, NV erionite
    sample for Cu^{2+} was 78 meq/g, but this could be improved by 15
    to 56% (90 to 122 meq/g) by eluting with Na^+ salts or by a pre-
    treatment to place the zeolite largely in the Na^+ form prior to
    subsequent Cu^{2+} exchange.

7. Elution of the Cu^{2+} from the erionite sample with KCl did not
    improve the CEC upon subsequent Cu^{2+} exchange, but use of Ca^{2+}
    or Mg^{2+} seriously reduced the CEC, probably because of the slow
    diffusion of these relatively large hydrated ions.

ACKNOWLEDGMENTS

REFERENCES

1. Sheppard, R. A. In United States Mineral Resources, U. S. Geol.
    Survey Prof. Paper 820, Brobst, D. A. and Pratt, W. P., eds.,
    U.S. Gov't. Ptg. Off. : Washington, DC, 1973, p. 689-695.
2. Mumpton, F. A. Utilization of Zeolites in Agriculture. In
    Background Papers for Innovative Biological Technologies for
    Lesser Developed Countries -- An Office of Technology Workshop,
    Nov. 24-25, 1980, Committee Print, U.S. Congress. U. S. Gov't.
    Ptg. Off: Washington, D. C., 1981.
3. Breck, D. W. Zeolite Molecular Sieves; John Wiley and Sons: New
    York, 1974.
4. Sherry, H. S. In Ion Exchange, Marinsky, J. A., ed., Marcel
    Dekker: New York, 1969, 2, 89-133.
5. Barrer, R. M. Zeolites and Clay Minerals as Sorbents and
    Molecular Sieves; Academic Press: New York, 1978.
6. Barrer, R. M. In Natural Zeolites, Sand, L. B. and Mumpton,
    F. A., eds.; Pergamon: Oxford, 1978; pp. 385-395.
7. Ames, L. L., Jr. American Mineralogist, 1961, 46, 1120-1131.
8. Barrer, R. M. and Munday, B. M. J. Chem. Soc., A, 1971,
    2904-2909.
9. Mercer, B. W. and Ames, L. L. In Natural Zeolites, ibid, pp.
    451-462.
10. Mondale, K. D., Mumpton, F. A. and Aplan, F. F. In Natural
    Zeolites, ibid, pp. 527-537.
11. Anon., DOWEX: Ion Exchange; Dow Chemical Co., Midland, MI, 1958.
12. Starkey, H.C. In U.S. G.S. Prof. Paper 475D, 1964, pp. D93-95.
13. Sheppard, R. A., Gude, A. J., 3rd and Edson, G. M. In Natural
    Zeolites, ibid, pp. 319-328.
14. Papke, K. G. Erionite and Other Associated Zeolites in Nevada,
    Nevada Bureau of Mines and Geology Bul. 79, 1972.
15. Rodrigues, A. E. and Tondeur, D., eds., Percolation Processes:
    Theory and Application, NATO Advanced Study Institutes: Series
    E, Applied Sciences No. 33, Sijthoff and Noordhoff, Rockville,
    MD, 1981.

16. Pauling, L. <u>The Nature of the Chemical Bond</u>, 3rd ed., Cornell University Press: Ithaca, NY, 1960.
17. Padova, J. <u>J. Chem. Phys.</u>, 1963, <u>39</u>, 1552-1557.
18. Padova, J. <u>J. Chem. Phys.</u>, 1964, <u>40</u>, 691-694.
19. Rosscinsky, R. M., <u>Chem. Rev.</u> 1965, <u>65</u>, 467-490.

Chapter 19

Recent Developments in Pillared Interlayered Clays

D. E. W. Vaughan

Exxon Research and Engineering Company, Route 22 East, Annandale, NJ 08801

The field of pillared clays has recently expanded by discoveries of new pillaring species, and extensions of the pillaring concept to several new layered materials, including micas, silicic acids, zirconium phosphates and layered metal hydroxides. Pillaring in various sheet materials has been done with clusters of cations, anions and neutral molecules, resulting in a new compositional versatility. Pillared layered materials now represent a rapidly expanding category of catalytic microporous materials having a high degree of chemical and structural diversity.

Since the first commercial announcements of Pillared Interlayered Clays (PILC) in 1979 (1), much interest has focused on these materials as potential sources of new materials in sorption, separations and catalysis. In this review I will attempt to summarise some of the recent developments that continue to make PILCs an exciting and opportunistic research area for the petroleum oriented industries. These developments can conveniently be divided into the following areas:

- New chemical understanding of clays and PILCs.
- New pillars
- New sheet structures

In the sense that much academic PILC research is industry-sponsored, only the first group may be viewed as not being closely intertwined with applications - both in direction and execution. Indeed, there seems to be little delay between the discovery of new PILC materials and their evaluation as catalysts. The original objectives in developing PILCs - the catalytic processing of heavy residual crude oils to transportation fuels (2,3) - continues to be the main focus of the technological developments in the field. This reflects not only a dearth of alternative catalysts in this important application, but also a conviction that they do represent a major

possible solution to the difficult catalytic problem of efficiently
converting heavy, metal laden, crude oils to transportation fuels.
PILCs essentially fill the pore size - activity gap between zeolites
and the larger pore amorphous gel catalysts.

The stimulus to create new compositions is to meet several
major perceived needed improvements to make PILCs effective
commercial fluid cracking catalysts (FCC):

- **Larger spacings between the clay sheets
  (to accommodate large 'resid' molecules)**
- **Higher thermal and steam stability
  (so as to survive FCC regeneration).**
- **Build novel catalytic activity into the pillar
  (to expand process applications).**

Despite this apparent focus, new materials and new materials
concepts are developing rapidly, and it is probably only a matter of
time before broader applications are discovered and developed for
PILCs in both separations and catalysis. There are many processes
other than FCC (alkylation, isomerisation etc.) that do not require
any of the above improvements, and in such applications PILCs
represent high surface area solids having unique structures. In
some cases, however, it must be noted that the pores in PILCs may be
too large for high specificity in many small molecule petrochemical
processes. ZSM-5 and related structures have become successful
catalysts because they have pore structures of 5 to 6Å - a
relatively restricted environment which significantly affects the
catalytic transition states or diffusion modes, creating novel
selectivities. PILCs will be more useful where the reactants are
substituted multi-ring aromatics or napthenic molecules, too large
to efficiently react in conventional zeolites. Hydrocracking and
dewaxing are the most probable areas of initial applications given
the present status of PILC stability.

For the present, the catalyst and petroleum patent literature
remain the major sources of new information and developments. Two
reviews provide a background for this paper (4,5).

New Chemistry

Studies of the solution chemistry of potential pillaring
species are of major interest in PILC studies, but have only
recently achieved the level of observing specific species in
solution prior to, during, and after pillaring (6). Although
solution NMR methods offer the opportunity for Al, Si and Zr polymer
definition, and have been demonstrated for specific Al (7,8) and Si
(9-11) cases, these studies are largely topics for future research.
Examination of a comprehensive text on metal species in solution,
such as reference (12), and recent literature, clearly demonstrate
large gaps in our knowledge of the detailed nature of complex
multi-atomic polymers in aqueous solutions indicated by many
potentiometric titration studies. Recent PILC developments
described in this paper demonstrate that important solution species
exist, and can be "sized" by PILC spacings and pore volumes, but
specific and direct information on bonding, structure and

dimensionality is lacking in most cases. However, the trends have clearly been demonstrated by several recent studies of zeolite precursor species in solution using both ^{29}Si solution NMR (13,14) and Raman spectroscopy (15). In these cases small polyhedral clusters have been identified in syntheses of zeolites A and ZSM-5, and these same techniques should be quite adaptable to study the character of some pillar precursors. As with many difficult problems, this area of science needs the simultaneous application of several complimentary techniques to elucidate cluster species in solution. If successful, such an approach will yield several families of new pillared materials.

    Some of the most important developments have taken place in the elucidation of new details of the structure of the clays themselves, together with some initial and provocative studies of the effects of pillaring - all using various magic angle spinning nuclear magnetic resonance techniques (MASNMR). ^{27}Al and ^{29}Si-MASNMR studies of clays by Herrero et al. (16) have demonstrated that tetrahedral layer ordering of Si and Al follows the general rules of Al avoidance characteristic of zeolites proposed by Loewenstein (17) and extended by Melchior et al. (18). This implies that cations, including pillaring cations, are likely to be evenly spaced within the interlayer space. Assuming an absence of pillar agglomeration on dehydration, the original assumption is supported that a PILC may be regarded as a molecular sieve having evenly spaced pillars propping open the layers (19). An alternative model is that in some clays pillars may cluster, and possibly in the initial stages of calcination or steaming, pillar clustering may be an important mechanism of stabilization. This particularly may apply in clays where the amount of pillar species fills the interlayer in the hydrated state. As more work on PILCs is published, it becomes clear that the clay itself is an important variable, and that more than one model may be needed to explain the experimental data.

    The molecular sieve sorption properties of PILCs (19,20) indicate zeolite like behaviour as shown in Figure 1, often with a sharp cut-off in molecular size separation, but these experiments do not adequately differentiate between large rectangular pores (a clustered PILC model) and the smaller, more uniform, zeolite-like (e.g., as in heulandite or stilbite) pores thought to be characteristic of PILCs in the isolated pillar model. More sophisticated molecular probing is therefore needed, together with analysis of interlayer cation ordering experiments, to further elucidate the pillaring models. One interesting new method of pore analysis developed at Exxon (21), and recently commercialized, uses the very low pressure part of the sorption isotherm to resolve pores in the molecular range. A comparison of such an analysis for zeolites 5A, NaX and an Al-PILC is shown in Figure 2, and gives a pore diameter for the PILC larger than faujasite, but showing a more dispersed pore size distribution than observed for the zeolites, and very close to the model proposed for an Al-PILC. Note that the zeolites have pore diameters close to their crystallographic window dimensions in this analysis. As the measurements were made at 87°K and represent a relatively rigid lattice, they are remarkably close to actuality. At or close to room temperature the breathing modes
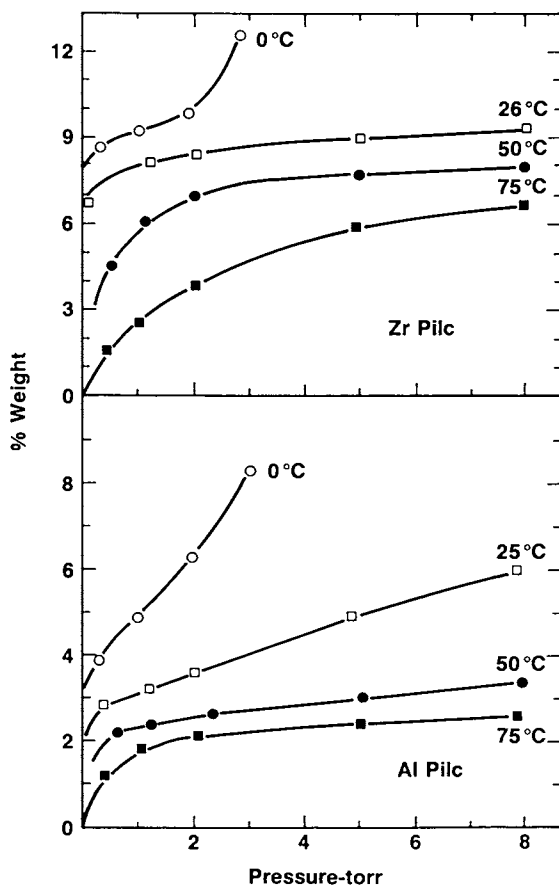
Figure 1. Absorption isotherms at 0°C, 25°C, 50°C and 75°C for n-octane in an Al-PILC and a Zr-PILC, using a bentonite-325 base clay (American Colloid Co.). The shape is typically "zeolitic" (Type I), with some capillary condensation between the small crystals at low temperatures.
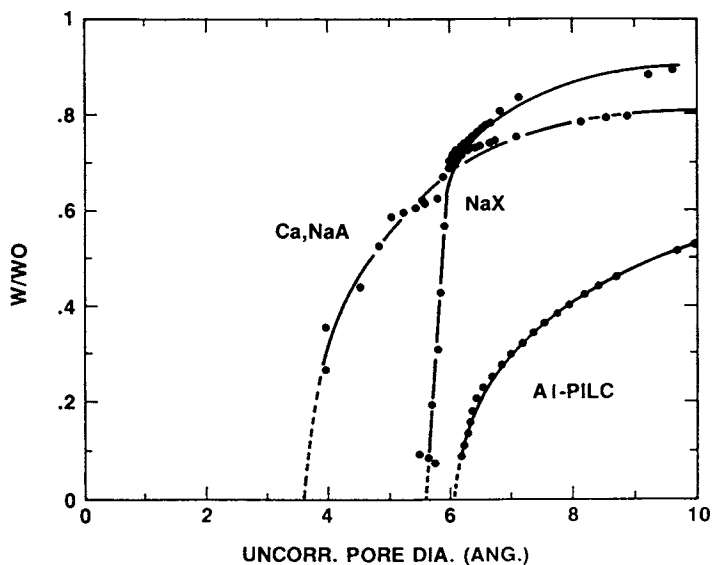
Figure 2. A comparison of the nitrogen pore size distribution
analysis for Ca, NaA (5A), NaX and an Al-PILC obtained using an
Omnisorb 360 in the partial pressure range of 10^{-5} to 10^{-3}. The
relative order of the pore sizes is in good agreement with other
experiments.

of faujasite increase the actual window diameter to about 8Å, and if similar structural vibrational amplitudes are assumed for the PILC, the room temperature PILC pore diameter would be about 9 to 10Å - very close to the predicted size based on a uniform pore model.

Exploration of the pillar-clay sheet reactivity and connectivity also indicate the important role of the specific clay type. ^{27}Al and ^{29}Si-MASNMR experiments have shown distinctive differences between pillaring mechanisms in trioctahedral hectorite and dioctahedral montmorillonite. Whereas Plee et al. (22) concluded that chemical crosslinking may occur between the pillar and tetrahedral layer in a beidellite montmorillonite, Pinnavaia et al. (23) showed that it did not occur in a hectorite. These are the first observations of a complex process that may depend upon several structural and chemical factors, such as substitution of Al in the tetrahedral layer, or the need for vacancies in the octahedral layer to allow rotation of structural units or migration of reactant species to facilitate crosslinking. Ongoing research should further elucidate refinements on these mechanisms, and direct the technology towards more optimized catalysts - presumably those which form chemical bonds between the pillar and clay layer.

New Pillar Compositions

The original PILC compositions proposed a family of pillaring species that resulted in a broad spectrum of quite different PILC products (1,5,24,25), based primarily on $(Al)_{13}$ or $(Zr)_4$ polymers, or such polymers modified primarily with Mg, Si and Ti species. New pillar compositions include:

- **Creation of new groups of polymers of $(TiO_2)_x$.**

- **Extention of some of the original polymers by substitution of part of the Al in the Keggin ion with secondary elements.**

- **Cluster small or colloid compositions of transition metal oxides or metal hydroxides.**

The synthesis of large spacing TiO_2 PILCs is one of the most important recent developments, in that materials having a high degree of ordering, with about 30Å (001) basal spacings, have been reported. Clay-alcohol intercalates with larger than 50Å basal spacings are known, but it is unlikely that inorganic pillared clays of such dimensions would have either stability or significant internal free volume. The 30Å PILCs of Sterte (26) have high surface areas, and hydrothermal stability comparable to Zr-PILCs, and within the range useful for FCC catalysts. Although lowered spacing TiO_2 PILCs were proposed in the original PILC patents (1,23,24), together with Zr-Ti and Al-Ti PILCs, precipitation reactions inhibited the development of significant ordered pillaring, or major surface areas. Sterte observed a high level of order, but at this time no hypotheses have been advanced to elucidate the structure of the near-20Å titania complexes participating in the intercalation reaction. In addition to 30Å

spacing PILCs, Sterte reports 25Å layered materials using a smaller
TiO_2 species. This has a similar basal spacing to the previously
reported 25.5Å ZrO_2-PILC (1), which presumed crosslinking of the Zr_4
square planar complex reported by Clearfield and Vaughan (27).
However, there are significant differences in the aqueous solution
chemistry of the smaller titanium cation (radius 0.61Å) compared to
the zirconium cation (radius 0.72Å). It has been reported that the
chain like $(Ti-O)^{2+}$ cations (e.g., as in $TiOSO_4$) prefer not to
crosslink in the manner of similar Zr cations (28). Yamanaka and
co-workers (29) have also made 25Å layered TiO_2-PILCs, but using
hydrolysed tetraethoxy titanium complexes. These too have high
stability and high internal pore volume, as shown in Table I.

TABLE I COMPARISON OF THE PROPERTIES OF
Al, Zr, Si and Ti-PILCs

Polymer Species	(001) Clay Spacing	Surface Area	Reference
Al_{13}	17.8Å - 18.5Å	400	1
$(Si_8)_n$	19Å	300	34
Zr_4	18.0Å	260	1
$(Zr_4)_x$	21.5	290	1
$(Zr_4)_y$	21.5 + 25.6	250	1
$(TiO_2)_a$	25Å	300	26
$(TiO_2)_b$	29Å	330	29

The titanium alkoxides are used extensively in surface coating
preparations for metals and plastics, and are thought to form sheet
like two-dimensional polymers (30), based on the structural unit
shown in Figure 3, in contrast with other one-dimensional Ti chain
polymers, and Zr_4 planar clusters. It is possible that the 25Å
Ti-PILC of Sterte, made via an inorganic route, may be different
from the similar sized 25Å Ti-PILC of Yamanaka et al made via the
alkoxide, and therefore these may have different properties. As for
Zr polymers, the low molecular weight Ti solution polymers are
difficult to characterize, and await the development of new
experimental techniques before their nature can be fully elucidated.
Zr and Ti NMR should have major impact here, if suitable techniques
can be developed. In contrast to ZrO_2, titanium may form a range of
non-stoichiometic oxides in addition to the three stoichiometric
TiO_2 forms of rutile, anatase and brookite. This raises the
possibility of having several "titania" pillar types, particularly
under reducing reaction conditions characteristic of many catalytic
processes, and presents a major challenge to present instrumental
capability to specifically identify the "real pillar" compositions.
This will be an issue of some importance in the patent area if some
compositions show novel properties.
        The modification of the Al_{13} species by substitution of
secondary metal ions into the complex (31), rather than by addition
polymerization (25), or post ion exchange (24), as originally
proposed, adds a new and wide ranging versatility to the pillar
itself. These materials may be expected to show not just a
different catalytic reactivity, but changes in the way the pillars

[TiO(OH)$_2$]$_x$

Si$_8$O$_{12}$(OH)$_8$

[Al$_{11}$M$_2$O$_4$(OH)$_{24}$]$^{7+}$

[Zr$_4$(OH)$_8$(H$_2$O)$_{16}$Cl$_x$]$^{(8-x)+}$
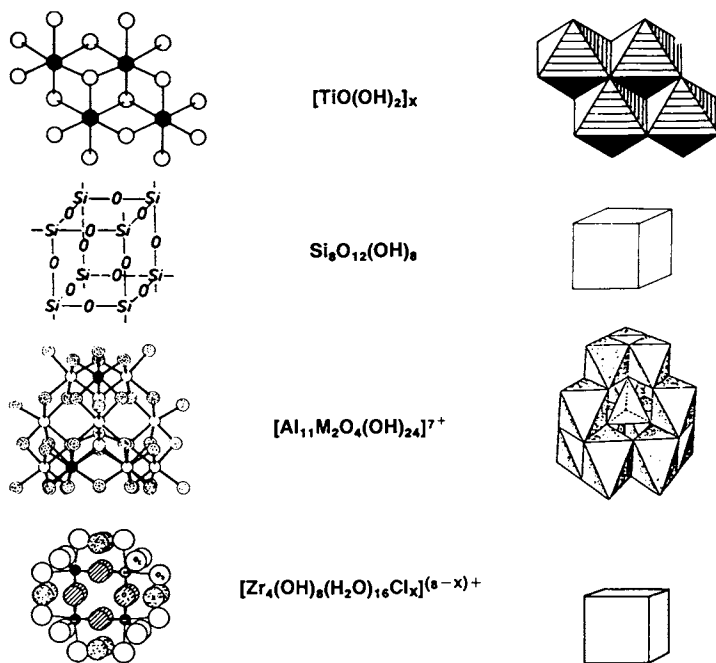
Possible (Cr)$_3$ and (Cr)$_4$hydroxy complexes
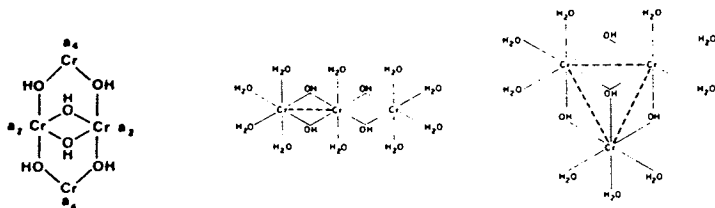
Figure 3. Models of various oxy-hydroxy inorganic polymers possibly used to pillar several layer structures, including complexes of Ti (29); (Si,Al) (9,34); (Al,M)$_{13}$(31); Zr(27) and Cr(39,40).

may react with the sheet structures. Preliminary evaluation of a similar Cr-Al-PILC polymer by Carrado et al. (32) indicates novel reactivity. In contrast to the case of the mica-montmorillonite PILC substituted with Ni^{2+} in the octahedral sheet (33), the pillar may now also act as a reservoir for creating catalytic metal clusters in the interlayer, leading to novel and enhanced reactivities.

Attention recently focused on a wide range of silica polymers (selsequisiloxanes) pillaring montmorillonites (34), and these can also be Al^{3+} substituted in the manner demonstrated by Hoebbel et al (9). This large group of potential pillars also offers the possibility of creating interlayer spacings comparable to those observed for TiO_2. However, as is well known in silicate chemistry, the stability of such materials in the presence of water will be relatively low.

Transition metal oxide pillars, first investigated as intercalates by Yamanaka and Brindley (35,36), have received renewed attention by Pinnavia and co-workers (37,38), who have created large spacing PILCs propped by new transition metal hydroxide cluster structures. In these cases, transition metal solutions were treated in an manner analogous to that used to make the Al_{13} polymer from Al solutions, yielding similar sized 8-10Å solution species which pillar the clay to basal spacings of over 20Å. The structures of the pillaring species have not yet been identified, but several polymeric chromium hydroxide polymers have been proposed (39,40), as shown in Figure 3. These are the first highly ordered, large spacing PILCs, having interesting transition metal catalyst possibilities, in that they have high void volumes and metal loadings.

Figure 3 summarizes the structures of possible pillaring species described above, based on known structures of species present prior to addition of the clay component. Multiples of these basic units probably constitute the actual pillars in many cases. Coalescence of such clusters is particularly expected during calcination or setting of the cluster to form the pillar, especially in the presence of low water partial pressures.

New Sheet Compositions

Hitherto the most successful pillaring has been carried out on smectite type clays. The original research on pillaring included several series of unsuccessful experiments on mica, vermiculite and the sheet silicic acid minerals magadiite, silhydrite and kenyaite. Recently renewed attention has focused on these and other alternative sheet structures. They include rectorite, zirconium phosphates, tetrasilicic micas, hydrotalcites and silicic acids, the general structural features of which are shown in Figure 4.

Rectorite is one of an almost infinite number of randomly mixed layer clays (41), collectively called 'illites', which include several other ordered interstratified varieties, including chlorite, corrensite and allevardite. Rectorite has the advantages of a mica and a smectite, in that alternate interlayers are expanding and non-expanding. It may be viewed as an ordered synthetic mica-montmorillonite (SMM) in the nomenclature familiar to catalytic

Rectorite
$Na[Al_2(Si_3Al)O_{10}(OH)_2]$

Tetrasilicic mica
$Na[Mg_{2.5}Si_4O_{10}F_2]$

Silicic acid
$H_2Si_2O_5$ (type I)

α-Zirconium phosphate
$[Zr(PO_4)_2]H_2.H_2O$

Brucite
$Mg(OH)_2$
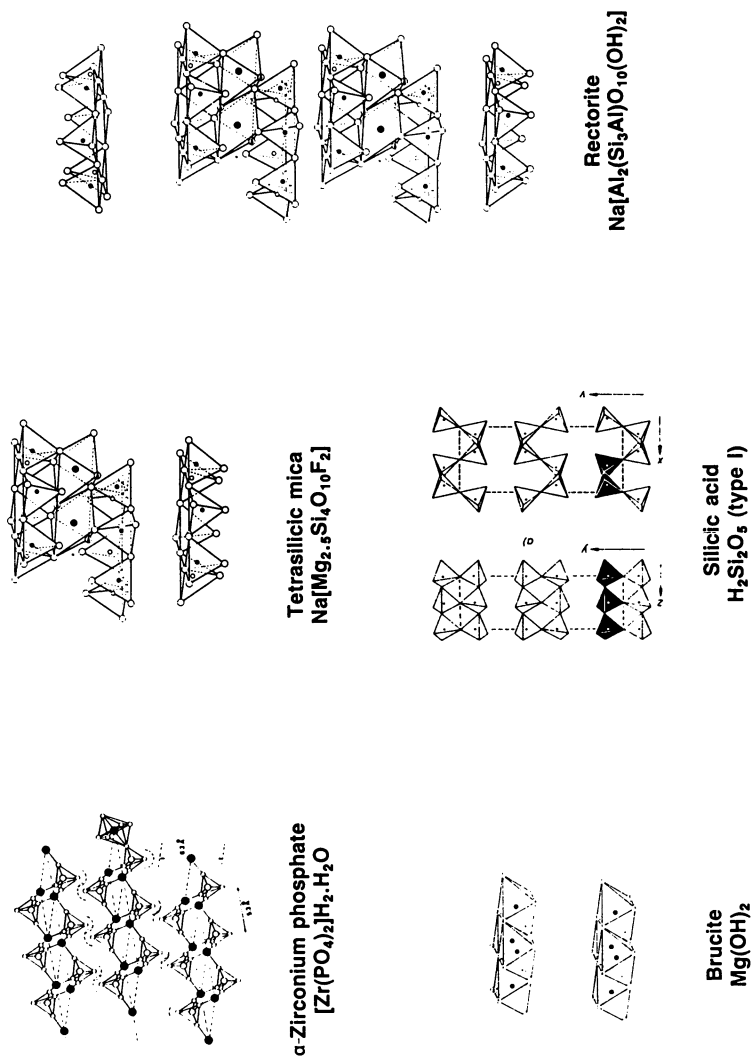
Figure 4. Most pillaring has been done with smectite clays. This figure shows a variety of new sheet structures recently pillared with various species shown in Figure 3, or related polymers.

chemists. The resulting double sheet between the pillared expanded layers in the PILC form, gives the pillared structure enhanced stability, which shows up as superior activity in catalytic reactions carried out after catalyst deactivation (42). Even though the total interlayer void volume is theoretically only half that expected of a fully expanded and pillared smectite, the enhanced deactivation survivability of that interlayer compensates for the smaller initial interlayer volume. Comparative catalytic activities, after severe deactivation, of PILC and conventional FCC catalysts are shown in Figure 5, and dramatically demonstrate the improvements due to the enhanced sheet stability, and the potential for these materials in FCC. The addition of zeolite to such PILC catalysts should give an even greater enhancement in activity, and added selectivity control. These data clearly demonstrate that the pillar may have very high stability, and this is probably another case of strong sheet-pillar connectivity.

It seems highly improbable that a non-"crosslinked" pillar would survive the stated deactivation conditions, and re-enforces the proposal of Plee, et al. (22) that chemical reaction between sheet and pillar plays a major role in PILC stabilization and catalyst survivability. Plee et al. focused their attention on beidellite, having a high tetrahedral Al^{3+} component, which has not yet been found in major mineral accumulations. Rectorite is more abundant, but again occurs in small deposits. The advantages shown by pillared rectorite warrant a re-evaluation of some of the pillared synthetic mica-montmorillonites made by Granquist and co-workers (e.g. 43), previously investigated for hydrocracking (44) and hydroisomerization (45), and having the advantage of no iron oxide admixed with the clay - a major problem with most mineral clays.

Although early attempts to pillar magadiite, silhydrite and kenyaite with Al_{13} and Zr_4 polymers failed to demonstrate intercalation, recent advances in the structural understanding of these sheet silicas have shown that some can be intercallated (46). These materials represent a large group of reactive hydroxylated silicas (47) of potential interest in pillaring reactions. In many cases the density of reactive "surface 'OH'" groups is such that the density of crosslinking with species such as selsesquisiloxanes will produce filled interlayers, and poor sorption properties (48). Pillaring the sheet silicic acids to produce open structures will therefore depend on very selective partial pillaring, or the capability of pillaring only a few structures. One recent example using a synthetic silicic acid, of undisclosed structure, indicates surface areas in the range of 580 m^2/gm, and pores large enough to sorb cyclohexane in copious amounts (49).

The tetrasilicic micas (TSM) are synthetic expandable fluoromicas (50) recently made available by Topy Industries (Japan) (51). They can be effectively pillared (52), and show interesting catalytic activity and enhanced stability, although not at the level of the rectorite-PILC. The chemical and physical properties of this group of materials do not yet seem to have been optimized, and probably require more extensive synthesis work before the full potential of TSM can be realized in pillared systems.
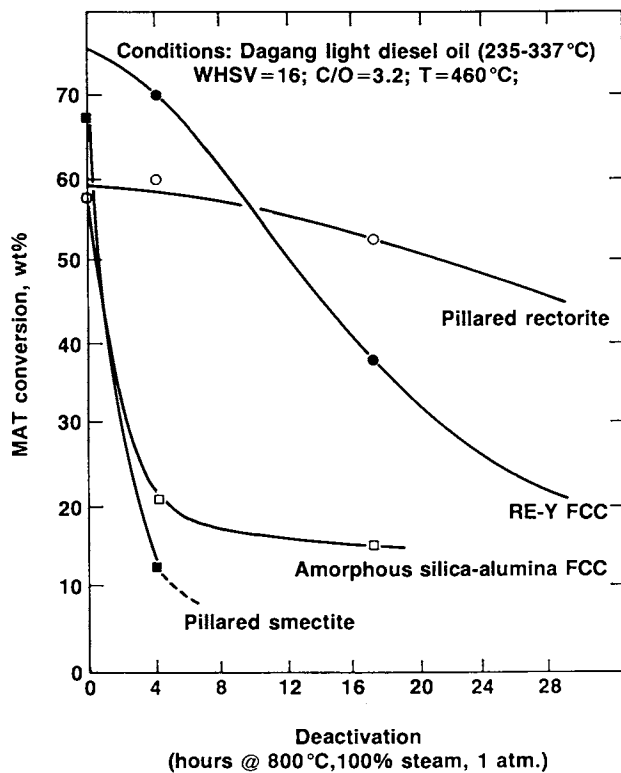
Figure 5. A comparison of catalytic activities using a light cycle oil over deactivated catalysts based on pillared montmorillonite, pillared rectorite, NaY and an amorphous silica-alumina FCC.

     Zirconium phosphates have been extensively investigated as
intercalation hosts (53), and the catalytic properties of some
pillared zirconium phosphates has been reviewed by Clearfield (54).
A recent Shell patent indicates that these materials can be pillared
with selsesquisiloxanes (55), and that they offer potential as
catalyst systems; opening up yet another class of inorganic
microporous materials to petrochemical and petroleum catalysis.
     The several new chemical and structural systems proposed in
recent discoveries are summarized in Table II, and greatly expand on
the available versatility of PILCs.

                    TABLE II   NEW PILC MATERIALS

Pillar	Layer	Advantage	Reference
$(Al_{(13-x)}M_x)$	Smectites	Active Pillar	31
$Al_{13}, (Al_{13})_x$	Rectorite	High Stability	42
Al_{13}, Zr_4	Tetrasilicic Mica	High Stability	51,52
$(SiO_2)_x$	Smectites	Pillar Versatility	34
$(TiO_2)_x$	Smectites	> 15Å Spaces	26,29
Cr_2O_3, Fe_2O_3, CoO	Smectites	Active Pillar	35,36,37,38
$(SiO_2)_x$	$ZrPO_4$	Novel Sheet	55
$(SiO_2)x$	SiO_2	Novel Sheet/chain	49

Our experience with several kinds of sheet structures is that the
smectites are the most versatile host materials, and that most other
classes are very specific for the kinds of species that will pillar.

Colloid-Clay Systems

     Colloid-clay agglomerates have been recognized for many years
as offering novel properties that neither alone possess. The
semi-synthetic fluid cracking catalysts of the early 1950's were
such materials, comprising various clays in a silica or
silica-alumina gel or colloid matrix. Similar materials are used as
a matrix for the current families of zeolite promoted fluid cracking
catalysts. Although several such materials have been 'lumped' with
PILCs, they in fact represent a separate family of materials which
are characterized by crystallographic disorder, although they may in
some cases show distinctive sharp pore size distributions. The
latter result from uniformity in the colloid or clay size
distributions used in their preparation, rather than from the
specific ordered interlayering of each clay layer with a uniform
molecular colloid entity. The transition from full order typical of
zeolites, to full disorder as in the colloid clay agglomerate
system, passes through the PILC which invariably has some
characteristics of both - a majority of micro-pores of the former
type together with a minority of meso-pores characteristic of the
latter. Several recent patents focus on the use of larger
cluster-colloid species of the trasition metals to form materials of
this general form (e.g. 56,57). They constitute an important class
of catalysts, but do not fall within the scope of this review.

Pillared Sheet Hydroxides

Brucite, $Mg(OH)_2$, comprises a single sheet of bridged octahedra analogous to the octahedral layer in talc. Although this sheet has no net layer charge, substitution of trivalent metal cations for Mg^{2+} creates a net positive charge on the sheet, and the resultant materials exchange anions between the sheets. Al^{3+} readily substitutes into this magnesium hydroxide sheet to form a mineral called hydrotalcite (58), and a large number of these mixed hydroxides are readily synthesized. Similar substituted materials occur in nature in great diversity, in some cases comprising important mineral ores (eg. takovite, $Ni_6Al_2(OH)_{16}CO_3$ - a Ni equivalent of hydrotalcite). Many such materials have been investigated as ion exchangers, and shown to have specific sorption properties in forms expanded with CO_3^{2-}, Cl^-, CN^- etc. (60,61). Recent work by Woltermann (62) has shown that in some cases various homopoly and heteropoly-acid anions, including those having the Keggin ion structure identical to the Al_{13} polymer, can effectively pillar these materials. The thermal and hydrothermal properties of these products are poor compared with conventional cation pillared smectites, and they collapse on dehydroxylation - usually below about 400°C. However, the compositional diversity of the pillars and the layers make them a chemically versatile group of potential catalysts. The pillaring reactions seem to be far more restrictive than initially proposed by Woltermann, and in many cases may be primarily of colloid-clay sheet random packed type, particularly as many of the synthetic hydroxides form crystals of only several hundred angstroms diameter. However, they comprise a very large group of microporous materials, both ordered and disordered, and offer many catalyst opportunities. The catalyst literature contains many examples of precipitated mixed metal oxides and hydroxides of "amorphous" structure, and probably includes many materials of this type.

Conclusions

Pillared sheet structures continue to expand their interest and diversity, with major developments taking place in increasing the number of both pillar and sheet compositions. Unfortunately the specific understanding and characterization of pillar precursors and PILC products greatly lags the technological "pull" for new materials - a classic catalyst scenario. With major interest now turning to relatively rare clays (or ones not available in quantity) such as beidellite and rectorite, the time may be ripe for a re-examination of specific clay synthesis methods, and dedicated projects to synthesize these kinds of materials. Tetrasilicic mica is a recent success in the synthesis area, which could be followed by others. Major opportunities exist for the application of various spectroscopic techniques in both the solution and solid states, and modeling studies on the products would further promote understanding and improvment in PILCs having applications as sorbents and catalysts.

Literature Cited

1. Vaughan, D.E.W., Lussier, R.J. and Magee, J.S., <u>U.S. Patent</u> 4,176,090, (1979).
2. Lussier, R.J., Magee, J.S., and Vaughan, D.E.W., <u>7th Canadian Symp. on Catalysis</u>, Preprints, Chem. Inst. Canada, 1980, 80.
3. Shabtai, J., Lazar, R., and Oblad, A.G., <u>7th Intl. Catalysis Congr.</u>, (Tokyo), 1980, 828. Ed. Seiyama, T. and Tanabe, K., Kodansha/Elsevier.
4. Pinnavaia, T.J., <u>Science</u>, 1983, <u>220</u>, 365.
5. Vaughan, D.E.W., in <u>"Pillared Clays"</u>, 1987, in press. Ed. Burch, R. and Delmon, B., Elsevier (Amsterdam).
6. Schutz, A., Stone, W.E.E., Poncelet, G., and Fripiat, J.J., <u>Clays and Clay Minerals</u>, 1987, <u>35</u>, 251.
7. Akitt, J.W., and Farthing, A., <u>J. Chem. Soc. (Dalton)</u>, 1981, 1617.
8. Akitt, J.W., and Farthing, A., <u>ibid</u>, 1624.
9. Hoebbel, D., Garzo, G., Ujszaszi, K., Engelhardt, G., Fahlke, B., and Vargha, A., <u>Z. Anorg. Allg. Chem.</u>, 1982, <u>484</u>, 7.
10. Boxhoorn, G., Sudmeijer, O., and van Kasteren, P.H.G., <u>J. Chem. Soc. Chem. Commun.</u>, 1986, 66.
11. Knight, C.T.G., Kirkpatrick, R.J., and Oldfield, E., <u>J. Chem. Soc. Chem. Commun.</u>, 1986, 66.
12. Baes, G.F., and Mesmer, R.E., <u>"The Hydrolysis of Cations"</u>, J. Wiley (New York), 1976.
13. Griebeb, E.J.J., Kortbeek, A.G.T.G., Mackay, M., and Sudmeijer, O., <u>Zeolites</u>, 1986, <u>6</u>, 403.
14. McCormick, A.V., and Bell, A.T., <u>Zeolites</u>, 1987, <u>7</u>, 183.
15. Dutta, P.K., and Shieh, D.C., <u>J. Phys. Chem.</u>, 1986, <u>90</u>, 2331.
16. Herrero, C.P., Sanz, J., and Sarratosa, J.M., <u>Solid State Commun.</u>, 1985, <u>53</u>, 151.
17. Loewenstein, W., <u>Amer. Mineral</u>, 1954, <u>39</u>, 92.
18. Melchior, M.T., Vaughan, D.E.W., and Jacobson, A.J., <u>J. Amer. Chem. Soc.</u>, 1982, <u>104</u>, 4859.
19. Vaughan, D.E.W., and Lussier, R.J., <u>Proc. 5th Intl. Zeolite Conf.</u>, 1980, 94, Ed. L.V.C. Rees, Heyden Press, London.
20. Occelli, M.L., Parvlekar, V.N., and Hightower, J.W., Proc. 8th Intl. Congr. Catalysis, Berlin, 1984, <u>4</u>, 725. Springer-Verlag (Frankfurt).
21. Pieters, W.J.M., and Venero, A.F., in <u>"Catalysis on the Energy Scene"</u>, 1984, 156. Ed Kaliaguine, S. and Mahay, A., Elsevier (Amsterdam).
22. Plee, D., Borg, F., Gatineau, L., and Fripiat, J.J., <u>J. Amer. Chem. Soc.</u> 1985, <u>107</u>, 2362.
23. Pinnavaia, T.J., Landau, S.D., Tzou, M.S., Johnson, I.D., and Lipsicas, M., <u>J. Amer. Chem. Soc.</u>, 1985, <u>107</u>, 7222.
24. Vaughan, D.E.W., Lussier, R.J., Magee, J.S., <u>U.S. Patent</u> 4,271,043 (1981).
25. Vaughan, D.E.W., Lussier, R.J., Magee, J.S., <u>U.S. Patent</u> 4,248,739 (1981).
26. Sterte, J., <u>Clays and Clay Miner.</u>, 1986, <u>34</u>, 658.
27. Clearfield, A., and Vaughan, P. <u>Acta Cryst.</u>, 1975, <u>B31</u>, 511.
28. Ellis, <u>J. Chem. Soc. (Dalton)</u>, 1973, 537.
29. Yamanaka, S. Tatsoo, N., and Hottori, M., <u>Materials Chem. and Phys.</u>, 1987, <u>17</u>, 87.

30. Ibers, J.A., <u>Nature</u>, 1963, <u>197</u>, 686.
31. Vaughan, D.E.W., <u>U.S. Patent</u> 4,666,877, 1987.
32. Carrado, K.A., Suib, S.L., and Coughlin, R.W., <u>Inorg. Chem.</u>, 1986, <u>25</u>, 4217.
33. Gaaf, J. van Santen, R., Knoester, A., and Van Wingerden, B. <u>J. Chem. Soc. Chem. Comm.</u>, 1983, 655. Also <u>European Pat. Appl.</u> 090,442 (1983).
34. Lewis, R.A., Ott, K.C., and Van Santen, R., <u>U.S. Patent</u> 4,510,257, 1985.
35. Yamanaka, S., and Brindley, G.W., <u>Clays and Clay Minerals</u>, 1978, <u>26</u>, 21.
36. Yamanaka, S., and Brindley, G.W., <u>Amer. Mineral</u>, 1979, <u>64</u>, 830.
37. Pinna vaia, T.J., Tzou, M-S., and Landau, S.D., <u>J. Amer. Chem. Soc.</u>, 1985, <u>107</u>, 4783.
38. Pinnavaia, T.J., and Tzou, M-S., <u>U.S. Patent</u> 4,665,044 (1987).
39. Stüzi, H., and Marty, W. <u>Inorg. Chem.</u>, 1983, <u>22</u>, 2145.
40. Finholt, J.E., Thompson, M.E., and Connick, R.E., <u>Inorg. Chem.</u>, 1981, <u>20</u>, 4151.
41. Sudo, T., and Shimoda, S., <u>Minerals Sc. Engng.</u>, 1977, <u>9</u>, 3.
42. Jie, G.J., Ze, M.E., Zhiqing, Y., <u>Eur. Pat. Appl.</u> 197,012;1986.
43. Wright, A.C., Granquist, W.T., and Kennedy, J.V., <u>J. Catalysis</u>, 1972, <u>25</u>, 65. Also <u>British Patent</u> 1,447,403; 1976.
44. Swift, H.E., and Black, E.R., <u>Ind. Eng. Chem. Proc. Res. Develop</u>, 1974, <u>13</u>, 106.
45. Heinerman, J.J.L., Freriks, I.L.C., Gaaf, J., Pott, G.T. and Coolegem, J.G.F., <u>J. Catalysis</u>, 1983, <u>80</u>, 145.
46. Lagaly, G., <u>Adv. Colloid and Interf. Sc.</u>, 1979, <u>11</u>, 105.
47. Liebau, F., <u>"Structural Chemistry of Silicates"</u>, Springer-Verlag (Berlin), 1985.
48. Rojo, J.M., Ruiz-Hitzky, E., Sanz, J., and Serratosa, J.M., <u>Revue Chemie Minerals</u>, <u>20</u>, p. 807, (1983).
49. Kuhl, G.H., Landis, M.E., and Chu, P., <u>European Pat. Appl.</u> 222,597, (1987).
50. Kitajima, K., Koyama, F., and Takusagawa, N., <u>Bull. Chem. Soc. Jpn.</u>, 1985, <u>58</u>, 1325.
51. Otsuka, K., and Ono, M., <u>Japanese Pat.</u> 56-142982, 1983.
52. Johnson, J.W., and Brody, J.F., in <u>"Microstructure and Properties of Catalysts"</u>, Materials Res. Soc. (Pittsburg), Ed. Treacy, M.M.J., Thomas, J.M., and White, J.M., 1988.
53. Alberti, G., and Costantino, U., in <u>"Intercalation Chemistry"</u>, Ed. Whittingham, M.S., and Jacobson, A.J., Academic Press (New York), 1982, 147.
54. Clearfield, A., <u>J. Mol. Catalysis</u>, 1984, <u>27</u>, 262.
55. Lewis, R.M., van Santen, R., and Ott, K.C., <u>European Pat. Appl.</u> 159,756; 1985.
56. Lewis, R.M. and van Santen, R., <u>U.S. Patent</u> 4,637,992; 1987.
57. Pinnavaia, T.J., and Tzou, M-S., <u>U.S. Patent</u> 4,665,044; 1987.
58. Reichle, W.T., <u>Chemtech</u>, 1986, 58.
59. Miyata, S., <u>Clays and Clay Minerals</u>, 1980, <u>28</u>, 50.
60. Miyata, S., <u>Clays and Clay Minerals</u>, 1975, <u>23</u>, 369.
61. Miyata, S., ibid, 1977, <u>25</u>, 14.
62. Woltermann, G.M., <u>U.S. Patent</u>, 4,454,244; 1984.

Chapter 20

Acid–Base Properties of Catalysts Derived from Anionic Hydroxides

C. P. Kelkar, A. Schutz[1], and G. Marcelin[2]

Chemical and Petroleum Engineering Department,
University of Pittsburgh, Pittsburgh, PA 15261

Layered double metal hydroxides consist of positively charged brucite-type layers in which part of the divalent cations are substituted by trivalent cations. This results in a net positive charge in the layers which is balanced by charge compensating anions in the interlayer. Upon heating, the hydroxides undergo progressive dehydration, dehydroxylation, and decomposition of the anion, leading to catalytically active materials. This work describes studies into the role of the nature of the cations and the layer composition on the acid-base properties of the resulting mixed oxides. The decomposition of 2-propanol was used as a model reaction to examine the acid-base characteristics. Some of the materials were shown to behave as highly active, strong solid bases. The selectivity towards a base catalyzed pathway, as shown by ketone formation, was found to depend on the nature of the cations as: Zn-Cr, Ca-Al > Ni-Al > Mg-Al. IR spectroscopy was used to elucidate the nature of the acid-base sites.

Layered double metal hydroxides are isomorphous with the naturally occuring mineral hydrotalcite, having the general formula $\{[M^{II}_{1-x}M^{III}_x(OH)_2] \cdot A^{y-}_{x/y} \cdot nH_2O\}$. The resulting positive charge of the layer is balanced by anions present in the interlayer. The trivalent cation substitution can be varied between 17% and 33%, and substitution outside of this range leads to the formation of additional single hydroxides (1). Anions with

different charges or sizes can be incorporated into the interlayer
of these hydroxides leading to interlayer distances ranging from
3.6 Å to 21.8 Å.   The remaining interlayer space is taken up by
water molecules.

The thermal stability of these materials has been previously
studied by Miyata ($\underline{2}$) and Reichle ($\underline{3}$).   Upon heating, below $200^{o}C$,
the interlayer water is lost.   Between $250^{o}C$ and $500^{o}C$ the
materials dehydroxylate accompanied by the decomposition of the
anion.   Reichle ($\underline{3}$) has shown that this process is reversible up
to $600^{o}C$, and takes place without exfoliation of the layers while
maintaining the morphological structure of the hydroxide.   In
their layered form, these hydroxides have found wide use as anion
exchangers ($\underline{4}$), and sorbents for various hydrocarbon molecules ($\underline{5}$)
and water.   Intercalation of heteropoly anions ($\underline{6}$) and polymerized
bidimensional silicate anions into the interlayer has also been
reported ($\underline{7}$).

The   layered   hydroxides   by   themselves   are   catalytically
inactive, probably due to a lack of accessible sites.   Upon
calcination up to $450^{o}C$, materials intercalated with CO_3^{2-} or NO_3^{-}
anions have been found active for aldol condensation ($\underline{8}$), olefin
isomerization and β–propiolactone polymerization ($\underline{9}$).   Although
many elimination reactions have been studied over decomposed
double metal hydroxides, the nature of the sites involved is still
unclear.

It was the purpose of this work to study the acid/base sites
generated   upon   calcination   of   layered   hydroxides   using   the
decomposition of 2–propanol as a test reaction.   Although most of
the previously reported catalytic work on this class of materials
has involved the Mg–Al hydroxide, other combinations of divalent
and trivalent cations are possible and were thus investigated.

Experimental Methods

Synthesis   and   Characterization   of   Layered   Precursors.
Hydrotalcite–like materials of Mg–Al, Zn–Cr, Ca–Al, and Ni–Al were
prepared from the nitrate salts.   A mixed solution of the
appropriate divalent and the trivalent cation salts in the
required molar ratios was co–precipitated with a base, typically
NaOH, at room temperature.   The pH of the suspension was
maintained between ·8 and 10 during the addition, which required
approximately 1 hour.   After complete addition, the precipitate
was allowed to age for 16 hours and later washed with deionized
water.   The purity and crystallinity of the material was verified
by X–ray diffraction.   DTA/TGA analysis was used to study the
thermal stability as well as the accompanying weight loss of the
materials.

IR spectroscopy and ^{27}Al NMR studies were performed on the
calcined materials.   IR spectra were obtained from a thin
transparent wafer of a finely ground mixture of approximately 1 mg
of the calcined sample with 100 mg of KBr using a Perkin Elmer 680
spectrometer.   NMR   spectra   of ^{27}Al–containing   samples   were
obtained employing magic angle spinning, at 162 Hz in a 14.8 Tesla
NMR instrument.

Reaction Studies. The reaction system consisted of a flow micro-reactor using helium as a carrier gas bubbled through a saturator containing 2-propanol. The partial pressure of 2-propanol was adjusted by controlling the temperature of the saturator. Approximately 200-400 mg of the layered hydroxide were heated in the reactor under a flow of helium in order dehydrate and dehydroxylate the material. The partial pressure of 2-propanol was maintained at 100 torr and the helium flow was varied between 10-20 ml/min. The in-situ calcination temperature was varied between 400-500°C and the reaction temperature between 150-350°C. Analyses of the reactants and the products were performed by an on-line GC fitted with a capillary column.

    The reaction order for 2-propanol decomposition was estimated by varying the residence times and was found to be approximately zero order at low conversions. Reaction rates were estimated based on this reaction order. The derived activation energies are approximate due to lack of precise knowledge of the particle size in the catalyst bed.

Results and Discussion

Table I summarizes the stoichiometric composition and crystal phases determined by XRD for the different layered hydroxides immediately after synthesis. The hydroxides were calcined at temperatures between 400°C and 500°C. The effect of calcination temperature on catalytic activity is shown in Table II for the Ni-Al hydroxide. This hydroxide was found to be most active when calcined at 450°C. Similar results were found for the other hydroxides.

<div align="center">

Table I. Chemical Formula and Crystalline Phase of
Materials upon Synthesis via Precipitation

</div>

Sample No.	Chemical Formula	Major Phase
A	$[Zn_{0.75}Cr_{0.25}(OH)_2](NO_3)_{0.25} \cdot nH_2O$	Hydrotalcite
B	$[Ca_{0.75}Al_{0.25}(OH)_2](NO_3)_{0.25} \cdot nH_2O$	diffuse-Hydrotalcite
C	$[Ni_{0.75}Al_{0.25}(OH)_2](NO_3)_{0.25} \cdot nH_2O$	Hydrotalcite
D	$[Mg_{0.75}Al_{0.25}(OH)_2](NO_3)_{0.25} \cdot nH_2O$	Hydrotalcite
E	$[Mg_{0.80}Al_{0.20}(OH)_2](NO_3)_{0.20} \cdot nH_2O$	Hydrotalcite
F	$[Mg_{0.70}Al_{0.30}(OH)_2](NO_3)_{0.30} \cdot nH_2O$	Hydrotalcite
G	$Ni(OH)_2$	---
H	$Mg(OH)_2$	Brucite
I	$Al(OH)_3$	Boehmite

Differential thermal analysis has shown that the dehydroxylation of the material occurs between 400 to 450°C (3). It is postulated that higher catalytic activty observed for materials calcined at 450°C indicates complete dehydroxylation. At higher calcination temperature, i.e. 500°C it is possible that the materials start spinel formation and hence lower catalytic activity. Thus, a calcination temperature of 450°C was used in all the reported work.

Table II. Effect on Catalytic Activity of Calcination
Temperature of Ni–Al Hydroxide
at GHSV=5 x 10^{-4} at 273°C

Calcination Temperature (°C)	Conversion (%)	k_9 mol/m^2/s
400	15.02	9.8 x 10^{-10}
450	24.07	1.6 x 10^{-9}
500	12.97	8.5 x 10^{-10}

Table III lists the physical and XRD characteristics of the samples after calcination at 450°C. During 2–propanol decomposition at low conversions (<5%) the only products detected were acetone and propylene. At higher conversions secondary

Table III. Physical and Structural Characteristics of the
Materials after Calcination at 450°C

Sample No.	Surface Area m^2/g	weight loss %	Phases observed via XRD
A	40	42.6	$ZnCr_2O_4$,ZnO crystalline
B	24	56.6	possibly $CaAl_6O_{14}$
C	128	41.5	NiO, crystalline
D	192	42.1	MgO, diffuse
E	159	41.3	MgO, diffuse
F	73	43.1	MgO, diffuse
G	48	21.5	NiO
H	113	30.9	MgO
I	250	62.5	$\gamma-Al_2O_3$

reactions, e.g., oligomerization of propylene and acetone condensation, complicated the analysis due to imprecise identification of the products. The total conversion activity of the double hydroxides (samples A through D) after calcination at 450°C is shown in Figure 1. It should be noted here that these materials were used after calcination and hence were no longer hydroxides, but they will be referred to as such for sake of continuity. The Zn—Cr double hydroxide was most active, whereas the Ca—Al hydroxide proved to be the least active. The selectivity to base catalyzed pathway, showed by preferential formation of ketone over propylene, for samples A through D is shown in Figure 2. Except for the Mg—Al hydroxide, which showed almost equal amounts of both acid and base sites, all the other three hydroxides showed distinctly basic character. The activation energies for samples A through D for ketone and propylene formation are listed in Table IV and are similar to those reported by other investigators (10).

Table IV. Apparent Activation Energies for
2-Propanol Decomposition over
Calcined Double Hydroxides

| | Activation Energy (kcal/mol) | |
Sample	PROPYLENE formation	ACETONE formation
A	—	20
B	—	28
C	—	25
D	29	24

    Due to the quite different selectivities shown by the Ni—Al and the Mg—Al hydroxide, comparison experiments of 2-propanol decomposition were also carried out on the respective single hydroxides (samples G through I). Sample I consisted of boehmite phase prior to calcination. Upon calcination, these hydroxides lead to MgO, NiO and γ-Al_2O_3 respectively. The NiO was found to be highly active and purely basic in character, whereas γ-Al_2O_3 displayed high activity mainly for the acid catalyzed pathway. MgO displayed poor activity but good selectivity towards ketone formation. These results are summarized in Figure 3.
    The effect of the ratio of divalent to trivalent cation on 2-propanol decomposition was investigated for the Mg—Al system. As Figure 4 shows the Mg—Al hydroxide with the highest Al/Mg ratio displayed poorest activity but the highest selectivity towards ketone formation.
    The behavior of the calcined Mg—Al and Ni—Al hydroxides can be better understood by considering the structure of the calcined products. The XRD patterns of the calcined samples D through F
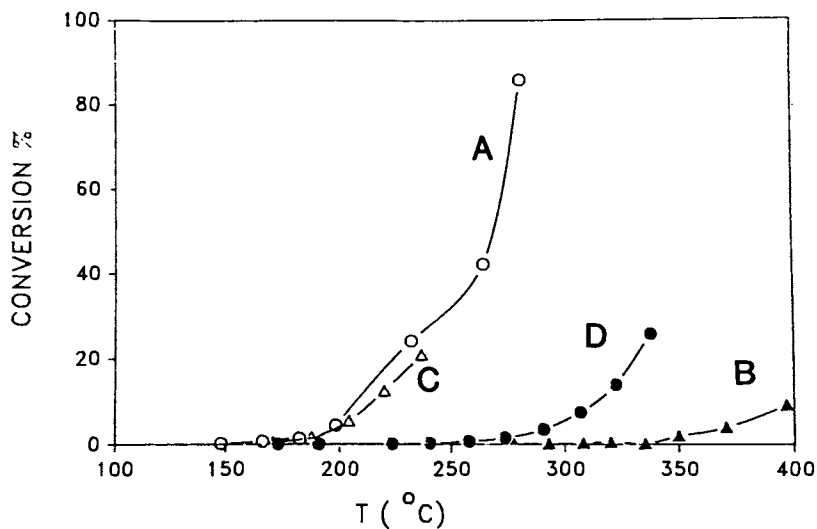
Figure 1. Total conversion activity (%) for sample A through D calcined at 450°C.
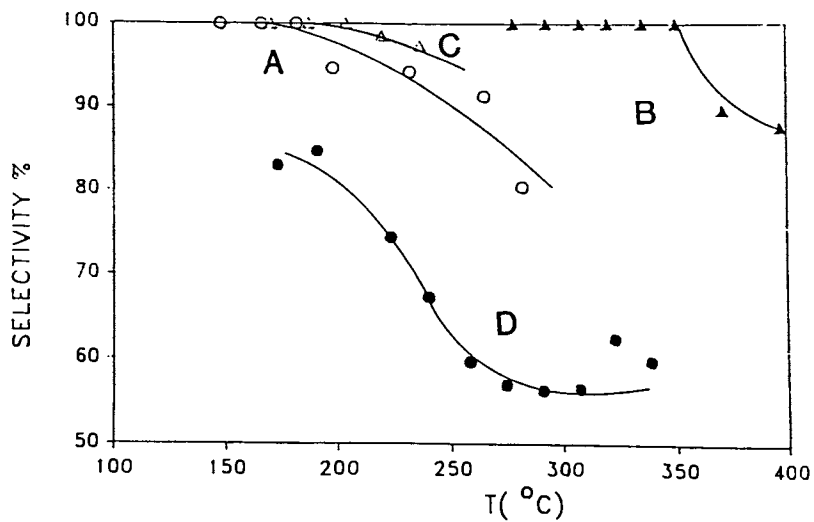
Figure 2. Selectivity (%) toward ketone formation for sample A through D.
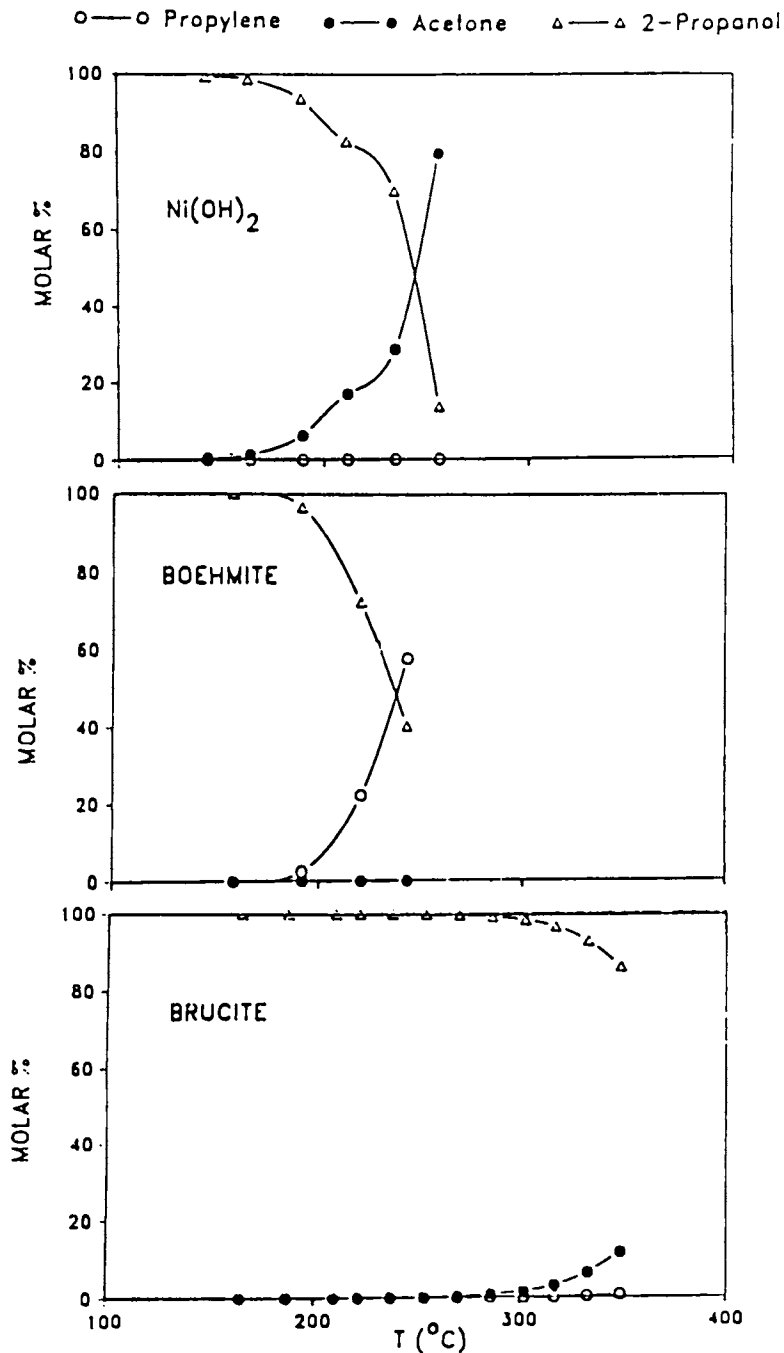
Figure 3. Product distribution for 2-Propanol decomposition over samples G through I.
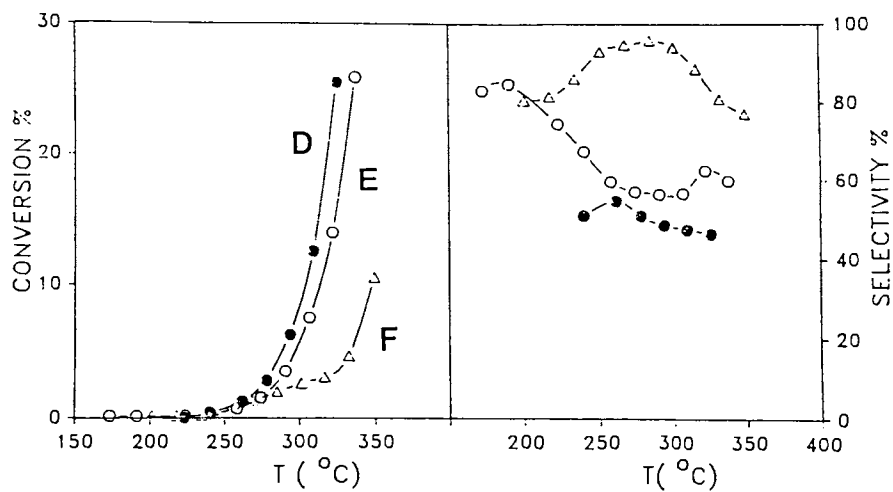
Figure 4. Total conversion and selectivity toward ketone formation for sample D through F.

revealed very broad and diffuse patterns, with a major peak which
was ascribed to MgO. Sample C, on the contrary, showed a very
crystalline pattern of NiO and no indication of either a spinel
structure or crystalline alumina. The ^{27}Al NMR spectra of sample
D, shown in Figure 5, revealed the presence of large amounts of
octahedrally coordinated Al and only small amounts of
tetrahedrally coordinated Al. No signal could be obtained on the
Ni-Al sample, possibly due to the presence of paramagnetic Ni.

IR spectroscopy was performed in the lattice wavenumber region
for samples C through F. The IR spectra, shown in Figure 6,
indicated two important characteristics: a strong band in the
400-450 cm^{-1} region, and weak bands in the region 500-900 cm^{-1}.
By comparison to spectra of MgO and NiO, the former was attributed
to the M-O stretches of each oxide. The higher wavenumber bands
are in the region of Al-O stretch, and the specific position of
the band is related to the coordination of Al. The 500-680 cm^{-1}
bands can be attributed to octahedral Al, and bands in the region
700-900 cm^{-1} can be attributed to tetrahedral Al (11). IR spectra
did not indicate spinel formation in any of the materials. The
Ni-Al calcined material showed a strong band at 825 cm^{-1}
corresponding to tetrahedral Al and absence of octahedrally
coordinated Al. In contrast all three Mg-Al showed presence of
both octahedrally as well as tetrahedrally coordinated Al, in
agreement with the NMR measurements.

The combination of spectral techniques and reaction results
revealed contrasting features for the Ni-Al and Mg-Al hydroxide
systems as they undergo calcination. The Ni-Al hydroxide after
calcination showed the distinct presence of NiO and tetrahedrally
coordinated Al, and a lack of octahedrally coordinated Al. 2-
Propanol decomposition studies showed that Ni-Al and Ni systems
display similar selectivity. This suggests that during
calcination the Ni can migrate to the outer portions of the
crystallites and it is the O-anion attached to the Ni which acts
as a basic site. The role of tetrahedral Al in this system cannot
be fully explained and may simply serve to dilute the system, thus
resulting in the observed lower activities. The Mg-Al systems, in
contrast, showed diffuse XRD patterns of MgO and the presence of
tetrahedral as well as large amounts of octahedral Al sites. It
can be tentatively proposed that the octahedrally coordinated Al
can act as a Lewis acid site while the O-anion attached to the Mg
is the basic site. An interesting feature of the Mg-Al materials
is seen in Figure 4. Sample F which contained the highest Al/Mg
ratio displayed higher selectivity towards ketone formation. This
increase in selectivity with more Al substitution cannot be
explained clearly. It has been proposed previously (8) that
hydroxyl groups present at the apices of tetrahedral Al can act as
basic sites. This finding is also consistent with the result that
tetrahedral coordination of Al is necessary for the formation of
carbonate species (12) upon adsorption of CO_2 in Al-containing
oxides. The increase in Al/Mg ratio probably causes an increase
in the amount of tetrahedral Al, and hence the higher selectivity
to base catalyzed products.
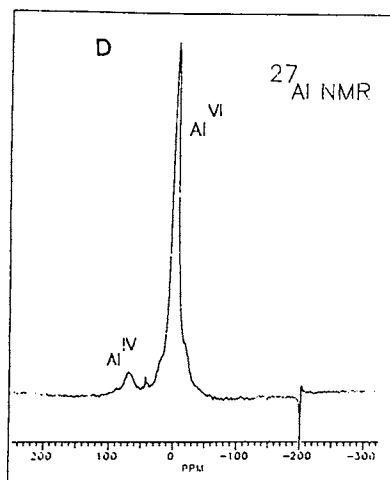
Figure 5. ^{27}Al NMR of sample D calcined at 450°C.
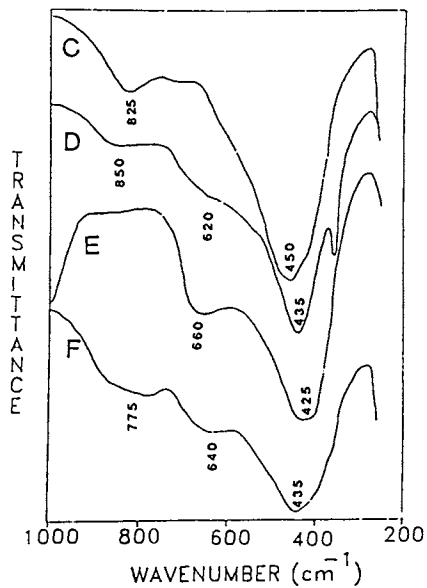
Figure 6. IR spectra of samples C through F calcined at 450°C.

Conclusions

The above work has demonstrated that not all double metal hydroxides display purely basic character upon calcination. Basic character in some cases appears due to the formation of single oxides. The active sites for ketone formation have been proposed to be the surface O-anion and the hydroxyl anion. The role of tetrahedral Al in the Ni-Al and Mg-Al systems is not clear; however, it does appear to contribute to the formation of basic sites at least for the Mg-Al system. Structural considerations have showed that Mg-Al and Ni-Al hydroxides behave differently upon calcination and therefore generate different types of active sites. In this paper a preliminary picture is presented of the coordination of the cations, particularly Al, and their effect on catalytic selectivity.

Acknowledgments

Literature Cited

1. Brindley, G.W.; Kikkawa, S. Am. Min. 1979, 64, 836.
2. Miyata, S. Clays Clay Miner. 1975, 23, 369.
3. Reichle, W.T.; Kang, S.Y.; Everhardt, D.S. J. Catal. 1986, 101, 352.
4. Miyata, S. Clays Clay Miner. 1983, 31, 305.
5. Cavalcanti, F.A.P.; Schutz, A.; Biloen, P. Preparation of Catalysts IV, Delmon, B. et al. (Editors) Amsterdam, 1987.
6. Woltermann, G.M. U.S. Patent 4 454 244, 1984.
7. Schutz, A.; Biloen, P. J. Solid State Chem. 1987, 68, 360.
8. Reichle, W.T.; J. Catal. 1985, 94, 547.
9. Nakatsuka, T.; Kawasaki, H.; Yamashita, S.; Kohjiya, S. Bull. Chem. Soc. Japan 1979, 52, 2449.
10. Kibby, C.L.; Hall, W.K. J. Catal. 1973, 31 65.
11. Tarte, P. Spectrochim. Acta 1966, 22, 1201.
12. Morterra, C.; Ghiotti, G.; Boccuzzi, F.; Coluccia, S. J. Catal. 1978, 51, 299.

Chapter 21

Carbon Molecular Sieves

Properties and Applications in Perspective

Henry C. Foley

Department of Chemical Engineering and The Center for Catalytic Science and Technology, University of Delaware, Newark, DE 19716

In this paper we briefly review the important aspects of carbon molecular sieve materials with special emphasis on their use in catalysis, and our most recent results with composite structures that we have termed inorganic oxide-modified carbon molecular sieves (IOM-CMS). The literature on carbon molecular sieves, particularly patents, is large and growing, with European and Japanese researchers dominating in recent years.

Carbon molecular sieve research can best be divided into three main areas: (A) fundamentals of preparation and properties, (B) gas separations, and (C) catalytic applications. Research and technological development concerning the carbon-based materials has been devoted primarily to the first two areas, with considerably less attention focused on their catalytic properties and utility. A number of good reviews of the separation applications, particularly pressure swing adsorption technology, have been published recently. This account will briefly summarize the properties of the carbon molecular sieves, review reports dealing with catalytic applications, and then describe our own research which has focused on preparation of composite materials, comprised of molecular sieving carbon and inorganic oxides. These composites contain functionality that is not present in the pure carbons, and ultramicroporosity for molecular sieving properties not found in the inorganic oxides. Recent results concerning the preparation and adsorptive properties of these inorganic oxide modified-carbon molecular sieves (IOM-CMS) will be discussed in the context of carbon molecular sieves in general.

Carbon molecular sieves are amorphous materials with average pore dimensions similar to the critical dimensions of small molecules. They are prepared by the pyrolysis of natural and synthetic precursors, including coal, coconut shells, pitch, phenol-formaldehyde resin, polyfurfuryl alcohol, polyacrylonitrile, and polyvinylidene chloride. Properties of the carbon molecular sieves are quite variable, spanning pore sizes from 3 to 12Å, pore volumes from 0.2 to 0.5 cm^3-g^{-1} and surface areas from 300 to 1500 m^2-g^{-1}. Properties of a particular carbon are controlled by the choice of precursor, additives or pore formers, and pyrolysis conditions (1). The surface of molecular sieving carbon is hydrophobic and inert in a net reducing environment. However, treatment of the carbon in a net oxidizing environment can convert surfaces to a more active and hydrophilic form. The hydrophilic state is generally thermally unstable, reverting to the hydrophobic form upon heating in an inert or reducing environment.

The pore structure in molecular sieving carbon is typically ascribed to arise from at least three different mechanisms. In the first the structure of the carbon is derived from the precursor, but in shrunken form. In this way the structure of wood charcoal is similar to the cellular structure of the wood (2). Another type of porosity arises in the fissures and cracks left behind in the carbon matrix. These faults relieve the thermally-induced, mechanical stresses brought on by pyrolysis. Ultramicroporosity can also originate from the volatilization of small molecules. These molecules are formed during pyrolysis, and leave molecularly-sized channels in the solidifying carbon matrix (3-6). Pyrolysis of polyfurfuryl alcohol, polyvinylidenechloride, and polyacrylonitrile lead to the formation of formaldehyde and water, hydrogen chloride, and hydrogen cyanide, respectively.

Since carbon molecular sieves are amorphous materials, the dimensions of their pore structures must be measured phenomenologically by the adsorption of small probe molecules with different critical dimensions. There is insufficient long range order to utilize standard x-Ray diffraction methods for characterization. The earliest reports of molecular sieving carbons dealt primarily with coals and charcoals. Sorption of helium, water, methanol, n-hexane, and benzene was measured and related to the porosity of the carbon. Pore-sizes were estimated to be two to six angstroms (3-6). In a classic paper P.H. Emmett described methods for tailoring the adsorptive properties and pore size distributions of carbon Whetlerites. The method combined steam and heat treatments of the carbon which had been treated with various metals and their oxides or chlorides (7).

Shortly thereafter, it was realized that molecular sieving carbons could be prepared by controlled pyrolysis of polymeric precursors (8). Early estimates of pore sizes for this carbon were seven to eight angstroms, but progressive activation increased surface area, pore volume, and pore dimensions. Factors of 1/100 and more were observed in the adsorption rates for bulky molecules like 3,3-diethylpentane compared to linear and planar molecules. The rate differences were attributed to steric limitations on the adsorption of the bulkier molecules. Separation of n-butane from isobutane was accomplished both on Saran- and other polyvinylidenechloride-derived carbons (9-11).

Based on these and other results it was concluded that molecular sieving carbons have slit-shaped pores (9-11). This view of the pore geometry of carbon molecular sieves persists and is still consistent with the bulk of experimental evidence.

Recently, carbon molecular sieves have been fabricated in the form of planar membranes and hollow tubes by the pyrolysis of polyacrylonitrile in suitable forms (12-16). Very high separation selectivities have been reported with these materials. Their pore sizes are in the range from 3 to 5.2Å. Selectivities of greater than 100:1 are observed between molecules which differ by as little as 0.2Å in their critical dimensions. Kinetics of adsorption on these materials have been determined (2,15,16).

By far the most fully developed application for carbon molecular sieves is in the separation of small gas molecules. A large number of patents describe claims for materials and processes that include carbon-based sieves. Separations that have been accomplished include: oxygen and nitrogen, hydrogen and coke gases, methane and carbon dioxide, methane and xenon, ethylene and ethane, propylene and propane. A number of companies in Europe and the United States have recently offered commercial systems for the separation of nitrogen from air. A review of the use of carbon molecular sieves in separation technology is well beyond the scope of this article and the interested reader is referred to recent reviews and references sited therein (17,18).

Catalytic applications of the carbon molecular sieves have been much fewer in number. The research groups of Walker and Trimm were the first to have investigated the reactant shape-selectivity of metal-containing carbon molecular sieves. In a series of papers and patents Trimm and Cooper reported the preparation, adsorptive, and catalytic properties of a variety of metal-containing carbon molecular sieves. In 1970 they showed that platinum-containing carbon molecular sieves hydrogenated 1-butene but not 3-methyl-1-butene. In contrast a platinum catalyst on activated carbon hydrogenated both substrates equally effectively (19-21). Schmitt and Walker also described the preparation of a platinum-containing carbon molecular sieve from polyfurfuryl alcohol and also tested its shape-selectivity studying the products from a mixture of linear and branched olefin that was passed over the catalyst with hydrogen. As in the work of Trimm, these results indicated that the linear olefin was reduced but the branched was largely unreacted (22-24). These demonstrations suggested that the steric bulk of the branched molecule prevented access to the platinum sites within the pores   of the carbon molecular sieve material. This was an example of reactant shape-selectivity since, the catalyst particles made a chromatographic separation of the reactants and then hydrogenated the sterically unhindered molecule.

More recently Walker and Vannice have examined iron carbon molecular sieves, Fe-CMS, for the hydrogenation of carbon monoxide. The report was particularly thorough and rich in detail regarding the preparation of the Fe-CMS materials. Chemisorption of CO and H_2, as well as the kinetics of CO hydrogenation and methanation were described (25). In other investigations Walker and coworkers have examined the effect of

heat treatments on the pore structure of carbon molecular sieve catalysts used for hydrodesulfurization and coal liquefaction (26).

Bragin has reported a study of three reactions: cis-trans isomerization of 1,2 dimethylcyclopentane, aromatization of cyclohexane, and the dehydrocyclization of isooctane. The catalysts contained Pt on various carbon molecular sieve supports with varying pore radii. The highest specific activity for the first two reactions was observed over the catalysts with the smallest pore size. In contrast the catalysts with the smallest pore radii had immeasurably low activity for the last reaction (27). Connor demonstrated the utility of carbon molecular sieves as supports for molten indium metal catalysts, which are used to produce aldehyde and ketones by dehydration of primary and secondary alcohols. The molten indium is apparently held in the pores of the carbon molecular sieve even at loadings as high as 7.5 wt% with a relatively high metal surface area resulting in commensurately high activity (28). Dessau has shown that large-pore carbon molecular sieves will cyclodimerize alkydienes in an Diels-Alder fashion. An example is the conversion of 1,3- butadiene into 4-vinylcyclohexene (30%), over a fixed bed of carbon molecular sieve (29).

As is evident relatively little research has been devoted to catalysis with carbon molecular sieves. This is especially surprising in view of the amount of recent interest there has been in novel catalytic materials. The latter two reports dealing with alcohol dehydration over In-CMS and Diels-Alder dimerizations with CMS materials are very interesting. Although carbon-based molecular sieves have had considerable impact upon the science and technology of small molecule separations, they have been much less important in catalysis.

This investigation has set out to explore the preparation and characterization of new carbon-based molecular sieves, which are functionalized with inorganic oxides and supported metals. The objective is to combine the molecular sieving properties of the carbon with the surface chemical and physical properties of the inorganic oxides in one composite structure. The advantage of composites is that they can be designed and engineered for specific applications. Incorporating functionalities like metals and acidic or basic oxides with high pore volume at the core of these composite materials can be an advantage in the application of these materials to gas separations. Similarly, combining molecular sieving carbon with active catalyst phases, the composite structure can provide separation with catalysis for enhanced selectivity. Weak chemisorption or enhanced physisorption can provide an additional driving force for mass transfer and separation over that provided by pure carbon. The balance of this paper deals with our recent results in the preparation and characterization of the inorganic oxide modified-carbon molecular sieve (IOM-CMS) composites.

Experimental

Characterization of IOM-CMS Materials by Molecular Probe Adsorption. Since carbon molecular sieves, and the IOM-CMS materials prepared herein, are both polycrystalline and amorphous, we have characterized their sieving properties phenomenologically by molecular probe adsorption. The probe

molecules utilized are: CO_2, n-butane, isobutane, and neopentane with critical dimensions of 3.3, 4.3, 5.0, and 6.2Å respectively. Comparisons are made between the specific adsorption of each of these molecules on both the pure inorganic oxides, and the IOM-CMS composites. The latter had different specific adsorptions depending upon the amount of carbon present.

   The molecular probe apparatus had to be able to generate reliable adsorption data at high throughput. With this in mind a system was constructed based on a Cahn electrobalance (see Figure 1). A high vacuum chamber, containing a carousel capable of holding up to six samples was fitted to the balance. The carousel was attached to a heater block, which contained cartridge heaters and a thermocouple. Carousel temperature was set and maintained with a Wizard 1601 programmable controller. All six samples in the carousel were conditioned, and subsequently exposed to the adsorbate, simultaneously, and for one hour following the methods of Walker and co-workers (9-11, 22-26). The carousel was rotated so that each sample could be separately picked up and hung on the balance to gravimetrically measure adsorptive uptake of the probe molecules. After an analysis with one probe molecule, the samples were heated in vacuo to recondition them, and then exposed to the next molecular probe molecule. This cycle was repeated until all four probe molecules had been exposed to all of the samples. The analyses always began with the smallest probe molecules first since these gave reversible adsorption in an acceptable time frame with a minimum of pore plugging due to entrappment of residual amounts of the larger probe molecules. In this way a large number of samples were characterized rapidly. The results of the molecular probe analyses on the IOM-CMS materials are described in the next section of this paper.

Preparation of IOM-CMS Materials. The Type I materials were prepared by building a carbon overlayer in a series of successive steps. The steps involved contacting the particle of the inorganic oxide with polyfurfuryl alcohol, draining off the excess, and heating in a flowing inert gas to convert the resin to carbon. These steps were repeated until a sufficient amount of carbon was added to produce the desired molecular sieving properties, diagnosed by molecular probe adsorption. The evolution of the pore structure of the inorganic oxides with carbon-coating cycles was examined with titania pellets and large-pore silica particles.

   The Type IIa samples were prepared by mixing the polyfurfuryl alcohol with metal alkoxides and then pyrolyzing the mixture in a tube furnace under flowing nitrogen. The Type IIb IOM-CMS samples were prepared by mixing metal oxide powders, formed by hydrolytic precipitation of the metal alkoxides and calcination of the precipitate, with the PFA and then pyrolyzing. Following the heat treatment the Type IIa and IIb samples were crushed and screened to retain the 40x80 mesh particles for molecular probe analysis.

   The Type III IOM-CMS materials were prepared by modifying the surface of a porous carbon with an inorganic oxide, combining this with polyfurfuryl alcohol, and pyrolyzing the mixture. Each of the examples described below were chosen to

represent the general methods used to prepare various
compositions of each type of IOM-CMS material.

C-SiO$_2$ (beads). Type I.   50 g of microporous silica beads
(Aldrich, No. 25,562-9, 3mm diam., N$_2$ BET S.A.= 600 m^2-g^{-1},
p.v.=0.39 cm3-g^{-1}, pore diam. = 25Å) were immersed in
polyfurfuryl alcohol (Occidental Chemical Corporation, No.
16470, Durez Resin , Lot No. 57VIBIA), and then drained of the
excess. The beads with adsorbed PFA were heated in a tube
furnace under flowing nitrogen with the following heat cycle:
100-300°C, in 50°C increments every 30 min, and 300°C for 2hr.
These steps were repeated up to twelve times. In addition
during the fourth, eighth, and last heating cycles the
temperature was raised to 500°C and soaked for 6hr. After this
the furnace was cooled down to room temperature in flowing
nitrogen and the sample removed, and stored in a capped vial.

C-TiO$_2$. Type IIa. Titanium (IV) butoxide was mixed with PFA in
seven different weight ratios to obtain theoretical weight
ratios of TiO$_2$ to carbon of 1:2, 1:1, 2:1, 4:1, 10:1, 15:1, and
20:1. These mixtures were heated by the cycle: 100°C for 1 hr,
30 min each in 100°C intervals from 200-600°C, and soak at 600°C
for 3 hr.

C-TiO$_2$. Type IIb. Titania was prepared by hydrolyzing
titanium(IV) butoxide (Alfa Products, # 77124) to produce a
powder, which was calcined at 500°C for two hours in air.
Titania powder was mixed with PFA in these weight ratios: 1:2,
1:4, and 1:8. The samples were heated at 100°C for 1hr, 200°C
for 1hr, 300°C for 2 hr, and finally 500°C for 6 hr.

C-TiO$_2$. C-ZrO$_2$. C-TiO$_2$-ZrO$_2$ Type III. Wide-Pore carbon (560
m^2/gm, 0.96cm^3/gm, ~60Å pore radius, American Cyanamid) was ball-
milled for 16 hr and then functionalized by contacting it with
Ti(IV) n-butoxide, dissolved in a volume of isopropyl alcohol
sufficient to fill the pore volume of the carbon. In order not
to exceed the pore volume of the carbon the contacting step was
repeated three times, with heat treatments of 200°C in air for
2-3 hr after each contacting step. This resulted in 20 wt%
titania on the carbon. The same process was followed to prepare
titania-modified and zirconia-modified (using Zr(IV) propoxide)
Raven 8000 carbon beads, also at the 20 wt% level. Three
samples of Type III materials were prepared with each of the
three surface-modified porous carbons by separately mixing 20 g
of the modified carbon base with 20, 80, and 160 g of PFA. The
mixtures were then heated in flowing nitrogen at 20°C/min to
500°C, soaked at 500°C for 2 hr, then heated again at 20°C/min
to 600°C, and soaked for 5 hr.

Results and Discussion

In this research program we have sought to prepare novel shape-
selective materials comprised of carbon molecular sieves and
selected inorganic oxides, referred to as Inorganic Oxide-
modified Carbon Molecular Sieves or IOM-CMS materials. An
incentive for conducting this investigation was that the IOM-CMS
materials could combine the best properties of inorganic oxides
with the molecular sieving properties of the carbon. The

inorganic oxides, such as alumina, silica, silica-alumina,
titania, and titania-zirconia have a variety of desirable
properties not available with pure carbon. These include macro-
and mesopore structures, metal support interactions, and acidity
or basicity. In contrast the polymer-derived carbons have the
ultramicroporosity needed to provide for molecular sieving but
are relatively inert and offer little in the way of variable
acidity and basicity or metal support interactions. Therefore
it seemed logical that a combination of the two materials into
one composite sieve could make possible synergistic properties,
and provide a degree of tailorability available only in a
composite material. With these features in mind three separate
types of IOM-CMS materials were conceptualized.

Type I IOM-CMS Materials

The Type I material is ideally comprised of a particle of
inorganic oxide surrounded by a shell-coating of the molecular
sieving carbon. In this way the inner non-sieving particle is
surrounded by a molecular sieving gate of carbon (see Figure 2).
Molecular communication to the inorganic oxide is regulated by
the pore restrictions of the carbon; however, once through the
gate the reactants experience the same catalytic environment
present in the untreated inorganic oxide. In many respects the
structure of the Type I material is similar to that of the all-
carbon composite molecular sieves, first prepared and
characterized by Walker and Metcalfe. In their system a
molecular sieving overlayer of polymer-derived carbon was
deposited on particles of porous active carbon, rendering the
combination a molecular sieve (9-11).
      The carbon overlayer of the Type I materials is prepared by
a series of successive steps, involving contacting the particle
of the inorganic oxide with polyfurfuryl alcohol, and heating in
a flowing inert gas to convert the resin to carbon. These steps
are repeated until a sufficient amount of carbon has been added
to produce the desired molecular sieving properties. A wide
range of materials were used for the Type I, IOM-CMS including
the following support and catalytic materials: silica, alumina,
silica-alumina, silica-supported iron, silica-supported
potassium-promoted iron, titania, titania-zirconia, silica-
supported ruthenium, a precipitated iron Fischer-Tropsch (FT)
catalyst ($Fe_2O_3:CuO:K_2O$), alone and in combination with a
hydrocracking catalyst (3% CoO-15% MoO_3/ Al_2O_3).
      The results of the molecular probe analyses on these
materials are displayed in Table I. Specific adsorptions of the
gases are given for each inorganic oxide as a function of the
number of cycles of carbon coating. The first two entries are
for a high surface area (>600 $m^2 \cdot g^{-1}$) microporous silica and a
lower surface area (<300$m^2 \cdot g^{-1}$) large pore silica. Both of the
silicas in their untreated states display specific adsorption of
all the probe molecules that are quite high. The differences in
magnitude are due to their different physical properties. The
stepwise addition of carbon dropped the adsorptivities of the
probe molecules on each sample. After twelve carbon coating
cycles both materials adsorb CO_2 in reasonably high quantities,
comparable to that of the untreated oxide itself, but
adsorptions of the larger hydrocarbon molecules are negligible.
We also note that the CO_2 surface area increases with carbon
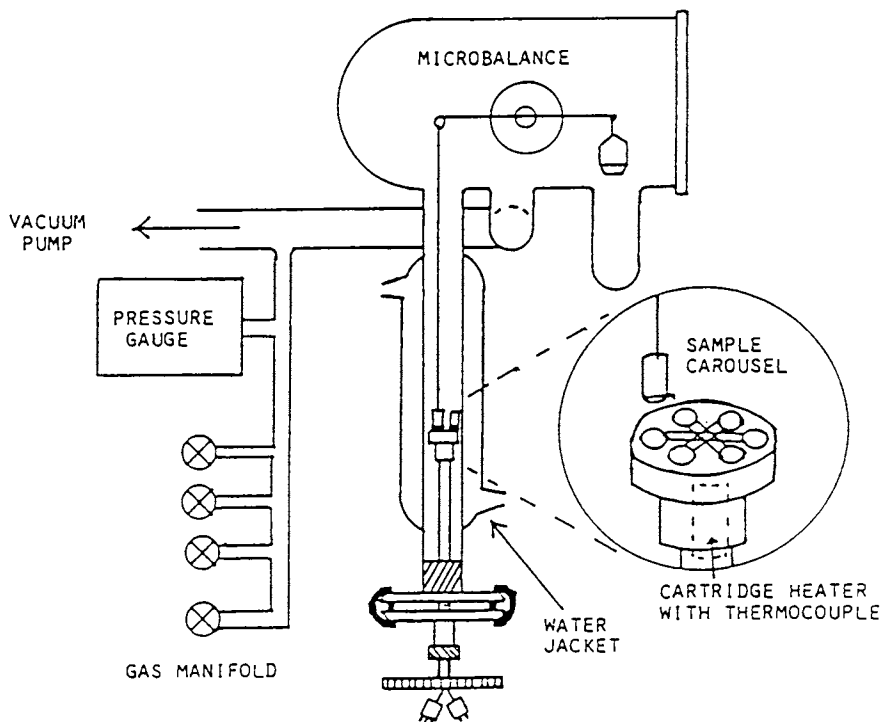
Figure 1. Specific Adsorption Apparatus
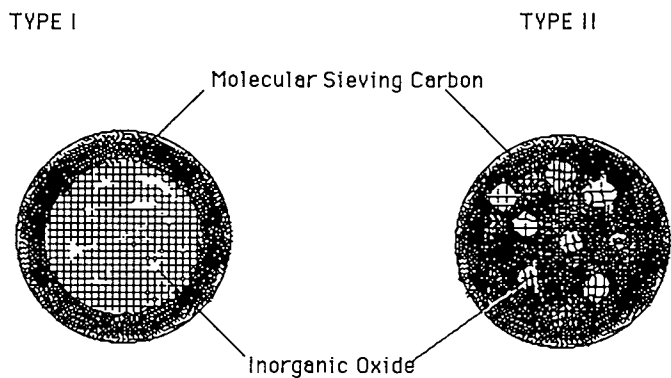
Figure 2. Schematic of Type I and Type II Structures

TABLE I. Specific Adsorptions for the Type I IOM-CMS Materials

INORGANIC OXIDE	FORM	COATING NUMBER	CO_2	SPECIFIC ADSORPTION (mg per gm)		
				n -BUTANE	ISOBUTANE	NEOPENTANE
SiO_2[a]	spheres	0	46	151	134	158
		2	32	35	32	38
		4	16	13	11	9
		6	14	4	8	5
		8	31	9	9	4
SiO_2[b]	irregular	0	16	40	40	50
		2	37	25	16	15
		4	42	12	10	6
		6	33	5	4	2
		8	31	0	0	1
SiO_2[c]	irregular	0	16	42	45	57
		4	19	45	25	61
		6	25	69	53	67
		8	33	74	54	47
		10	29	61	4	10
		12	33	39	2	6
Al_2O_3[d]	trilobes	0	33	69	66	80
		4	30	47	44	52
		6	30	38	37	38
		10	27	37	34	37

a = Silica Gel Spheres, 3 mm diam., 600 m^2/gm, 0.38 cm^3/gm, 25 Å pore diam. – Aldrich No. 25,562-9

b = Large Pore Silica, 8 x12 mesh, 300 m^2/gm, 1cm^3/gm, ~ 70 Å pore diam.– Alfa No. 89436

c = Cabosil Silica

d = gamma – Alumina, trilobes 2.5 x 10 mm, 1 cm^3/gm, ~ 80 Å pore diam. – American Cyanamid

Table I. (continued) Specific Adsorptions and Carbon Content on Type I IOM-CMS Materials

INORGANIC OXIDE	FORM	COATING NUMBER	SPECIFIC ADSORPTION (mg per gm)			
			CO_2	n-BUTANE	ISOBUTANE	NEOPENTANE
SiO_2-Al_2O_3[e]	pellets	0	20	49	47	60
		4	29	40	37	34
		6	30	23	17	9
		8	22	10	11	3
		10	28	10	3	0
		12	30	10	8	5
TiO_2[f]	pellets	0	8	11	13	15
		5	8	2	0	1
		8	19	2	0	1
TiO_2-ZrO_2[g]	pellets	0	29	54	54	68
		4	27	21	16	7
		8	11	6	5	1
ZrO_2[h]	pellets	0	30	26	21	21
		4	24	31	25	25
		6	17	38	26	31
		8	20	11	1	1
CARBON[i]	irregular	-	56	0	0	0

e = Silica-alumina pellets, 3.2 x 3.2 mm, Alfa No. 11839
f = Titania pellets, 5 x 7 mm, 60 m^2/gm, prepared by hydrolysis of Ti(i-OBu)$_4$
g = Titania-zirconia pellets, 5 x 7 mm, ~240 m^2/gm, > 40 Å pore diameter, prepared by hydrolysis of Zr(i-Opr)$_4$ & Ti(i-OBu)$_4$
h = zirconia pellets, 5 x 7 mm, 5 x 7 mm, ~ 200 m^2/gm, < 40 Å pore diameter, prepared by hydrolysis of Zr(i-Opr)$_4$
i = Carbon, 8 x 18 mesh, prepared by pyrolysis of Durez Resin - Hooker Chemical

content. This is not surprising since the added carbon contains
ultramicroporosity that provides very high surface area. Based
on these results the Type I IOM-CMS materials behave similarly
to a 4A zeolite, adsorbing only CO_2. Similar results were
observed with the other inorganic oxides, with some variation in
the amount of carbon neccessary for the material to be converted
to a molecular sieve (see Table I). However, even after ten
carbon-coating cycles the gamma-alumina sample was not converted
into a molecular sieving material, despite measurable decreases
in the specific adsorptions of hydrocarbon probe molecules. At
this time it is not clear whether this result is due to the
chemical or physical properties of gamma-alumina, or both.
     These specific adsorption results for the Type I IOM-CMS
materials indicate that a wide variety of inorganic oxides with
markedly different chemical compositions, physical properties,
and forms can be rendered molecular sieving by the carbon. Also
for the majority of the inorganic oxides used, the onset of
molecular sieving began after eight carbon coating cycles. This
suggested a relationship between the weight percent of carbon
present and the molecular sieving properties of the materials.
It seemed likely that the amount of carbon needed to produce the
sieving properties might depend on the surface area and pore
structure of the particular inorganic oxide. To determine if
this were true, the carbon content of the IOM-CMS materials was
evaluated after each carbon-coating step. The evaluation was
done by measuring the specific adsorption of the probe molecules
and the nitrogen adsorption isotherms after each carbon coating
cycle.
     The change with carbon content in the specific adsorption
of the gaseous probes was made on titania pellets and large-pore
silica particles. These two samples had different chemical
compositions, surface areas, and porosities. These oxides were
converted into Type I IOM-CMS materials by successive cycles of
contacting in polyfurfuryl alcohol and pyrolysis in flowing
nitrogen. To relate the carbon content to the coating cycle
number, the sample was weighed before and after each complete
cycle, and the amount of carbon added was calculated by
difference. Samples were also saved after each coating step,
and a portion carefully weighed, then burned in flowing air.
The residual oxide was carefully isolated and weighed. The
difference in weight before and after burning gave another
independent measure of the total amount of carbon present on the
sample at that point in the preparative process. The data from
these experiments over twelve cycles are displayed graphically
in Figure 3.
     The specific adsorptivities and nitrogen isotherms were
also determined on these samples after each coating cycle. The
specific adsorption results are plotted in Figures 4 and 5 for
titania and silica, respectively. In both cases the carbon
dioxide adsorption increases with the addition of carbon. This
is because the added carbon is ultramicroporous and has a large
surface area available for carbon dioxide adsorption, larger
than that of the pure inorganic oxide. As the carbon content
increases the adsorption of the larger probe molecules drops
because the large inner pores are made inaccessible by the
carbon.
     In general it is noted that eight carbon- coating cycles
were usually needed to induce molecular sieving properties in
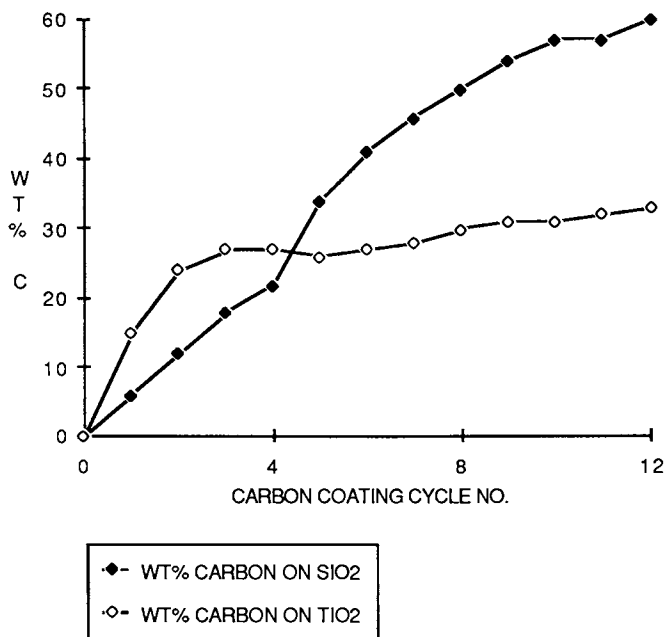
Figure 3. Change in Carbon Content with Coating Cycle Number for TiO_2 and SiO_2 Type I IOM-CMS Materials
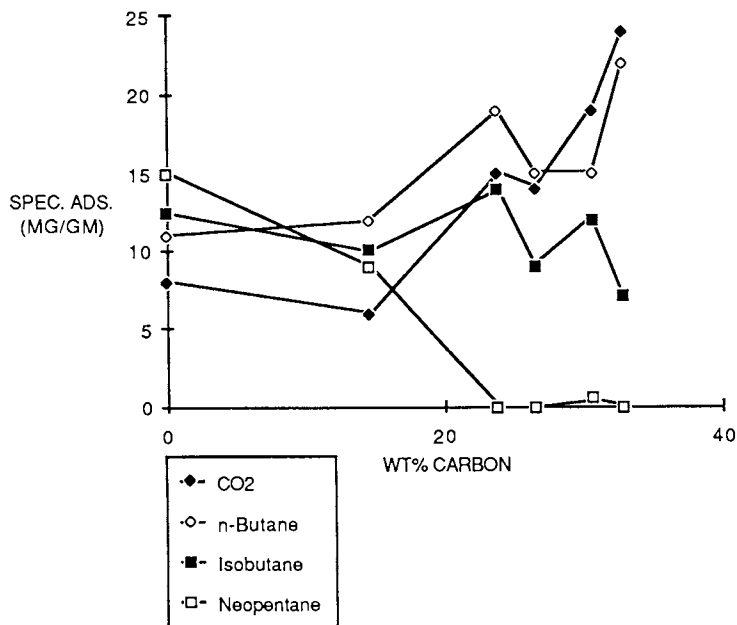
Figure 4. Specific Adsorption of Probe Molecules on Titania as a
Function of Carbon Content
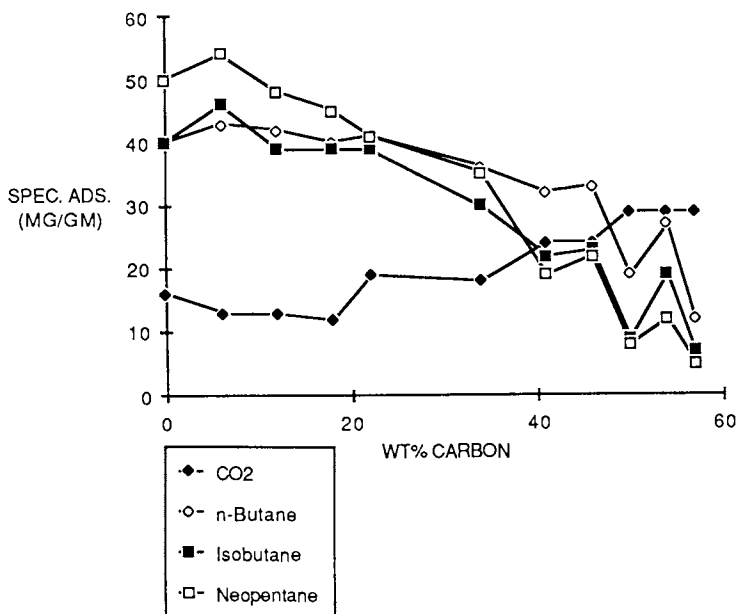
Figure 5. Specific Adsorption of Probe Molecules on Silica as a
Function of Carbon Content

American Chemical Society
Library
1155 16th St., N.W.
Washington, D.C. 20036

most of the inorganic oxides used for the Type I IOM-CMS
materials. For titania the eighth coating step corresponds to
30% carbon, while for silica it corresponds to 43-49% carbon.
The nitrogen isotherm and molecular probe adsorption data both
suggest that the carbon must reach some minimum value, set by
the physical and chemical properties of the oxide, before it
converts the composite into a molecular sieve.

Type II IOM-CMS Materials

Type II materials were conceptualized as a dispersion of very
fine inorganic oxide particles, distributed through the carbon
matrix (see Figure 2). This is in contrast to the idealized
form of the Type I material in which the inorganic oxide
particle is large and in effect supports the molecular sieving
carbon. We have found that the Type II materials can be
prepared in two different ways. In the first method a
hydrolytically unstable metal alkoxide compound was used as a
precursor to the inorganic oxide, and was mixed with the
polyfurfuryl alcohol resin. The mixture was then pyrolyzed
under flowing nitrogen. The pyrolysis of the polyfurfuryl
alcohol leads to the formation of water as well as carbon. The
metal alkoxide compounds break down to the corresponding metal
hydrous oxide in the presence of water. Therefore it is logical
to expect that the metal alkoxide, which was dispersed in the
PFA resin, broke down to the metal hydrous oxide and alcohols
during the initial stages of pyrolysis. The metal hydrous oxide
was then dehydrated to the metal oxide with further heating at
the elevated temperatures. This process resulted in the
formation of a highly dispersed metal oxide phase in the carbon
matrix. Release of the alcohols and their subsequent
volatilization is expected to also give rise to enhanced pore
formation.

$$PFA \xrightarrow{\text{600 C, } N_2} Carbon + H_2O + CO_2$$

$$M(OR)_4 + H_2O \xrightarrow{\text{600 C, } N_2} M(O)(OH)_2 \xrightarrow{\text{600 C, } N_2} MO_2$$

$$\{M = Ti, Zr\}$$
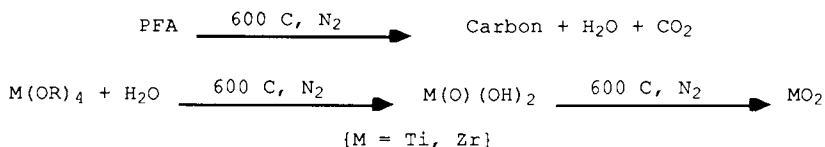
     Molecular probe analyses of the Type IIa materials
demonstrated that all of these materials were molecular sieves
(see Table 2, Figures 6a and b). They adsorbed nearly as much
CO_2 as the pure carbon alone, but near zero amounts of the
larger probe molecules. Based on this data, these materials are
classified as 4A size sieves. It was somewhat surprising to
discover that at metal oxide contents over 60 wt% molecular
sieving properties still persist. This result is consistent
with the notion that the metal oxide particles, produced from
the alkoxide during pyrolysis, are present at high dispersion.
     In order to determine the composition of the Type IIa
materials the samples were oxidized in air. This was done to
burn off the carbon and leave behind the metal oxide. By
careful weighing before and after the oxidation process, the
amounts of carbon and inorganic oxide contained in each sample
were calculated. The results of these analyses, as well as the
metal alkoxide and polyfurfuryl alcohol conversions, are also

Table II. Specific Adsorptions and Carbon Content on Type IIa IOM-CMS Materials

INORGANIC OXIDE	OXIDE PRECURSOR	WT% CARBON	WT% Metal Oxide	SPECIFIC ADSORPTION (mg per gm)			
				CO_2	n-BUTANE	ISOBUTANE	NEOPENTANE
TiO_2	Ti(i-OBu)$_4$	100	0	51	0	0	0
		91	9	45	0	0	0
		86	14	65	0	0	0
		80	20	58	0	0	0
		64	36	65	0	0	0
		58	42	34	0	0	0
		44	56	39	0	0	0
		40	60	31	0	0	0
		37	63	30	0	0	0
ZrO_2	Zr(i-OPr)$_4$	100	0	70	0	0	0
		88	12	59	0	0	0
		80	20	48	0	0	0
		70	30	31	0	0	0
Al_2O_3	Al(s-OBu)$_3$	100	0	66	0	0	0
		87	13	62	0	0	0
		87	13	63	0	0	0
		60	40	55	0	0	0
TiO_2-ZrO_2	Ti(i-OBu)$_4$	100	0	59	0	0	0
	Zr(i-OPr)$_4$	68	32	57	0	0	0
		56	44	50	0	0	0
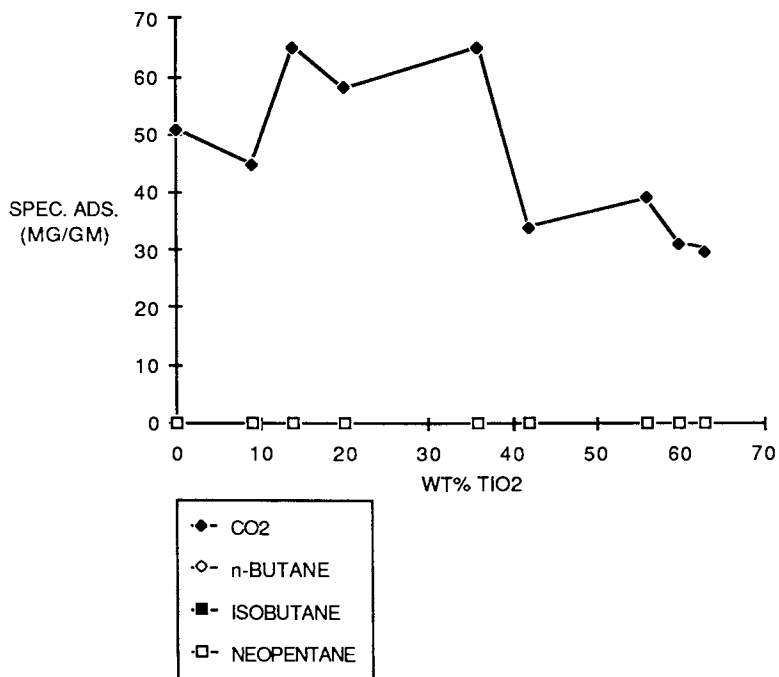
Figure 6a Specific Adsorption of Probe Molecules on TiO_2 Type IIa
IOM-CMS Materials versus Wt% TiO_2
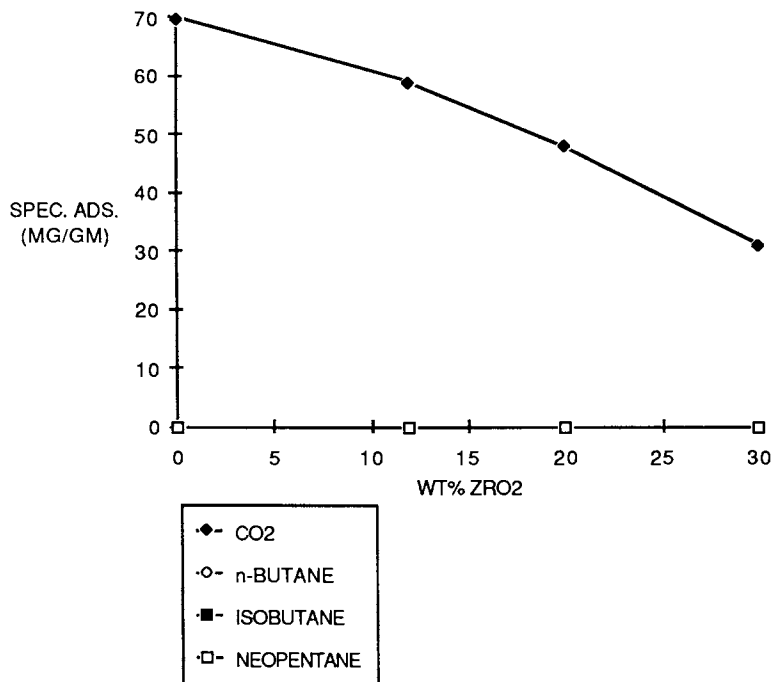
Figure 6b   Specific Adsorption of Probe Molecules on ZrO_2 Type IIa
             IOM-CMS Materials versus Wt% ZrO_2

collected in Table 3. The titania series ranged in oxide
content from 9 to 63 wt%, the zirconia series from 12 to 30 wt%,
the alumina series from 13 to 40 wt%, and the titania-zirconia
series from 10 to 26 wt%. In the course of this analysis it was
noted that the carbon yield from pyrolysis of polyfurfuryl
alcohol improved in the presence of the metal alkoxide compared
to the yield obtained from the pure resin. In the case of
Ti(IV) butoxide, the carbon yield was observed to go as high as
50% (weight carbon produced/weight resin used), versus typical
yields of about 25% for the resin alone. With the other
alkoxides the effect was not as great, leading to carbon yields
of about 30-35%. The enhanced carbon yield may be a result of
metal alkoxide-catalysed dehydration or crosslinking of the
resin, or both.

     The Type IIb IOM-CMS materials were prepared by mixing fine
powders of the metal oxides with PFA. The metal alkoxide
powders were prepared by hydrolysis of the same alkoxides used
in the preparation of the Type IIa sieves with PFA. After
calcination and mechanical grinding, the powders were mixed in
different weight ratios with the polfurfuryl alcohol and
pyrolyzed.

     Molecular probe analyses of the Type IIb materials showed
that they adsorbed significant quantities of CO_2 and n-butane,
but nearly zero amounts of the two larger probe molecules (see
Table 3, Figures 7a and b). Because of this selective
adsorption, these materials behaved similarly to the 5A size
molecular sieves, but without the sharp cutoffs displayed by
zeolites. However, it is remarkable that these Type IIb
materials adsorbed more of n-butane than the Type IIa materials.
It may be that the addition of the fine oxidic particles led to
interstices, which did not form in the preparation starting with
the metal alkoxides. These interstices may provide adsorption
sites for the larger molecules. Further investigations will be
conducted to determine the structural factors that give rise to
these different adsorptive properties.

     Carbon burnoff experiments were also used with the Type IIb
samples to determine the carbon and inorganic oxide contents of
these materials. In the titania series the metal oxide content
ranged from 46 to 61 wt%, the zirconia series from 32 to 60 wt%,
and in the titania-zirconia series from 38 to 44 wt% (see Table
3). In this preparative procedure the addition of the oxidic
powders did nothing to improve the yield of carbon from the
resin.

     As a further diagnostic of the adsorptive properties of the
IOM-CMS composite materials, the extent of water adsorption was
determined on various Type I, IIa, and IIb samples. It is
important to assess the water adsorption isotherms on the IOM-
CMS materials, since it is a standard method of comparison
between adsorbents. The water adsorption data are displayed in
Figure 8 for IOM-CMS materials, the pure inorganic oxides, and
zeolite 3A. The zeolite showed the characteristically high
adsorption of water at low relative pressures. The three Type I
samples of SiO_2-Al_2O_3, SiO_2 beads, and large pore SiO_2, adsorbed
amounts of water similar to the carbon alone. This is
consistent with a Type I structure in which the surface
adsorbing the water is carbon.

     The most interesting IOM-CMS sample was the Type IIa Al_2O_3-
carbon sample which has a different water adsorption isotherm

TABLE III. Specific Adsorptions and Carbon Content on Type IIb IOM-CMS Materials

INORGANIC OXIDE	OXIDE PRECURSOR	WT% CARBON	WT% Metal Oxides	CO_2	SPECIFIC ADSORPTION (mg per gm) n-BUTANE	ISOBUTANE	NEOPENTANE
TiO_2	$Ti(i-OBu)_4$	39	61	27	15	0	2
		43	57	22	6	0	1
		53	47	32	13	0	0
		54	46	29	6	0	0
ZrO_2	$Zr(i-OPr)_4$	40	60	28	26	4	1
		56	44	35	15	0	0
		68	32	41	0	0	0
SiO_2	CABOSIL		94	11	26	25	28
			90	14	28	30	30
			80	10	27	20	25
			66	28	19	13	22
			40	24	2	2	2
			33	25	2	2	2
TiO_2-ZrO_2	$Ti(i-OBu)_4$	68	45	0	0	0	
	$Zr(i-OPr)_4$		56	38	8	0	0
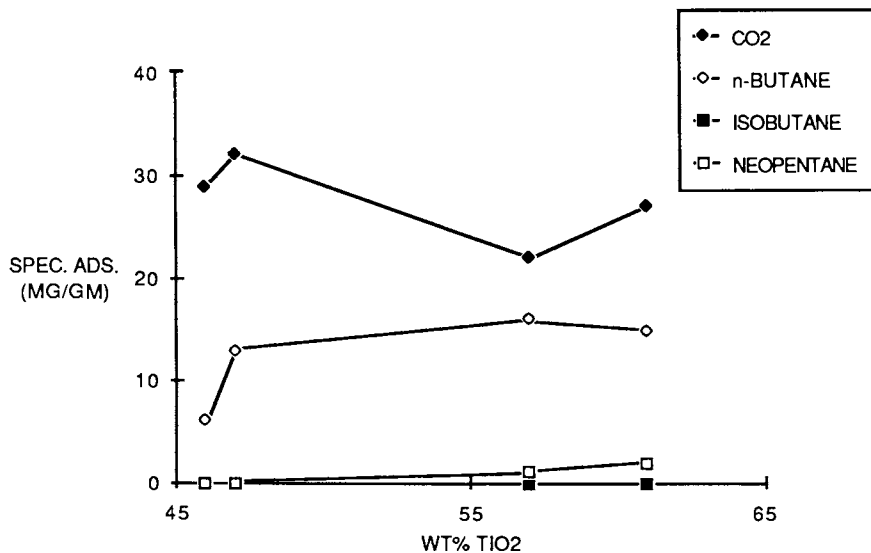
Figure 7a. Specific Adsorption of Probe Molecules on TiO$_2$ Type IIb
            IOM-CMS Materials versus Wt% TiO$_2$
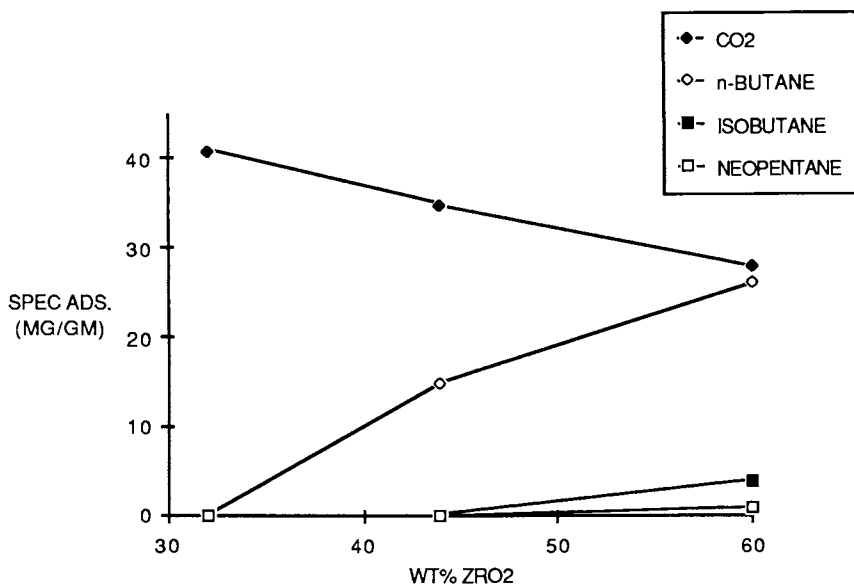
Figure 7 b Specific Adsorption of Probe Molecules on ZrO$_2$ Type IIa
            IOM-CMS Materials versus Wt% ZrO$_2$
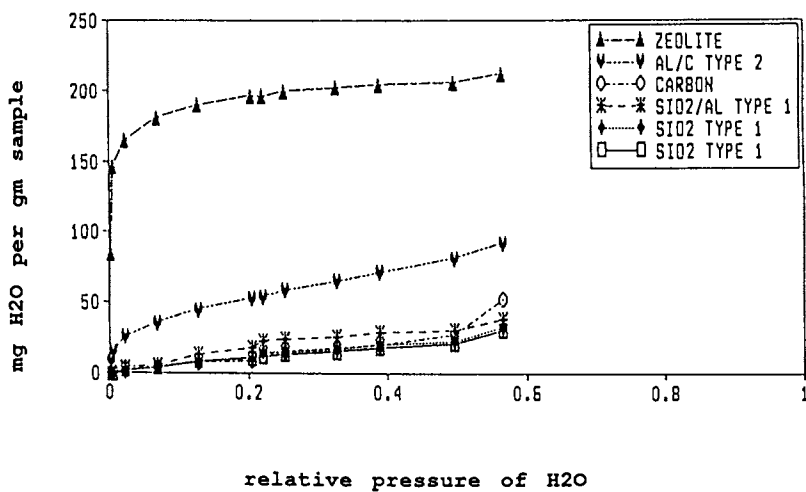
Figure 8.   Water Adsorption Data For IOM-CMS Materials

than the Type I materials, carbon, or the pure inorganic oxides. It displayed somewhat stronger water adsorption than the other samples at the lower relative pressures. Although much lower on an absolute scale, this is reminiscent of the result obtained with the 3A zeolite sample. The adsorptive behavior of the IOM-CMS materials, especially of Type II, is under continued investigation and analysis.

The Type III materials were conceptualized as Type IIb materials, except that the inorganic oxide was to be dispersed as a coating on the surface of a porous, but not molecular sieving, carbon support. The surface-modified carbon could then be mixed with the resin as a fine powder, and pyrolyzed. The molecular probe analyses of the nine Type III samples are very interesting (see Table 4, and Figures 9a and b). The three sets of samples each showed the same trends. At the lowest ratio of polymer resin to surface-modified porous carbon the materials all behaved as 5A size molecular sieves, adsorbing relatively large quantities of CO_2 and n-butane, but nearly zero amounts of isobutane and neopentane. This holds for the both the titania-modified wide pore carbon and the Raven 8000 beads, and the zirconia-modified Raven 8000 beads. At the middle ratio of polymer resin to base material, the two titania-modified samples displayed 4A size molecular sieving properties, adsorbing CO_2 in large quantities, but only negligible amounts of the other larger probe molecules. The zirconia-modified Raven 8000 beads behaved more like the 5A size sieve even at this middle ratio of polymer resin to surface-modified carbon base. At the highest ratio of polymer resin to surface-modified carbon base, all three of the samples displayed 4A size sieving properties.

Summary and Conclusions

Carbon molecular sieves can be made with a wide range of physical properties, and from a variety of natural and synthetic materials. The primary use of these materials has been in separation processes, the most notable of which is pressure swing adsorption for the separation of nitrogen from air. Relatively little attention has been given to the catalytic properties of these materials beyond the early work by Walker and Trimm. However, some of the more recent reports in the patent literature are very intriguing, and suggest that the use of carbon molecular sieves in catalysis merits further attention.

This work has aimed at adding functionality to the carbon molecular sieves by preparing composite structures of carbon and inorganic oxides. The objective is to combine the surface chemical properties of the inorganic oxides with the molecular sieving properties of the carbon. The results obtained to date indicate that composite structures can be made with molecular sieving properties in at least four forms. The data on the Type III materials, combined with those obtained for the Type IIa and IIb samples, indicate that by proper control of the inorganic oxide precursor chemistry, and the physical properties of the solid additives, one can begin to control the molecular sieving properties of the IOM-CMS materials. The molecular sieving properties of the Type IIa IOM-CMS materials are maintained even at low carbon to inorganic oxide ratios. These properties are dependent upon the preparation variables, but a systematic

TABLE IV. Specific Adsorptions and Carbon Content on Type III IOM-CMS Materials

INORGANIC OXIDE	OXIDE PRECURSOR	WT% CARBON	WT% Metal Oxides	CO$_2$	SPECIFIC ADSORPTION (mg per gm) n-BUTANE	ISOBUTANE	NEOPENTANE
TiO$_2$	Ti(i-OBu)$_4$	86	14	50	30	0	6
		92	8	62	4	0	3
		95	5	64	1	0	2
ZrO$_2$	Zr(i-OPr)$_4$	86	14	57	39	0	6
		92	8	59	27	0	5
		95	5	55	1	0	2
TiO$_2$/ZrO$_2$	Ti(i-OBu)$_4$	86	14	54	44	0	6
	Zr(i-OPr)$_4$	92	8	47	6	0	3
		95	5	57	1	0	2
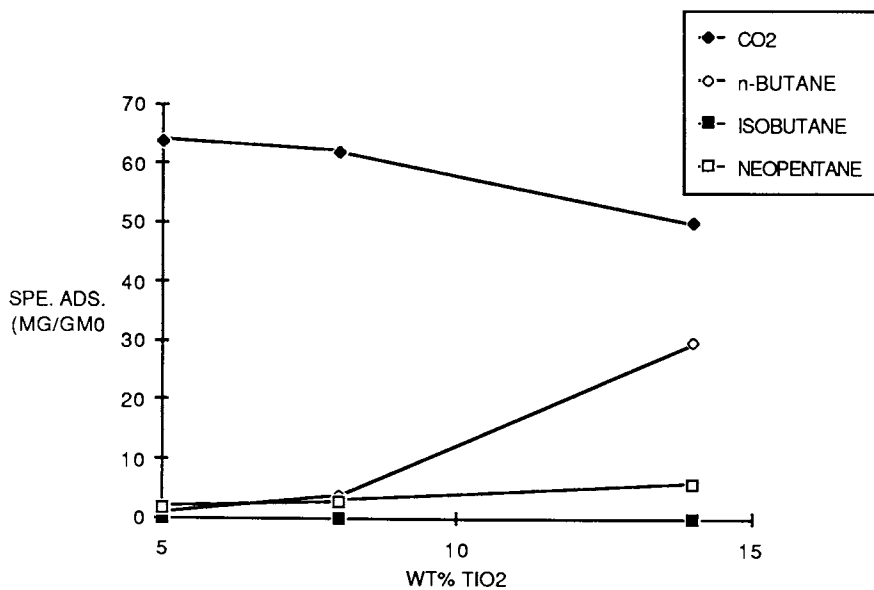
Figure 9. a   Specific Adsorption of Probe Molecules on TiO_2 Type III
               IOM-CMS Materials versus Wt% TiO_2
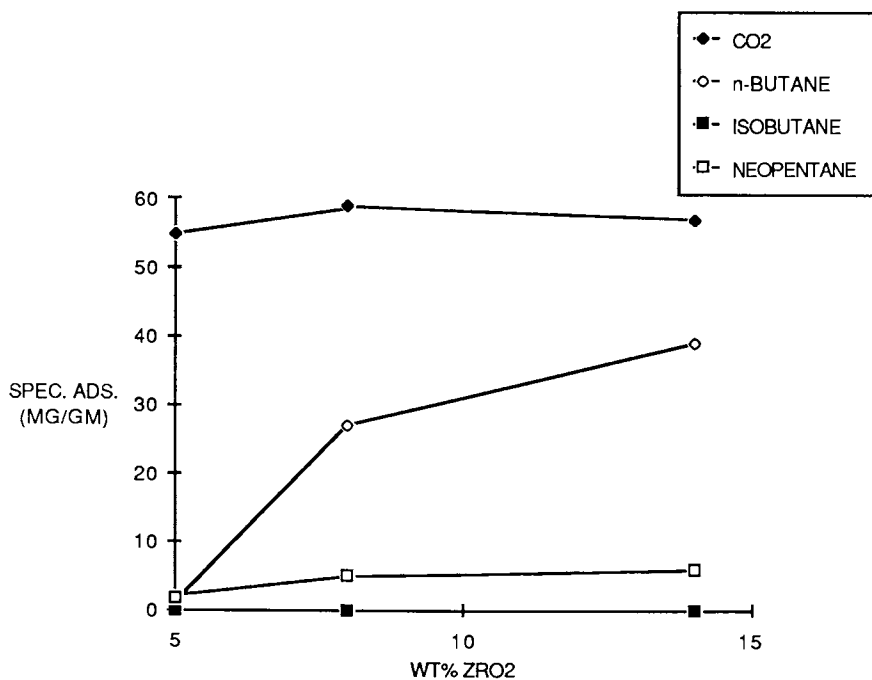
Figure 9. b   Specific Adsorption of Probe Molecules on ZrO_2 Type III
               IOM-CMS Materials versus Wt% ZrO_2

investigation will be carried out to clearly define the
dependencies. Continued studies will define the relationships
between composition, structure, and molecular sieving properties
of the IOM-CMS materials, and relate these properties to
catalytic activities and selectivities for specific reactions.

Literature Cited

 1. Foley, H.C., "Novel Carbon Molecular Sieve Catalysts for Wax
    Suppression in the Fischer-Tropsch Reaction;" **Dept. of
    Energy Contract No. DE-AC22-84PC70031, Final
    Report,** June (1987) and references therein.
 2. Koresh, J.E., Sofer, A., **Sep. Sci. and Technol.,** *18,* 723
    (1983).
 3. Franklin, R.E., **Trans. Farad. Soc.,** *45,* 274 (1949)
 4. Franklin, R.E., **Trans. Farad. Soc.,** *45,* 668 (1949)
 5. Anderson, R.B., Hall, W.K., Lecky, T.A., Stein, K.S., **J.
    Phys. Chem.,** *60,* 1548 (1956).
 6. Pierce, D., Wiley, J.W., Smith, R.N., **J. Phys. Chem.,** *53,*
    669 (1949).
 7. Emmett, P.H., **Chem. Rev.,** *43,* 69 (1948).
 8. Dacey, J.R., Thomas, D.G., **Trans. Faraday Soc.,** *50,* 740
    (1954).
 9. Walker, P.L., Jr., Lamond, T.G., Metcalfe, J.E., III, **Proc.
    2nd Conf. on Ind. Carbon Graphite, Society of the
    Chemical Industry,** London (1966).
10. Lamond, T.G., Metcalfe, J.E., III, Walker, P.L., Jr.,
    Carbon, *3,* 59 (1965).
11. Metcalfe, J.E., III, Ph.D. Thesis, The Pennsylvania State
    University (1965).
12. Koresh, J., Soffer, A., **J. Chem. Soc., Faraday Trans.
    1,** *76,* 2457 (1980).
13. Barton, S.S., Koresh, J., **J. Chem. Soc., Faraday Trans.
    1,** *79,* 1147 (1983).
14. Koresh, J., Soffer, A., **J. Chem. Soc., Faraday Trans.
    1,** *76,* 2507 (1980).
15. Koresh, J., Soffer, A., **J. Chem. Soc., Faraday Trans.
    1,** *76,* 2472 (1980).
16. Koresh, J., Soffer, A., **J. Chem. Soc., Faraday Trans.
    1,** *77,* 3005 (1981).
17. Yang, R.T., **Gas Separations by Adsorption Processes,**
    Butterworths, Boston (1987).
18. Ray, M.S., **Sep. Sci. and Technol.,** *21,* 1 (1986).
19. Trimm, D.L., Cooper, B.J., **J.Chem. Soc. D,** *8,* 477 (1970).
20. Cooper, B.J., Trimm, D.L., **Conf. on Ind. Carbon
    Graphite, 3rd Mtg. Date,** Soc. Chem. Ind., London,
    (1970).
21. Cooper, B.J., **Plat. Metals Rev.,** *14,* 133 (1970).
22. Schmitt, J.L. Jr., Walker, P.L. Jr., **Carbon,** *10,* 791
    (1971).
23. Schmitt, J.L. Jr., Walker, P.L. Jr., **Carbon,** *10,* 87
    (1971).

24. Schmitt, J.L. Jr., Diss. Abstr. Int. B 1971, 32, 807 (1970).
25. Moreno-Castilla, C., Mahajan, O.P., Walker, P.L. Jr., Jung,
     H.J., Vannice, M.A., **Carbon**, *18,* 271 (1980).
26. Walker, P.L. Jr., Oya, A., Mahajan, O.P., **Carbon**, *18,* 377
     (1980).
27. Bragin, O.V., Olfereva, T.G., Ludwig, J., Fiebig, W., Heise,
     K., Schnabel, K.H., **Z. Chem.**, *20,* 387 (1980).
28. Connor, H. , **DE 3006105** (1980).
29. Dessau, R.M., **US 4413154** (1983).

Chapter 22

Intracrystalline Diffusion in Zeolites

Douglas M. Ruthven and Mladen Eic

Department of Chemical Engineering, University of New Brunswick, Fredericton, New Brunswick E3B 5A3, Canada

A new experimental technique (ZLC) has been developed and applied to study the diffusion of a range of hydrocarbons (xylene, benzene, cyclohexane and linear paraffins) in unaggregated crystals of zeolites A and X. The validity of the method was confirmed by varying the crystal size and the nature and flowrate of the purge gas. The method has advantages of speed and simplicity but the major advantage is that the intrusion of extraneous heat and mass transfer resistances is much less significant than in conventional uptake rate measurements. As a result, the new method can be applied to systems in which diffusion is too rapid to follow in a conventional sorption experiment.

Several of the systems studied have also been investigated by NMR, as well as by uptake and exchange rate measurements using large crystals. For all sorbates in both A and X zeolites the results obtained by the new ZLC method are consistent with our earlier sorption rate data but the diffusivities are much smaller than the values obtained by the NMR PFG method. Agreement between ZLC and NMR measurements was found only for butane in large 5A crystals. The large difference in diffusivity between large laboratory synthesized crystals and small commercial crystals is also confirmed for this system.

The problem of determining reliable intra-crystalline diffusivities for hydrocarbons and other simple molecules in zeolite crystals has exercised zeolite scientists for many years. During the early 1970s Pfeifer, Karger and their colleagues at Leipzig extended the nuclear magnetic resonance pulsed field gradient (NMR PFG) self diffusion measurement technique, originally developed for measuring diffusion in liquids (1), to permit measurement of the lower diffusivities encountered in intracrystalline diffusion in

zeolites.(2,3) The diffusivities obtained by this method were much higher than the reported diffusivities derived from more conventional experimental techniques such as the measurement of uptake rates but the validity of the NMR data was confirmed by a number of experimental checks. Most of the uptake rate diffusivities had been obtained with the small commercially available synthetic zeolite crystals. Detailed re-examination of these data revealed that, at least for some systems, the intrusion of extraneous heat and/or mass transfer resistances (such as extracrystalline diffusion) was more significant than had been originally assumed (4-6) and the discrepancy with the NMR results could be explained on this basis. The remaining discrepancies were generally attributed to differences in preparation or pre-treatment of the zeolite crystals or to the existence of a 'surface barrier' to mass transfer.(7)

More detailed uptake rate studies carried out with larger crystals and with a range of different crystal sizes, however, showed no evidence of any surface barrier.(7-9) For diffusion of propane and n-butane in laboratory synthesized 5A crystals the uptake results show reasonably close agreement with the NMR.(10) However, for some other systems such as benzene-NaX the NMR diffusivities were still much higher. The uptake rates, however, close to the limit of the experimental technique so the possible intrusion of extraneous heat or mass transfer resistances could not be unequivocally excluded.

More recently, a detailed study of diffusion of the xylene isomers in large crystals of NaX and natural faujasite was undertaken by both sorption rate and tracer exchange.(11-14) The data obtained by both these techniques using several different crystal sizes were entirely consistent but the diffusivities were much smaller than the values derived for the same systems by NMR PFG measurements. In an attempt to resolve this discrepancy we have developed a new chromatographic technique (zero length column or ZLC) which is less sensitive than conventional sorption methods to the intrusion of external heat and mass transfer resistances and which is therefore useful for following relatively rapid diffusion processes. The method has now been applied to study the diffusion of a range of different hydrocarbons in both A and X zeolite crystals and the results of these studies are summarized here.

Experimental Method

The method depends on following the desorption curve obtained when a very small sample (1 - 2 mg) of zeolite crystals, previously equilibrated with sorbate at a known (low) concentration, is purged with an inert carrier. A high purge gas flowrate is used in order to maintain a low sorbate concentration at the external surface of the crystals thus minimizing any external heat or mass transfer resistance. The initial sorbate concentration is kept low, preferably within the Henry's Law region, in order to permit a simple and unambiguous interpretation of the desorption rate curves. By taking advantage of the high sensitivity of a flame ionization detector it is possible to follow the desorption curve accurately even at very low concentrations and thus to approach in

practice the ideal isothermal situation in which the external concentration is maintained close to zero and the desorption rate is controlled entirely by intracrystalline diffusion. The absence of any significant extracrystalline resistance can be confirmed by using two different purge gases with different molecular diffusivities (He and Ar) and by varying the purge flowrate.

In the above limit (zero concentration at the crystal surface) the desorption curve is given by:

$$\frac{c}{co} = 2L \sum_{n=1}^{\infty} \frac{\exp(-\beta_n^2 Dt/R^2)}{[\beta_n^2 + L(L-1)]} \qquad (1)$$

where β_n is given by the roots of the equation:

$$\beta_n \cot \beta_n + L - 1 = 0 \qquad (2)$$

$$L = \frac{1}{3}\left(\frac{R^2}{D}\right)\frac{\varepsilon v}{(1-\varepsilon)Kz} = \frac{1}{3}\cdot\frac{R^2}{KD}\left(\frac{\text{Purge Flowrate}}{\text{Crystal Volume}}\right) \qquad (3)$$

In the long time region only the first term of the summation is significant so equation 1 reduces to:

$$\frac{c}{co} = 2L \cdot \frac{\exp(-\beta_1^2 Dt/R^2)}{[\beta_1^2 + L(L-1)]} \qquad (4)$$

A plot of $\ln(c/c_o)$ vs t should therefore approach linearity with slope $-\beta_1^2 D/R^2$ and this is the region in which the basic assumption of the model ($c/c_o \ll 1.0$) is a valid approximation.

In the extreme limit of a very low purge flowrate, equilibrium is approached. Diffusion through the crystal is fast enough to maintain a uniform (equilibrium) concentration through the crystal at all times and the desorption rate is controlled simply by the rate at which sorbate is removed in the purge gas. Under these conditions the desorption curve is given by:

$$\frac{c}{co} = \exp\left[\frac{-\varepsilon vt}{(1-\varepsilon)Kz}\right] \qquad (5)$$

$$\text{or} \quad \ln\left(\frac{c}{co}\right) = -st \quad \text{where} \quad s = \frac{\varepsilon v}{(1-\varepsilon)Kz} \qquad (6)$$

If a desorption curve is measured under these conditions (purge velocity v', slope $s=s'$) then at a much higher gas velocity v (corresponding to L):

$$LD/R^2 = \frac{1}{3}\left(\frac{v}{v'}\right)s' \qquad (7)$$

The diffusional time constant (D/R^2) may thus be found from the solution of the three equations 2, 4 and 7 relating D/R^2, L and β_1. To achieve sensitivity of the solution to D/R^2 it is necessary to

ensure that L > 1.0. It is therefore desirable to make measurements at several purge flowrates in order to confirm consistency of the data.

It is clear from equation 3 that for a rapid diffusion process (D/R^2 large) the requirement L > 1 can be achieved only by using high purge flowrates and small zeolite sample volumes. Meeting this requirement becomes increasingly difficult for strongly adsorbed species (large K), necessitating the use of larger crystals. In any case the desorption curve must be on a measureable time scale (a few seconds) which requires D/R^2 < 0.01 s^{-1} and it is this constraint which imposes the main limitation on the application of the ZLC technique with small crystals and rapidly diffusing sorbates.

A more detailed account of the method and its range of applicability has been given elsewhere.(15,16)

Results and Discussion

NMR PFG measurements determine the tracer or self-diffusivity (D_s) under equilibrium conditions with no concentration gradient. In any sorption rate measurement it is the transport diffusivity under the influence of a concentration gradient which is measured. In general these two quantities are not the same but the relationship between them can be established from irreversible thermodynamics. (17,18) In the low concentration limit the thermodynamic correction factor vanishes and the transport and self diffusivities should approach the same limit. Since ZLC measurements are made at low concentrations within the Henry's Law region the diffusivity values should be directly comparable with the NMR self-diffusivities.

ZLC desorption curves were measured over a wide range of conditions for several different hydrocarbon sorbates in a range of different sizes of NaX and 5A zeolite crystals. In general He was used as the purge gas but numerous checks were made with an Ar purge to confirm the absence of any extracrystalline resistance. The form of the desorption curves was consistent with the theoretical model outlined above and consistent diffusivity values were obtained at different flowrates and with different crystal sizes. A few representative curves are shown in figure 1.

o-Xylene-NaX

Diffusion of o-xylene in 50 μm and 100 μm NaX crystals was studied over the temperature range 125-250°C. The derived parameter values are summarized in Table 1 which includes also the sorption rate and tracer exchange measurements of Goddard.(11-14) The agreement between the ZLC diffusivity values obtained with different crystal sizes, different purge gases and different purge flowrates is seen to be excellent and the diffusivity values derived from the ZLC measurements are entirely consistent with the limiting sorption and tracer diffusivities derived from the uptake and exchange measurements. The comparison with the NMR PFG self-diffusivity data (19) is shown in figure 2 from which it is apparent that there
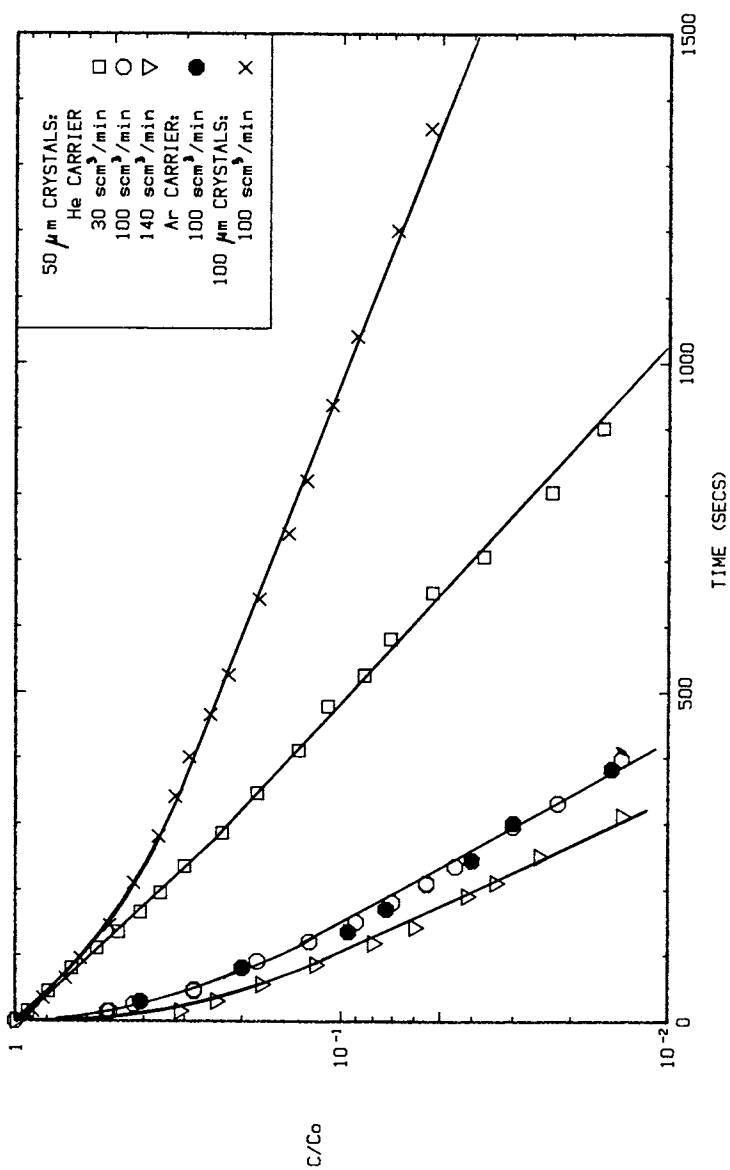
Figure 1. Representative ZLC desorption curves for o-Xylene in different size 13X zeolite crystals at 200°C.

Table I.   Summary of ZLC Diffusivity Data for
o-Xylene and Benzene in NaX Zeolites Crystals

Sorbate	T (K)	$P \times 10^3$ (Torr)	2R (μm)	PFR^+ (cm^3/min)	$10^3 \times D/R^2$ (s^{-1})	ZLC $D_{av} \times 10^8$ ($cm.^2 s^{-1}$)	Sorption/Exch $D_{av} \times 10^8$ ($cm^2.s^{-1}$)
o-Xylene	473	7.7	50	30	1.33		
				100	1.37		
				100*	1.37	0.87	
				140	1.39		
	473	7.7	100	100	0.35	0.9	0.96
				160	0.37		
	473	3.8	50	100	1.5	0.94	
	523	7.7	50	100	2.4	1.52	1.42
		3.8	50	100	2.47		
	423	8.5	100	100	0.156		
		8.5	50	140	0.592	0.375	0.38
Benzene	443	28	100	60	3.56		
			50	30	13.4	8.8	
			50	60	3.6		
	473	26	100	30	5.76		
			100	50	6.1	14.3	
			50	25	21.1		
	403	30	100	200	1.88	4.7	
		30	100	200*	1.88	4.7	4.1

+ PFR - purge flowrate, cm^3/min at STP.
* Ar purge.
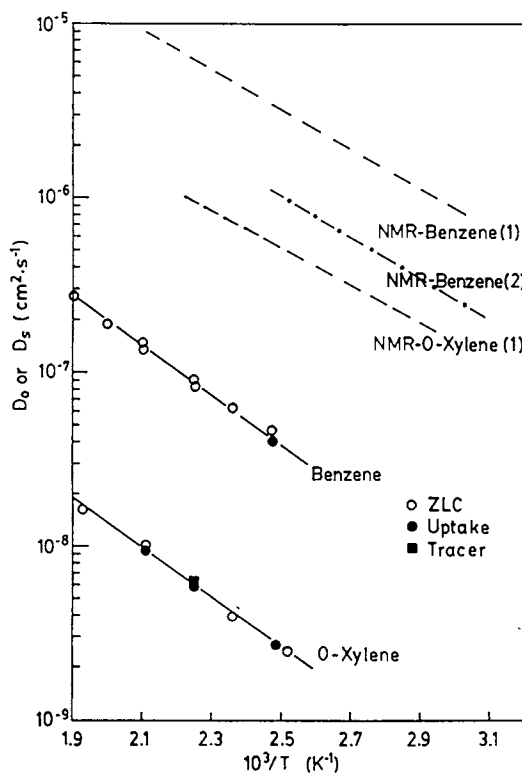
Figure 2. Arrhenius plot showing comparison of NMR and sorption diffusivities for benzene and o-xylene in NaX zeolite crystals. NMR data from (1) Germanus et al. (19) and (2) Karger and Ruthven (10). Uptake (corrected diffusivity) and tracer exchange data of Goddard (11-13) (50 μm and 100 μm NaX, 250 μm faujasite). ZLC data of Eic (15,16).

is a very large discrepancy. The only agreement is in the activation energy for which similar values are obtained from both the sorption and NMR data.

Benzene-NaX

Diffusion of benzene was studied in 250 μm natural faujasite crystals by sorption rate measurements and in 50 μm and 100 μm NaX by ZLC. Diffusion in 100 μm NaX was too fast to measure with confidence by conventional sorption methods. The results are summarized in Table 1 and figure 2 in which the NMR self diffusivity data are also shown. The ZLC data for 50 μm and 100 μm crystals are consistent and in good agreement with the sorption rate measurements for 250 μm faujasite, suggesting that, as with the xylene isomers, under comparable conditions, there is no significant difference in diffusivity between NaX and natural faujasite. The NMR diffusivities(10,19) are again much larger but with a similar activation energy.

In contrast with the results obtained in this laboratory, the piezometric uptake rate data of Bulow et al.(25,26) lie very much closer to the NMR data. It should, however, be noted that the corrections introduced to account for 'valve effects' and other extraneous factors were very large, thus inevitably reducing the confidence level.

Linear Paraffins and Cyclohexane-NaX

Diffusion of saturated hydrocarbons is very much faster than diffusion of the aromatics and the diffusivities for these systems are well beyond the range amenable to direct sorption rate measurement, even in relatively large crystals. ZLC measurements in 50 μm and 100 μm crystals were, however, straightforward and yielded consistent diffusivity values. The results are summarized as Arrhenius parameters in Table 2 and the comparison with the NMR data(20) is shown in figure 3 in which the diffusivity at 150°C and the diffusional activation energy are plotted against carbon number. The general trends are obviously similar but we see the same 100-fold discrepancy between the diffusivity values as well as higher activation energies for the ZLC data (except for butane). A further point of interest is that, according to both NMR and ZLC data, the diffusivity of cyclohexane is essentially the same as that of n-hexane. Clearly, in its diffusional behaviour cylohexane resembles a saturated paraffin far more closely than benzene.

Linear Paraffins-5A

Diffusion of linear paraffins was studied in a wide range of 5A zeolite crystals including both the small commercial (Linde) crystals and larger crystals synthesized in our laboratory by Charnell's method (31). Whereas in the case of NaX we found no significant difference between the diffusivities for large laboratory synthesized and small commercial crystals (15), for 5A we see large differences. In particular, for n-butane, the large

Table II. Parameters D_o and E Giving Temperature
Dependence of ZLC Diffusivities [$D=D_o$ exp (-E/RT)]

Sorbent	Sorbate	D_o $cm^2 sec^{-1}$	E kcal/mole
NaX	n C_4H_{10}	2.8×10^{-6}	1.47
	C_5H_{12}	1.68×10^{-5}	3.0
	C_7H_{16}	7.41×10^{-5}	4.7
	$C_{10}H_{22}$	6.2×10^{-5}	5.2
	$C_{14}H_{30}$	2.65×10^{-5}	4.8
	Cyclohexane	2.17×10^{-5}	3.6
	Benzene	1.24×10^{-4}	6.4
	o-Xylene	9.7×10^{-6}	6.5
5A	n C_4H_{10}	5.31×10^{-7}	3.8
(Lab	C_7H_{16}	4.26×10^{-6}	8.1
synthesized	$C_{10}H_{22}$	4.8×10^{-5}	11.2
crystals)	$C_{13}H_{28}$	1.97×10^{-5}	12.0
	$C_{16}H_{34}$	8.24×10^{-5}	13.1
5A Linde lot 550045	C_4H_{10}	0.06×10^{-7}	3.9
5A Linde lot 550043	C_7H_{16}	1.24×10^{-7}	8.0

a)

b)
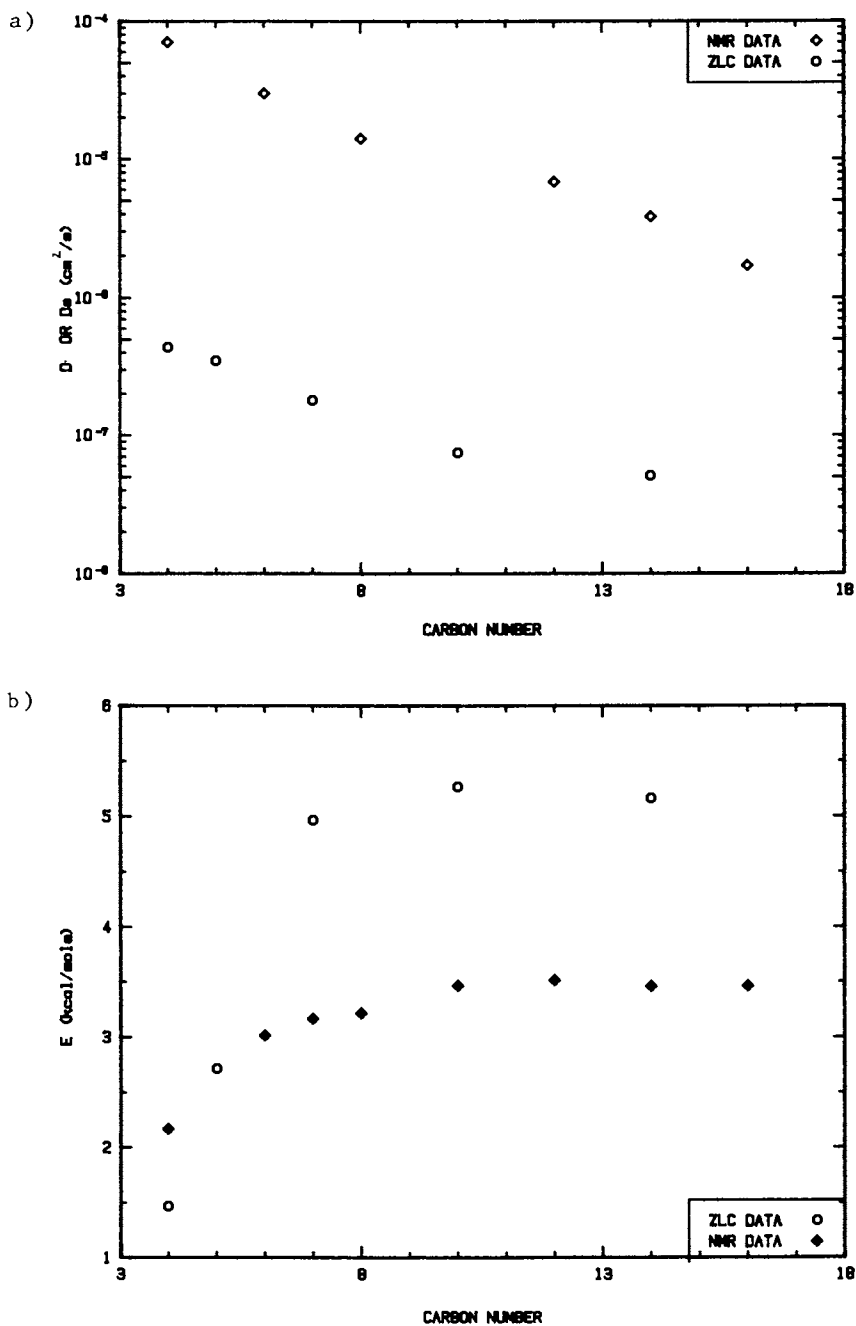
Figure 3. Comparison of ZLC (15) and NMR PFG (20) diffusivity data for n-paraffins in NaX zeolite crystals (a) Values of D and D_s at 150°C (b) Activation energies.

difference in diffusivity between Linde 3.6 μm (lot 550045) crystals and large laboratory synthesized crystals, which was observed in our earlier uptake rate studies, (9,10,21) is confirmed by the ZLC results. Similar differences are observed also for n-heptane (see Table 2) Furthermore the previously observed agreement between the NMR and sorption diffusivities for n-butane in the large 5A crystals (10) is confirmed by the ZLC data. Recent NMR studies by the tracer desorption technique (23,24) have suggested that this difference may be due to the presence of a surface barrier in the small commercial crystals. The ZLC data do not support this contention. The forms of both the uptake rate curves and the ZLC desorption curves are consistent with a diffusion controlled process rather than with a surface barrier resistance.

Arrhenius plots showing the temperature dependence of diffusivity for n-butane in various 5A samples are shown in figure 4 while figure 5 shows the trend of activation energy with carbon number. For linear paraffins higher than n-butane, diffusion, even in the large 5A crystals, is too slow to measure by the NMR PFG method so it is only for butane that a direct comparison between ZLC and PFG NMR data is possible.

Conclusion

The ZLC method provides a simple and practically useful experimental technique for measuring intracrystalline diffusivities in zeolite crystals and this method can be used to study somewhat faster processes than are amenable to study by more conventional sorption rate measurements. The validity of the new method is confirmed by the consistency of the results obtained with different crystal sizes, different purge gases and different purge flowrates as well as by the consistency of the diffusivities with values derived from independent uptake rate and tracer exchange measurements. For diffusion in NaX crystals the diffusivity appears quite insensitive to the origin of the crystals as well as to small differences in dehydration procedure. Differences for 5A zeolite crystals are very much greater and the previously observed large difference in diffusivity between commercial 5A zeolite crystals and carefully dehydrated laboratory samples is confirmed by the ZLC results.

For the n-butane-5A system both sorption and ZLC results are in substantial agreement with NMR PFG self diffusivity data. However, for all NaX systems studied the NMR self diffusivities are approximately two orders of magnitude larger than the ZLC values. This discrepancy is difficult to understand. Most of the more obvious explanations can be ruled out on the basis of the experimental evidence. For example, the possible intrusion of extraneous heat and/or mass transfer resistances is excluded by the agreement between the sorption, exchange and ZLC results. For NaX crystals both NMR and ZLC results show that differences in the origin of the sample and the initial dehydration procedure have only a relatively small effect on the diffusivity. (27) The absence of significant surface barriers (for aromatics-NaX) is
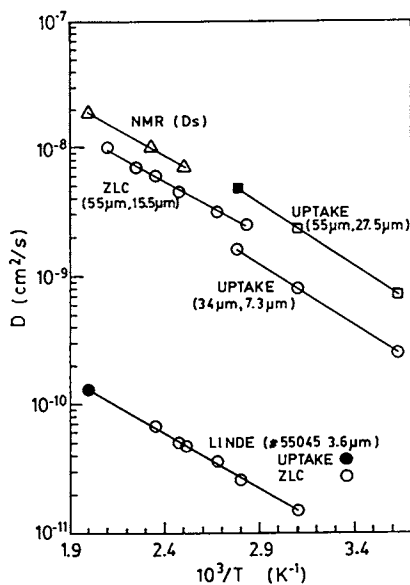
Figure 4. Arrhenius plot showing comparison between sorption, ZLC and NMR diffusivity data for n-butane in 5A zeolite crystals. Data from Karger and Ruthven (10), Yucel and Ruthven (9) and Eic (15).
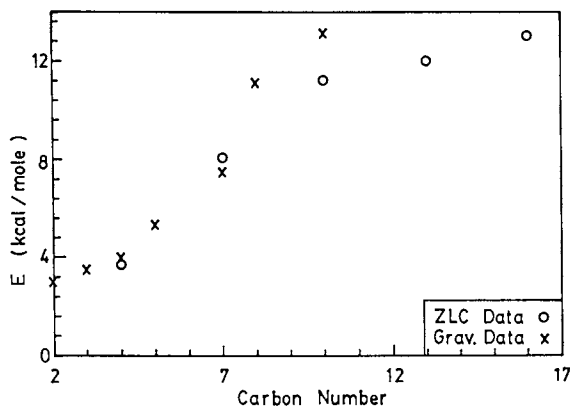
Figure 5. Variation of diffusional activation energy with carbon number for n-paraffins in 5A zeolite crystals. (Data from refs. 9, 21, 22, 29, 15.)

confirmed by the conformity between NMR PFG and NMR tracer desorption rate measurements (28) as well as by the form of the uptake, exchange and ZLC curves and the consistency of data obtained with different crystal sizes. The NMR method follows movement of the protons and it is implicitly assumed that there is no H-exchange under experimental conditions. Since protons diffuse very rapidly, a small degree of exchange could lead to erroneously high apparent diffusivities. However, the agreement between the sorption and NMR diffusional activation energies, which is observed at least for benzene and xylene in NaX, then becomes hard to explain.

It must be recognized that the time scales of the two techniques are very different, so if there were a rapid exchange between a few rapidly diffusing molecules with the large majority of the adsorbed molecules being relatively immobile, one would expect to find different diffusivities by the two techniques. However, the intensity of the NMR signal evidently corresponds to the expected response of all the adsorbed molecules so, on that basis, the existence of an exchange between mobile and immobile molecules does not appear to be supported.(3)

In recent years there has been a tendency to accept NMR diffusivity data as correct and to assume that where lower diffusivity values are obtained from sorption rate measurements the latter must be in error. The present results suggest that this perspective may not always be correct. Until the origins of the discrepancy are resolved, one must be cautious of accepting NMR self diffusivity data without independent confirmation.

NOTATION

c   gas phase concentration of sorbate (moles/cm^3)
D   intracrystalline diffusivity (cm^2/s)
D_o pre-exponential factor (Table 2) (cm^2/s)
D_s self-diffusivity (tracer or NMR), cm^2/s
E   activation energy of diffusion (k cal/mol)
K   dimensionless adsorption equilibrium constant (Henry's Law constant)
R   crystal radius (cm)
s   slope of plot of $\ln (c/c_o)$ vs t
t   time (sec)
v   interstitial gas velocity (cm/s)
z   bed depth (cm)
β   roots of equation (2)
ε   voidage

Subscript o denotes initial steady state value.

References

1.   E.O. Stejskal and J.E. Tanner, J. Chem. Phys. 42, 288 (1965) and 49, 1768 (1968).
2.   J. Karger and H. Pfeifer, Z. Chemie 16, 85-90 (1976).

3. J. Karger and J. Caro, J. Chem. Soc. Faraday Trans I 73, 1363 (1977).
4. L-K. Lee and D.M. Ruthven, J. Chem. Soc. Faraday Trans. I 75, 2406 (1979).
5. D.M. Ruthven, L-K. Lee and H. Yucel, AIChE Jl. 26, 16 (1980).
6. D.M. Ruthven and L-K. Lee, AIChE Jl. 27, 654 (1981).
7. J. Karger, W. Heink, H. Pfeifer, M. Rauscher and J. Hoffmann, Zeolites 2, 275 (1982).
8. H. Yucel and D.M. Ruthven, J. Colloid Interface Sci. 74, 186 (1980).
9. H. Yucel and D.M. Ruthven, J. Chem. Soc. Faraday Trans I, 76, 60 (1980) and 76, 71 (1980).
10. J. Karger and D.M. Ruthven, J. Chem. Soc. Faraday Trans I, 77, 1485 (1981).
11. M. Goddard, Ph.D. Thesis, University of New Brunswick, Fredericton, N.B., Canada (1985).
12. M. Goddard and D.M. Ruthven, Zeolites 6, 283 (1986).
13. M. Goddard and D.M. Ruthven, Zeolites 6, 445 (1986).
14. M. Goddard and D.M. Ruthven, Proc. Seventh Internat. Zeolite Conference, p. 467, Y. Murakami, A., Lijima and J.W. Ward eds. Kodansha, Tokyo (1986).
15. M. Eic., Ph.D. Thesis, University of New Brunswick, Fredericton, N.B., Canada (1987).
16. M. Eic and D.M. Ruthven, Zeolites - to be published.
17. R. Ash and R.M. Barrer, Surface Sci. 8, 461 (1967).
18. J. Karger, Surface Sci. 36, 797 (1973).
19. A. Germanus, J. Karger, H. Pfeifer, N.N. Samulevic and S.P. Shdanov, Zeolites 5, 91 (1985).
20. J. Karger H. Pfeifer, M. Rauscher and A. Walter, J. Chem. Soc. Faraday Trans I, 76, 717 (1980).
21. D.M. Ruthven and K.F. Loughlin, Chem. Eng. Sci. 26, 1145 (1971).
22. I.H. Doetsch, D.M. Ruthven and K.F. Loughlin, Can. J. Chem. 52, 2717 (1974).
23. J. Karger, AIChE Jl. 28, 417 (1982).
24. J. Karger, H. Pfeifer, M. Rauscher, M. Bulow, N. Samulevic and S.P. Shdanov. Z. Phys. Chem. (Leipzig) 262, 567 (1981).
25. M. Bulow, M. Mietk, P. Struve and A. Zikanova, Z. Phys. Chem. (Leipzig) 264, 298 (1983).
26. M. Bulow, W. Mietk, P. Struve and P. Lorenz, J. Chem. Soc. Faraday Trans I, 79, 2457 (1983).
27. J. Karger, H. Pfeifer and W. Heink in Proc. 6th Internat. Conf. on Zeolites p. 184, D.H. Olson and A. Bisio eds.
28. J. Karger - personal communication.
29. A.P. Vavlitis, D.M. Ruthven and K.F. Loughlin, J. Colloid Interface Sci. 84, 526 (1981).
30. M. Bulow, P. Struve and L.V.C. Rees, Zeolites 5, 113 (1985).
31. J.F. Charnell, J. Crystal Growth, 8, 291 (1971).

Chapter 23

Transport Properties of Molecular Sieves Studied by the NMR Pulsed Field Gradient Technique

J. Kärger and H. Pfeifer

Sektion Physik der Karl-Marx-Universität, Linnéstrasse 5, DDR-7010 Leipzig, German Democratic Republic

The basic principles of both the nmr pulsed field gradient and nmr tracer desorption techniques are presented. It is shown that these methods allow the measurement of the coefficients of intracrystalline and of long-range self-diffusion as well as of the intracrystalline mean life times of the adsorbate molecules. By combining this information, a unique possibility for the direct proof of the existence of surface barriers is provided. The nmr methods are applied to study the transport properties of adsorbate molecules in zeolite NaX, NaCaA and ZSM-5, with particular emphasis on the existence of surface barriers. It is shown that not only the preparation and pre-treatment but also the use of molecular sieves to separate linear paraffins may lead to the formation of surface barriers controlling the net molecular transport in these systems.

Invention and application of synthetic zeolites (1,2) have led to a most peculiar process of innovation in chemical industry, initiated by the prospects of the three main fields of zeolite application as cation exchanger, molecular sieves and catalysts. In all these cases, the relevant processes in the adsorbate-adsorbent system are inevitably accompanied by a succession of transport phenomena, maintaining the molecular exchange between the active sites and the surrounding fluid. The investigation of mass transfer in zeolitic adsorbate-adsorbent systems has become therefore a major objective of both fundamental research and industrial application.

The traditional way of studying molecular transport in zeolites is to follow the time response of the adsorbate-adsorbent system after changing the pressure or the composition of the surrounding atmosphere. If it is possible to eliminate the influence of non-diffusive processes, either experimentally or through suitable data processing, from analysis of the observed response curve the contributing coefficients may be calculated (3,4). As a general feature of such "sorption experiments", molecular transport is

studied under the influence of concentration gradients: It is the existence of these very gradients (and thus of the gradients of the chemical potential (4)) which gives rise to the observed transport phenomena.

In contrast to the traditional method, the nmr pulsed field gradient technique (4-10) is applied to samples under macroscopic equilibrium. By monitoring the precessional phases of the nuclear spins around an external magnetic field, this technique allows the determination of the displacements $r(\Delta)$ of the individual molecules of the sample during an observation time Δ of typically 1...100 ms. Using Einstein's relation

$$D = \langle r(\Delta)^2 \rangle / 6\Delta \tag{1}$$

the mean square displacement may be straightforwardly transferred into the self-diffusion coefficient. This definition of the self-diffusion coefficient is completely equivalent to that by Fick's first law

$$j^* = - D \; grad \; c^* \tag{2}$$

with j^* and c^* denoting the diffusion flux of labelled molecules and their concentration, respectively.

Equation 2 is to be compared with the corresponding relation

$$j = - D' grad \; c \tag{3}$$

for the overall diffusion flux under the influence of a concentration gradient. Equation 3 defines the diffusion coefficient. It is this quantity which may be determined in the sorption experiments.

Being based on the same elementary processes of molecular migration, the coefficients D and D' of self-diffusion and of diffusion, respectively, cannot be independent from each other. In many cases the relation between these quantities is given by the expression (4)

$$D' = D \; d \; \ln p \; / \; d \; \ln c \tag{4}$$

with p denoting the adsorbate pressure at equilibrium with the sorbate concentration c.

In contrast to the sorption method, nmr pulsed field gradient experiments may be performed "in situ" in the closed sample, without the necessity of any sample manipulation. This is of especial relevance for the investigation of compacted and granulated material.

In addition to the conventional application of nmr pulsed field gradient experiments to self-diffusion studies, it is also possible to determine the intracrystalline molecular life times. Referring to the corresponding classical experiment, this method has been termed nmr tracer desorption technique (7). Together with the self-diffusion measurements it provides an excellent tool for characterizing the transport properties in the intra- and intercrystalline spaces, as well as at the interface between them. So far, the nmr techniques provide the only possibility for a direct determination of the existence and of the intensity of transport resistances at this

interface. The investigation of the formation of such surface
barriers on zeolite crystallites of different type and origin is
the main objective of this contribution.

Fundamentals of NMR Self-Diffusion Measurement of Molecules Adsorbed on Zeolites

The quantity observed in nmr spectroscopy (8-10) is the vector sum of
the magnetic moments of the resonating nuclear spins. Under the
influence of a constant magnetic field, the individual nuclear
spins precess around the magnetic field at a rate proportional to
its magnitude ("Larmor" precession). Hence, by applying an additional
inhomogeneous field (the "field gradients"), the positions of the
molecules with respect to the coordinate along the direction of
these field gradients may be recorded via the precessional phases
of the spins. Since the interaction energy between the magnetic
field and the nuclear spins is much less than the thermal energy,
this kind of labelling has no influence on the microdynamic
processes within the sample.

The nmr pulsed field gradient experiments (4-10) are based on
the application of the spin-echo method. In this technique, the nmr
signal ("spin echo") is produced by a sequence of rf pulses of
appropriate duration. In general, one applies a two-pulse sequence
consisting of a $\pi/2$ and a π pulse (primary echo). In order to achieve
larger observation times (and provided that the longitudinal nuclear
magnetic relaxation time is sufficiently exceeding the transverse
relaxation time), a three-pulse sequence ("stimulated" echo) is to be
preferred.

Under the influence of the applied gradients and the thus
effected space dependence of the Larmor frequencies, molecular
migration leads to a decrease of the signal intensity. The echo
attenuation due to diffusion becomes (cf., e.g., (6,8-10))

$$\psi(\delta g, \Delta) = \exp \left\{ - \gamma_P^2 \delta^2 g^2 \langle r^2(\Delta) \rangle / 6 \right\} \qquad (5)$$

with g, δ and Δ denoting respectively the intensity, duration and
separation of the two pulsed field gradients applied. For simplicity,
it has been assumed that $\delta \ll \Delta$. γ_P stands for the gyromagnetic ratio
of the considered nuclei. For protons, which provide the best
measuring conditions, it holds $\gamma_P = 2.68 \times 10^{8}$ $T^{-1}s^{-1}$. With Equation 1,
Equation 5 may be transformed into

$$\psi(\delta g, \Delta) = \exp \left\{ - \gamma_P^2 \delta^2 g^2 D\Delta \right\} \qquad (6)$$

According to these equations, the self-diffusion coefficients, as
well as the molecular mean square displacements, may be determined
from the slope of a semi-logarithmic plot of the echo attenuation
ψ vs $(\delta g)^2$.

For root mean square displacements $\langle r(\Delta)^2 \rangle^{1/2}$ much less
than the mean crystallite diameters, the thus determined self-diffusion
coefficient exclusively refers to migration in the intracrystalline
space. In the opposite limiting case of large molecular dis-
placements one obtains the coefficient of long-range self-diffusion
($D_{l.r.}$). This quantity is related to the relative

amount p_{inter} of molecules in the intercrystalline space
and to their self-diffusion coefficient D_{inter} through the
equation

$$D_{l.r.} = p_{inter}D_{inter} \tag{7}$$

For systems with $D_{intra} \ll p_{inter}D_{inter}$, molecules which leave the
individual crystallites may cover significantly larger mean square
displacements than those remaining in the intracrystalline space.
In this case, echo attenuation may be approximated by a super-
position of two exponentials of the type of Equation 5 representing
the contributions of the molecules which have left or which did
not leave their crystallites during the observation time Δ (7).
One obtains

$$\Psi(\delta g, \Delta) = \gamma(\Delta)\exp\{-\gamma_p{}^2\delta^2 g^2 \langle r^2(\Delta)\rangle_{inter}/6\}$$
$$+ (1-\gamma(\Delta))\exp\{-\gamma_p{}^2\delta^2 g^2\langle r^2(\Delta)\rangle_{intra}/6\} \tag{8}$$

with $\gamma(\Delta)$ denoting the relative amount of molecules which have
left their crystallites during the observation time Δ, and with
$\langle r^2(\Delta)\rangle_{inter}$ and $\langle r^2(\Delta)\rangle_{intra}$ denoting the molecular mean square
displacements due to long-range diffusion and due to diffusion in
the interior of an individual crystallite, respectively. Since as
a consequence of the above introduced condition, $\langle r^2(\Delta)\rangle_{intra}$ is
much less than $\langle r^2(\Delta)\rangle_{inter}$, $\gamma(\Delta)$ may be straightforwardly
determined from the plots of $\ln\Psi$ vs. $(\delta g)^2$ for different values
of Δ (cf. Figure 1). Obviously, the quantity $\gamma(\Delta)$ contains the
identical information of tracer desorption curves. The method to
determine $\gamma(\Delta)$ from nmr pulsed field gradient experiments has
been termed, therefore, nmr tracer desorption technique (7).
    In general, nmr tracer desorption data are represented by the
molecular intracrystalline life time τ_{intra} which is determined
as the first statistical moment of the tracer desorption curve (2)

$$\tau_{intra} = \int_0^\infty (1 - \gamma(\Delta))\, d\Delta \tag{9}$$

With commercial samples, the range of measurement may be considerably
enhanced by applying a large constant field gradient in addition to
the pulsed field gradients. It has been shown (11) that in this case
by the nmr tracer desorption technique a time constant τ'_{intra} is
obtained which in the limit of small values coincides with the
intracrystalline mean life times (in general for $\tau'_{intra} < 5$ ms), and
which increases with increasing values of τ_{intra} at a rate above
that expected from a linear interdependence. Hence, differences in
the kinetics of intracrystalline molecular exchange in different
samples may more easily be determined. For simplicity, in our further
discussion we shall only use the term τ_{intra}. One should
have in mind, however, that in some cases in fact we have to do
with the quantity τ'_{intra}.
    If molecular exchange is controlled by intracrystalline diffusion
one has (7)

$$\tau_{intra} = \langle R^2\rangle/15D_{intra} \tag{10}$$
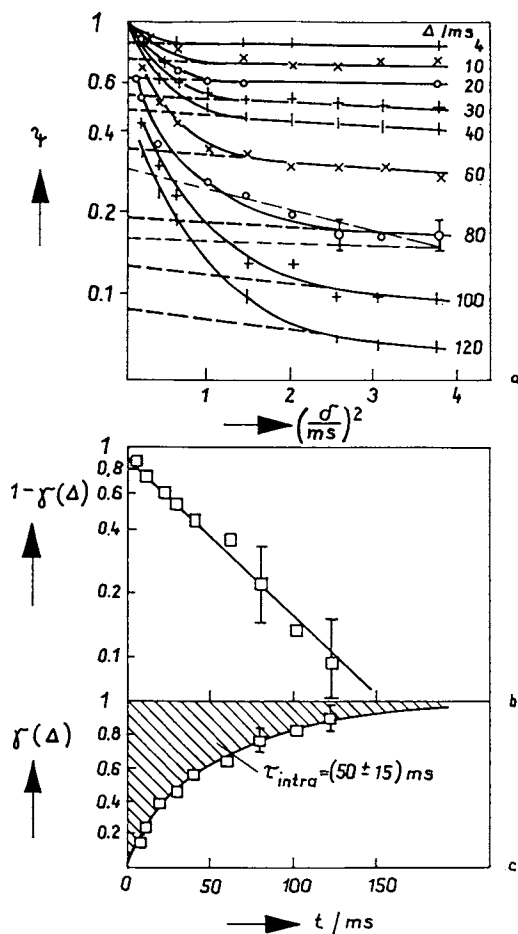
Figure 1: Analysis of the nmr data for tracer desorption studies (in the example: butane/NaX, 165 mg g^{-1}, R = 25 µm, 353 K). 1a: The dependence of echo attenuation ψ on gradient pulse width δ (g has been kept constant during the experiment) for different observation times Δ. As an example, the uncertainty in these values is indicated for Δ = 80 ms. 1b: Nmr tracer desorption curve as determined from Figure 1a. 1c: Determination of τ_{intra} from the desorption curve (= shaded area) by Equation 9 (Reproduced with permission from Ref. 7. Copyright 1982, American Institute of Chemical Engineers)

where the adsorbent crystallites have been assumed to be approximated
by spheres with the mean square radius $\langle R^2 \rangle$. On the basis
of Equation 10 one may introduce a limiting intracrystalline mean
life time

$$\tau_{intra}^{Diff} = \langle R^2 \rangle / 15 D_{intra} \qquad (11)$$

which may be calculated from the intracrystalline self-diffusion
coefficient and the mean square crystallite radius. Clearly,
τ_{intra}^{Diff} coincides with the directly measured τ_{intra}, if
desorption is controlled by intracrystalline diffusion. However,
if the rate of molecular exchange is additionally reduced by
transport resistances at the crystallite boundary ("surface
barriers") τ_{intra} is significantly exceeded by τ_{intra}^{Diff}.

Experimental

Nmr self-diffusion measurements are generally carried out by applying
sealed sample tubes containing the adsorbate-adsorbent system. In
general, activation of the zeolite material is accomplished by
evacuating and heating the samples up to a temperature of 400°C
and by keeping them at the final temperature for about 20 h at a
pressure of less than 5×10^{-3} Pa. Subsequently, either by adsorption
from a gas reservoir at ambient temperature, or - more commonly -
by freezing the adsorbate from a dosing volume at the temperature
of liquid nitrogen, the adsorbate is introduced into the activated
adsorbent. Then the sample tubes are fused by flame. The amount
sorbed may be checked gravimetrically or by the intensity of the
nmr signal.
        Nmr self-diffusion measurements may be carried out with any
nmr pulse spectrometer equipped with a pulsed field gradient
unit. In our experiments, we have applied both a pulse spectrometer
specially built in our laboratory for self-diffusion measurements
(FEGRIS) as well as a conventional spectrometer with an iron
magnet equipped with a pulsed field gradient unit produced
by the Department for Scientific Instrumentation (Zentrale
Abteilung Wissenschaftlicher Gerätebau) of the Karl-Marx-
University, Leipzig. In both cases, pulsed field gradients
with intensities g up to 10 Tm⁻¹ and with rise and fall
times of the order of 20 μs could be produced. The width δ
of the gradient pulses was varied between 0.1 and 5 ms.
Depending on the nuclear magnetic relaxation times of the
samples, observation times Δ up to 1 s could be realized.
        The examples given in Figures 1a-c visualize our way of
analysing the primary data in the nmr tracer desorption
experiments (7). Since, according to Equation 5, molecules with
the smaller mean displacements give rise to $\ln\psi$ - vs - $(g\delta)^2$
representations with the smaller slope, one obtains the relative
number $(1-\gamma(\Delta))$ of molecules which have not left the crystallites
during Δ, simply by extrapolating the asymptote of the
$\ln\psi$ - vs - δ^2 plot for large values of δ to the ordinate.
The uncertainty in these values is due to the uncertainty
in determining echo attenuation and in extrapolating the

asymptotes to the ordinate. The corresponding error bars of Figure 1b
illustrate that it is not reasonable to deduce more information from
the functional dependence of $\gamma(\Delta)$ than that contained in τ_{intra}.

Molecular Transport in Zeolite NaX

X type zeolites provide favourable conditions for nmr self-diffusion
measurements, since in comparison with most other zeolite types, the
open pore structure leads to higher molecular mobilities, as well
as to larger (transverse) nuclear magnetic relaxation times, which –
in turn – allow the application of larger observation times Δ.
Hence, the nmr pulsed field gradient technique could be applied
to study the diffusion behaviour of a large variety of adsorbate
molecules. The data for intracrystalline self-diffusion are summarized
in the review (6). In the following, we shall restrict ourselves
to the discussion of experimental results referring to the existence
of surface barriers.
      Due to the higher intracrystalline mobility, it is in general
more difficult to fulfill the condition $D_{intra} \ll D_{l.r.}$ in zeolite
NaX than in small-port zeolites such as NaCaA. For hydrocarbons
in NaX it has been found that the coefficients of intracrystalline
self-diffusion decrease with increasing concentration (concentration
dependences of type I and II (6)). By contrast, for not too high
gas phase concentrations (i.e., as long as molecular transfer
in the intercrystalline space proceeds by Knudsen diffusion)
$D_{l.r.}$ increases with increasing sorbate concentration (12). Optimum
conditions for the application of the nmr tracer desorption technique
to zeolite NaX are in general provided, therefore, at higher sorbate
concentrations. The nmr tracer desorption experiments on zeolite
NaX have been carried out with n-paraffins and with aromatic
compounds as adsorbates.

n-Paraffins in NaX. Figure 2 gives a comparison of the results of
nmr tracer desorption studies and self-diffusion measurements of
short chain length paraffins in zeolite NaX (7). The zeolite specimens
have been synthesized by S.P.Shdanov and N.N.Samulevitsch (13) in Lenin-
grad, and were applied as a loose assembly of crystallites. For
illustration, Figure 2 also presents the complete tracer desorption
curves at selected temperatures.
      Covering temperatures from -140 up to 200°C and chain
lengths from one to six carbon atoms, the intracrystalline mean
life times are found to coincide with the values of $\tau_{intra}^{D,l.r.}$
calculated from the nmr self-diffusion coefficients. This clearly
indicates that molecular exchange is controlled by intracrystalline
self-diffusion, and that for the considered adsorbate-adsorbent
systems there are no perceptible surface barriers.
      It would be worthwhile to find out, whether such a
characterization would also hold true of commercially available
zeolites NaX. For this purpose, we have investigated specimens of
granulated zeolite NaX with a mean crystallite radius R of about
1 μm, provided by CECA, France. Applying methane as an adsorbate,
in contrast to Figure 1a in no case a deviation from linearity in the
$\ln\gamma$ – vs – $(\delta g)^2$ plots became visible. Taking into account
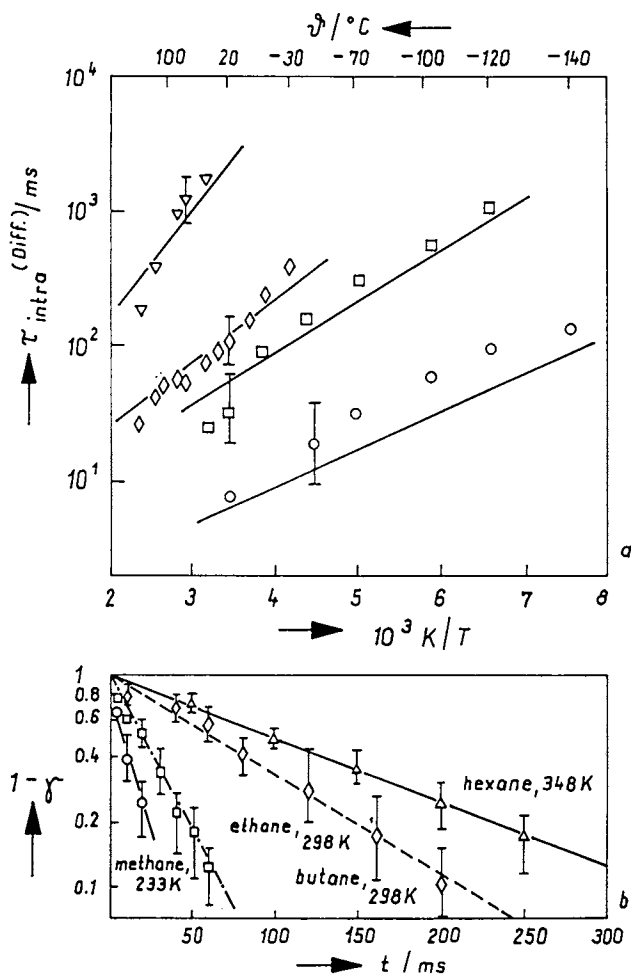
Figure 2a: Intracrystalline mean life times determined from nmr tracer desorption studies on zeolite NaX for methane (●, c = 94 mgg⁻¹, R = 25 μm); ethane (▢, 113 mgg⁻¹; 25 μm); n-butane (◇, 165 mgg⁻¹; 25 μm) and n-hexane (△, 165 mgg⁻¹, 10 μm (data recalculated on the basis of Equations 10 and 11 for a mean crystallite radius of 25 μm, for comparison with the other values)), and comparison with the values of $\tau_{intra}^{Diff.}$ calculated from the coefficients of intracrystalline self-diffusion (full lines) 2b: Tracer desorption curves at selected temperatures (Reproduced with permission from Ref. 7. Copyright 1982 American Institute of Chemical Engineers)

that for a minimum observation time Δ of 0.5 ms, echo attenuation could be followed over more than 1 order of magnitude, a quantitative estimate (14) yields the intracrystalline mean life time to be much less than 0.2 ms. Evidently, for the given intra-crystalline molecular mobility the small size of the zeolite crystallites applied prohibits a direct determination of the intra-crystalline mean life times, so that no direct information on the existence of surface barriers may result. This is a general problem on characterizing the transport properties of commercial zeolite NaX.

In the present case, the intracrystalline mean life times should be compared with a value of $\tau_{intra}^{Diff} = 0.007$ ms, which results from inserting the mean crystallite radius and the intra-crystalline self-diffusion coefficient ($\simeq 10^{-8}$ m²s⁻¹) at the given temperature and concentration (15) into Equation 10. Since in the nmr measurement τ_{intra} is found to be much less than 0.2 ms, a possible transport resistance due to surface barriers can be estimated to be, at the most, of the order of magnitude of the transport resistance due to intracrystalline diffusion.

<u>Aromatic Compounds in NaX</u>. Molecular transport of aromatic compounds in zeolite NaX has been studied by both nmr and uptake measurements. On the basis of Equation 4, and if surface barriers are absent, both methods should lead to comparable results. Though uptake measurements by the variable – pressure, constant – volume method by Bülow and coworkers (16,17) apparently are in satisfactory agreement with the nmr data (18), extensive uptake measurements including chromatographic methods are continuously found to yield diffusivities of about two orders of magnitude below these values (19,20). In principle, this discrepancy might be explained by the existence of surface barriers, which remain invisible for nmr studies of intra-crystalline diffusion, but which may control the uptake rate. However, uptake studies with zeolite specimens of different crystallite radii lead to radius dependences of the uptake constants as to be expected for intracrystalline rather than for surface resistances (19,20).

For a direct check of the existence or non-existence of surface barriers we have applied the nmr tracer desorption technique. For a few selected systems, Table I gives a comparison between the intracrystalline mean life times τ_{intra} and the quantities τ_{intra}^{Diff} calculated from the coefficients of intra-crystalline diffusion on the basis of Equation 11. The order of – magnitude agreement between these quantities indicates that under the given conditions in fact a substantial influence of surface barriers on molecular transport may be excluded.

If one implies the validity of Equation 4, as well as the correctness of either of the experimental techniques, the stated difference has to be explained by differences between the investigated adsorbate – adsorbent systems. As one possibility, differences in the amount of residual water might be taken into consideration. For short chain length paraffins and olefins in NaX it has been shown (6,21) that molecular diffusion may be significantly affected by the existence of co-adsorbed water molecules. However, for benzene in NaX such an influence has been found to be of minor importance (22).

Table I. Comparison of the Intracrystalline Mean Life Times τ_{intra}
and the Quantities τ_{intra}^{Diff}, calculated on the
Basis of the Coefficients of Intracrystalline Self-Diffusion
for Aromatic Compounds in Zeolite NaX

Mean crystallite radius (μm)	Sorbate	Sorbate concentration (molecules per cavity)	Temperature (K)	τ_{intra} (ms)	D_{intra} $(10^{-11} m^2 s^{-1})$	τ_{intra}^{Diff} (ms)
2	benzene	4.7	393	12	1.5	18
2	benzene	4.3	423	20	2.0	13
18	toluene	2.1	463	37	40	54
18	meta-xylene	1.65	463	98	15	140

Comparison between zeolitic diffusion and self-diffusion is a most
actual topic of zeolite research (3,4,23-25), and it is still far
from being conclusively treated. Nmr self-diffusion studies on
the very adsorbate – adsorbent system of the uptake device are
most likely to help to clarify this problem, since in this case
one in fact has to do with the identical system in both experiments.

Transport Properties of Zeolite NaCaA

Influence of Zeolite Texture. Table II shows the results of
combined nmr pulsed field gradient and nmr tracer desorption studies
of zeolite NaCaA as a powder and in the granulated form with
methane as an adsorbate (6,11). The zeolite specimens have been
activated under both "shallow bed" (SB: filling height ≤ 3mm, heating
rate 10K/h, continuous evacuation) and "deep bed" (DB: filling height

Table II. Influence of the Processes of Sample Activation and
Granulation on Molecular Transport of Methane in NaCaA at 293 K

	sample activation	τ_{intra}^{Diff} (ms)	τ_{intra} (ms)	$D_{l.r.}$ $(10^{-9} m^2 s^{-1})$
NaCaA powder	SB	0.3 ± 0.1	0.3 ± 0.1	18 ± 7
	DB	0.3 ± 0.1	2.5 ± 0.5	21 ± 8
NaCaA granule	SB	0.3 ± 0.1	1.8 ± 0.4	2.5 ± 1.0
	DB	0.3 ± 0.1	5.6 ± 1.1	2.9 ± 1.1

about 15 mm, heating rate 100K/h, evacuation only at the final
temperature) conditions (26).
    From the constancy of the values for τ_{intra}^{Diff} it follows
that neither the granulation procedure nor the mode of sample
preparation significantly affects the intracrystalline mobility. As a
consequence of the reduction of the intercrystalline void volume,
however, there is a significant reduction of the long-range

diffusivity due to granulation. In accordance with this inter-
pretation, sample preparation does not affect long-range diffusivity.

Comparing the values τ_{intra}^{nmr} and τ_{intra}, only for the SB-
treated powder satisfactory agreement is observed. Hence, in this
case the existence of surface barriers may be excluded. Both the DB-
activation and the granulation procedure lead to the formation of
surface barriers, which are found to be of comparable intensity. DB-
activation of the granule leads to a further enhancement of these
barriers.

<u>Influence of Hydrothermal Pretreatment</u>. During the processes of
both DB-activation and granulation the zeolite crystallites are
subjected to hydrothermal conditions. In complete agreement with
the results of Kondis and Dranoff (28), the nature of the hydro-
thermal conditions is found to be of decisive influence on the
transport properties of the zeolites. In addition to these former
studies, nmr tracer desorption measurement in combination with
the nmr pulsed field gradient technique allow a localization
of the structural changes leading to the reduced diffusion rates.

As an example (6,27), Figure 3 presents molecular transport
parameters of methane in zeolite NaCaA, which has previously been
subjected to an atmosphere of extreme humidity ($p_{water} \approx 90$ kPa)
at different temperatures (373 - 873 K) over a period of 7 and 14 h,
respectively. Whilst D_{intra} is found to be essentially independent
of the pretreatment conditions, changes in both D_{intra} and τ_{intra} are
observed. However, from a comparison of τ_{intra}^{nmr} it becomes
obvious that it is exclusively the transport resistance of the
surface barriers which controls intercrystalline molecular exchange.
The most intense effect is evidently brought about at temperatures
around 200°C.

In Figures 3e and f, these changes are demonstrated to lead to
substantial deteriorations of the macroscopic transport properties,
represented by the retention volumes V_R for n-pentane at 523 K,
and the break-through capacities K_D of a hydroraffinate in the
boiling range 461 - 594 K, at 653 K.

<u>NaCaA under Hydrocarbon Atmosphere at Elevated Temperatures</u>. One
of the main applications of NaCaA type zeolites is for the separation
of linear paraffins (Leuna-Werke process "Parex" (4,29)). To simulate
the conditions of technical separation columns, the molecular sieve
NaCaA was subjected alternately to a carrier gas stream (H_2)
containing the paraffin distillate, and to an ammonia stream to
displace the hydrocarbons. The data given in Table III (6) have been
determined after 10 cycles. From the large differences between the
values of τ_{intra} and τ_{intra}^{nmr} it may again be concluded that
molecular exchange is limited by surface barriers rather than by
intracrystalline transport. As in the case of hydrothermal
deterioration a distinct correlation between overall transport (V_R)
and tracer desorption is observed. Since there are only minor
changes in the intracrystalline mobility, one has to conclude that
the transport properties of the molecular sieves are mainly
affected by the deposition of the reaction products on or
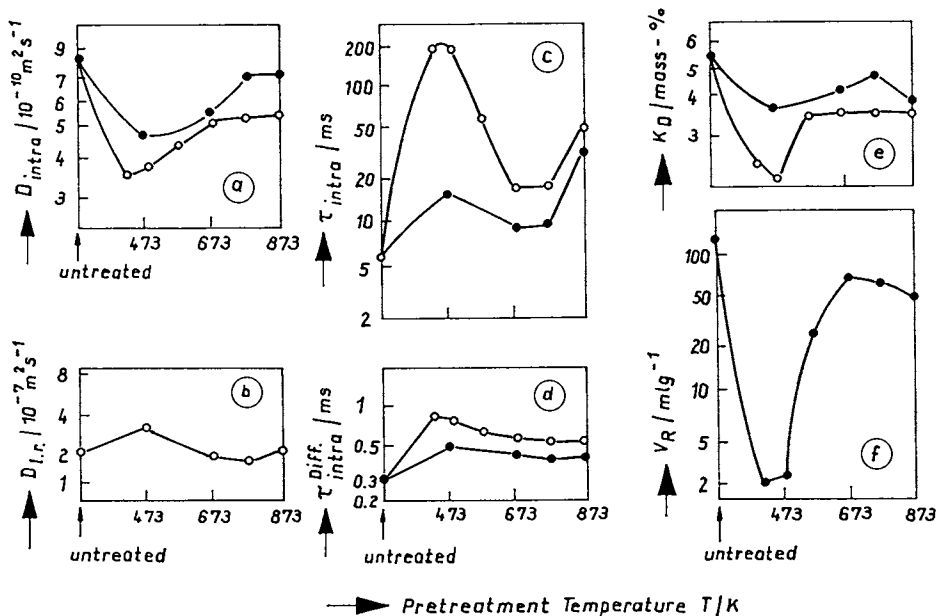
Figure 3: Intracrystalline (a) and long-range (b) self-diffusion coefficients and intracrystalline mean life times τ_{intra} (c) and $\tau_{intra}^{Diff.}$ (d) of methane in granulated zeolite NaCaA, and comparison with the break-through capacities for a petroleum raffinate (e) and the specific retention volume for n-pentane (f), in dependence on the temperature of hydrothermal pretreatment applied over a time interval of 7 h (●) and 14 h (○), respectively (Reproduced with permission from Ref. 6. Copyright 1987 Butterworth)

Table III.   Parameters of Molecular Transport in Granulated Zeolite
             NaCaA after Deterioration by Contact with Hydrocarbons of
             Different Boiling Ranges

Boiling range	T_{intra} (ms)	D_{intra} (10^{-11} m^2 s^{-1})	T_{intra}'''' (ms)	V_{br} (ml g^{-1})
Starting material	2	9	0.3	115
190° – 290° C	3	9	0.3	85
190° – 320° C	5	7	0.4	70
260° – 320° C	17	5	0.5	64
290° – 320° C	19	5	0.5	52

in the vicitnity of the crystallite surface, rather than by
depositions in the crystalline bulk phase. The intensity of
these barriers is found to increase with increasing boiling range
of the petrol distillate.

     Figure 4 provides a comparison of the nmr data on molecular
diffusion with the break-through capacity of a granulated Linde
NaCaA molecular sieve after different times on stream in a petroleum
refinery (6). The increasing deterioration of the dynamic
properties of the molecular sieves with increasing times on stream
is clearly reflected by the decreasing break-through capacities.

Transport Properties of Pentasils

Influence of the Crystal Morphology. Figure 5 compares the self-
diffusion coefficients of methane and propane in two different
specimens of zeolite ZSM-5: polyhedral crystals with elongated
hexagonal form and nearly spherulitic poly-crystals (30). It turns
out that molecular mobility in the ZSM-5 poly-crystals is somewhat
higher than in well-shaped crystals. This experimental finding must
be explained by a promotion of molecular transport due to additional
fast diffusion paths which are most likely to result from a
secondary pore system between the individual crystallites of the
intergrowths. An influence of possible transport resistances at the
interfaces of the individual crystallites must be assumed either to
be negligibly small or to be overcompensated by the effects of
transport promotion, since transport barriers would clearly reduce
rather than enhance the molecular mobility in comparison with
the well-shaped crystals.

     The constancy of the self-diffusion coefficients with varying
observation time indicates that in the time and space scale of the
nmr pulsed field gradient experiments both the crystals and
polycrystals can be considered to be quasi-homogeneous, i.e.,
that the adsorbent particle sizes significantly exceed the
observed molecular displacements, but that, on the other hand,
these displacements are large enough to exceed significantly the
dimensions of heterogeneity caused by the substructure. The
deviating behaviour of propane in poly-crystalline ZSM-5 may be
explained by assuming that with decreasing observation times
an increasing number of propane molecules does not escape into
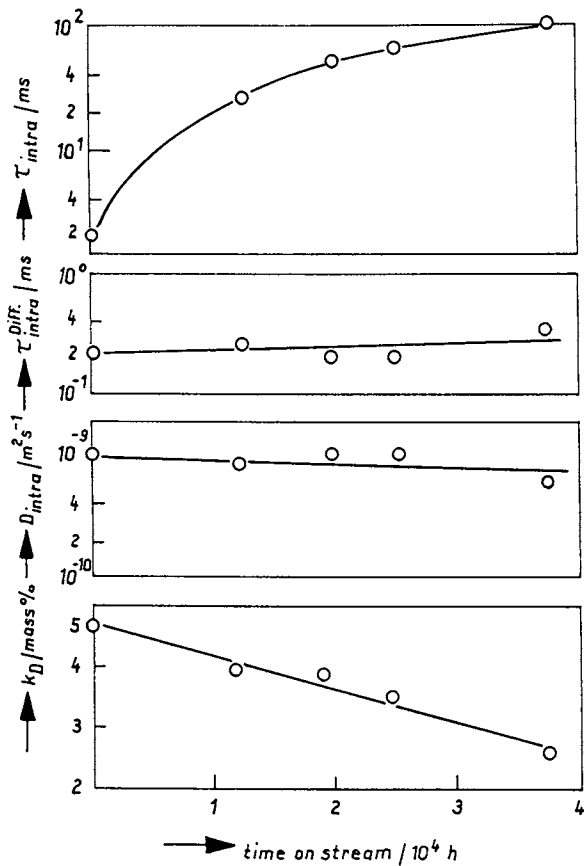
Figure 4:   Parameters of molecular transport in granulated zeolite NaCaA in dependence on the time on stream in a petroleum refinery (Reproduced with permission from Ref. 6. Copyright 1987 Butterworth)
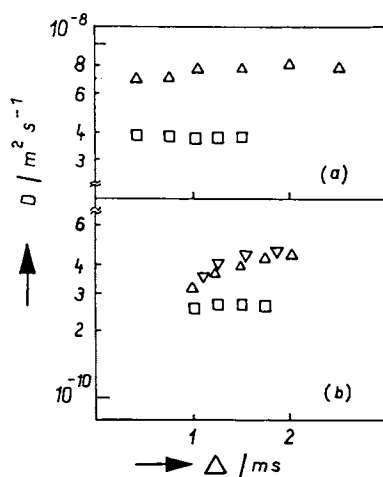
Figure 5: Self-diffusion coefficients of (a) methane (loading
ca. 3.5 molecules per channel intersection) and (b) propane
(2.5 molecules per channel intersection) in H ZSM-5 crystals
(□) and in polycrystals (△) for different observation times
Δ at 296 K (Reproduced with permission from Ref. 30. Copyright
1986 Elsevier)

the regions of higher mobility. Due to their higher mobility, for methane molecules such behaviour should occur at much shorter observation times than accessible at present.

Influence of Coke Depositions. Following an idea of Gilson and Derouane (31), n-hexane and mesitylene have been applied as starting materials for the coke deposition. n-Hexane coking was achieved by directing a continuous stream of hydrogen (2 l/h x g_{cat}) saturated with n-hexane at 16°C into a fixed bed - type glass reactor. For mesitylene coking more severe conditions had to be used. We have applied a nitrogen stream (9 l/h x g_{cat}) saturated with mesitylene at 40°C, at a temperature of 530°C.

Figure 6 gives a comparison of the intracrystalline mean life times of methane in ZSM-5 type monocrystals after different coking times, and the values of $\tau_{intra}^{(...)}$, calculated from the intracrystalline self-diffusion coefficients (6,32,33). The two starting chemicals lead to completely different dependences: For n-hexane, τ_{intra} and $\tau_{intra}^{(...)}$ coincide over a large range of coking times, whereas with mesitylene τ_{intra} is found to increase, whilst the intracrystalline mobility represented by $\tau_{intra}^{(...)}$ remains unaffected.

During mesitylene coking, the carbonaceous compounds are found to be exclusively deposited on the outer surface. For n-hexane, two stages of the coke deposition become visible: At shorter coking times n-hexane is mainly deposited in the intracrystalline space, thus simultaneously affecting a retardation of intracrystalline diffusion and tracer desorption. In a second stage, similar to the behaviour observed with mesitylene, coke is predominantly deposited on the crystallite surface.

Figure 7 shows the ratio of the quantities $\tau_{intra}^{(...)}$ and τ_{intra} as represented by Figure 6, in dependence on the total amount of coke deposited. While for coking with n-hexane the two stages of coking become clearly visible, for mesitylene $\tau_{intra}^{(...)}/\tau_{intra}$ decreases from the very beginning. Since the mesitylene molecules are too large to penetrate into the intracrystalline channel system, this result is in accordance with the expected behaviour.

Figure 8 shows the ratio $\tau_{intra}^{(...)}/\tau_{intra}$ for HZSM-5 crystals of different morphology as a function of the amount of n-hexane coke deposited (33): poly-crystalline spherical particles and polyhedral crystals. Once again, two stages of coke formation can be distinguished. The beginning of the second stage is virtually the same for all polyhedral crystals; however, a distinct delay of this onset is to be seen with the polycrystalline grain. This experimental finding can be explained by the existence of the secondary pore system represented by the free space between the crystallites. Thus, an additional amount of coke may be deposited on "neutral" spots outside the zeolite channel network, causing a delay of the onset of the second period of coke formation.

Figure 9 shows the self-diffusion coefficients of propane in the poly-crystalline grains after different coking times corresponding to different amounts of coke deposited (33). In complete agreement with the proposed model, the time dependence is determined by the amount of coke deposits: In the fresh specimen
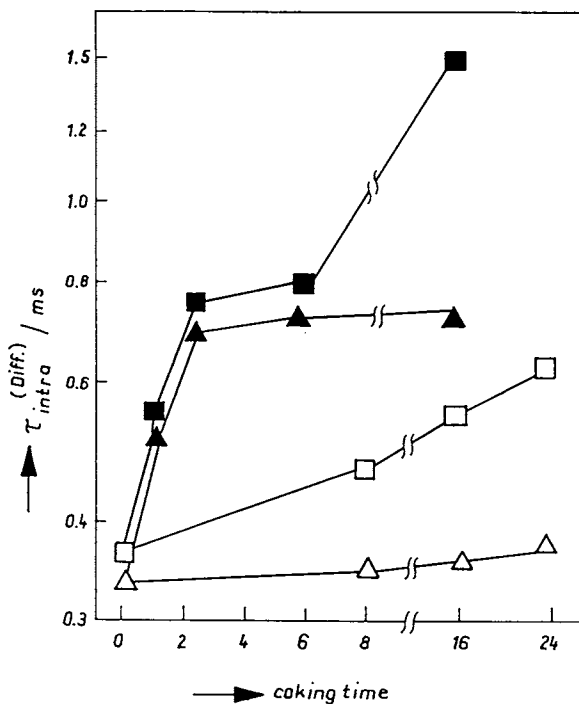
Figure 6: Intracrystalline mean life times τ_{intra} ($\square$) and τ_{intra}^{Diff} ($\triangle$) for methane at 296 K and a sorbate concentration of 3 molecules per channel intersection in H ZSM-5 coked by n-hexane (full symbols) and mesitylene (open symbols) in dependence on the time on stream (Reproduced with permission from Ref. 6. Copyright 1987 Butterworth)
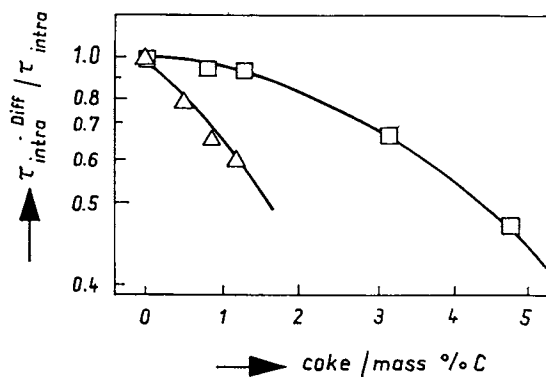
Figure 7: Ratio $\tau_{intra}^{Diff}/\tau_{intra}$ for methane in H ZSM-5
(Experimetnal values of Figure 6) as a function of the amount
of coke deposited: □ n-hexane coke, △ mesitylene coke
(Reproduced with permission from Ref. 33.   Copyright 1987
Elsevier)
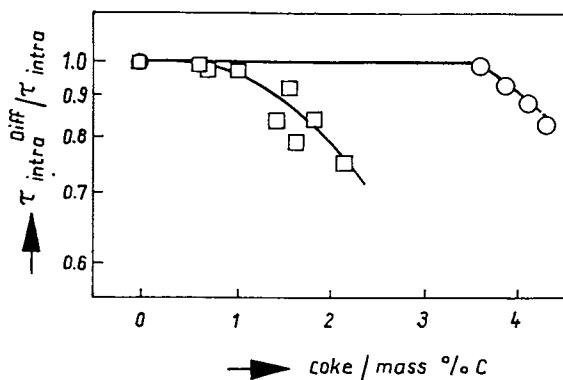
Figure 8: Ratio $\tau_{intra}^{Diff}/\tau_{intra}$ for H ZSM-5 samples of
different morphology as a function of the amount of coke
deposited: □ polyhedral crystals, O polycrystalline grains
(Reproduced with permission from Ref. 33. Copyright 1987
Elsevier)
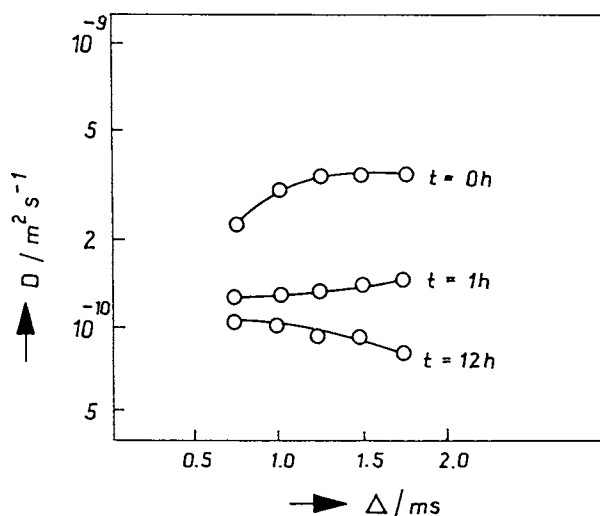
Figure 9: Self-diffusion coefficients of propane (loading ca 2.5 molecules per channel intersection) in polycrystalline grains of fresh H ZSM-5 and after 1 h (corresponding to 3.6 mass % coke) and 12 h (corresponding to 4.3 mass % coke) on n-hexane stream for different observation times Δ at 296 K (Reproduced with permission from Ref. 33. Copyright 1987 Elsevier)

the observed mobilities increase with increasing observation times, since – as above discussed – an increasing number of molecules may escape into the regions of higher mobility, i.e., into the secondary pore system. With increasing amount of coke, however, these pores are blocked, so that now with increasing observation times molecular diffusion is more and more restricted, since an increasing number of molecules comes into contact with the restricting coke deposits in the secondary pore system. Thus the secondary pore system is found to exhibit two remarkable properties: an enhancement of intraparticle diffusion in the fresh sieve, and the representation of a region of preferential coke deposition.

Acknowledgments

Literature Cited

1. Breck, D. W. Zeolite Molecular Sieves; Wiley: New York, 1974
2. Barrer, R. M. Zeolites and Clay Minerals as Adsorbents and Catalysts; Academic Press: London, 1978
3. Riekert, L. Adv. Catal. 1970, 21, 281-322
4. Ruthven, D. M. Principles of Adsorption and Adsorption Processes; Wiley: New York, 1984
5. Stejskal, E. O.; Tanner, J. E. J. Chem. Phys. 1965, 42, 288-292
6. Karger, J.; Pfeifer, H. Zeolites 1987, 7, 90-107
7. Karger, J. AIChE-Journal 1982, 28, 417-423
8. Pfeifer, H. Physics Rep. 1976, 26, 293-338
9. Farrar, T. C.; Becker, E. D. Pulse and Fourier Transform NMR; Academic Press: New York, 1971
10. Tyrrell, H. J. V.; Harris, K. R. Diffusion in Liquids; Butterworths: London, 1984
11. Richter.R.; Seidel, R.; Karger, J.; Heink, W.; Pfeifer, H.; Furtig, H.; Hose, W.; Roscher, W. Z. phys. Chem. (Leipzig) 1986, 267, 841-850
12. Karger, J.; Samulevitsch, N. N. Z. Chemie 1978, 18, 155-157
13. Shdanov, S. P.; Khvoschtschov, S. S.; Samulevitsch, N. N. Synthetic Zeolites; Khimia: Moscow, 1981
14. Karger, J. Adv. Coll. Interf. Sci. 1985, 23, 129-148
15. Karger, J.; Pfeifer, H.; Rauscher, M.; Walter, A. J.C.S. Faraday I 1980, 76, 717-737
16. Bulow, M.; Mietk, W.; Struve, P.; Zikanova, A. Z. phys. Chem. (Leipzig) 1983, 264, 598-602
17. Bülow, M. and Öhlmann, G. In New Developments in Zeolite Science and Technology – Discussion, Tominaga, H. Ed.; Japan Association of Zeolites, Tokyo, 1986, p 68
18. Germanus, A.; Karger, J.; Pfeifer, H.; Samulevitsch, N. N.; Shdanov, S. P. Zeolites 1985, 5, 91-95
19. Goddart, M.; Ruthven, D. M. Zeolites 1986, 6, 283-290 and 445-448

20. Goddart, M.; Ruthven, D. M. In New Developments in Zeolite Science and Technology; Murakami, Y.; Iijima, A.; Ward, J. W., Ed.; Kodansha: Tokyo, 1986, p 467

21. Germanus, A.; Kärger, J.; Pfeifer, H. Zeolites 1984, 4, 188-190

22. Kärger, J.; Pfeifer, H.; Heink, W. In Proceedings of the Sixth International Zeolite Conference; Olson, D.; Bisio, A., Ed.; Butterworths: Surrey, 1984, p 184

23. Haag, W. O.; Lago, R. M.; Weisz, P. B. Faraday Disc. 1982, 72, 317-330

24. Bülow, M. Z. Chem. 1985, 25, 81-88

25. Garcia, S. F.; Weisz, P. B. Ann. Meeting of the Am. Inst. Chem. Engr. Nov. 15-17, 1987, New York, Paper 16 E

26. Kerr, G. J. Catal. 1969, 15, 200-206

27. Richter, R.; Seidel, R.; Karger, J.; Heink, W.; Pfeifer, H.; Furtig, H.; Hose, W.; Roscher, W. Z. phys. Chem. (Leipzig) 1986, 267 1145-1151

28. Kondis, E. F.; Dranoff, J. S. Ind. Eng. Chem. Process Design Develop. 1971, 10, 108-114

29. Seidel, G.; Welker, J.; Ermischer, W.; Wehner, K. Chem. Techn. 1979, 31, 405-409

30. Kärger, J.; Pfeifer, H.; Caro, J.; Bülow, M.; Richter-Mendau, J.; Fahlke, B.; Rees, L. V. C. Appl. Catal. 1986, 24, 187-198

31. Gilson, J. P.; Derouane, E. G. J. Catal. 1984, 88, 538

32. Karger, J.; Pfeifer, H.; Caro, J.; Bulow, M.; Schlodder, H.; Mostowicz, R.; Völter, J. Appl. Catal. 1987, 29, 21-30

33. Bulow, M.; Caro, J.; Volter, J.; Karger, J. In Catalyst Deactivation; Delmon, B.; Froment, G. F., Ed.; Elsevier: Amsterdam, 1987, p 343

Chapter 24

Isothermal Three-Dimensional Diagram for Adsorption from Oxygen–Nitrogen Mixtures on Clinoptilolite

I. M. Galabova and G. A. Haralampiev

Higher Chemical Technological Institute, Boulevard "Kliment Ochridsky", No. 8, Sofia 1156, Bulgaria

A threedimensional diagram, expressing the amount adsorbed as a function of sorbate equilibrium concentration and total pressure, is drawn using both direct experimental data and computed data for O_2/N_2 mixtures on K–clinoptilolite at room temperature. The real adsorption isotherms follow the Freundlich law for N_2 and Henry's law for O_2. Freundlich and Henry constants are computed and correlated to sorbate equilibrium concentration. Selectivity coefficients, $\propto$, equilibrium constants, K, and the changes in the standard Gibbs free energy, ΔG^o, are determined. Selectivity towards N_2 is satisfactory and K–clinoptilolite could be used for industrial air enrichment.

Selectivity of some zeolites towards N_2 from O_2/N_2 mixtures is the basis of the adsorption process of oxygen enrichment of air. This process has certain advantages compared with the cryogenic process: it is more efficient for small or medium scales of production; it is flexible and easily adaptable in changing the production needs; it employs simpler machinery and operation, etc. The general principles of the adsorption enrichment of air have been discussed mainly with respect to synthetic zeolites or mordenite as the sorbents (1-3). The possibility of using clinoptilolite is a subject both of papers and patents (4,5) and has attracted much attention, since clinoptilolite is one of the most widely spread natural zeolite.
    The present paper deals with the threedimensional diagram for description of the equilibrium adsorption of O_2/N_2 mixtures on clinoptilolite. This diagram shows the dependence of the amount adsorbed on the total pressure, as well as the equilibrium concentration of the gas mixtures. Adsorption from binary mixtures involves theoretical and experimental problems. Ruthven's and Loughlin's works (7,8) provide much detail and they succeed in describing fully enough the complicated systems, but all at the expense of considerable characteristic constants used and elaborate computation. The experimental

difficulties ensure from the need to determine the concentration of
the components and to estimate the amount adsorbed, using elaborate
calibrations, measurements and computation (9).

The aim of the present paper is to present the adsorption equi-
librium of binary O_2/N_2 systems, as well as of pure sorbates on
natural clinoptilolite and to try to predict the behaviour of each
sorbate in mixtures under arbitrary pressures and concentration.

Sorbates and Sorbent Characteristics. K-clinoptilolite, obtained
from natural clinoptilolite from Olygocene 3 horizon (10), is used
as a sorbent. The natural sample chosen is with a fairly high pota
sium content, because K-form has high selectivity towards N_2 (10) –
the following ion-exchange increases K^+ content in the sorbent up to
7.83%.

Sorbates – N_2 and O_2 – are supplied in metal cylinders under
pressure of about 20 bar. The purity of N_2 is 99.999% and O_2 – 99.0%.

Experimental equipment. Figure 1 presents the apparatus used. The
system works at room temperature. Adsorption column, 1, contains
340 g dehydrated zeolite. The column has 44 mm diameter and 275 mm
height. Mercury manometer, 5, measures precisely the equilibrium
pressure in 1, while 5a and 5b (factory made manometers) are attach-
ed to 1 and to dosing column 2. Circulating pump 3 (Hartman and
Braun AC) operates between 0.6 and 1.4 bar, the range suitable for
industrial applications. It effects the circulation of the sorbates
until equilibrium is achieved. Vacuum pump 4 (MR-5-GDR) is used for
regeneration between runs. Gas-chromatographer 6 ("Thermochrom 23"
with an integrator IZ-21 and a printer "Seiko-310") is the analyser
of O_2/N_2 mixtures – Table I.

Table I. Parameters of gas-chromatographer column

Parameters	Value
Dispersity of the sorbent, mm	+0.2 – 0.3
Column diameter, mm	4
Column length, cm	120
Mass of the sorbent 5A, g	11.6
Temperature, K	323 + 0.5
Volume of the gas sample, cm^3	0.025

Sorbates O_2 and N_2, as well as H_2 and He, are kept in bottles 8
(H_2 – gas carrier for the chromatographer and He – used for adsorp-
tion experiments under lower pressures); 1' – 10' valves. Gases are
dried in column 7 by native clinoptilolite down to at least 40 ppm
moisture.

Gas mixtures are prepared in advance, analysed and stored in 8.
Dosing column 2 is filled with sorbate under constant pressure and
calibrated beforehand so the reading on 5a gives the sorbate amount
allowed to 1. Samples taken for analysis should be of the smallest
amounts (Table I) so that the equilibrium would not be disturbed.
Initial and equilibrium concentrations of O_2, N_2, resp., are used to
estimate the amounts of O_2, N_2, resp. adsorbed (a, cm^3 g^{-1}). The
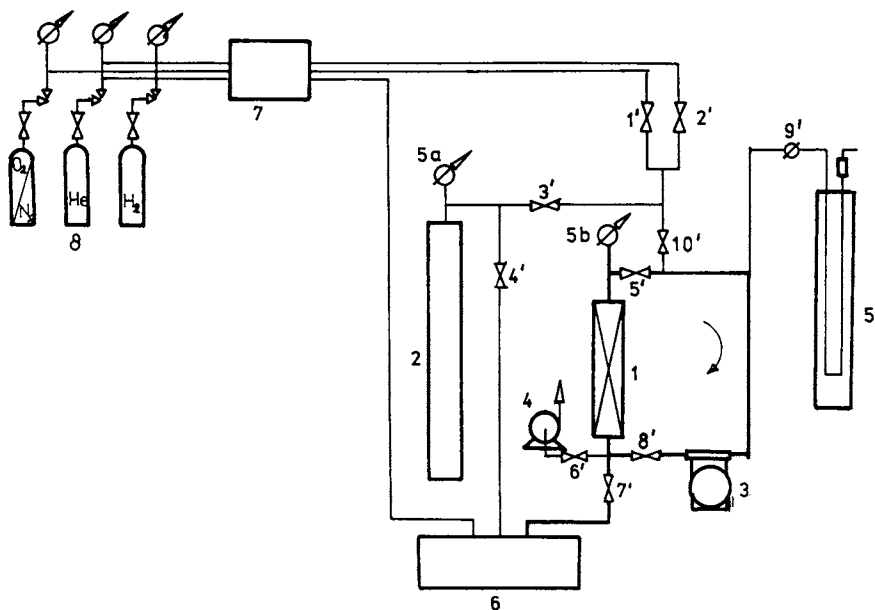
Figure 1. Experimental equipment.

dosing volumes are evaluated with the aid of a calibration burette and a calibration equation is derived: v (cm^3) = 1483$\triangle$p (bar) (Regression coefficient being R = 0.99). Helium is used to estimate the dead volume as a sum of the communications, free volume of the adsorption column, pores between sorbent grains and transport pores. The weight of the dehydrated sorbent is measured (340.0 $\pm$ 1 g). Errors of the adsorption capacities are aroung 3% at high pressures and about 8% at low pressures.

Experimental data and discussion

Adsorption isotherms of pure N_2 and 99% O_2 are presented on Figure 2. The selectivity towards N_2 is noticeable. On the same figure, the amounts of N_2 and O_2 adsorbed from a mixture (equilibrium concentration - $\overline{C}_{O_2}$ = 41%) are drawn as functions of the total pressure, to illustrate the difference of adsorption from mixtures compared with that from pure components.

The threedimensional diagram for N_2 and O_2, for various mixtures, is shown on Figure 3. Cuts at constant total pressure give isobars, an example of which is given in Figure 4, and represents ability of adsorption of each sorbate at different equilibrium concentrations of O_2 in the gas phase ($C_{gas}^{O_2}$). Cuts at constant equilibrium concentrations, $\overline{C}_{O_2}$, give functions of the amount adsorbed $a_{N_2(O_2)}$ as function of the total pressure P_{tot}. Such curves (Figures 5 and 6) are very similar to adsorption isotherms, but they differ from them - since for an adsorption isotherm the amount adsorbed of a given sorbate should be represented as a function of its partial pressure, so the curves on Figures 5 and 6 are fictitious isotherms - "isotherms". However, they are very convenient to present adsorption data from mixtures. Regression analysis is applied to functions as those on Figures 5 and 6. For chosen equilibrium concentration ($\overline{C}_{O_2}$) a virial equation of type

$$a_{N_2(O_2)} = a_o + a_1 P_{tot} + a_2 P_{tot}^2 + a_3 P_{tot}^3$$

is found, where a_o, a_1, a_2 and a_3 are virial coefficients (Table II). Data from Table II allow computation of amount adsorbed ($a_{N_2(O_2)}$) under various pressures in the experimental range 0.6 - 1.4 bar. Threedimensional diagram provides possibility to read off amount adsorbed at any equilibrium concentration, $\overline{C}$, and total pressure, P_{tot}.

Actual adsorption isotherm of N_2 and O_2 are shown on Figures 7 and 8. The isotherms for N_2 in the experimental region are well described as Freundich type of isotherm - the amount adsorbed (a) as a function of the partial pressure, P_i. Table III contains Freundich constants n_F and K_F. It is a challenge to correlate those constants with equilibrium concentration, $\overline{C}$, as that would give a chance to calculate the amount adsorbed at arbitrary partial pressures and equilibrium concentrations. Such a correlation for k_F is expressed by a function of type $k_F = m + q \ln \overline{C}_{N_2}$, where m = 7.779 and q = 3.665.
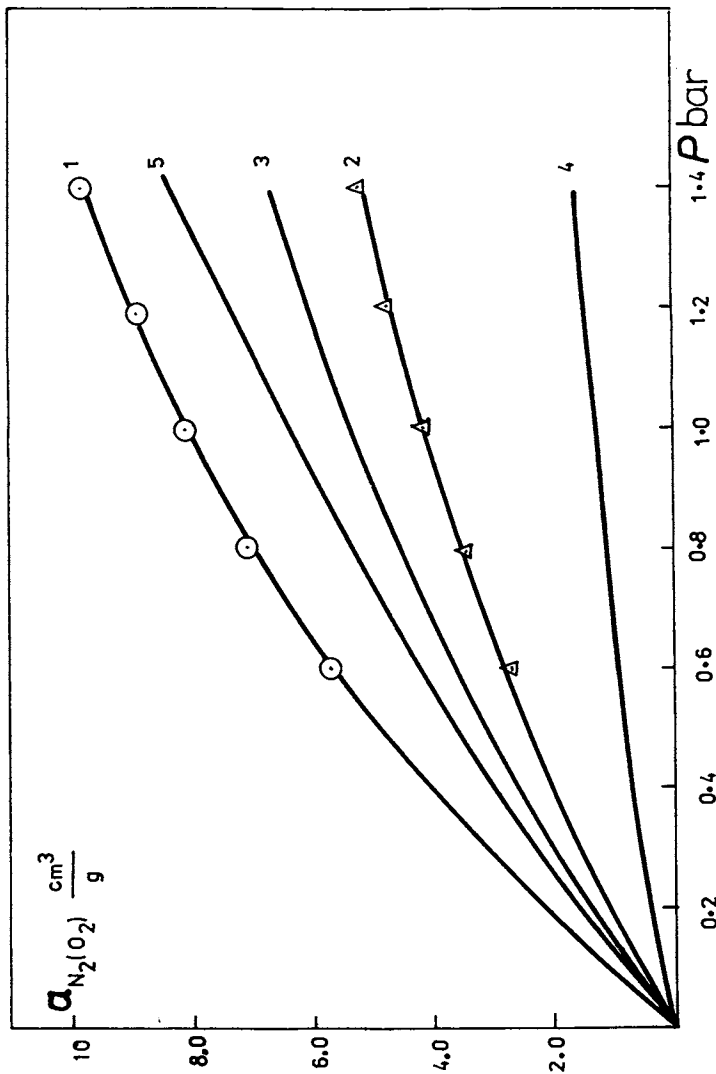
Figure 2. Adsorption isotherm of N_2 and O_2 from pure gases $(1 - N_2, 2 - O_2)$ and from sorbate mixture $(\bar{C}_{O_2} = 0.41, 3 - N_2, 4 - O_2, 5 - (N_2 + O_2))$.
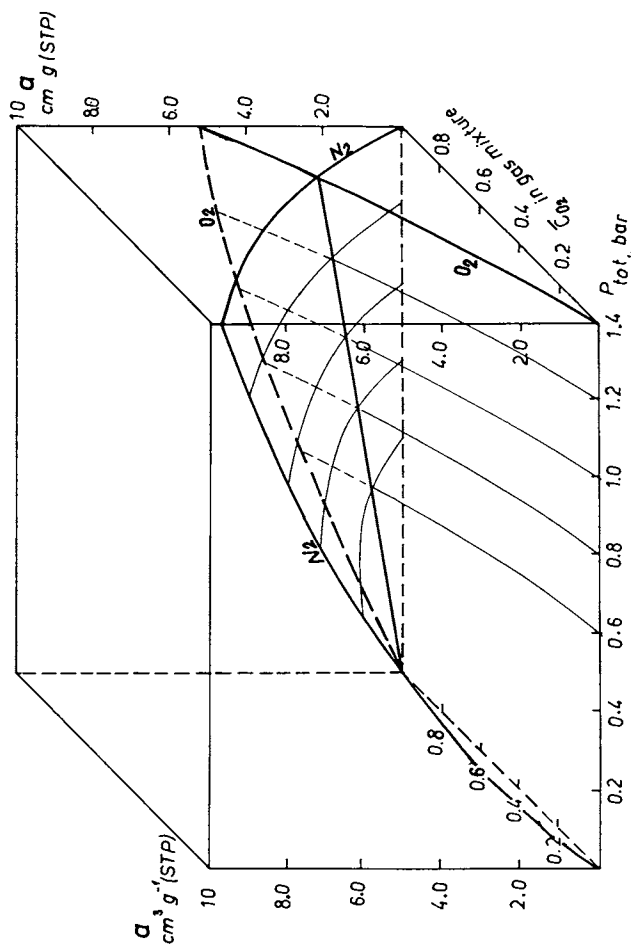
Figure 3. Threedimensional diagram for adsorption from N_2/O_2 mixtures ($a_{N_2(O_2)}$ - amount adsorbed for N_2, O_2 resp.), P_{tot} - total pressure, C_{O_2} - equilibrium oxygen concentration in the gas mixture.
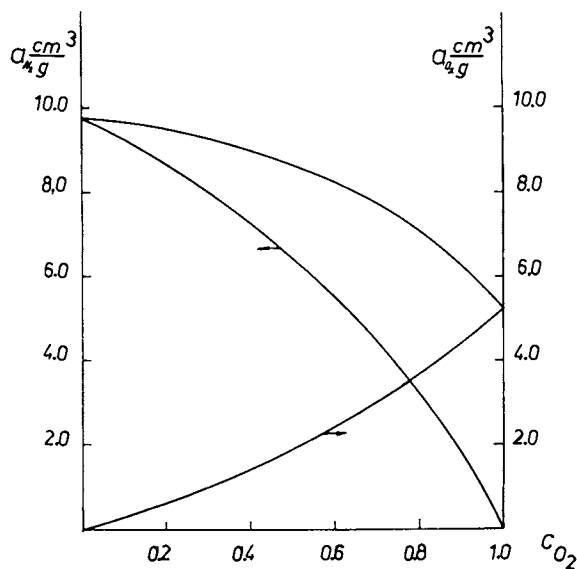
Figure 4. Isobaric cuts from the threedimensional diagram at p = 1.4 bar. $\bar{C}_{ads}$ equilibrium mole fraction of O_2 in the sorbed phase.
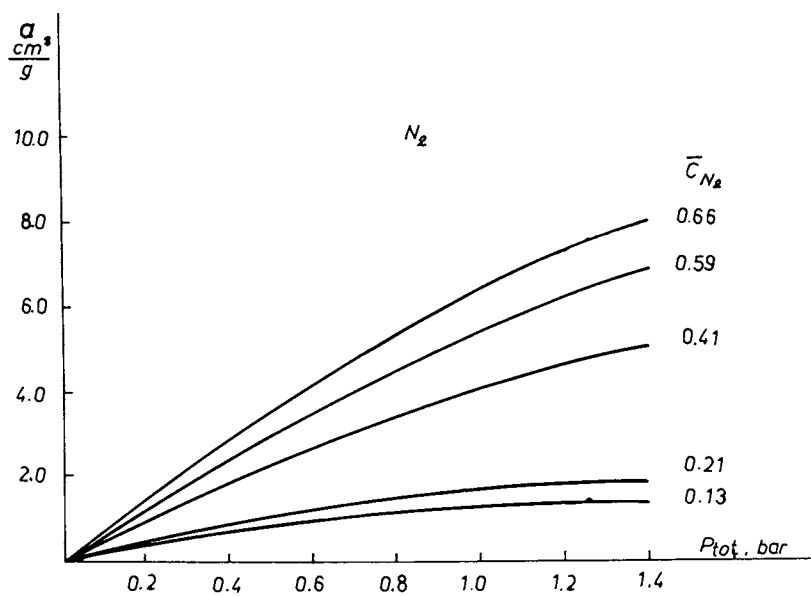
Figure 5. Adsorption "isotherms" for N_2 from O_2/N_2 mixtures.
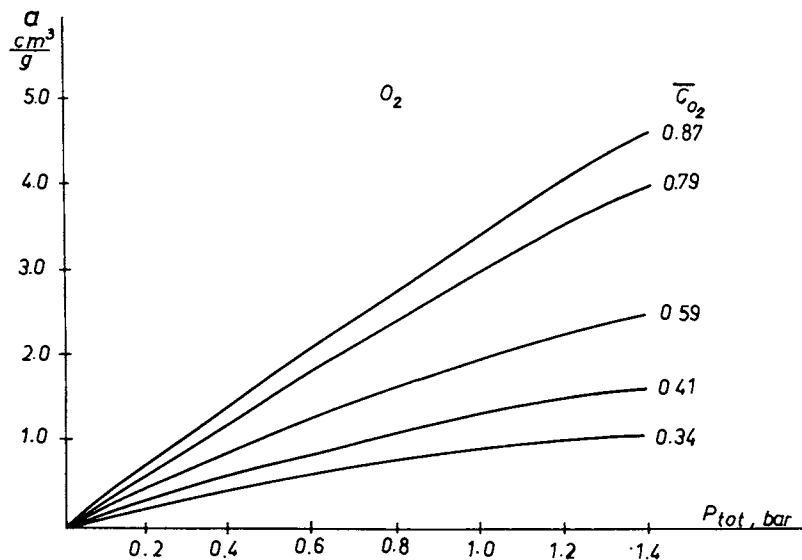
Figure 6. Adsorption "isotherms" for O_2 from O_2/N_2 mixtures.

$$a = k_F P_i^{n_F}$$
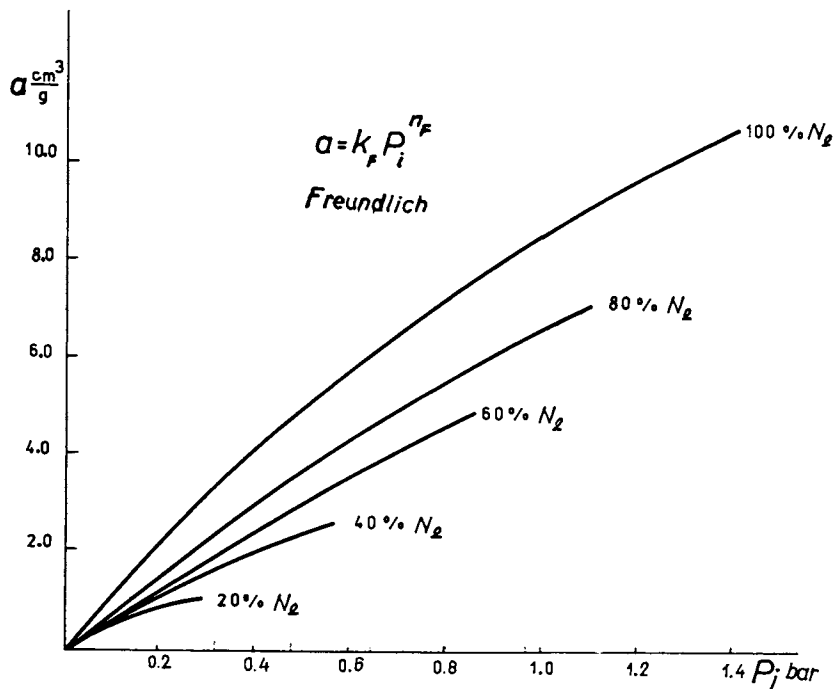
Freundlich

Figure 7. Freundlich type isotherms for N_2 from O_2/N_2 mixtures.
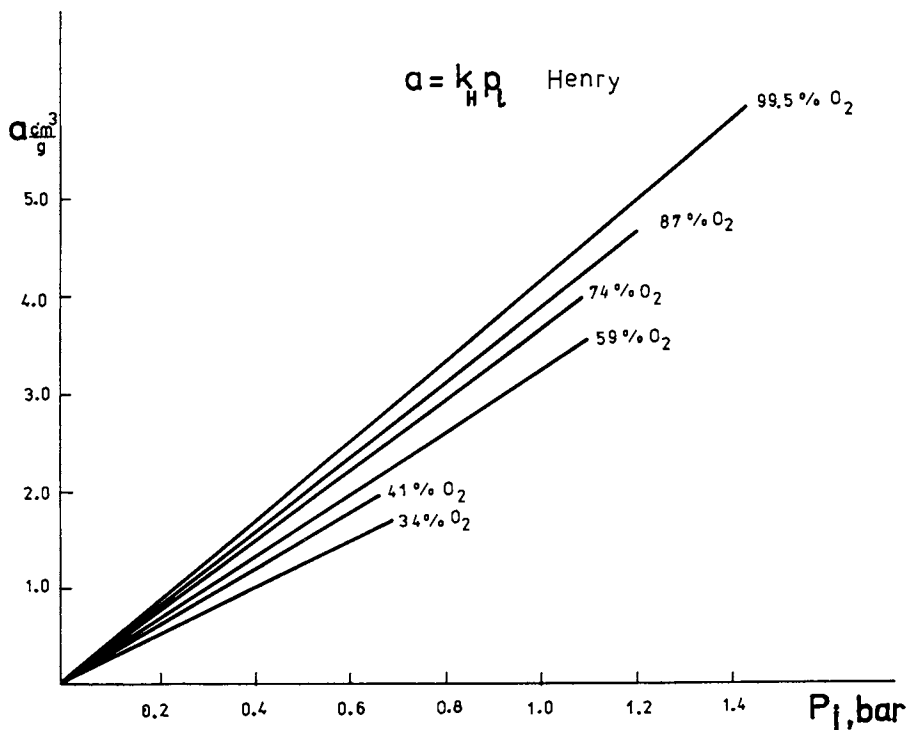
Figure 8. Henry type isotherms for O_2 from O_2/N_2 mixtures.

Table II. Virial coefficients

$\bar{C}_{O_2}$,	Coefficients	a_o	a_1	a_2	a_3
0.00	N_2	-0.190	14,335	-8.678	2.558
0.34	O_2	-0.001	1.035	-0.077	-0.075
	N_2	-0.004	7.396	-0.495	-0.521
0.41	O_2	-0.001	1.957	-1.389	0.644
	N_2	-0.002	5.537	0.435	-0.651
0.59	O_2	0.001	1.666	0.826	-0.508
	N_2	0.001	3.618	1.179	-0.807
0.79	O_2	-0.002	2.900	0.183	-0.172
	N_2	-0.001	1.984	-0.206	-0.189
0.87	O_2	0.002	1.755	3.176	-1.479
	N_2	-0.001	0.844	0.750	-0.352
0.995	O_2	-0.030	4.860	-0.367	-0.267

Table III. Freundich constants

$\bar{C}_{N_2}$ Constants	0.20	0.40	0.60	0.80	1.00
n_F	0.535	0.958	0.995	0.860	0.680
k_F	1.97	4.41	5.75	6.73	8.09
n_{FSPL}	0.498	0.884	0.960	0.850	0.720

Regression coefficient is R = 0.98. Constants n_F are in more complex functionality with $\bar{C}_{N_2}$ which could be described by a cubic parametric B-spline. The spline computed values (n_{FSPL}) are listed in Table III.
Oxygen adsorption isotherms, in the experimental region, is Henry type isotherm (Figure 8). Table IV gives Henry constants.

Table IV. Henry constants

$\bar{C}_{O_2}$	0.34	0.41	0.59	0.79	0.87	0.995
k_H	1.96	2.5	3.10	3.19	3.36	3.91

Dependence of Henry constant (k_H) on equilibrium concentration is also of interest. The dependence is of logarithmic type as that for k_F. The equation for k_H is: $k_H = 3.737 + 1.530 \ln \overline{C}_{O_2}$ (Regression coefficient R = 0.93). The similarity of $k_F = f(\overline{C}_{N_2})$ and $k_H = f(\overline{C}_{O_2})$ is logical, as for $n_F = 1$ Freundlich isotherm turns into Henry type. With the equilibrium data at our disposal it is possible to compute the separation coefficient, $\propto$,

$$\propto\; = \; Ya, Xg\; /\; Xa, Yg$$

where Ya and Xa are the equilibrium concentrations of N_2 and O_2, resp. in the sorbed phase; Yg and Xg – the corresponding concentrations in the gas phase. Separation coefficients in the following values are determined: $2.0 < \propto_{N_2} < 3.9$. The selectivity coefficient, $\propto$, of K-clinoptilolite towards N_2 is satisfactory, as compared to $\propto = 2.54$ for 5A (11); $\propto = 3$ for KX and $\propto = 4.9$ for NaX at $-78^{o}C$ (6).

As the data presented refer to an equilibrium, it is of interest to further establish some thermodynamic data, such as equilibrium constants $K = \overline{C}_{ads,N_2(O_2)}\; /\; \overline{C}_{g,N_2(O_2)}$ and changes in standard Gibbs free energy, $\triangle G^o$. Values of $K_{N_2(O_2)}$ and $\triangle G_{N_2(O_2)}$ are in Table V.

Table V. Equilibrium constant, K, and change in Gibbs free energy, $\triangle G^o$

$\overline{C}_{O_2}$	0.34	0.41	0.56	0.79	0.87
K_{O_2}	0.35	0.51	0.58	0.77	0.83
$\triangle G^o_{O_2}$, $\frac{kJ}{mol}$	25.7	18.5	13.7	6.4	4.7
$\overline{C}_{N_2}$	0.14	0.20	0.4	0.59	0.63
K_{N_2}	2.00	1.95	1.68	1.34	1.33
$\triangle G^o_{N_2}$, $\frac{kJ}{mol}$	-17.17	-16.6	-12.8	-7.24	-7.11

The negative values of the changes in Gibbs free energy for N_2 are another good quantitative evaluation of the selectivity of K-clinoptilolite towards N_2.

Conclusions

The threedimensional diagram obtained could serve both theoretical
and technological computations concerning oxygen enrichment of air
on K-clinoptilolite. It is a basis for determining of adsorption
isobars, fictitious and real isotherms, as well as thermodynamic
data for adsorption from binary O_2/N_2 mixtures. Freundlich and Henry
constants (for the real adsorption isotherms) correlated with the
equilibrium concentration are useful for computation of the amounts
adsorbed at arbitrary partial pressures and equilibrium concentra-
tions.

Acknowledgment

Literature Cited

1. Scarstrom, C. W., U.S. Patent 3 237 377, 1966.
2. Domine, D.; Hay, L., Proc. 1st Int.Conf.Mol.Sieves, 1968, p.204,
   Soc.Chem.Ind., London.
3. Davis, J. C., Chem.Eng., 1972, 79, 88.
4. Galabova, I. M. et al., Bul.Not.Bureau for Inv. 18 223, 1973.
5. Torii, K. et al., J.Chem.Soc.Japan, Chem.and Ind.Chem., 1973. 2,
   225.
6. Breck, D. W., Zeolite Mol.Sieves, John Wiley & Sons, New York,
   1974, p.689; p.695.
7. Ruthven, D. M., Loughlin, K. F., Faraday Trans., 1972, 68, 696.
8. Ruthven, D. M., Loughlin, K. F., Mol.Sieves (3rd Int.Conf.),
   American Chemical Society: Washington D.C., 1973, p.330.
9. Murphy, V. E., Ph.D.Thesis, Imp.Coll.of Sci. and Technol., Lon-
   don, 1968.
10. Galabova, I. M. et al., Proc.Natural Zeol.Occ., Prop.Use, Perg.
    Press, 1978, p.431.
11. Townsend, R. P.; The Properties and Applications of Zeolites,
    1980, p.95.

Chapter 25

Binary Sorption Equilibria
by Pulse Chromatography

Dhananjai B. Shah

Department of Chemical Engineering, Cleveland State University,
Cleveland, OH 44115

A chromatographic method has been used to measure
single component sorption isotherms of O_2, N_2, CH_4,
C_2H_6, C_3H_8 and cyclopropane and binary sorption
isotherms of O_2-N_2, CH_4-C_2H_6 and C_3H_8-cyclopropane
mixtures on Linde 5A zeolite. The Van der Vlist-Van
der Meijden Method was used to analyze the response
peaks. This method provides a reliable way to
measure single component isotherms but does not work
as well for binary sorption isotherms for two of the
three binary systems studied here (CH_4-C_2H_6 and
C_3H_8-cyclopropane). The difficulty appears to lie
in the nature of the experimental technique and the
method of data analysis.

A significant amount of work has been done on determining sorption
capacity and the kinetics of sorption in zeolites because of their
applications as adsorbents and as catalysts in the chemical process
industry. However, most of this work has been done with single
components, whereas all practical applications involve
multicomponent mixtures. Hence, measurement of binary or
multicomponent equilibria on zeolites is of considerable
importance.

Adsorption isotherms for single components have generally been
determined by gravimetric and volumetric methods. These methods
involve following the changes in either the weight of the sample or
the volume and/or pressure of the gas phase to measure the amount
of adsorption. However, these techniques are cumbersome and
time-consuming for measuring binary sorption isotherms as both the
total amount of adsorption and the adsorbed phase composition have
to be determined. The chromatographic method, on the other hand,
provides a simpler alternative for determining binary sorption
equilibria.

    The method consists of monitoring and analyzing the response
of an adsorption column to a pulse input or a step change in
concentration of an adsorbate. The carrier gas is a mixture of an
inert gas and the adsorbate of known composition. The retention
time of the pulse is related to slope of the equilibrium curve at
the carrier gas composition. The slopes of the equilibrium curve
at different points on the curve can be determined by carrying out
experiments with different carrier gas compositions. The
equilibrium curve can, then, be easily obtained by integration of
the slopes of the isotherm curve. For binary sorption equilibria,
the experiments are similar except the carrier gas is a mixture of
the two adsorbates.
    The chromatographic method has been used extensively to
determine various process parameters (1). Schneider and Smith (2)
and Hashimoto and Smith (3, 4) determined Henry constants for
different gases on alumina and silica gel by analyzing the first
moments of the response peaks. Peterson and Helffrich (5) and
Peterson et al. (6) used tracer pulse chromatography to measure
single component adsorption isotherms. Haydel and Kobayashi (7)
used a similar method to measure adsorption equilibria of
methane-propane mixtures on silica gel. Their method used
radioactive tracer pulsing and hence required a special detection
system for radioisotopes. Van der Vlist and Van der Meijden (8)
used this method to determine binary sorption equilibria of
nitrogen-oxygen mixture on Linde 5A molecular sieve. Ruthven and
Kumar (9) and Ruthven and Wong (10) have used the chromatographic
method successfully to measure binary adsorption of different gases
in 4A and 5A zeolites.
    In this work, a gas chromatographic system has been used to
obtain binary sorption equilibria for nitrogen-oxygen,
methane-ethane and propane-cyclopropane mixtures on 5A molecular
sieve. The experimental measurements have also been compared with
the predictions from the statistical thermodynamic model of Ruthven
(11). The model is capable of predicting binary sorption
equilibria from the parameters derived from the pure-component
isotherm measurements.

Theoretical

When a pulse of an adsorbate is introduced in an adsorption column,
its retention time t in the column is related to the slopes of the
isotherms of each component in the carrier gas (7):

$$t/t' = 1 + ((1 - \varepsilon)/\varepsilon)*(K_1(1 - x_1) + K_2 x_1) \qquad (1)$$

Here K_1 and K_2 are the dimensionless slopes of the sorption
isotherms of components 1 and 2, x_1 and x_2 are the mole fractions
of the two components in the carrier gas, t' is the retention time
of a non-adsorbing species in the column and   is the column
voidage. After multiplication with appropriate conversion factors,
K_1 and K_2 may also be written as dq_1/dx_1 and dq_2/dx_2 where q_1 and
q_2 are the adsorbate concentrations on zeolite in molecules per
cavity.

Pure-Component Isotherm. When one of the components in the carrier
gas is non-adsorbing such as helium, the above equation reduces to
$$t/t' = 1 + ((1 - \varepsilon)/\varepsilon)* K_1(1 - x_1) \qquad (2)$$
Knowledge of the retention time (t) of the pulse and the mole
fraction of the adsorbing component in the carrier gas (x_1) enables
one to calculate the slope of the isotherm K_1 at x_1. If the values
of K_1 are obtained at various compositions of the carrier gas, the
sorption isotherm can be easily obtained by integrating the slopes
over the composition range from 0 to 1.

Binary Isotherm. The method to calculate the binary sorption
isotherm from the pure component isotherms is outlined below.
Equation (1) can be rearranged to obtain
$$(t/t' - 1)*(\varepsilon/(1 - \varepsilon)) = K_1(1 - x_1) + k_2 x_1 = f(x_1) \quad (3)$$
The above equation has been derived from a column mass balance and
is valid under the conditions of constant temperature and pressure.
It is also required to assume that the isotherms are linear in the
concentration range studied. The left side of the equation is
known experimentally as a function of x_1 from the response peaks
obtained by pulsing an adsorbate into a carrier gas of composition
x_1. To obtain the isotherms q_1 and q_2 as a function of
concentration, an integration procedure is followed. In general,
$f(x_1)$, $q_1(x_1)$ and $q_2(x_2)$ can be expressed as third order
polynomials
$$f(x_1) = A_o + A_1 x_1 + A_2 x_1^2 + A_3 x_1^3$$
$$q_1(x_1) = a_1 x_1 + a_2 x_1^2 + a_3 x_1^3 \qquad (4)$$
$$q_2(x_2) = b_1 x_2 + b_2 x_2^2 + b_3 x_2^3$$
where $x_2 = 1 - x_1$. The experimental values of $f(x_1)$ are fitted to
a third order polynomial and the coefficients A_o, A_1, A_2 and A_3 are
calculated. When Equation (4) is substituted in Equation (3) and
the coefficients of x_1^o, x_1^1, x_1^2 and x_1^3 are compared, four
equations involving six unknowns are obtained. Two additional
equations arise by noting that both $q_1(x_1)$ and $q_2(x_2)$ must pass
through the end points defined by the single component isotherms in
the limit as x_1 and x_2 approach 1. This system of six equations is
solved for the coefficient a's and b's from which the sorption
isotherms of the binary gas mixture can be calculated from Equation
(4).
     The above method has been applied to determine the binary
sorption isotherms of N_2-O_2, CH_4-C_2H_6 and C_3H_8-cyclopropane
mixtures. The equilibrium sorption data obtained from the gas
chromatograph have been compared with the predictions of the
statistical thermodynamic model proposed by Ruthven (11, 12).
Parameters used in the thermodynamic model are the Henry constants

and v/β the number of adsorbate molecules that can be accomodated
in the zeolitic cavity for each of the components. Experimentally
obtained pure-component isotherms were fitted to the model isotherm
equation to calculate the Henry constant and the effective volume
of the adsorbate molecule. The values of these parameters obtained
from the curve fitting technique are listed in Table I for each of
the component studied. These, in turn, were used to predict the
binary sorption equilibria from the model equations as outlined by
Ruthven (11).

Table I. Henry constants and molecular parameters used in
          predicting binary sorption equilibria from
          statistical thermodynamic model

| Component | | Temp | v/β | | Henry constants molecule/cavity/torr | |
1	2	K	1	2	K_1	K_2
N_2	O_2	298	8.9	11.7	0.00125	0.00055
C_2H_6	CH_4	298	9.5	10.0	0.00566	0.00188
		348	6.0	9.5	0.00877	0.00081
cyclo propane	C_3H_8	398	5.0	5.0	0.099	0.0158

Experimental

The experimental system consisted of an adsorption column fitted
with a thermal conductivity detector. The adsorbate gas mixture
was passed through the column packed with Linde 5A molecular sieve.
The details of the packed column are given in Table II. The
carrier gas mixture was dried prior to introduction to the column.
The gas flow rates were adjusted and measured until a desired
carrier gas composition was achieved. A six-port valve with
interchangeable loops was used for introducing a pulse in the
carrier gas. The pressure drop across the column was measured with
a manometer and was found to be negligible. The dead volume in the
system between the points where the pulse was introduced and the
response was measured was minimized.

Table II. Details of column and adsorbent
Column: packed length = 33 cm x 0.95 cm diameter
Bed voidage = 0.37
Adsorbent: Linde 5A 30-40 mesh pelleted molecular sieve
            (Lot MX 1582)

The inert gas used for the study was high purity helium and
all other gases were of chemical purity (99.0%). The adsorption

column was regenerated by passing helium over the sieve at 673K for 24-36 hours. The column voidage was determined from the volume of the packed column, the amount of adsorbent charged and the bulk density of the adsorbent. The linearity of the system was checked by varying the pulse size.

Results and Discussion

Pure-Component Isotherms.   The single component isotherms (obtained using helium as the carrier gas) are shown in Figures 1(a), 2(a), 3(a) and 4(a). Nitrogen and oxygen isotherms are shown in Figure 1(a). Both the isotherms are nearly linear and compare well with the experimental data of Huang (13) who used a static method to measure the pure-component isotherms. Figures 2(a) and 3(a) show pure component isotherms for methane and ethane at 298 and 348K. The sorption capacity of 5A zeolites for methane is not as high as that for ethane (q = 1 molecule per cavity for methane versus 5 for ethane at 298K and 760 torr). These single component isotherms have been compared with the gravimetric data of Loughlin (14). The data for ethane at 298K compare well whereas the data for methane at 298K fall below the gravimetric data at 273K as expected. The gravimetric data for ethane at 345K also compare reasonably well with the chromatographic data. The pure-component isotherms for propane and cyclopropane are shown in Figure 4(a) and are also compared with the data of Laughlin (14) and Derrah (15). Comparison between the two sets of data is good. The chromatographic method, therefore, can be used to accurately measure the pure-component isotherms. This has been pointed out by other workers as well (9, 10, 16).

Binary Isotherms. Of the three systems studied, the N_2-O_2 mixture contains components which are not strongly adsorbed by the molecular sieve. Since the thermal conductivity of nitrogen and oxygen is quite close to one another, the problem of baseline drift was encountered and a servomax oxygen analyzer was used for this system. The binary sorption isotherms obtained from the chromatographic method are nearly linear and are shown in Figure 1(b). These isotherms are compared with the isotherms predicted from the statistical thermodynamic model. Both the results compare quite well.

Figures 2(b) and 3(b) show the experimental binary sorption equilibria for the CH_4-C_2H_6 mixture at two different temperatures along with the theoretical prediction of the statistical thermodynamic model. The comparison between the two sets of data is good. However, the nature of the experimental binary sorption isotherm curve for ethane is different from that predicted by the thermodynamic model in the region of high ethane concentrations. The experimental curve shows an increase in the slope of the curve in the region where the mole fraction of ethane approaches 1 whereas the isotherm predicted by the thermodynamic model is concave with respect to the gas phase composition axis for the entire concentration range.

For the system of propane-cyclopropane, the problem of baseline drift and noise was encountered because of the closeness
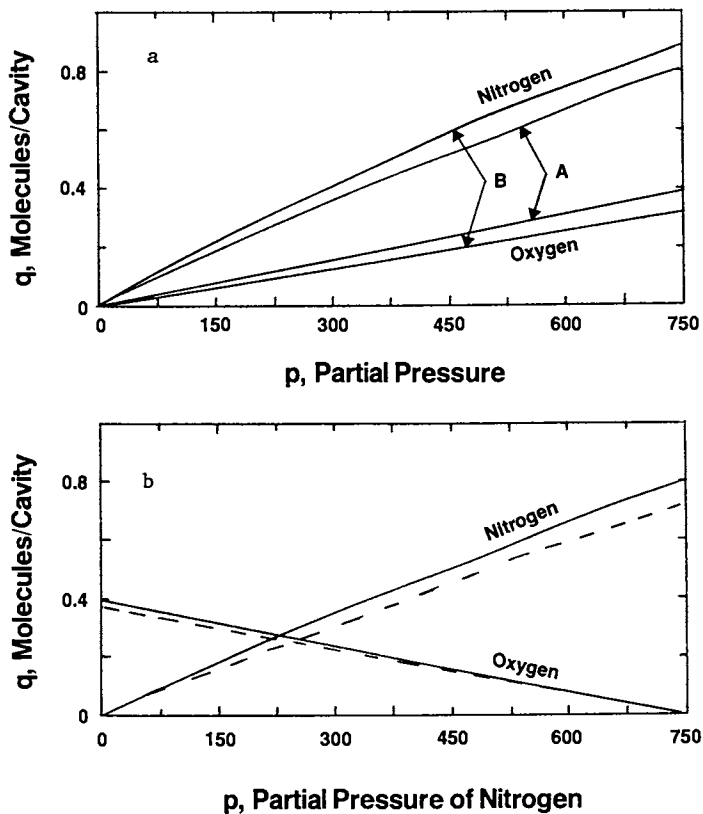
Figure 1. (a) Pure-component isotherms for oxygen and nitrogen at 298K. A - Present experimental data. B - Experimental data of Huang (13). (b) Binary sorption isotherms for nitrogen-oxygen mixture at 298K and 750 torr. ———— Present experimental data. ----- Theoretical prediction from the thermodynamic model.
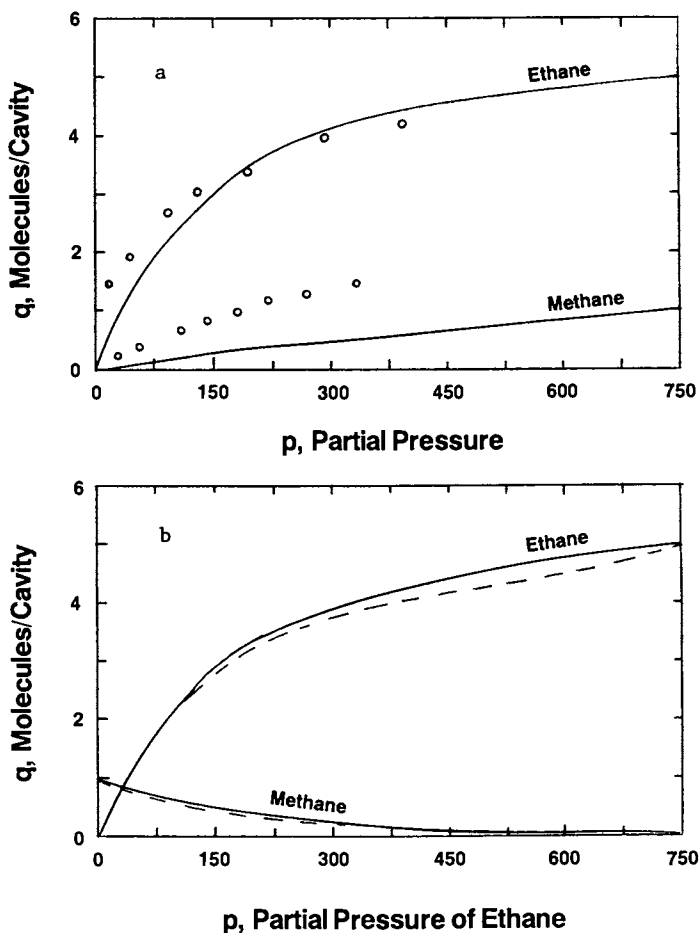
Figure 2. (a) Pure-component isotherms for ethane and methane at 298K. o - Gravimetric data of Loughlin (14) (Data for methane are at 273K). (b) Binary sorption isotherms for ethane-methane mixture at 298K and 750 torr. ———— Present experimental data. ----- Theoretical prediction from the thermodynamic model.
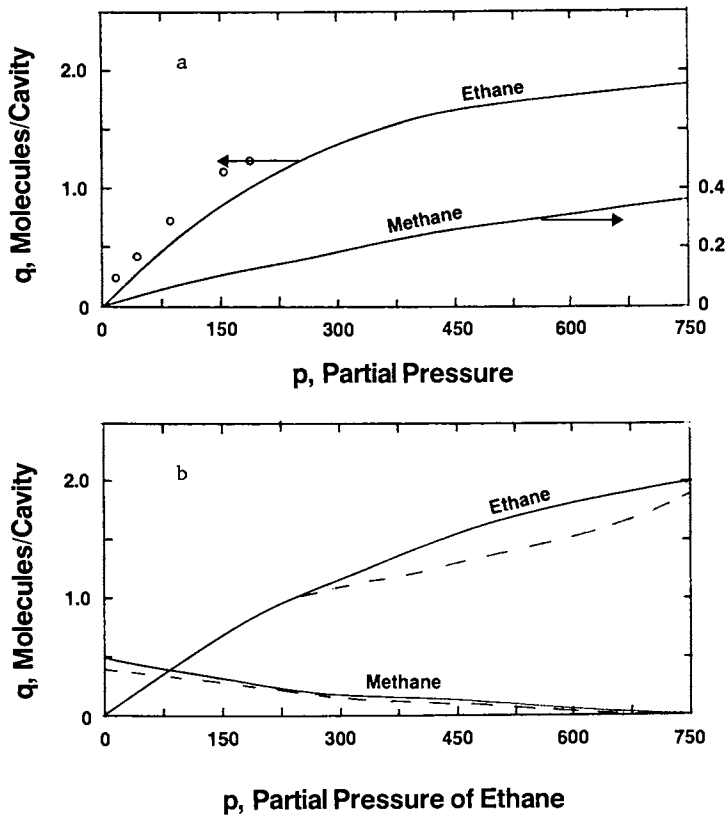
Figure 3. (a) Pure-component isotherms for ethane and methane at
348K. o - Gravimetric data of Loughlin (14). (b) Binary
sorption isotherms for ethane-methane mixture at 348K and 750
torr. ----- Present experimental data. ——— Theoretical
prediction from the thermodynamic model.
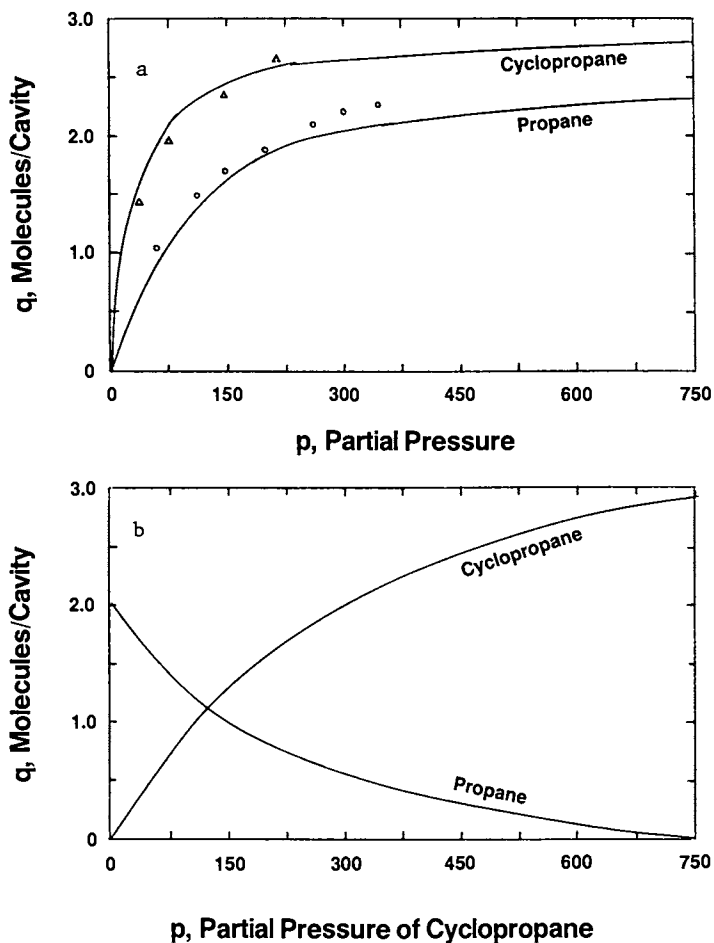
Figure 4.   (a) Pure-component isotherms for cyclopropane and propane at 398K.   (Reproduced with permission from Ref. 17. Copyright 1977 American Institute of Chemical Engineers.) O.- Gravimetric data of Loughlin (14).   Δ - Gravimetric data of Derrah (15).   (b) Binary sorption isotherms for propane-cyclopropane mixture at 398K and 750 torr as predicted from the thermodynamic model.

of their thermal conductivities. A few experiments in the middle
of the composition range were performed but these were not
sufficient to construct the binary sorption equilibria curves.
However, the Henry constants and molecular volumes of the two
sorbates were determined from the pure component isotherms and the
binary sorption equilibria were calculated from the thermodynamic
model. These isotherms are shown in Figure 4(b). The experimental
constants $K_1(1-x) + K_2x$ were compared with the theoretical values
by taking slopes of the isotherms at the required compositions.
The results are shown in Table III. The experimental values go
through a minimum at the composition of 55.8% cyclopropane and then
increase with the composition. This behavior appears to be similar
to that of methane-ethane system and the chromatographic
experimental measurements over the entire composition range are
likely to show an increase in the slope of the cyclopropane
isotherm in the region where the mole fraction of cyclopropane
approaches 1.

Table III.   Comparison of experimental and predicted slopes for
             propane-cyclopropane mixture at 398K and different
             compositions

| Mole fraction | $K_1x_2 + K_2x_1$ | |
cyclopropane	Experimental	From Figure 4(b)
0.4153	38	69
0.558	30	47
0.677	35	36

    If the two components form a non-ideal adsorbed solution
mixture, then the behavior as outlined above can be expected for
the binary sorption equilibria. Indeed, such data have been
reported for $i\text{-}C_4H_{10}\text{-}C_2H_4$ on molecular sieve 13X ([16]). The
presence of one component may reduce the sorption capacity of the
molecular sieve for the other component. However, as the pure
component regions are approached (x → 0 and x → 1), the sorption
capacity must increase to match that of the pure component. Such a
phenomenon may conceivably give rise to an abrupt increase in the
slopes of the isotherm curves.
    Another possible cause for such a behavior may not be due to
the non-ideality of the system but may be rooted in the nature of
the experimental technique and the method of data analysis. The
binary sorption equilibria (total amount adsorbed and the
composition of the adsorbed phase) are not measured directly in the
chromatographic method but are deduced from integration of the
slopes of the isotherms at different gas phase compositions. Such
an integration may give rise to a significant cumulative error
which, in turn, may be responsible for underpredicting the binary

sorption isotherm. The method of data analysis, however, requires the binary sorption isotherm to have the same end value as the pure component isotherm. This forces the isotherm to curve up as is observed for the case of ethane.

Hyun and Danner (16) have noted a similar shortcoming of the chromatographic method for measuring the binary sorption equilibria. They measured binary sorption equilibria for C_2H_6-C_2H_4 mixture using the chromatographic and static methods. The volumetric data for ethylene adsorption showed concave curvature for the entire concentration range but the chromatographically determined isotherm considerably underpredicted the volumetric data upto ethylene mole fraction of 0.8. Thereafter, the slope of the isotherm increased sharply as the isotherm was forced to go through the pure-component value at the ethylene mole fraction of 1.0.

For all the binary mixtures examined in this study, molecular volumes of the components are nearly similar and hence all the binary systems are expected to exhibit ideal behavior. However, the chromatographically derived data show non-ideal behavior for CH_4-C_2H_6 and cyclopropane-propane mixtures. The chromatographic method seems to work for the N_2-O_2 mixture probably because both the components are not adsorbed strongly on the molecular sieve. But for systems where either one or both components are strongly adsorbed, the chromatographic method should be used with caution to measure the binary sorption equilibria.

Conclusions

The chromatographic method has been shown to be useful in measuring pure component sorption isotherms. The single component isotherms of N_2, O_2, CH_4, C_2H_6, C_3H_8 and cyclopropane on Linde 5A have been experimentally measured and they compare well with the data obtained with other methods. The binary sorption equilibria are for the most part reasonable but for CH_4-C_2H_6 and C_3H_8-cyclopropane systems, the measurements show unexpected behavior of the sorption isotherm near the region of high concentration of the more strongly adsorbed component. Such a behavior may be expected for gas mixtures that form non-ideal adsorbed phase solution but not for the binary systems studied here. It is, therefore, concluded that the uncharacteristic shape of the binary sorption isotherm arises from the nature of the method of data analysis employed here. At present, it is not possible to predict a priori for which binary systems the chromatographic method would work and therefore, the binary sorption equilibria measured using this method should be used with caution.

Acknowledgments

Legend of Symbols

A, a, b	coefficients in Equation 4
K_1, K_2	slopes of isotherms for component 1 and 2, molecules per cavity per torr
q_1, q_2	sorbate concentration on zeolites in molecules per cavity
x_1, x_2	mole fractions of components 1 and 2 in gas phase
t, t'	retention times for adsorbing and a nonadsorbing species
v	volume of cavity
ε	bed voidage
β	molecular volume

Literature Cited

1. Ramachandran, P.A.; Smith, J.M. Ind. Eng. Chem. Fundam. 1978, 17, 148-60.
2. Schneider, P; Smith, J.M. AIChE J. 1968, 14, 762-71.
3. Hashimoto, N.; Smith, J.M. Ind. Eng. Chem. Fundam. 1973, 12, 353-59.
4. Hashimoto, N.; Smith, J.M. Ind. Eng. Chem. Fundam. 1974, 13, 115-20.
5. Peterson, D.L.; Helfferich, F. J. Phys. Chem. 1965, 69, 1283- 93.
6. Peterson, D.L.; Helfferich, F.; Carr, R.J. AIChE J. 1966, 12, 903-05.
7. Haydel, J.M.; Kobayashi, R. Ind. Eng. Chem. Fundam. 1967, 6, 546-54.
8. Van der Vlist, E.; Van der Meijden, J. J. Chromatography 1973, 79, 1-13.
9. Ruthven, D.M.; Kumar, R. Ind. Eng. Chem. Fundam. 1980, 19, 27-32.
10. Ruthven, D.M.; Wong, F. Ind. Eng. Chem. Fundam. 1985, 24, 27-32.
11. Ruthven, D.M. AIChE J. 1976, 22, 753-59.
12. Ruthven, D.M. Principles of Adsorption and Adsorption Processes; John Wiley and Sons: New York, 1984; pp112-114.
13. Huang, J.T. M.Sc. Thesis, Worcester Polytechnic Institute, Massachusetts, 1970.
14. Loughlin, K.F. Ph.D. Thesis, University of New Brunswick, New Brunswick, Canada, 1970.
15. Derrah, R.I. Ph.D. Thesis, University of New Brunswick, New Brunswick, Canada, 1973.
16. Hyun, S.H.; Danner, R.P. AIChE Symposium Series, 1982, No. 219, 78, 19-28.
17. Shah, D.B.; Ruthven, D.M. AIChE J. 1977, 23, 804-809.

Chapter 26

Dynamic Adsorption of SO_2 on an Annular Bed of Molecular Sieve 5A

Ephraim Kehat, Joseph Berkovici, and Aluf Orell

Department of Chemical Engineering, Technion-Israel Institute of Technology, Haifa 32000, Israel

The objective of this work was to study the feasibility of dynamic adsorption of SO_2 from nitrogen in an annular packed bed of molecular sieve 5A. The annular bed, 20 mm I.D., 44 mm O.D. and 0.6 m long, was packed with pellets of 1.6 mm O.D. and 3-4 mm long. The parameters tested were: temperature, 100-180°C, pressure, 890-1610 mm Hg, flow rate, 5-10 liters/min, and SO_2 concentration of 1% and 4%. The maximal amount of SO_2 adsorbed under dynamic conditions was found to increase by increasing the SO_2 concentration and operating pressure and decreasing the temperature and flow rate. The efficiency of the dynamic adsorption ranged from 5% to 40% within the investigated test conditions. The Kehat-Abrahami model showed better agreement with the experimental results than the spherical diffusion model.

An annular packed bed of an adsorbent has the advantage of low resistance to flow during the desorption stage of a pressure swing cycle. However, the adsorption stage breakthrough times are much shorter than those of a conventional tubular packed bed. The objective of this work was to study the feasibility and characteristics of dynamic adsorption of SO_2 on an annular bed of molecular sieve 5A. In an earlier study (1) it was shown that the rate of desorption in an annular bed of molecular sieves is comparable to that of a single particle. This indicates that there is a considerable advantage of an annular bed over the traditional tubular packed bed, at least in the desorption stage.

The use of an annular bed, however, has two disadvantages. The mass transfer zone concept, suggested by Michaels (2), indicates that due to a short flow path, breakthrough of the adsorbed species is expected to occur shortly after the start of the adsorption stage. In addition, the concentric tube structure containing the annular bed is more complex than that of a tubular bed and reduces the effective bed volume due to the existence of an empty core.

In view of the above limitations the potential use of an
annular bed for adsorption was initially assessed by conducting
preliminary experiments in a small unit at room temperature and
determining the breakthrough time. The obtained results demonstrated
that breakthrough did not take place immediately and were thus
encouraging.

The choice of SO_2 as the adsorbed component was made in view of
the successful operation of a commercial unit for separating SO_2
from the tail gas of a sulfuric acid unit using Zeolon molecular
sieve (3). In this work, however, use was made of molecular sieve
5A, which unlike Zeolon is not acid-resistant, due to the existence
of fairly accurate equilibrium adsorption data (4) for SO_2
adsorption on this specific adsorbent. It should be noted that
additional equilibrium adsorption data for SO_2 on a variety of
natural and commercial molecular sieves are available (5-12).
However, the agreement between the different sets of data is not
satisfactory. Nitrogen was used as a carrier gas for SO_2 since its
adsorption rate on molecular sieve 5A is by far smaller than that of
SO_2 in the temperature range studied in this work.

Experimental

A schematic description of the experimental system is shown in
Figure 1. The annular bed was formed by two concentric Poral type
porous stainless steel tubes 0.60 meters long. The external tube
O.D. was 50 mm with a wall thickness of 3 mm and limiting pore size
of 35 microns. The internal tube O.D. was 20 mm with a wall
thickness of 1 mm and limiting pore size of 20 microns. The
concentric tubes were housed in a stainless steel tube of 75 mm O.D.
The adsorption unit was immersed in an oil circulation thermostat,
150 mm O.D. and 1.5 meters long. The oil could be heated up to 350°C.
and its temperature was controlled within 2°C. Oil and selected bed
temperatures were measured by Copper-Constantan thermocouples.

The metered feed stream was first preheated by passing it
through two coils immersed in the oil bath. It was then introduced
into the outer annular space of the adsorption unit housing, that
was closed on all sides, through two feed tubes 50 cm long and
4.8 mm in diameter. The tubes were equipped with a large number of
holes to ensure a uniform feed distribution to the bed. Adsorption
took place along a radial flow path of 12 mm in length. The effluent
gas was withdrawn from the adsorption unit through the inner 20 mm
O.D. tube.

The adsorbent was Linde Molecular Sieve 5A pellets 1.6 mm in
diameter and 3-4 mm long. The dry weight of the molecular sieves was
508.7 grams. The feed was composed of mixtures of SO_2 in nitrogen of
specified concentrations that were prepared in advance and stored in
pressure cylinders. The SO_2 concentration in the effluent was
measured continuously by a thermal conductivity cell that was
recalibrated after every few runs. The estimated accuracy of the
measured SO_2 concentration was within 1.5%. The SO_2 material balance
was checked for many runs by absorbing the SO_2 from the effluent gas
in an NaOH solution. The agreement was better than 5% in all cases.
The accuracy of the pressure measurement at the outlet of the bed was
within 15 mm Hg and that of the temperature in the bed was within
0.25°C. The reproducibility of duplicate runs was better than 5%.
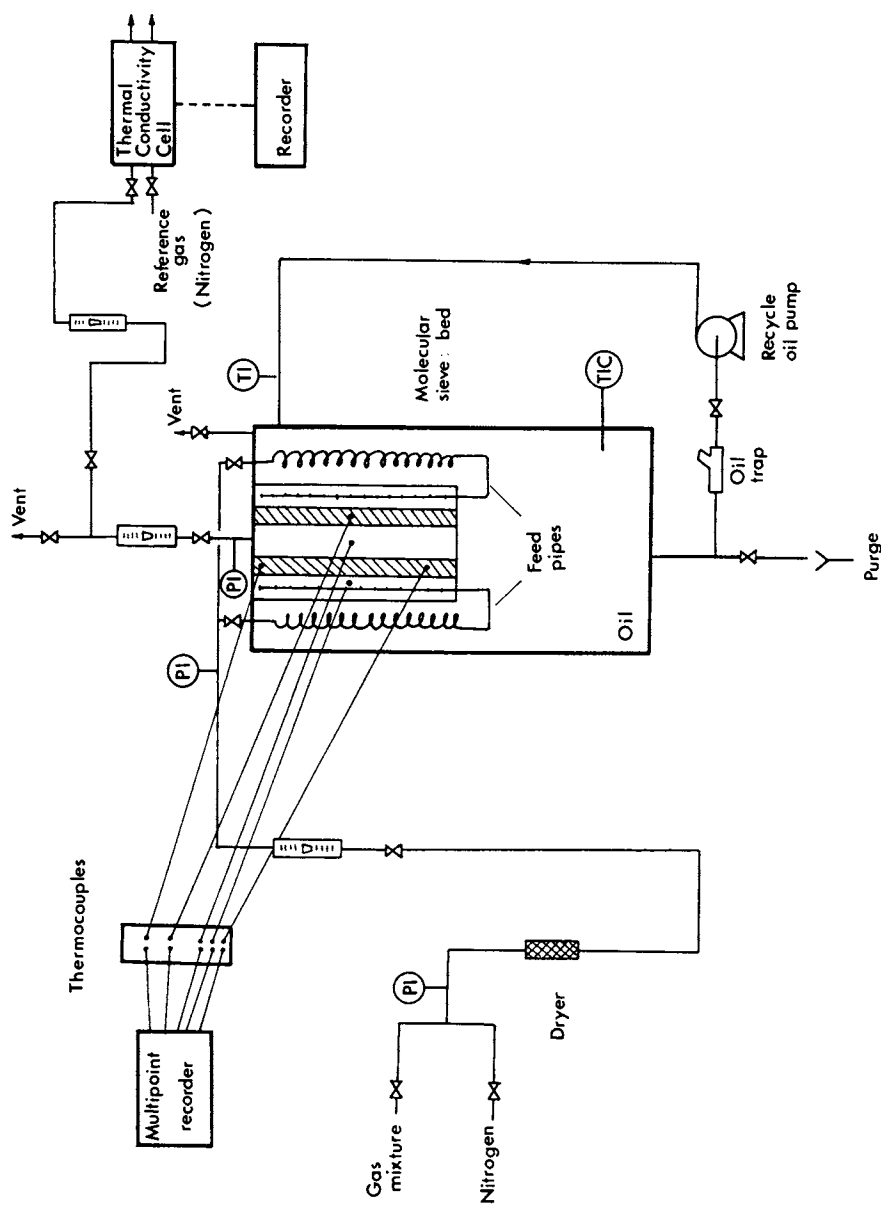
Figure 1. Experimental apparatus.

The experimental procedure was to bring the bed to the desired temperature under dry nitrogen flow. After attaining a constant bed temperature the nitrogen flow was cut off. A feed gas of a predetermined composition was then introduced into the bed at the desired flow rate and outlet pressure. The SO_2 concentration in the effluent was monitored continuously. The run was terminated after the effluent concentration had reached the feed concentration and was maintained at that level for a few minutes.

In several runs the adsorption stage was followed by a desorption stage, using dry nitrogen, that was carried out at the adsorption operating conditions. Typical normalized concentration vs. time curves for both adsorption and desorption are shown in Figure 2.

At the end of each run the bed was heated to 320°C for several hours under dry nitrogen flow and then put under vacuum for a few hours. Finally, the heating was stopped and the bed was placed under dry nitrogen flow.

Results

Experimental runs were performed at two feed concentration levels: 1% by volume SO_2 in nitrogen at 100, 140 and 180°C, and 4% SO_2 in nitrogen at 140°C. The additional tested parameters were: feed gas flow rate, in the range of 5 to 10 liters per minute, and outlet pressure ranging from 890 to 1610 mm Hg. The SO_2 breakthrough time was defined as the time at which the effluent concentration level reached 5% of the feed concentration. The dynamic equilibrium time was defined as the time at which the effluent concentration reached 95% of the feed concentration.

It should be noted that in this study the term dynamic equilibrium applies to the situation where two components are adsorbed simultaneously on an adsorbent in a flow system. Consequently, the pore volume of the molecular sieves is occupied by both nitrogen, the less strongly adsorbed species, and SO_2. The dynamic equilibrium is consequently characterized by adsorption and desorption of molecules of both species at different rates. In contrast, static equilibrium applies to adsorption of a pure gas in a non-flowing system and is attained when the adsorption and desorption rates of the single component are equal.

The dynamic adsorption capacity of the annular bed was calculated by integrating the concentration vs. time curves up to a point close to the dynamic equilibrium time. Typical results of the dynamic adsorption capacity as a function of the SO_2 inlet partial pressure, the feed flow rate and the feed concentration are shown in Figures 3 to 5. The effect of temperature on the dynamic adsorption capacity is shown in Figure 6 where the higher temperature data were taken from reference (5).

The fractional approach to the dynamic equilibrium concentration was defined as the SO_2 concentration at a given time divided by the concentration at dynamic equilibrium. Representative results of the time dependence of the normalized SO_2 concentration are shown in Figures 7 and 8.

The efficiency of the dynamic adsorption process was defined as the ratio of the dynamic adsorption capacity to the static
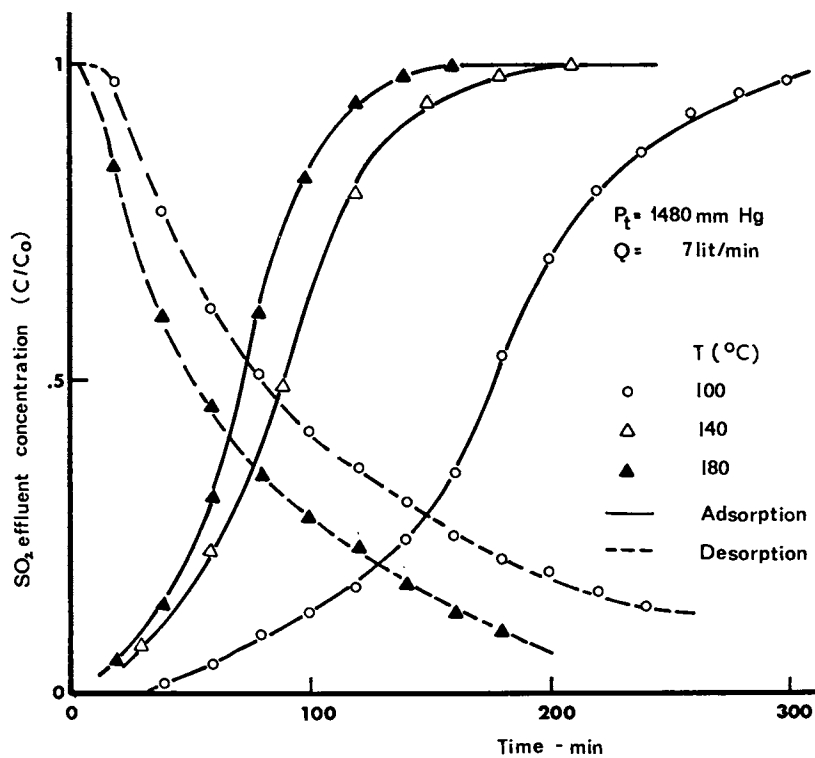
Figure 2.   Typical concentration vs. time curves.
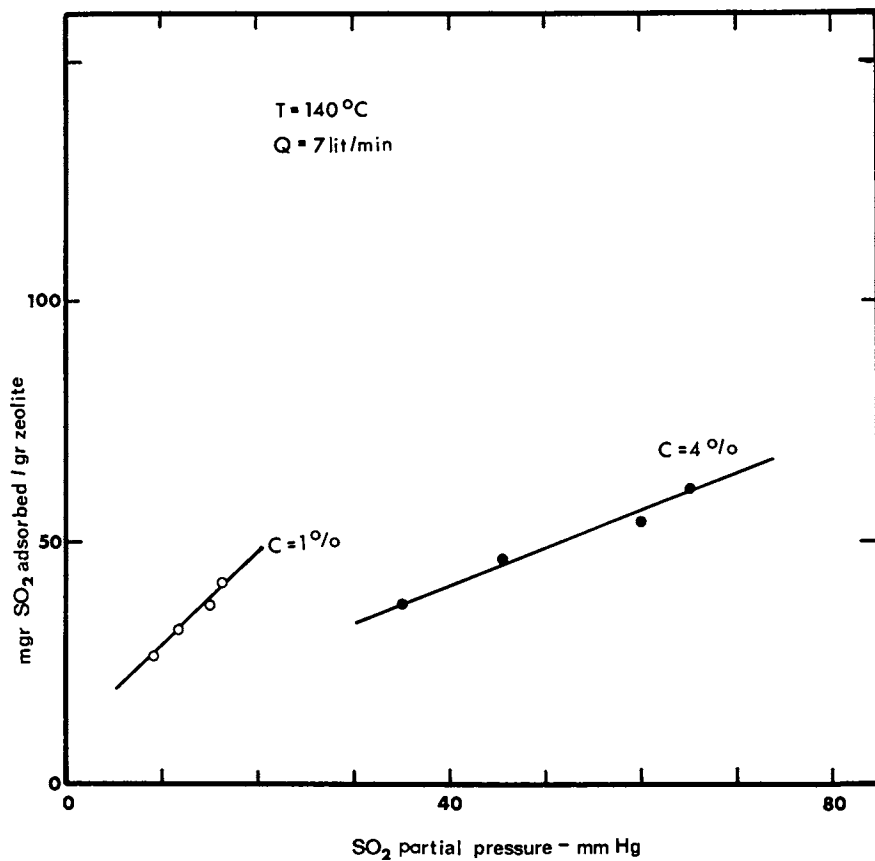
Figure 3. The effect of SO$_2$ concentration on the dynamic adsorption capacity

T≈100°C

Q =5lit/min
7
10

mgr SO₂ adsorbed / gr zeolite

SO₂ Partial pressure ⁻ mm Hg
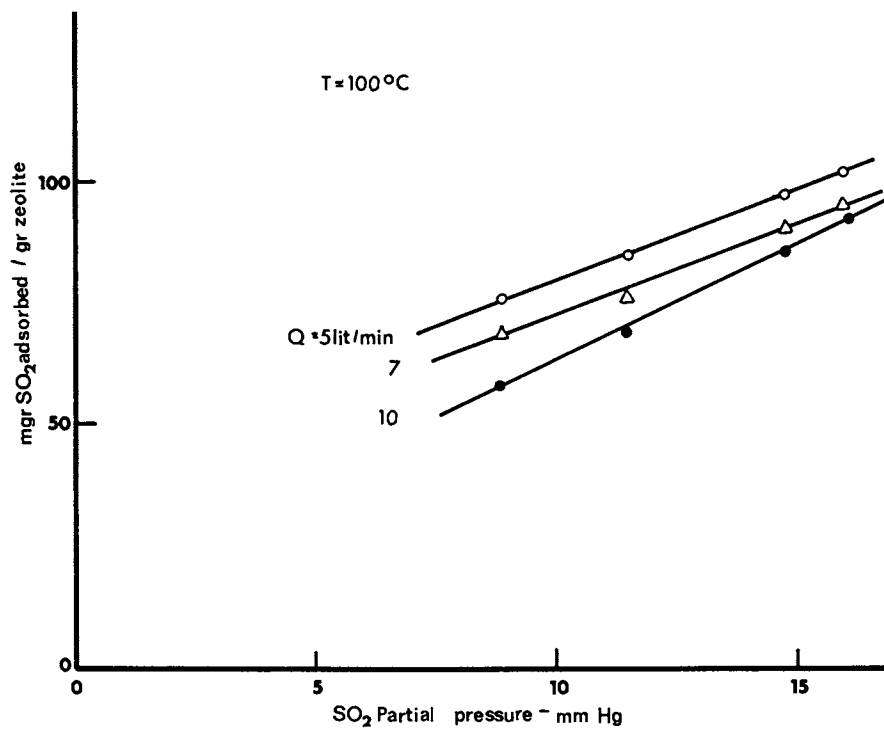
Figure 4. The effect of SO₂ partial pressure on the dynamic
adsorption capacity.
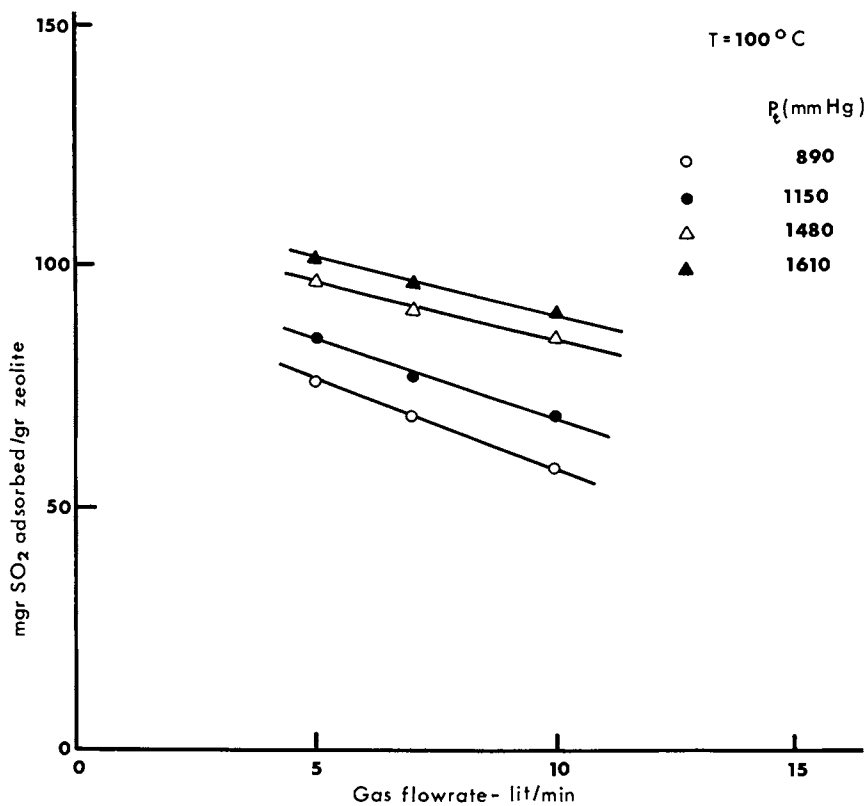
Figure 5.   The effect of feed flow rate on the dynamic
            adsorption capacity.
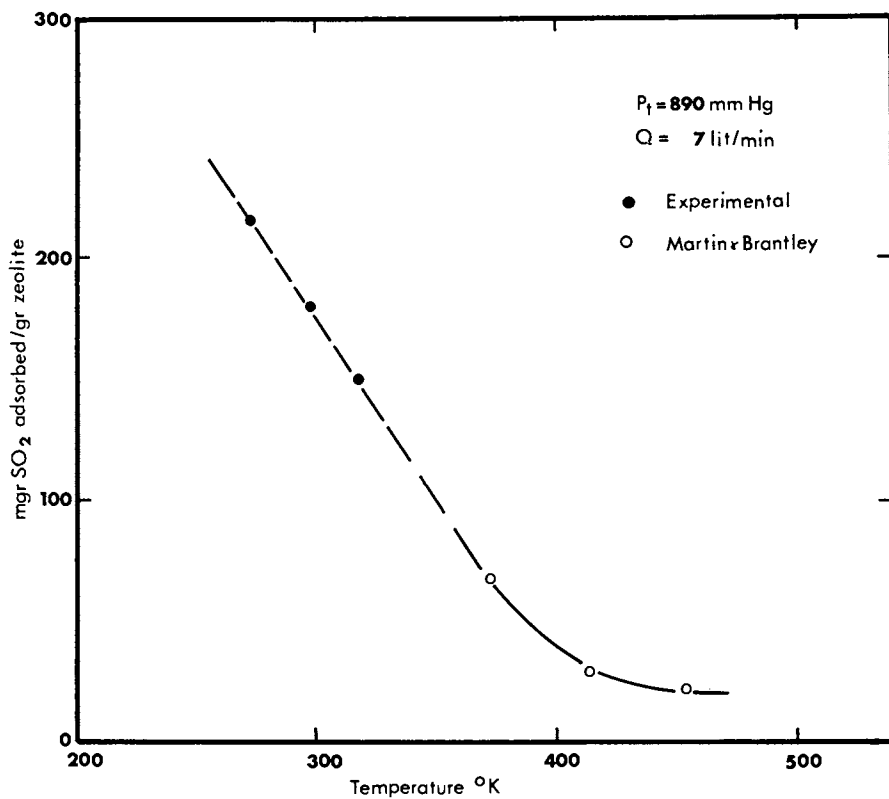
Figure 6. The effect of temperature on the dynamic adsorption capacity.
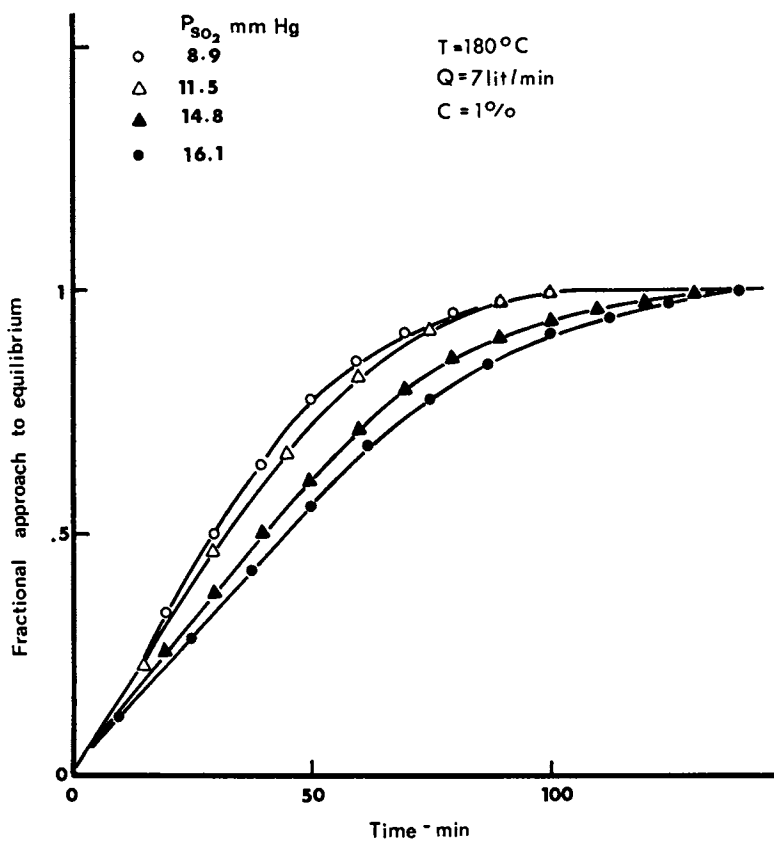
Figure 7.   The effect of SO_2 partial pressure on the rate of adsorption.

T $=$ 140 °C

P$_t$ $=$ 1410 mm Hg

Q   lit/min

○   10

●   7

▽   5
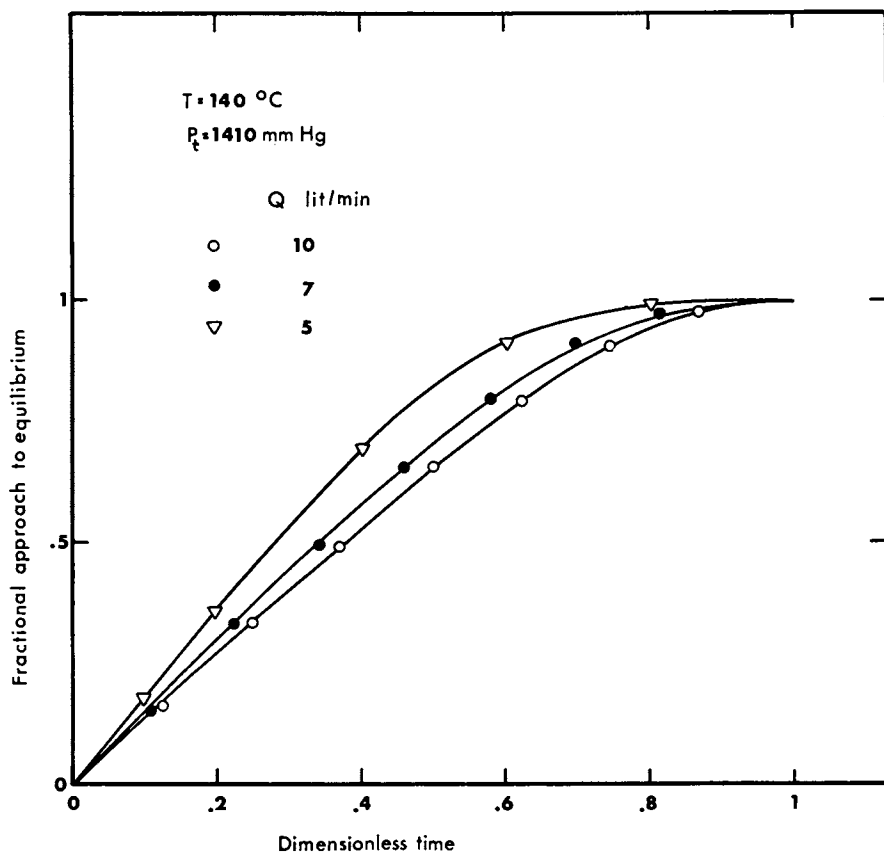
Figure 8.   The effect of flow rate on the rate of adsorption.

adsorption capacity at the same SO_2 partial pressure and temperature. The data of the static adsorption capacity were taken from Abrahami (4). Representative results are shown in Table I and the effect of the partial pressure of SO_2 in the feed on the efficiency is shown in Figure 9.

Table I. Dynamic Adsorption Efficiency

Temperature,°C	Efficiency of Dynamic Adsorption, %			
	Total Pressure, mm Hg			
	890	1150	1480	1610
100	19.4	13.5	11.9	9.4
140	40.8	27.7	19.5	16.9
180	19.2	12.0	8.1	5.5

Discussion of Results

The dynamic adsorption capacity of the bed ranged from 23.2 mg SO_2 per gram of adsorbent, at 890 mm Hg, 180°C and 7 liters/minute, to 101.6 mg SO_2 per gram of adsorbent, at 1610 mm Hg, 100°C and 5 liters per minute. It increased with the SO_2 feed concentration, or partial pressure, and decreasing flow rate, as can be seen in Figures 3 to 5. The dynamic adsorption capacity decreased markedly with increasing temperature as can be seen in Figure 6.
     Figure 7 shows that the rate of adsorption, expressed as the time dependence of the fractional approach to equilibrium, decreased with increased partial pressure of SO_2, which is rather unexpected. A possible explanation is that in these runs the SO_2 concentration in the feed gas was 1% and its partial pressure was a linear function of the total pressure of the feed. Consequently, the decrease of the rate of adsorption is a net result of two opposing effects. Higher pressures, on one hand, increase the number of collisions between gas molecules and the external surface of the adsorbent, and on the other hand decrease the flexibility of the orientation of the gas molecules in the direction that will allow them to enter the adsorbent pores. The last effect is apparently dominant and offsets the gain in adsorption rate due to higher collision frequency.
     The rate of adsorption also decreased with increasing the feed flow rate, as is shown in Figure 8. As the flow rate is increased the residence time of the SO_2 molecules at the adsorbent surface decreases. Consequently, this effect is analogous to the one of increasing the gas total pressure.
     The temperature effect on the dynamic adsorbent capacity is shown in Figure 6. Although the rate of adsorption increases with temperature the total amount adsorbed decreases, as it does in the case of static equilibrium. Possibly, the higher effective volume of molecules at higher temperatures decreases the number of molecules that can be accommodated per unit volume of the adsorbent.
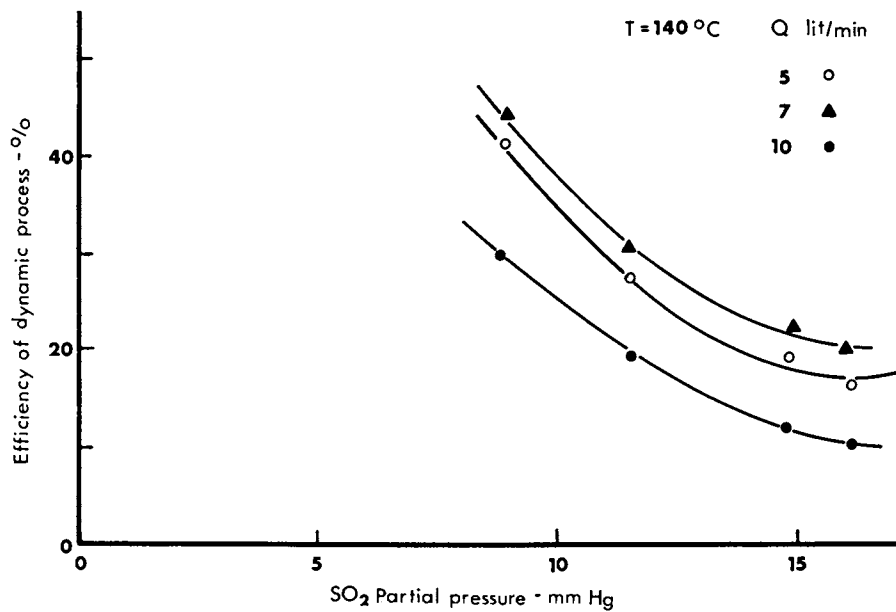
Figure 9. The effect of SO$_2$ partial pressure on the efficiency of dynamic adsorption.

The efficiency of dynamic adsorption at constant temperature decreased with increasing the SO_2 partial pressure, as shown in Figure 9. Within the flow rate range of 5-10 liters/min the adsorption efficiency at a given partial pressure was found first to increase with the flow rate and then to decrease.

The effect of temperature on the efficiency of dynamic adsorption at constant total pressure is illustrated in Table I. As can be seen, the efficiency reaches a maximum value at 140°C at each level of the total pressure. This result may be attributed to two opposing effects. Increasing the temperature increases the adsorption rate but decreases the dynamic adsorption capacity. At high temperatures the second effect becomes more dominant resulting in lower efficiencies.

The ratio of the flow path length to a single pellet size in this work is rather small, of the order of 8:1. Consequently, the annular bed characteristics are closer to those of a single pellet. This is manifested in the rather low values of the efficiency of the dynamic adsorption, as defined in this work. If this efficiency had been defined at the breakthrough conditions its values would have been approximately one half of the reported efficiency values. Consequently, the results of this study should not be applied directly to thicker annular beds, that have yet to be investigated. It is expected, however, that thicker annular beds would yield higher dynamic adsorption efficiencies. This would merit considering their use as an adsorption-desorption pressure swing system, at a cost of small loss of efficiency in the desorption stage of the cycle.

Theoretical Models

The experimental data were used to test the following two theoretical models.

Spherical Diffusion Model. This simple model assumes that diffusion occurs within a spherical particle. The model, however, cannot yield the diffusion coefficient directly since it contains a dimensional length parameter whose numerical value depends on the assumed diffusion mechanism. If intradiffusion predominates, the characteristic length parameter is assumed to be the size of a single crystal of the adsorbent. Consequently, the resulting diffusion coefficients are very small. If interdiffusion predominates, the characteristic length parameter is assumed to be the adsorbent particle diameter. The diffusion coefficient values in this case are much higher than the former ones.

As shown in Figure 10 the spherical diffusion model does not fit the experimental results except at the last stage of the adsorption process where the adsorption rate is rather low.

Consequently, diffusion coefficients were calculated for all runs assuming that intraparticle diffusion predominates and that the characteristic length value is 2 microns. Typical values of the diffusion coefficients as a function of the SO_2 partial pressures are shown in Figure 11. The order of magnitude of the diffusion coefficients, -10 to -12, is within the usual range of intraparticle diffusion coefficients in molecular sieves. The diffusion coefficient decreased both with the flow rate and temperature (not

T = 140 °C

P$_t$ = 1650 mm Hg

Q = 10 lit/min

—— Calculated

▽ Experimental

$(\frac{D\ t}{r^2})$ Dimensionless time parameter

Fractional approach to equilibrium
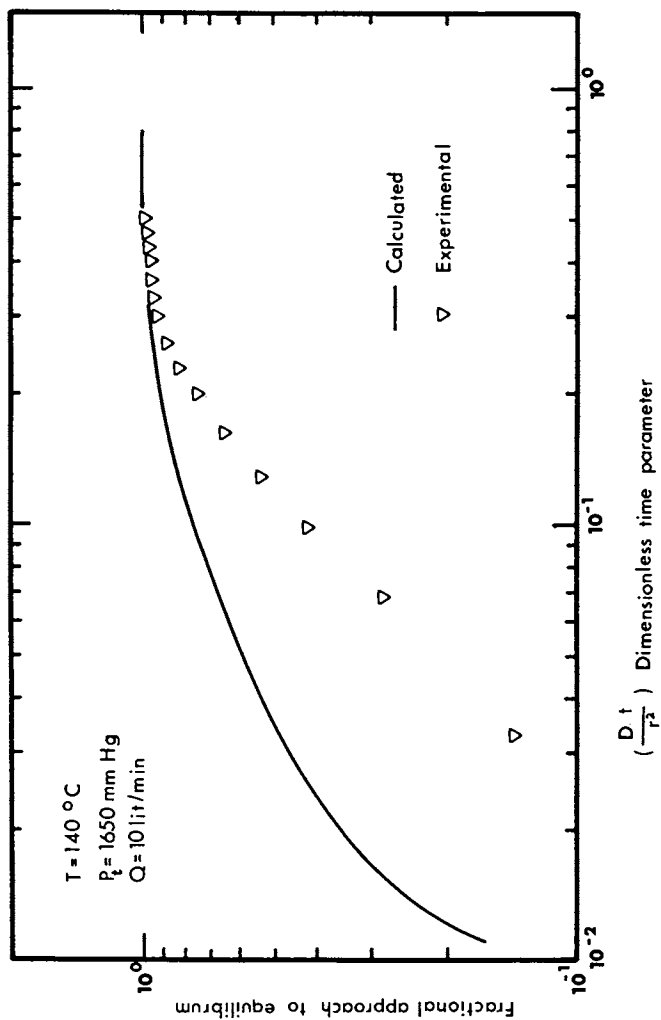
Figure 10. Test of the Spherical diffusion model.
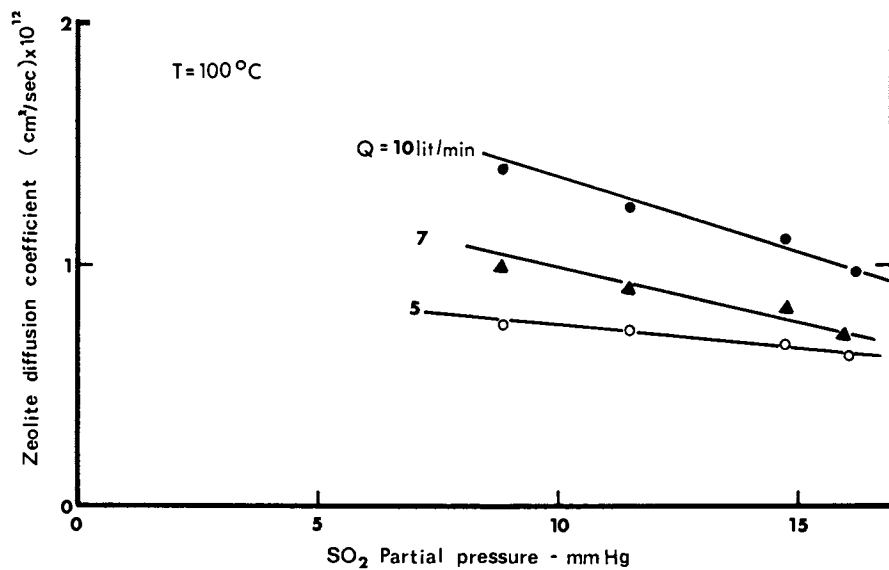
Figure 11. The effect of SO$_2$ partial pressure on diffusion
          coefficients.

T = 140 °C
P$_t$ = 890 mm Hg
K = 6$_x$10^{16}
η = 0.005
C = 3 $\times$ 10^{-7}

Dimensionless time

Fractional approach to equilibrium
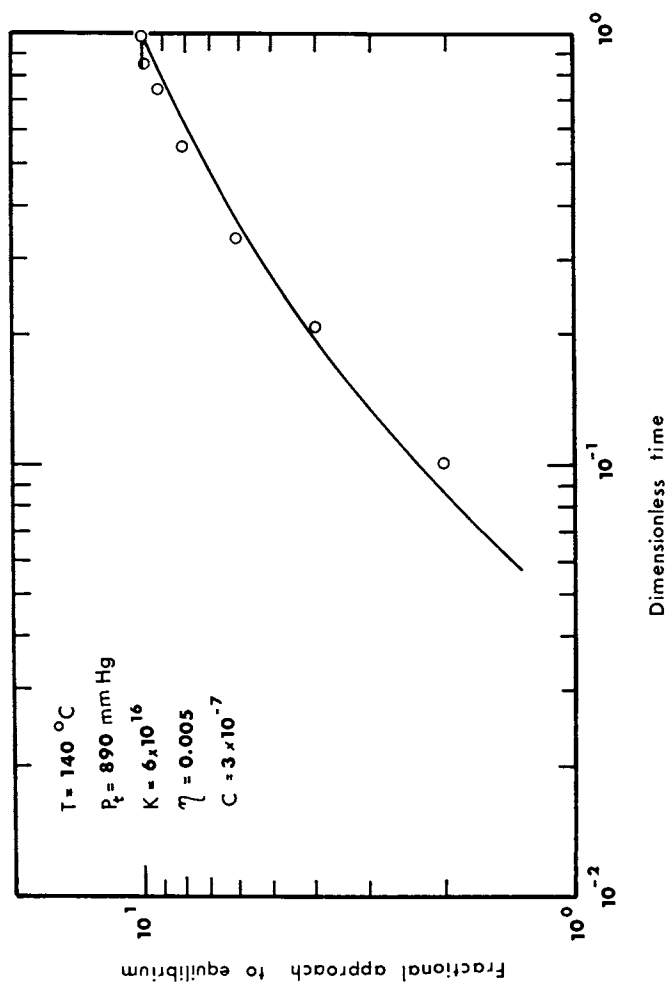
Figure 12. Test of the Kehat–Abrahami model.

shown here). These two trends are expected and seem reasonable. However, the diffusion coefficient was found to decrease with increasing SO_2 partial pressure, or effectively SO_2 concentration. This effect is even more pronounced at higher temperatures and flow rates and does not concur with the accepted diffusion model.

Arrhenius plots of the diffusion coefficient yielded values of activation energies in the range of 8–10 kcal/grmole that are of the same order of magnitude as the heat of adsorption on molecular sieves. The activation energy was found to increase slightly with increasing SO_2 partial pressure.

No attempt was made in this study to test the bidisperse diffusion model.

Kehat-Abrahami Model (4). This model assumes that the adsorbent pellet is composed of spherical concentric layers and that movement of molecules can take place only in the radial direction. The center of the pellet, however, is considered to be impervious to molecules. Since the pore apertures are of about the same size as the molecules, the driving force for movement of molecules between adjacent layers is proportional to the number of filled pores in a given layer and to the fraction of unfilled pores in the adjacent layers. Only molecules that have adequate energy can move to an adjacent layer. At the outer surface of the adsorbent pellet the number of molecules entering the surface layer is a function of the rate of collision of molecules with the surface and the probability that a molecule will be oriented so that if it collides with an external pore aperture it will pass through it.

The model uses three parameters that have to be fitted to the data: K – a concentration distribution coefficient between the outermost layer and the first inner layer, C – the preexponential constant in an Arrhenius-type rate equation, and η – the efficiency of collisions with the external surface. The model contains additional parameters that can be determined from the characteristics of the adsorbent pellet and the operating conditions.

The parameters of the model could be fitted to yield good agreement with the experimental data. A representative result is shown in Figure 12 for one run. Within the studied range of the operating parameters the values of the three fitted parameters were found to be insensitive to the SO_2 partial pressure, an advantage over the diffusion model. The parameter K was found to increase with temperature. Such an effect is typical of distribution coefficients. The parameters C and η were found to be insensitive to the operating parameters. This is quite reasonable for C. η, however, is expected to be slightly temperature dependent.

In conclusion, the good agreement between the model and the experimental results is based on a rather narrow range of operating parameters studied here. The test of the general validity of the model must await further experimental data.

Literature Cited

1. Kehat, E.; Heinemann, M. I&EC Proc. Design and Develop., 1970, 9, 72–78.
2. Michaels, A.S. Ind. Eng. Chem., 1952, 44, 1922–1930.

3. Kiovski, J.R.; Koradia, P.B. <u>Chem. Eng. Progress</u>, 1976, <u>72</u>(8), 98–103.
4. Abrahami, S. Ph.D. Thesis, Technion, Haifa, 1973.
5. Martin, D.A.; Brantly, F.E. Bureau of Mines Report 6321, (1963).
6. Tamboli, J.K.; Sand, L.B. <u>Proc. 2nd Clear Air Congress</u>, 1970, p.861.
7. Joubert, J.I.; Zwiebel, I. <u>Advances in Chemistry Series</u> No.102, 1971, p.209.
8. Gupta, J.C.; Ma, Y.H.; Sand, L.B. <u>AIChE Symp. Series</u> No. 117, 1971, <u>67</u>, p.51.
9. Ma, Y.H.; Mancel, C. <u>AIChE J.</u>, 1972, <u>18</u>, 1148–1153.
10. Ma, Y.H.; Roux, A.J. <u>AIChE J.</u>, 1973, <u>19</u>, 1055–1059.
11. Roux, A.J.; Huang, A.A.; Ma, Y.H.; Zwiebel, I. <u>AIChE Symp. Series</u> No. 134, 1973, <u>69</u>, p.46.
12. Debrun, D.; Francois, M.; Grillet, Y.; Guerin, H.C.R. <u>Compt. Rendu Acad. Sci. Paris</u>, 1973, <u>276 Ser C.</u>, 971.

Chapter 27

Temperature-Programmed Desorption of Hydrocarbons from ZSM-5, ZSM-11, and Theta-1

n-Hexane from Different Cation Forms

Chen Li-feng[1] and Lovat V. C. Rees

Physical Chemistry Laboratories, Imperial College of Science and Technology, London SW7 2AY, England

The temperature programmed desorption (t.p.d) of n-hexane
from the sodium and hydrogen forms of ZSM-5, ZSM-11 and
THETA-1 have been studied. The t.p.d profiles have been
analysed by a newly developed method. From these analyses
peak temperatures, peak widths, maximum rates of desorption
and activation energies of desorption as a function of
coverage have been obtained. The saturation capacities of
these high silica zeolites for n-hexane have also been
determined. The effect of change of cation on all of these
quantities is demonstrated.

In Part I([1]) the temperature programmed desorption (tpd) of n-hexane
and n-octane from the (Na, H) forms for ZSM-5, ZSM-11 and Theta-1
was reported. In Part II([2]) the tpd of p-xylene and benzene from the
same zeolite samples was presented. In the latter study the
desorption of p-xylene from ZSM-5 and ZSM-11 zeolites of varying
Si/Al ratio was also included. In the present study the effect of
different cations in the channels and intersections of ZSM-5, ZSM-11
and Theta-1 on the desorption of n-hexane is reported.

Experimental

The (NaH)- Theta-1 used previously([1,2]) with a unit cell (u.c)
composition of $H_{0.45}$ $Na_{2.46}$ $Al_{2.91}$ $Si_{93.09}$ O_{192} was converted by

ion exchange into its sodium and hydrogen forms. The u.c.
compositions of these forms were $Na_{2.91}$ $Al_{2.91}$ $Si_{93.09}$ O_{192} and

$Na_{0.09}$ $H_{2.82}$ $Al_{2.91}$ $Si_{93.09}$ O_{192} respectively. The pure sodium forms

NOTE: This chapter is part 3 in a series.

[1]Current address: Nanchang Institute of Aeronautical Technology, No. 2 Shanghai Road, Nanchang Jiangxi, China

of the (NaH)- forms of ZSM-5 and ZSM-11 used in Parts I([1])
and II([2]) were also prepared by ion exchange. The u.c.
compositions of the starting materials were $H_{4.48}$ $Na_{1.52}$ Al_6 Si_{90}
O_{192} and $H_{4.36}$ $Na_{1.64}$ Al_6 Si_{90} O_{192} respectively. After exchange
both of these samples had the same u.c. composition of Na_6 Al_6
Si_{90} O_{192}; i.e. both ZSM-5 and ZSM-11 samples have the same Si/Al
ratio of 15. To prepare the pure sodium form 0.1M NaCl solution
at pH ∼10 was used while the hydrogen form was prepared using
0.1M NH_4Cl solution at pH 5∼6. In both exchanges the zeolite
phase was contacted with excess solution phase with continuous
stirring for 48 hours at room temperature. The hydrogen form was
formed by calcination of the ammonium exchanged samples at 500°C
for 1 hour.
     The crystallinity of the starting materials and the ion
exchanged forms was determined in all cases by x-ray diffraction.
All samples gave good diffraction patterns indicating high
crystallinity.
     The tpd profiles were determined using a Stanton-Redcroft TG
762 thermogravimetric balance with on-line Commodore CBM computer
for data collation and analyses.([3,4]) The profiles were analysed
using the single heating rate, variable coverage (SHR) method.([4])
     In this method first-order desorption kinetics, the
Arrhenius equation and a linear sample heating rate are combined
to give

$$-d\theta/\theta = (A/\beta)\ exp\ (-E/RT)\ dT \qquad\qquad (1)$$

where θ is the degree of coverage, A is the pre-exponential
factor and E the activation energy of desorption from the
Arrhenius equation and β is the heating rate. Equation (1) was
integrated between the limits (θ_o, T_o) and (θ_i, T_i) which
represent the starting conditions and those after some time t
respectively to give

$$\int_{\theta_o}^{\theta i} -\frac{d\theta}{\theta} = \frac{A}{\beta} \int_{T_o}^{T_i} exp\ (-E/RT)\ dT \qquad\qquad (2)$$

However, the temperature integral in equation 2 has no exact
analytical solution. In the SHR method of analysis([4]) a new
variable u = E/RT is introduced and on integration the right hand
side (RHS) of equation 2 becomes

$$RHS = \frac{AE}{\beta R} \left[p(x) - p(x_o) \right]$$

where $p(x) = \dfrac{\exp(-x)}{x} + \displaystyle\int_x^\infty \dfrac{\exp(-u)}{u}\,du$ (3)

On integration equation (2) can now be written as:

$$-\ln \theta_i = \frac{AE}{\beta R}\left[p(E/RT_i)-p(E/RT_o)\right]$$ (4)

Equation (4) was fitted to the experimental data through the relationship

$$Q = \overline{\sum_i}\left[\ln \theta_i + \frac{AE}{\beta R}\{p(E/RT_i) - p(E/RT_o)\}\right]^2$$ (5)

In equation (5) variable θ_i changes as T_i changes and A and E are independent variables. To obtain the best fit two conditions involving the partial derivatives of the summation with respect to the two independent variables have to be satisfied, i.e. $\partial Q/\partial A$ = 0 and $\partial Q/\partial E$ = o. A reiterative programme is used to obtain the optimum values of A and E over limited areas of θ from θ = 0 to 1. From the analysis peak temperatures, peak widths, maximum rates of desorption and activation energies, Ed, as a function of coverage were obtained in the same manner as before.(1,2)

A heating rate of 10Kmin^{-1} was used in all tpd runs. The n-hexane vapour, at a relative pressure of p/po ∾ 0.5, was flowed over the zeolite sample, in situ in the TG balance at room temperature using argon as the carrier gas until sorption equilibrium was attained.

Results and Discussion

The saturation capacities of the Na-, (Na/H)- and H- forms of Theta-1 for n-hexane are listed in Table I. From the saturation capacity of H-Theta-1 the micropore volume, w_o, is calculated to be 0.084cm^{3}g^{-1}, a value close to that reported previously(5) for the volume of the one-dimensional channel network of Theta-1 of 0.089cm^{3}g^{-1}. Table I clearly shows that the introduction of ∾ 2.8Na$^+$ ions per u.c. into the H-form decreases the saturation capacity for n-hexane from 3.66 to 2.30 molecules per u.c. (m/u.c.). This decrease is much greater than the volume of the Na$^+$ ions introduced, suggesting that the steric hindrance of the Na$^+$ ions in the one-dimensional channel system is large. Since there are no intersections in the channel system which would allow n-hexane molecules to by-pass Na$^+$ barriers, n-hexane molecules must diffuse over these barriers to be sorbed up

TABLE I: Saturation Capacities and $\bar{E}_{\underline{d}}$ Values Obtained by SHR

Method of Analysis. β = 10 K.min^{-1}

	n-hexane		
	Na Theta-1	(Na.H) Theta-1	H Theta-1
amount adsorbed (m/u.c)[+]	2.30	2.72	3.66
average activation energy, $\bar{E}_d$ [*] (kJ.mol^{-1})	80	74	69

[*] the activation energy averaged over the whole coverage range

[+] molecules per u.c.

to the 2.30 m/u.c limit. The large decrease in the saturation
capacity of the Na- form over that of the H- form must,
therefore, be the result of inefficient packing of the n-hexane
molecules in the channel system. It would seem that n-hexane
molecules are excluded from channel segments between adjacent Na^{+}
ions if these Na^{+} ions are closer than 1.03nm apart, the length
of a n-hexane molecule. This interpretation of the packing of n-
hexane is supported by the large decrease of 0.42 m/u.c of n-
hexane resulting from the introduction of an additional 0.46Na[+]
per u.c. into the (Na/H)- form (the difference in saturation
capacities of the (Na/H)- and Na- forms of Theta-1). The
additional 0.46 Na^{+} per u.c. would significantly increase the
number of such channel segments.

The tpd profiles of n-hexane desorbing from the Na-Theta-1
and H-Theta-1 are shown in Figures 1 and 2 respectively. The
values of the peak temperature, peak width and maximum rate of
desorption obtained from these tpd profiles are listed in Table 2,
which also lists the corresponding values found in Part I([1])
for the (Na,H)- form of Theta-1 for comparison.

Table II demonstrates the increase in peak temperatures and
widths and the decrease in desorption rate caused by the
introduction of Na^{+} ions into the channel system of Theta-1.
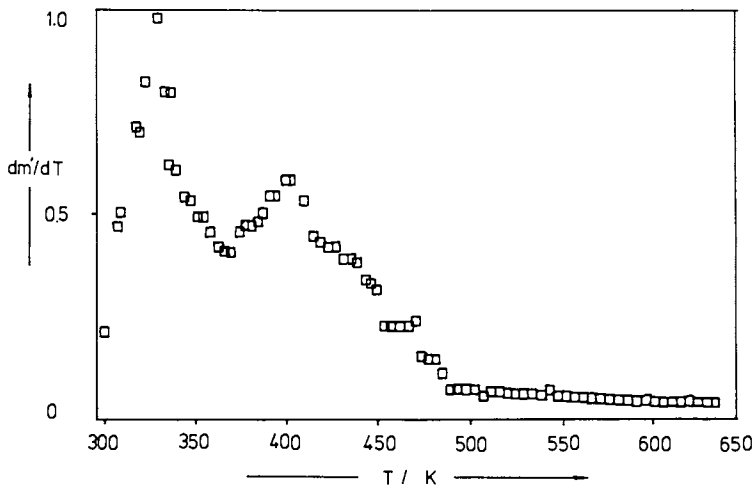
Figure 1. Temperature programmed desorption of n-hexane from Na-
Theta-1. β = 10Kmin^{-1} m' = mass of sample and sorbate.
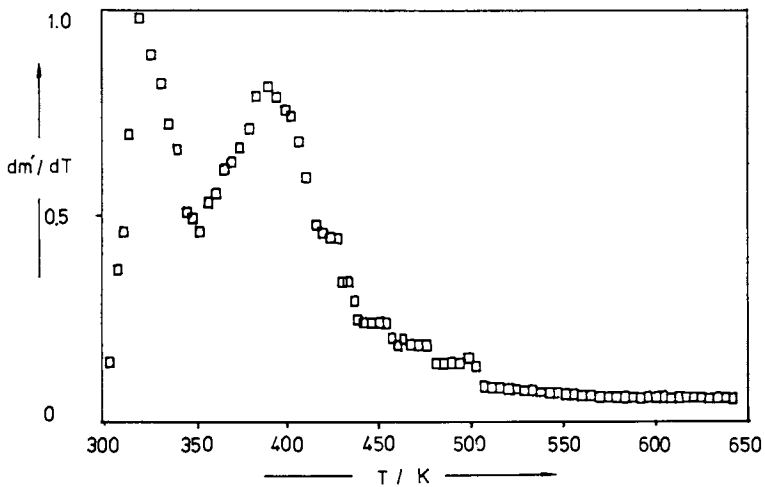
Figure 2. Temperature programmed desorption of n-hexane from H-
Theta-1 β = 10Kmin^{-1}

TABLE II: Peak Temperatures and Widths and Maximum Rates of

Desorption of n-hexane from Theta-1.   β = 10 K.min^{-1}

		Na-Theta-1	(NaH)-Theta-1	H-Theta-1
peak temperature (K)	peak I	330	320	315
	peak II	405	395	390
larger peak		peak I	peak I	peak I
maximum rate (mg.s^{-1})		1.323E-03	1.662E-03	2.186E-03
peak width (K)	peak I	300~370	300~350	300~350
	peak II	370~450	350~410	350~410

From the results in Table II (as proposed previously([6,7]))
the activation energies of desorption, Ed, should follow the
order Na-Theta-1 > (Na/H)-Theta-1 > H-Theta-1. The activation
energies obtained by the SHR method([4]) for these three samples as
a function of coverage are shown in Figure 3 and the activation
energies averaged over the whole coverage range, $\bar{E}_d$, are given in
Table I.   These average energies do follow the above predicted
order but Figure 3 shows that the desorption energies of the last
1.5m/u$_+$c. to be desorbed are very similar in all three samples.
The Na$^+$ ions should introduce an additional electrostatic
interaction with the n-hexane molecules which should increase the
initial heat of adsorption and thus increase, Ed, the activation
energy for desorption of the later molecules to be desorbed.
Since the channel system of Theta-1 is one-dimensional the

electrostatic interaction introduced by the Na$^+$ ions will tend to
be limited to the end CH$_3$ group of the n-hexane molecule. This
additional interaction energy seems to be too small to be
observed by the SHR method of analysis even though the peak
temperatures and widths do show a small effect of the Na$^+$ ions.
Although the Na$^+$ ions must enhance the activation energy for
diffusion of n-hexane molecules in the channel system of Theta-1
the SHR method of analysis assumes that desorption is not
diffusion controlled and thus any increase in Ed with Na$^+$ content
cannot be interpreted as due to an increase in the activation
energy of diffusion. Although the activation energy of diffusion
of n-hexane has not been measured, as yet, as a function of
cation content or type, it is certain that this energy will be
much smaller than the values of $\bar{E}_d$ reported in Table I.

Corresponding studies were carried out on the pure Na- forms
of ZSM-5 and ZSM-11 both samples of which had Si/Al ratios of 15.
The saturation capacities of these samples for n-hexane are given
in Table III, where the values may be compared with the
corresponding saturation capacities for the (Na/H)- forms
obtained previously.([1]) All saturation capacities listed in
Table III are much smaller than the theoretical saturation
capacities of the pure silica forms of these frameworks.
Silicalite-1 has a theoretical channel volume of $0.19 cm^3 g^{-1}$ which
corresponds to 8.42 molecules of n-hexane per u.c. at saturation
indicating that segments of two different n-hexane molecules are
located at each intersection. The theoretical saturation
capacity of silicalite-2 is somewhat greater due to the 30%
greater volume of the straight channel segments which replace the
sinusoidal channel segments of silicalite-1.

TABLE III: Saturation Capacities and $\bar{E}_d$ Values Obtained

by SHR Method. $\beta = 10K.min^{-1}$

	ZSM-5		ZSM-11	
	NaZSM-5	(NaH)ZSM-5	NaZSM-11	(NaH)ZSM-11
amount adsorbed (m/u.c)	6.18	6.80	6.42	6.99
average activation energies; $\bar{E}_d$ * ($kJ.mol^{-1}$)	92	84	91	87

*   the activation energy averaged over the whole coverage range

Table III shows that the introduction of $1.52Na^+$ ions per

u.c. into ZSM-5 and $1.66Na^+$ ions per u.c. into ZSM-11 reduces the
saturation capacity of n-hexane to 6.80 and 6.99 m/u.c

respectively. Like Theta-1, introduction of Na^+ into the channel
network decreases the packing efficiency of n-hexane molecules.

However, on increasing the Na^+ ion concentrations to 6 per u.c.,
the saturation capacities only decrease slightly to 6.18 and
6.42 m/u.c. respectively. Now, unlike the Theta-1 case, these

quite large Na^+ ion concentration increases have little effect on
the n-hexane saturation capacities. Thus, the channel

intersections which are present in both ZSM-5 and ZSM-11 allow
more efficient packing of n-hexane molecules in the presence of

high Na$^+$ ion contents.

The tpd profiles of n-hexane desorbing from Na-ZSM-5 and Na-
ZSM-11 are shown in Figures 4 and 5 respectively. The values of
the peak temperature, peak width and maximum rate of desorption
obtained from these profiles are listed in Table IV. The
corresponding values for the (Na/H)- forms obtained previously([1])
are included for comparison.

TABLE IV: Peak Temperatures and Widths and Maximum Rates of

Desorption of n-hexane from ZSM-5 and ZSM-11. β = 10K.min^{-1}

		ZSM-5		ZSM-11	
		NaZSM-5	(NaH)ZSM-5	NaZSM-11	(NaH)ZSM-11
peak temperature (K)	peak I	350	340	350	340
	peak II	415	405	415	405
larger peak		peak I	peak I	peak I	peak I
maximum rate (mg.s^{-1})		2.312E-3	2.89E-03	2.653E-03	3.234E-03
peak width	peak I	300~380	300~370	300~380	300~370
	peak II	380~460	370~440	380~460	370~440

As found with Theta-1, Table IV clearly shows that

increasing Na$^+$ contents in the channels of ZSM-5 and ZSM-11
increases the peak temperatures and widths and decreases the
rates of desorption.

On analysis of the tpd profiles in Figures 4 and 5 by the
SHR method([4]) the variation of the activation energy of
desorption, E_d, with coverage shown in Figures 6 and 7 for the

ZSM-5 and ZSM-11 samples respectively was obtained. The

activation energy, $\bar{E}_d$, averaged over the whole coverage range for

these ZSM-5 and ZSM-11 samples are listed in Table III. As in
the case of Theta-1 and in agreement with the data in Table IV,
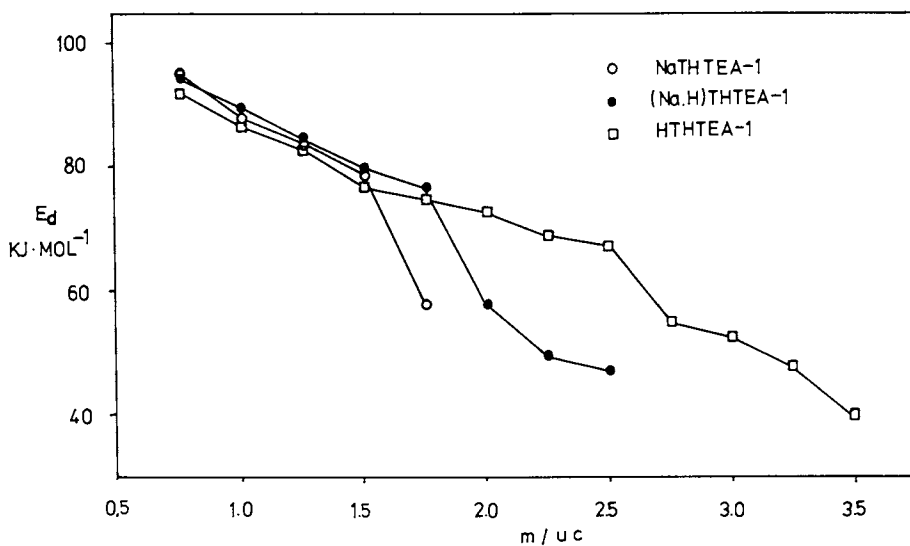
Figure 3. Activation energy of desorption of n-hexane from
O Na-Theta-1; ● (Na,H)-Theta-1; □ H-Theta-1 as a function of
sorbate loading in molecules per unit cell. Single heating rate
(SHR) method of analysis.
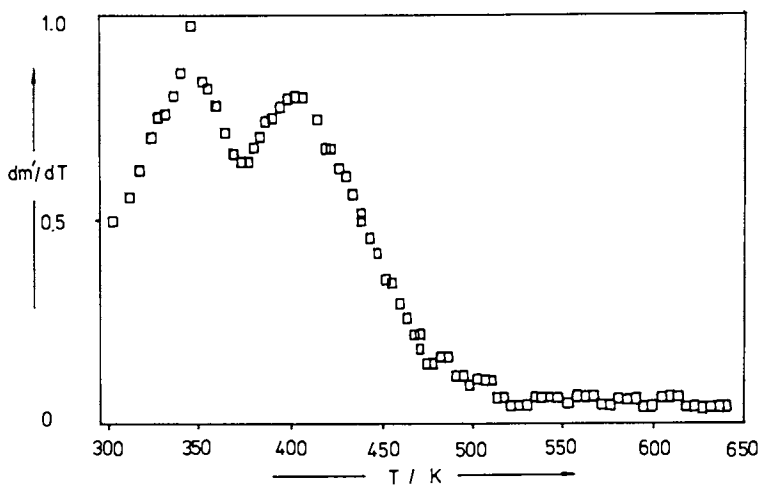
Figure 4. Temperature programmed desorption of n-hexane from Na-
ZSM-5.   β = 10Kmin⁻¹
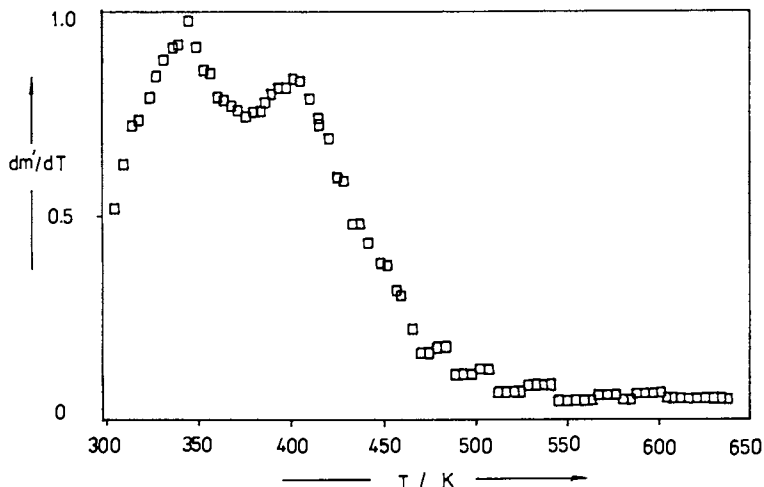
Figure 5.   Temperature programmed desorption of n-hexane from Na-ZSM-11. β = 10Kmin^{-1}.
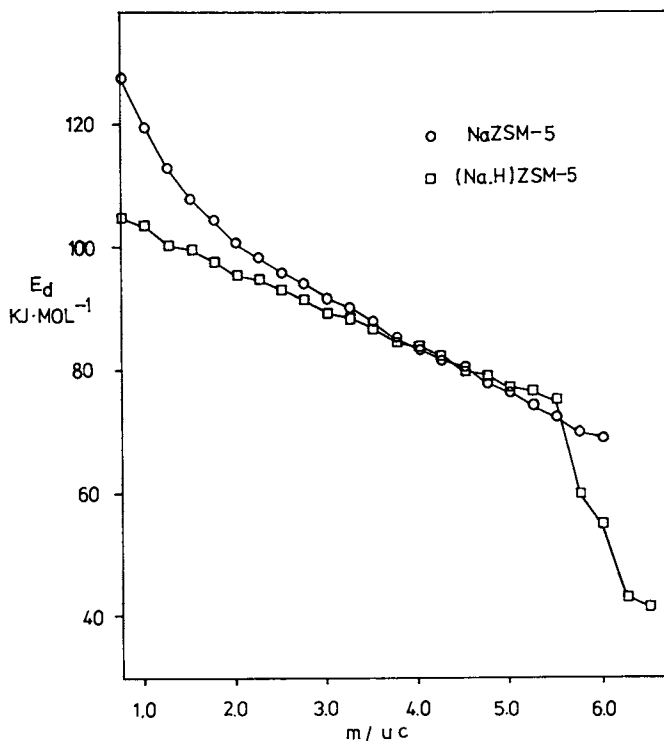
Figure 6.   Activation energy of desorption of n-hexane from O Na-ZSM-5; □ (Na,H)-ZSM-5 as a function of sorbate loading in molecules per unit cell.   SHR method of analysis.
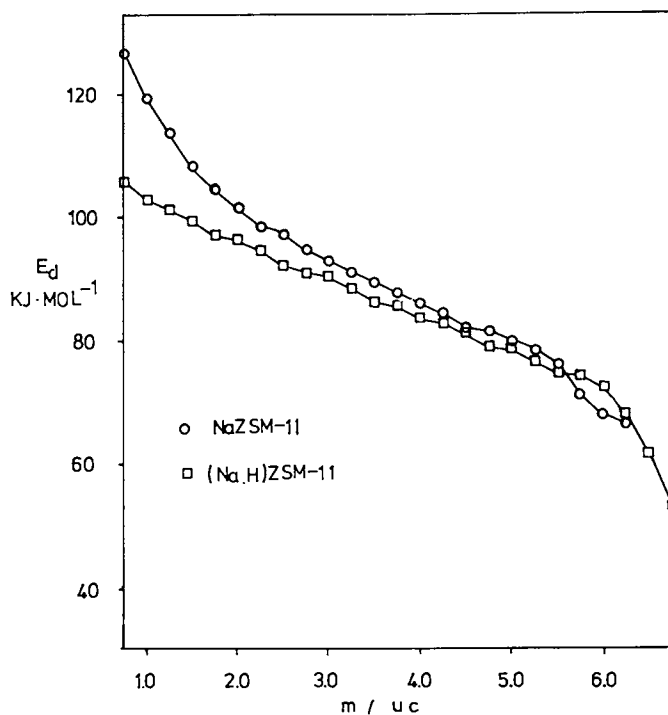
Figure 7. Activation energy of desorption of n-hexane from
O Na-ZSM-11; ☐ (Na,H)-ZSM-11 as a function of sorbate loading in
molecules per unit cell. SHR method of analysis.

these energies increase with increasing Na^+ content per u.c. It is also interesting to note that these energies have similar values in these ZSM-5 and ZSM-11 samples which have the same Na^+ ion concentrations. (N.B: Both of these zeolites had the same Si/Al ratios.) Unlike the case of Theta-1 the E_d values at low loadings are much larger for the pure Na^+ forms of both ZSM-5 and ZSM-11, indicating that the electric field around each Na^+ ion is introducing a significant electrostatic component to the total interaction energy.

It is interesting to note on comparing the $\bar{E}d$ values in Table I and III that the average desorption energies in the one-dimensional channel network of Theta-1 are smaller than the corresponding energies for the three dimensional channel networks of ZSM-5 and ZSM-11, which have four intersections per u.c. These results are further evidence that Ed is closely related to the heat of adsorption of n-hexane rather than the activation energy for diffusion in these frameworks. The higher $\bar{E}d$ values for ZSM-5 and ZSM-11 over those for Theta-1 are the result of the stronger electrostatic interactions which exist in the frameworks with higher Al concentrations.

REFERENCES

1.   Chen, L.F. and Rees, L.V.C., Zeolites, in press.
2.   Chen, L.F. and Rees, L.V.C., Zeolites, in press.
3.   Richards, R.E. and Rees, L.V.C., Zeolites, 1986, 6, 17.
4.   Dima, E. and Rees, L.V.C., Zeolites, 1987, 7, 219.
5.   Barri, S.A.I., Smith, G.W., White, D. and Young, D., Nature, 1984, 312, 533.
6.   Tokoro, Y., Misono, M., Uchijima, T. and Yoneda, Y., Bull. Chem. Soc. Japan, 1978, 51, 85.
7.   Czanderna, A.W., Biegen, J.R. and Kollen, W., J. Coll. Interface Science, 1970, 34, 406.

Chapter 28

Liquid Diffusion and Adsorption of Aqueous Ethanol, Propanols, and Butanols in Silicalite by HPLC

Y. S. Lin and Yi Hua Ma

Chemical Engineering Department, Worcester Polytechnic Institute, Worcester, MA 01609

The diffusion and equilibrium adsorption of aqueous alcohols in silicalite crystals have been studied using a novel HPLC technique. With a nonlinear mathematical model, the adsorption isotherms and intracrystalline diffusivities have been determined at 10, 30, 50, 70°C for ethanol, i-propanol, i-butanol, and at 30°C for n-propanol and n-butanol. The liquid intracrystalline diffusivities are found to be in the range of 10^{-9} to 10^{-11} cm^2/s and decrease in the folowing order: n-butanol> n-propanol> ethanol >i-propanol> i-butanol. The adsorption equilibrium results determined by the present HPLC technique are compared with those measured by the conventional batch method and good agreement is found between the two methods.

Silicalite is a microporous crystalline silica molecular sieve with remarkable hydrophobic properties (1) and has been considered to offer practical applications in the clean-up of water contaminated with hydrocarbons and the separation of ethanol from dilute fermentation aqueous solutions (2, 3, 4, 5). Many studies have been reported on the properties of adsorption and diffusion of gases in silicalite (e.g., 6, 7, 8, 9, 10). However, despite the many potential applications of silicalite as an adsorbent in liquid phase, studies on liquid phase diffusion and adsorption in silicalite are rather scarce. Early work on liquid phase adsorption in silicalite includes studies by Milestone and Bibby (3) on the adsorption of alcohols, Narita et al. (11) on adsorption of phenols, cresols and benzyl alcohol, both from aqueous solution, and Ma and Lin (12) on liquid hydrocarbon adsorption. Due to considerable difficulty involved in liquid diffusion measurements in molecular sieves, however, no liquid diffusion studies on silicalite were reported until recently. Ma and Lin (13) applied an HPLC technique to the measurements of liquid diffusion and adsorption in silicalite. The intracrystalline diffusivities for methanol, ethanol, acetone from aqueous solution and acetone, toluene from cyclohexane solution in silicalite were reported to be in the range from 10^{-10} to 10^{-11} cm^2/s.

Liquid chromatography (LC) has been, in the past decade, increasingly used for the measurement of liquid adsorption equilibrium (14, 15, 16, 17). But the application of the LC technique for the measurement of liquid diffusion in molecular sieves was rather limited (18, 19). The recently developed LC technique using a commercial HPLC system (13), with many advantages over the conventional batch techniques, enables us to determine liquid phase diffusion and adsorption equilibrium in molecular sieve crystals in a simpler, more accurate and rapid way.

The present study reports the measurements of intracrystalline diffusion and adsorption equilibrium for ethanol, propanols and butanols from aqueous solution in silicalite using a modified HPLC technique. The unique feature of the present work is the use of a mathematical model with a nonlinear adsorption isotherm equation to obtain the intracrystalline diffusivity and adsorption isotherm parameters. The adsorption equilibrium data for alcohols from aqueous solution in silicalite measured by the conventional batch method are also reported and compared with the results measured by the HPLC technique.

EXPERIMENTAL

The liquid adsorption and diffusion measurements were carried out in a BECKMAN HPLC system, which consists of one model 421 system controller, two model 110 solvent metering pumps, one solvent mixer and one model 210 sample injector with a 20 μl sample loop. A Hitachi model 100-40 UV-Vis Spectrometer was used as the detector. To increase the pressure in the UV-VIS detector cell, a back pressure regulator was connected to the effluent stream from the detector to avoid formation of air bubbles due to vaporization in the detector cell. Figure 1 shows the schematic of the HPLC system used in the experiments.

In performing experiments, the silicalite samples were first activated at 300°C overnight and then cooled in a desiccator to room temperature. A column 2.0(L)x0.20(ID) cm was packed with the silicalite powder by a dry-packing method. After the column was packed, it was necessary to stabilize it by flowing the carrier solvent (water in the present study) through the column in the HPLC system over an extended period of time. The details on the column packing and stabilization for the silicalite LC column were given by Ma and Lin (13).

In the measurements of the adsorption equilibrium and intracrystalline diffusion data, the injection sample loop was first filled with a sample solution (water as solvent) of a known sorbate concentration by a syringe. The sample was then injected into the column after a stable base line in the recorder had been obtained. For each adsorbate at a given temperature, about 4 to 6 samples of different adsorbate concentration (C_0 from about 0.015 to 0.06 g/ml) and at different carrier flow rate (Q from 0.5 to 2.0 ml/min) were injected to give the corresponding response peaks at the outlet of the column. The response peaks were recorded and then directly read from the recording chart and input to a DEC-20 computer for further analysis. Figure 2 shows some recorded response peaks from the silicalite LC column for ethanol, n-propanol and n-butanol.

The dead volume of the HPLC system was minimized using the connecting tubing of smallest inner diameter (d_t=0.0254cm) and the fittings with a very small dead volume. The dead volume of the system
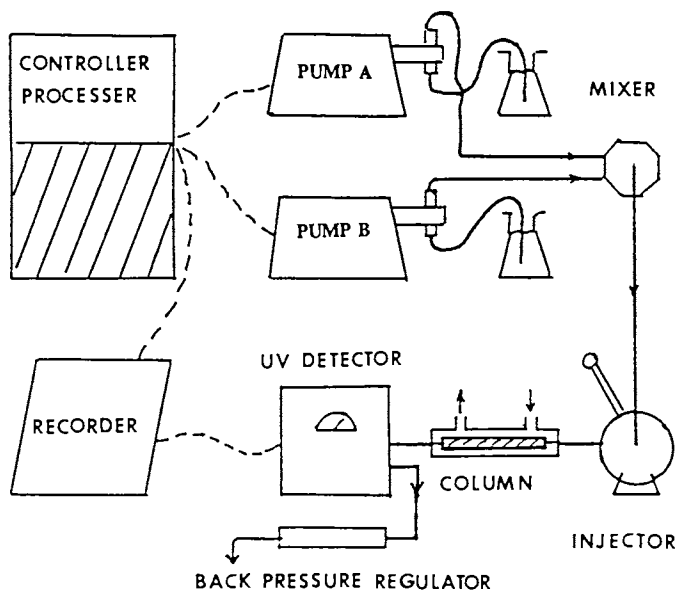
Figure 1. Schematic of HPLC Experimental Apparatus.
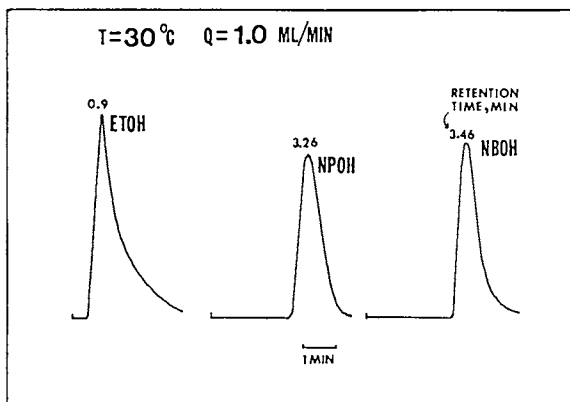
Figure 2. Recorded Response Peaks from Silicalite LC Column.

was determined (13) to be 0.022 ml. The dead volume effect on the first moment was corrected for all the measured response peak data. The effect of the dead volume on the second moment of the response peaks was found to be negligible in the present LC systems.

The batch measurement for the equilibrium adsorption of alcohols from aqueous solution in silicalite was conducted in air-tight bottles which were immersed in a thermal bath at 30°C (12). Amounts of activated silicalite sample, solute (alcohols) and solvent (water) in each bottle were measured gravimetrically. The bottles in the thermal bath were intermittently shaken to hasten the equilibrium. After the bottles had been kept in the thermal bath for over 10 hr, the equilibrium solution was withdrawn and analyzed by gas chromatography. The packing material of the gas chromatography column was poropak Q (Waters Associates, Inc.). Details of the adsorption equilibrium measurement by the batch method can be found in Ma and Lin (12)

The silicalite in spherical crystal particle (powder) form was obtained from Union Carbide Corp. The results of particle size distribution analyzed by an Electrozone Celloscope particle size analyzer showed very narrow crystal size distribution (in the range from 1.5 to 3.5 microns in diameter). The approximately spherical form and the size of the crystal particles were verified by scanning electron micrographs. The specification of the silicalite sample and some of the column parameters are given in Table I. All solvents used were of HPLC grade. In handling water, special care was taken to prevent it from being chemically or biologically contaminated.

Table I   Specification of silicalite and
LC column parameters

Average crystal radius R (μl)	1.17
Crystal pore volume v_p (ml/g)	0.19
Crystal porosity ε_p	0.33
Column size (cm)	2.0(L)x0.2(ID)
Bed porosity ε_b	0.46

MATHEMATICAL MODEL AND ANALYSIS

The mathematical model for the mass transfer of an adsorbate in the LC column packed with the silicalite crystal particles is based on the assumptions of (1) axial-dispersed plug-flow for the mobile phase with a constant interstitial flow velocity; (2) Fickian diffusion in the silicalite crystal pore with an intracrystalline diffusivity independent of concentration and pressure; and (3) spherical silicalite crystal particles with a uniform particle size distribution. A detailed discussion of these assumptions can be found in (13). The differential mass balances over an element of the LC column and silicalite crystal result in the following two partial differential equations:

for the mass transfer in the mobile phase:

$$\frac{\partial C}{\partial t} + U \frac{\partial C}{\partial Z} + \frac{1-\varepsilon_b}{\varepsilon_b} \dot{q} = D_1 \frac{\partial^2 C}{\partial Z^2} \tag{1}$$

with the adsorption rate $\dot{q}$ expressed by:

$$\dot{q} = D_p \frac{3}{R} \frac{\partial C_p}{\partial r} \Bigg|_{r=R} \tag{2}$$

for the diffusion in the crystals:

$$D_p \left(\frac{\partial^2 C_p}{\partial r^2} + \frac{2}{r} \frac{\partial C_p}{\partial r} \right) = \varepsilon_p \frac{\partial C_p}{\partial t} \tag{3}$$

where C and C_p are the concentration of adsorbate in the mobile phase and in the silicalite crystal pore, respectively; D_1 is the axial dispersion coefficient (its estimation was given in (13)). D_p is the intracrystalline diffusivity based on the total area of the crystal particle perpendicular to the diffusion direction. Other symbols are identified in the nomenclature.

For a column initially flowed with a pure solvent, the initial conditions are:

for the mobile phase:

$$C(Z, t) = 0 \quad \text{at} \quad t = 0 \tag{4}$$

for the silicalite crystal:

$$C_p(Z, r, t) = 0 \quad \text{at} \ t = 0 \tag{5}$$

The following equations are used as the boundary conditions for the mobile phase at the outlet of the column:

$$\frac{\partial C}{\partial Z} = 0 \quad \text{at} \quad Z = L \tag{6}$$

and at the inlet of the column:

$$C = \Gamma + \frac{D_L}{U} \frac{\partial C}{\partial Z} \quad \text{at} \quad Z = 0 \tag{7}$$

where Γ is the square pulse input function:

$$\Gamma = \begin{cases} C_o & (0 \le t \le t_{in}) \\ 0 & (\text{otherwise}) \end{cases} \tag{8}$$

The spherical symmetrical condition is applied to the silicalite crystal particle:

$$\frac{\partial C_p}{\partial r} = 0 \quad \text{at} \ r = 0 \tag{9}$$

As the mass transfer resistance at the external surface of the silicalite crystal particle has negligible effects on the overall mass transfer in the present LC system (13), local equilibrium at the external surface thus can be assumed to simplify the mathematics involved in the numerical solution. Since the adsorption isotherm data of alcohols from dilute aqueous solution in silicalite, as reported by Milestone and Bibby (3), can be described by a Langmuir type equation, the following Langmuir type equation is used as the boundary condition at the external surface of the silicalite crystal particle:

$$q = \frac{n \cdot b \cdot C}{1 + b \cdot C} \quad \text{at } r = R \tag{10a}$$

with

$$q = C_p\, v_p \tag{10b}$$

Equations 1 and 3 with the initial and boundary conditions as given above were first non-dimensionalized and then solved by the orthogonal collocation numerical technique (20). The concentration in the mobile phase and crystal pore was divided by $(C_o \cdot V_1 / \varepsilon_b \cdot V_c)$ to give the dimensionless concentration. The parametric analysis shows that varying any of the parameters of n, b and D_p can result in substantial change in the location (retention time) and the shape (broadness and symmetry) of the LC response peaks. A variation on the axial dispersion coefficient D_1, however, has very small effect on the response peaks for the present LC system. The details of the numerical solution and parametric analysis will be given in a separate paper.
    The direct time domain fitting method was used for calculating the adsorption equilibrium parameters, n and b, and intracrystalline diffusivity D_p. For the adsorption systems with nonlinear adsorption isotherm, both experimental and simulated response peaks for pulse injections showed that variation on the injection sample concentration, C_o, or the carrier solvent flow rate, Q, can drastically affect both the shape and location of the LC response peaks, indicating that the LC response peaks are rather sensitive to these two experimentally controllable variables. Thus, to ensure the uniqueness of a set of the calculated values for n, b and D_p, the direct time domain fitting was done by fitting four response peaks at different C_o and Q with a single set of values for n, b and D_p for a given temperature. The IMSL routine ZXSSQ using the Levenberg-Marquadt algorithm was used for the optimum parameter search with the objective function as:

$$F(n,b,D_p) = \sum_{pks} \sum_{pks} (C_{exp} - C_{cal})^2 \tag{11}$$

where C_{cal} and C_{exp} are respectively the concentration at the outlet of the LC column calculated from the mathematical model and measured experimentally. After the optimum set of values for n, b and D_p were found, their uniqueness was verified by examining whether a good agreement was obtained between all the experimentally determined peaks and those computed from the mathematical model using the estimated values of n, b and D_p at different C_o and Q for a given temperature.

RESULTS AND DISCUSSION

From the experimental response peaks at different C_o and Q, the intra-crystalline diffusivity and isotherm parameters were obtained for ethanol, i-propanol, i-butanol at 10, 30, 50, 70°C and n-propanol, n-butanol at 30°C from aqueous solutions in silicalite. The results are presented in Table II. The error limit (95% confidence interval) for most parameter values listed in Table II is less than 10%. Fig-ures 3 and 4 show some typical experimental response peaks (points) and the corresponding theoretical peaks (solid lines) for ethanol and n-propanol. For an adsorbate at a given temperature, the four theor-etical peaks were calculated with the same set of the optimum values for D_p, n and b as given in Table II using the nonlinear mathematical model. As shown in the figures, a fairly good agreement is achieved between the theoretical and experimental data for all four response peaks at different Q and C_o, which ensures the uniqueness of the set of the optimum values for D_p, n and b and the applicability of the Langmuir type isotherm equation for the adsorption equilibrium of the alcohols from aqueous solution in silicalite.

Table II   Intracrystalline diffusivity and adsorption isotherm
parameters of liquid alcohols in silicalite

Adsorbate	T (°C)	$D_p \times 10^{-10}$ (cm^2/s)	n (mmol/g)	b (ml/mmol)
ethanol	10	1.3	1.90	16.6
	30	1.6	1.94	14.7
	50	3.0	1.92	12.8
	70	4.0	1.75	11.5
i-propanol	10	0.60	1.52	50.5
	30	0.79	1.58	45.7
	50	1.0	1.44	41.7
	70	2.1	1.45	35.5
i-butanol	10	0.32	1.26	35.6
	30	0.41	1.22	35.2
	50	0.75	1.23	23.0
	70	2.5	1.25	16.4
n-propanol	30	7.9	1.79	58.7
n-butanol	30	15.2	1.42	106

An examination of the results reported in the previous studies on adsorption equilibrium for alcohols from aqueous solution in different silicalite samples (3, 5, 21) shows considerable differences in equil-ibrium adsorption capacities among different batches of silicalite samples. Thus, in order to compare the results determined by the HPLC
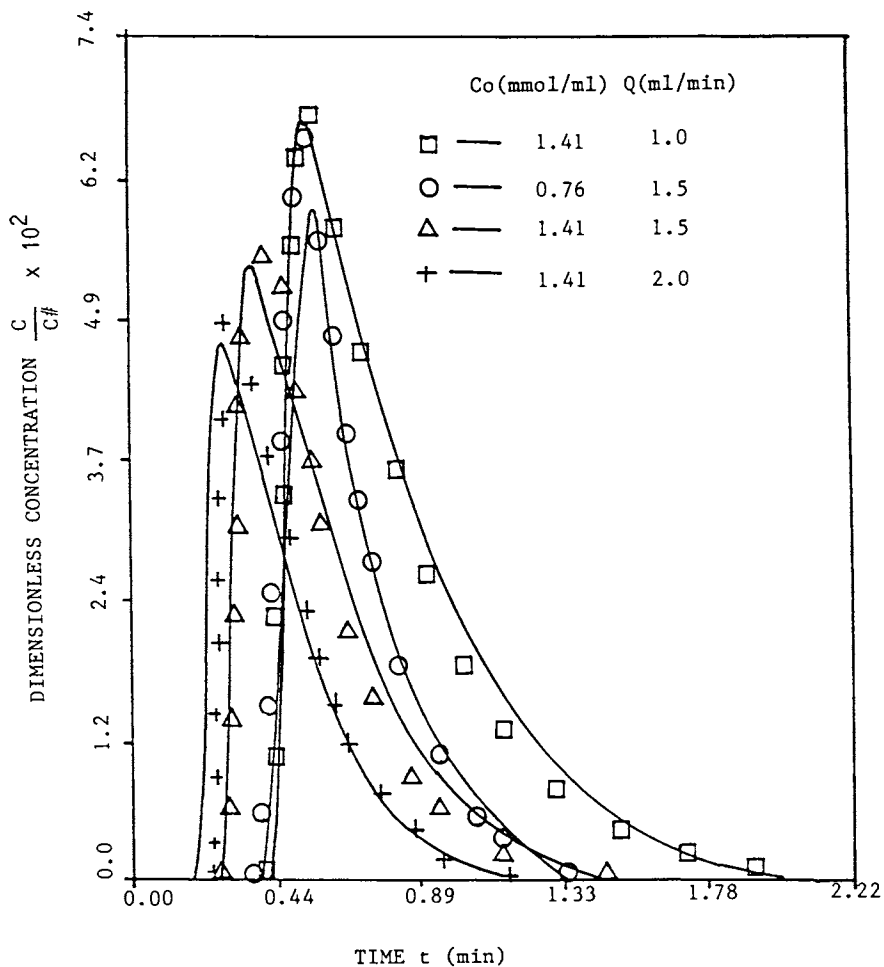
Figure 3.   Comparison of Simulated and Experimental Response
Peaks for Ethanol at 50°C.
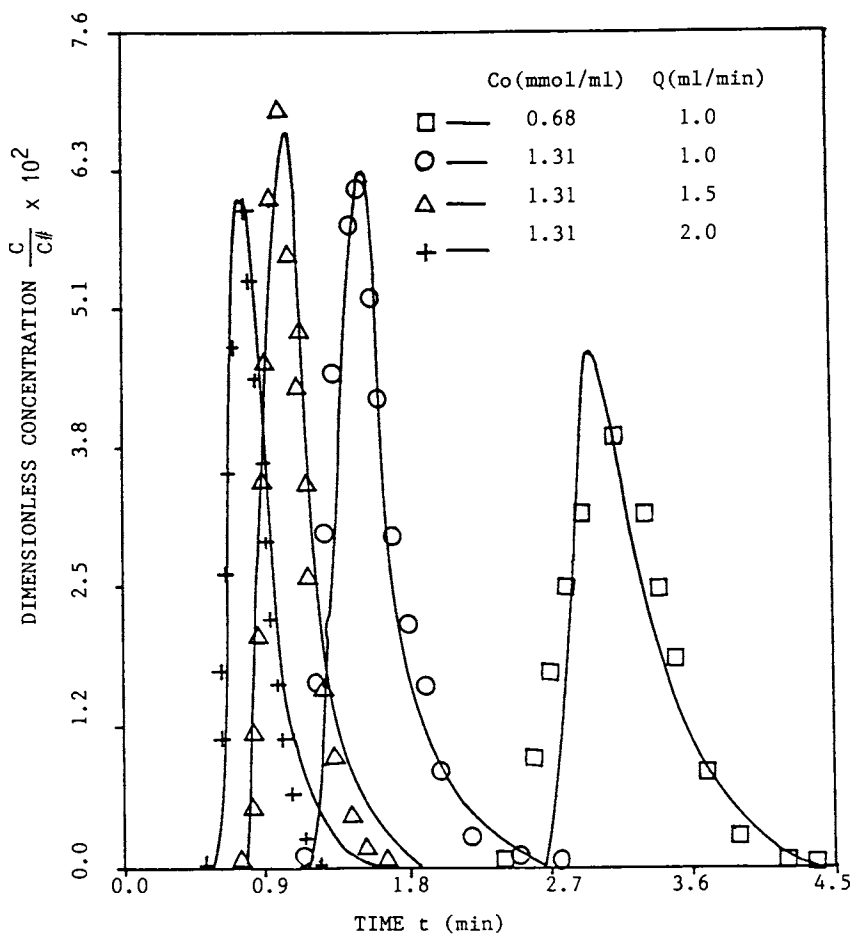
Figure 4. Comparison of Simulated and Experimental Response
           for N-propanol at 30°C.

technique with those determined by the conventional batch method, the adsorption equilibrium capacities for the five alcohols from aqueous solution in the same silicalite (also under the same pretreatment condition) were determined by the batch method at 30°C. Figure 5 shows the adsorption isotherm data for the five alcohols measured by the batch method. The solid curves in Figure 5 are the results fitted by Langmuir equation, Equation (10a). A comparison of the solid curves with the experimental data shows that the adsorption isotherm can be well described by the Langmuir equation, further verifying the use of Equation (10a) in the mathematical model.

For the adsorption from a solution into a solid, the Langmuir equation is often used to describe the equilibrium isotherms. But the parameters in the Langmuir equation should not be considered as having the same physical meaning as those used for the vapor adsorption. Nevertheless, the parameters n and b in Equation (10a) can be used for comparison as n may indicate the "saturated" adsorption capacity and b is related to the initial slope of the isotherm. The liquid adsorption equilibrium results given in Table II show that the saturation adsorption capacity for the five alcohols decrease in the following order (based on the adsorption quantity in mmol/g):

ethanol > n-propanol > i-propanol > n-butanol > i-butanol

which agrees with the results reported in the previous studies on adsorption of liquid alcohols in silicalite (3, 21). Such an order of variation in the saturation capacity may be due to the difference in the molecular size of the five alcohols.

The effect of temperature on equilibrium for liquid adsorption is generally much more complex than that for pure vapor phase adsorption due, partially, to the involvement of a solvent in liquid adsorption systems (22). The amount of an adsorbate adsorbed in liquid adsorption may decrease or increase with increasing temperature, depending mainly on the difference of the heats of immersion for the adsorbate (solute) and solvent (22). In the present study, the saturation adsorption capacity n for ethanol, i-propanol and i-butanol are insensitive to temperature, while the parameter b for the three alcohols decreases as the temperature increases. Bui et al. (4) reported a similar temperature dependence of n and b for the adsorption of ethanol from an aqueous solution in silicalite.

A comparison of the adsorption isotherm data measured by the batch method with those measured by the HPLC method for the five alcohols in silicalite is given in Figure 6. As shown in Figure 6, a remarkably good agreement is found between the two methods, verifying the validity of the present HPLC technique for the measurement of adsorption equilibrium as well as diffusion in molecular sieve crystals

The diffusion of the alcohols in silicalite with water as the carrier solvent in the LC system may be considered similar to the counterdiffusion of an adsorbate into silicalite already saturated with a less adsorptive solvent (23). The diffusivities thus measured by the HPLC technique depend on the properties of the sorbate, the adsorbent and the carrier solvent. The diffusivities reported in Table II are in the range of 10^{-9} to 10^{-11} cm^2/s. This is approximately in the same order of magnitude as those of pure vapor diffusion by the adsorption uptake measurements (6) and the GC measurements (7)
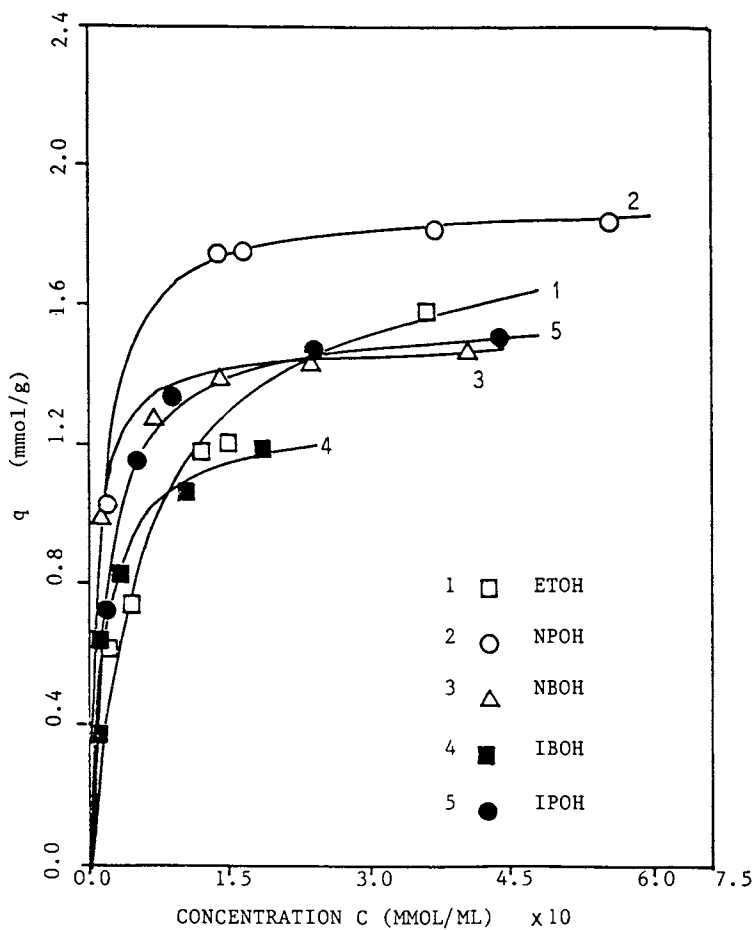
Figure 5.   Isotherm Data Measured by Batch Method (Dot points---
            Experimental Data; Solid Curves---Results fitted by
            Langmuir Equation).
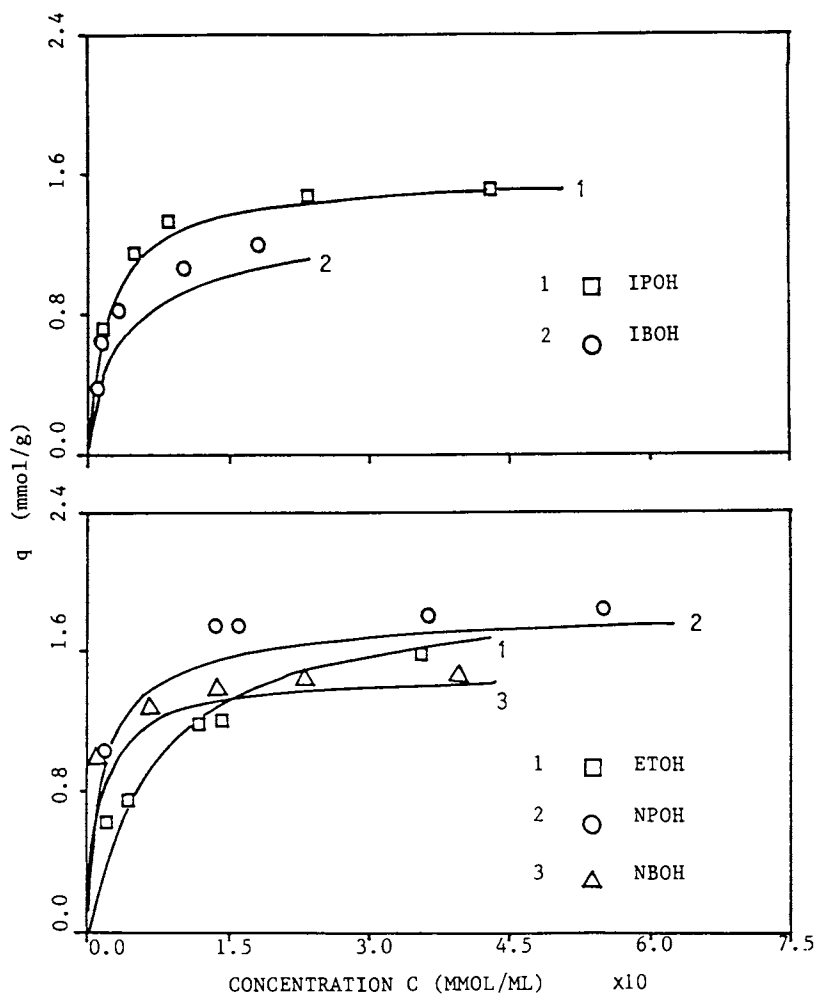
Figure 6. Comparison of Isotherm Results Measured by HPLC Method
and Batch Method (Dot points---Batch Results; Solid
Curves---HPLC Results).

in silicalite crystals. However, the liquid intracrystalline diffus-
ivities reported here are found to be considerably smaller than the
self-diffusivity of methanol in methanol-water mixture in silicalite
($\underline{24}$). An intracrystalline diffusivity of about 3×10^{11} was reported
for cumene in NaY zeolite crystals with cyclohexane as the solvent
(at 30°C), which is close to the diffusivity of i-butanol reported in
Table II. A detailed comparison of the present liquid diffusion data
with others is difficult as no other liquid diffusion data in silica-
lite under similar conditions were reported.

   The intracrystalline diffusivities reported here for alcohols
from aqueous solution in silicalite are found to decrease in the
following order:

   n-butanol > n-propanol > ethanol > i-propanol > i-butanol
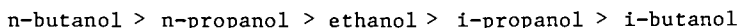
The lower diffusivities for the branched alcohols are due probably
to their branched structure which may hinder the molecules from diff-
using in the silicalite channels. For the three straight-chain normal
alcohols, however, the diffusivities increase as the chain length
increases. This somewhat unusual variation of the diffusivity with
the molecular size may be explained by examining the polar nature of
the adsorbate molecules. As the sizes of ethanol, n-propanol and
n-butanol molecules are smaller than the pore openings of the silic-
alite samples. In this situation, it appears that the diffusion will
be primarily affected by the interaction between the adsorbate mol-
ecules and the silicalite framework. Since silicalite is hydrophobic
and the polarity of the alcohols decreases as the chain length in-
creases, it is reasonable that the diffusivity increases as the chain
length increases due, mainly, to the fact that the interaction between
the adsorbate molecules and the silicalite framework is less severe
for molecules with smaller polarity. This makes it easier for the
molecules to diffuse through the silicalite channels, resulting in a
higher value of diffusivity. Furthermore, the larger value of the
adsorption equilibrium constant K (K≈n.b in dilute solution) for
n-butanol and n-propanol than that for ethanol indicates a higher
solute concentration of n-butanol and n-propanol on the surface of the
silicalite channels. Thus, surface diffusion may also occur for n-
butanol and n-propanol, which may cause a higher value of the effective
intracrystalline diffusivity ($\underline{25}$).

CONCLUSIONS

(1) An HPLC experimental technique has been developed to determine the
intracrystalline diffusivity and nonlinear adsorption isotherm for the
adsorption of liquids in molecular sieve crystals. The application of
the experimental technique was demonstrated by the determination of
the adsorption isotherms and diffusivities of the five alcohols (eth-
anol, i-propanol, n-propanol, i-butanol and n-butanol) from aqueous
solutions in silicalite crystals.
   (2) The saturation adsorption capacity for the adsorption of the
five alcohols from aqueous solution in silicalite decreases in the
following order as the molecular size increases:

   ethanol > n-propanol > i-propanol > n-butanol > i-butanol
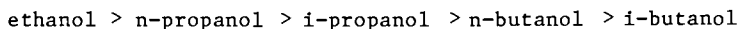
The determined intracrystalline diffusivities for the five alcohols from aqueous solution in silicalite are found to be in the range from 10^{-9} to 10^{-11} cm^2/s and decrease in the following order:

n-butanol > n-propanol > ethanol > i-propanol > i-butanol

(3) The adsorption equilibrium results measured by the present HPLC technique are found to be in good agreement with the results measured by the conventional batch method.

ACKNOWLEDGMENT

The authors are grateful for the silicalite samples provided by the Union Carbide Corporation.

NOMENCLATURE

b --- Isotherm parameter in Langmuir equation (ml/mmol)
C --- Concentration of the adsorbate in the mobile phase (g/ml or mmol/ml)
C_o--- Injection sample concentration (g/ml or mmol/ml)
C_p--- Concentration of the adsorbate in silicalite crystal pore (g/ml or mmol/g)
$C_{\#}$--- = $C_o V_1 / \varepsilon_b V_c$ (g/ml or mmol/ml)
D_p--- Intracrystalline diffusivity (cm^2/s)
D_1--- Axial dispersion coefficient (cm^2/s)
L --- Length of the packing in the column (cm)
n --- Isotherm parameter in Langmuir equation (mmol/g)
Q --- Volumetrical flow rate (ml/min)
$\dot{q}$--- Adsorption rate on surface of silicalite crystal particle (g/ml.s)
q --- Adsorption amount (mmol/g)
R --- Radius of silicalite crystal particle (cm)
r --- Radius in silicalite crystal particle (cm)
t --- Time (sec or min)
t_{in}-- Injection time, t_{in} = V1/Q (sec or min)
U --- Interstitial flow velocity (cm/s)
V_c--- Volume of empty LC column (ml)
V_d--- Dead volume of LC system (ml)
V_1--- Volume of the injection sample loop (ml)
V_p--- Pore volume of adsorbent particle (ml/g)
Z --- Distance along the column axial direction (cm)

Greek Letters

ε_p--- Porosity of adsorbent particle
ε_b--- Porosity of the packed column
Γ --- Square pulse function

LITERATURE CITED

1. Flanigen, E.M., Bennett, J.M., Grose, R.W., Cohen, J.R., Patton, R.L., Kirchner, R.M., and Smith, J.V., *Nature* (London), 1978, <u>257</u>, 512.

2.   Oulman, C.S. and Chriswell, C.D., U.S. Pat. #4277635 (7 July, 1981).
3.   Milestone, N.B. and Bibby, D.M., J. Chem. Tech. Biotech., 1981, 31, 732.
4.   Bui, S., Verykios, X. and Mutharasan, R., Ind. Eng. Chem. Proc. Des. Dev., 1985, 24, 1209.
5.   Haegh, G.S., in Zeolites, Ed. Drzaj, B., Hocevar, S. and Pejovnik, S., Elsevir Science Publisher, 1985, p. 606.
6.   Wu, P.D., Debebe, A. and Ma, Y.H., Zeolites, 1983, 3, 117.
7.   Chiang, A.S.C., Dixon, A.G., Ma, Y.H., Chem. Eng. Sci., 1984, 39, 1461.
8.   Bulow, M., Schlodder, H., Rees, L.V.C. and Richards, R.E., Proc. of 7th Internat. Zeol. Conf., Ed. Murakami, Y., Iijima, A. and Ward, J.W., Elsevier, 1986, p. 579.
9.   Zikanova, A., Bulow, M. and Schlodder, H., Zeolites, 1987, 7, 115.
10. Richards, R.E. and Rees, L.V.C., Langmuir, 1987, 3, 335.
11. Narita, E., Horiguchi, N. and Okabe, T., Chem Lett., 1985, 787.
12. Ma, Y.H. and Lin, Y.S., AIChE Symp. Series, 1985, Vol. 81, 242, 39.
13. Ma, Y.H. and Lin, Y.S., AIChE Symp. Series, 1987, Vol. 83, 259, 1.
14. Wang, H.L., Duda, J.L. and Radke, C.J., J. Coll. Interf. Sci., 1978, 66, 153.
15. Koster, H. and Findenegg, G.H., J. Chromatog., 1982, 15, 743.
16. Jacobson, J., Frenz, J. and Horvath, C., J. Chromatog., 1985, 316, 53.
17. Kibby, N.F., Slater, N.K.H., Weisenberger, K.H., Addoyobo, F. and Doulia, D., Chem. Eng. Sci., 1986, 8, 2005.
18. Lee, T.K. and Ruthven, D.M., Ind. Chem. Eng. Fundam., 1977, 16, 290.
19. Haq, N., Ph.D. thesis, Univ. of New Brunswick, Canada, 1983.
20. Villadsen, J. and Michelsen, M.L., Solution of Differential Equation Models by Polynomial Approximation, Pretice-Hall, 1978, Chapter 3.
21. Milestone, N.B. and Bibby, D.M., J. Chem. Tech. Biotech., 1983, 34A, 73.
22. Sircar, S., Novosad, J. and Myers, A.L., Ind. Eng. Chem. Fundam., 1972, 11, 249.
23. Satterfield, C.N. and Cheng, C.S., AIChE J., 1972, 18, 724.
24. Caro, J., Bulow, M. Richter-Mendau, J., Karger, J., Hunger, M., Freude, D. and Rees, L.V.C., J. Chem. Soc. Faraday Trans. I., 1987, 83, 1843.
25. Komiyama, H., Smith, J.M., AIChE J., 1974, 20, 1110.

Chapter 29

Shape-Selective Catalysis at the 30-Year Mark

N. Y. Chen

Central Research Laboratory, Mobil Research and Development Corporation, Princeton, NJ 08540

Summary

Shape selective catalysis with molecular sieve zeolites has progressed in its first thirty years to become an established branch of catalytic science. Since the first demonstration of selective n-paraffin conversion over 5A molecular sieves, increased insight into how these catalysts function has created opportunities for the development of a number of new industrial processes.

In the meantime, new characterization tools such as NMR, STEM, EXAFS, FTIR, and synchrotron XRD, etc., have allowed us to peer into the very heart of the zeolite and discern the nature and orientation of the active tetrahedral sites as well as determine the dimensions and connectivity of the zeolite pore systems.

Today we find shape selective catalysis 30 years old but far from mature. Synthesis and preparation of molecular sieves has expanded to over 200 combinations of chemical compositions and crystal structures. Indeed, the number of elements which can be inserted into the crystal framework either by isomorphous substitution or by direct synthesis has grown dramatically in recent years.

This paper presents a personal overview of the past progress and future horizons of shape selective catalysis from a practitioner's viewpoint.

After 30 years of effort, we can now safely say that shape selective catalysis has established itself as a new and continually evolving branch of heterogeneous catalysis. I would like to give you a personal view of the major advances made with respect to the general principles of catalyst design and the industrial applications of shape selective catalysis.

Molecular sieve zeolites

As we all know, there are two aspects that make
zeolites unique. First of all, being crystals, their
intracrystalline surface is an inherent part of the
crystal structure and hence they are topologically well
defined. This is in sharp distinction to the ill-
defined amorphous solids we are familiar with. The
availability of solids with such a large and well
defined surface area is certainly exciting and
welcoming news to us.

Secondly, the diameter of their pores is of
similar magnitude to that of many organic molecules of
interest. Molecular sieving and shape selectivity,
previously unknown, became possible with man-made
catalysts. Therefore, with zeolites we can begin to
discuss the concept of designing novel catalysts on a
molecular level – it is a fashionable thing these days
to talk about molecular engineering or nanotechnology.
Of course, we are far from being satisfied with the
current status of catalyst design.

To begin with, we have yet to synthesize a new
structure entirely by the principles of molecular
engineering. In fact, all of the new structures were
discovered by chance and by experience rather than by
design. Nevertheless, many advances have been made.

For example, the synthesis and preparation of new
materials has expanded to over 200 combinations of
chemical compositions and crystal structures, not to
mention the possible variety of molecularly engineered
layered structures such as the MELS from Catalytica (1)
and many other pillared clays.

While classical zeolites contain Si and Al, the
substitution of additional elements such as Ga, Ge, B,
P, etc., in framework positions has been achieved.
Indeed, the number of elements which can be inserted
into the crystal framework either by isomorphous
substitution or by direct synthesis has grown
dramatically in recent years (2). The synthesis of
aluminum phosphate-based materials has also led to some
new frameworks and new compositions of known
frameworks. Extensive work on these new materials has
just begun (3-4).

Zeolites derive their acidity or catalytic
activity from the proton associated with the framework
aluminum. Replacement of aluminum by the other three-
valent elements could also lead to the generation of
Bronsted acid sites. However, one needs to exercise
caution in proclaiming unusual catalytic properties
before one thoroughly understands the nature of these
materials. For example, many studies have been
reported on the nature of the acidity of boron ZSM-5
(5-6-7-8). Although physical measurements (8-9)
indicate that the protonic site associated with the

framework boron exhibits some weak acidic properties,
the studies of Chu and Chang (8) showed that the
catalytic activity of Boron ZSM-5 was due to the
aluminum contaminant in the sample.

As far as shape selective catalysis is concerned,
the structure characteristic of greatest interest is
the pore/channel system of these molecular sieves. As
we know, depending on the largest channel, zeolites are
characterized as small, medium or large pore if they
contain apertures made by rings of 8, 10 or 12 linked
tetrahedra.

In addition to the difference in size and shape,
the channel system in these zeolites may be one-
dimensional as in ZSM-48 (10) or multidimensional as in
ZSM-5. These channels could be relatively uniform in
size or they consist of interconnecting supercages.

Principles of catalyst design

The design of shape selective catalysts may be
described as the science of coupling chemical reactions
with sorption and diffusion characteristics of the
zeolite to alter the reaction pathway and the product
selectivity of known chemical reactions.

Reaction selectivity based on the principle of
molecular exclusion or molecular sieving action was
demonstrated many years ago.

Steric inhibition of the formation of bulky
reaction intermediates can also lead to unexpected
selectivity. This is known as spatioselectivity or
transition state selectivity. Csicsery first proposed
this in 1978 in his study with mordenite (11). With
medium pore zeolites, the relatively slow rate of
cracking of 3-methylpentane compared to that of n-
hexane, known as the Constraint Index of these zeolites
(12) is a typical example of this type of shape
selectivity. The reaction intermediate for
3-methylpentane is sterically constrained in the pores
of ZSM-5.

In addition to size exclusion and steric
inhibition, the intermolecular forces between the
zeolite and sorbate molecules offer opportunities to
achieve unique selectivity based on competitive
sorption properties of various zeolites. Variables
such as silica to alumina ratio, the nature of the
cation species and the geometry of the channels have
been shown to be important factors for consideration
(13-14). They also can contribute to catalyst
stability and reduced coking propensity, two important
characteristics of commercially useful catalysts.

Design for diffusion constrained systems

One may wish to take advantage of the difference in the diffusivity of the molecules in the zeolite channels to achieve high selectivity. In this case, besides the selection of a specific zeolite structure and chemical composition, the successful design of a shape selective catalyst often depends on the ability to alter and control the morphology of the crystals and the means to adjust the concentration of active sites within each crystal.

High selectivity will result when the rate of the reactions involving the undesirable bulkier molecules is in the severely diffusion constrained regime. The observed selectivity depends on the relative rate of reaction to that of diffusion of these molecules. It is obvious that the degree of selectivity can be adjusted by varying the diffusion pathway and its acid site density (15).

The advances of our capability in this area were aided by a number of remarkable new developments in analytical instrumentation. These new characterization tools include, among many, NMR, which provides information on the local environment of atoms in the structure (16-17), synchrotron XRD, which provides very high resolution x-ray data from powders (18-19), the application of Rietveld analysis of x-ray or neutron diffraction data to zeolite structure determination (20), and STEM, which provides atomic resolution of the crystal structure and its chemical composition (21), to name just a few.

Equally significant is the development of a variety of catalytic diagnostic tools which complement the physical chemical characterization tools and provide a link to the real world of industrial catalysis.

On the other hand, our knowledge of configurational diffusion in zeolites is far from being adequate. While Fick's law on diffusion has been commonly used to obtain diffusion coefficients in zeolites, there is experimental data such as the window or cage effect observed in erionite which cannot be interpreted by such equations. Data on diffusion of high molecular weight molecules in zeolites are almost nonexistent. Discrepancies also remain unresolved between diffusion coefficients determined by NMR and uptake data (22-23). Needless to say, much remains to be investigated, both in theory (24-25) and in experimental measurement (26).

Catalytic acidity

When zeolites were first shown to have acidity for catalytic conversion nearly 30 years ago, we were

filled with the expectation that these porous
crystalline materials of high surface area would
provide us with the opportunity to work with well
defined pores of known dimensions and active sites,
which could be related to the structure of the crystal.
This expectation has been only partially realized. As
we showed many years ago, the protonic sites associated
with the framework aluminum can have acid activity many
orders of magnitude higher than that of the amorphous
catalyst of similar aluminum concentration. But this
should not be construed as an indication that the
correlation between structure and activity is
completely understood. In fact, there is still
disagreement as to the nature of the acid site in
different chemical environments and different
structural configurations. Questions such as the
relationship between site density and site strength,
and the nature of defect sites and activated sites (27)
remain unresolved.

In addition, the substitution of additional
elements, such as Ga, Ge, B, P, etc., adds to the
complexity of the system, which is also far from being
completely understood. But I believe that the most
important challenge at hand is to devise rapid and
reliable screening tests to identify the practical
utility of this large variety of catalysts.

Industrial applications

Perhaps for obvious reasons, most of the current
commercial processes using shape selective catalysts
are in the petroleum and petrochemical industries.
These processes also largely fall into the category of
hydrocarbon conversion or conversion of non-
hydrocarbons to hydrocarbons over acid catalysts. They
include the reactions of olefins, paraffins, aromatics
and their mixtures in the production of high octane
gasoline, high quality diesel, jet fuel, distillate
fuels and lubricants. Table 1 shows a partial list of
these processes.
The benefits of shape selectivity can be discussed in
terms of tangible goals of [1] reducing the cost of
production, [2] improving the quality of the product,
[3] increasing the supply of product from
unconventional feedstocks and [4] creating totally new
products.

The octane boosting processes allow us to reduce
cost by increasing yield without sacrificing product
quality. To reduce cost, a new catalytic dewaxing
process replaces an expensive noncatalytic process.
Catalytic dewaxing does not have the temperature
limitation of a solvent dewaxing process. Thus, it
creates a new class of super-low freeze point or pour
point products for low temperature applications. The

Table 1 Processes Utilizing Shape Selective Zeolite
Catalysts

Selectoforming (28-29)	Octane boosting
M-Forming (30)	Octane boosting
Catalytic cracking (31-32-33-34-35)	Octane boosting
MDDW (36-37-38-39-40)	Distillate dewaxing
MLDW (41-42)	Lube dewaxing
M2-Forming (43)	Gas to aromatics
Cyclar (44-45)	Gas to Aromatics
MOGD (46-47-48)	Light olefins to gasoline and distillate
MTG (49-50-51-52)	Methanol to gasoline
MTO (53-54)	Methanol to light olefins
MVPI, MLPI, MHTI (15-55)	Xylene isomerization
MTDP (15)	Toluene disproportionation
MEB (56)	Ethylbenzene synthesis
Para-selective reactions (57-58-59)	p-Xylene synthesis p-ethyltoluene synthesis

ability to produce fuels and chemicals from
unconventional feedstocks by shape selective catalysts
is exemplified by aromatization of light gases,
production of gasoline and distillate from light
olefins, and production of light olefins and gasoline
from oxygenates, such as methanol. In the
petrochemical area, there are a number of processes
involving the production of aromatics.

However, there is little doubt that the
application of shape selective catalysis will be
extended from hydrocarbons to the conversion of non-
hydrocarbons and from acid catalysis to metal catalyzed
and bi-functional catalysis.

A cursory look at the patent literature shows
that, for example, the double bond of unsaturated
aldehydes and ketones can be isomerized over low
acidity medium pore zeolites without cleaving the
carbonyl group, and aldehydes and ketones can be
interconverted by skeletal isomerization (60-61).

In spite of the fact that acid sites are prone to
be poisoned by basic nitrogen compounds and phenols,
nitrogen compounds such as amines, pyridines, anilines,
nitriles and phenols have been synthesized with medium
pore zeolites with the desired selectivity (62-63).

Aromatic alkylation reactions which led to a
number of para-selective products have been duplicated
on phenols and thiophenes (64-65-66-67). So have
halogenation and nitration reactions (68-69).

Therefore, we are not only addressing the issue of
providing improved catalysts for existing process
technology, but also expecting the creation of totally
new processes and new products heretofore non-existent.

Literature Cited

1. *Catalytica Highlights*. 1986, 12, (4) 1.
2. Flanigan, E. M., Lok, B. M., Patton, R. L. and Wilson, S. T., *Proc. 7th Int. Zeol. Conf.*, Murakami, Y., Iijima, A. and Ward, J. W., eds., Kodansha/Elsevier, 1986; p 103.
3. Pellet, R. J., Rabo, J. A., Long, G. N. and Coughlin, P. K., *paper presented at the 10th North Am. Mtg. Catal. Society*, May 17-22, 1987; paper No. B-2.
4. Pellet, R. J., Rabo, J. A., Long, G. N., *Poster 75 presented at the 10th North Am. Mtg. Catal. Society*, May 17-22, 1987.
5. Taramasso, M., Perego, G. and Notari, B., *Proc. 5th Int. Conf. on Zeolites*, Rees, L. V., ed., Heyden, London, 1980; p 40.
6. Ione, K. G., Vostrikova, L. A., Paukshtis, E. A., Yurchenko, E., and Stepanov, V. G., *Akad. Nauk SSSR*, 1981, 27, 1160.
7. Hoelderich, W., Eichhorn, H., Lehnert, R., Marosi, L., Mross W., Reinke, R., Ruppel, W., and Schlimper, H., *Proc. 6th Int. Zeol Conf.*, Olson, D. H. and Bisio, A., eds., Butterworths, 1984, p 545.
8. Chu, C. T-W, and Chang, C. D., *J. Phys. Chem.*, 1985, 89, 1569.
9. Scholle, K. F. M. G. J., Kentgens, A. P. M., Veeman, W. S., Frenken, P. and van der Welden, G. P.M., *J. Phys. Chem.*, 1984, 88, 5.
10. Schlenker, J. L., Rohrbaugh, W. J., Chu, P., Valyocsik, E. W., and Kokotailo, G. T., *Zeolites*, 1985, 5, 355.
11. Csicsery, S. M., *J. Catal.*, 1978, 52, 453.
12. Frilette, F. J., Haag W. O., and Lago, R. M., *J. Catal*. 1981 67, 218.
13. Dessau, R. M., *Am. Chem. Soc. Symp. Ser*. 1980, 135, 123.
14. Santilli, D. S., *J. Catal*., 1986, 99, 327.
15. Olson, D. H. and Haag, W. O., *Am. Chem. Soc. Symp. Ser*., 1984, 248, 275.
16. Engelharde, G., Lohse, U., Lippmaa, E., Tarmak, M., Magi, M. Z., *Anorg. Alleg. Chem*. 1981, 482, 49.
17. Ramdas, S., Thomas, J. M., Klinowski, J., Fyfe, C. A., Fyfe, J. S., Hartman, J. S., *Nature* 1981, 292, 228.
18. Eisenberger, P., Newsam, J. M., Leonowicz, M. E. and Vaughan, D. E. W., *Nature*, 1984, 309, 45.
19. Cox, D. E., Hastings, J. B., Cardoso, L. P. and Finger, L. W., "*Materials Science Forum*", High Resolution Powder Diffraction, C.R.A. Catlow, Ed. 1986; vol. 9, p 1-20.
20. Baerlocher, C., *Proc. Sixth Intern. Zeolite Conf.*, Olson, D., and Bisio, A., Editors, Butterworths, Guildford, UK, 1984, p 823.

21. Thomas, J. M., New Scientist, 1980, August 21, 580.
22. Karger, J., Pfeifer, H., Freude, D., Caro, J., Buelow, M. and Uehlmann, G., Proc. 7th Int. Zeol. Conf., Murakami, Y., Iijima, A. and Ward, J. W., eds., Kodansha/Elsevier, 1986, p633.
23. Ma, Y. H.,Tang, T. D., Sand, L. B. and Hou, L. Y., ibid, 1986, p 531.
24. Doros, T., Wei, J., J. Catal., 1983, 83, 205.
25. Sundaresan, S., Hall, C. K., Chem. Eng. Sci., 1986, 41, 1631.
26. Chang, A. S., Dixon, A. G. and Ma, Y. H., Chem. Eng. Sci., 1984, 39, 1461.
27. Haag, W. O. and Dessau, R. M., Proc. 8th Intern. Congr. Catal. 1984, 2, 305.
28. Chen, N. Y., Maziuk, J, Schwartz, A. B. and Weisz, P. B.,Oil Gas J., 1968, 66 (47) 154.
29. Roselius, R. R., Gibson, K. R., Ormiston, R. M., Maziuk, J. and Smith, F. A., paper presented at the NPRA Annual Meeting, San Antonio, TX, Apr. 1973.
30. Chen, N. Y., Garwood, W. E. and Heck, R. H., Ind. Chem. Eng. Res., 1986, 26, 706.
31. Anderson, C. D., Dwyer, F. G., Koch, G. and Niiranen, P., paper presented at the 9th Iberoamerican Symp. Catal.,Lisbon, Portugal, Jul. 1984.
32. Yanik, S. J., Demmel, E. J., Humphries, A. P. and Campagna, R. J., Oil Gas J., 1985, 83 (19), 108.
33. Sparrell, P. T., Donnelly, S. P. and Schipper, P. H., paper presented at the 10th North Am. Catal. Soc. Mtg., San Diego, CA, May 17-22, 1987.
34. Dwyer, F. G. and Schipper, P. H., paper presented at the Ketjen Motor Octane Symposium, Amsterdam, Netherlands, June 25-26, 1987.
35. Donnelly, S. P., Mizrahi, S, Sparrell, P. T., Huss, Jr., A., Schipper, P. H. and Herbst, J. A., paper presented at the 19th Nat. Am. Chem. Soc. Mtg., New Orleans, LA, Aug. 30 - Sep. 4, 1987.
36. Chen, N.Y., Gorring, R. L., Ireland, H. R. and Stein, T. R., Oil Gas J. 1977, 75 (23) 165.
37. Perry, Jr., R. H., Davis, Jr., F. E. and Smith, R. B., Oil Gas J., 1978, 76, (21) 78.
38. Ireland, H.R., Redini, C., Raff, A. S. and Fava, L., Hydrocarbon Proc. 1979, 58, (5) 119.
39. Donnelly, S. P. and Green, J. R., paper presented at the Symp. Japan Petrol. Inst., Oct. 1980.
40. Graven, R. G. and Green, J. R., paper presented at the Congr. Australia Inst. Petrol., Sidney, Australia, Sept. 1980.
41. Smith, K. W., Starr, W. C. and Chen, N. Y., Oil Gas J. 1980, 78 (21) 75.

42. Wise, J. J., Katzer, J. R. and Chen, N. Y.,
    "Catalytic dewaxing in petroleum processing",
    paper presented at the Am. Chem. Soc. 173rd Annual
    Mtg., New York, NY, Apr. 14-15, 1986.
43. Chen, N. Y. and Yan, T. Y., Ind. Eng. Chem.,
    Process Res. Devel. 1986, 25, 151.
44. Johnson, J. A. and Hilder, G. K., paper presented
    at the NPRA Annual Mtg., San Antonio, TX, March
    1984.
45. Anderson, R. F., Johnson, J. A. and Mowry, J. R.,
    paper presented at the AIChE Spring National Mtg.,
    Houston, TX, March 24-28, 1985.
46. Garwood, W. E., Am. Chem. Soc. Symp. Ser., 1983,
    218, 383.
47. Tabak, S. A., paper presented at the AIChE National
    Meeting, Phila. PA, Aug. 1984.
48. Tabak, S. A., Krambeck, F. J.and Garwood, W. E.,
    paper presented at the AIChE Mtg., San Francisco,
    CA, Nov., 1984.
49. Chang, C. D., Catal. Rev. - Sci. Eng. 1983, 25, 1.
    "Hydrocarbons from Methanol", Marcel Dekker, N. Y.,
    1983.
50. Penick, J. E., Lee, W. and Maziuk, J., paper
    presented at the Intern. Symp. Chem. Reactor Eng.,
    (ISCRE-7) Boston, MA, Oct. 1982.
51. Gierlich, H. H., Keim, K. H., Thiagarajan, N.,
    Nitschke, E., Kam, A. Y., Daviduk, N., paper
    presented at the 2nd EPRI Conf. "Synthetic Fuels -
    Status and Directions", San Francisco, CA, Apr.
    1985.
52. Yurchak, S., paper presented at the Symp.
    Production of Fuels and Chemicals from Natural Gas,
    Auckland, NZ, Apr. 1987.
53. Chang, C. D., Chu, C. T-W. and Socha, R. F., J.
    Catal. 1984, 86, 289.
54. Gould, R. M., Avidan, A. A., Soto, J. L., Chang, C.
    D. and Socha, R. F., "Scale-up of a Fluid-bed
    Process for Production of Light Olefins from
    Methanol", paper presented at the AIChE National
    Mtg., New Orleans, LA, April 6-10, 1986.
55. Haag, W. O. and Dwyer, F. G., paper presented at
    the AIChE 8th Natl. Mtg., Boston, August 1979.
56. Dwyer, F. G., Lewis, P. J. and Schneider, F. M.,
    Chem. Eng., 1976, 83, (1) 90.
57. Chen, N. Y., Kaeding, W. W. and Dwyer, F. G., J.
    Am. Chem. Soc. 1979, 101, 6783.
58. Kaeding, W. W., Chu, C., Young, L. B., Weinstein,
    B. and Butter, S. A., J. Catal. 1981, 67, 159.
59. Kaeding, W. W., Young, L. B. and Prapas, A. G.,
    Chemtech. 1982, 12, 556.
60. Hoelderich, W., Merger, F., Mross, W. D. and
    Fischer, R. European Patent 162,387, Nov. 27,
    1985.

61. Hoelderich, W., <u>Proceedings 7th Intern. Zeolite Conf.</u>, Murakami, Y., Iijima, A. and Ward, J. W., Eds,. Kodadansha/Elsevier, 1986; p 827.
62. Chang, C. D. and Lang, W. H., U.S. Patent 4,220,783, Sept. 2, 1980. U.S. Patent 4,380,669, Apr. 19, 1983; U.S. Patent 4,434,299, Feb. 28, 1984.
63. Chang, C. D. and Perkins, P. D., U.S. Patent 4,388,461, Jun. 14, 1983. U.S. Patent 4,395,554, Jul. 26, 1983.
64. Cullo, L. A., Restelli, E. F., Shiring, F. J., <u>Intern. Pub.</u> No. WO 8604834, Aug. 28, 1986.
65. Swanson, B. J., Shubkin, R. L., U. S. Patent 4,532,368, Jul. 30, 1985.
66. Toray Ind., Japan Patent 61050933, Mar. 13, 1986.
67. Baltes, H., Leupold, E. I, European Patent 144760, Jun. 19, 1985.
68. Japan Syn. Rubber, Japan Patent 59216851, Dec. 5, 1984.
69. Ihara Chem., Japan Patent 59206322, Nov. 22, 1984; 60048943, Mar. 16, 1985; 61053234, Mar. 17, 1986; European Patent 154236, Sept. 11, 1985.

Chapter 30

Molecularly Engineered, High-Performance Adsorbent

Self-Bound Low-Silica X Zeolite

C. G. Coe, S. M. Kuznicki[1], R. Srinivasan, and R. J. Jenkins

Corporate Science and Technology Center, Air Products and Chemicals, Inc., Allentown, PA 18195

We prepared highly crystalline, low-silica X zeolite (LSX) in a self-bound form directly from porous, preformed metakaolin pellets. In the appropriate cation form, these materials should have improved adsorption properties for weakly interacting adsorbates such as nitrogen. The composition of the synthesis medium, substrate porosity, aging period, and crystallization conditions affected both the total amount of zeolite produced and the relative amount of X and A phases formed. Materials were characterized by elemental analysis, X-ray diffraction, scanning electron microscopy, N_2 adsorption, and ^{29}Si MAS NMR. Pellets converted in situ under optimum conditions contained >95% X zeolite having a Si/Al ratio equal to 1.0. These properties, combined with a large median pore diameter and acceptable crush strength, make this material a superior adsorbent. As predicted, a calcium low-silica X zeolite, properly activated, possesses higher N_2 capacity (1.37 moles/g at 30°C, 1 atm) and N_2/O_2 selectivity (11.5 from air at 30°C) than any other adsorbent.

Synthetic faujasites have substantial utility in a wide variety of adsorptive, catalytic, and ion exchange processes. Typically, Y zeolites are used as catalysts whereas X zeolites, having comparatively more cations and a higher framework charge, have been used for adsorptive and ion exchange applications.

The typical X zeolite possesses a framework Si/Al ratio of about 1.25. However, the aluminum-rich end member of the faujasite family, in accordance with Lowenstein's rule, has a ratio of 1.0, and consequently the maximum possible number of

[1]Current address: Engelhard Corporation, Menlo Park, CN 28, Edison, NJ 08818

exchangeable cations. In previous work we have shown that highly exchanged CaX (Si/Al = 1.23), with most of the calcium in the dehydrated/dehydroxylated state, possesses N₂ capacities and N₂/O₂ selectivities that are much larger than typically reported.(1) Since the strength of cation/sorbate interactions is relatively independent of the number of cations present(2), the adsorption capacity for weakly interacting adsorbates such as nitrogen should be directly related to the number of sorbate-accessible cations available. Improving the dynamic capacity is a prime consideration and goal for all separation and adsorption applications.(3) Thus, we felt it would be worthwhile to prepare an X zeolite having the maximum aluminum content. This zeolite is referred to as "reduced silica X" or "low-silica X" (LSX).(4) In addition, in accordance with Lowenstein's rule the LSX would have an ordered, uniform distribution of aluminum atoms leading to a more energetically homogeneous surface.

The utility of an adsorbent in a given process is affected not only by its chemical composition, but also by its physical form. For most commercial applications, zeolites must be pelletized to produce a particle having 1) sufficient size to eliminate massive pressure drops through a packed bed, 2) adequate crush strength and attrition resistance, and 3) enough macroporosity to minimize diffusion resistance. Generally in order to formulate a pelletized material the active zeolitic component must be diluted with an inorganic binder and then extruded or formed into beads. Adding a binder, however, dilutes the active zeolite phase, lowering its capacity. Thus our goal was to produce a self-bound LSX pellet, eliminating the need for a binder.

Some information on self-bound zeolites has been published.(5) Howell and Acara (6) have converted preformed aggregates of reactive kaolin-type clay, under appropriate conditions, directly to a zeolitic phase. Metakaolin having a Si/Al ratio of 1.0 was easily converted to zeolite A. Also, Breck (5) discusses the fabrication of pure self-bound A zeolite particles several inches in size by converting metakaolin in situ.

Since LSX and A zeolite have the same overall chemical composition and both are constructed by linking sodalite cages, we postulated that preformed metakaolin could be converted directly to LSX. Several reports show that kaolin-type clays can be transformed to X- or Y-type zeolites having Si/Al ratios exceeding 1.2 by either adding silica to or removing alumina from the metakaolin.(7-9) In each case, without addition of silica or deletion of alumina, only A zeolite is formed.

Only scattered reports are available on the preparation of LSX even in an unbound form. Simply extrapolating the standard synthesis reagents and conditions used to produce typical X zeolite will not yield a Si/Al ratio of less than 1.2. Kuhl and Sherry have published the most comprehensive information on LSX synthesis.(10) In a British patent, they describe a preparation wherein aluminosilicate gels in highly alkaline mixed Na⁺/K⁺ are subjected to a multiday aging period at 40°C, followed by

crystallization at higher temperature. They claim the long
aging period is critical to eliminating the formation of A
zeolite.(10) They also stated that many reactive silica-alumina
sources may be used to prepare LSX, including calcined clays,
but give no examples.(10) Barrer has carefully studied the
hydrothermal reactions of metakaolin in both single and mixed
bases at temperatures of 80°C and above but did not observe the
formation of LSX.(11) We found no reports of the direct
preparation of LSX from metakaolin in either a powder or
self-bound pelletized form. In addition, the air separation
properties for any ion form of LSX have never been reported.
      The work reported here describes the preparation and
characterization of highly crystalline self-bound LSX from a
porous metakaolin precursor and the superior air separation
properties observed for the calcium form.

Experimental

Porous metakaolin pellets were prepared from Engelhard ASP-400
kaolin using food grade corn starch as the pore former. Pellets
containing 30% starch gave the best results. After 30% starch
was mulled into the kaolin clay, the mixture was extruded by
standard techniques to form 1/8 inch diameter pellets of
starch-filled kaolin clay. Extrusion was followed by a heat
treatment at 700°C similar to that described by Howell and
Acara.(6)
      The heat treatments were carefully controlled since the
pellets have a high organic fraction. Uncontrolled "burnout" of
the organics may cause localized hot spots in the pellets.
Therefore, prior to treatment at 700°C in air, the samples were
heated at a lower temperature under an inert atmosphere to
remove most of the organics. Heat treatment tubes loaded with
the dried pellets were lowered into 595°C ovens under a nitrogen
atmosphere. The pellet temperature rose rapidly to 480-540°C;
as the organics burned off a black smoke evolved. The N_2
atmosphere was maintained until smoke formation ceased. To
remove the balance of the organics, a small fraction (5-10%) of
the nitrogen was replaced with air. The rate of air addition
was controlled to maintain the ΔT in the treatment vessel
below 40°C so that the pellet temperature was maintained below
700°C. After all the organic material had burned out and
nitrogen had been replaced by air, the pellet bed temperature
was raised to 700°C and held for 2 hrs. The total heat
treatment time was typically from 4 to 6 hrs.
      The self-bound LSX pellets were prepared directly from the
porous metakaolin pellets. In a typical preparation 22.2 g of
the pellets was mixed with 39.0 g of NaOH, 18.2 g of KOH and 234
cc of H_2O so that SiO_2/Al_2O_3 = 2.0, (Na_2O +
K_2O)/SiO_2 = 3.25, $Na_2O/(Na_2O + K_2O)$ = 0.75, and
$H_2O/(Na_2O + K_2O)$ = 20. Aging and/or crystallization
temperatures and times were varied to ascertain optimal
conditions. The best results were obtained when the above
mixture was allowed to react with constant circulation at about
50°C for a period of 10 days.

One pound lots of selected adsorbents were prepared by a direct scaleup of the above procedure, for conversion to other ion forms and application studies.

The self-bound LSX is readily converted to other ion forms using standard ion exchange techniques. The calcium form was prepared in most cases directly from the mixed Na/K adsorbents. Four 2-hr. exchanges, with at least a fourfold excess of 1 M $CaCl_2$ at temperatures between 90 and 100°C, generally produced samples having >98% of their exchange capacity in the calcium form.

The amounts of X and A zeolites present in the adsorbents were determined by X-ray diffraction. The sodium forms were used in all cases. The method involved adding $\alpha-Al_2O_3$ to the sample as an internal standard and then establishing the ratios of the integrated peak areas for selected zeolite lines in the sample of interest to those of pure zeolites in the sodium form. Total micropore accessibility was determined by oxygen adsorption at −196°C and 20 torr on a vacuum microbalance after activation of the zeolite at 1 to 2°C per minute to a final temperature of 400°C.

^{29}Si NMR spectra were obtained at ambient temperature using the Bruker CXP-200 FT-NMR (4.77 T) spectrometer equipped with a magic angle spinning multinuclear probe. The Delrin rotor was spun at about 3 kHz, and the pulse repetition time was 10 sec. The chemical shift scale was calibrated using hexamethyldisiloxane as an external reference ($\delta = 6.83$ ppm).

Crush strengths were measured using a Chatillon apparatus. Values reported were the average of 20 determinations. Pore size distributions were measured by mercury intrusion using a Micromeritics Autopore 9220. A contact angle of 130° was assumed for all measurements.

The equilibrium capacities of nitrogen and oxygen from air and the adsorbent capacities for pure nitrogen were determined for an 8-inch bed of each adsorbent contained in a 1-inch I.D. by 24 in. stainless steel tube. The packed bed was placed in a three-zone tube furnace. The adsorbents were activated under a flow of dry nitrogen and controlled temperature ramp, in a manner we previously found leaves a high proportion of the zeolite cations in a dehydroxylated state.(12)

To ascertain the nitrogen capacity and nitrogen selectivity of each adsorbent at 30°C and 1 atm pressure, we passed a stream of dry CO_2-free air through the activated adsorbent bed at 30°C for sufficient time to ensure equilibrium (approximately 12 hrs). To analyze the adsorbed product, the adsorbent bed was thermally desorbed at about 400°C into a gas burette collection chamber at atmospheric pressure. Void volumes in the adsorbent beds were determined by helium displacement. Measurements of the displaced volume in the gas collector, coupled with void volume measurements, yielded the amount of nitrogen plus oxygen adsorbed. The compositions of the adsorbed gases were determined by gas chromatography.

The selectivity (α) of the nitrogen/oxygen separation is calculated from:

$$\alpha \frac{N_2}{O_2} = \frac{[N_2] \text{ adsorbed}}{[O_2] \text{ adsorbed}} \cdot \frac{[O_2] \text{ gas phase}}{[N_2] \text{ gas phase}}$$

Nitrogen capacities for pure gas were determined in a similar manner. Following activation, the adsorbent beds were allowed to equilibrate in a stream of dry nitrogen at 30°C. Thermal desorption coupled with void volume measurements by helium displacement into a gas buret at atmospheric pressure yielded the amount of nitrogen adsorbed.

Results and Discussion

Synthesis. Extrapolation of standard synthesis techniques for X zeolite will not produce synthetic faujasites having a Si/Al below 1.2. Kuhl and Sherry's methods for preparing LSX vary from usual X-type syntheses in several ways.(10) They synthesized LSX in a mixed base (NaOH + KOH) system, whereas typical X-synthesis is conducted in pure aqueous NaOH using a $SiO_2/Al_2O_3 = 3.0$. However, the chemical composition of unmodified metakaolin fixes the SiO_2/Al_2O_3 at 2.0 for these reactant compositions. Thus without elevating this ratio, the mixture will typically be converted to zeolite A. The ratio of total base to silica is high, $(Na_2O + K_2O)/SiO_2$ ~ 3.25 compared to Na_2O/SiO_2 ~ 1.0-1.5 in a more typical X zeolite synthesis. The water content of the system is simultaneously low, $H_2O/(Na_2O + K_2O) = 20$, compared to H_2O/Na_2O ~40 for X zeolites. We presumed that the increased alkalinity of the system elevates the Al/Si ratio in both the solution and crystalline zeolite product. This presumption is supported by Barrer's observation that a general correlation exists between alkalinity and the framework Si/Al ratio of the zeolite product.(13)
    Kuhl and Sherry also claim that precrystallization aging conditions of the system are crucial. Due to the low SiO_2/Al_2O_3 (~1.0) employed immediate crystallization resulted in the formation of predominantly zeolite A. The aging process is reported to be highly sensitive to both time and temperature. These workers suggested that nucleation centers leading to faujasite form more rapidly than those for A zeolite at temperatures below 50°C.
    The highly reactive metakaolin used in our work is formed during the 700°C heat treatment which is also needed to remove the organic pore former in the pelletized adsorbents. Metakaolin is believed to exist as a defect phase where silica layers of the original clay are in close proximity to AlO_4 tetrahedral units coming from the original octahedral layer.(14)
    Figure 1 shows the overall scheme for the preparation of a self-bound LSX adsorbent, from metakaolin pellets which after calcium exchange have improved performance as adsorbents for air separation. We have made self-bound LSX by contacting the porous metakaolin pellet with a mixture of sodium and potassium hydroxides at relatively low temperatures and pressures. Depending on the conditions, these aggregates are either converted to a mixture of A and LSX or transformed entirely to

an essentially pure LSX. The formation of LSX does not require any silica source in addition to the metakaolin. The time required for aging and/or crystallization of LSX and the porosity of the metakaolin pellet vary greatly depending on the conditions employed (vide infra). Both Na^+ and K^+ are necessary for the formation of LSX from metakaolin. Similar preparations lacking K^+ produced predominantly hydroxysodalite, and removing the Na^+ produced a phase identified by XRD as KF. As synthesized, the self-bound LSX pellets are in the mixed ion form containing about 75% Na^+ and 25% K^+. Other cation forms are readily prepared using standard ion exchange procedures. The pellets maintain their macroscopic integrity during their conversion to zeolite.

We carried out our initial synthetic work using finely powdered metakaolin. Its optimum aging period was about 5 days at 40°C; aging was followed by crystallization at 100°C. These results were unanticipated in light of Kuhl and Sherry's results for aluminosilicate gels. Kuhl and Sherry showing a continuous rise in LSX purity with extended aging.(10) Even after the optimum aging period, we found that the converted metakaolin contained about 75% LSX with 10% A zeolite as a minor phase.

Having learned how the powdered metakaolin reacts, we focused our attention on in situ conversion of pelletized materials. We found that a pore-formed metakaolin was necessary for preparing self-bound LSX; attempts to convert extruded metakaolin pellets made without a pore former were unsuccessful. Apparently the dense pellets do not have sufficient macroporosity to interact with the synthesis medium. When a pore former such as starch is extruded with the kaolin clay and subsequently burned out, the resulting metakaolin aggregate has a median pore diameter an order of magnitude larger than typically found in a commercial pelletized X or A-type adsorbent.

We carried out aging studies on both powdered and pelletized metakaolin. Exposing porous metakaolin pellets to the same synthesis conditions used for powdered metakaolin at 40°C produced a similar optimum aging period (about 5 days) but a low level of zeolites. In contrast, when aged at 50°C prior to crystallization the powder could be crystallized at 100°C to pure LSX after 7 days whereas the pellets always contained an A zeolite impurity (about 10%) and a maximum of 75% LSX. The results from aging studies at 50°C are plotted in Figure 2. Agitating the aging mixture had no effect on the conversion of metakaolin to LSX.

However, we found that circulating the alkaline solution during the <u>crystallization</u> step improved the degree of conversion to zeolite and increased the fraction of LSX produced in both powders and pellets. For samples aged for 5 days at 40°C circulating the alkaline solution during crystallization at 100°C completely converted metakaolin to zeolite having about 80% LSX and 20% A. The beneficial effect of agitation during crystallization in the formation of LSX has not been recognized. In fact, previous workers have stated that quiescent conditions are preferred during the crystallization of synthetic faujasite or A zeolites from metakaolin.(6)

KAOLIN CLAY + PORE FORMER

↓ EXTRUSION

SOLID PELLET

↓ CALCINATION, 700°C

POROUS METAKAOLIN

↓ NaOH/KOH, 40-80°C

SELF-BOUND LSX

↓ POST MODIFICATION

ADSORP-
TION

ION
EXCHANGE | CATALYSIS
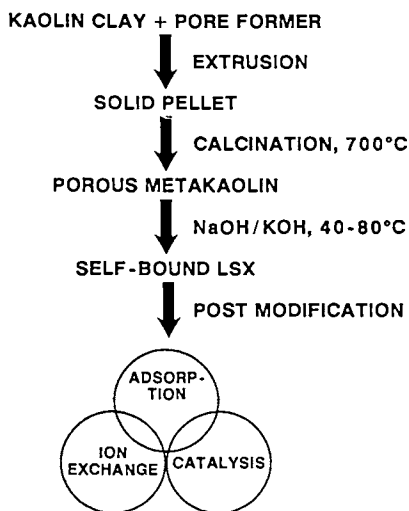
Figure 1. Insitu preparation of a versatile self-bound LSX.

● SELF-BOUND PELLET
○ FINELY POWDERED
── LSX ZEOLITE
── A ZEOLITE
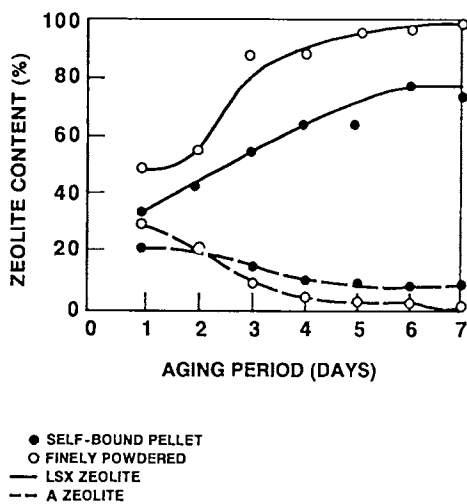
ALL SAMPLES WERE CRYSTALLIZED FOR 8 HOURS AT 100°C
WITH NO AGITATION.

Figure 2. Effect of 50°C aging period on LSX formation.

Extensive work on the formation of LSX from finely powdered metakaolin resulted in the discovery that essentially pure LSX could be prepared in a one-step synthesis without aging using a temperature of 50°C or slightly higher. Crystallization curves for LSX produced by circulating the alkaline mixture continually over the metakaolin at 50°C are shown in Figure 3. In both the powdered and porous pellets, A zeolite did not form if the bases were circulated and the temperature maintained at 50°C. At this temperature, classical crystallization behavior was observed. After an induction period, the LSX crystallinity formation exhibits a smooth S-shaped curve.

Attempts to accelerate LSX formation by increasing the reaction temperature enhanced the formation of A zeolite but diminished the yield of LSX. However, additional studies on powdered metakaolin showed the formation of LSX can be significantly accelerated by chemical means. Ciric has shown that A zeolite, which has a Si/Al ratio of 1.0 and the same structural components as faujasite, has a rate of formation proportional to $[OH^-]^2$ at a given temperature.([15]) Therefore, we were interested in examining how hydroxide concentration influences LSX formation. By reducing the water content to half the amount used in the standard reaction mixture (doubling the concentration of hydroxides), the synthesis was shortened from several days to approximately 1 day. An additional benefit of using less water was a large increase in the amount of LSX produced per unit volume of the reactor. Attempts to apply this to the porous metakaolin pellets were hampered by the lack of sufficient circulation of the viscous synthesis medium. However, we feel there is no chemical reason why similar results for the pellets should not be possible.

Characterization. Our self-bound pellets contained different amounts of LSX and A zeolites depending on the synthetic procedures. The amounts of A and X present were determined using the X-ray diffraction techniques described in the Experimental section. On a line-by-line basis the LSX phase in these products display significantly different X-ray diffraction pattern intensities compared to a standard X zeolite (Si/Al = 1.25). However, summation of all the major peaks for a pure LSX gives a total intensity that is virtually identical to the standard X zeolite. We measured the framework Si/Al ratio present in the pellets directly using solid-state ^{29}Si NMR and also estimated the ratio from the unit cell constant, a_0, using an extrapolation of the linear relationship developed by Breck and Flanigen.([16]) Extrapolation of this correlation gives a lattice constant of 25.02 A for a faujasite having a 1:1 Si/Al ratio. The preferred LSX product, which was crystallized at 50°C, had a unit cell constant of 25.03 A, corresponding to a framework Si/Al of 0.99. Figure 4 shows the ^{29}Si NMR is a single resonance at -85.7 ppm, characteristic of the Si (4Al) group in the zeolite.([17]) The absence of a resonance at -90 ppm indicates there is <5% zeolite A in the pellets.

Bulk elemental analysis confirmed that the calcium form of self-bound LSX pellets has a Si/Al ratio of 0.99 and a calcium exchange capacity of 7.03 mequiv./g on a dry basis. The calcium

exchange capacity was identical to the theoretical value for
pure faujasite or A zeolite having a Si/Al ratio of 1. Also,
the micropore volume determined by oxygen adsorption for the LSX
pellets in the calcium form was 0.325 g/g. This value is
slightly less than that measured for pure CaLSX powder (0.336
g/g), strongly implying that the pellets are completely
converted to a zeolitic phase. The lower value for the LSX is
consistent with the trend observed in going from CaY to CaX
powder (0.378 vs. 0.342) and is due to the presence of
additional cations in the α cage.

   Scanning electron micrographs show that both the porous
metakaolin and the resulting LSX adsorbents have a similar
morphology. A typical micrograph for the LSX pellets (Figure 5)
shows aggregates of cubic crystals with a massive habit, which
incorporate extensive void volume within the pellet. The
self-bound LSX pellets contain well-defined cubic crystalline
masses ranging in size from 1 to 40 μm. The cross-section
shows that to some extent the products of the in situ zeolite
synthesis retain the large macropores present throughout the
porous metakaolin precursor.

   The physical characteristics of the LSX pellets are both
similar to and different from those of typical pelletized X
zeolites. In both cases the total nonzeolitic pore volume is
about 0.25 cc/g, with a bulk density of about 0.65 g/cc on a dry
basis. However, the LSX pellets have a substantially larger
macroporosity than commercially available adsorbents. Median
pore diameters for the self-bound adsorbents vary from 1.5 to
5.0 μm whereas those for typical pelletized X adsorbents are
around 0.1 μm.

   Table 1 compares the pore properties for the starting
metakaolin and the LSX pellets, and Figure 6 plots differential
pore volume distributions for both materials. The pore
distribution data show that the macroporosity of the LSX pellets
is approximately half that of the starting metakaolin. The
difference between pore volumes measured with helium and mercury
is used as an indicator for the microporosity of the sample.
The LSX pellets contain approximately half of their pore volume
in micropores, whereas the porous metakaolin has a negligible
micropore content. The increase in the median pore diameter for
the LSX pellets may be due to a preferential conversion of the
material which surrounds the smaller macropores to zeolite,
resulting in an apparent shift to larger pores.

Table I.   Pore Properties Before and After Conversion to LSX

	Total Pore Volume[a] (cc/g)		Microporosity[b] (cc/g)	Median[c] Pore Dia (μm)
	He	Hg		
Porous Metakaolin	0.716	0.699	0.017	1.64
Self-Bound CaLSX	0.599	0.313	0.286	3.33

a)   1/δHg - 1/δHe equals total pore volume by He
b)   Difference in mercury and helium pore volumes, i.e., <30 A
c)   From mercury intrusion
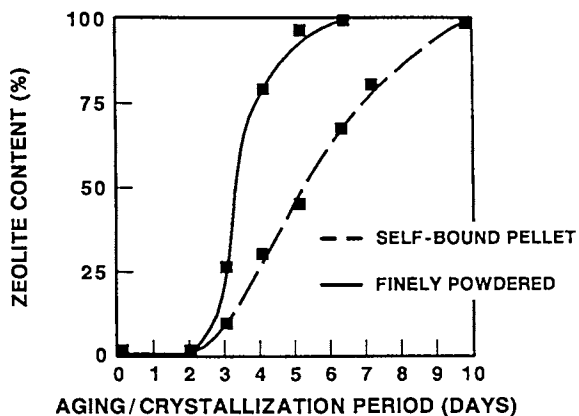
Figure 3. Crystallization of LSX with agitation from standard synthesis mixture at 50°C.
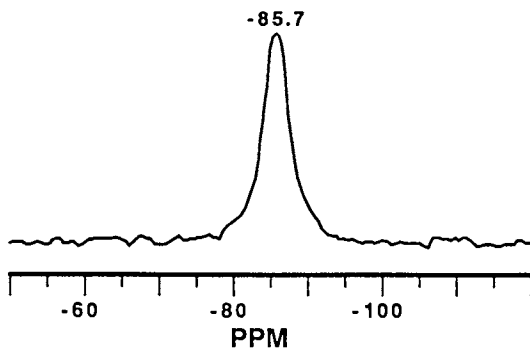
Figure 4. ^{29}Si NMR of self-bound CaLSX.
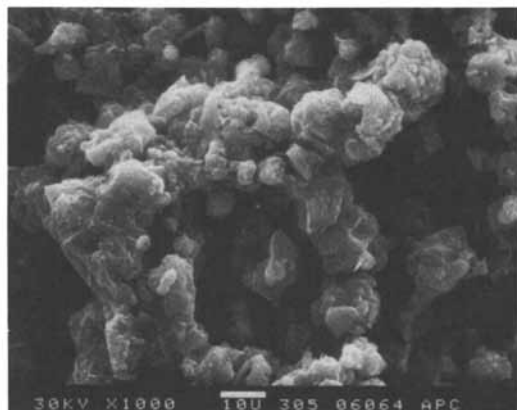
Figure 5. Secondary electron micrograph of the exposed interior of self-bound CaLSX.

The crush strength of the LSX pellets is three to five times higher than that of the starting metakaolin. Crush strengths for the 1/8-in. LSX pellets were about 1.5 lb/mm, compared to 0.3-0.5 lb/mm for the porous metakaolin. Evidently, the conversion to zeolite substantially improves the overall hardness of the pellet, rendering it sturdy enough for use in packed-bed applications.

Air Separation Properties. Self-bound LSX adsorbents have an enhanced ability to selectively adsorb nitrogen from air. For thermodynamically driven adsorption processes, the quantity of a gas adsorbed by a zeolite at a given pressure and temperature is a function of its the affinity for the cationic adsorption sites as well as the quantity of sites available for interaction. Electronic charge balance dictates that the LSX will have the maximum number of cationic sites available for direct interaction with weakly interacting adsorbates. The electric field within the zeolite cavity is dependent on both structure and the charge density of the extra-framework cation. Small polyvalent cations in the dehydrated/dehydroxylated state, especially calcium, show high selectivity for N_2 from air.(12)

We postulated that in the calcium form pure LSX should have about a 20% increase in N_2 capacity due to the increased number of accessible calcium ions. Figure 7 illustrates a typical faujasite structure including the location of selected accessible and inaccessible cation sites. The accessible cation content increases in CaLSX. Standard CaX zeolite (Si/Al = 1.25) has 43 calcium ions per unit cell, whereas LSX has 48. In standard dehydrated CaX, 16 of the calcium ions are in N_2-inaccessible (site I) positions.(18) Assuming that the same siting occurs in LSX, there are 32 N_2 accessible calcium ions in LSX, compared to only 27 in a standard X. This results in an 18.5% increase in the number of accessible cations. This increase has a direct effect on the N_2 equilibrium capacity which for pure LSX showed a 20% increase over conventional X zeolites. Furthermore, compared to commercially available X adsorbents which all contain binders, the self-bound LSX adsorbents do not have any binder to "dilute" the active component and lower the gas capacity.

We carried out packed-bed studies in order to assess the performance of a self-bound CaLSX as an air separation adsorbent. The results from these studies are summarized in Table II. For comparison to standard CaX, we studied a commercial X-type zeolite which is, in fact, a mixture of X and A zeolites (Sample 1, Table II). A-type zeolite in the calcium form is a nitrogen-selective adsorbent in its own right and is commercially employed as such. While the nitrogen capacity of the A phase contributes to the overall nitrogen capacity of the commercial adsorbents, the nitrogen-oxygen selectivity of CaA is known to be significantly lower than that of properly activated CaX. Thus the presence of the A phase acts to dilute the selectivity of mixed-phase adsorbents. To ascertain the properties of a nitrogen-selective adsorbent employing only CaX as the active phase, a sample of commercial Davison NaX
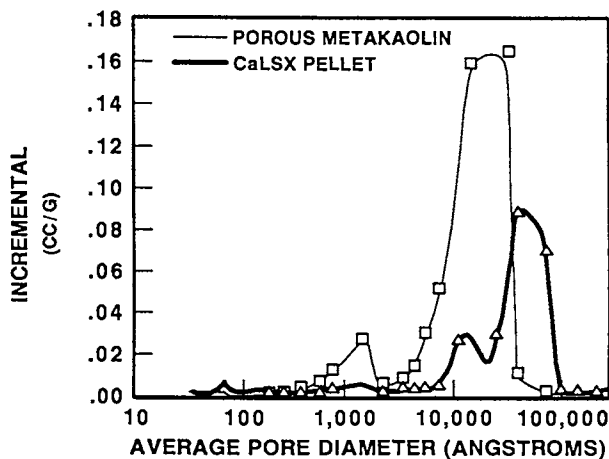
Figure 6.   Pore distribution of self-bound samples.
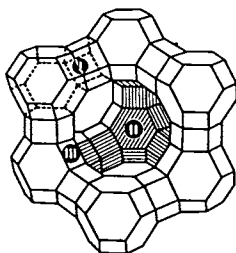
INACCESSIBLE (I)
ACCESSIBLE (II), (III)

	CaX	CaLSX
FORM	PURE POWDER	SELF-BOUND PELLET
Si / Al	1.25	1.0
CHARGES TO BALANCE	86	96
OCCUPIED SITES	43	48
INACCESSIBLE	16	16
ACCESSIBLE	27	32 (18.5%)*
N_2 CAPACITY AT 30°C, 1 ATM (MMOLE/G)	1.15	1.37 (20.0%)*

*IMPROVEMENT OBSERVED OVER PURE CaX POWDER

Figure 7.   Effect of accessible calcium on N_2 adsorption.

containing about 20% inert binder was converted to the calcium
form. CaX exhibited about a 10% enhancement in both N_2/O_2
selectivity and N_2 capacity for the CaX compared to the
mixture of CaX and CaA (Sample 2, Table II).

Table II. Nitrogen Capacity and Selectivity at 30°C and
One Atmosphere Pressure for Selected Adsorbents

Sample No.	% X	% LSX	% A	Calcium Exchange %	N_2/O_2 Selectivity	mequiv./g	
						N_2 Capacity (From Air)	N_2 Capacity (Pure Gas)
1	50	--	20	98	6.8	0.64	0.71
2	75	--	--	98	7.3	0.70	0.78
3	--	60	20	98	8.6	0.88	0.97
4	--	95+	<5	100	10.6	0.83	N.A.
5	--	95+	<5	100	11.5	1.08	1.18

N.A. = Not Available

A self-bound sample containing a mixture of LSX and A zeolite
(sample 3) showed better N_2 adsorption properties than the
standard CaX adsorbents. Not only was the nitrogen capacity
notably higher, but the N_2/O_2 selectivity was improved even
with the A zeolite present. This result was surprising
considering that the A zeolite, having inferior N_2 adsorption
properties, reduced the overall properties of the LSX adsorbent.
    We also studied an essentially pure self-bound LSX in the
calcium form. Our initial evaluation (sample 4) showed the
anticipated rise in selectivity but a nitrogen capacity
significantly below that measured for pure unbound CaLSX. We
postulated that the low capacity resulted from improper thermal
activation of the LSX, since this aluminum-rich adsorbent is
more prone to hydrothermal degradation. The N_2 adsorption
properties of pure CaLSX powder were increased by decreasing the
purge gas residence time during the dehydration of the CaLSX
from 1.4 to 0.6 sec and including three thermal plateaus.
However, even after this vigorous activation, the capacity at
30°C and 1 atmosphere for a packed-bed of CaLSX was about 15%
less than that measured on a 0.5 g sample activated at 400°C in
the vacuum microbalance, i.e., 1.18 vs. 1.37 mmoles of N_2/g.
We believe that the difference in N_2 capacity for a packed-bed
vs. a shallow bed is directly attributable to the poor
hydrothermal stability of this adsorbent. Nevertheless, the
self-bound CaLSX after dehydration in a packed-bed displays the
best air separation properties of any pelletized N_2-selective
adsorbent reported.

Conclusion

We prepared effective LSX type adsorbents on a laboratory scale
as essentially pure self-bound aggregates. At 50°C under
continual circulation in a highly alkaline solution of mixed

sodium and potassium hydroxide, porous metakaolin pellets are converted to LSX. The LSX pellets maintain morphology of the metakaolin and have acceptable physical properties for use in packed-bed adsorption processes. The N_2 capacity observed for the calcium form of this adsorbent is that predicted for a pure faujasite having the maximum number of accessible calcium ions. Air separation properties (both N_2/O_2 selectivity and N_2 capacity) for CaLSX are superior to any other pelletized N_2 selective adsorbent reported.

Acknowledgments

Literature Cited

1. Coe, C. G.; Parris, G. E.; Srinivasan, R.; Auvil, S. R. In *New Developments in Zeolite Science and Technology- Proceedings of the 7th International Zeolite Conference, Tokyo*, Iijima, A.; Ward, J. W.; Murakami, Y.; Ed., Elsevier, New York, 1986, p. 1033.
2. Neddenriep, R. J. *J. Colloid Interface Sci.* 1968, 28, 293.
3. Roberts, C. W. In *The Properties and Applications of Zeolites*; Chemical Society, London, 1980, Special Publication No. 33, p. 103.
4. Kuhl, G. H.; Sherry, H. S. *Proceedings of the Fifth International Conference on Zeolites*; Rees, L. V., Ed.; Heyden Publications: London, 1980; p. 813.
5. Breck, D. W. In *Zeolite Molecular Sieves*; John Wiley & Sons: New York, 1974, p. 315.
6. Howell, P. A.; Acara, Nancy A. U.S. Patent 3 119 660, 1964.
7. Hoffman, G. W. U.S. Patent 3 733 391, 1973.
8. Plank, C. J.; Rosinski, E. J. U.S. Patent 3 459 501, 1969.
9. Flank, W. H.; McEvoy, J. E.; Mills, G. A. U.S. Patent 3 515 681, 1970.
10. Kuhl, G. H.; Sherry, H. S. G.B. Patent 1 580 928, 1980.
11. Barrer, R. M.; Mainwaring, D. E. *JCS Dalton*, 1972, 2534.
12. Coe, C. G.; Kuznicki, S. M. U.S. Patent 4 481 018, 1984.
13. Barrer, R. M. In *Hydrothermal Chemistry of Zeolites*, Academic Press: New York, 1982, p. 256.
14. Breck, D. W. op. cit. p. 314.
15. Ciric, J. *J. Colloid Interface Science*, 1968, 28, 315.
16. Breck, D. W.; Flanigen, E. M. In *Molecular Sieves*, Society of Chemical Industry, London, 1968, p. 47.
17. Klinowski, J.; Ramdas, S.; Thomas, J. M.; Fyfe, C. A.; Hartman, J. S. *J. Chem. Soc., Faraday Trans. 2*, 1982, 78, 1025-1050.
18. Mortier, J. "Compilation of Extra Framework Sites in Zeolites", Butterworth & Co.: London, 1982.

Chapter 31

Methanol Conversion on Ceramic Honeycombs Coated with Silicalite

M. D. Patil and I. M. Lachman

Corning Glass Works, SP–DV–19, Corning, NY 14831

Silicalite, a pentasil type zeolite was washcoated on a
cordierite ceramic honeycomb using a silica binder
derived from prehydrolyzed ethyl-orthosilicate. Binder
content in the washcoat was varied from 10% to 40% to
determine the effect on blocking the zeolite active
sites. Methanol conversions on H-silicalite/honeycombs
were conducted on four samples with different binder
contents. Percentage of methanol conversion was
calculated per gram of zeolite present in the washcoat.
Highest methanol conversions for 10% and 20% binder in
washcoat indicate maximum availability of active sites
of the zeolite; whereas, lower methanol conversion was
observed for 30% and 40% binder content indicating the
blockage of some active sites of the zeolite. A washcoat
with 20% and 30% binder content gave higher loading than
10% binder and good binding to the cordierite surface.
The washcoat made with 40% binder content gave the
highest loading and excellent binding to the honeycomb
substrate. Thus 20-30% binder in the washcoat combines
excellent adhesion, high loading of catalyst with high
catalytic activity. A methanol conversion was also
conducted on extruded silicalite honeycomb with alumina
binder.

Catalysts in thin-wall honeycomb form offer the advantages of low
pressure drop, high geometric surface area, and short diffusion
distance as compared to conventional pellets and beads in fixed bed
reactors (1). Active zeolite catalysts may be extruded in the form
of a honeycomb structure or they may be washcoated on ceramic
honeycomb substrates. The latter technique has been widely used in
automotive emissions control (2), woodstove combustors (3), control
of volatile organic emissions from organic solvents (4), ozone
abatement in jet aircraft passenger cabins (5), and NO_x abatement

from industrial emissions (6). However, washcoats of zeolite catalysts have not yet been exploited in the chemical process industries.

A pentasil type zeolite (ZSM-5) is being used in a methanol to gasoline (MTG) conversion process (7) in a fixed bed reactor. This type of zeolite when washcoated on ceramic honeycomb substrates should offer the advantages of lower pressure drop and high geometric surface area in the reactor. Such washcoated zeolite catalysts must be strongly bound to the honeycomb substrate and should have the maximum number of active sites for highest catalytic activity for chemical process applications.

Thus the objective of this study is to find the best combination of binder and zeolite composition for washcoating silicalite (a pentasil type zeolite) on a ceramic honeycomb substrate, and to evaluate the catalytic activity for methanol conversion. This will demonstrate the utility of zeolite honeycomb catalysts for chemical processing.

Silicalite honeycombs were also prepared by extrusion and similarly evaluated.

Experimental

Standard cordierite honeycombs (Corning code 9475) with 400 channels/in.^{2} were core-drilled (1" diameter) and cut into 1" length pieces. These pieces were acid leached (8) in 1.5 N HNO_3 solution for 2 hours at 95°C in preparation for washcoating. A leached cordierite surface provides better bonding for the subsequent washcoat than the as-fired surface. After leaching and washing, the samples were dried in an oven at 100°C for 16 hours. The percentage weight loss is given in Table 1.

Table 1: Percentage weight loss of cordierite honeycomb pieces (1" diameter x 1" length) after leaching in 1.5 N HNO_3 at 95°C for 2 hours

Sample No.	Wt. before leaching (g)	Wt. after leaching (g)	% Wt. Loss
1	5.15	4.90	4.85
2	5.24	4.98	4.96
3	5.16	4.91	4.84
4	5.31	5.05	4.90
5	5.73	5.46	4.71
6	5.47	5.20	4.94

Cordierite is Corning's Celcor substrate code 9475 with 400 squares/in.^{2}, 0.16 mm wall.

For washcoat preparation silicalite zeolite powder (S-115 from
Union Carbide Corp.) was dried at 100°C in an oven overnight.
Prehydrolyzed ethyl-orthosilicate containing 19.5% silica (Silbond
H-5 from Stauffer Chemical Co.) was the source of the silica binder.
Absolute ethanol (from U.S. Industrial Chemicals Co.) and absolute
methanol (reagent grade from J. T. Baker Company) were used without
further purification for the liquid portion of the washcoat slurry
and for the methanol conversion reaction, respectively. Reagent
grade ammonium nitrate (from J. T. Baker) was used for ion-exchange
purposes.

The washcoat slurry was prepared by slowly adding a known
amount of silicalite to a stirred solution of a known amount of
Silbond H-5. After complete addition of silicalite the mixture was
stirred for another 15-30 minutes. Slurry mixtures with different
solid to liquid ratios were made by diluting the mixtures with
absolute ethanol.

Leached cordierite honeycomb pieces were immersed completely
into stirred washcoat slurries and after removal the channels were
cleared of excess slurry by blowing with compressed air. Samples
were then dried in air for 3-5 hours. This coating procedure was
repeated, generally two more times, until sufficient coating was
achieved. After coating, samples were dried in an oven at 100°C for
16 hours and fired at 500°C for 6 hours. The percentage of washcoat
loading, Table 2, was calculated by weighing the samples before and
after coating.

Table 2: Silicalite concentration in washcoated (silica binder) or
extruded (alumina binder) honeycomb pieces, 1" (diameter) x 1"
(length)

Sample* Code	Zeolite/ Binder	Wt. Before Coating(g)	Wt. after coating(g)	%Wt. loading	Silicalite (g)
A	90:10	5.16	5.81	11.2	0.58
B	90:10	5.19	5.84	11.1	0.58
C	80:20	5.15	6.30	18.2	0.92
D	80:20	5.29	6.08	13.0	0.63
E	70:30	5.21	6.53	20.2	0.92
F	70:30	5.20	6.48	19.7	0.90
G	60:40	5.12	7.31	30.0	1.31
H	60:40	5.16	7.44	30.6	1.37
I (Extruded)	84:16	--	--	--	3.80

* Samples A to H were washcoated on leached cordierite honeycombs
and sample I was extruded with 16% alumina binder.
All washcoat slurry mixtures had 30% (wt.) of solids.

Selected samples were immersed in 10% ammonium nitrate solution overnight at room temperature to exchange NH_4^+ for Na^+ ions in the silicalite. The immersed samples were washed with distilled water, dried, and fired at 500°C for 6 hours to decompose the NH_4^+ ion to H^+ ion and thus give a H-silicalite coated honeycomb.

Extruded silicalite zeolite honeycombs were also prepared by well known procedures (9,10). Silicalite zeolite powder (Union Carbide Corp. S-115) was extruded with a boehmite alumina (Vista Chemical Catapal D) which forms a gamma alumina binder phase after heat treatment. The final composition is 84% silicalite + 16% gamma alumina. These extruded honeycomb samples were ion-exchanged and evaluated in the same way as the washcoated ones.

The methanol conversion reaction was carried out over these H-silicalite/honeycomb samples in a reactor set up as shown in Figure 1. Absolute methanol was injected into an evaporator at the rate of 0.49 ml/hour. Dry helium, a diluent gas, was passed into the evaporator at a rate of 45 ml/minute. Gaseous products were directly passed via a heated line through a six port Valco valve with a 0.25 ml sample loop. The products were analyzed by a Varian 6000 GC with a Chromosorb-102 column. For each sample, reaction runs were made for at least 50 hours and steady state conversion data were collected. Methanol conversion was monitored at different catalytic reaction temperatures: 100°C, 150°C, and 250°C. However, percent methanol conversions were calculated only for the 100°C and 150°C runs. Methanol conversion, calculated per gram of zeolite in the washcoat, was plotted (Figure 2) vs. percentage binder content.

Results and Discussion

Automotive emission control catalysts and woodstove combustor catalysts are washcoated on highly porous cordierite honeycomb substrates. Gamma alumina is the principle binding phase for these commercial products. Silicalite zeolite catalysts in this study were washcoated similarly onto porous cordierite honeycomb substrates but with a silica binder. In preparation for washcoating, the cordierite honeycomb substrates were acid leached (8) for two hours at 95°C with 1.5 N HNO_3 because leaching selectively removes alumina and magnesia from cordierite crystallites and leaves a high surface area microporous silica phase. Acid leaching of cordierite honeycomb substrates under these conditions (Table 1) shows a weight loss of 5%. Earlier results by Elmer (8), suggest a surface area of 20-40 m2/g for similarly leached honeycombs, which still retain 80% of their original crushing strength. A surface of microporous silica is desirable for washcoating with zeolites using a silica binder because strong binding appears to develop between the coating and the leached substrate.

Silicalite washcoat results given in Table 2 indicate the weight loadings attained with different binder contents in the washcoat slurry. Generally weight loading increases as the binder content in the slurry increases. Sometimes loading with the same composition slurry may not be reproducible (e.g., samples C and D) because of channel blocking with the slurry. Generally a continuously mixed slurry gives consistent loading of the washcoat on the cordierite substrate. A thick viscous slurry (with high

solids content) gives a non-uniform and inconsistent loading, whereas a thin fluid slurry with a low solids content gives a low but consistent loading. Thus a compromise in the solids content of the slurry is necessary to get good washcoating with consistent loading. A solids content of 30-40% by weight in the slurry gave best results in this case for uniformity and consistent loading.

Figure 3 shows three optical micrographs: (a) an uncoated cordierite honeycomb substrate and two washcoated honeycomb substrates, (b) 20% silica binder, and (c) 40% silica binder. Figure 3(c), 40% silica binder, shows shrinkage cracks, whereas in Figure 3(b), 20% silica binder, there are no apparent cracks. Higher drying and firing shrinkage is expected in case of 40% silica binder content as compared to the 20% silica binder. The washcoats were uniform for all the samples and appeared strongly bound to the honeycomb substrates.

All washcoated samples and extruded honeycomb samples were exchanged with NH_4^+ ion to get H-silicalite after firing at 500°C for 6 hrs. H-silicalite coated or extruded honeycombs were loaded into a 1" diameter reactor as shown in Figure 1. Methanol conversion was monitored by gas chromatographic analysis of gaseous products. Percent methanol conversions were calculated only for the 100°C and 150°C temperature runs. There was virtually no conversion at 100°C. It is assumed only active zeolite sites convert methanol to hydrocarbons and the degree of conversion at 150°C is therefore a function of total available active zeolite sites. Thus percent methanol conversion is calculated per gram of zeolite in the honeycomb sample in order to compare the blockage of active sites. Methanol conversion (Figure 2) per gram of zeolite decreases as the percentage binder content increases in the washcoat. The washcoated sample with 90% zeolite and 10% silica binder has the highest methanol conversion, 37.6%, whereas the lowest methanol conversion, 15.3%, is observed for the sample with 60% zeolite and 40% silica binder. This indicates the available active zeolite sites decrease as the binder content in the washcoat increases. Blockage from the binder is the most likely cause of the decrease in these active zeolite sites. These results indicate about 60 percent of the active sites are blocked in sample G (40% silica binder) as compared to sample A (10% silica binder). For this calculation it is assumed that there is no blockage in sample A, even though a small amount must be present.

A low 12% methanol conversion per gram of zeolite was observed for extruded H-silicalite with 16% alumina binder. A comparison of 12% methanol conversion activity to 37.6% for the washcoated zeolite with 10% silica binder indicates about 68% blockage or impedance to the active sites under the given test conditions.

Conclusions

Zeolite catalysts, either in extruded honeycombs or washcoated on honeycomb substrates, show good catalytic activity for methanol conversion.

Availability of active zeolite sites is important for catalytic reactions. The data show that active zeolite sites in washcoated honeycombs may be optimized by the amount of binder in the washcoat.
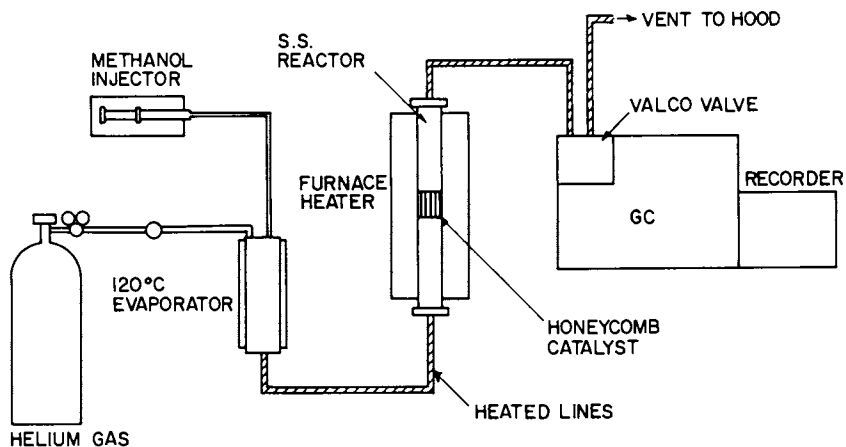
Figure 1.   Schematic of reactor system.
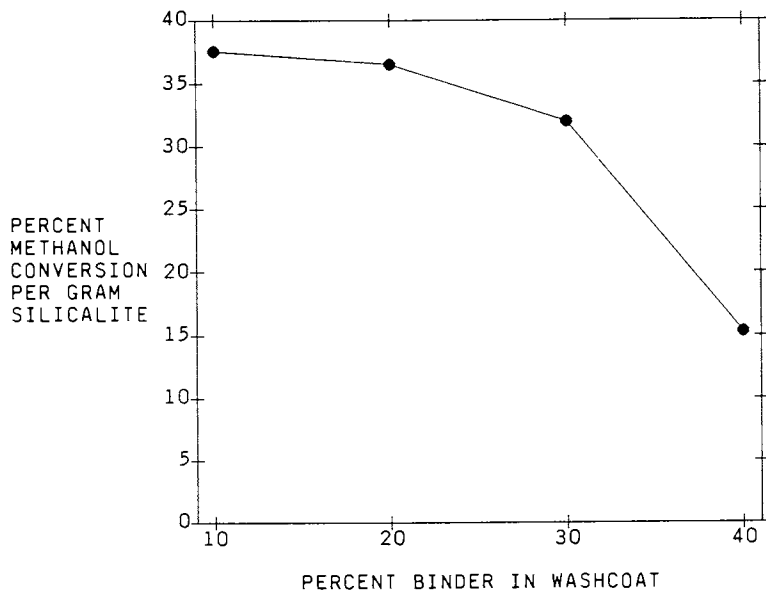
Figure 2.   Percent methanol conversion per gram of silicalite versus percent binder in washcoat.
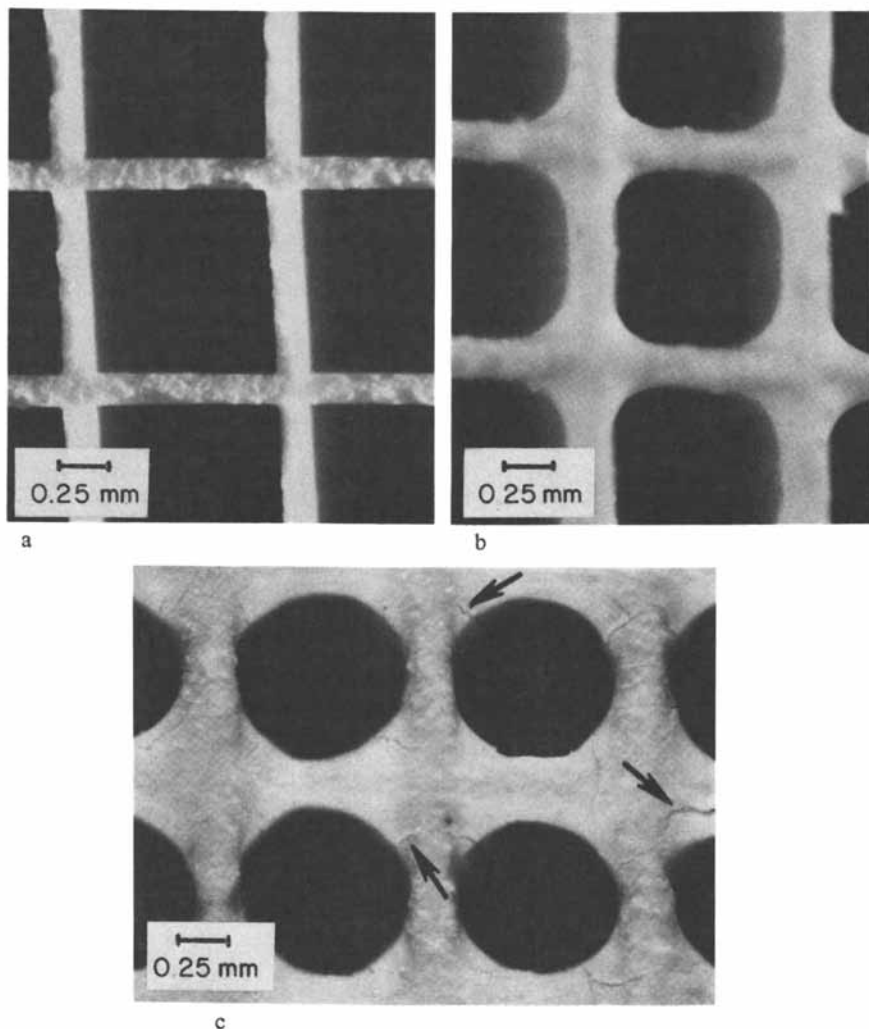
Figure 3. Optical micrographs of uncoated and washcoated cordierite honeycomb substrates. (a) Uncoated honeycomb, (b) 18.2% washcoat (80% silicalite + 20% silica binder), and (c) 30% washcoat (60% silicalite + 40% silica binder).

Extruded zeolite catalysts offer higher zeolite content per unit volume, which increases the overall catalytic activity.

These results demonstrate that zeolite catalysts perform well in honeycomb form. This is similar to the well established use of noble metals/gamma alumina washcoats on cordierite honeycombs for automotive emission control. This geometrical form offers the advantages of low pressure drop, high geometric surface area, and short diffusion distance in a fixed bed reactor.

References

1)   Deluca, J. P., and Campbell, L. L., Thin Wall Ceramics as Monolithic Catalyst Supports; Advanced Materials in Catalysis, Academic Press, Inc., 1977; Chapter 10.
2)   Howitt, J. S., Ceramic Industry 1975, 104, 19; Thin Wall Ceramics as Monolithic Catalyst Supports; SAE Tech Paper No. 800082 (1980).
3)   Vara, J., Woodburning: The Catalytic Combustor comes of Age; Country Journal, Nov. 1982, pp 92–99.
4)   Kenson, R. E., Chemical Engineering Progress. Nov. 1985, 57.
5)   Bonacci, J. C., Egbert, W., Collions, M. F., and Heck, R. M., Proceedings of the 6th Annual Conference held at Newport Beach CA, 1982; Precious Metals 1983, pp 29–44.
6)   Harrison, B., Diwell, A. F., and Wyatt, M., Platinum Metals Rev. 1985, 29, (2) 50–56.
7)   Chang, C. D., Kuo, J. C. W., Lang, W. H., Jacob, S. M., Wise, J. J., and Silvestri, A. J., Ind. Eng. Chem. Process Res. Dev. 1978, Vol. 17, 225.
8)   Elmer, T. H., Ceramic Eng. and Sci. Proceedings 1986, Vol. 7, No. 1–2, 40–51.
9)   Lachman, I. M., Bagley, R. D., and Lewis, R. M., Amer. Ceramic Soc. Bull. 1981, 60, No. 2, p. 202–5.
10) Lachman, I. M., and Nordlie, L. A., U.S. Patent No. 4,631,267, Dec. 23, 1986.

Chapter 32

Lead Removal from Wastewaters Using Chabazite Tuff

Carmine Colella[1] and Michele Pansini[2]

[1]Dipartimento di Chimica, Ingegneria Chimica e Materiali, Università de L'Aquila, 67040 Monteluco di Roio (AQ), Italy
[2]Dipartimento di Ingegneria dei Materiali e della Produzione, Università di Napoli, Piazzale Tecchio 80, 80125 Napoli, Italy

The possible use of Campanian tuff, namely chabazite tuff, in the removal of lead from wastewaters has been evaluated, either in static experiments or testing fixed beds eluted by solutions of the pollutant with or without the addition of interfering cations. Through the computation of breakthrough curves, ion exchange dynamic data have been collected, pointing out the good performances of the beds, at least when the concentration of interfering cations is comparable to that of lead. On the ground of the results obtained, perspectives of use in lead decontamination from wastewaters of storage batteries manufacturing industries and ceramic factories have been at last foreseen.

Among the various applications of natural zeolites in sectors of technical significance, the use in the control and abatement of environmental pollution is gaining increasing interest all over the world. Copious references on this are found in the introductory plenary lectures of the three International Conferences on natural zeolites held in the last years (1-3). Focusing our attention on the wastawaters pollution abatement, it may be observed that not more than two or three zeolites (clinoptilolite, mordenite and phillipsite) have been considered until now for removal of cationic pollutants from waters, and that the recourse to ion exchange processes has been limited to the treatment of few cations, substantially ammonium, cesium and strontium. Lack of data is found for instance in the literature on the use of natural zeolites for the removal of heavy metals (4-5), even if these are common

pollutants and several zeolites are known to have excellent selectivies for them (6). Moreover, ion exchange may be particularly attractive, either because it may allow the recovery of removed species, or because it gives rise to stoichiometric reactions even when pollutant concentration is not constant over time.

        An example of a cationic pollutant which might be treated by ion exchange is lead, a metal widely employed by several industries and discharged at levels of tens and sometimes hundreds of milligrams per liter (7). Lead removal is usually performed by precipitation as hydroxide or sulfide, but the results are sometimes unsatisfactory (hydroxide) (8), sometimes good but conditioned by the abatement of the excess reactant (sulfide) (9). A careful lead removal (usually up to 0.1 $mg \cdot l^{-1}$ or less) is on the other hand necessary, since the metal which reaches man directly or, more frequently, through the food chain, may give rise to saturnism at levels as low as 0.8 $mg \cdot Kg^{-1}$ (10).

        The previous considerations and the knowledge of the high selectivity of chabazite for lead (11) suggest research on the possible use of Campanian tuff (namely chabazite tuff) (12) for lead removal from wastewater. Recent studies have emphasized the good behaviour of the tuff either in equilibrium (E. Torracca, P. Galli, private communication) or dynamic tests, carried out with model solutions of only lead (M. Pansini, C. Colella, to be published).

        The aim of the present research is to complete the preliminary investigation on a fixed bed, extending it to model waters containing interfering cations, which simulate wastewaters of the main industries employing lead.

Experimental

Materials. Campanian tuff is a volcanic rock cropping out over an area of about 500 Km^2, mainly in the Campanian Plain, north of Naples. It consists substantially of volcanic ash with scant pumice, lithic and scoriaceous lapilli, and crystals of sanidine, pyroxene and biotite, cemented all together by finely crystalline zeolite, usually chabazite and phillipsite, the former being normally predominant over the latter. The tuff sample used in the present study, coming from the quarries of San Mango sul Calore, 50 Km east of Naples, is typically monozeolitic, containing only chabazite. Data on its chemical, mineralogical and technical features have been reported elsewhere (12).

        The above sample has been ground and sieved and the 30x50 mesh grain size fraction chosen for the column tests. The chemical analysis of the grains has given the following results: SiO_2 51.60%; Al_2O_3 17.20%; Fe_2O_3 4.15%; Na_2O 1.45%; K_2O 5.50%; CaO 3.45%;

MgO 1.50%; BaO 0.20%; H_2O 14.80%, which is very close to those
reported for the parent rock (12), showing the substantial chemical
uniformity of the material. Chabazite content of the grains evaluat-
ed through water vapour desorption technique (12,13) on both Na-
and K-exchanged samples, has turned out to be close to 55% (mean
value).

Cation exchange capacity (CEC). CEC has been measured by several
techniques: i) it has been calculated, starting from zeolite content
(see above), on the basis of the known CEC of the pure phase, 3.12
$meq \cdot g^{-1}$ (12); ii) it has been measured, evaluating Na^+, K^+, Ca^{++}
and Mg^{++} amounts eluted by percolating 1M Na^+ or K^+ warm solutions
through two weighed samples of tuff grains, until the concentration
of the released ions was less than $0.5 \cdot mg \ l^{-1}$; iii) it has been
determined from the lead breakthrough curves, estimating through
graphical integration the area above the S-curve up to exhaustion
(M. Pansini, C. Colella, to be published). Figure 1 summarizes
the data collected. The mean value of CEC has turned out to be
$1.70 \pm 0.03 \ meq \cdot g^{-1}$. This value looks also as the most probable,
since the data from ion exchange tests might be too high (run ii),
because of some cation amounts contributed by the volcanic ash
contained in the tuff (14), or too low (run iii), because of the
greater difficulty of the entering cation (Pb^{++}) to occupy some
less accessible exchange sites in column runs.

Ion exchange runs. Fixed beds have been obtained, allowing wet
tuff grains to tightly accomodate into glass columns. Bed have
been Na-exchanged beforehand and percolated by lead solutions with
or without interfering cations, usually prepared from reagent grade
nitrates or chlorides. Flow rate constancy has been assured by
a peristaltic pump (Pharmacia Mod. P-3), effluent solutions collect-
ed by a fraction collector (Pharmacia Mod. PF-3). As a rule tuff
beds have been eluted until completion of lead breakthrough curves
(exhaustion) and then regenerated downwards by 1M $NaNO_3$ solutions.
Table I reports the operating conditions adopted in the dynamic
runs.

Table I
Column Operating Conditions

Equipment Specifications			Service Conditions	
Column diameter	1.43	cm	Feed composition	3.0-110 $mg \cdot l^{-1}$ Pb^{++}
Bed depth	40	cm	Feed flow rate	6.0-10.8 $ml \cdot min^{-1}$
Weight of tuff	51.6	g	Holdup Time	5.9-10.7 min

Referring to feed flow rate it has to be pointed out that values
higher than about 10 $ml \cdot min^{-1}$ result in unreliable column operations
(M. Pansini, C. Colella, to be published).
    Lead uptake curves have been obtained, evaluating Na^+ amount

released, as a function of time, by 1-gram samples of Na-exchanged tuff grains, contacted under stirring with 1-liter of 2.5 or 5 meq·l^{-1} Pb^{++} solutions.

Analytical procedures. Outgoing or released cations (Pb^{++}, Na^{+}, K^{+}, Ca^{++}, Mg^{++}) have been determined by atomic absorption spectrofotometry (Perkin-Elmer 300 S).

Results and Discussion

Figure 2 shows the elongated form of the lead breakthrough curve on Campanian tuff in its original composition, treated by 110 mg· l^{-1} Pb^{++} solution at a feed flow rate equal to 6 ml·min^{-1}. The remaining curves reported in the same figure point out the sequence of cation elution, in relation to: i) affinity for the zeolite; ii) exchange kinetics ; iii) cation concentration in the zeolite. Calcium appears to be more difficultly removable than the other cations, most likely because of kinetic reasons, being that chabazite is surely more selective for potassium and sodium than for calcium (6); sodium, for which chabazite is less selective than for lead (11) , is on the contrary easily exchangeable, supporting the choice of such cation as regenerant, and suggesting accordingly to operate with Na-exchanged tuff beds.

Figure 3A shows the kinetic curves of lead uptake from 2.5 or 5 meq·l^{-1} Pb^{++} solutions by Na-exchanged tuff grains. Points are rather scattered because kinetics are conditioned by solution diffusion into tuff grains and ion migration to the outside. Nevertheless it is clear that exchange is very fast, so much so that equilibrium is attained in about one hour. From the interpolated curves of Fig. 3A the kinetic order of the exchange reaction may be worked out. The straight line of Fig. 3B, obtained from the more reliable upper curve of Fig. 3A, demonstrates that the kinetic order is two, since the reciprocal of the number of exchange sites per mass unit (c_o - c) available in the zeolite is a linear function of time, according to the relation obtained from integration of the differential equation:

$$- \frac{dc}{dt} = K (c_o - c)^2$$

The slope of the line, which is the rate constant K, turns out to be 0.13 l·meq^{-1}·min^{-1}, a value very close to, but higher than that obtained with clinoptilolite and the same cation (4).

Figure 4 reports a typical lead breakthrough curve (squares) obtained with a solution of only Pb^{++}, i.e. without any interfering cation (feed composition: 100 mg·l^{-1} Pb^{++}, feed flow rate: 6 ml· min^{-1}). The curve appears very narrow and sharp, confirming the
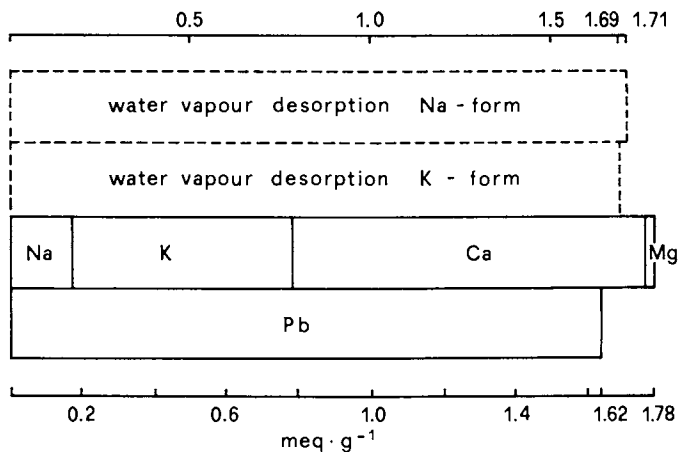
Figure 1. Schematic representation of chabazite tuff cation exchange capacity (CEC). Solid lines : CEC from ion exchange tests; dashed lines : CEC calculated from zeolite content (see experimental).
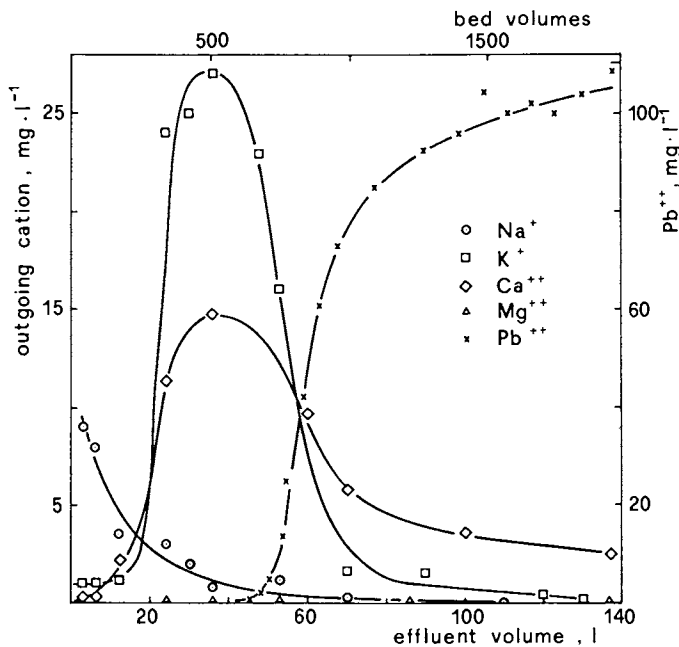
Figure 2. Cation elution curves (left scale) and lead break-through curve (right scale) on chabazite tuff bed in its original cationic composition. Feed composition: 110 mg·l^{-1} Pb^{++}; feed flow rate: 6 ml·min^{-1} .
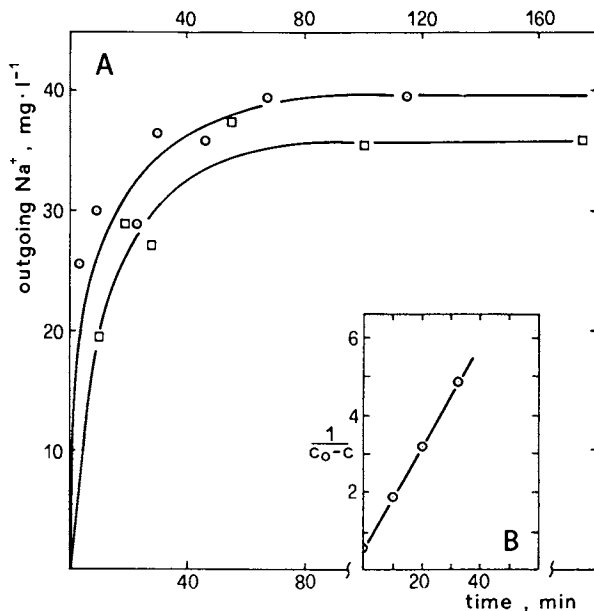
Figure 3.   A: Kinetics of lead uptake from 2.5 (squares) or 5 mN (circles) Pb^{++} solutions by Na-exchanged tuff grains. Solid to liquid ratio 1:1000. B: Reaction order kinetic plot, c,c_o =actual and final Pb^{++} concentration in the zeolite $(meq \cdot g^{-1})$ or actual and final Na^+ concentration in the solution $(meq \cdot l^{-1})$.
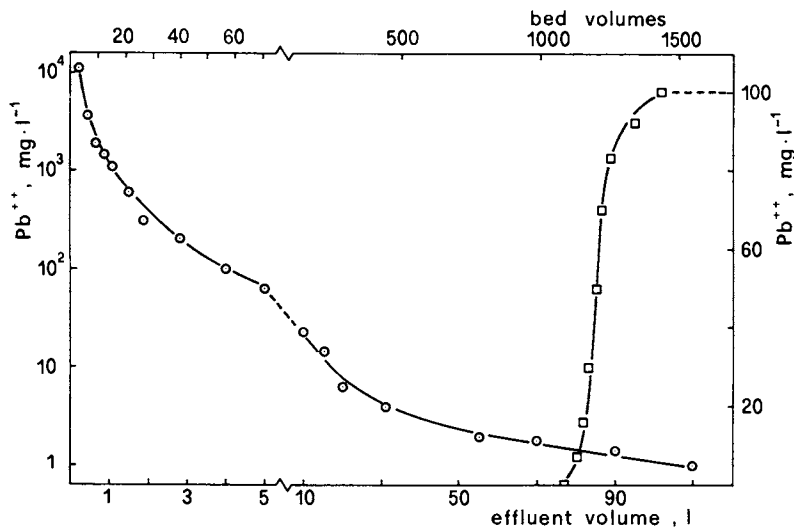
Figure 4.   Typical lead breakthrough curve (squares, right scale) and lead elution curve (circles, left scale) on Na-exchanged chabazite tuff bed. Feed or regenerant flow rate: 6 $ml \cdot min^{-1}$; feed composition: 100 $mg \cdot l^{-1}$ Pb^{++}.

considerable affinity of the cation for the Na-form of chabazite. In the same figure a bed regeneration curve (circles) is also reported (regenerant flow rate: 6 ml·min^{-1}). Regeneration has been carried out by NaNO$_3$. NaCl must be avoided, because of the possibility of PbCl$_2$ precipitation in the early stages of the operation, when Pb^{++} concentration in solution is very high. The regeneration curve appears rather steep, at least in the first tract, which indicates that most of the lead may be removed rather easily. As an example, a rough computation of the two curves in Fig. 4 shows that, using 20 regenerant bed volumes ($\simeq$1.4 l), the extent of regeneration approximates 80%, while with 200 bed volumes ($\simeq$14 l), it reaches hardly 85%. The optimization of this operation, however, is not an object of the present research and is deferred to a successive more specific study.

The investigation of the role played by interfering cations on lead removal by chabazite tuff has been performed, keeping in mind real cases. As the main industries discharging lead are those manufacturing storage batteries and antiknock compounds (7), both of them involving more or less directly sodium as interferent, lead removal runs have been carried out in the presence of variable amounts of that cation. Fig. 5 shows three lead breakthrough curves on Na-exchanged chabazite tuff bed, treated at a feed flow rate of 6 ml·min^{-1} with 100 mg·l^{-1} Pb^{++} solutions, containing in addition 1 g·l^{-1} (triangles), 5 g·l^{-1} (squares) or 15 g·l^{-1} (circles) NaCl (note that in these cases the PbCl$_2$ solubility product is not reached). Table II reports the values of the dynamic parameters obtained using the mass transfer zone (MTZ) method (15) and the mathematics describing the relative column model (16).

Table II

Dynamic Data from Lead Breakthrough Curve

Ref.	Interferent	MTZ length cm	Pb-CEC[1] meq·g^{-1}	WEC[2] meq·g^{-1}	S[*]	E[**]
Fig. 4	–	11.9	1.62	1.44	1.00	0.89
Fig. 5	NaCl 1g·l^{-1}	27.3	1.48	1.24	0.91	0.76
Fig. 5	NaCl 5g·l^{-1}	56.6	1.07	0.66	0.66	0.41
Fig. 5	NaCl 15g·l^{-1}	143.9	0.43	0.18	0.26	0.11
Fig. 6	§	51.4	0.93	0.42	0.57	0.26

§ Na$^+$ =Mg^{++} =1·10^{-3}M; Ca^{++}=1.5·10^{-3}M; K$^+$ =1·10^{-4}M.

[1]CEC= cation exchange capacity; [2]WEC= working Pb-CEC (i.e., lead CEC at the breakthrough point); [*]Selectivity (Pb-CEC /CEC); [**] Overall efficiency (WEC /CEC).

It may be seen that the addition of 5 or especially 15 $g \cdot l^{-1}$ NaCl gives rise to unreliable column data, as MTZ length turns out longer than bed depth (17). This is perhaps the reason why some lead leakage is recorded before breakthrough points (Fig. 5). These runs point out moreover low dynamic selectivities of tuff bed for lead and low overall efficiencies. This leaves out the possibility that chabazite tuff may be used for removing lead from tetraethyl lead industry wastewaters, because of the elevated NaCl content of these waters (18). On the contrary Table 2 shows that Na^+ contents corresponding to 1 $g \cdot l^{-1}$ NaCl or less do not cut down significantly either selectivity or efficiency. This allows us to foresee a possible application of chabazite tuff in lead removal from rinse waters of storage battery cells, provided that sulfuric acid is beforehand neutralized by NaOH solution. That is why a simulation test has been programmed, starting from a 3 $mg \cdot l^{-1}$ Pb^{++} solution, saturated with H_2SO_4 (pH= 2.6) and then neutralized. This leads to a Na^+ content of about 65 $mg \cdot l^{-1}$. Given the very low Pb^{++} concentration, a long lasting run is expected: at present about 600 l (roughly 8500 bed volumes) have been already percolated and only about 20% of total exchange capacity utilized.

Another simple model of water lead pollution is that of the wastewaters of ceramic industries (9,19). Here Pb^{++} concentration is at a level of a few tens of $mg \cdot l^{-1}$ and the interfering cations are only those present in the natural water matrix. A simulation test has been performed, treating the tuff bed with 28 $mg \cdot l^{-1}$ Pb^{++} solution, containing also Na^+ ($1 \cdot 10^{-3}$M), K^+ ($1 \cdot 10^{-4}$M), Ca^{++} ($1.5 \cdot 10^{-3}$M) and Mg^{++} ($1 \cdot 10^{-3}$M). A higher feed flow rate (10.8 $ml \cdot min^{-1}$) has been tested for obtaining data at lower holdup times (5.9 min in this case compared with 10.7 min in the previous ones). Fig. 6 reports the lead breakthrough curve obtained in this run and Table II (last line) presents the dynamic data deduced from the curve. It may be noticed that also in this experiment MTZ length is larger than bed depth. This may be corrected using higher bed depths and lower feed flow rates, which possibly eliminate also some lead leakage before the breakthrough point. The data of Table II show however that, even in unfavourable conditions, about 57% of the original cation exchange capacity is kept for lead and that more than 45% of this is employable for lead abatement.

Conclusions

The results of the present research allow one to foresee good perspectives on the use of Campanian tuff in lead abatement from wastewaters. Chabazite in fact shows good selectivity for the pollutant, also in the presence of considerable amounts of interfering cations, and high exchange rate. Applications may be expected
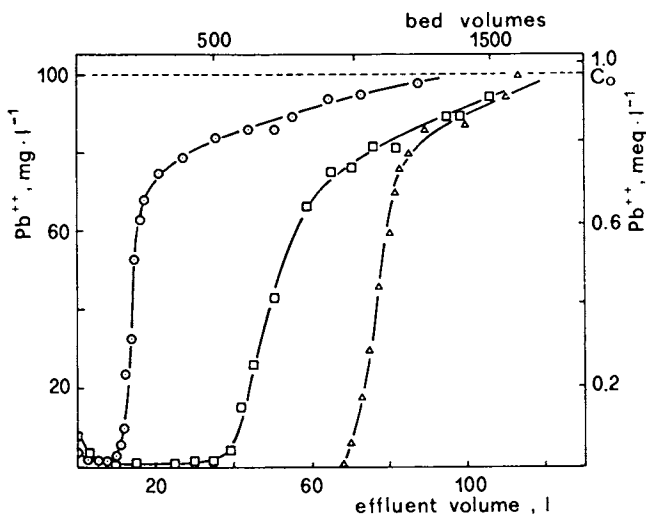
Figure 5.   Lead breakthrough curves on Na-exchanged chabazite tuff bed, treated by 100 mg·l^{-1} Pb^{++} solutions, containing 393 (triangles), 1967 (squares) or 5900 (circles) mg·l^{-1} Na^{+}, as interfering cation. Feed flow rate: 6 ml·min^{-1}.
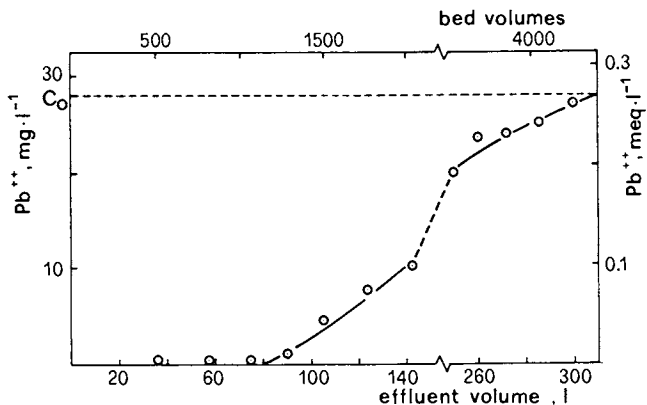
Figure 6.   Lead breakthrough curve on Na-exchanged chabazite tuff bed, treated by 28 mg·l^{-1} Pb^{++} solution, containing 23 mg·l^{-1} Na^{+}, 4 mg·l^{-1} K^{+}, 60 mg·l^{-1} Ca^{++} and 24 mg·l^{-1} Mg^{++}, as interfering cations. Feed flow rate: 10.8 ml·min^{-1}.

in the sectors of storage batteries manufacture, provided the
wastewaters are neutralized beforehand, and in ceramic industries,
while the excessive salinity of tetraethyl lead manufacturing
industry wastewaters excludes the employment of chabazite tuff
in this sector.

     To be noticed is that the overall efficiency may be improved
by using materials richer in chabazite, either natural or arti-
ficial, e.g., self-bonded chabazite pellets obtained from highly
zeolitized tuff powders (20).

Acknowledgments

Literature cited

 1. Mumpton, F.A.   In Natural Zeolites. Occurrences, Properties,
     Use (Proc. Zeolite '76, Tucson 1976); Sand, L.B.; Mumpton,
     F.A., Eds.; Pergamon Press: Oxford, 1978; p 3.
 2. Mumpton, F.A.   In Zeo-Agriculture. Use of Natural Zeolites
     in Agriculture and Aquaculture (Proc. Zeo-Agriculture '82,
     Rochester 1982); Pond, W.G.; Mumpton, F.A., Eds.; Westview
     Press: Boulder, 1984; p 3.
 3. Mumpton, F.A. Proc. Zeolite '85, Budapest 1985.
 4. Blanchard, G.; Maunaye, M.; Martin, G.   Water Research 1984,
     18, 1501.
 5. Komarneni, S. Nucl. Chem. Waste Manage. 1985, 5, 247.
 6. Sherman, J.D.   Linde Molecular Sieves. Ion Exchange Bulletin;
     Union Carbide Corp.: New York, 1977.
 7. Patterson, J.W.   Wastewaters Treatment Technology; Ann Arbor
     Science Publisher Inc.: Ann Arbor, 1975; p 129.
 8. Nilsson, R. Water Research 1971, 5, 51.
 9. Mazzocco, F. Inquinamento 1977, 19 (9), 129.
10. Fontana, U.; Mazzocco, F.   Ingegneria Ambientale 1975, 4,
     591.
11. Barrer, R.M.; Davies, J.A.; Rees, L.V.C.   J. Inorg. Nucl.
     Chem. 1969, 31, 219.
12. de' Gennaro, M.; Colella, C.; Aiello, R.; Franco, E.   In-
     dustrial Minerals 1984, n° 204, 97.
13. Colella, C.; de' Gennaro, M.   Atti VI Convegno Associazione
     Ital. Calorimetria e Analisi Termica; AICAT: Napoli, 1984;
     p P129.
14. Colella, C.; de' Gennaro, M.; Franco, E.; Aiello, R.   Rend.
     Soc. Ital. Min. Petr. 1982-83, 38, 1423.

15. Michaels, A.S. Ind. Eng. Chem. 1952, 44, 1922.
16. Nastro, A.; Colella, C. Ing. Chim. Ital. 1983, 19, 41.
17. Luckis, G.M. Chem. Eng. 1973, 80 (13), 111.
18. Nozaki, M.; Hatotami, H. Water Research 1967, 1, 167.
19. Mariani, I.; Tenti, L. La Ceramica 1973 26, (7-8), 22.
20. Aiello, R.; Colella, C.; Nastro, A.; Sersale, R. Proc. Sixth Int. Zeolite Conf.; Olson, D.; Bisio, A. Eds.; Butterworths: Guildford, 1984; p 957.

Chapter 33

Skeletal Rearrangement Reactions of Olefins, Paraffins, and Aromatics over Aluminophosphate-Based Molecular Sieve Catalysts

Regis J. Pellet, Peter K. Coughlin, Edwar S. Shamshoum, and Jule A. Rabo

Union Carbide Corporation, Old Saw Mill River Road, Tarrytown, NY 10591

Medium pore aluminophosphate based molecular
sieves with the -11, -31 and -41 crystal
structures are active and selective catalysts for
1-hexene isomerization, hexane dehydrocyclization
and C_8 aromatic reactions. With olefin feeds,
they promote isomerization with little loss to
competing hydride transfer and cracking
reactions. With C_8 aromatics, they effectively
catalyze xylene isomerization and ethylbenzene
disproportionation at very low xylene loss. As
acid components in bifunctional catalysts, they
are selective for paraffin and cycloparaffin
isomerization with low cracking activity. In
these reactions the medium pore aluminophosphate
based sieves are generally less active but
significantly more selective than the medium pore
zeolites. Similarity with medium pore zeolites
is displayed by an outstanding resistance to coke
induced deactivation and by a variety of shape
selective actions in catalysis. The excellent
selectivities observed with medium pore
aluminophosphate based sieves is attributed to a
unique combination of mild acidity and shape
selectivity. Selectivity is also enhanced by the
presence of transition metal framework
constituents such as cobalt and manganese which
may exert a chemical influence on reaction
intermediates.

A large family of novel aluminophosphate based molecular sieves has
recently been described in the literature(1-3). The individual
crystal species of these molecular sieves represent a wide variety
of crystal structures and chemical compositions. Structures
include several novel crystal types and various intracrystalline
pore sizes. Thus aluminophosphate-based molecular sieves have been

synthesized having small, medium and large-pore apertures, presumably defined by O_8, O_{10} and O_{12} rings, respectively. The aluminophosphate molecular sieves (AlPO4's) consist of aluminum and phosphorus linked by oxide ions. In the larger family of aluminophosphate based molecular sieves with three or more framework cations an additional 13 elements have been incorporated with a variety of crystal structures. The whole aluminophosphate based molecular sieve family comprises more than two dozen crystal structures and about two hundred compositions. While AlPO4 molecular sieves with only two framework elements are catalytically inactive, most of the three or multi-component aluminophosphate based molecular sieves possess cation exchange capacity, and in the protic form they display carboniogenic catalytic activity.

According to recent reports, the aluminophosphate based molecular sieves have acidic catalytic activity for a broad array of petroleum refining and petrochemical reactions. In early studies(2) n-butane cracking activities were reported for a number of silicoaluminophosphate (SAPO) molecular sieves. These SAPO molecular sieves showed weak acidity by comparison with zeolites. Subsequently, it was found that transition metal substitution into certain aluminophosphate crystals resulted in enhanced acidity as indicated by enhanced butane cracking activity(3). With medium pore species the generally mild acidity combined with unique shape selectivity has resulted in improved catalytic selectivity in several reactions. Thus, a review of the patent literature reveals that aluminophosphate based molecular sieves have shown catalytic activity in fluid catalytic cracking(4), hydrocracking(5), dewaxing(6), reforming(7), aromatic alkylations(8), methanol to olefin conversion(9,10) and in olefin oligomerization(8,11). In several cases olefins play an important role, either as feed constituents or as reaction intermediates. The enhanced selectivity of certain SAPO's for olefin reactions has already been noted. Thus, small pore SAPO's, such as SAPO-34, were found very effective at interconverting light olefins such as ethylene, propylene and butylenes with little loss to paraffinic or oligomeric products(12). The medium pore SAPO's were also active and very selective for oligomerization of propylene and butenes to olefinic gasoline(11) or to distillates without the production of paraffins or aromatics.

The present paper reports on the catalytic properties of selected aluminophosphate molecular sieves in model hydrocarbon reactions. The molecular sieves were selected to represent large and medium pore sizes with a variety of framework elements including transition metals, in addition to aluminum and phosphorus. Model reactions were chosen to explore catalytic performance in paraffin, olefin and aromatic rearrangement reactions to probe molecular sieve character, shape selectivity and catalytic activity, particularly for reactions involving olefins or olefin reaction intermediates.

EXPERIMENTAL

Molecular Sieve Catalyst Preparation. The aluminophosphate based molecular sieves used in the present study were prepared according

to procedures described in US Patent references(2,13,14). The preparation of medium pore reference molecular sieves, LZ-105 zeolite and silicalite, have also been described elsewhere(15,16). All aluminophosphate-based molecular sieves were calcined prior to incorporation into catalyst formulations. This calcination is necessary in order to remove the organic template used in synthesis, to free the intracrystalline pore system. The LZ-105 zeolite reference material, a zeolite similar in structure and chemistry to ZSM-5, which was synthesized without an organic templating agent, was acid washed prior to use, to lower its soda content and to form Bronsted acid sites.

For 1-hexene isomerization and for acid catalyzed C_8 aromatic reactions all molecular sieves were evaluated in their calcined, powdered state. For the study of C_8 aromatics, selected SAPO molecular sieves were aluminum exchanged or steam treated as noted in Table IV. For bifunctional catalysts used in paraffin cyclization/isomerization and ethylbenzene-xylene interconversions, the calcined molecular sieve powder was mixed with platinum-loaded chlorided gamma alumina powder. These mixtures were then bound using silica sol and extruded to form 1/16" extrudates which were dried and calcined at 500°C. The bifunctional catalysts were prepared to contain about 0.5% platinum and about 40 to 50% SAPO molecular sieve in the finished catalysts.

Catalyst Evaluation. The powdered molecular sieves were evaluated following the treatment described above, without further activation. The 1-hexene isomerization and C_8 aromatic isomerization tests were conducted in tubular, fixed bed, continuous flow microreactors. The catalyst bed contained one gram molecular sieve powder and one to three grams of similarly sized quartz chips used as diluent. The reactor was heated to the chosen reaction temperatures in a fluidized sand bath, and the reaction temperature was monitored by a thermocouple located in the catalyst bed. Typical runs lasted 3 to 5 hours during which samples were collected every 30 minutes.

Liquid feeds (i.e., 1-hexene or xylene and xylene-ethylbenzene mixtures) were fed to the reactor by syringe pump through a preheat zone to insure complete vaporization and mixing, prior to entering the catalyst bed. Reactor effluent was cooled via cold water trap to collect condensable liquid products while gaseous product volumes were monitored by standard dry test meter. Both gas and liquid products were analyzed by gas chromatography.

Paraffin cyclization and isomerization studies were also conducted in the microreactor system. The feed used in this study was technical grade n-hexane containing 87% n-hexane, 9% methylcyclopentane and 4% isopentanes. Typically about 0.35 g of ground extrudates (20/80 mesh) were mixed with quartz chips and loaded to the reactor. The reactor was heated to the reaction temperature in flowing hydrogen, prior to hexane feed introduction. Runs lasted for 24 hours and samples were collected only after 20 hours on feed to permit catalyst line-out. Liquid and gaseous products were collected and analyzed as described above.

The bifunctional platinum - SAPO catalysts were evaluated for C_8 aromatic reactions in the presence of hydrogen in bench scale

reactors. Typically, 25 to 50 cc catalyst extrudates were diluted with about four volumes of similarly sized quartz chips, and placed in a 1 1/4" ID reactor with quartz chips placed in both end zones. The reactor had a central thermowell containing six bed thermocouples. Catalysts were activated with hydrogen and then subsequently sulfided with 5% H_2S/95% H_2 mixture at atmospheric pressure and at run temperature. The run was started with the pressurization of the reactor and the setting of the H_2 flowrate. Feed which consisted of either 17% ethylbenzene + 83% m-xylene or 40% ethylbenzene + 60% m-xylene was then pumped over the catalyst bed. Bench scale runs lasted several days and products were collected daily. Both gas and liquid products were quantified and analyzed and material balances were determined. Typically these balances were within 2% of closure.

The reaction conditions for all catalyst tests are given along with the test results in Tables I to V.

RESULTS AND DISCUSSION

Reactions of Olefins. Olefins play a key role as intermediates in a number of petroleum refining and petrochemical reactions. Therefore, to better understand the function and utility of aluminophosphate-based catalysts, it is desirable to examine their catalytic chemistry with model olefins. As mentioned above, the silicoaluminophosphate molecular sieves have already been reported to be active for oligomerization of light olefins to gasoline range products(11). The results of that study are reproduced in Table I which presents conversion and selectivity data for propylene oligomerization to liquid products. These data were obtained using large, medium and small-pore SAPO's and medium pore reference LZ-105 zeolite.

TABLE I. Vapor Phase Propylene Oligomerization

Molecular Sieve	SAPO-5	SAPO-11	SAPO-31	SAPO-34	LZ-105
Pore Size, A	8	6	7	4.3	6
Run Temperature,°F	700	700	700	700	703
Pressure, psig	25	25	50	25	25
Propylene WHSV	0.98	0.94	1.04	0.53	0.90
Time on Stream,hr.	4.3	4.2	5.5	2.33	3.5
Propylene Conversion, %	0	86.3	76.2	41.6	81.6
C5+ Selectivity[a]	-	77.0	82.7	19.5	37.2

a) C_5+ Selectivity = (C_5+ yield, wt%)/(C_3= conversion, wt%)x100.

The data show that the large pore SAPO-5 with a undirectional non intersecting channel system(17) was inactive for oligomerization by the time the first sample had been taken. Since SAPO-5 exhibited significant activity for butane cracking(2), the lack of oligomerization activity was attributed to rapid catalyst coking, resulting in deactivation.

The small pore SAPO-34 having a crystal structure analogous to chabazite was also ineffective for propylene oligomerization. While 40% propylene conversion was observed, most of the products consisted of ethylene and butenes, with only 20% selectivity to liquid products. Larger oligomers were conceivably formed in the cages of the -34 crystal structure but could not escape through the molecular sieve's small pore openings. The light olefin products observed, were presumably formed by the cracking of trapped propylene oligomers. This scrambling of light olefins by SAPO-34 was also observed by Kaiser(12).

In contrast to SAPO-5 and SAPO-34, the medium pore SAPO-11 and SAPO-31 exhibited significant oligomerization activity and selectivity to liquid products. While the structure of the SAPO-31 is as yet unknown, the structure of SAPO-11 has been reported. It comprises unidirectional, non intersecting channels formed by 10 member oxygen rings(17). Conversions as high as 86%, with C5+ product selectivities as high as 83%, were reported under the screening conditions. The performance of the medium pore SAPO's also differed significantly from that of the medium pore zeolite reference, LZ-105, which also achieved high propylene conversion, but at only 37% C_5+ selectivity. The LZ-105 is structurally related to ZSM-5 but is prepared without an organic template. The liquid products formed over LZ-105 were highly aromatic, in contrast to the SAPO products which were predominantly olefinic. Furthermore, the major gas product formed over LZ-105 consisted of light paraffins. The LZ-105 product distribution was attributed to the preponderance of hydrogen transfer reactions in which olefin feed and oligomerizate underwent secondary reactions, presumably over strong acid sites, to produce light paraffins and aromatics. It was concluded that, the medium pore SAPO'S lacked the acid strength required to catalyze hydride shift reactions, and possibly lacked spatial requirements to form the bulky transition states envisioned for these hydride shift reactions(11). This lack of hydride shift activity resulted in high selectivity to olefinic gasoline.

While the reactions with propylene feed provide information about acid strength and perhaps about shape selective effects, further information on reaction chemistry is expected by observing the reactions of higher olefins. In the present study, the reactions of 1-hexene as catalyzed by a number of these molecular sieves are summarized in Table II. As before, data are presented for large, medium and small pore SAPO's. The influence of transition metal framework elements is also explored with selected MeAPO and MeAPSO molecular sieves. In addition to oligomerization and hydride transfer reactions observed with propylene feed, double bond and skeletal isomerizations, cyclization and cracking are also possible using 1-hexene as model reactant. The data presented in Table II were collected under somewhat milder reaction conditions

Table II. Reactions of 1-Hexene over
Aluminophosphate-Based Molecular Sieves

Run Conditions:

Run Temperature   650°F
Pressure   40 psig
WHSV   5.5 l/hr

Molecular Sieve	SAPO-5	SAPO-11	FAPO-11	MnAPO-11	SAPO-31	FAPO-31	MnAPSO-31	LZ-105
Pore Size, A	8	6	6	6	7	7	7	6
Total Conversion, %	85.1	84.5	90.1	89.6	86.0	89.1	94.5	93.7
Selectivities:								
Double Bond Isomerization, %	79.1	46.2	22.1	28.0	82.2	42.5	43.2	2.4
Skeletal Isomerization, %	10.9	41.9	70.6	63.6	14.3	52.8	44.6	12.2
Oligomerization, %	5.6	4.3	2.4	0.9	1.7	0.9	4.1	55.1
Cracking, %	3.2	3.3	1.5	1.9	0.9	1.3	2.6	25.6

than those reported in the propylene oligomerization study. Under these conditions listed in Table II, the large pore SAPO-5 molecular sieve exhibited high conversion of the 1-hexene feed, forming only double bond isomers, 2- and 3-hexene. Again, little oligomerization activity was observed and skeletal isomerization and cracking activity were also low. Since very weak acids will catalyze double bond isomerization, the lack of additional catalysis on the part of SAPO-5 is consistent with the conclusion of the previously published propylene results and with rapid coke-induced deactivation.

As with propylene, the medium pore SAPO's are again quite active and also quite selective. Thus, SAPO-11 gave over 90% 1-hexene conversion with over 90% selectivity to isomerized products, half of which were skeletal isomers. It is important to note that medium pore SAPO-11 is several orders of magnitude more coke resistant than the large pore SAPO-5. After only 30 minutes on hexene feed, the SAPO-5 was catalytically inactive whereas isomerization activity with SAPO-11 remained unchanged throughout the three hour long micro screening test. It is envisioned that the enhanced coke resistance of the medium pore SAPO-11 is due to a product shape selectivity. Due to spatial constraints within the SAPO-11 structure, bulky coke precursors are formed at a greatly reduced rate relative to their rate of formation in SAPO-5. Until now this resistance to coke formation has only been observed with the medium pore ZSM type molecular sieves(18). Under the milder conditions of this screening study with SAPO-11, little oligomerization activity was observed, but importantly, almost no cracking of hexene occurred. In contrast, under identical test conditions, the zeolite reference LZ-105 had very high activity for both oligomerization and cracking, forming over 30% light products. Most of the isomerized hexene olefins were consumed in these secondary reactions. The high isomerization selectivity observed with the medium pore SAPO's is probably attributable to significantly milder acid strength than that possessed by the reference zeolite catalyst.

The incorporation of transition elements into the crystal structure of medium pore aluminophosphate molecular sieves enhances skeletal isomerization selectivity even beyond that observed with the SAPO's. Thus, the silicoaluminophosphate SAPO-11 gives 42% conversion to skeletal isomers with 3% cracked product while the same aluminophosphate crystal phase containing manganese as a framework constituent, MnAPO-11, gives 64% skeletal isomerization with only 2% cracked product. The iron containing FAPO-11 was even more active and selective with 71% and 1.5% isomerization and cracking activities, respectively. Similar trends can be seen for the manganese and iron substituted aluminophosphates with the -31 structure.

Paraffin Reactions. The high selectivity observed with aluminophosphate based molecular sieves in olefin skeletal isomerization relative to cracking suggests that these molecular sieves may be used advantageously in several petroleum and petrochemical reactions where olefins serve as reaction intermediates, and where skeletal rearrangements are desired. Gasoline reforming involving paraffin isomerization and

dehydrocyclization is one area where improved selectivity is needed.
    The dehydrocyclization of paraffins represents a very important
class of reactions occurring in the gasoline reforming process.
Through dehydrocyclization low octane paraffins are converted to
high octane aromatics. Paraffin isomerization also boosts gasoline
octane in reforming since branched isomers typically have very
significantly enhanced octane numbers relative to normal
paraffins. Dehydrocyclization and isomerization are very often
accompanied by undesirable cracking reactions enhancing product
octane at the expense of gasoline yield. Shape selective cracking
can enhance octane by cracking away the low octane paraffins to
form gas. The intermediacy of olefins in these reactions has been
previously demonstrated(19). A simplified mechanism for the
dehydrocyclization, isomerization and cracking of n-hexane is
summarized below:

$$
\begin{array}{c}
\qquad\qquad\qquad\qquad\qquad Pt \\[2pt]
\qquad H^+ \qquad\quad iC_6^= \longleftrightarrow iC_6 \\[6pt]
Pt \qquad\qquad \nearrow \\[2pt]
nC_6 \longleftrightarrow nC_6^= \longrightarrow \text{Cyclo } C_6 \longleftrightarrow \text{Benzene} \\[6pt]
\qquad\qquad \searrow \\[2pt]
\qquad\qquad\quad \text{light olefins} \longleftrightarrow \text{light paraffins}
\end{array}
$$
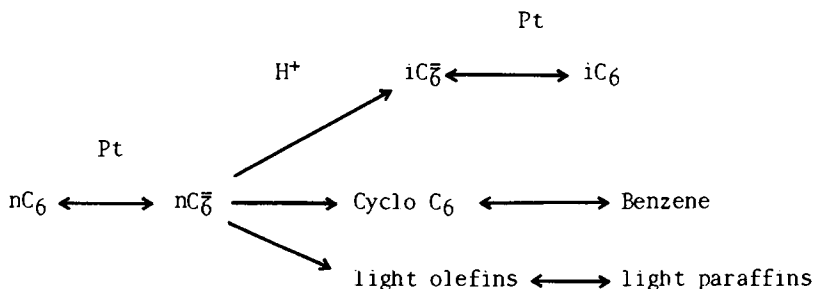
    Here, first olefinic intermediates are generated over
platinum. These intermediates are either cracked to form lighter
olefins or cyclized and isomerized over the acidic chlorided
alumina. The olefins and naphthenes thus formed are finally
dehydrogenated over the platinum to form paraffins and aromatics.
Zeolitic acids such as mordenite(20) and ZSM-5(21) have been
substituted for the chlorided alumina as acid catalyst components.
All of these acid components have been reported to boost reformed
product octane. However, much of the enhanced octane observed with
these materials is accompanied by enhanced cracking activity and by
reduced yields.
    In the present study, mixtures of supported platinum and
aluminophosphate based molecular sieves have been tested for
n-hexane rearrangement reactions under reforming conditions (900°
F, 200 psig). Results are summarized graphically in Figures 1 and
2, where selectivities are plotted as functions of n-hexane
conversion. Data are presented for the large, medium and small
pore SAPO molecular sieves mixed with a Pt-alumina catalyst. Data
for platinum mixed with chlorided alumina or mixed with silicalite
are presented for reference. In Figure 1, the ratio of iso-hexanes
to cracked products is plotted against conversion. The catalyst
consisting of platinum and large pore SAPO-5 is less active than
reference platinum-chlorided alumina; however, it appears similar
in selectivity, in that it produces a similar distribution of
isomerized and cracked products. Mixed platinum and small pore
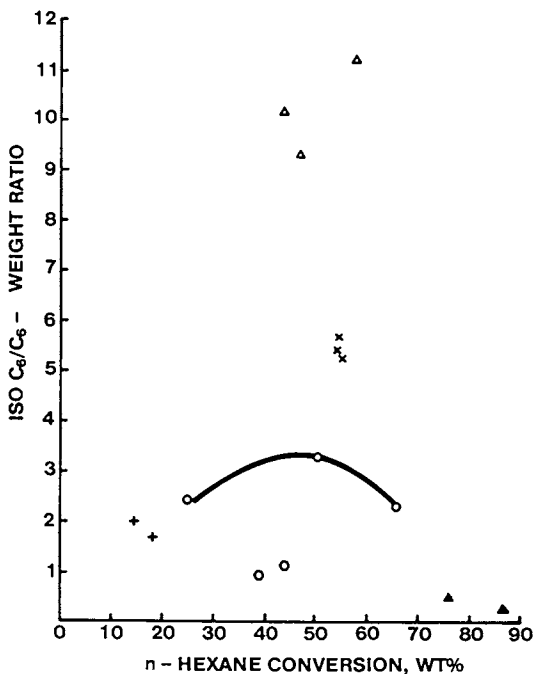
Figure 1. Isomerization/Cracking Selectivity Ratio plotted as a function of n-hexane conversion: △ SAPO-11, ✗ SAPO-41, + SAPO-5, ⭕ SAPO-34, ▲ Silicalite and ⭘ Pt/chlorided-alumina reference.
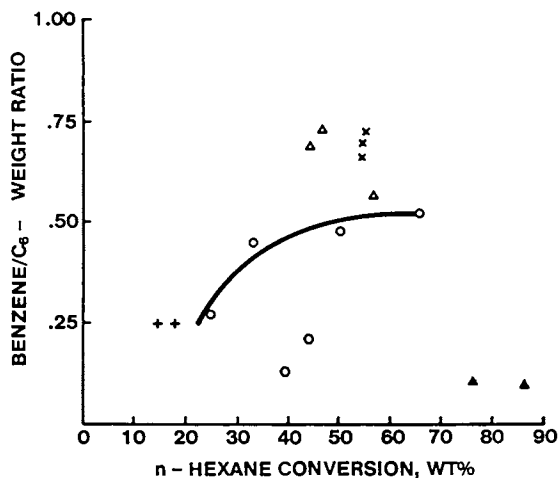
Figure 2. Dehydrocyclization/Cracking Selectivity Ratio plotted as a function of n-hexane conversion: △ SAPO-11, ✗ SAPO-41, + SAPO-5, ⭕ SAPO-34, ▲ Silicalite and ⭘ Pt/chlorided-alumina reference.

SAPO-34 is quite active for hexane conversions but selectivity for isomerized hexanes is significantly lower than observed with the reference, and a significant increase in the amount of light cracked products is observed. These results are to be expected. SAPO-34 with the chabazite-type structure possesses cages in which the large hexene isomers can form; however, due to the small pore opening of the -34 structure, the isomers once formed can not escape without cracking to lighter products. The noble metal-loaded medium pore SAPO's -11 and -41 exhibit excellent hexane isomerization selectivities when applied together with platinum, producing 2 to 4 times the amount of isomers compared to reference platinum-chlorided alumina catalyst. In contrast, the medium pore silicalite and supported platinum catalyst mixture, while achieving significantly higher n-hexane conversion, is far less selective than the medium pore SAPO catalyst mixture and the chlorided alumina-platinum reference, producing a large amount of cracked products. Similar selectivity trends are observed for the dehydrocyclization reactions of n-hexane. Thus in Figure 2 the benzene to light products ratio is plotted against conversion for the same set of catalysts, and again the medium pore SAPO's exhibit superior selectivity to both reference materials and to both large and small pore SAPO catalyst systems. These results are in complete agreement with the hexene isomerization data described above, wherein the medium pore SAPO's show significantly reduced activity for cracking reactions while maintaining high skeletal isomerization activity.

Aromatic Reactions. In addition to reforming, the isomerization of C_8 aromatics to produce para-xylene is another area where olefinic intermediates may play a significant mechanistic role. The production of para-xylene is of interest to the petrochemical industry because of its use as monomer in polyester production. In addition to C_8 aromatic isomerization, there are a number of important routes to para-xylene including the alkylation of toluene with methanol and the disproportionation of toluene. The catalytic properties of the SAPO molecular sieves for toluene methylation reactions have been described(11). While both large and medium pore SAPO's were active for the alkylation reaction, the medium pore materials were distinguished by remarkably high selectivity for methylation reactions, with disproportionation of the toluene feed representing less than 2% of the total conversion. By comparison, large pore SAPO-5 had nearly 60% disproportionation selectivity and the zeolite reference LZ-105 had nearly 80% disproportionation selectivity. The very low disproportionation activity of the medium pore SAPO's, attributed to their mild acid character, resulted in reduced losses of toluene to benzene and increased xylene yields relative to LZ-105 and SAPO-5.

In the present study, silicon and transition metal substituted aluminophosphate molecular sieves have also been evaluated for activity and selectivity for para-xylene production via C_8 aromatic isomerization. In commercial practice, C_8 aromatic cuts are obtained from reformate gasoline and from pyrolysis naphtha streams. Both feeds contain a significant fraction of ethylbenzene which is difficult to separate from xylenes by physical techniques,

and must be catalytically converted to other products. This catalytic conversion can be accomplished by one of two commercially available approaches. In one approach, mono-functional acid catalysts such as ZSM-5 (22) isomerize xylenes and also convert ethylbenzene to non C_8 aromatics by selective ethyl group disproportionation. Disproportionation of xylenes to non C_8 aromatics is a competing side reaction lowering the ultimate para-xylene yield. Acid catalysis alone can not convert the ethylbenzene to xylenes. To this end, bifunctional catalysts containing both a hydrogenation-dehydrogenation function such as platinum as well as an acidic function such as mordenite(23), have typically been employed. In the latter approach, ethylbenzene is hydrogenated over Pt to ethylcyclohexene which is then isomerized to dimethylcyclohexene over the acid catalyst function, and finally converted to xylenes by dehydrogenation over the platinum.

Cracked Products
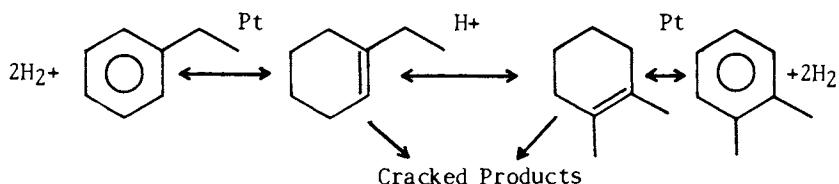
Conceptually, this route offers the possibility of enhanced xylene yields, but since naphthenic intermediates are present, significant acid catalyzed ring opening and yield loss of aromatics are also possible. A review of available patent literature data(22,23b) suggests that because of these undesirable side reactions, the bifunctional approach to isomerization yields about the same amount of xylene as does the monofunctional route.

C_8 Aromatic Reactions Without Hydrogen. In the present study, the aluminophosphate molecular sieves have been used alone and with added platinum and hydrogen to isomerize C_8 aromatic feeds. In an initial screening study, a series of large to medium pore size molecular sieves were evaluated for catalytic activity for m-xylene rearrangements at $1000°$ F without added metal and hydrogen. Under these conditions all molecular sieves evaluated give essentially complete isomerization of m-xylene feed to a thermodynamic equilibrium mixture of xylene isomers, while the disproportionation activity to toluene and trimethylbenzenes varies significantly. The results of this study are summarized in Table III and in Figure 3, where xylene disproportionation activity is plotted as a function of molecular sieve pore size. In general, a rough trend can be seen in which the molecular sieves with larger pore sizes are more active for this undesirable side reaction. Thus under the chosen screening conditions, SAPO-5, MAPO-5 and MAPO-36, all large pore molecular sieves with approximately 8 angstrom pore sizes, catalyze from 12 to 22 % disproportionation while SAPO-11, MAPO-11 and SAPO-41 with approximately 6 angstrom pores suffer only 2 to 7 % xylene losses. These results are consistent with the concept of transition state shape
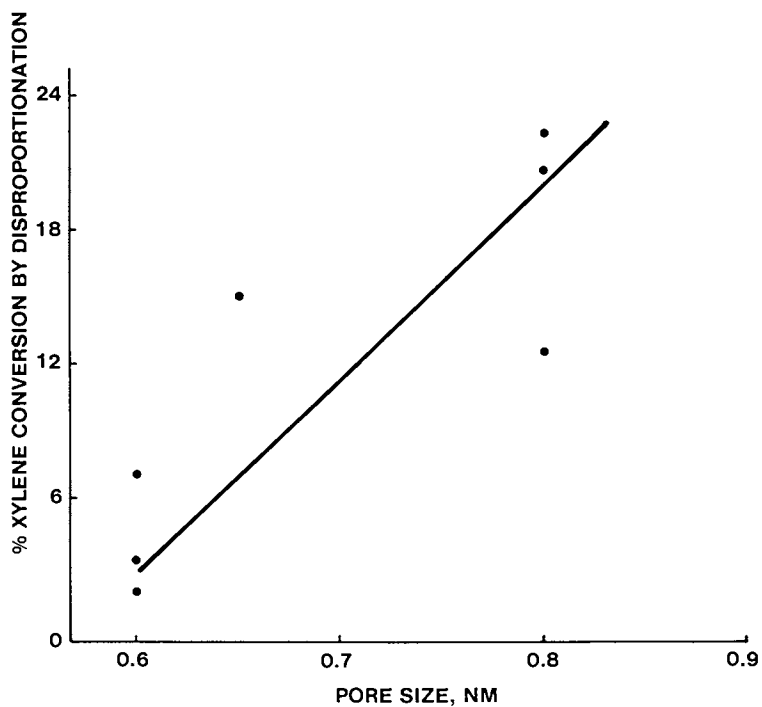
Figure 3. Xylene losses due to disproportionation are a function of the molecular sieve catalyst's pore size.

selectivity where a bulky, bimolecular interaction of two xylenes to form toluene and trimethylbenzene is difficult to achieve in the approximately 6 angstrom size channels.

Table III. m-Xylene Reactions Catalyzed by
Aluminophosphate-Based Molecular Sieves

Run Conditions:
Run Temperature   1000°F
Pressure   100 psig
WHSV   5.6 1/hr

Molecular Sieve	Pore Size a	Pore Volume b	m-Xylene Disproportionation, % Conversion
SAPO-5	0.8	0.31	20.7
MAPO-5	0.8	0.31	22.4
MAPO-36	0.8	0.31	12.6
SAPO-31	0.65	0.17	15.1
SAPO-41	0.6	0.22	7.1
SAPO-11	0.6	0.16	3.2
MAPO-11	0.6	0.16	1.8

a) Determined by McBain Bakr gravimetric adsorption studies(3).
b) Determined by water adsorption at saturation(3).

In the next phase of the present study, several medium pore molecular sieves were evaluated for catalytic performance with an ethylbenzene and m-xylene feed. Again, the molecular sieves were tested with no added metal or hydrogen. Several of these aluminophosphate based molecular sieves did contain transition metals as framework elements. The results of this study are summarized in Table IV and Figure 4. From the Table it can be seen that all molecular sieves yield para-xylene in amounts equivalent to thermodynamic equilibrium. Surprisingly, the cobalt and manganese-containing molecular sieves with the -31 type structure did not promote the equilibration of meta to ortho-xylene, so that very high para/ortho selectivities were observed. Since SAPO-31 with identical framework structure does not exhibit the high para and low ortho-xylene selectivity observed with the MeAPSO-31 molecular sieves, their high selectivity might possibly be interpreted as product shape selectivity due to restricted pore size. Obviously the Mn^{+2} framework cations are larger than the silicon and aluminum cations they are replacing, and this could conceivably result in restrictions in the molecular sieve channels. However, McBain-Bakr gravimetric adsorption studies with "plug gauge-sized" molecules suggest that MeAPSO-31's have pore sizes and volumes similar to those of the metal-free SAPO-31, which does not appear to be para selective(3). Furthermore, SAPO-11 with

Table IV. m-Xylene/Ethylbenzene Reactions with
Medium Pore Size Aluminophosphate Based Molecular Sieves

Run Conditions:
Run Temperature   800°F
Pressure   100 psig
WHSV   5.6 1/hr.

Molecular Sieve	Para/Ortho Xylene Ratio	%Para-Xylene Equilibration	% Disproportionation	
			Xylenes	Ethylbenzene
SAPO-11	0.97	96	9.9	23.2
SAPO-11 (Al^{+3} exchanged)	1.15	102	6.6	20.1
SAPO-11 (Steam treated)	1.52	63	0.2	6.0
SAPO-31	0.78	100	31.6	56.3
SAPO-31 (Steam treated)	1.56	102	1.7	10.4
MnAPSO-11	0.88	104	5.0	23.3
CoAPSO-11	1.81	91	0.0	7.7
MnAPSO-31	3.59	120	0.0	17.7
CoAPSO-31	3.06	111	1.7	23.0
LZ-105	0.99	100	23.6	58.5
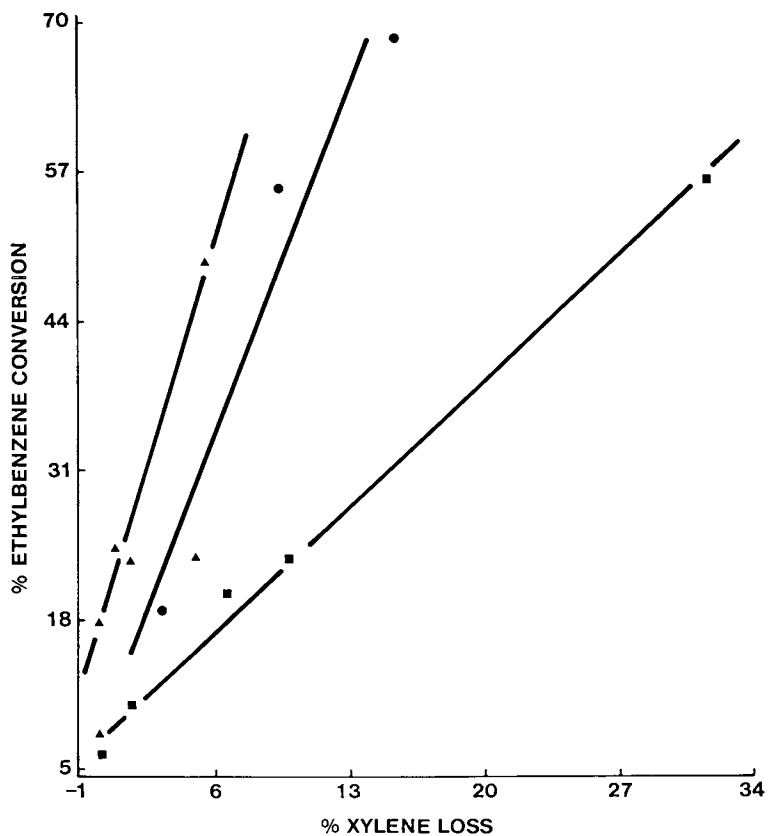
Figure 4. Selectivity for ethylbenzene conversion plotted
against xylene losses for ▲ MeAPSO's, ● LZ-105 and ■ SAPO's.

slightly smaller pore size than CoAPSO-31 and MnAPSO-31 does not show nearly the para selectivity observed with the transition metal-containing molecular sieves with the -31 crystal structure. An alternate explanation is needed. It may be that the framework transition metal ions in these molecular sieves exert a chemical influence on the intermediates in isomerization, favoring the formation of the para-isomer. Alternately, acid sites may be uniquely located in the MeAPSO molecular sieves such that access of reactants and reaction intermediates to these acid sites is spatially constrained, favoring para-selectivity.

Figure 4 plots ethylbenzene vs xylene disproportionation activity for the same series of catalysts. Data were obtained at a range of conversions by varying reaction temperature. Again all catalysts were tested without added metal or hydrogen. Data obtained with medium pore zeolite reference LZ-105 are also presented for comparison. The MeAPSO-31 molecular sieves are again distinguished by superior selectivity. Thus at comparable ethylbenzene conversions, the CoAPSO and MnAPSO-31 molecular sieves exhibit the lowest activity for the undesirable xylene disproportionation while SAPO-11 and SAPO-31 are considerably less selective. Data obtained with LZ-105 is intermediate in selectivity. Again the enhanced selectivity observed with the MeAPSO-31 molecular sieves may be due to a transition metal specific influence on the reaction intermediates. Shape selective effects by themselves cannot explain differences between these materials and the transition metal-free SAPO's.

C_8 Aromatic Reactions with Hydrogen. The mild acid nature of the family of aluminophosphate based sieves renders them selective for a number of rearrangements as observed in the reactions of olefins and paraffins described above. This property as well as their apparent low disproportionation activity observed in the alkylation of toluene suggests that they be evaluated as the acid function in bifunctional C_8 aromatic isomerization. As described above, cyclo-olefins are most likely involved in the conversion of ethylbenzene to xylenes. Strong acid functions, such as in mordenite, actively isomerize cyclo-olefinic intermediates but also catalyze ring-opening reactions which lead to loss of aromatics. A more selective acid function must still effectively interconvert ethylcyclohexene to dimethylcyclohexenes but must leave the cyclohexene rings intact.

In a final phase of the current study, catalysts consisting of selected SAPO's and supported platinum have been evaluated in the presence of hydrogen for bifunctional C_8 aromatic isomerization. Two catalysts were prepared, one containing 40% of the intermediate pore SAPO-11 and the other containing 40% of large pore SAPO-5. Both catalysts were prepared to contain about 0.6% platinum supported on alumina. The catalysts were evaluated at 800° F, 185 psig and at a space velocity of 1 and a hydrogen to hydrocarbon ratio of 14. The feed used for these tests contained 17% ethylbenzene and 83% m-xylene, simulating a C_8 aromatic cut obtained from reformate gasoline. Each catalyst was evaluated for several days on stream, and at the high hydrogen/hydrocarbon ratio employed, little or no deactivation was observed. In addition, the

SAPO-11-containing catalyst was evaluated with a 40% ethylbenzene + 60% m-xylene feed in order to better evaluate its effectiveness in converting ethylbenzene to xylenes, and to model a feed similar to a pyrolysis naphtha C_8 cut. Typical performance data for each catalyst after several hours on the 17% ethylbenzene feed are summarized in Table V. Performance indicators were calculated assuming that the naphthenes formed during processing would in commercial practice be recycled, and therefore their formation would contribute to neither ethylbenzene conversion nor to xylene losses. According to the tests both catalysts promote near-complete xylene equilibration, and the catalyst containing SAPO-5 achieves higher ethylbenzene conversion than the SAPO-11 catalyst, 68% and 44% respectively. However, the large pore molecular sieve incurs nearly 22% xylene losses while the SAPO-11 based catalyst actually produces 2.1% more xylenes than were present initially in the feed. With SAPO-5 these losses are due to disproportionation reactions producing benzene, toluene and C9+ aromatics, and also to non cyclic product formation, suggesting significant ring opening and cracking. With the SAPO-11 catalyst there is much less disproportionation activity, and almost no ring-opened paraffinic products are observed.

While the present study has not examined the performance of zeolite based catalysts, Table V summarizes patent literature data(23b) for a mordenite and platinum/alumina mixture. Data for the Pt and SAPO-11 mixture obtained under similar conditions are presented for comparison. The mordenite catalyst is significantly less selective than SAPO-11, giving 25.6% ethylbenzene conversion with only 0.5% net xylene production.

The data obtained with high ethylbenzene feed shows even more dramatically the efficient conversion of ethylbenzene to xylenes over the SAPO-11-containing catalyst. Thus at 23.6% ethylbenzene conversion, a nearly 13% increase in xylene yield is observed. This indicates that ethylbenzene has been converted with 75% selectivity to xylene isomers. The remaining conversion was to disproportionation products with again almost no ring opening.

CONCLUSIONS

The medium pore aluminophosphate based molecular sieves are active and selective catalysts for a variety of important hydrocarbon rearrangement reactions. As acid catalysts, they promote olefin isomerization and oligomerization while they are significantly less effective at the competing hydride transfer and cracking reactions. In the reactions of aromatics, the medium pore aluminophosphates are again effective for skeletal isomerization but show low ethyl group disproportionation activity. As acid components in bifunctional catalysts, they are selective for paraffin and cycloparaffin isomerization with low cracking activity.

These catalytic properties contrast sharply with those of medium pore zeolites such as LZ-105 and with silicalite. Thus, medium pore SAPO's are considerably less active than LZ-105 for olefin, paraffin and aromatic conversions when compared at the same temperature. However, they are more selective for olefin and paraffin isomerizations when evaluated at comparable conversions.

Table V. C$_8$ Aromatic Isomerization With

Bifunctional Catalysts

Molecular Sieve Component	SAPO-5	SAPO-11	SAPO-11	SAPO-11	Mordenite[b]
Molecular Sieve Content, %[a]	40	40	40	40	50
Run Temperature, °F	800	800	840	800	800
Run Temperature, psig	185	185	250	165	175
H$_2$/HC Ratio	14	14	8.3	14	8
WHSV	1	1	2.9	1	3.6
Ethylbenzene in Feed, %	17	17	17	40	15.5
Approach to p-xylene Equilibrium, %	94.9	97.3	94.5	96.2	99.3
Ethylbenzene Conversion, %	67.9	44.6	28.2	23.6	25.6
Net Xylene Production, %	-21.6	2.1	1.5	12.8	0.5

a) In addition to the quantity of molecular sieve listed, all
    catalysts contained 0.4-0.6% platinum.
b) Data obtained from U.S. Patent 4,255,606, Example 1.

Not surprisingly, the catalytic properties of medium pore aluminophosphates also contrast with large pore aluminophosphate-based molecular sieves of similar framework composition. With olefinic feeds, the large pore molecular sieves deactivate very rapidly, presumably due to pore plugging by higher molecular weight products. The medium pore SAPO's are dramatically more coke resistant. Under conditions that fully deactivate SAPO-5 in less than 30 minutes, SAPO-11's activity remains unchanged for several hours. With aromatic feeds, both large and medium pore molecular sieves are active for alkylation and isomerization. However, the large pore molecular sieves are significantly more active for the disproportionation of dialkyl aromatics, implying transition state shape selectivity for the medium pore molecular sieves. In bifunctional catalysis involving olefinic intermediates, large pore molecular sieves are more active for cracking and less selective for skeletal isomerization reactions.

The catalytic properties of the aluminophosphate molecular sieves are also influenced by chemical composition. The introduction of transition metals into framework positions enhances the activity and selectivity for olefin isomerization relative to the silicoaluminophosphates. The transition metal containing aluminophosphates are also surprisingly more selective for C_8 aromatic rearrangements than the corresponding SAPO molecular sieves, an effect which can not be attributed solely to improved shape selectivity.

The enhanced selectivities observed with medium pore silico- and metalloaluminophosphates may, to a large extent be attributed to a unique combination of mild acidity and shape selectivity. The lack of hydride shift and cracking activity in olefin-mediated reactions is suggestive of mild acidity. The observed resistance to coke deactivation and the enhanced selectivity to para-xylene in methylation and isomerization reactions is evidence of shape-selective catalysis.

In addition to these factors, however, transition metal framework constituents appear to exert a special chemical effect on catalytic performance which appears to be independent of molecular sieve acid strength and spatial constraints. This effect is evidenced by cobalt and manganese- containing molecular sieves as enhanced selectivity for ethylbenzene disproportionation in the presence of xylenes, and by enhanced para-selectivity in xylene isomerization. Thus, MnAPSO-31 has a larger pore size than SAPO-11 as judged by "plug gauge" molecules but is far more selective for para-xylene and for ethylbenzene disproportionation than the SAPO-11 under comparable test conditions. This enhanced selectivity may be due to a uniquely located acid site in the transition metal-containing molecular sieve with special and unexpected spatial requirements. Alternately, it may be due to a ligand or electronic effect of the transition metal, affecting the transition states in aromatic isomerization and disproportionation reactions.

LITERATURE CITED

1.   Wilson, S.T.; Lok, B.M.; Messina, C.A.; Cannan, T.R.; Flanigen, E.M. J. Am. Chem. Soc. 1982, 104, 1146.

2.   Lok, B.M.; Messina, C.A.; Patton, R.L.; Gajek, R.T.; Cannan, T.R.; Flanigen, E.M. J. Am. Chem. Soc. 1984, 106, 6092; U.S. Patent 4 440 871, 1984.
3.   Flanigen, E.M.; Lok, B.M.; Patton, R.L.; Wilson, S.T. In New Developments in Zeolite Science and Technology; Murakami, Y.; Iijima, A.; Ward, J.W., Eds.; Proceedings of the 7th International Zeolite Conference; Elsevier, New York, 1986, p.103.
4.   Pellet, R.J.; Coughlin, P.K.; Staniulis, M.T.; Long, G.N.; Rabo, J.A. U.S. Patent 4 666 875, 1987.
5.   Gortsema, F.P.; Pellet R.J.; Springer, A.R.; Rabo, J.A.; Long, G.N. Eur. Pat. Appl. 207 133, 1987.
6.   Gortsema, F.P.; Pellet R.J.; Springer, A.R.; Rabo, J.A.; Long, G.N. Eur. Pat. Appl. 185 329, 1986.
7.   Garska, D.C.; Lok, B.M. U.S. Patent 4 499 315, 1985.
8.   Pellet, R.J.; Long, G.N.; Rabo, J.A. In New Developments in Zeolite Science and Technology; Murakami, Y.; Iijima, A.; Ward, J.W., Eds.; Proceedings of the 7th International Zeolite Conference; Elsevier, New York, 1986, p. 843;
9.   Kaiser, S.W. U.S. Patent 4 524 234, 1985. 10. Kaiser, S.W. Arabian J. Sci. Eng., 1985, 10(4), 361-6;
11. Long, G.N.; Pellet, R.J.; Rabo, J.A. U.S. Patent 4 528 414, 1985;
12. Kaiser, S.W. Eur. Pat. Appl. 142 156, 1985. 13. Messina, C.A.; Lok, B.M.; Flanigen E.M. U.S. Patent 4 544 143, 1985.
14. Wilson, S.T.; Flanigen E.M. U.S. Patent 4 567 029, 1986.
15. Grose, R.W.; Flanigen E.M. U.S. Patent 4 257 885, 1981.
16. Grose, R.W.; Flanigen E.M. U.S. Patent 4 061 724, 1977.
17a. Bennett, J.M.; Cohen, J.P.; Flanigen, E.M.; Pluth, J.J.; Smith, J.V. In Intrazeolite Chemistry; ACS Symposium Series No. 218; American Chemical Society: Washington, D.C., 1983; pp 109-18.
   b. Bennett, J.M.; Smith J.V. Z. Krist. 1985, 171, 65-68.
18. Walsh, D.E.; Rollman, L.D. J. Catal. 1979, 56, 195-197.
19. Mills, G.A.; Heinemann, H.; Milliken, T.H.; Oblad, A.G. Ind. Eng. Chem. 1953, 45, 134.
20. Bertolacini, R.J. U.S. Patent 4 018 711, 1977.
21. Detz, C.M.; Field, L.M. U.S. Patent 4 347 394, 1982.
22. Haag, W.O.; Olson, D.H. U.S. Patent 3 856 871, 1974.
23a. Carr, W.C.; Polinski, L.M.; Hindin, S.G.; Kosco, J.L. U.S. Patent 4128 591, 1978.
   b. Tse, H.F. U.S. Patent 4 255 606, 1981.

Chapter 34

Borosilicate Molecular Sieves

Nancy A. Kutz

Amoco Research Center, Amoco Chemical Company, P.O. Box 400, Naperville, IL 60566

Crystalline borosilicate molecular sieves have been the object of an intensive investigation effort since they were reported in the open literature at the Fifth International Conference on Zeolites by Taramasso, et al. (1) A wide range of structures containing framework boron have been synthesized. The physical properties of these borosilicate molecular sieves have been studied by such techniques as X-ray diffraction, infrared and nuclear magnetic resonance spectroscopies, and temperature programmed desorption of ammonia. In addition, the catalytic performance of borosilicate molecular sieves has been reported for such reactions as xylene isomerization, benzene alkylation, butane dehydroisomerization, and methanol conversion. This paper will review currently available information about the synthesis, characterization, and catalytic performance of borosilicate molecular sieves.

The synthesis of zeolites and zeolitic materials has been pursued for nearly 50 years (2), and the literature is filled with reports of structures, methods of preparation, and uses for these materials. The substitution of aluminum or silicon in the framework structure has been performed using many main group elements (3,4) as well as some transition metals (3,5). New families of molecular sieves which are based on an aluminophosphate framework have been reported recently, some of which are also microporous (6,7). Of the various new materials which have been reported, this review will focus on crystalline borosilicate molecular sieves.

The growing interest in the properties of borosilicate molecular sieves has led to a significant increase in the number of reports which specify a borosilicate molecular sieve as the important component in catalyst compositions (8-11). The range of reactions which have been claimed include a variety of hydrocarbon conversions such as xylene isomerization (8,12),

butane dehydroisomerization (13), catalytic dewaxing (9,14), and methanol conversion (10,15).

Synthesis

Borosilicates have been prepared via hydrothermal synthesis in alkaline solutions (1,16-24). Alternatively, synthesis has been successful from neutral or slightly acidic media in the presence of fluoride anions (25). Borosilicate molecular sieves have been prepared through secondary synthesis techniques as reported by Derouane, et al. (26), in which the aluminosilicate ZSM-5 was treated with boron trichloride to replace aluminum with boron in tetrahedral sites.

Typical hydrothermal synthesis consists of the preparation of a gel comprising a source of silica, a source of boron, an organic compound, and a source of alkali. The gel is digested at a temperature generally between 80°C and 200°C until such time as a crystalline molecular sieve is obtained. The as-prepared molecular sieve contains the organic synthesis agent as well as any cations which may have been present (such as Na+ or Ca^{2+}). After calcination or firing, usually at temperatures in excess of 400°C, a mixed hydrogen/cation form results which can be converted to the hydrogen form through ammonium ion exchange followed by calcination, or by treatment with hydrochloric acid to generate the hydrogen form directly.

The preparation of a borosilicate molecular sieve (termed by the authors "borozeosilite") at relatively low pH, in the neutral to acidic range, has been reported (25). A reaction mixture comprising a silica source, boric acid, tetrapropyl-ammonium bromide and an ammonium fluoride salt was digested hydrothermally at 170°C. Subsequent calcination of the product in air at 550°C was performed to remove organic template and to provide the hydrogen form of the molecular sieve.

In a method which is analogous to the dealumination of zeolites by silicon tetrachloride (27), Derouane and co-workers reported the replacement of aluminum in the NH$_4$-ZSM-5 framework by boron from BCl$_3$ (26). By controlling the reaction conditions, particularly the exposure time to boron trichloride, the degree of substitution was varied. The zeolite was dried initially in a stream of flowing dry nitrogen, then was exposed to the boron trichloride at elevated temperature (500°C), followed by an additional treatment with dry nitrogen. After the reaction with BCl$_3$, the molecular sieve was ammonium exchanged and air-dried to preserve the ammonium form of the sieve for subsequent characterization.

A number of borosilicate molecular sieves have been discovered using these synthesis techniques. By changing the organic compound and other reaction variables, it is possible to prepare various borosilicate structures (1,11,24,28). Modifications of zeolites and molecular sieves with boron compounds which do not lead to tetrahedral (framework) boron will not be addressed in this article.

Characterization

X-Ray Diffraction.

Borosilicate molecular sieves have been studied by X-ray diffraction (1,16-20). X-ray diffraction techniques have been developed to determine the degree of substitution of the silicate framework by borate tetrahedra (29). The boron-oxygen bond is shorter than the the silicon-oxygen bond, which leads to a contraction of the unit cell for a borosilicate molecular sieve as boron substitution increases. The unit cell volume determined from peak positions in the ranges $20° < 2\theta < 35°$ and $45° < 2\theta < 50°$ or an empirical parameter termed ΣT (sum of four d spacings) correlated with structural boron content (29).

Changes in the ratios of line intensities were used to analyze the X-ray diffractograms of a series of isomorphously substituted MFI molecular sieves (30). The analysis revealed that, although large cations such as Al or Ga substitute in an ordered manner for Si, substitution by the small B cation leads to statistical replacement of Si. The results were interpreted as leading to a maximum theoretical substitution of about 4 (Al or Ga)/unit cell in the crystalline framework, but a Si/B mole ratio as low as 1 was predicted.

A detailed analysis of the X-ray powder diffraction pattern of two borosilicates was used to develop a model for their structures (31). The material called BOR-C is reported to have the MFI structure containing regular stackings of pentasil layers related by inversion centers. On the other hand, the BOR-D material was found to have the MEL structure. It was structurally disordered, consisting mainly of pentasil layers related by inversion centers as well as layers related by mirror planes. The disordered structure model for BOR-D also was proposed for the aluminosilicate ZSM-11 and the silicalite-2 analog (32).

Infrared Spectroscopy.

Infrared spectroscopy has been used to study borosilicate molecular sieves (22,25,33-36). Vibrational bands associated with trigonal framework boron occur near 900 cm^{-1} and 1400 cm^{-1} (22,25,33). The presence of the Si-O-B asymmetric stretching vibration, indicative of tetrahedral framework boron incorporation, cannot be observed directly because it is masked by the strong Si-O-Si band near 1100 cm^{-1} in the pentasil structures. The tetrahedral Si-O-B vibration has been observed for the borosilicate mineral danburite (33). Shifts of bands in the framework vibrational region at 550 cm^{-1} and 560 cm^{-1} to higher frequencies as a function of boron content has been used to study boron incorporation in the framework of AMS-1B borosilicate (36).

Evaluation of the hydroxyl region of the spectrum (4000-3000 cm^{-1}) has been reported by several authors for borosilicate molecular sieves (33,35-38). The well-known band near 3610 cm^{-1} associated with acidic hydroxyls in aluminum-containing ZSM-5 (36-40) is not observed for the borosilicate molecular sieve. Assignment of a band at 3725 cm^{-1} to hydroxyls associated with structural boron (37,38) was

questioned when the band was observed in silicalite and ZSM-5 samples (36). Recent unpublished data (41) suggest that, for borosilicate molecular sieves, the band near 3275 cm^{-1} is a combination of an acidic band and a non-acidic band, such as that observed in silicalite and ZSM-5. A sharp band near 3700 cm^{-1} has been observed in some samples of borosilicate molecular sieves. A similar band has been observed in porous glass and silica impregnated with boric acid (42). The hydroxyls associated with this band are not strongly acidic.

Nuclear Magnetic Resonance Spectroscopy. The use of ^{11}B NMR spectroscopy to examine the state of boron in borosilicate molecular sieves has been reported (21,22,24-26,43,44). Scholle and Veeman (43) reported that the boron resonance is characteristic of tetrahedral boron when the samples are hydrated. Dehydration of a borosilicate sample results in a shift to a trigonal environment, as evidenced by the lineshape and peak position. The trigonal boron remains in the framework, and the change between trigonal and tetrahedral environments is reversible. Boron NMR has also been used to show that boron from Pyrex liners can be incorporated in molecular sieve frameworks during synthesis of MFI and MOR structure types (21,44).

Proton NMR of a borosilicate molecular sieve was reported by Scholle and co-workers in a study of the hydroxyl groups in borosilicate, silicalite, and ZSM-5 (45). In this study, the silanol protons in both borosilicate and aluminosilicate materials were observed at a chemical shift of ~2 ppm relative to Me$_4$Si. A low field resonance attributed to hydroxyls associated with the heteroatom (B or Al) was shifted to higher field for the boron-containing sieve relative to the aluminum-containing sieve (~3.5 ppm vs ~6 ppm). This was interpreted as indicating that the borosilicate hydroxyls are less acidic than those of the aluminosilicate, consistent with the IR results reported above.

Temperature Programmed Desorption. Ammonia has been used as a probe molecule in a number of studies of crystalline borosilicate molecular sieve (22,33,45). It has been shown that the ammonia is desorbed from the borosilicate samples at low temperature, 465°K, indicating the weak acidity of the hydroxyls (33). The hydroxyls have been shown to have higher acidity than silanol groups and lower acidity than those of ZSM-5 (45). The results are consistent with IR and calorimetric data for NH$_3$ adsorption/desorption (35).

Quantum Chemical Characterization. Calculations have been performed using model compounds to determine the stability of framework boron (46-48). Due to the lengthy (hence costly) calculations involved, cluster sizes used for the calculations are usually small, involving as few as 6 to 16 atoms. The results obtained however, were consistent with experimental characterization data.

Three-coordinate boron was found to be more stable than four-coordinate boron, except when a sufficiently strong

electron donor O-atom is available to provide additional
stability ($\underline{46}$). Examination of calculated stabilities of
$(HO)_3$-Si-O(M)-T$(OH)_3$ dimers (M = H, Li, or Na) using GAUSSIAN-80
with the STO-3G basis set, led to the observation that the
H-form for the borosilicate dimer was unstable, suggesting poor
stability for tetrahedrally coordinated boron in borosilicates
of the hydrogen form ($\underline{47}$). For dehydrated samples, boron
assumes a position in which it is closer to a trigonal face of
the tetrahedral site than to the center of the site as indicated
by NMR spectroscopy ($\underline{43}$). Experimental evidence showed that
addition of an electron donor species (i.e., water) does serve
to stabilize the four-coordinate environment ($\underline{43}$).

O'Malley and Dwyer ($\underline{48}$) calculated the OH bond
characteristics of terminal silanol (H_3SiOH), bridged hydroxyl
on aluminum dimer ($H_3SiOHAlH_3$) and bridged hydroxyl for boron
dimer ($H_3SiOHBH_3$) using 3-21G basis set. They determined that
the hydroxyl bridge in the boron dimer had acidity intermediate
between terminal silanol and the bridged aluminum hydroxyl,
consistent with experimental results ($\underline{38,43}$).

Catalysis

Although adsorption processes represent an extremely large
application of molecular sieves ($\underline{49}$), applications in the area
of heterogeneous catalysis have received the most attention for
borosilicate molecular sieves. Due to the inherently weaker
acidity of borosilicates relative to aluminosilicates, a number
of advantages in using borosilicates have been reported due to
improved product distributions or reaction selectivities.

Xylene Isomerization. The first reported use of borosilicate
containing catalysts was for xylene isomerization ($\underline{12,16}$). In
this application, the purpose is to isomerize a reaction mixture
which is lean in p-xylene to an equilibrium mixture from which
the p-xylene can then be removed. In addition to the
isomerization of xylenes, the catalyst also must convert a
portion of the other components present in the feed to allow
easier separation of p-xylene from the product mixture. The
primary contaminant in the feedstock is ethylbenzene, which is
converted via transalkylation to higher molecular weight
compounds, which are valuable as gasoline blending components,
and benzene.

Borosilicate catalysts provide high approach to
thermodynamic equilibrium of the xylenes, and offer high
selectivity in the conversion of ethylbenzene ($\underline{8,12,22,50}$). In
addition, they have been shown to be less prone to the effects
of thermal and steam treatments than corresponding
aluminosilicate zeolite catalysts ($\underline{51}$). The catalytic activity
of borosilicate catalysts was demonstrated to be a function of
the structural boron content of the molecular sieve ($\underline{22,36,50}$).
In addition, the by-product distribution obtained from a
borosilicate catalyst in a xylene isomerization/ethylbenzene
conversion process was found to be distinctive ($\underline{50}$), with high
transethylation reactivity relative to transmethylation.

Methanol Conversion. Methanol conversion reactions based on borosilicate catalysts have been studied extensively (10,15,24,28,33,52-54). During the conversion of methanol, the reaction proceeds through a number of steps, to yield dimethylether, then olefins, followed by paraffins and aromatics. The weaker acid sites of borosilicate molecular sieves relative to those of aluminosilicates require higher reaction temperatures to yield aromatics. The use of less forceful process conditions leads to the formation of olefins selectively, instead of a mixture of paraffins, olefins, and aromatics (10,28,53,54).

Various borosilicates have been reported in the methanol conversion process. In a study reported in 1984, Hölderich gave details for the preparation of propene selectively from methanol using a borosilicate molecular sieve of the MFI structure type (10). Autocatalysis was observed when small amounts of olefin were added to the feed. Modification of the borosilicates using HF, HCl, or extrusion with amorphous silica-alumina led to changes in the observed product distribution to yield more C_2-C_4 olefins. Use of borosilicates of the MOR and ERI structure types for methanol conversion was reported by Ione, et al. (28). The selectivity to olefins was improved for borosilicates with these structures relative to the silicate of the same structure and aluminum impurity level.

Catalytic Dewaxing. Catalytic dewaxing has become a very important process recently due to the need to process oil feedstocks containing higher levels of nitrogen contaminants. Borosilicates can be used to reduce the pour point of these oils (9,14). Recently, Kuehl (9) has described a process for preparing a borosilicate catalyst which has better resistance to nitrogen poisoning than an aluminosilicate dewaxing catalyst. This improved resistance has been attributed to the molecular sieve calcination procedure which is performed in an oxygen- and water-free environment; this procedure is claimed to minimize the possibility of hydrolysis of boron from the molecular sieve framework.

Other Processes. Borosilicates have been used to catalyze a number of other reactions. Among these are dealkylation of cumene by faujasite-type sieves (11). The sieves used for this reaction were prepared by hydrothermal synthesis and contained some aluminum. The catalytic activity increased as the boron content increased.

According to U S Patent 4 672 049 (55), a borosilicate molecular sieve of the beta structure can be used as the active component in a hydrocracking catalyst. The advantage offered by the use of a borosilicate component in a hydrocracking catalyst was the ability to operate the process under low pressure, specified as 100-1000 psig (broad) or 300-770 psig (preferred).

A summary of some typical processes for which borosilicates are of interest was provided by Hölderich in 1986 (56). Advantages in their use were reported for double bond migrations in carbonyl containing compounds (aldehyde - ketone rearrangement), for the dehydration of aldehydes, for aldol

condensation reactions, and for the preparation of dicarboxylic acid nitriles. Borosilicates and iron silicates exhibited high selectivity in the reported reactions due to moderate acidity.

The conversion of propene to aromatics over borosilicates in the H-, Ga-, and Zn-forms was reported at the 7th International Zeolite Conference by Ono (57). The hydrogen form of the borosilicate exhibited low activity in the aromatization of propene, producing mainly butenes and C_5^+ (nonaromatic). The Zn exchanged borosilicate exhibited good conversion, with about half of the products being aromatic. The mechanism proposed was bifunctional, with Zn or Ga cations being responsible for the dehydrogenation of olefins.

Toluene alkylation by methanol was reported for various metallosilicates (58). Heteroatoms used were Al, B, Cr, and Fe. The selectivity toward p-xylene was highest for the borosilicate sieve (70% at 30% toluene conversion). The high selectivity was attributed to the moderate acidity of the borosilicate and its shape selectivity.

Summary

The growth of borosilicate molecular sieve technology during the past 8 years demonstrated the unique properties of borosilicate molecular sieves. The presence of moderately acidic sites in a shape selective environment has led to a number of novel application areas for borosilicate molecular sieves. Additional applications will arise as scientists turn to these interesting materials for their unique properties.

Literature Cited

1. Taramasso, M.; Perego, G.; Notari, B. In _Proceedings of The Fifth International Conference on Zeolites_; Rees, L. V. C., Ed.; Heyden: London 1980, pp 40-8.
2. Breck, D. W. _Zeolite Molecular Sieves_; John Wiley & Sons: New York 1974, p. 2.
3. Barrer, R. M. In _Proceedings of The Sixth International Zeolite Conference_; Olson, D.; Bisio, A., Eds.; Butterworths: Surrey 1984, pp 870-86.
4. Meier, W. M. _Pure Appl. Chem._ 1986, 58, 1323.
5. Szostak, R.; Nair, V.; Thomas, T. L. _J. Chem. Soc., Faraday Trans. 1_ 1987, 83, 487.
6. Flanigen, E. M.; Lok, B. M.; Patton, R. L.; Wilson, S. T. _Pure Appl. Chem._ 1986, 58, 1351.
7. Wilson, S. T.; Lok, B. M.; Flanigen, E. M. U.S. Patent 4 310 440, 1982.
8. Nimry, T. S. U.S. Patent 4 654 456, 1987.
9. Kuehl, G.H. U.S. Patent 4 661 467, 1987.
10. Hölderich, W.; Eichhorn, H.; Lehnert, R.; Marosi, L.; Mross, W.; Reinke, R.; Ruppel, W.; Schlimper, H. In _Proceedings of The Sixth International Zeolite Conference_; Olson, D.; Bisio, A., Eds.; Butterworths: Surrey 1984, pp 545-55.
11. Onu, P.; Ababi, V. _Rev. Chim._ 1981, 32, 142.
12. Klotz, M. R. U.S. Patent 4 268 420, 1981.

13. Sikkenga, D. L. U.S. Patent 4 503 282, 1985.
14. Angevine, P. J.; Kuehl, G. H.; Mizrahi, S. U.S. Patent
    4 431 518, 1984.
15. Ione, K. G.; Vostrikova, L. A.; Petrova, A. V.; Mastikhin,
    V. M. In <u>Structure and Reactivity of Modified Zeolites</u>;
    Jacobs, P. A.; Jaeger, N. I.; Jiru, P.; Kazansky, V. B.;
    Schulz-Ekloff, G., Eds.; Studies in Surface Science and
    Catalysis <u>18</u>; Elsevier: Amsterdam 1984, pp 151-8.
16. Klotz, M. R. U.S. Patent 4 269 813, 1981.
17. Klotz, M. R.; Ely, S. R. U.S. Patent 4 285 919, 1981.
18. Marosi, L.; Stabenow, J.; Schwarzmann, M. U.S. Patent
    4 401 637, 1983.
19. Taramasso, M.; Manara, G.; Fattore, V.; Notari, B. U.S.
    Patent 4 656 016, 1987.
20. Hoelderich, W.; Mross, W. D.; Schwarzmann, M. U.S. Patent
    4 554 142, 1985.
21. Gabelica, Z.; Debras, G.; Nagy; J. B. In <u>Catalysis on the
    Energy Scene</u>; Kaliaguine, S.; Mahay, A., Eds.; Studies in
    Surface Science and Catalysis <u>19</u>; Elsevier: Amsterdam 1984,
    p 113.
22. Kutz, N. A. In <u>Heterogeneous Catalysis</u>; Shapiro, B. L.,
    Ed.; Texas A&M University Press: College Station 1984, pp
    121-41.
23. Wenqin, P.; Xiaoyan, J.; Milin, G. <u>Gaodeng Xuexiao Huaxue
    Xuebao</u> 1982, <u>3</u>, 577.
24. Vostrikova, L. A.; Ione, K. G.; Mastikhin, V. M.; Petrova,
    A. V. <u>React. Kinet. Catal. Lett</u>. 1984, <u>26</u>, 291.
25. Kessler, H.; Chezeau, J. M.; Guth, J. L.; Strub, H.;
    Coudurier, G. <u>Zeolites</u> 1987, <u>7</u>, 360.
26. Derouane, E. G.; Baltusis, L.; Dessau, R. M.; Schmitt, K.
    D. In <u>Catalysis by Acids and Bases</u>; Imelik, B.; Naccache,
    C.; Coudurier, G.; Ben Taarit, Y.; Vedrine, J.C., Eds.;
    Studies in Surface Science and Catalysis <u>20</u>; Elsevier:
    Amsterdam 1985, pp 135-46.
27. Beyer, H. K.; Belenykaja, I. In <u>Catalysis by Zeolites</u>;
    Imelik, B.; Naccache, C.; Ben Taarit, Y.; Vedrine, J. C.;
    Coudurier, G.; Praliaud, H., Eds.; Studies in Surface
    Science and Catalysis <u>5</u>; Elsevier: Amsterdam 1980, pp
    203-10.
28. Ione, K. G.; Tien, N. D.; Klyueva, N. B.; Vostrikova, L. A.
    In <u>Proceedings of the 7th National Symposium on Advances in
    Catalysis Science and Technology</u>; Prasada Rao, T. S. R.,
    Ed.; John Wiley & Sons: New York 1985, pp 281-6.
29. Meyers, B. L.; Ely, S. R.; Kutz, N. A.; Kaduk, J. A.; van
    den Bossche, E. <u>J. Catal</u>. 1985, <u>91</u>, 352.
30. Solovieva, L. P.; Romanikov, V. N.; Olenkova, I. P.;
    Mastikhin, V. M.; Ione, K. G.; Plyasova, L. M. <u>React.
    Kinet. Catal. Lett</u>. 1986, <u>31</u>, 71.
31. Perego, G.; Cesari, M.; Allegra, G. <u>J. Appl. Cryst</u>. 1984,
    <u>17</u>, 403.
32. Olson, D. H.; Kokotailo, G. T.; Lawton, S. L.; Meier, W.M.
    <u>J. Phys. Chem.</u> 1981, <u>85</u>, 2238.
33. Coudurier, G.; Vedrine, J. C. <u>Pure Appl. Chem</u>. 1986, <u>10</u>,
    1389.

34. Chukin, G. D.; Nefedov, B. K.; Surin, S. A.; Polinina, E.
    V.; Khusid, B. L.; Sidel'kovskaya, V. G. Kinet. Katal.
    1985, 26, 1262.
35. Auroux, A.; Coudurier, G.; Shannon, R.; Vedrine, J. C.
    Calorim. Anal. Therm. 1985, 16, 68.
36. Amelse, J. A.; Nerheim, A. G.; Full, P. R. Advances in
    Catalytic Chemistry III, Salt Lake City, May 1985.
37. Chang, C. D.; Chu, C. T-W.; Kuehl, G. H.; Lago, R. M. Proc.
    Amer. Chem. Soc. Div. Petrol. Chem., April 1985, p. 195.
38. Chu, C. T-W.; Chang, C. D. J. Phys. Chem. 1985, 89, 1569.
39. Jacobs, P. A.; von Ballmoos, R. J. Phys. Chem. 1982, 86,
    3050.
40. Haag, W. O.; Lago, R. M.; Weisz, P. B. Nature 1985, 309,
    589.
41. Amelse, J. A., unpublished data.
42. Low, M. J. D.; Ramasubramanian, N. J. Phys. Chem. 1966, 70,
    2740.
43. Scholle, K. F. M. G. J.; Veeman, W. S. Zeolites 1985, 5,
    118.
44. Gabelica, Z.; Nagy, J. B.; Bodart, P.; Debras, G. Chem.
    Lett. 1984, 1054.
45. Scholle, K. F. M. G. J.; Kentgens, A. P. M.; Veeman, W. S.;
    Frenken, P.; van der Velden, G. P. M. J. Phys. Chem. 1984,
    88, 5.
46. Pelmentschikov, A. G.; Zhidomirov, G. M.; Khuroshvili,
    D. V.; Tsitsishvili, G. V. In Structure and Reactivity of
    Modified Zeolites; Jacobs, P. A.; Jaeger, N. I.; Jiru, P.;
    Kazansky, V. B.; Schulz-Ekloff, G., Eds.; Studies in
    Surface Science and Catalysis 18; Elsevier: Amsterdam 1984,
    pp 85-90.
47. Derouane, E. G.; Fripiat, J. G. J. Phys. Chem. 1987, 91,
    145.
48. O'Malley, P. J.; Dwyer, J. J. Chem. Soc., Chem. Commun.
    1987, 72.
49. Breck, D. W. Zeolite Molecular Sieves; John Wiley & Sons:
    New York 1974, pp 701-4.
50. Kutz, N. A.; Ray, G. J.; Meyers, B. L.; Hall, J. B.
    Advances in Catalytic Chemistry III, Salt Lake City, May
    1985.
51. Nefedov, B. K.; Chukin, G. D.; Lupina, M. I.; Polinina,
    E. V.; Khurib, B. L.; Morgachera, N. Yu.; Kukushkin, W. B.;
    Agievskii, D. A. Neftekhim. 1986, 26, 16.
52. Bragin, O. V.; Vasina, T. V.; Nefedov, B. K.; Lutovinova,
    V. N.; Alekseeva, T. V.; Minachev, Kh. M. Izv. Akad. Nauk
    SSSR Ser. Khim. 1981, 5, 1179.
53. Hegde, S. G.; Chandwadkar, A. J. In Proceedings of the 7th
    National Symposium on Advances in Catalysis Science and
    Technology; Prasada Rao, T. S. R., Ed.; John Wiley & Sons:
    New York 1985, pp 163-9.
54. Ratnasamy, P.; Hegde, S. G.; Chandwadkar, A. J. J. Catal.
    1986, 102, 467.
55. Chen, N. Y.; Huang, T. J. U.S. Patent 4 672 049, 1987.
56. Hölderich, W. Pure Appl. Chem. 1986, 58, 1383.

57. Shibata, M.; Kitagawa, H.; Senoda, Y.; Ono, Y. In <u>New Developments in Zeolite Science and Technology</u>; Murakami, Y.; Iijima, A.; Ward, J. W., Eds.; Studies in Surface Science and Catalysis <u>28</u>; Elsevier: Amsterdam 1986, pp 717-24.

58. Borade, R. B.; Halgeri, A. B.; Prasada Rao, T. S. R. In <u>New Developments in Zeolite Science and Technology</u>; Murakami, Y.; Iijima, A.; Ward, J. W., Eds.; Studies in Surface Science and Catalysis <u>28</u>; Elsevier: Amsterdam 1986, pp 851-8.

Parameters in Addition to the Unit Cell That Determine the Cracking Activity and Selectivity of Dealuminated HY Zeolites

A. Corma[1], V. Fornés[2], A. Martínez[1], and A. V. Orchillés[3]

[1]Instituto de Catálisis y Petroleoquímica, C.S.I.C., Serrano, 119, 28006-Madrid, Spain
[2]Instituto de Ciencia de Materiales, C.S.I.C., Serrano, 115 bis, 28006-Madrid, Spain
[3]Departamento de Ingenieria Química, Universidad Valencia, Burjasot Valencia, Spain

The cracking activity and selectivity for n-heptane and gas-oil, of a series of dealuminated HY zeolites (SiCl$_4$ or steam dealuminated) have been measured. The results have been related with the different types of aluminium and acid groups present and to the pore volume distribution. It is clearly shown that the unit cell parameter (framework Si/Al ratio) can not explain, by itself, the activity and selectivity of dealuminated zeolites. Moreover, the sharp changes in selectivity observed for samples with a_0 below 24.24 Å cannot be explained only on the bases of the strength and density of the acid sites. In order to explain those results, we must consider the different types of tetrahedral and octahedral extraframework aluminium as well as the texture and adsorption hydrophobicity characteristics of the zeolites. Finally, the existence of radical-type cracking, which becomes especially important on highly dealuminated HY zeolites, must be taken into account.

It was proposed recently ($\underline{1}$) that both activity and selectivity of zeolitic cracking catalysts could be correlated with a single zeolite parameter, i.e., the unit cell size of the Y zeolite, which is related to amount of framework aluminium (FAL). It has also become accepted that the cracking activity for gas-oil is directly related to the concentration of isolated aluminiums (Al with ONNN), which are those with the strongest acid hydroxyl groups. On the other hand, the selectivity to gases, gasoline, coke, and the hydrogen transfer reactions will depend not only on the strength of the acid sites, but also on their density.

In agreement with the above, a sharp increase in dry gas formation is observed ($\underline{1}$), while gasoline selectivity decreases, when the unit cell size decreases below 24.24 Å (~2 Al/u.c.).

This was attributed to the increase in acidity due to the completely isolated framework Al. On the other hand, the hydrogen transfer reactions, which are believed to be responsible for olefin saturation and, consequently, for the parallel decrease in the RON observed, have been related to the density of acid sites. These reasonable assumptions can not fully explain, however, the product distribution observed during the cracking of gas-oil on a series of Y zeolites dealuminated at different levels and by different procedures. This is due to the presence, besides the framework-associated Brönsted sites, of Brönsted and Lewis sites which are associated with extraframework aluminium (EFAL) and which can catalyze carbonium ion as well as radical cracking reactions.

The aim of this work is to show that acid strength and site density are not the only parameters controlling activity and selectivity during catalytic cracking. This is due on one hand, to a non-uniform chemical composition along the crystal, and on the other hand to the presence of more than one type of active site on which catalytic cracking takes place, not only via carbocations but also via radical-cation type species.

Experimental

Materials

The starting NaY zeolite was a SK-40 from Union Carbide with a 2.4 framework Si/Al ratio. Ultrastable HY zeolites were prepared by steaming (HYUS) or by $SiCl_4$ treatment (HYD). The HYUS samples were prepared by steam calcination at atmospheric pressure and 500-750°C for 3-20 hours of partially ammonium-exchanged zeolites. After steaming they were exchanged twice with a NH_4^+ solution at 80°C during one hour and then calcined at 550°C for 3 hours. In this way dealuminated samples containing less than 2% of the original Na^+ were obtained.

Samples dealuminated with $SiCl_4$ were prepared following (2) and working at 250-500°C. Textural and structural characteristics of the zeolite samples are given in Table I. The high purity (99.5%) n-heptane was from Carlo Erba. The physicochemical properties of the vacuum gas-oil are given elsewhere (3).

The unit cell constant of the zeolites was determined by X-ray diffraction using CuKα radiation and following ASTM procedure D-3942-80. The estimated standard deviation was $\pm$ 0.01 Å. The crystallinity of the samples was calculated by comparing the peak height of the (5, 3, 3) peak in the sample with that in the NaY SK-40, taken as 100% crystalline.

The ^{27}Al Mas-n.m.r. spectra were obtained in a Bruker AM-400 n.m.r. spectrometer (^{27}Al 104.25 MHz). The spinning frequency wasin the range 4-4.5 kHz. All measurements were carried out at room temperature with $Al(H_2O)_6^{3+}$ as standard reference. Cross polarization and proton decoupling were not used. Time intervals of 2 sec. between successive accumulations were chosen in order to avoid saturation effects. The number of accumulations was 400. The mean error in the measured isotopic chemical shift was 0.5 ppm.

Infrared spectroscopic measurements were carried out in a conventional greaseless i.r. cell. Wafers of 10 mg.cm^{-2} were pretreated overnight at 400°C and 1.33×10^{-2} Pa of dynamic vacuum. The spectra in the 4000-3300 cm^{-1} region were recorded at room tempera-

Table I. Textural and structural characteristics of the HYUS and HYD samples

Zeolite	Si/Al[a]	U.C. (Å)	Si/Al[b]	Al/u.c.[b]	Cryst. %	XPS Si/Al	Area Langmuir ($m^2 g^{-1}$)	Micropore ($m^2 g^{-1}$)
HYUS-1	2.9	24.48	5.9	28.0	85	2.6	847.2	770.7
HYUS-2	2.8	24.42	8.1	21.1	90	0.7	–	–
HYUS-3	2.8	24.34	14.1	12.6	90	–	805.2	707.8
HYUS-4	2.8	24.28	35.3	5.3	75	0.8	–	–
HYUS-5	2.3	24.24	141.0	1.4	70	0.7	616.9	525.2
HYD-1	3.4	24.45	6.9	24.3	95	–	854.3	810.6
HYD-2	3.9	24.39	9.9	17.6	100	0.8	876.9	823.3
HYD-3	4.0	24.31	21.2	8.6	90	–	739.5	688.1
HYD-4	10.4	24.22	–	0	90	–	685.1	606.3
HYD-5	10.2	24.20	–	0	30	–	–	–

a From Chemical Analysis.
b Calculated from Fichtner-Schmittler equation (15).

ture in a Perkin-Elmer 580B spectrophotometer equipped with Data Station. For the pyridine adsorption experiments 666 Pa of pyridine were introduced into the cell at room temperature. After equilibrium the samples were outgassed at temperatures in the range 250-400°C under vacuum, and the spectra recorded at room temperature.

The gas-oil cracking was carried out in a fixed-bed tubular reactor at atmospheric pressure and 482°C. The yields of the different reaction products, i.e., diesel (300°C), gasoline (210°C), methane, ethane, ethylene, propane, propylene, i-butene, n-butane, butenes and coke, were measured at total conversion levels in the range 30-80% wt/wt. The different conversions were achieved by varying the catalyst oil ratio in the range 0.025-0.40 $g.g^{-1}$, but always at 60 seconds the time on stream. The operational procedure is given elsewhere (4).

n-heptane cracking was carried out at 450°C at a catalyst to oil ratio of 0.017-0.180 $g.g^{-1}$ and 75 seconds of time on stream.

Results and Discussion
Variables Affecting Activity

In Figure 1 the catalytic activity for cracking n-heptane is given for the two series of dealuminated zeolites, HYUS and HYD. The n-heptane molecule is small enough for its cracking not to be severely diffusion limited. Two HY zeolites with the same unit cell size (same framework Si/Al) prepared by different procedures have different cracking activities, which may be one indication that other active sites besides the Brönsted acid groups associated with FAL are present. In any case, and since the only elements different from oxygens in the dealuminated samples are silicon and aluminium, any type of acidity present must be associated with aluminium.

Figure 2 shows for HYUS-5 that there are several types of differently coordinated aluminium. Indeed, there are bands at 60, 30 and 1.4 ppm, which are related to tetrahedral, pentahedral (5) or tetrahedrally distorted aluminium (6), and different types of octahedrally coordinated aluminium, respectively. The tetrahedral aluminium appearing at ~60 ppm has always being attributed to FAL^{IV} (7). However, the intensity of the 60 ppm lime (34%) becomes difficult to reconcile with the value of 140 for the zeolite framework Si/Al ratio obtained from the unit cell size (24.24 A). Indeed, from the X-ray unit cell contraction one should expect ~4% of the total aluminium to be in framework tetrahedral position. Then we conclude that in steam dealuminated zeolites there is some aluminium which is not in framework positions but it is also tetrahedrally coordinated (EFAL^{IV}). The same is observed in the HYD samples. We have recently claimed (8) that the EFAL^{IV} could be present as a special type of non-crystalline silica-alumina formed during dealumination. If this is so, there is not doubt that at least some of the EFAL^{IV} could be associated with Bronsted acid sites, which would not be taken into account if only the FAL^{IV} is considered to be related to active Brönsted sites.

In the extraframework octahedral aluminium (EFAL^{VI}) (Fig. 2) there are species appearing at 1.4 and higher ppm's whereas it is usually reported from -0.5 to 0 ppm (6). This is an indication that these EFAL^{VI} species are polymerized, forming an alumina type material. Therefore, in order to explain the cracking activity and selectivity of highly dealuminated zeolites we have to take into
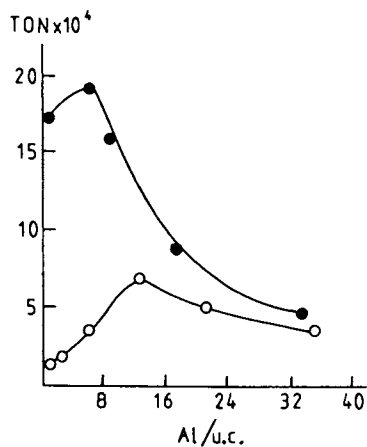
Figure 1. Turnover Frequency for cracking n-heptane on a series of HY dealuminated zeolites as a function of number of aluminiums per unit cell.
         ● SiCl$_4$ dealuminated zeolites
         ○ Steam dealuminated zeolites
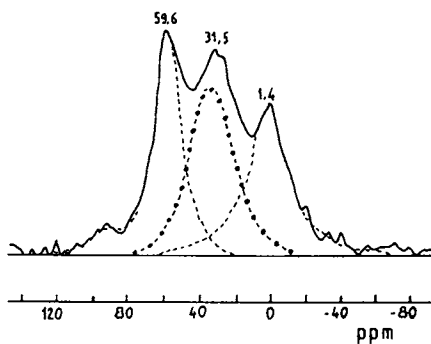
Figure 2. ^{27}Al MAS–NMR spectrum of HYUS–5 sample.

account not only the Brönsted acidity related to FAL^{IV}, but also the Brönsted acidity, which may be associated to $EFAL^{IV}$. Furthermore it looks as if in highly dealuminated HY zeolites there was alumina–like species, which according to the XPS results presented in Table I are accumulated on the surface. It is known that high surface alumina is active for cracking gas-oil, but not selective for gasoline formation, giving high amounts of dry gas and coke. Therefore, the observed final catalytic properties will not depend on one single parameter, i.e., FAL^{IV} or unit cell size dimension of the Y zeolite, but on the three parameters discussed above,i.e., FAL^{IV}, $EFAL^{IV}$ and the different types of $EFAL^{VI}$.

It is well known that the hydroxyl groups associated with FAL^{IV} show two bands in the i.r. region at 3630 cm^{-1} (HF) and 3555 cm^{-1} (LF). $EFAL^{IV}$ species such as the non–crystalline silico–alumina, which can be responsible for Brönsted sites other than that corresonding to the HF and LF hydroxyl bands, should appear in the same region, and would interact with pyridine. Indeed, very recently (8, 10) we have shown that in dealuminated Y zeolites some of the hydroxyl groups appearing at 3600 cm^{-1} which retain pyridine even after degassing the sample at 400°C under vacuum.

Figure 3 shows the µmols of pyridine remaining adsorbed on the strong Brönsted sites (1545 cm^{-1} band, associated with FAL^{IV} and $EFAL^{IV}$) after desorption at 350° and 400°C. As has been shown previously (5), the intensity of the 3600 cm^{-1} i.r. band assigned to acid hydroxyls is much more important for HYD than for HYUS samples. Moreover, the acid strength of this type of site is higher than that of the HF and LF sites (10). Consequently, the higher amount of Bronsted acidity shown by HYD samples in Figure 3 must be associated to $EFAL^{IV}$ (silico–alumina). This result explains the higher n–heptane cracking activity observed for HYD samples as compared with the HYUS. Moreover it appears that the amount of Brönsted sites related to the $EFAL^{IV}$ is maximum at framework Si/Al ratios > 10. It is also observed that in the steamed zeolites the acid hydroxyls appearing at the 3600-3610 cm^{-1} band have practically dissappeared for FAL^{IV} content lower than 10 Al/u.c.

The above results could be interpreted in the following way: A catalytically active non–crystalline silica–alumina is formed in samples steamed at temperatures in the range 500-600°C (samples with more than 20 Al/u.c.). However, if the steaming temperature is higher than 600°C (samples HYUS-2, 3 and 4) the silica–alumina formed starts to dealuminate, i.e., to loose Al^{IV}, and after steaming at 750°C during 20 hours (sample HYUS-5) most of the 3600-3610 cm^{-1} acid hydroxyls associated with the silico–alumina have disappeared, or at least the amount is not enough to be detected by i.r. spectroscopy. This has been confirmed by the ^{27}Al m.a.s.-n.m.r. spectra of commercial amorphous silica–alumina before and after steaming at the above conditions. We have observed that the intensity of the Al^{IV} line at 54 ppm decreases strongly, while the 30 and 0 ppm lines increase (5, 11). Nevertheless, the non–crystalline silica–alumina, if it could be stabilized, would be of great interest for both bottom conversion (since it should concentrate on the surface) and for reducing the RON–MON differences in the gasoline formed.

If we consider gas-oil cracking, from the point of view of the number of acid sites one should expect the HYD samples to be more active than the HYUS ones at a given unit cell size. However, in

Figure 4 just the opposite behaviour can be observed, i.e., the HYUS are more active for gas-oil cracking than the HYD zeolites. The comparison between Figures 1 and 4 shows that the cracking behaviour of the gasoline (n-heptane) and gas-oil are quite different, i.e., they do not see the same catalyst. In a first approximation one could think that this is due to a need of different active sites for n-heptane and gas-oil. However, taking into account that the gas-oil feed (3) is mainly formed of paraffins, naphthenes and alkyl polyaromatics, the cracking of all of which needs, as that of n-heptane does, bronsted acid sites (12), we have to rule out this possibility. Another possibility would be that the observed relative activities of the HY zeolites with respect to the two reactants considered are caused by differences in size of the gas-oil and n-heptane molecules, since the first does not penetrate as deeply as the second inside the zeolite crystals. Then, one should expect the gas-oil to be cracked only in an outer shell of the zeolite crystallites, while the gasoline could react much deeper inside the crystallites. If the observed difference is due to this, it could mean that the zeolites are not homogeneous in their composition,i.e., that the chemical composition at the surface and in the "bulk" are different. If this is so, in the case of gas-oil it is a hopeless task to try to relate bulk characteristics, i.e., unit cell size, pyridine or NH_3 adsorption-desorption, with catalytic activity, and one has to look instead at surface composition and surface accessibility. Since, as we have said above, other acid sites do exist besides those related with framework Al^{IV}, it should be better to calculate the activity per acid site by dividing the apparent rate constant by the μmols of pyridine adsorbed on the strong acid sites (ATOF), instead of dividing by the number of framework Al^{IV}. In this way one should take into account all acid sites independently of their association to Al^{IV} FAL or EFAL. If this is so, it should be expected that after 15-20 Al/u.c. the calculated ATOF should remain constant independently of the unit cell size or of the dealumination procedure. However, in Figure 5 it can be seen that for HYUS zeolites the apparent turnover frequency (ATOF) for gas oil, measured as kinetic rate constant at 60% level of conversion divided by the amount of pyridine remaining adsorbed after desorption at 350°C and 1.33 x 10⁻ Pa, increases up to 5 Al/u.c. and then stays constant. However, in the HYD samples the ATOF increases slightly with dealumination. These results indicate that pyridine, which can penetrate deep inside the crystallites, cannot correlate with the cracking of gas-oil, which reacts mainly on the surface. Moreover, if we correlate the adsorbed pyridine to the activity for cracking of n-heptane (Fig. 6), a molecule which can penetrate inside of the zeolite crystallites, it can be seen that ATOF is constant for highly dealuminated zeolites and the differences observed between zeolites dealuminated by different procedures have been strongly diminished with respect to those observed in Fig. 1. The mesopore volume of the zeolites, which gives an indication of its surface accessibility, supports the above hypothesis. Indeed, the pore volume, in the mesopore region, is much higher for HYUS than for HYD samples (Fig. 7), and this difference increases with dealumination. Finally, in Figures 5 and 6 we see the same evolution on both curves, i.e., the mesopore volume of HYUS strongly increases with dealumination
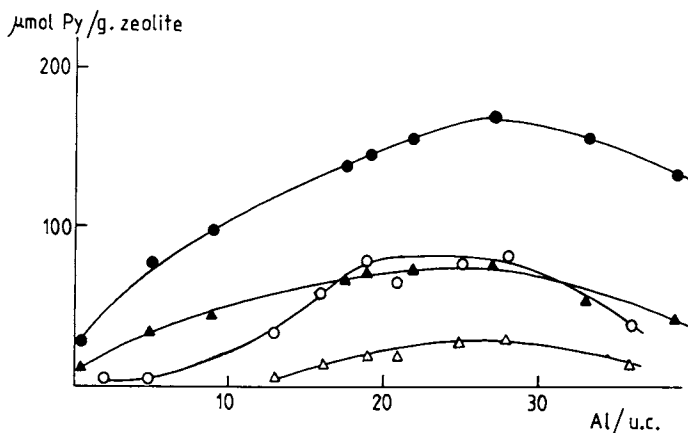
Figure 3. Brönsted acidity of dealuminated Y zeolites as a function of FAL per unit cell.
        O Pyridine retained after desorption at 350 °C and vacuum.
        △ Pyridine retained after desorption at 400 °C and vacuum.
      ●,▲ SiCl$_4$ dealuminated zeolites
      O,△ Steam dealuminated zeolites
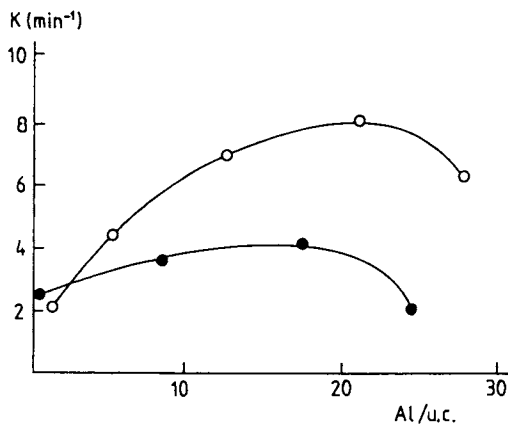
Figure 4. Activity for gas-oil cracking as a function of FAL per unit cell, for samples dealuminated by:
       ● SiCl$_4$
       O Steam
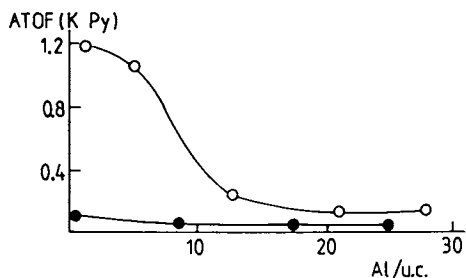
Figure 5. Apparent turnover frequency (ATOF) for gas-oil cracking as a function of FAL per unit cell.
● SiCl$_4$
○ Steam
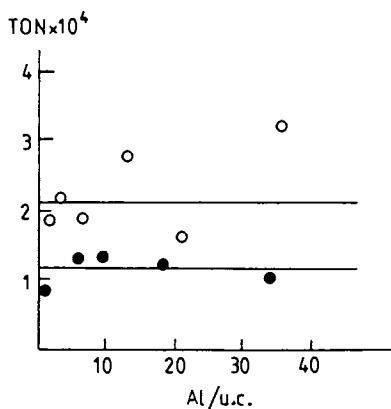
Figure 6. Turnover (Activity/Al$_{fw}$ +3600 cm^{-1}) for n-heptane cracking as a function of FAL per unit cell.
● SiCl$_4$
○ Steam
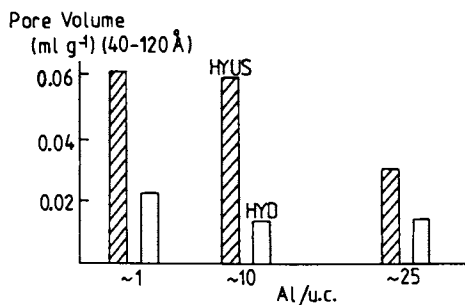
Figure 7. Pore volume (pore size between 40 and 120 Å) as a function of FAL per unit cell, for samples dealuminated by:
▨ Steam
☐ SiCl$_4$

(steaming temperature) up to 5 Al/u.c. and then remains constant, while in the HYD samples it slowly increases with the dealumination level.

Gas-oil Cracking Selectivity

Figure 8 shows that the selectivity of HYUS samples for dry gases strongly increases when the number of aluminiums per unit cell goes below 10 (unit cell size lower than 24.39). At these levels, and for a random aluminium distribution, practically all FAL^{IV} should be completely isolated, in agreement with the n.m.r. results reported in the literature (7). If this is so, further dealumination to 5 and 2 Al/u.c. should not change the acid strength of the remaining FAL. Then, we cannot explain the observed increase of $C_1 + C_2$ hydrocarbons as a consequence of the presence of stronger acid sites. Figure 9 shows that methane is a secondary product; if it is also a primary product the initial selectivity is very small. It is clearl that for a secondary product any increase in mesoporosity (decrease in diffusion limitation) should decrease its selectivity. However, in the HYUS the selectivity to $C_1 + C_2$ not only does not decrease but increases with increasing mesopore volume. Therefore, the increase in selectivity must be due to the increase, with dealumination, of the number of sites not selective for the formation of liquid products, at least relative to the number of Brönsted acid sites which are more selective for gasoline production.

We have said above that at high dealumination temperatures during steaming, a part of the extracted aluminium is polymerized, forming alumina-type species ($EFAL^{VI}$). This high surface alumina could give dry gases and coke by cracking via a radical mechanism. If this is so, the radicals could be formed and stabilized in electron deficient sites of the zeolite, such as Lewis acid sites, which are relatively abundant in alumina.

The formation of coke and the loss of RON have been associated (1) with the hydrogen transfer ability of a given catalyst: the higher the hydrogen transfer ability, the higher the selectivity to coke and the lower the RON of the gasoline due to olefin saturation. On the other hand, it has been reported (1) that the hydrogen transfer reactions need closely located Bronsted sites,and therefore, the advance of this reaction will depend on the density of Bronsted acid sites. There are, however, at least two facts that seriously question the hydrogen transfer mechanism based on a bimolecular reaction in the Langmuir-Hinshelwood sense. The first inconsistency is that it would be very difficult to draw a mechanism for hydrogen transfer involving two neighbour acid sites. This mechanism would imply the proximity of two positively charged molecules. In order to desorb one of those, it would be necessary to transfer the positive charge to the neighbouring adsorbed molecule, increasing, therefore the positive charge on the first one. The second inconsistency is that from Figure 8 and from other results reported in the literature (1), it is apparent that the RON is still increasing when the amount of FAL^{IV} per unit cell decreases from 5 to 1. Since one unit cell involves 8 supercavities, if the increase observed in RON is only due to a decrease in the density of acid sites, and therefore to a decrease in the hydrogen transfer reaction, then
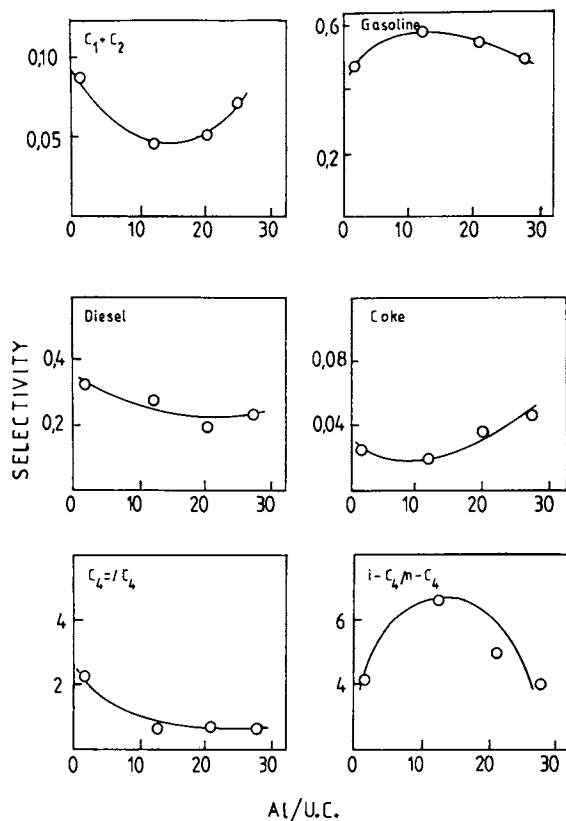
Figure 8. Selectivities to different products of cracking of gas-oil (60 % level of conversion) as a function of FAL per unit cell for steam dealuminated zeolites.
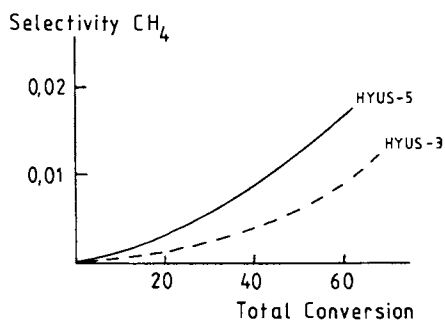
Figure 9. Selectivity to methane as a function of total conversion for two HYUS samples.

it would be difficult to explain the results at so low contents of FAL^{IV} , since the distance between sites is much higher than the distances required for bimolecular interactions.

There is an alterntive for explaining the high oleficinity of the gasoline obtained with highly dealuminated zeolites (unit cell size < 24.25 Å). It has been said before (1) that with a low unit cell size HY zeolite, the selectivity to gasoline decreases while that of gases increases. This can be attributed to a higher recracking of the gasoline occurring in highly dealuminated zeolites (Fig. 8). If this is so, it means that the higher the recracking, the higher the cracking of long chain olefins formed in the first cracking event will be. Since the cracking of one olefin gives two olefins, and the cracking of a paraffin gives one olefin and one paraffin, it is obvious that if more recracking takes place at the same level of total conversion, the higher the olefin to paraffin ratio will be in the gasoline and in the C_4 and C_3 fraction. Moreover, we have said above that in highly steam dealuminated zeolites a highly dispersed alumina phase is present on the surface of the zeolite. Since it is known that cracking on alumina produces a high proportion of olefins, the alumina ($EFAL^{VI}$) would be partially responsible for the increase in the olefin/paraffin ratio and therefore, for the increase in RON observed for highly steam dealuminated HY zeolites. However the cracking mechanism on the alumina and on the zeolite component does not have to be the same. Indeed, the zeolite framework presents only Bronsted acidity which cracks paraffins via carbonium ion intermediates. Alumina, on the other hand, shows only Lewis acidity and should crack paraffins via carbenium ions or via cation-radical intermediates. A characteristic of radical cracking of paraffins is the formation of a high proportion of olefins and a low ratio of branched to unbranched product (13). From Figure 8 it becomes clear that in highly dealuminated zeolites, a futher dealumination produces an increase in the olefin/paraffin ratio and a decrease in the branched to unbranched products in the C_4 fraction which has been taken here as a yardstick.

These results show that, together with the typical carbocation cracking, a radical cracking mechanism is also taking place, especially on highly steam dealuminated zeolites. This radical mechanism, which will become proportionally more important when the framework aluminium content of the zeolite will decrease, could explain the strong increase in ethylene formation and decrease in branched/unbranched C_4 ratio when decreasing the unit cell size of the zeolite.

Finally another parameter, which is very seldom taken into account when considering zeolite reactivity, is that of the changes in adsorption provoked by decreasing the framework Si/Al ratio. The higher activity of zeolites with respect to amorphous silica–alumina has been explained on the basis of two factors: higher amount of acid sites in zeolites, and higher concentration of reactants in the micropores of the zeolite (14). When dealuminating the zeolites, the concentration of reactants, especially the more polar ones, strongly decreases in the micropores. Therefore, bimolecular cracking will be more affected than unimolecular reactions (monomolecular cracking).

In conclusion, it can be said that gas–oil cracking activity does not depend only on the unit cell size. During dealumination

non-crystalline silica-alumina is formed, with strong Bronsted acidity, and therefore catalytic activity. The EFAL accumulates on the surface, and under hard steaming conditions is present as polymerized alumina, which is also active for catalytic cracking. The mesoporosity of the zeolite can be a determinant in the cracking of gas-oil. This is a consequence of the small penetration in the zeolite crystal of the gas-oil molecules and the different chemical composition of the surface and bulk of the zeolite.

The strong increase in C_1 and C_2 species for the low unit cell size can be explained on the basis of a competing radical-type cracking occuring on electron acceptor sites of the zeolite. Finally, the product olefin content, and therefore the RON of the gasoline and the coke formed, will depend on the amount of recracking, relative amount of radical to carbocation cracking and on the concentration of reactants in the micropores.

Acknowledgments

Literature Cited

1. Pine, L.A.; Maher, P.J.; Watcher, W.A. J. Catal. 1984, 85, 466.
2. Beyer, H.K.; Belenkaya, I. In Catalysis of Zeolites; Imelik, B., et al., Ed.; Elsevier, Amsterdam, 1980; p 203.
3. Corma, A.; Juan, J.; Martos, J.; Molina, J. J. Proc. 8th Int. Congr. Catal., 1984, II, p 293.
4. Corma, A.; Herrero, E., Martínez, A.; Prieto, J. Symposium in Advances in Fluid Catalytic Cracking, New Orleans, 1987.
5. Gilson, J.P.; Edwards, G.C.; Peters, A.K.; Rajagopalan, K.; Wormsbecher, R.F.; Roberie, T.G.; Shatlock, M.P. J. Chem. Soc. Chem. Comm. 1987, 91.
6. Samoson, A.; Lippmaa, E.; Engelhardt, G.; Lohse, D.; Jerschmitz, H.G. Chemical Physics Letters. 1987, 134, 589.
7. Thomas, J.M.; Klinoswki, J.K. Adv. Catal. 1986, 33, 200.
8. Corma, A.; Fornés, V., Martínez, A.; Melo, F.; Pallota, O. Int. Symposium on Innovation in Zeol. Materials Science, Niewpoort (Belgium) 1987.
9. Frende, D.; Hunger, M.; Pfeifer, H. Zeits. Phys. Chemie. Neue Folge Bd. 1987, 152, 5183.
10. Garralón, G.; Sanz, J.; Fornés, V.; Corma, A. J. Chem. Soc. Chem. Comm. (in press).
11. Sanz, J.; Fornés, V.; Corma, A. J.C.S. Faraday I (submitted for publication).
12. Corma, A.; Fornés, V.; Montón, J.B.; Orchillés, A.V. Ind. Eng. Chem. Prod. Res. Dev. 1986, 25, 231; ibid 1987, 26, 882.
13. Wojciechowski, B.W.; Corma, A. Catalytic Cracking: Catalysts, Chemistry and Kinetics; Marcel Dekker, Chem. Ind. Ser., 1986, 25.
14. Gates, B.C.; Katzer, J.R.; Schmit, G.C.A. Chemistry of Catalytic Processes, New York, McGraw-Hill, 1979.
15. Fichtner-Schmittler, H.; Lohse, V.; Engelhardt, G.; Patzelova, V. Crys. Res. Technol. 1984, 19 (1), k1-k3.

Chapter 36

Relation Between the Aluminum Content of the Faujasite Framework and the Isomerization and Disproportionation of m-Xylene

A. Corma[1], V. Fornés[2], J. Perez-Pariente[1], E. Sastre[1], J. A. Martens[3], and P. A. Jacobs[3]

[1]Instituto de Catálisis y Petroleoquímica, C.S.I.C., Serrano, 119, 28006–Madrid, Spain
[2]Instituto de Ciencia de Materiales, C.S.I.C., Serrano, 115 bis, 28006–Madrid, Spain
[3]Laboratorium voor Oppervlaktechemie, Katholieke Universiteit Leuven, Kardinaal Mercierlaan 92, B–3030 Leuven (Heverlee), Belgium

For the conversion of m-xylene, the activity of H-faujasite depends strongly on its degree of dealumination. Maximum catalytic activity is obtained for aluminum T-atom fractions equal to 0.10. Surprisingly, in contrast to both theoretical predictions and to the behaviour of H-ZSM-5, for dealuminated H-faujasites the turnover frequency per protonic aluminum site exhibits a pronounced maximum when the aluminum T-atom fraction is 0.09. The present results can be rationalized if, besides the classical predictions on zeolite acidity, a new concept of "hidden acid sites" is handled. Changes of the m-xylene isomerisation and disproportionation selectivities with the degree of dealumination of faujasite are in agreement with this concept.

It is well established that the catalytic activity of decationated zeolites for Brønsted acid catalysed reactions is related to the presence of protons, associated with tetrahedral framework aluminum (Al_F). Convincing evidence for the nature of the active sites in high-silica acidic zeolites has been provided by Haag et al. ([1]), who showed that in H-ZSM-5 the catalytic activity for n-hexane or n-hexene cracking and for the double bond shift in 1-hexene is proportional to the number of Al_F atoms. This relation holds for aluminum T-

atom fractions ($Al_F/Al_F + Si_F$) ranging from 0.03 to zero. The proportionality between catalytic activity and aluminum content of H-ZSM-5 has been ascribed to the presence of active sites with constant acid strength, associated with the presence of a single type of Al_F (1,2).

For the last two decades the acidity changes of H-faujasite upon removal of Al_F atoms have received continuous research interest (3). Essentially two approaches have been followed to rationalize these changes. In one approach, the strength of the acid sites is correlated with the presence of aluminum in the second coordination sphere of a given aluminum atom (4-6). The second approach considers the influence of the overall chemical composition on the protons and results in expressions for the mean acid strength in terms of activity coefficients (7) or of the electronegativity of the framework and the atomic charges on the protons (8,9). The common feature of all approaches is that they predict a continuous increase of the average acid strength per site with decreasing numbers of Al_F atoms. The topological approach predicts that all acid sites become strong when less than 29 Al_F per unit cell (UC) are present, corresponding to a value of 0.15 for $Al_F/Al_F + Si_F$ (10).

Correlations between the catalytic activity and the aluminum content of decationated faujasites have been reported (11-14). DeCanio et al. (12,14) derived from their data that rates of hexane cracking and cumene dealkylation, expressed on a weight basis of catalyst, are linearly related to the number of Al_F atoms in faujasite. The aluminum T-atom fractions of the samples varied from 0.18 to 0.004. However, from the discrepancy between overall and framework aluminum contents of these samples it can be concluded that all materials contained significant amounts of extra-framework aluminum (Al_{EF}). Therefore, we have recalculated the rate data of DeCanio et al. (12,14) assuming that Al_{EF} is catalytically inactive and has Al_2O_3 as overall stoichiometry. In Figure 1 the turnover frequencies per Al_F obtained in this way are plotted against the aluminum T-atom fraction. Surprisingly, for both reactions the turnover frequencies exhibit a maximum for a specific composition of the faujasite catalyst. Other literature data on cumene cracking (13) determined for less siliceous samples are complementary in this respect.

In this paper we will provide another example of the occurrence of a maximum catalytic turnover frequency for a specific composition of the faujasite catalysts. We also will present further evidence that for every Brønsted acid catalysed reaction in H-faujasites, this is the generally expected behaviour and will introduce a new concept to rationalize this.
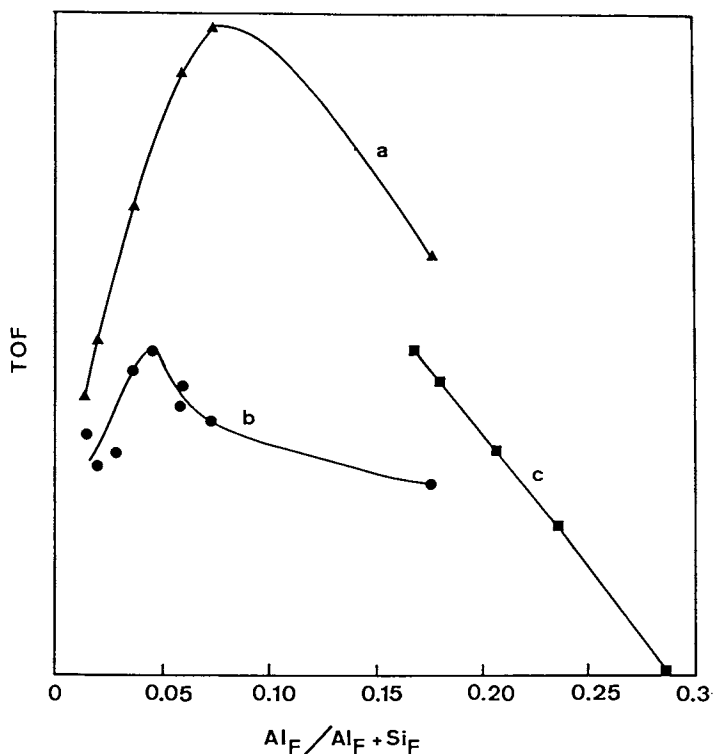
Figure 1. Literature data on the evolution of the catalytic turnover frequency (TOF) per framework aluminum site of H-faujasite: (a), cumene cracking (4); (b), hexane cracking (6) and (c), cumene cracking (3).

Experimental

Dealumination procedure. NaY (Linde SK-40, with Si/Al=2.4) was dealuminated with $SiCl_4$ as described in literature (15). Powder of NaY was compressed, crushed and sieved to obtain pellets with a diameter between 0.6 and 0.9 mm. The pellets were loaded in a tubular reactor and dried at 773K in flowing nitrogen for 2h. Subsequently, the reactor was cooled to the desired dealumination temperature and the zeolite contacted with a stream of nitrogen, saturated at room temperature with $SiCl_4$ vapor. The degree of dealumination was changed by varying the reaction temperature between 473 and 773K. Sample 8 was obtained by dealuminating subsequently at 523, 623 and 723K, each time for a period of 2h. The dealuminated sample was recovered after flushing the reactor with nitrogen at the final temperature. The final product was obtained by washing thoroughly with deionised water, exchange with NH_4^+ and calcination at 823K in deep-bed conditions. Exchange with NH_4^+ and deep-bed calcination was repeated three times at 823K to remove any sodium left.
    The degree of crystallinity of the samples was determined using the intensity of the [5,3,3] reflection with XRD and considering the parent NaY to be 100% crystalline. The Al_F content was derived from the unit cell size, a_o, applying the relation of Fitchner-Schmittler et al. (16). Lattice constants, Al_F/Al_F+Si_F ratio's and degrees of crystallinity of the dealuminated faujasites are listed in Table I.

Infrared spectroscopy. Infrared spectra were scanned using a PE580B instrument with data station. The zeolite powder was compressed in wafers of 10 mg cm^{-2} and mounted

Table I. Lattice constant, aluminum T-atom fraction and degree of crystallinity of NaY dealuminated with $SiCl_4$

Sample number	a_o (nm)	Al_F/Al_F+Si_F	crystallinity (%)
1	2.452	0.180	80
2	2.446	0.115	90
3	2.443	0.110	50
4	2.440	0.100	100
5	2.439	0.090	70
6	2.435	0.070	80
7	2.430	0.040	65
8	2.426	0.015	90

in a vacuum cell. All spectra were recorded at room temperature. The samples were pretreated overnight at 673K and 1.33 mPa. For the pyridine adsorption experiments, 660 Pa of base was introduced at room temperature in the cell. The cell was then outgassed in vacuo at 423K before recording the spectrum.

Catalytic testing. The reaction of essentially pure m-xylene was carried out in a fixed bed, tubular glass reactor with an internal diameter of 1.5 cm. Catalyst particles with a diameter of 0.1 mm were prepared by compressing the zeolite powder and crushing of the flakes. A typical experiment was performed in the following way. First the catalyst was heated in nitrogen to 623K and kept there for 0.5h. Thereafter it was increased to 723K for another hour. The reaction temperature was always kept at 623K, while the molar ratio nitrogen/m-xylene was 4. W/F_o, in which W stands for the amount of catalyst and F_o for the molar flow of m-xylene at the reactor inlet, was varied between 0.02 and 2.00 kg mmole^{-1}s^{-1}. During the first 40 minutes on-stream, the reaction products were collected at regular time intervals. The liquid products were analysed with GLC using a packed column with 16% DC-200 methyl silicone oil and 3% Bentone 34 on 80-100 mesh Chromosorb W. A Konic-200C GC with F.I.D. detector was used.

As deactivation was observed for all catalysts, the initial conversion, X_o, was obtained from conversion against time curves by fitting the experimental results to the following equation:

$$X_t = X_o \exp(-kt^{0.5}) \qquad (1)$$

Initial selectivities were calculated as the ratio of the initial rates of formation of the products.

Results and Discussion

The "Hidden Site" Concept in Faujasite. The infrared active hydroxyl vibrations in H-faujasite absorb at two distinct frequency regions, commonly denoted as high-frequency (HF) and low-frequency (LF) hydroxyl bands (17). In the structure of faujasite, there are four crystallographically distinct oxygen atoms. The HF band vibrating in the 3680-3625 cm^{-1} range is generally assigned to O_1H groups vibrating in the supercage and therefore corresponding to a free and unperturbed OH vibration (18). The LF band vibrating around 3560 cm^{-1} has been assigned to O_2H, O_3H and O_4H groups, which are necessarily associated with six-membered rings (6-MR) (18). Although the detailed assignment of both bands has

been subject of much debate, particularly in the older literature, general agreement exists now that the proton distribution over the crystallographically different oxygen atoms is not random in faujasite, although each oxygen type is a possible proton capturing site ([17]). The batochromic shift of the LF band with respect to the unperturbed position seems to be the result of its hidden location and can be explained by an electrostatic interaction with the nearest oxygen atom in the 6-MR ([19]). From the adsorption experiments of pyridine on H-Y zeolite it follows that the entire HF OH band can be converted to pyridinium ions, while in the same conditions only part of the LF band undergoes this reaction ([20]). Recent ^{1}H MAS NMR experiments in the presence and absence of pyridine confirm the infrared results ([21,22]).

In hydrothermally treated NH_4-Y samples, both sorts of bridging OH groups are accessible to pyridine, but the interaction with the OH groups of the line at 5.2 ppm, corresponding to the LF infrared band, remains weaker than with those of the 4.2 ppm resonance line, corresponding to the HF band ([22]). It is well established that in such samples extra-framework aluminum species are present giving rise to new OH bands at 3600 and 3670 cm^{-1} disappearing only partially upon adsorption of pyridine ([20,23]).

In faujasite, the Al content must necessarily be varied by dealumination of a low-silica zeolite, as no synthesis recipe for high-silica faujasite is available. Because the aim of this work was to study the acidity of the zeolite itself, the $SiCl_4$ dealumination method was selected in order to minimise the formation of extra-lattice aluminum ([24]).

OH spectra of the present series of faujasite samples, dealuminated to various extent with $SiCl_4$, are shown in Figure 2. The OH spectra taken before and after pyridine addition as well as the corresponding difference spectra are compared. On the first sample, the HF band disappears completely, while the LF band reacts only partially (Figure 2a). For all other samples the OH spectra are of such complexity that clear statements about this behaviour cannot be made. However, the difference spectra of these samples show again the typical HF and LF pattern, indicating that out of all major OH bands initially present, only these two bands show an acidic behaviour towards pyridine. For a highly dealuminated sample (Figure 2d) a minor acidic component emerges at 3610 cm^{-1}. Very probably this component will be also present on the other samples, but, for obvious reasons cannot be resolved. Thus, dealumination in the present conditions at the level of the OH spectra creates two new bands, a non-acidic one at 3600 cm^{-1} and an acidic one at 3610 cm^{-1}. The former band has often been attributed to the presence of extra-framework Al-OH

species (20,23), the latter one has been tentatively assigned to Brønsted acid sites belonging to an extra-framework silica-alumina phase, formed upon dealumination (25). Indeed, highly acidic OH groups on amorphous silica-alumina also absorb at 3610 cm^{-1} (25). In line with this is the observation that in pyridine poisoned samples, the OH vibration at 3610 cm^{-1} remains extinguished up to desorption temperatures as high as 623K.

Provided that the preference of protons for the different types of oxygens does not change with the degree of dealumination and consequently that the ratio of the average acid strength of both sites does not change, the ratio of the intensities of the LF and HF OH bands is also expected to remain unchanged. In Figure 3, this ratio is shown to remain constant for all samples. For the highly dealuminated samples (sample 2-7) it was determined with the help of the difference spectra. For the first sample it was measured on the original spectrum. From all this can be concluded that not only the ratio of hidden to readily available Brønsted acid sites remains constant with the degree of dealumination, but also that on highly dealuminated samples all OH groups contained in the LF band should be accessible to pyridine.

Catalytic Activity for m-Xylene Conversion and Degree of Dealumination. In the reaction conditions used, the following reaction products were formed: p- and o-xylene, toluene and the trimethylbenzene isomers. At high conversion benzene and tetramethylbenzenes were also detected. The initial rate of formation of the products is given in Figure 4, against the Al T-atom fraction. A maximum in the catalytic activity is obtained when $Al_F/Al_F+Si_F=0.10$. As the isomerisation and disproportionation of m-xylene is catalysed by Brønsted acid sites (26) and their total number increases gradually with the T-atom fraction, the data of Fig.4 indicate that the average turnover number per Brønsted acid site cannot be constant.

Average turnover frequencies (TOF) were calculated by dividing the initial rates of formation of the products by the framework aluminium content per weight of catalyst. A maximum TOF is found when the aluminum T-atom fraction is 0.10 (Figure 5a and c). From the present results and those presented in Figure 1, it seems that with faujasite generally a maximum TOF is found for a specific aluminum fraction of the T-atoms.

Because the catalytic activity exerted by the non-framework Brønsted acid sites is neglected in this approach, an alternative way of determining average turnover frequencies was used. TOF[*] values were determined by dividing the initial rates by the number of strong Brønsted acid sites, measured as the intensity of
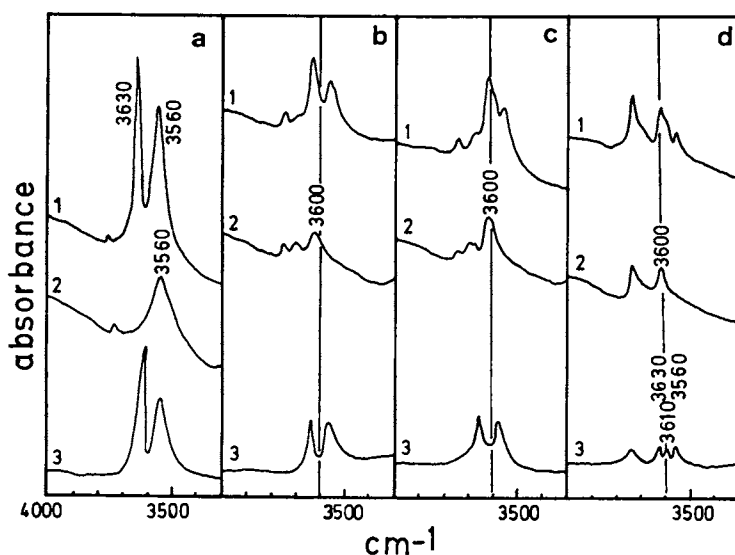
Figure 2. Hydroxyl stretching vibration spectra of sample 1 (a), 2 (b), 4 (c) and 6 (d) before adsorption of pyridine (1) and after evacuation of pyridine at 423K (2); (3) is the difference spectrum between (1) and (2).
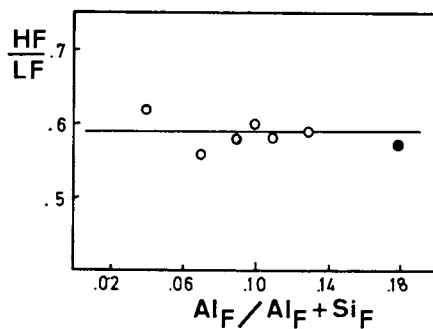
Figure 3. Ratio of the intensities of the HF and LF OH bands in function of the aluminum T-atom fraction.
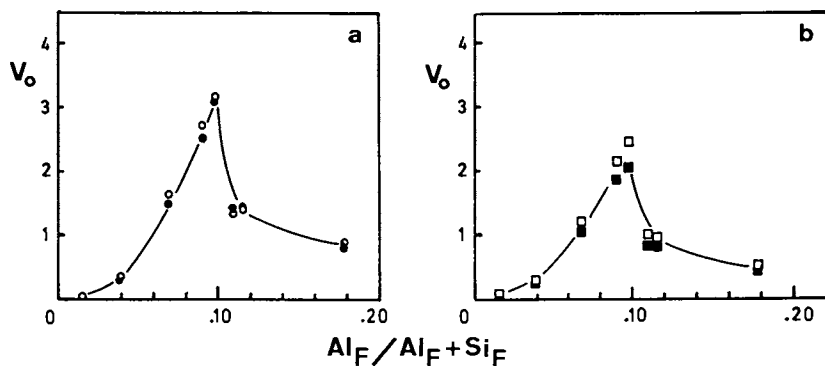
Figure 4. Relative initial rates of formation (Vo) of (a), p- (o) and o-xylene (●), and (b), toluene (■) and trimethylbenzenes (□) in function of the aluminum T-atom fraction.
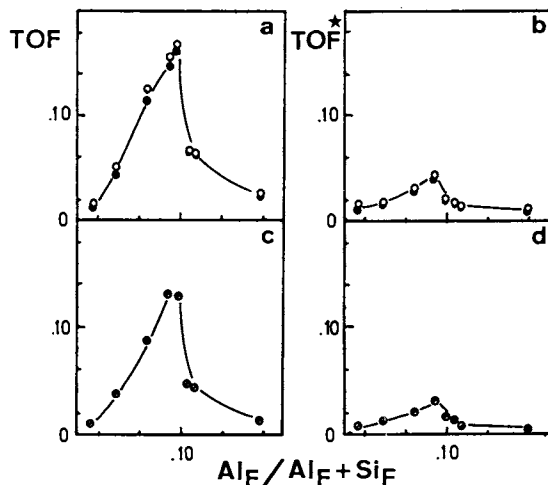
Figure 5. TOF and TOF* of the formation of p- (o) and o-xylene (●), and trimethylbenzenes (Ø) in function of the aluminum T-atom fraction.

the infrared absorption of pyridinium ions in the samples after degassing at 623K. In this way differences in degree of crystallinity or of surface area between the various samples can be eliminated. Furthermore, as the kinetic diameter of pyridine and m-xylene are similar, differences in the porosity of the samples are also accounted for. In Figure 5b and d it is shown that TOF* exhibits a maximum for aluminium T-atom fractions equal to 0.09.

All theoretical models on zeolite acidity predict that the acid strength, and consequently the turnover frequency decreases with increasing aluminum T-atom fraction. In line with these predictions, a decrease of TOF* is observed for aluminum T-atom fractions higher than 0.09 (Figure 5b and d). However, the increase of TOF* with increasing aluminum T-atom fraction from 0.015 to 0.09 is in contradiction with the theoretical predictions. One explanation for the increase of TOF* for aluminum T-atom fractions lower than 0.09 is that the turnover frequencies of extra-framework acid sites, e.g. those belonging to the amorphous silica-alumina intra-crystalline phase, are lower than those of the framework itself. If the number of extra-framework acid sites is lower for lower degrees of dealumination, an increase of TOF* with the aluminum T-atom fractions in the range from 0.015 to 0.09 can be explained. However, no fundamental reason seems to exist why the turnover frequencies of the extra-framework acid sites should be lower than of the framework sites, as both exhibit strong acidity towards pyridine.

The hidden acid sites might exert a negative effect on TOF* of highly dealuminated faujasites in the following way. As there is a physical limit to the number of m-xylene molecules that have access to the faujasite supercages, for high Al_F contents an excess of readily available acid sites that can protonate pyridine should be present. As a result, part of the readily available sites and all the weaker framework sites will be catalytically inactive. Upon dealumination both types of sites become diluted and from a certain degree of dealumination on, the screening of the "hidden sites" by the readily available ones will cease. The m-xylene molecules which are adsorbed on the hidden proton sites, characterized by a lower acidity towards pyridine, are converted at a lower rate and this results in low TOF*.

At this point a factor should be stressed which is frequently neglected when the influence of dealumination on the catalytic activity is considered, namely the influence of the $Al_F/Al_F + Si_F$ ratio on the concentration of the reactants in the zeolite pores. It is clear that when all Al_F atoms are isolated, a further dealumination will cause a decrease of not only the number of active sites, but also of the concentration of reactants in the zeolite cavities, even if the macroscopic partial

pressure of the reactants in the bulk of the system remains constant. This "concentration" effect will become especially important in the case of bimolecular reactions, even for those of the Eley-Rideal type. This concentration effect, the presence of hidden framework acid sites and of extra-framework acid sites should be reflected in the selectivity of the reaction of m-xylene.

p/o-Selectivity of the m-Xylene Reaction and Aluminum Content. In a previous paper (27), it was illustrated that in 12-MR zeolites the p/o-selectivity of m-xylene isomerisation varies between 1.0 and 1.4. It was concluded that the p/o selectivity should be governed by transition state shape-selectivity, exerted by the walls of the zeolite pores (27). With this series of dealuminated faujasites some more light was shed on this phenomenon. When Al_F/Al_F+Si_F varies from 0.115 to 0.015 as a result of dealumination, the p/o selectivity is enhanced gradually from 1.03 to 1.2 (Figure 6a). Consequently, for a given zeolite sample, the p/o selectivity depends on its Al_F content. One explanation is that the isomerisation of m-xylene on the hidden acid sites yields p-xylene preferentially. On these sites the protonation of m-xylene at position 2 (in between the two methyl groups) is most difficult, what would result in a suppressed o-xylene formation (28,29). An alternative explanation is that the strong Brønsted acid sites, which are associated with Al_{EF} in the amorphous silica-alumina phase, are responsible for the observed increase of the p/o selectivity. Anyway, the presence and action of hidden acid sites will result in an increased p/o-selectivity.

Isomerisation/Disproportionation-Selectivity in the m-Xylene Conversion and Degree of Dealumination. For samples with Al_F/Al_F+Si_F varying from 0.115 to 0.015, the isomerisation/disproportionation-selectivity increases (Figure 6b). Disproportionation has been shown to occur on strong, isolated Brønsted acid sites (27). Provided that hidden acid sites are less appropriate for catalysing this kind of conversion, the increase of the isomerisation/disproportionation-selectivity of m-xylene with decreasing Al_F content can be understood. The sample with an aluminum T-atom fraction equal to 0.18 shows a high isomerisation/disproportionation selectivity as well. The behaviour of this sample is in line with its lower acid strength due to its high Al_F content.
      The concentration effect could explain the observed changes as well. If the concentration of molecules in the cavities decreases with decreasing Al_F content, the rate of bimolecular reactions (disproportionation) should decrease faster than the rate of unimolecular reactions (isomerisation).
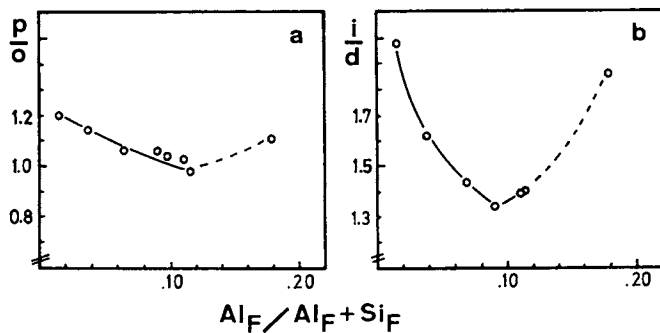
Figure 6. Initial p/o-selectivities (p/o) (a) and initial isomerisation/disproportionation-selectivities (i/d) (b) in function of the aluminum T-atom fraction.

m-Xylene Disproportionation Selectivity and the Degree of Dealumination of Zeolite Y. The shape and dimensions of the intracrystalline cavities in 12-MR zeolites are important factors that govern the disproportionation selectivity (27). Lobate pores favour the formation of 1,3,5-trimethylbenzene over the 1,2,3-isomer and show an initial 1,2,3-/1,3,5-trimethylbenzene ratio which is lower than 0.30 (27). If the contribution to disproportionation of the hidden acid sites could be negligeable, the 1,2,3-/1,3,5-trimethylbenzene initial product ratio should not be influenced by the Al_F content of H-faujasite. This is consistent with the experimental observations shown in Table II.

Table II. Composition of the trimethylbenzene products at low levels of conversion of m-xylene

Al_F/Al_F+Si_F	conv. (%)	1,3,5- (%)	1,2,4- (%)	1,2,3- (%)	1,2,3-/1,3,5 isomer ratio
0.110	3.6	29.2	64.3	6.5	0.22
0.090	5.5	28.3	63.3	8.4	0.30
0.070	4.8	27.4	64.8	7.8	0.28
0.040	3.2	26.5	67.3	6.1	0.23
0.015	3.7	25.8	68.0	6.2	0.24

Acknowledgments

Literature Cited

1. Haag, W. O.; Lago, R. M.; Weisz, P. B. Nature 1984, 309, 589.
2. Weisz, P. B. Ind. Eng. Chem. Fundam. 1986, 25, 53.
3. Barthomeuf, D. In Zeolites: Science and Technology; Ribeiro, F. R.; Rodrigues, A. E.; Rollmann, L. D. and Naccache, C., Eds.; NATO ASI Ser.E No.80, Nijhoff: The Hague, Boston, Lancaster 1984, p 317.
4. Dempsey, E. J. of Catal. 1974, 33, 497; 1975, 39, 155.
5. Wachter, W. A. Proc. 6th Int. Zeolite Conf., 1984, p 141.
6. Beagley, B.; Dwyer, J.; Fitch, F. R.; Mann, R.; Walters, J. J. Phys. Chem. 1984, 88, 1744.
7. Barthomeuf, D. J. Phys. Chem. 1979, 83, 249.
8. Mortier, W. J. J. of Catal. 1978, 55, 138.
9. Jacobs, P. A. Catal. Rev.-Sci. Eng. 1982, 24, 415.
10. Mikovsky, R. J.; Marshall, J. F. J. of Catal. 1976, 44, 170.

11. Tsutsumi, K.; Takahashi, H. J. of Catal. 1972, 24, 1.
12. DeCanio, S. J.; Sohn, J. R.; Fritz, P. O.; Lunsford, J. H. J. of Catal. 1986, 101, 132.
13. Namba, S.; Hosonuma, N.; Yashima, T. J. of Catal. 1981, 72, 16.
14. Sohn, J. R.; DeCanio, S. J.; Fritz, P. O.; Lunsford, J. H. J. Phys. Chem. 1986, 90, 4847.
15. Beyer, H. K.; Belenykaja, I. M. Stud. Surf. Sci. Catal. 1980, 5, 203.
16. Fitchner-Schmittler, H.; Lohse, V.; Engelhardt, G.; Patzelova, V. Crystal Res. Tech. 1984, 19, 1, K1-K3.
17. For a review see: Jacobs, P. A. Carboniogenic Activity of Zeolites, Elsevier 1977, p 50.
18. Jacobs, P. A.; Uytterhoeven, J. B. J. Chem. Soc., Faraday Trans. I 1973, 69, 359.
19. Jacobs, P. A.; Mortier, W. J. Zeolites 1982, 2, 226.
20. For a review see: Ward, J. W. In Zeolite Chemistry and Catalysis; Rabo, J., Ed.; ACS Monograph No. 171; American Chemical Society: Washington, DC, 1976, p 118.
21. Pfeifer, H.; Freude, D.; Hunger, M. Zeolites 1985, 5, 274.
22. Freude, D.; Hunger, M.; Pfeifer, H. Chem. Phys. Lett. 1986, 128, 62.
23. Jacobs, P. A.; Uytterhoeven, J. B. J. Chem. Soc., Faraday Trans. I 1973, 69, 373.
24. Beyer, H. K.; Belenykaja, I. M.; Hange, F.; Tielen, M.; Grobet, P.; Jacobs, P.A. J. Chem. Soc., Faraday Trans. I 1985, 81, 2889.
25. Corma, A.; Fornés, V.; Martinez, A.; Melo, F.; Pallota, O. Proc. Int. Symp. Innovation in Zeolite Materials Science, Nieuwpoort, Sept. 1987, to be published Stud. Surf. Sci. Catal..
26. Poutsma, M. L. In Zeolite Chemistry and Catalysis; Rabo, J., Ed.; ACS Monograph No. 171; American Chemical Society: Washington, DC, 1976, p 437.
27. Martens, J. A.; Perez-Pariente, J.; Sastre, E.; Corma, A.; Jacobs, P. A. submitted for publication in Zeolites.
28. Corma, A.; Cortés, A.; Nebot, I.; Tomás, F. J. of Catal. 1979, 57, 44.
29. Cortés, A.; Corma, A. J. of Catal. 1978, 51, 338.

Chapter 37

Structure-Sensitive Reactions of Cyclopropane with Cobalt and Iron Zeolite Catalysts

Steven L. Suib[1] and Zongchao Zhang[2]

[1]Departments of Chemical Engineering and Chemistry, and Institute of Materials Science, University of Connecticut, Storrs, CT 06268
[2]Department of Chemistry and Institute of Materials Science, U-60, University of Connecticut, Storrs, CT 06268

This paper concerns the preparation of various size particles of cobalt and iron in zeolite NaX and their use in cracking reactions of cyclopropane. Characterization of the catalysts has been done with X-ray diffraction, Mössbauer, ferromagnetic resonance, FMR, transmission electron microscopy and spin echo nuclear magnetic resonance methods. Metal particles ranging in size from 5 Å to 20 Å have been prepared. Catalytic reactions have been done with these materials in a 10 to 1 mixture of hydrogen to cyclopropane. Ring opening, hydrogenolysis, and hydrogenation reactions have all been observed but the extent of each of these reactions can be controlled by varying the nature of the metal in the zeolite and by the size and shape of the metal particles. The structure sensitivity of these metal particles in zeolites for these catalytic reactions will be discussed.

Several studies in recent years have focussed on the preparation and characterization of metal particles in zeolites (1). Various ways have been developed to introduce metals and metal precursors including sublimation (2), adsorption (3), and ion-exchange (4). If it is desirable to remove the ligands from the precursor metal complexes many approaches can be used including high temperature reduction in hydrogen (5), photochemical degradation (6), sodium (7) or cadmium (8) reduction, H atom reduction (9), low temperature vacuum treatments (10) and plasma methods (11).

The primary reason for preparing metal particles in zeolites is that such particles might be great catalysts. In general it is often believed that the smaller the particle size of metals the greater the surface area and consequently the greater the catalytic activity. For this reason researchers have tried to prepare extremely small

metal particles in and on several supports like zeolites (5-11), carbon (12), silica (13), and alumina (14). A zeolite provides a cage environment that can prevent large particles of metals from growing provided that the metal particles stay in the cages.

Researchers in the area of heterogeneous catalysis have recently focussed considerable attention to the relationships among catalytic activity, product selectivity and the size and shape of metal particles for reactions catalyzed by metals (15). Reactions that are influenced by the size and shape of metal particles or electronic interactions of the metal particles with the support are known as structure sensitive reactions. Theoretical calculations of various crystallographic structures (16) have shown that the number of specific type of surface atoms (face, corner, edge) change as a function of particle size. For example, for a face centered cubic system, the number of face atoms decreases as particle size decreases. If, therefore, a reaction is catalyzed on a face and there are a substantial number of face atoms necessary for catalysis to occur, then as particle size decreases catalytic activity will decrease. This idea often runs counter to principles discussed in general science texts (17).

We have been interested in the preparation of highly dispersed iron and cobalt metal particles in zeolites for several years (11, 18-20). It is widely known that iron readily oxidizes and is difficult to prepare as small iron particles especially in an oxidizing environment. In general we have found that if the iron starts out in an oxidized form, then it is not possible to fully reduce the iron to the metallic state (18-20). Standard methods of reduction usually lead to sintering or aggregation of the metal.

Microwave plasma techniques can lead to the preparation of highly dispersed metallic iron and cobalt particles in zeolites (11) that cannot be obtained by thermal or photochemical methods. The microwave power can be used to control the particle size. A 3 watt microwave power in an argon plasma leads to metal particles smaller than 5 Å whereas a 10 watt power leads to metal particles that are 20 Å in size. Particles as large as 175 Å can be prepared with this method.

The goal of the research reported here is to understand the role of the size and shape of these small metal particles in the cracking, hydrogenation, oligomerization and ring opening of cyclopropane. It is well known that Brönsted sites in zeolites cause cyclopropane to oligomerize (21,22). It has also been shown that ring opening, hydrogenation, and hydrogenolysis reactions of cyclopropane occur for both iron and cobalt wire and thin film catalysts (23,24). We will discuss the role of the size and shape of iron and cobalt metal particles in reactions of cyclopropane and hydrogen over these metal-containing zeolite catalysts. By dual function we refer to the presence of both metal and Brönsted type sites in zeolites.

Experimental

Sample Preparation.
Cobalt catalysts were prepared by subliming $Co_2(CO)_8$ into the pores of dehydrated NaX zeolite in a vacuum line at pressures of 1×10^{-4} torr. Argon was flowed over the metal loaded zeolite sample at a pressure of 0.3 torr. A microwave plasma was induced with a static gun and the decomposition of the metal carbonyl precursor occurred for two hours. After total decomposition of the metal carbonyl which can be determined by the color of the plasma, the argon flow was stopped and the sample was sealed off by closing the Teflon stopcocks at both ends of the reactor. The sample was then brought into a drybox and loaded into catalytic reactors or holders for spectroscopic experiments. Further details of this procedure can be found elsewhere (11, 25). Iron samples were prepared in a similar fashion except ferrocene was used as a metal precursor.

Characterization.
The characterization of the cobalt NaX catalyst prepared by microwave plasma methods has been reported elsewhere (11,20) except for particle size determinations by transmission electron microscopy, and metal content determinations. Transmission electron microscopy experiments were done by dispersing the cobalt zeolite materials in a polymer and microtoming them. A Philips model CM12 transmission electron microscope was used for all TEM experiments. An energy dispersive X-ray analyzer was used for chemical analysis of these samples. Magnification as high as 600,000 X was used in these experiments. Metal content was determined by dissolving the samples in HF and by subsequent analysis with atomic absorption spectroscopy. Mössbauer experiments were done in the transmission mode on a home-built spectrometer with a 80 mCi Co^{57} source. All data were analyzed with a curve fitting program that fits Lorentzian peak shapes. Further details concerning similar Mössbauer experiments can be found elsewhere (26).

Catalysis Experiments.
All catalysis experiments were done by loading 0.25 grams of metal loaded zeolite into a tubular flow reactor. Temperatures used in all catalytic reactions were 120°C. A mixture of 10 parts hydrogen to 1 part cyclopropane was made in a premixing chamber before the mixture entered the reactor. All reactions were done at atmospheric pressure. A gas sampling valve was installed after the reactor for product insertion into the gas chromatograph. A Hewlett Packard model 5880A gas chromatograph with an attached integrator was used for all product analyses. Standard gas samples of methane, ethylene, ethane, propylene, and propane were used to determine their retention times on the Poropack Q column. The calculated turnover numbers were determined by assuming that all of the metal sites are active.

Results

The cobalt catalysts prior to catalysis experiments have been shown to be less than 10 Å in size by several methods including chemisorption methods, ferromagnetic resonance and spin echo nuclear magnetic resonance techniques (11, 20, 27). The transmission

electron microscopy experiments of the cobalt and iron catalysts reported here do not show any small metal particles on the surface of the catalyst even at a magnification of 600,000 X. Lattice images of the zeolite were observed and electron diffraction experiments as shown in Figure 1 suggest that the zeolite is still crystalline. These results are in agreement with earlier X-ray diffraction data. An energy dispersive X-ray analysis of the cobalt loaded NaX sample is shown in Figure 2. Signals for Na, Al, Si, Cl, K, Ca, and Co are observed. The K, Cl, Ca signals are due to the epoxy matrix.

Mössbauer data for the iron loaded zeolite NaX sample are given in Figure 3. A broad singlet is observed with an isomer shift of 0.10 mm/sec relative to iron foil. No quadrupolar splitting is readily observed in this sample. Heating this sample to 120°C in an in-situ Mössbauer cell does not change the intensity or the position (isomer shift) of this signal. Exposure of this sample to air produces 2 quadrupole split doublets with isomer shifts of 0.35 mm/sec and 0.46 mm/sec. The quadrupole splittings for these 2 signals are 0.75 mm/sec and 2.38, respectively.

Turnover numbers at various times on stream for reactions of the cobalt NaX zeolite catalysts at 1 weight percent and 2 weight percent loadings are given in Figures 4 and 5, respectively. For the low loading material, only propylene was observed by gas chromatography methods. The sample with higher metal loading on the other hand produces methane, ethane and propane when exposed to hydrogen/cyclopropane mixtures. The percent conversion and percent selectivity of products for these two catalysts and the corresponding iron loaded catalysts are given in Table I for comparison. The weight percent of metal and metal particle size are also included.

Discussion

Samples prepared by the microwave plasma technique (11) have been shown to contain highly dispersed cobalt and iron metal particles. The particle size of the iron and cobalt particles is less than 5 Å as determined by chemisorption (20), transmission electron microscopy, ferromagnetic resonance (11), and spin echo nuclear magnetic resonance methods (27). This is so only if the power used in the microwave plasma decomposition reaction is lower than 3 watts and if low loadings (< 1 weight %) of metal precursor are used. For loadings greater than 1 weight percent aggregation of the metal particles occurs. Mössbauer, ferromagnetic resonance (11), transmission electron microscopy, and spin echo nuclear magnetic resonance methods (27) clearly show that this is the case. Higher power (>3 watts) in the microwave plasma decomposition, temperatures above 120°C, and nonzeolitic supports (silica, alumina) (11) give rise to larger metallic particles of iron and cobalt than with the 3 watt, low temperature (thermal) microwave plasma procedure described above.

The transmission electron microscopy experiments reported here show that the particles of iron and cobalt are extremely small and that the microwave plasma procedure does not lead to degradation of

Figure 1. Electron Diffraction Pattern for Cobalt loaded (1 weight %) NaX Zeolite.
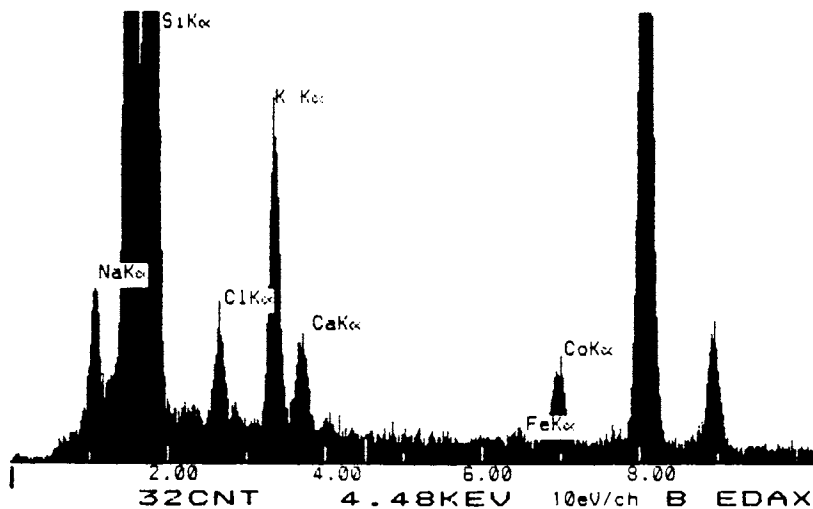
Figure 2. Energy Dispersive X-ray analysis for Cobalt loaded (1 weight %) NaX Zeolite.
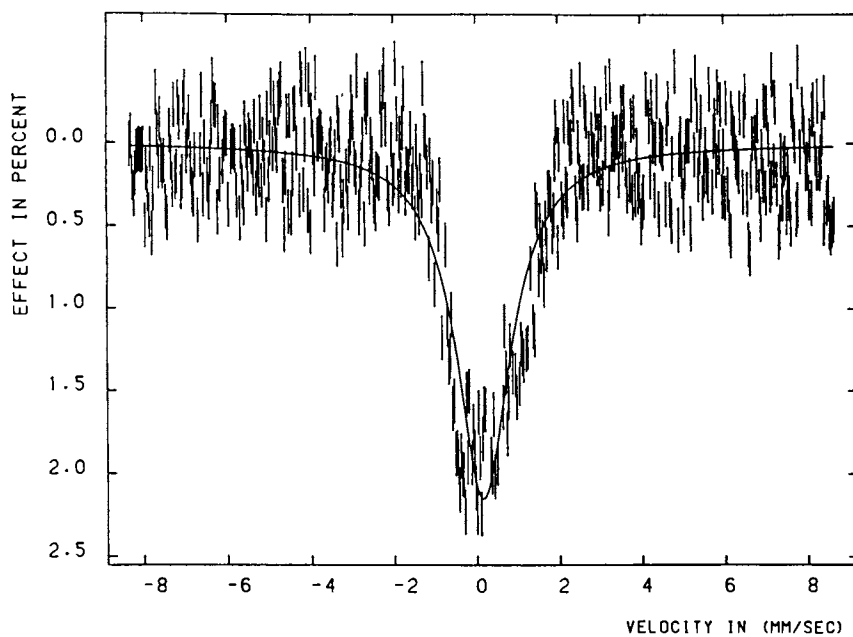
Figure 3. Mössbauer spectrum for Iron loaded (1 weight %) NaX Zeolite.
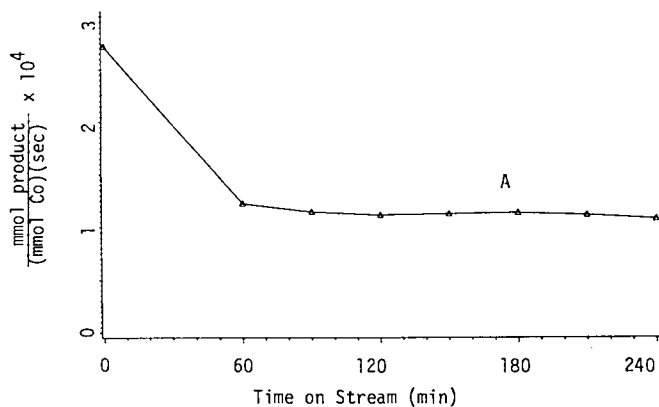
Figure 4. Catalytic Data of Turnover Number versus Time on Stream for Cobalt loaded (1 weight %) NaX Zeolite.
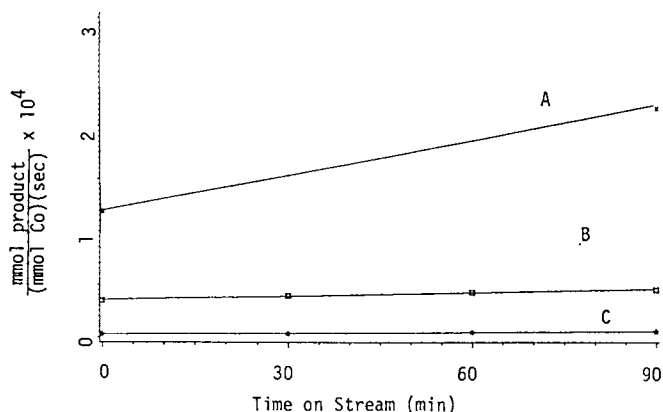
Figure 5. Catalytic Data of Turnover Number versus Time on Stream for Cobalt loaded (2 weight %) NaX Zeolite.

Table I. Summary of Particle Size and Catalysis Results

Sample[*]	P.S.[**]	% Conv.	Selectivity (%)				
			CH_4	C_2H_4	C_2H_6	C_3H_6	C_3H_8
Fe(1)	< 5 Å	0.3	a	a	a	100	a
Fe(2)	>20 Å	0.3	a	a	a	a	100
Co(1)	< 5 Å	0.6	a	a	a	100	a
Co(2)	>20 Å	1.7	81	a	2	a	17

   * = Transition metal NaX zeolite catalyst, # in parentheses is weight % loading of metal.

  ** = Particle size determined from TEM, FMR, SENMR and chemisorption methods, in Angstroms.

   ' = Reactions done @ 120°C, 1 atm pressure, 10/1 H_2 to cyclopropane, time on stream is 90 min.

   a = Not observed.

the zeolite. X-ray powder diffraction (11) experiments of these samples after microwave decomposition procedures also show that there is no loss in crystallinity. The data of Figure 1 also show that there is no loss in crystallinity as a result of electron bombardment during the TEM experiments. Certain microtomed samples were destroyed by the electron beam especially if the magnification was rapidly increased. The data of Figure 2 show that cobalt is incorporated into the zeolite. The extra signals that are observed such as K, Cl, and Ca are due to contaminants of the polymer epoxy used to disperse the zeolite samples.

Mössbauer data for the iron samples show that superparamagnetic iron particles are formed during the microwave plasma decomposition. Similar particles have been stabilized on carbon supports (12) and characterized by Mössbauer spectroscopy. Since the Mössbauer signal does not significantly change during heat treatment of these superparamagnetic particles this means that the particles are stable up to this temperature. Spin echo nuclear magnetic resonance (SENMR) experiments (27) on similar samples also show that significant sintering does not occur. The SENMR technique is more sensitive than Mössbauer and ferromagnetic resonance methods for determination of small changes in particle size for these particles in the temperature range of 120°C to 250°C.

The assignments for the intentionally oxidized species are based on known iron compounds (28). The species with an isomer shift of 0.35 mm/sec and a quadrupole splitting of 0.75 mm/sec is due to small iron (III) oxide particles (28). It is reasonable that small oxide particles of iron could form from small metallic iron precursor particles. The signal with an isomer shift of 0.46 mm/sec and a quadrupole splitting of 2.42 mm/sec is due to unreacted ferrocene (28). This latter signal is not apparent in Figure 3 because the signal is so broad although curve fitting procedures can be used and a doublet for the precursor can be fitted. It is clear then that the Mössbauer data suggest that most of the iron after microwave decomposition is reduced to the metallic state and is highly dispersed.

The catalytic data of Figure 4 show that small cobalt particles in NaX zeolite selectivity convert cyclopropane to propylene by ring opening reactions. We believe that these reactions are catalyzed at cobalt sites and not at Brönsted sites since we have tried to poison any Brönsted sites in additional experiments with sodium vapor. These materials show the same conversion and selectivity as catalysts not treated with sodium.

The catalytic data of Figure 5 should be compared to that of Figure 4. It is clear that the larger cobalt particles when reacted with hydrogen and cyclopropane catalyze hydrogenolysis and hydrogenation reactions as shown in Figure 5. For the case of iron particles, the larger particles selectively form propane via hydrogenation reactions as shown in Table I.

The data of Table I, Figure 1 and Figure 2 suggest that small particles of either cobalt or iron catalyze the ring opening of cyclopropane and act very similarly. The large particles of iron and cobalt both catalyze hydrogenation reactions to propane but the primary product in the case of large cobalt particles is methane. These data suggest that hydrogenolysis reactions are important with large clusters of cobalt.

The catalyst with small cobalt particles initially shows appreciable loss in activity although ring opening is still the primary reaction pathway. We are not certain what contributes to this deactivation since a steady state is reached soon after this initial decay. Microscopy studies do not show large cobalt particles at this stage and FMR data do not significantly change. The total percent conversion for these four catalysts varies from 0.3% to 1.7% which is a reasonable range for comparison among these materials.

Conclusions

The catalytic and spectroscopic data reported in this paper show that small particles of iron and cobalt (<5 A) primarily catalyze the ring opening of cyclopropane even in the presence of large amounts of hydrogen. The data also suggest that large (>5 A) particles of iron or cobalt catalysts both catalyze hydrogenation reactions and that large cobalt particles also catalyze hydrogenation reactions. The structure sensitivity of cyclopropane ring openings hydrogenation, hydrogenolysis and oligomerization have all been observed over cobalt and zeolites. Bronsted sites on the NaX zeolites have been minimized since it is well known that such sites lead to oligomerized species like butane (21,22). Bronsted sites are also known to oxidize iron particles in redox type reactions in zeolites. We have shown here that these cyclopropane/hydrogen reactions are structure sensitive and at least depend on the size of the metal particles. Further attempts to study particle shapes and electron effects in such systems are now underway in our laboratory.

Acknowledgment

Literature Cited

1. Delafosse, D. *J. Chim. Phys.*, 1986, **83**, 791-799.
2. Schneider, R. L.; Howe, R. F.; Watters, K. L. *Inorg. Chem.*, 1984, **23**, 4600-4605.
3. Bein, T.; Jacobs, P. A. *J. Chem. Soc.*, Faraday Trans.. I, 1983, **79**, 1819-1831.
4. Verdonck, J. J.; Jacobs, P. A., Uytterhoeven, J. B. *J. Chem. Soc.*, *Chem. Comm.*, 1979, 18-20.

5. Suib, S. L.; McMahon, K. C.; Tau, L. M.; Bennett, C. O. J. Catal., 1984, 89, 20-34.
6. Nagy, J. B. M.; Van Eenoo, M.; Derouane, E. G. J. Catal., 1979, 58, 230-237.
7. Lee, J. B. J. Catal.,1981, 68, 27-32.
8. Fraenkel, D.; Gates, B. C. J. Am. Chem. Soc., 102, 2478-2480.
9. Olivier, D.; Richard, M.; Bonneviot, L.; Che, M., In "Growth and Properties of Metal Clusters", (J. Bourdon, Ed.) p. 193, Elsevier, Amsterdam, 1980.
10. Nazar, L. F.; Ozin, G. A.; Hugues, F.; Godber, J.; Rancourt, D. Angew. Chem. Int. Ed., 1983, 22, 624-625.
11. Zeger, R. P.; McMahon, K. C.; Seltzer, M. D.; Michel, R. G. J. Catal., 1986, 99, 498-505.
12. Niemantsverdriet, J. W.; Van der Kraan, A. M.; Delgass, W. N.; Vannice, M. A. J. Phys. Chem., 1985, 89, 67-72.
13. Kip, B. J.; Duivenvoorden, F. B. M.; Koningsberger, D. C.; Prins, R. J. Am. Chem. Soc., 1986, 108, 5633-5634.
14. Reuel, R. C.; Bartholomew, C. H. J. Catal., 1984, 85, 78-88.
15. (a). Goodman, D. W.; Houston, J. E. Science, 1987, 236, 403-409. (b). Goudart, M. Adv. Catal., 1968, 20, 153.
16. van Hardeveld, R.; Hartog, F. Surf. Sci., 1969, 15, 189-230.
17. Mortimer, C. E. Chemistry, A Conceptual Approach, Van Nostrand Reinhold, New York, 1967, p. 405.
18. Suib, S. L.; McMahon, K. C.; Psaras, D. In Intrazeolite Chemistry, ACS Symposium Series, 218, G. D. Stucky, F. G. Dwyer, Eds., 1983, 301-317.
19. Suib, S. L.; Kostapapas, A.; McMahon, K. C.; Baxter, J. C.; Winiecki, A. M. Inorg. Chem., 1985, 24, 858-863.
20. McMahon, K. C.; Suib, S. L.; Johnson, B. G.; Bartholomew, C. H. J. Catal., 1987, 106, 47-53.
21. Hall, W. K.; Lutinski, F. E.; Gerberich, H. R. J. Catal., 1964, 3, 512-527.
22. Kirisci, I.; Hannus, I.; Varca, K.; Fejes, P. J. Catal., 1980, 63, 501-504.
23. Anderson, J. R.; Avery, N. R. J. Catal., 1967, 8, 48-63.
24. Sinfelt, J. H.; Yates, D. J. C.; Taylor, W. F. J. Phys. Chem., 1965, 69, 1877-1882.
25. McMahon, K. C.; Ph.D. Thesis, University of Connecticut, 1985.
26. Suib, S. L.; Zerger, R. P.; Stucky, G. D.; Emberson, R. M.; Debrunner, P. G.; Iton, L. E. Inorg. Chem., 1980, 19, 1858-1862.
27. Zhang, Z.; Suib, S. L. 1988, J. Am. Chem. Soc., to be submitted.
28. Greenwood, N. N.; Gibb, T. C. Mössbauer Spectroscopy, Chapman and Hall, New York, 1972.

Chapter 38

Hydrogenation and Cracking Catalyzed by Nickel Sulfide in Dealuminated Y Zeolites

S. Delahaie, A. Chambellan, D. Cornet, and J. F. Hemidy

Laboratoire de Spectrochimie, Groupe Catalyse et Spectrochimie, Unité Associée No. 414, I.S.M.Ra, Université de Caen, 14032 Caen, Cedex, France

A series of NiHY zeolites with different Si/Al ratios (2.7, 15 and 45) and nickel contents (0.3 to 9 wt %) were evaluated as catalysts for benzene hydrogenation under sulfiding conditions at 40 bars total pressure. The selectivity in hydrogenation varies with the extent of dealumination, as zeolites with high Si/Al ratios give less secondary cracking. The total hydrogenation activity increases moderately with nickel loading. The number and distribution of the zeolitic OH groups, as well as the state of nickel ions, were examined by diffuse reflectance spectroscopy, and correlated well with the catalytic behavior.

Numerous studies have been devoted to zeolites containing transition metals under cationic form, or as reduced metal particles, or as coordination complexes (1, 2, 3). Among these, very few deal with encaged transition metal sulfides. We recently examined the transformation of nickel ions into sulfide in various zeolite structures, mainly from the stoichiometric point of view (4, 5). It appeared that sulfidation was generally incomplete, but the fraction of nickel which could be converted into a sulfide increased with the Al/Si framework ratio (6). As nickel sulfide has some activity as an hydrogenation catalyst, its combination with an acidic zeolite should lead to a bifunctional catalyst of the type required for hydrocracking processes (7).

We examine here the catalytic behavior of a series of sulfided NiHY zeolites, with various extents of dealumination and several nickel loadings. As the hydrogenation capacity of these systems is rather low, a

high hydrogen pressure is required for the reaction. However, the benzene molecule used in the test undergoes a complex transformation, and the reaction is thus very sensitive to variations in the catalyst properties. In the same time, the structural modifications occurring as a result of zeolite dealumination or introduction of nickel are examined by means of Diffuse Reflectance in the NIR and Visible spectral range.

Experimental

Catalyst preparations.   Y zeolites with overall Si/Al ratio equal to 2.7, 15 and 45 were used as supports. The $Y_{2.7}$ sample was a stabilized zeolite available from Union Carbide (LZY 82). This material when submitted to self-steaming and acid leaching yielded HY_{45}. The HY_{15} sample derived from a commercial NaY (Union Carbide LZY 52) : the transformation involved successive ammonium exchange, self-steaming and acid washing.
     Nickel was introduced in three different ways, according to the desired concentration.
     Process E is a room-temperature cation exchange using a 0.4 molar nickel acetate solution. It leads to a low nickel loading, smaller than the theoretical exchange capacity of the zeolite.
     Process R involves contacting the zeolite with an excess of boiling solution under reflux for 24 h, followed by washing. Higher nickel loadings (4 to 9 % by weight) exceeding the nominal exchange capacity can be achieved in this way.
     Finally, process I is a dry impregnation of the zeolite powder with an adjusted amount of nickel acetate solution.
     In all cases the wet samples are calcined at 773 K under pure oxygen flow. The composition of the nickel zeolites Ni_xHY is given in Table I, where x is the weight fraction of nickel present on the dry material.

Table I.   Summary of catalyst compositions

Support Catalyst	Low Ni Weight % Ni	S/Ni	Medium Ni Weight % Ni	S/Ni	High Ni Weight % Ni	S/Ni
LZY 82 $Ni_xHY_{2.7}$	1.1(E)	0.4	3.0(E)	0.6	6.4(I)	0.7
NH_4Y_{15} Ni_xHY_{15}	0.9(E)	0.75	4.3(R)	0.6	9.0(R)	0.6
HY_{45} Ni_xHY_{45}	0.3(E)	0.1	–		9.3(R)	0.8

Spectroscopic characterizations. Reflectance spectra are recorded on a Beckman 5240 spectrometer equipped with a reflectance sphere. Data processing by a microcomputer provides a plot of the Kubelka function $F_{R\infty}$ versus wavenumber $\bar{\nu}$. The zeolite powder, with an average grain size 1 μm, can be treated and evacuated before being transferred into the spectrometer cell made of Suprasil.

Catalytic measurements. The high pressure reactor for benzene hydrogenation has been previously described (8). The reaction was conducted at 598 K under 40 bars total pressure. The benzene feed contained 1.5 % by weight of dimethyldisulfide (DMDS) which was fully decomposed on the catalyst, so that the H_2S/H_2 and benzene/H_2 molar ratios during reaction amounted to 10^{-4} and 4×10^{-3} respectively. The catalyst mass was 0.4 g and the liquid feed rate 1.6 μl mn^{-1}. Catalyst sulfidation was performed in the reactor itself but at atmospheric pressure, using a H_2-H_2S feed. Details of the complete procedure are following :

Step	Dehydration	Purge	Sulfidation	Reaction
Total Pressure P/bar	1	1	1	40
Temperature/K	598	598	Rises from 353 to 598	598
Feed	O_2	He	H_2+H_2S+CH_4	H_2+C_6H_6 +DMDS
P H_2S/bar	O	O	0.125	0.004

   After sulfidation the reactor temperature was lowered to 353 K and the pressure fixed at 40 bars. Then benzene reaction was started and the reactor temperature was increased from 353 to 598 K.
   Hydrocarbon analysis was performed by on-line gas chromatography, using an OV 17 silicone column. After the catalytic test had been completed, the catalyst was swept under helium and its sulfur content determined by microanalysis. Sulfur contents, expressed as S/Ni atomic ratios, are given in Table I.

Results

Conversion of benzene. In the above stated conditions benzene conversion varied from 0 to 10 % depending on the catalyst considered. The more dealuminated support HY_{45} gave no conversion at all. The only other hydrocarbon detected at the reactor exit was methane, resulting from the decomposition of DMDS.
   On all other solids, a more or less complex reaction occurred, leading to four categories of products :

- direct hydrogenation products, cyclohexane and methylcyclopentane,
- alkylation products, toluene and C_8 aromatics,
- products involving ring opening, mainly 2-methyl pentane, 3-methyl pentane and n-hexane,
- cracked products namely ethane, propane, butane and isobutane.

Since appreciable amounts of the two latter categories appeared only on the nickel-containing zeolites, it is likely that the ring-opening and cracking processes are preceded by benzene ring hydrogenation, so that all saturated products were taken into account to evaluate the hydrogenation conversion:

$$x_H = \frac{\text{mass benzene converted into } C_2\text{-}C_6}{\text{mass initial benzene}}$$

whereas the alkylation conversion was arbitrarily taken as :

$$x_A = \frac{\text{moles (toluene + xylene)}}{\text{moles initial benzene}}$$

The variation of product distribution with time-on-stream was peculiar. During the first four hours after the reactor temperature has been raised to 593 K, the conversions into various products generally go through a maximum, and then steadily decrease. There are several reasons for the variation in activity during the initial period, i) a steady state of adsorption-desorption is long to establish, ii) the extent of catalyst sulfidation slowly changes as the gas phase composition changes between sulfidation and reaction. The experimental conversions reported in Figure 1a, b, refer to time-on-stream longer than the initial period. After that period, both x_A and x_H generally decrease and a constant conversion level is reached only after 25 h. The only exception is the support $HY_{2.7}$ for which the alkylation conversion still increases after 25 h. and eventually goes through a maximum for much longer time on stream. So we shall compare the catalyst activities recorded at that time. Conversions recorded for the four processes of hydrogenation into cycloalkanes, alkylation, ring opening and cracking are collected in Figure 2. For the catalysts derived from each of the three supports conversions are plotted as a function of nickel content. It clearly appears that the selectivity of benzene transformation drastically changes as both the Si/Al ratio and the nickel content in the zeolite are changed. Alkylation is the prominent process for the bare zeolites, except for the inactive HY_{45} but, as expected, incorporating nickel favors hydrogenation and related processes, at the expense of alkylation.
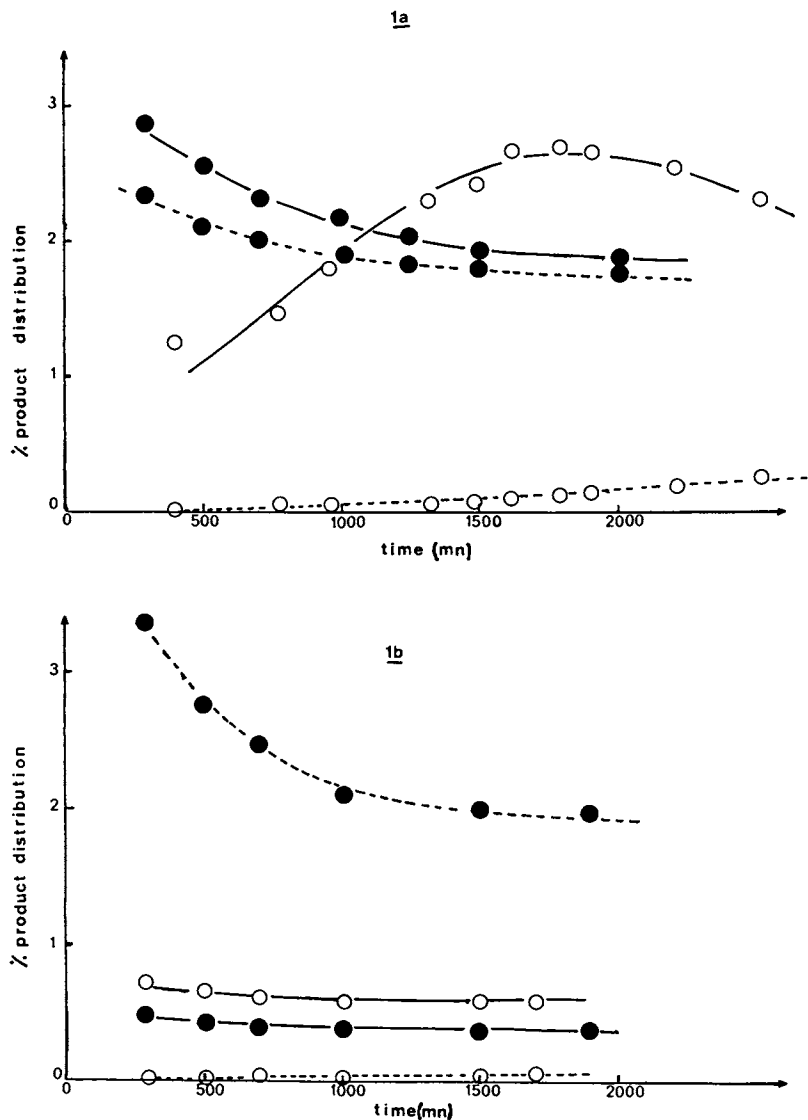
Figure 1. Product distribution versus time on stream for benzene conversion at 593 K and 40 bars.
1a. Zeolites $HY_{2.7}$ (open symbols) and $Ni_3HY_{2.7}$ (filled symbols)
1b. Zeolites HY_{15} (open symbols) and $Ni_{4.3}HY_{15}$ (filled symbols).
———— alkylated products (x_A) ;
-------- total hydrogenated products (x_H).
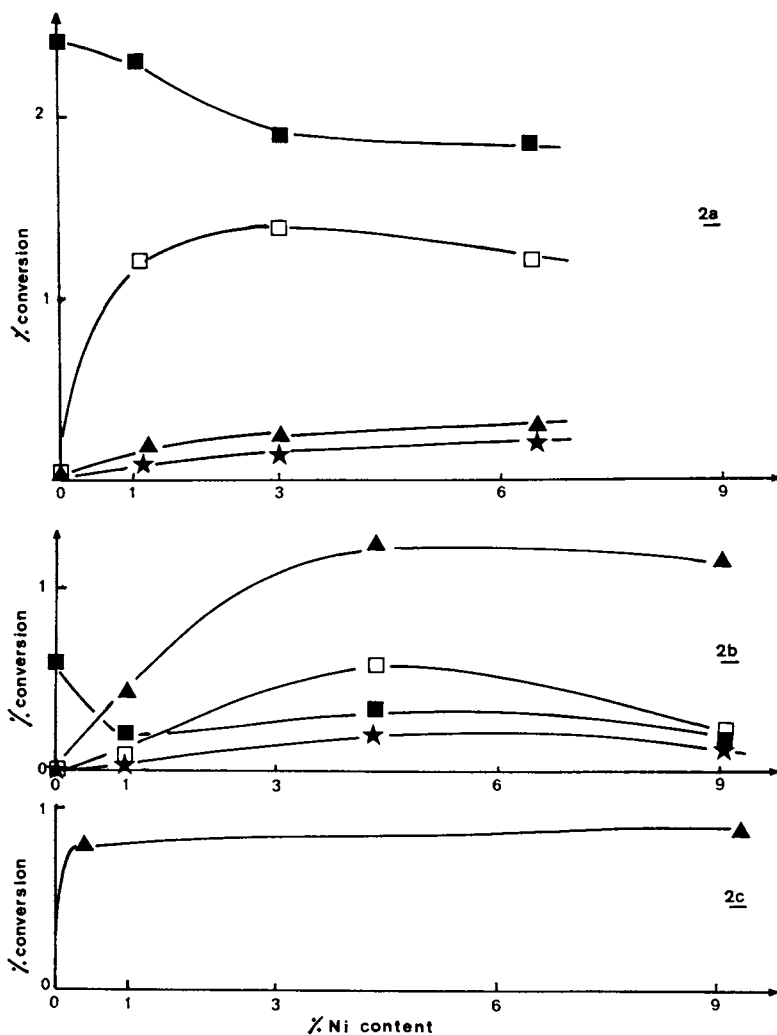
Figure 2. Product distribution at steady state versus
          nickel loading for benzene conversion at
          593 K and 40 bars.
          2a. Zeolites $Y_{2.7}$; 2b. Zeolites Y_{15}
          2c. Zeolites Y_{45}.
          Conversion into : ■ alkylated products ;
          ▲ methylcyclopentane and cyclohexane ;
          ★ open-chain hexanes ; □ cracked products.

Alkylation seems characteristic of the support acidity. Over $Ni_9HY_{2.7}$, the alkylaromatics distribution reveals 62 % toluene and 38 % C_8 when dimethyldisulfide is used as a sulfiding agent, and shifts to 22 % C_7–78 % C_8 when diethyldisulfide is injected in place of DMDS. Therefore the alkylation reaction is mainly due to the presence of an alkyldisulfide. The initial formation of toluene is immediately followed by disproportionation, yielding xylenes. But product analysis also reveals that with the (benzene + DMDS) mixture, more methane is produced with $HY_{2.7}$ catalyst where alkylation goes on, than over HY_{45} where no benzene conversion occurs. Thus, some of the methane may arise from a deep degradation of benzene, and such a reaction may also be considered as a minor source of alkylaromatics.

As seen on Figure 2 the extent of alkylation is not greatly affected by nickel. However, high nickel contents in zeolites $Y_{2.7}$ and Y_{15} make alkylation less important. Considering the influence of the Si/Al ratio the trend in alkylation activity is :

$$Y_{2.7} > Y_{15} > Y_{45}$$

suggesting that alkylation is mainly related to the number of acid sites.

Benzene hydrogenation into cycloalkanes occurs to a very limited extent on zeolite $HY_{2.7}$ and is greatly enhanced by addition of nickel. It is the only reaction observed on $NiHY_{45}$. The yield in cycloalkanes is highest with the medium nickel loaded $Ni_{4.3}HY_{15}$ but apart from the $Ni_{0.9}HY_{15}$ it does not vary much with nickel content. It is remarkable that even 0.3 % nickel added to zeolite HY_{45} is enough to confer some hydrogenation ability.

In every case, the methylcyclopentane to cyclohexane ratio is very large and exceeds the equilibrium level (5.7). C_7 and C_8 cycloalkanes, which could arise from the hydrogenation of toluene and xylene, were not detected.

Finally, the ring-opening and cracking reactions are very sensitive towards the Si/Al ratio. In fact, they run parallel to the alkylation activity, decreasing with aluminium content. In all cases, cracking is more important than ring opening into hexanes, particularly with zeolite $Y_{2.7}$ where cracked products are clearly formed at the expense of the cycloalkanes. Therefore, it is likely that primary hydrogenation products undergo acid-catalyzed bond breaking and the activities for this process run in the order :

$$NiHY_{2.7} > NiHY_{15} > NiHY_{45}$$

the last catalysts being inactive. The variation with nickel content is not so clear, as the highest cracking rates are observed at medium nickel loadings.

An additional hydrogenation reaction of limited importance is observed on zeolite $HY_{2.7}$ which is devoid of nickel. Mainly cracked products are formed, probably via hydrogenation of the benzene cycle as a result of hydrogen transfer ultimately yielding coke. This process is likely to occur on all zeolites with many acidic OH groups.

In conclusion, addition of nickel to the zeolites followed by sulfidation make them moderatily active for hydrogenation. Medium loadings seem to give the best results with respect to activity and rate of deactivation. The overall hydrogenation activity associated with nickel does not vary greatly with Si/Al ratio, but secondary cracking reactions appear on catalysts bearing a large number of acid sites, thus lowering the yield in hydrogenated products.

This flexibility affords a convenient way in obtaining the desired balance between hydrogenating and acidic function.

Spectroscopic characterization of the zeolites. Diffuse reflectance spectroscopy reaches the spectral range comprised between 4000 and 40000 cm^{-1}. Two types of transitions are of interest. In the first place, 4000-10000 cm^{-1} region contains vibrations associated with the OH groups : combination bands near 4500-5000 cm^{-1} and the first overtone $2\nu_{OH}$ near 7200 cm^{-1}. Secondly, the d-d transitions of the nickel ions show up between 4000 and 30000 cm^{-1}.

- Hydroxyl vibrations. The spectral print of the hydroxyls reveals the influence of steaming and acid washing performed on the support. The stabilized zeolite LZY 82 (Si/Al = 2.7) shows a broad absorption at 4690 cm^{-1} corresponding to a $(\nu + \delta)$ combination, and another at 6410 cm^{-1}, due to the first overtone of the NH vibrator (Figure 3a). In addition bands due to adsorbed water appear at 5220 and 7020 cm^{-1}. Upon dehydration all of these bands progressively disappear, while the narrow bands characteristic of hydroxyls develop : we note that the $2\nu_{OH}$ is split into a triplet at 6950, 7140, 7330 cm^{-1}, while the $(\nu + \delta)$ combinations yield an ill-resolved doublet near 4670 cm^{-1}. Figure 3b-c shows that complete transformation of ammonium into hydroxyl groups is achieved upon calcining at 773 K.

The profiles of the combinations and overtones are affected by the thermal treatment leading to stabilization of the zeolite and further modified upon washing with an HCl solution. Figure 4 compares the spectra of our three dehydrated HY zeolites with those of the non-stabilized $HY_{2.5}$ and of silica. The high frequency OH appearing at 7140 and 4670 cm^{-1} on $HY_{2.5}$ are strongly affected by the steaming procedure leading to $HY_{8.7}$ and completely absent on the acid-washed HY_{48}.
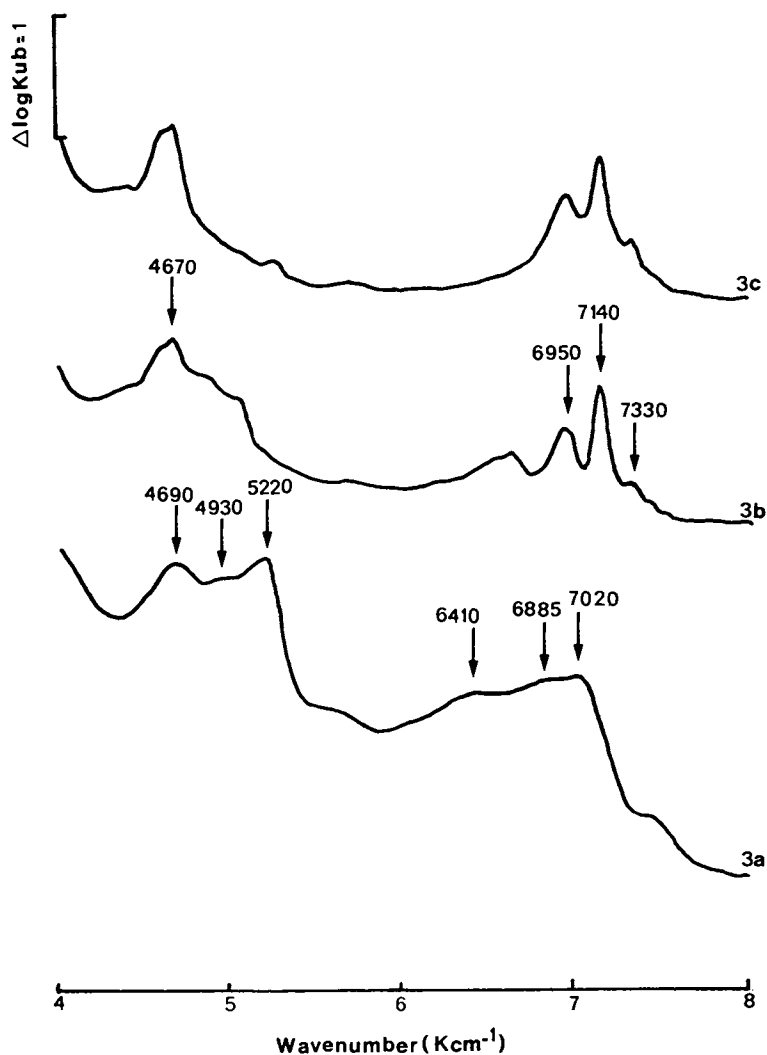
Figure 3. Reflectance spectra of zeolite $NH_4Y_{2.5}$:
OH overtones and combinations :
3a. Non-activated (wet) ; 3b. Activated at
573 K ; 3c. Activated at 793 K.
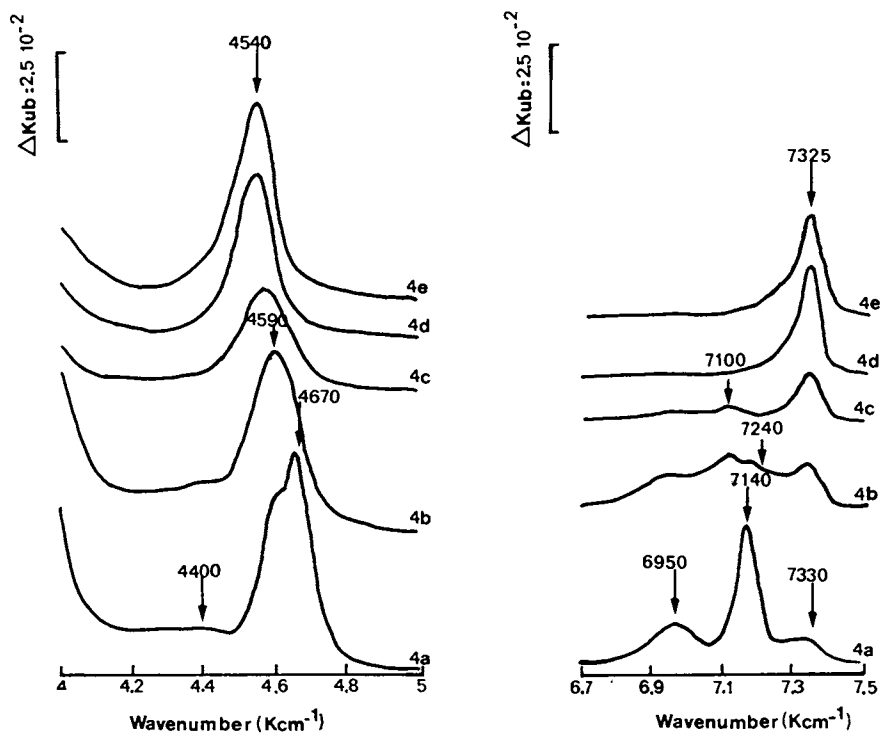
Figure 4. Reflectance spectra of HY zeolites and
          silica gel dehydrated at 793 K : OH
          combinations (left side) and overtones
          (right side).
          4a. $HY_{2.5}$; 4b. $HY_{2.7}$; 4c. HY_{15} ; 4d. HY_{45};
          4e. SiO_2 gel.

Similarly, the low frequency overtone at 6950 cm^{-1} associated with acidic OH vanishes, while the silanol overtone band develops at 7325 cm^{-1} (9) and the ($\nu + \delta$) combination shifts to 4540 cm^{-1}. These observations are consistent with the creation of silicon defects in the structure of dealuminated Y zeolites (10) while the weak overtone band at 7240 cm^{-1} is probably related to hydroxylated aluminium species extracted from the lattice (11, 12). Thus, the near-IR spectra give evidence for the decrease of the number of Brönsted acid sites as a result of dealumination.

Introduction of nickel ions followed by dehydration does not appreciably affect the intensity of the silanol OH bands. Figure 5 compares the spectra obtained with zeolite HY_{15} at various nickel loadings. The zeolitic OH however are strongly diminished in the presence of nickel but they are never completely suppressed, even at the highest nickel loading. Therefore, incorporation of nickel seems to neutralize only a fraction of the zeolitic acid sites.

- Transitions due to nickel ions. On spectra recorded immediately after the ion-exchange or impregnation procedure, three absorption bands appear on all samples at 9400, 15000 and 25100 cm^{-1}. These bands are typical for Ni^{2+} ions in octahedral coordination (13). A closer inspection of Figure 6, reveals some differences according to the amount of nickel on the mildly dealuminated HY_{15}. For the lowest concentrations, nickel ions are likely to be hydrated, as in solution. But for the more concentrated Ni_9HY_{15}, the high wavenumber band broadens and the shape of the doublet around 15000 cm^{-1} is modified, indicating the presence of hydroxylated species similar to nickel hydroxyde.

With calcined samples, the spectra fall into three categories, represented on Figure 7a, b, c. The first kind of spectrum is found on zeolite $Ni_{1.1}HY_{2.7}$ and shown on Figure 7a. The position of the three bands indicates that nickel ions are again in octahedral coordination. They are likely to be stabilized at S_1 sites of the HY structure (14). The same type of spectrum is observed with all non dealuminated HY zeolites, and also at small nickel concentration over the mildly dealuminated HY_{15}. However a splitting of the absorption near 15000 cm^{-1} and a weak additional band at 5000 cm^{-1} indicate that some nickel ions are located in sites with a symmetry lower than S_1 in the zeolite structure.

The second type of spectrum is examplified by zeolite $Ni_{0.3}HY_{45}$, with a high Si/Al ratio and low nickel concentration. This complex spectrum is reported in Figure 7b and cannot be attributed to Ni^{2+} ions in a single environment. The presence of tetrahedral nickel may be inferred from the bands at 18820, 14930 and 6245 cm^{-1} similar to those observed with an activated
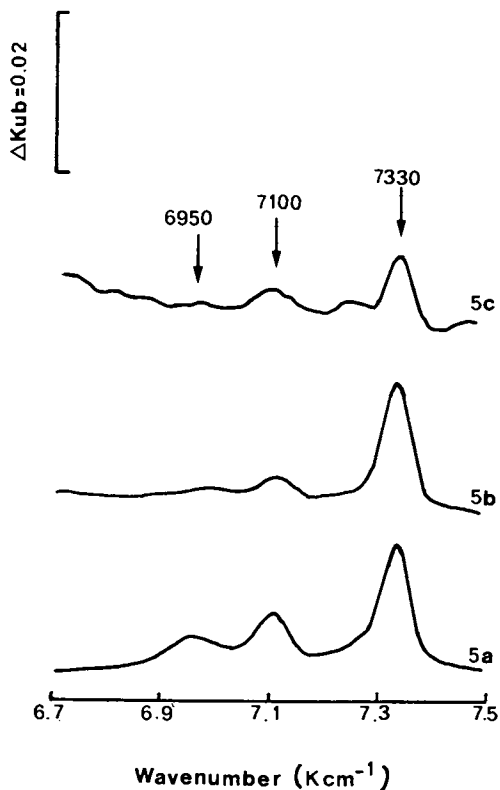
Figure 5. Reflectance spectra of $NiHY_{15}$ zeolites :
OH overtones on dehydrated samples.
5a. HY_{15} support ; 5b. $Ni_{0.9}HY_{15}$;
5c. Ni_9HY_{15}.
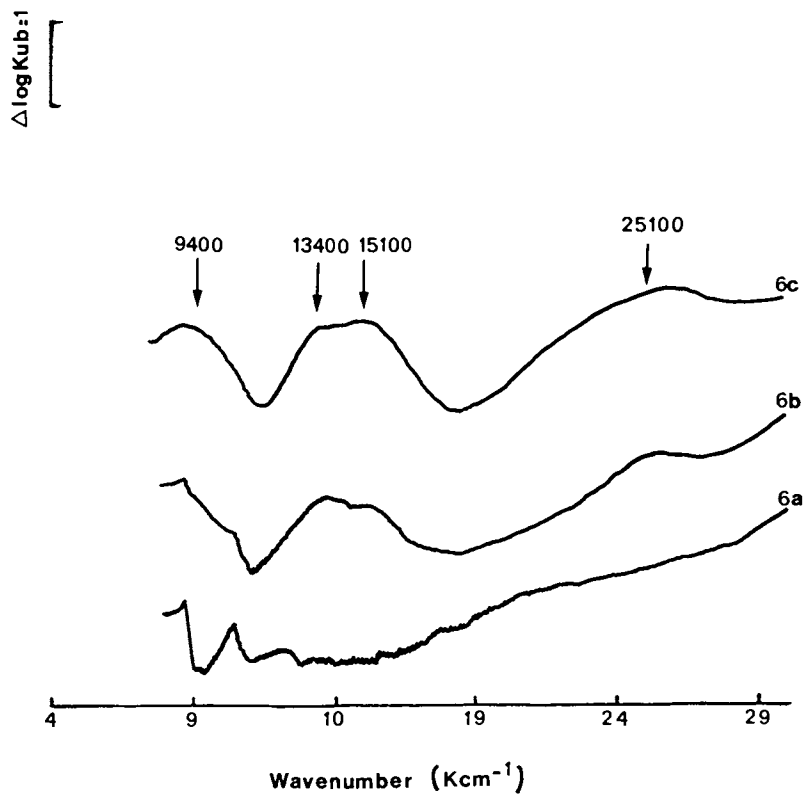
Figure 6. Reflectance spectra of $NiHY_{15}$ zeolites in their hydrated state : Effect of nickel loading.
6a. HY_{15} support ; 6b. $Ni_{1.6}HY_{15}$;
6c. Ni_9HY_{15}.
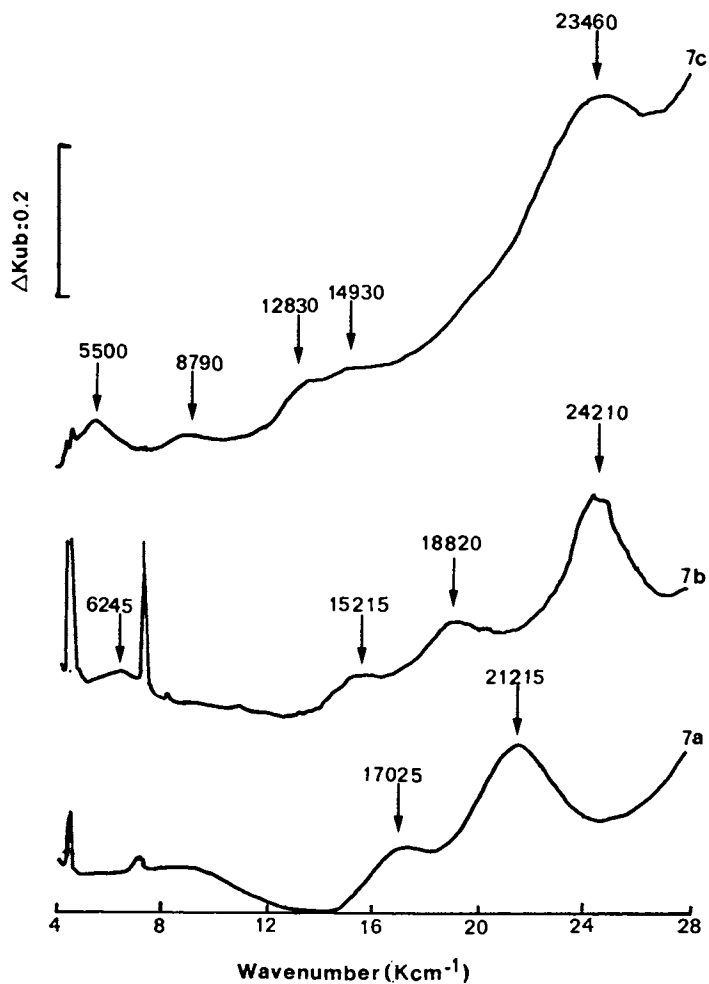
Figure 7. Reflectance spectra of NiHY zeolites
dehydrated at 773 K.
7a. $Ni_{1.1}HY_{2.7}$ (intensity x 2) ;
7b. $Ni_{0.3}HY_{45}$ (intensity x 10) ; 7c. Ni_9HY_{15}

Ni/SiO$_2$ catalyst (15). The additional strong band at 24210 cm^{-1} is associated with coordinatively unsaturated nickel species.

The third kind of spectrum, pictured on Figure 7c, is found on dealuminated zeolites Y$_{15}$ and Y$_{45}$ at medium and high nickel loadings. This spectrum reveals that only a small part of nickel is stabilized in the cationic sites. But the bands at 23460 cm^{-1} and 5500 cm^{-1} are inconsistent with an octahedral coordination. Such bands may be attributed to coordinatively unsaturated nickel ions. A similar type of nickel species was recently found on an alumina surface after moderate heating (16) with characteristic bands at 5830 and 23500 cm^{-1}.

Spectra 7a, b correspond to samples which, in the hydrated state, contained hydrated and presumably isolated ions, whereas spectrum 7c corresponds to the case where wet sample contained some nickel hydroxyde. In these dealuminated zeolites, a high nickel loading exceeding the exchange capacity may be achieved by treatment with a hot solution, but upon heating, the nickel ions form a new phase which has the characteristics of a disperse nickel oxide with many coordinatively unsaturated nickel ions at the surface.

Discussion

Spectroscopic results show that nickel is located in the cationic sites of the zeolite only if the exchange capacity of the starting material is high enough. In other cases it forms a separate phase mostly located outside of the grains. In any case, the sulfidation procedure is efficient, as shown by sulfur analysis : the sulfur over nickel ratio is close to 1. In their sulfided forms, the zeolites do not differ much in hydrogenation ability, as the rates of benzene hydrogenation do not vary greatly, when secondary processes are taken into account. Hence, the hydrogenation function is nearly insensitive to the Si/Al ratio ; moreover, it increases only slightly at high nickel loadings. We note that a remarkably small nickel loading (ca 1 %) introduced into the zeolite accounts for the major part of the hydrogenation activity. This small nickel amount when directly incorporated appears more efficient that would be a separate Ni/Al$_2$O$_3$ component mixed with the zeolite. However, the favourable properties of nickel loaded onto the zeolites cannot be extended beyond a certain amount. On the other hand the acidity of the zeolite strikingly influences the secondary processes, namely ring opening into hexanes, cracking and alkylation in our case. As shown by infrared results (17) the sulfidation procedure does not affect the zeolitic OH groups connected with acidity. We observed indeed that the secondary acid-catalyzed processes decreased as Si/Al ratio increased, and were negligible over zeolite Y$_{45}$.

Reflectance spectroscopy brings evidence for a parallel decrease in hydroxyl number. Such a conclusion agrees well with the results of IR absorption : the bands at 6950 and 7140 cm^{-1} are overtones of the fundamental bands at 3560 and 3630 cm^{-1}. The latter is associated with the more acidic OH groups (18). These bands progressively weaken as dealumination increases. In highly dealuminated materials, the band at 7325 cm^{-1} is the overtone of the silanol absorption at 3740 cm^{-1}, but contrary to the fundamental (18) no splitting of the overtone was observed.

Examination of both harmonic and fundamental OH absorptions leads to the same conclusion : the number of acid sites decreases upon dealumination. The strongly dealuminated zeolites Y_{45} is likely to be a useful hydrocracking component as secondary reactions are absent and the hydrogenation activity brought about by nickel is resistant towards deactivation.

Literature Cited

1. Pérot, G. ; Hilaireau, P. ; Guisnet, M. Proc. 6th Int. Zeolite Conf. , Olson, D. ; Bisio, A., Eds. : Reno, USA, 1983 ; p. 427.
2. Galich, P.N. ; Guturya, V.S. ; Galinski, A.A. Proc. 5th Int. Conf. Zeolites , Rees, L.V.C., Ed. : Naples, Italy, 1980 ; p. 661.
3. Bager, K.H. ; Vogt, F. ; Bremer, H. in Molecular Sieves II ; Katzer, J.R., Ed. ; ACS Symposium Series n° 40 ; American Chemical Society : Washington, D.C., 1977 ; p. 528.
4. Ezzamarty, A. ; Hémidy, J.F. ; Hennebert, P. ; Cornet, D. Proc. 5th Int. Conf. Zeolites ; Rees, L.V.C., Ed ; Naples, Italy, 1980 ; p. 424.
5. Cornet, D. ; Ezzamarty, A. ; Hémidy, J.F. ; Proc. 6th Int. Zeolite Conf. ; Olson, D. ; Bisio, A. Eds Reno, USA, 1983 ; p. 377.
6. Ezzamarty, A. Thesis, Caen University, France, 1983.
7. Myers, C.G. ; Rope, G. ; Garwood, W.E. ; US Patent 3384 572, 1968.
8. Chambellan, A. ; Delahaie, S. ; Cornet, D. ; Hemidy, J.F. Applied Catalysis ; 1987, 34, 181.
9. Kustov, L.M. ; Borovkov, V. Yu ; Kazanskii, V.B. J. Catal., 1981, 72, 149.
10. Hanke, W. ; Moller, K. Zeolites, 1984, 4, 244.
11. Shannon, R.D. ; Gardner, K.H. ; Staley, R.H. J Phys. Chem., 1985, 89, 4778.
12. Lohse, U. ; Loffler, E. Zeolites, 1987, 7, 11.

13. Garbowski, E. ; Kodratoff, Y. ; Mathieu, M.V. ; Imelik, B., <u>J. Chem. Phys.</u>, 1972, <u>69</u>, 1360.
14. Gallezot, P. ; Imelik, B. <u>J. Phys. Chem.</u>, 1973, <u>77</u>, 652.
15. Rebenstorf, B., <u>Acta Chem. Scand.</u>, 1978, <u>32</u>, 195.
16. Cornet, D. ; Hémidy, J.F. ; Mariette, L. <u>Nouveau Journal de Chimie</u>, 1984, <u>8</u>, 159.
17. Cornac, M. Thesis, Caen University, France, 1986.
18. See paper by Janin, A. ; Lavalley, J.C. ; Macedo, A.; Raatz, F. ; at the same symposium.

Chapter 39

Methanol-to-Gasoline Process

Reaction Mechanism

Clarence D. Chang

Central Research Laboratory, Mobil Research and Development
Corporation, Princeton, NJ 08540

Mobil's Methanol-to-Gasoline (MTG) Process [1] is the
first new synfuels process to be commercialized since
the Fischer-Tropsch process of the 1920's. The MTG
process was chosen by New Zealand to convert natural
gas from their extensive offshore Maui field into
gasoline via methanol. Started up in late 1985, the
plant at Motonui produces 14,500 BPD of premium
gasoline, which is one third of New Zealand's total
demand.

The successful development and scale-up of the MTG
process [2] was a triumph of modern catalytic and
reaction engineering. Ironically the detailed
chemistry of methanol transformation to hydrocarbons
remains unknown to this date, and is a widely debated
issue. Indeed, some two dozen more or less distinct
mechanistic proposals may be found in the current
literature. This paper presents an overview, focussing
on several of the more popular concepts, as well as the
sparse experimental evidence pro and con the various
schemes.

GENERAL CHARACTERISTICS AND REACTION PATH

Hydrocarbon formation from methanol is catalyzed by
Bronsted acids. The general reaction path for
hydrocarbon formation from methanol over zeolite ZSM-5
[3], the catalyst of choice [4], was defined in early
Mobil studies [1b], and is represented by:

$$\frac{n}{2}\,[2CH_3OH \rightleftharpoons CH_3OCH_3 + H_2O] \xrightarrow{-nH_2O} C_nH_{2n} \longrightarrow n[CH_2]$$
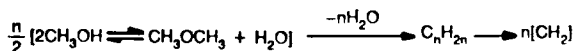
where $[CH_2]$ = average formula of a paraffin-aromatic mixture.

Methanol rapidly equilibrates to a dimethyl ether (DME) and water mixture. Further dehydration affords light olefins, which undergo subsequent reaction to form gasoline-range aromatics and paraffins. The reaction is exothermic [1b] and autocatalytic [5-7].

The mechanisms of etherification and olefin aromatization are well-understood [4,8]. The controversy centers on the mechanism of formation of the first C-C bond from a single-carbon source. The question whether ethylene is the "first" olefin has also been debated [4], but will not be considered in this paper.

MECHANISM OF INITIAL C-C BOND FORMATION

Virtually every possible reactive C_1 intermediate has been invoked to explain the crucial step of initial C-C bond formation from methanol/DME. Proposed mechanisms can be broadly classified as carbenic, carbocationic, ylide, and free radical. In some proposals several of these categories are combined.

Carbenes were the earliest proposed C_1 intermediates. These were considered to be generated via α-elimination of water from methanol itself [9,10], or from catalyst surface methoxyls [11]. The reaction may be assisted by cooperative action of acid and base sites on the catalyst [10]. Olefins would be formed by polymerization of the (free) $:CH_2$. To overcome the high energetic requirements of carbene generation (vide infra), and the low probability of $:CH_2$ self-condensation, Chang and Silvestri [1b] proposed a concerted mechanism of carbene generation with sp^3 insertion into the C-H bond of DME to form MeOEt.

$$Z^\ominus \quad \overset{H}{\underset{H}{\overset{\diagdown}{\underset{\diagup}{C}}}}H_2 \overset{OR}{\diagup} \quad H^\oplus \quad \xrightarrow{-HZ} CH_3CH_2OR' + ROH$$
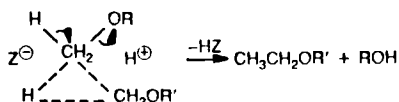
β-Elimination affords ethylene.

Indirect evidence in support of carbene intermediacy was obtained through isotope labelling studies of the interaction of MeOH with propane diluent over HZSM-5 [11]. MTG hydrocarbons are rich in isoparaffins along with the aromatics. For example, the ratio of iso- to normal butane (i/n) is typically greater than 2. In

the presence of propane diluent under conditions where
propane itself was unreactive, however, this ratio
drops from 4 (with He diluent) to 1, approaching the
thermodynamic ratio, 0.75. When isotopically labelled
MeOH (90% ^{13}C, 10% ^{12}C) was used, the product butanes
had a nonrandom isotope distribution high in singly-
substituted butane (Figure 1a). Furthermore, the i/n
ratio of singly-labelled butanes was ca. 1, while that
of the fully-labelled butanes was ca. 3 (from self
reaction of ^{13}C MeOH), (Figure 1b). The presence of
doubly and triply-labelled butanes indicates some
isotope scrambling. These observations were taken as
evidence that the propane diluent served to intercept
the reactive C_1 intermediate from MeOH to form butane,
and that this C_1 intermediate was carbenic, inserting
into the C-H bond of propane. Such insertions are
random because of the high reactivity of carbene. A
carbocationic intermediate would tend to give isobutane
predominantly, via the relatively stable t-butyl cation
[12].

$$:CH_2 + CH_3CH_2CH_3 \xrightarrow{75\%} CH_3CH_2CH_2CH_3$$

$$\xrightarrow{25\%}$$

$$CH_3^{\oplus} + CH_3CH_2CH_3 \xrightarrow[-H^{\oplus}]{\sim 100\%} CH_3\overset{CH_3}{\underset{|}{CH}}CH_3$$

A carbenic mechanism was also favored by Lee and
Wu [13], who proposed that the carbene intermediate
would be stabilized by the zeolite framework (Figure
2). They attempted to model the reaction by studying
the interaction of singlet methylene (from CH_2N_2) with
various surfaces, including ZSM-5. Although olefins
were observed even in the presence of "inert" materials
such as Vycor, hydrocarbon yields increased substan-
tially in the presence of acidic surfaces.

a. ^{13}C distribution in butanes. Comparison against the random distribution (broken line) for a 90% ^{13}C + 10% ^{12}C mixture.

b. Iso/normal ratio of ^{13}C-labeled butanes.

Figure 1 Butanes from Interaction of $^{13}CH_3OH$ with C_3H_8 over HZSM-5
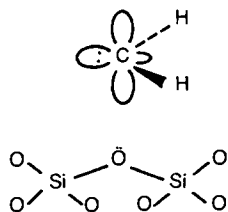
Figure 2. Surface-Stabilized Singlet Carbene

Theoretical justification for framework-stabili-
zation of carbene was provided by ab initio (MINDO3)
calculations of Drenth et al. [14]. The zeolite acid
site was simulated using HOAlO, HOF, and H_3O^+ as
electron acceptors of increasing strength, with two
hydroxyl anions as electron donors. The interaction of
CH_2 with this assemblage was examined (Figure 3). It
was found that H_3O^+ protonated CH_2 while the weaker
acids tended to retain their proton. Calculated
stabilization energies were 284-313 kJ/mol. The heat
of formation of CH_2 from MeOH is 349 kJ/mol; thus,
framework-stabilization CH_2 is not unreasonable.

Carbocationic mechanisms were proposed by Uno and
Mori [15] and others [16,17]. According to Uno and
Mori, surface methoxyls may behave as incipient methyl
cations, which add to the C-H of DME, forming a penta-
valent carbonium transition state. MeOEt is formed
upon proton loss.

$$CH_3^+ + CH_3OR \longrightarrow \left[\begin{array}{c} H \\ \diagdown \\ CH_3 \diagup \end{array} CH_2OR \right]^+ \longrightarrow CH_3CH_2OR + H^+$$
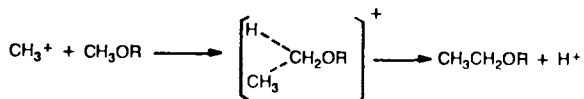
Since HCl addition did not poison the reaction,
these workers concluded that basic sites were not
involved.

Whether the C-H bond of DME or MeOH is suffi-
ciently nucleophilic to undergo substitution by CH_3^+ is
debatable. The gas phase reaction of CH_3^+ with MeOH
was studied by Smith and Futrell [18] using ion
cyclotron resonance techniques. Hydride abstraction
forming CH_4 and CH_2OH^+ were seen to be the predominant
reaction (85-90%).

$$CH_3^+ + CH_3OH \longrightarrow \overset{CH_3}{\underset{+}{\overset{|}{CH_3-O-H}}} \longrightarrow [CH_2OH]^+ + CH_4 \qquad (80\%)$$

$$\Delta H = -255 \text{ kJ/mol}$$

$$CH_3^+ + CH_3OH \longrightarrow CH_3^+OH_2 + CH_2 \qquad (7\%)$$

$$\Delta H = 84 \text{ kJ/mol}$$

$$CH_3^+ + CH_3OH \longrightarrow [CH_2OH]^+ + CH_4 \qquad (5-10\%)$$
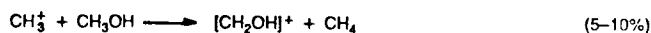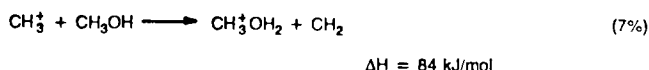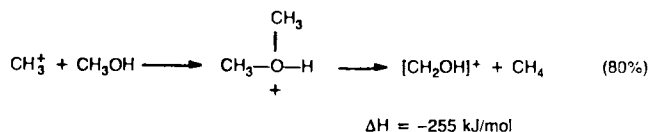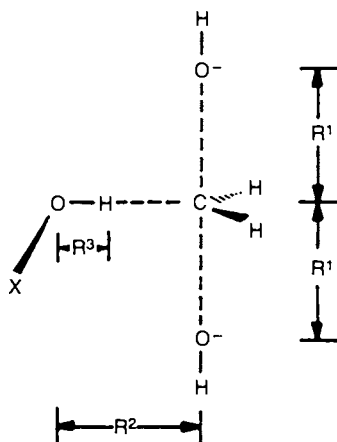
Optimized bonding energy of CH_2, ΔE, and bond lengths (in pm)

Acid	R_3 90 pm			Varying R_3	
	R_1	R_2	ΔE (kJ mol^{-1})	R_3[a]	ΔE[b] (kJ mol^{-1})
HOAlO	190	275	255	105	284
HOF	190	270	267	115	313
H_3O^+	190	240	485	132	c

[a] Value of R_3 in the CH_2 complex.
[b] R_1 and R_2 as in this Table; R_3 optimized both in the complex and in the CH_2-free model.
[c] Variation of R_3 does not yield a meaningful ΔE since in the CH_2-free model, the proton is transferred to one of the OH$^-$ groups.

Fig. 3. Zeolite model for *ab initio* molecular orbital calculations.

Interestingly, proton transfer from CH_3^+ to MeOH forming CH_2 occurs to a significant extent (7%), but C_2 species were not detected.

In superacid systems, methylation of DME gives trimethyloxonium (TMO) ion [19]. Mechanisms invoking hypervalent carbon intermediates therefore seem unlikely.

The most popular mechanisms at present invoke oxonium ylides as intermediates. van den Berg et al. [20] proposed that DME is protonated by a Bronsted site, and the resultant ion suffers nucleophilic attack by a second molecule of DME to form TMO with release of MeOH. The TMO ion is then deprotonated by a basic site to form the dimethyloxonium methylide, which undergoes a Stevens-type rearrangement to give methylethyl-oxonium ion. MeOEt is subsequently formed upon β-elimination. No experimental evidence was offered in support of the scheme.
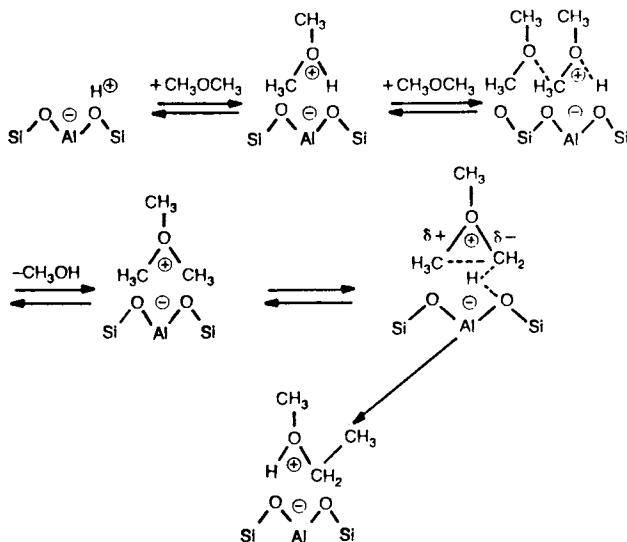
Olah [21] also proposed an ylide mechanism, mediated by a bifunctional acid-base catalyst (e.g., WO_3/Al_2O_3). However, based on isotopic labelling, Olah concludes that the putative ylide would not undergo a Stevens rearrangement, but rather an intermolecular methylation.
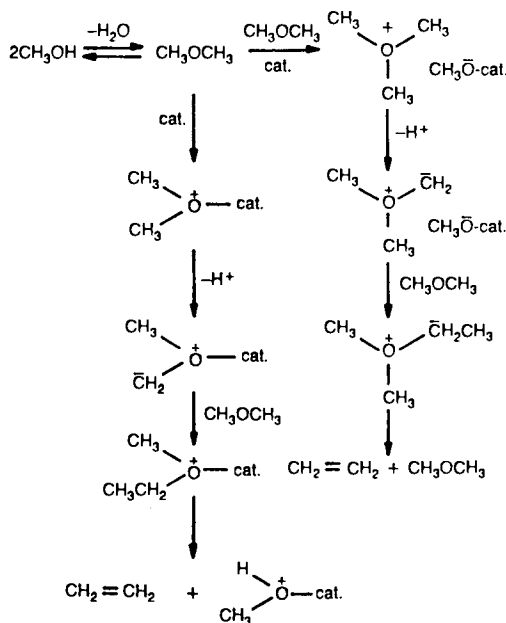
At this point, three questions must be addressed. Do oxonium ylides indeed exist? If so, will they undergo a Stevens-type rearrangement? Finally, will a zeolite conjugate base be sufficiently basic for proton abstraction from an oxonium ion to generate the ylide? Rimmelin et al. [22] treated $TMO^+SbCl_6^-$ with the strong hindered base 2,2,6,6-tetramethylpiperidyl-lithium (TMPLi) and obtained MeOEt as well as C_2–C_4 hydrocarbons (Table 1). The TMO ion appears therefore at least plausible as an intermediate in C–C bond formation. A Stevens rearrangement would also be plausible but not proven. When t-butyllithium was used in place of TMPLi, isopentane rather than MeOEt was formed, showing the criticality of a sterically hindered base.
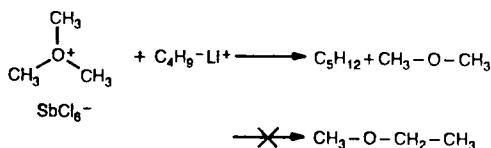
Olah approached the problem by attempting to synthesize the ylide directly, via three routes: deprotonation of TMO ion, desilylation of dimethyl ((trimethylsilyl)methyl)oxonium ion, and the reaction of photolytically generated methylcarbene with DME [23,24].
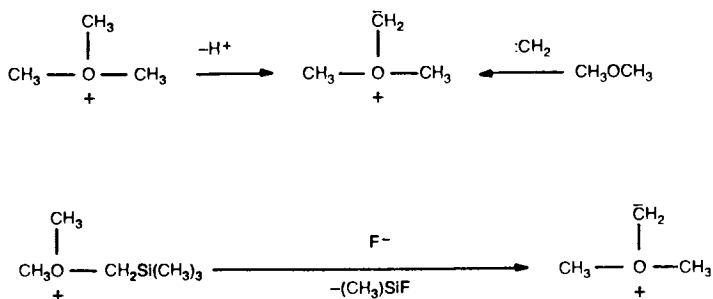
In none of these experiments was the ylide isolated, but its existence was inferred from product and isotope distributions. The deprotonation of TMO^+ (^{13}C and D labelled) was attempted by heating the BF_4^- salt with NaH until a vigorous reaction occurred. Although hydride methylation forming CH_4, and TMO decomposition to DME were the major reactions, analysis of the head gas showed ethylene (0.3-2.5%) and ethane (0.3-2.1%), (Table 2 and 3). Based on ^{13}C isotope distributions (Table 2) it was concluded that TMO^+ was deprotonated to an ylide, which is then methylated intermolecularly by excess TMO^+ to Me_2EtO^+.
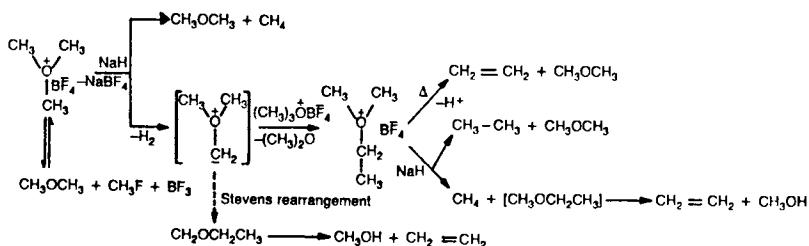
The desilylation of $Me_3SiCH_2O^+(CD_3)CH_3BF_4^-$ was carried out by reaction with CsF. Again small amounts of C_2 products were observed (Table 4), while F^- alkylation was the major reaction. It was postulated that desilylation gave the ylide, which is trans-methylated by CH_3 and CD_3 to Me_2EtO^+, which in turn was cleaved by F^- to labelled MeOEt and EtF.

Table 1. Composition of the head space gases

Experiment		CH$_4$	C$_2$H$_4$	C$_2$H$_6$	C$_3$H$_8$	mol % MeCl	MeOMe	C$_4$H$_{10}$	EtOMe	EtOEt
1(a)	30 min at room temperature	0.5	0.5	0.5	0.5	15.0	70.0	1.0	0.6	11.0
1(b)	30 min at 70°C	2.0	2.0	2.0	5.0	15.0	32.0	3.0	25.0	12.0
2	Oxonium salt + TMPH 30 min at 70°C	—	—	—	—	22.0	70.0	—	—	8.0
3	Oxonium salt + EtOEt 30 min at 70°C	—	—	—	—	5.0	10.0	—	—	85.0
4	Oxonium salt + 2,6-di-t-butylpyridine 30 min at 70°C	—	—	—	—	53.0	47.0	—	—	—

Table 2 Reaction of $^{13}CH_3O^+(CH_3)_2BF_4^{-a}$ with NaH

products	yield, %^{b}	isotopic distribution, %		
		$^{13}C_0$	$^{13}C_1$	$^{13}C_2$
methane	58.4	60.3	39.7	
MeF	4.6	c		
ethylene	2.5	55.0^d	36.9	8.1
ethane	2.1	c		
Me$_2$O	32.4	41.0	51.3	7.7

^{a} $^{13}CH_3$ group 90% labeled.
^{b} Unlabeled trimethyloxonium ion with BF$_4^-$, PF$_6^-$, and SbCl$_6^-$ as counter ion gave similar product distributions.
^{c} Not determined.
^{d} Calculated for intermolecular path: 49.0 $^{13}C_0$, 42.0 $^{13}C_1$, 9.0 $^{13}C_2$. Calculated for intramolecular path: 36.6 $^{13}C_0$, 63.4 $^{13}C_1$.

Table 3 Reaction of $(CD_3)_3O^+BF_4^{-a}$ with NaH

products	yield, %	isotopic distribution, %						
		d_0	d_1	d_2	d_3	d_4	d_5	d_6
methane	9.1				~84	~16		
MeF	16.8	b						
ethylene	0.3	5.5	16.4	18.3	26.5	33.3		
ethane	0.3	b						
Me_2O	73.5						7.0	93.0

[a]Isotopic purity 99%.
[b]Not determined.

Table 4 Reaction of $Me_3SiCH_2O^+(CD_3)CH_3BF_4^{-a}$ with CsF

products	yield, %[b]	isotopic distribution,[c]%
methane	0.1[d]	e
MeF	12.1[d]	60.6 CD_3F
		39.4 CH_3F
ethylene	1.0[d]	e
EtF	0.5	48.4 CD_3CH_2F
		51.6 CH_3CH_2F
Me_2O	55.9	16.8 CD_3OCD_3
		69.2 CD_3OCH_3
		14.0 CH_3OCH_3
MeOEt	1.6	29.0 $CD_3CH_2OCD_3$[f]
		27.0 $CD_3CH_2OCH_3$
		22.7 $CH_3CH_2OCD_3$
		21.3 $CH_3CH_2OCH_3$
Me_3SiF	3.4	no D
$Me_2Si(Et)F$	4.1	no D
Me_3SiCH_2F	9.2	no D
Me_3SiCH_2OMe	12.1	g

[a]CD_3 group 99% labeled.
[b]Three experiments with the unlabeled oxonium salt showed similar product distributions.
[c]Similar isotopic distributions were obtained in two other runs.
[d]Values obtained from analysis of gas phase and converted under the assumption mol % MeF = mol % Me_3SiCH_2OMe.
[e]Not determined.
[f]Calculated distribution for Stevens rearrangement: 16.8:34.6:34.6:14.0.
[g]MS data did not allow differentiation between $Me_3SiCH_2OCD_3$ and $Me_3SiCH_2OCH_3$.

$$CH_3F + CD_3OCH_2SiMe_3$$
$$+$$
$$CD_3F + CH_3OCH_2SiMe_3$$
$$+$$
$$CD_3OCH_3 + FCH_2SiMe_3$$
$$+$$
$$(CH_3)_2Si(Et)F$$

Stevens rearrangement //→ $CD_3OCH_2CH_3 + CH_3OCH_2CD_3$

$$CH_3F + CD_3F + CD_3OCH_3$$
$$+$$
$$CH_3OCH_2CD_3 + CD_3OCH_2CD_3$$
$$+$$
$$CD_3CH_2F + CH_2 = CD_2$$

$$CH_3F + CD_3F + CD_3OCH_3$$
$$+$$
$$CH_3OCH_2CH_3 + CD_3OCH_2CH_3$$
$$+$$
$$CH_3CH_2F + CH_2 = CH_2$$
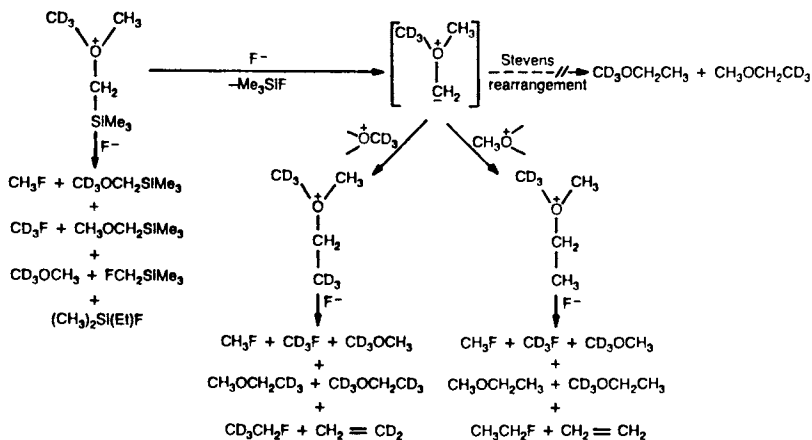
The observed deuterium distribution in MeOEt appeared to rule out the intermolecular Stevens-type rearrangement.

The photolytic reaction of CH_2N_2 with dialkyl ethers was first described by Meerwein et al. [25]. According to Huisgen [26] the reaction proceeds via ylide formation followed by a Stevens-type rearrangement. This was disputed by Franzen and Fikentscher [27] who found, using $^{14}CH_2$, that EtOPr from EtOEt was labelled in the γ-position rather than the α-position expected from an ylide rearrangement.

$$C_2H_5O\overset{\oplus}{-}CH_2-CH_3 \longrightarrow C_2H_5O-^{14}CH_2-CH_2-CH_3$$
$$\underset{^{14}CH_2\ominus}{} \qquad\qquad \alpha \quad \beta \quad \gamma$$

$$C_2H_5O-CH_2-CH_3 + :^{14}CH_2$$

$$C_2H_5O-CH_2-CH_2-^{14}CH_3$$
$$\alpha \quad \beta \quad \gamma$$
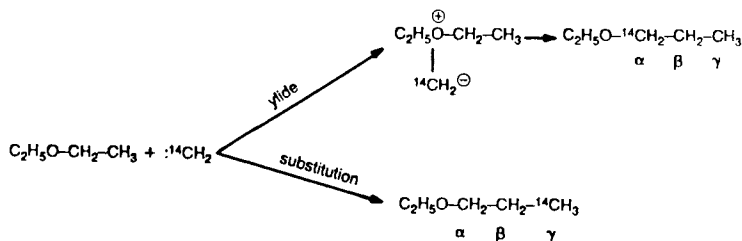
Olah [24] reexamined this reaction using CD_2N_2 with unlabelled ethers (MeOEt, MeO-n-Pr, EtOEt, EtO-n-Pr, and THF). In addition to products of C-H insertion, evidence was found for competing methylene attack on oxygen to form the ylide. The reaction of

CD_2 with MeOEt is illustrative. Aside from the insertion products MeOPr and EtOEt, small amounts of DME are formed. Analysis of deuterium distribution in DME showed significant amounts of d_0, d_2, and d_3. Small amounts of unlabelled ethylene were also detected. These results were rationalized by the scheme below:

$$CH_3-O-Et \xrightarrow{:CD_2} \left[\begin{array}{c} \bar{C}D_2 \\ | \\ CH_3^+ O-Et \end{array} \right] \longrightarrow CH_2=CH_2 + CH_3OCD_2H$$

$$\downarrow CD_3OD$$

$$\begin{array}{c} CD_3 \\ | \\ CH_3^- O-O-CD_3 + EtOCH_3 + EtOCD_3 \longleftarrow CH_3^+ O-Et \xrightarrow{CH_3OEt} CH_3^+ O-Et + CH_3^+ O-Et + Et-O-Et \\ | \\ \bar{O}CD_3 \end{array}$$

$$\downarrow \bar{O}CD_3$$

$$CH_3-O-CH_3 + Et-OCH_3 + Et-OCD_3 +$$
$$CH_3OCD_3 + CD_3OCD_3 + Et_2O$$
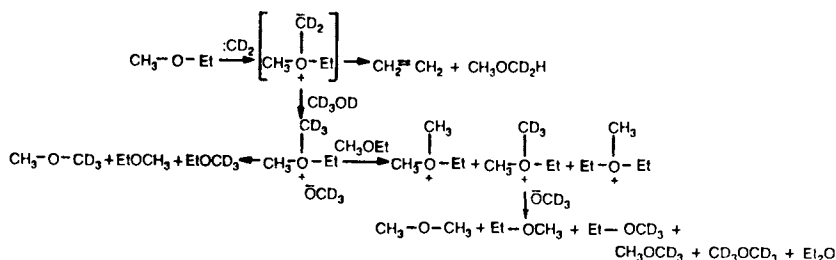
In this interpretation, attack of CD_2 on the oxygen of MeOEt yields the ylide, which can undergo β-elimination to ethylene and d_2-DME, or protonation (deuteration) by impurities (D_2O or deuterated MeOH produced during CD_2 generation) to form a labelled oxonium ion. This undergoes a series of rapid methyl transfers to give d_0, d_3 and d_6-DME. In contradiction, the deuterium distributions from the THF experiment are inconsistent with the hypothesis. In this case the DME produced should be d_6 (and d_5 reflecting isotopic purity) exclusively, while the observed DME-d_6 was the smallest component. Furthermore, some tetrahydropyran, the expected product of a Stevens rearrangement, was found.
    These model experiments provide new insights into the question of initial C-C bond formation in MTG. However, they cannot be considered definitive. Assuming, nevertheless, that oxonium ylides are intermediates in C-C bond formation in MTG, there remains the question whether the zeolite conjugate base can effect ylide generation from alkyloxonium precursors.
    Hunter and Hutchings [28] modelled the zeolite conjugate base with lithium tetraisopropoxide, and studied its reaction with $TMO^+SbCl_6^-$. No MeOEt was detected, but only products of isopropoxide decomposition or nucleophilic chloride or isopropoxide attack.

$$(CH_3)_3O^+ SbCl_6^- + LiAl(OP i)_4 \longrightarrow P i OMe + P i Cl + P i OH$$
$$ 27\% \quad 31\% \quad 42\%$$
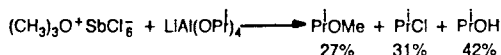
(7% conversion to P i OMe)

The Al–O bond is therefore more nucleophilic than basic. These same workers then studied the decomposition of various methylating agents MeX (X = OH, I, OSO_3Me) over ZSM-5 [29] (Table 5). The fact that hydrocarbons were formed from dimethyl sulfate argues against TMO ion as a key intermediate, since the oxygen in dimethyl sulfate is too weakly nucleophilic to form an oxonium ion. Hunter and Hutchings propose the initial formation of a surface-bound methoxyl, which is deprotonated to a surface-bound ylide. This surface-bound ylide is isoelectronic with surface-bound carbene [13,30],

Surface incorporated ylide   Surface carbene
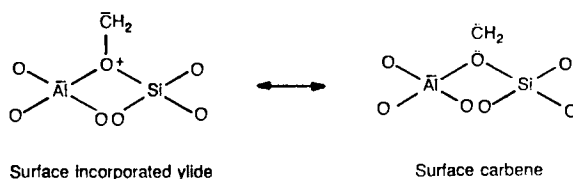
which inserts into C–H to form C–C. The nature of the basic site remains unspecified.

The question of zeolite basicity was recently addressed by Hellring and co-workers [31], who synthesized TMO-ZSM-5 and monitored its decomposition by ^{13}C magic angle spinning NMR (MASNMR). TMO-ZSM-5 was synthesized by ion exchange of TMO$^+$BF$_4^-$ (in CH$_3$NO$_2$) with HZSM-5 at T<253 K. Figure 4 shows the ^{13}C MASNMR spectra of TMO-ZSM-5 as it is warmed to room temperature. It is seen that the sample decomposes to methyl ZSM-5 and DME, confirming that the conjugate base of HZSM-5 is nucleophilic rather than basic toward TMO$^+$. This is further evidence against a Stevens rearrangement.

Forester et al. [32], using in situ FTIR, studied the MTG reaction over ZSM-5 at elevated temperature (T>473 K) and observed the appearance of surface AlOMe, coincidental with hydrocarbon formation.

These two studies provide additional evidence that surface methoxyls are implicated in the mechanism.

A free radical chain mechanism for MTG was suggested by Zatorski and Krzyzanowski [33] some time ago, but without experimental support. Recently, Clarke et al. [34] detected free radicals in DME decomposition over ZSM-5, using a spin-trapping

Table 5 Decomposition of Various Methylating Agents over ZSM-5

Catalyst	Methylating agent	W.H.S.V.	T, °C	Time on line, min	Total conversion, %	Product selectivity, mole %			
						CH_4	C_2H_4	C_3H_6	$\geq C_4$
H-ZSM-5	MeOH	0.15	250	15	7.1	4.0	3.9	4.1	92.0
		0.15	250	60	16.7	1.1	14.1	5.6	79.2
		0.15	250	100	22.6	0.9	24.3	6.3	68.5
H-ZSM-5	Me_2SO_4	0.075	250	15	0.12	81.5	18.5	0	0
		0.075	250	60	3.3	20.5	44.9	28.2	6.4
		0.075	250	100	12.9	2.5	28.9	11.2	57.4
		0.075	250	230	21.2	1.5	45.2	15.1	38.2
H-ZSM-5	MeI[a]	0.8	250	60	0.02	66.1	33.9	0	0
		0.8	250	100	0.13	7.0	44.1	32.5	16.4
Na-ZSM-5	MeOH[b]	0.075	300	200	0.001	64.4	35.6	0	0
Na-ZSM-5	Me_2SO_4	0.075	250	90	0.06	52.4	47.6	0	0
		0.075	300	130	2.0	48.1	51.9	Trace	0
Na-ZSM-5	MeI	0.1	250	15	0.05	66.0	34.0	0	0
		0.1	300	90	0.07	70.0	30.0	0	0

[a] No conversion observed after 15 min.   [b] No conversion observed for 160 min at 250 °C.
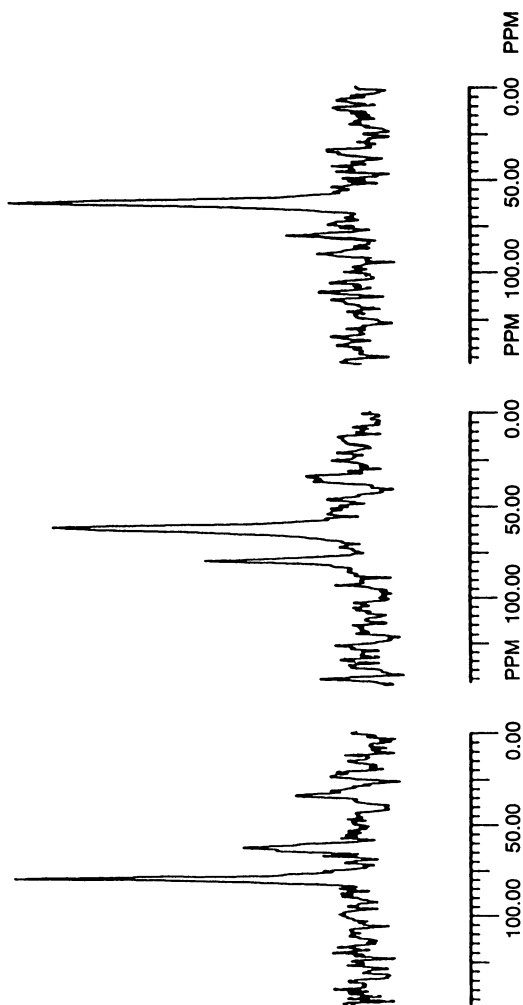
Figure 4   50.1MHz CP-MAS ^{13}C-NMR spectra of trimethyloxonium ion in ZSM-5 (left to right) 4:20P.M., 9:20P.M., and 11:20P.M. Spectra show the slow decomposition of TMO-ZSM-5 (δ=79ppm) and appearance of methyl-ZSM-5 (δ=62ppm).

reagent. These workers postulate that radicals are generated at paramagnetic centers (solid-state defects) in the zeolite, and proposed the following schemes for C-C bond formation:

$$S\cdot + CH_3OCH_3 \longrightarrow S-H + \cdot CH_2-O-CH_3$$
$$2 \cdot CH_2-O-CH_3 \longrightarrow CH_3-O-[CH_2]_2-O-CH_3$$
$$S-H \longrightarrow S\cdot + H\cdot$$

or

$$\cdot CH_2-O-CH_3 \longrightarrow :CH_2 + \cdot O-CH_3$$
$$:CH_2 + CH_3-O-CH_3 \longrightarrow CH_3CH_2-O-CH_3$$
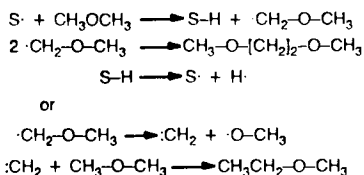
It must be noted, however, that the proposed glycol diether from radical recombination has never been detected in the products of DME reaction.

The proposal of Clarke et al. eliminates the requirement of strongly basic sites for proton removal from C-H, a major drawback of most schemes. Assuming that radicals can be generated by thermolysis of surface methoxyls, and that the radical scission of Clarke et al. occurs, the following initiation mechanism would seem plausible:

$$CH_3OH + ZOH \longrightarrow CH_3OZ + H_2O$$
$$CH_3OZ + R\cdot \longrightarrow \cdot CH_2OZ + RH$$

$$RH + \cdot OZ \longrightarrow R\cdot + ZOH$$
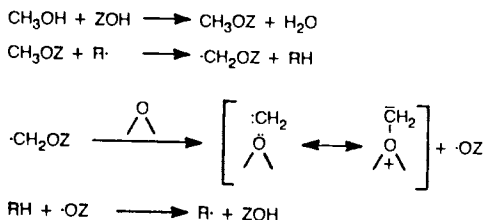
SUMMARY

A survey of current opinion on the mechanism of initial C-C bond formation in MTG has been presented. Proposals for the reactive C_1 intermediate range from carbocationic to radical. However, the various intermediates may be shown to be related to one another as follows:
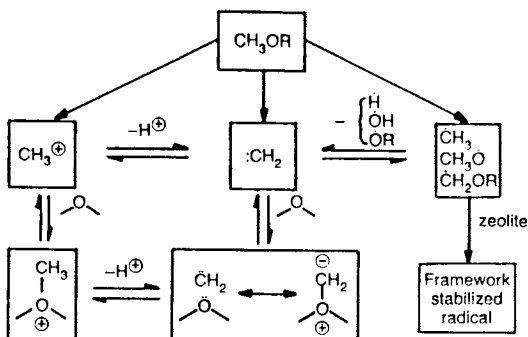
Definitive evidence in support of any particular pathway is lacking at present.

REFERENCES

1.   a) S. L. Meisel, J.. P. McCullough, C. H. Lechthaler and P. B. Weisz, Chemtech, 1976, 6, 86.
     b) C. D. Chang and A. J. Silvestri, J. Catal., 1977, 47, 249.
2.   A. Y. Kam, M. Schreiner and S. Yurchak, "Handbook of Synfuels Technology" (R. A. Meyers, ed.), McGraw-Hill, New York, 1984, ch. 2-3.
3.   D. H. Olson, G. T. Kokotailo and S. L. Lawton, J. Phys. Chem., 1981, 85, 2238.
4.   C. D. Chang, "Hydrocarbons from Methanol", M. Dekker, New York, 1983, ch. 5.
5.   N. Y. Chen and W. J. Reagan, J. Catal., 1979, 59, 123.
6.   Y. Ono, E. Imai and T. Mori, Z. Phys. Chem., N.F., 1979, 115, 99.
7.   C. D. Chang, Chem. Eng. Sci., 1980, 35, 619.
8.   M. L. Poutsma, "Zeolite Chemistry and Catalysis", (J. A. Rabo, ed.), ACS Monograph 171, Amer. Chem. Soc., Washington, D.C., 1976, p. 437.
9.   P. B. Venuto and P. S. Landis, Adv. Catal., 1968, 18, 259.
10. F. A. Swabb and B. C. Gates, Ind. Eng. Chem., Fundam., 1972, 11, 540.
11. C. D. Chang and C. T-W. Chu, J. Catal., 1982, 74, 203.
12. G. A. Olah, G. Klopman and R. H. Schlosberg, J. Amer. Chem. Soc., 1969, 91, 3261.
13. C. S. Lee and M. M. Wu, J. Chem. Soc., Chem. Commun., 1985, 250.
14. W. Drenth, W. T. M. Andriessen and F. B. van Duijneveldt, J. Mol. Catal., 1983, 21, 291.
15. Y. Ono and T. Mori, J. Chem. Soc., Faraday Trans. I, 1981, 77, 2209.
16. J. B. Nagy, J. P. Gilson and E. G. Derouane, J. Mol. Catal., 1979, 5, 393.
17. D. Kagi, J. Catal., 1981, 69, 242.
18. R. D. Smith and J. H. Futrell, Chem. Phys. Lett., 1976, 41, 64.
19. G. A. Olah, H. Doggweiler, J. D. Felberg, S. Frohlich, M. J. Grdina, R. Karpeles, T. Keumi, S. Inaba, W.M. Ip, K. Lammertsma, G. Salem and D. C. Tabor, J. Amer. Chem. Soc., 1984, 106, 2143.
20. J. P. van den Berg, J. P. Wolthuizen and J. H. C. van Hooff, Proc. 5th Int. Conf. on Zeolites, (L.V. Rees, ed.), Heyden, London, 1980, p. 649.
21. G. A. Olah, Pure Appl. Chem., 1981, 53, 201.
22. P. Rimmelin, H. Taghavi and J. Sommer, J. Chem. Soc., Chem. Commun., 1984, 1210.

23. G. A. Olah, H. Doggweiler and J. D. Felberg, J.
     Org. Chem., 1984, 49, 2112.
24. Ibid., 2116.
25. H. Meerwein, H. Rathjen and H. Werner, Chem. Ber.,
     1942, 75, 1610.
26. R. Huisgen, Angew. Chem., 1955, 67, 439.
27. V. Franzen and L. Fikentscher, Liebigs Ann. Chem.,
     1958, 617, 1.
28. R. Hunter and G. J. Hutchings, J. Chem. Soc.,
     Chem. Commun., 1985, 886.
29. Ibid., 1643.
30. C. T-W. Chu and C. D. Chang, J. Catal., 1984, 86,
     297.
31. S. D. Hellring and C. D. Chang, reported at 21st
     ACS State-of-the-Art Symp., "Methanol as a Raw
     Material for Fuels and Chemicals", Marco Is., FL,
     June 1986.
32. T. R. Forester, S-T. Wong and R. F. Howe, J. Chem.
     Soc., Chem. Commun., 1986, 1611.
33. W. Zatorski and S. Krzyzanowski, Acta Phys. Chem.,
     1978, 29, 347.
34. J. K. A. Clarke, R. Darcy, B. F. Hegarty, E.
     O'Donoghue, V. Amir-Ebrahimi and J. J. Rooney, J.
     Chem. Soc., Chem. Commun., 1986, 425.

Author Index

Affiliation Index

Subject Index

Affiliation Index

Subject Index